THE UNIVERSITY
of EDINBURGH

Supercritical CO_2 flow through fractured low permeability geological media: experimental investigation under varying mechanical and thermal conditions

Claire Aarti McCraw

Thesis submitted for the degree of Doctor of Philosophy

School of GeoSciences

The University of Edinburgh

2016

Abstract

To ensure secure geological storage of carbon dioxide it is necessary to establish the integrity of the overlying sealing rock. Seal rock fractures are key potential leakage pathways for storage systems; understanding their behaviour in the presence of CO_2 under reservoir conditions is therefore of great importance. This thesis presents experimental investigations into the hydraulic behaviour of discrete fractures within low permeability seal rocks during single phase supercritical CO_2 flow, under varying mechanical and thermal conditions representative of in-situ conditions.

An experimental rig was designed and built to enable the controlled study of supercritical CO_2 flow through 38 mm diameter samples under high pressures and temperatures. Samples are placed within a Hassler-type uniaxial pressure cell and CO_2 flow is controlled via high precision syringe pumps. Flow experiments with supercritical CO_2 within the pressure range 10-50 MPa were undertaken at temperatures of 38°C and 58°C with confining pressures of 35-55 MPa. The effects of stress loading and temperature change on the hydraulic properties of the fractured sample were studied; continuous differential pressure measurement enabled analysis of hydraulic response.

Experiments were undertaken on a pre-existing Wissey field Zechstein Dolomite fracture and three artificial fractures (two East Brae field Kimmeridge Clay samples and one Cambrian shale quarry sample). Fracture permeabilities ranged from 8×10^{-14} m^2 to 6×10^{-11} m^2 with higher permeabilities observed within the harder rock samples. A broadly linear flow regime, consistent with Darcy's law, was observed in the lowest permeability sample (East Brae). A Forchheimer-type non-linear flow regime was observed in the other samples.

Transmissivity variations during experiments were used to infer the mechanical impact of stress and temperature changes. An increase in effective stress resulted in transmissivity reduction, suggesting fracture aperture closure. During initial stress loading cycles, and subsequent higher temperature stress loading, a component of this transmissivity reduction was found to be inelastic, suggesting permanent modification of fracture geometry during closure. Pre- and post-experiment fracture surface characterisation

provides further evidence for the occurrence of plastic deformation. Transmissivity-stress relationships were elastic during subsequent external stress-loading cycles, suggesting elastic closure and opening of fractures without additional permanent fracture geometry changes.

The impact of fluid property variations on fracture hydraulic conductivity, K_{frac}, was also analysed. Under constant effective stress K_{frac} was found to be higher within high temperature and low fluid pressure scenarios, due to higher density/viscosity ratios. However, under constant confining pressure, fluid pressure changes are coupled both to mechanical effects (from effective stress alteration) and hydraulic effects (from viscosity variation), with opposing impacts on fracture hydraulic conductivity. At lower effective stresses mechanical effects were found to be dominant, with fluid pressure increase resulting in a notable increase to K_{frac} due to aperture opening. At higher effective stresses, mechanical changes are much smaller due to increased contact area between fracture surfaces, and thus increased stiffness of fractures. Under such conditions hydraulic effects may be dominant and result in a small K_{frac} reduction as fluid pressure increases, due to a reduction in the density/viscosity ratio. These results highlight that CO_2 fluid property variation can have a notable influence on hydraulic conductivity under certain in-situ conditions.

The single phase CO_2 fracture flow experiments undertaken during this study were designed to enable a study of hydraulic and mechanical processes in isolation, without the influence of chemical processes. In-situ, the additional presence of brine and thus multi-phase fluid behaviour and associated chemical processes makes the hydraulic behaviour of fractures considerably more complex. Coupled process modelling enables the relative influence of these processes to be simulated, but relies on experiments for validation. These unique experimental findings are of great value for enabling validation of such models as well as for informing analyses of geological and field studies.

Lay Summary

Human-induced climate change is currently occurring as a result of increased concentrations of greenhouse gases, such as CO_2, trapping heat within the Earth's atmosphere. Burning fossil fuels produces large quantities of CO_2, and is the main cause. Carbon capture and storage (CCS) is a technology designed to mitigate these negative impacts of burning fossil fuels by capturing and storing the CO_2 produced, limiting its release into the Earth's atmosphere. In order for CCS to contribute to mitigating climate change, the captured CO_2 must be stored for over 10,000 years. It is proposed that CO_2 could be geologically stored by pumping it into porous rock deep underground (around 1 km depth or more). To ensure the CO_2 does not escape, the storage location must be beneath layers of impermeable rock that naturally trap the CO_2 in place, preventing its escape. However, the presence of fractures within the impermeable seal rock layers could potentially create pathways for the CO_2 to escape upwards, out of the storage location.

To contribute to understanding the risk of CO_2 leakage through such fractures, and the rate at which leakage may occur under a variety of scenarios, laboratory experiments have been undertaken. The experiments measure the permeability of the fractures (the ease at which CO_2 flows through the fracture) under a range of pressure and temperature conditions, typical of those found in-situ. The experiments analyse the flow behaviour (whether it is smooth (laminar) or rough (turbulent)). Analysis of how the permeability is affected by changes to the external forces acting on the fracture; changes to the CO_2 fluid pressure (internal forces); and changes to temperature were also undertaken.

The experimental findings suggest that changes to the fracture geometry through mechanical closure and opening of the fracture can be significant, both as a result of changes to external and internal forces (CO_2 pressure) acting on the fracture. Unprecedented increases to external forces acting on the fracture result in permanent fracture aperture reduction and associated permanent permeability decrease. These permanent changes are more significant at higher temperatures. For low permeability fractures (small fracture apertures), flow is found to be smooth; for higher permeability fractures (larger apertures), rough or turbulent flow occurs.

The experiments focus on the mechanical and hydraulic (flow) behaviours associated with CO_2 fluid flow through fractures. In reality, the presence of other fluids such as brine or oil, and the occurrence of chemical reactions also affect how easily CO_2 flows through fractures, and how this changes with time. Other studies have assessed these contributing processes. As the combination of processes that occur is complex, studying each of the processes in isolation enables an improved understanding of the importance of each, and thus helps the scientific community to build a full picture of the resulting behaviour.

Declaration

I declare that this thesis has been composed solely by myself and that it has not been submitted, either in whole or in part, in any previous application for a degree. Except where otherwise acknowledged, the work presented is entirely my own.

The publication, McCraw et al. [2016], contains material included within this thesis. The publication utilises experiment details and results associated with the Wissey field Zechstein Dolomite fractured sample (W3) within a hybrid numerical analytical hydraulic mechanical simulation study. The publication is a joint paper that presents experimental work undertaken by myself as part of this PhD study in conjunction with numerical simulation undertaken by Christopher McDermott. The publication indicates that numerical simulation utilising a statistical approximation of the Wissey fracture surface and combined application of standard nonlinear flow models and analytical mechanical solutions can replicate the key hydro-mechanical behaviour of supercritical fluid flow through the fractured sample observed experimentally. It should be noted that this thesis contains significantly more comprehensive and extensive analysis of experimental results than that included within the publication.

Claire Aarti McCraw

Acknowledgements

First and foremost, I would like to acknowledge and thank my primary supervisors. I am extremely grateful to Katriona Edlmann, who has consistently provided invaluable experimental guidance, technical support and bucketloads of encouragement. Thank you for the many hours spent helping me in the lab, the helpful discussions, and latterly for your cheery disposition and patience when faced with reading thesis chapters multiple times over. Thank you also to Chris McDermott, who has provided a helpful steer at key moments during the project, informative discussions and useful feedback.

In addition to my primary supervisors, I have benefited from help and guidance from many others. Thank you to Ian Butler for expert experimental advice on several occasions, for the loan of the reliable Validyne differential pressure transducer, and for undertaking x-ray CT scanning of my Cambrian shale sample. Thank you to Mark Wilkinson, Mark Naylor and Stuart Haszeldine for valuable discussions and guidance during the project and to the Geofluids group for helpful feedback and debate. Thanks to Mark Naylor for also allowing me to use his CO_2 properties R program during my data analysis. I am grateful to Kate Heal, my advisor, for being available to provide helpful guidance and support when required.

Experimental support was provided by many. Thank you to Nic Odling for undertaking XRD analysis on my rock samples, to Alex Jackson for coring my samples, and to Mike Hall for assistance and access to core trimming equipment. I am extremely grateful to Bob, Grant and Alex from the workshop for their practical assistance and metalwork skills during the building of the rig, for creating the fracturing core support, and for their patience when smoothing and polishing the coreholder platens on numerous occasions throughout the project. Thanks also to Colin Kay for wiring help and to Jimmy and Alan for assistance in overcoming practical challenges on a number of occasions. Thank you also to Justin and Ross from IT for your assistance in setting up my logging software.

Funding for this project has been provided by the European Community's Seventh framework Programme FP7/2007-2013, as part of the PANACEA project. Without this support, this project would not have been possible. Thank you also to my PANACEA colleagues, who provided support and encouragement at group meetings.

Thanks to Marathon Oil for provision of the East Brae samples, to Tullow Oil and Kirk Petrophysics for the Wissey and Wildcat samples, to the MUSTANG EC Seventh Framework project for the Heletz samples, and to Forth Stone Ltd for the Cambrian shale.

I am extremely grateful to Ian Murray and Grainne El Mountassir at the University of Strathclyde for both enabling access, and providing assistance in use of the Micro-Epsilon ScanCONTROL laser scanner.

Thank you to my supportive PhD office mates for their understanding, advice, and intelligent discussions, and for making my time at the University of Edinburgh enjoyable. Thanks also to my non-PhD friends for your patience and understanding over the last few years, and for very welcome distractions!

Finally I would like to thank my family. Both of my parents have supported my decisions over the years and made my education possible. During my PhD, my mum has provided valuable advice and countless food parcels, while my dad has willingly taken on the daunting task of reviewing my thesis at relatively short notice and with little context provided. My husband, Dave, has provided unwavering support throughout, hundreds of cooked meals, and endless patience with taking over household responsibilities to enable to me to write up. He has also assisted me with resolving programming bugs, and offered valuable proofreading skills. I could not have succeeded without his support.

Contents

List of Figures

List of Tables

List of Equations

Symbols

A	cross sectional area	m^2
e	aperture	m
e_h	hydraulic aperture	m
F_0	Forchheimer number	-
g	acceleration due to gravity	m/s^2
k	intrinsic permeability	m^2
k_a	apparent permeability (Klinkenberg)	m^2
K	hydraulic conductivity	m/s
L	sample length	m
P	pressure	MPa
ΔP	differential pressure	MPa
∇P	pressure gradient	Pa/m
Q	volumetric flow rate	m^3/s
r	pore radius	m
Re	Reynolds number	-
T	transmissivity	m^4
T_0	true transmissivity	m^4
T_{app}	apparent transmissivity	m^4
$\mathbf{u}$	flow velocity	m/s
V	volume	m^3
w	sample diameter/fracture width	m
z	elevation	m

θ	temperature	°C
μ	viscosity	Pa s
ρ	density	kg/m^3
ϕ	porosity	-
σ	stress	MPa
$\bar{\lambda}$	mean free path of molecules	m

Chapter 1

Introduction

1.1 Background

1.1.1 Geological storage of CO_2

The long term secure storage of CO_2 in the subsurface is key to the success of Carbon Capture and Storage (CCS), the only industrial-scale technology currently designed to reduce CO_2 emissions from fossil fuel power stations and large industrial plants. For CCS to be successful in contributing to climate mitigation efforts, CO_2 must be securely stored for over 10,000 years [Metz et al., 2005].

Geological storage of CO_2 is typically proposed within porous sedimentary rock formations such as depleted oil and gas reservoirs and deep saline aquifers. Under the high pressure, high temperature conditions present within such storage reservoirs, CO_2 is in its supercritical phase (see section 2.5.1). Supercritical CO_2 is less dense than brine, and thus CO_2 travels upwards through interconnected high permeability pathways within the formation [Gunter et al., 2004].

There are four main mechanisms that trap CO_2 within such brine-saturated aquifers [Chadwick et al., 2008]. Overlying low permeability rock such as shale or salt beds can prevent upwards migration by physically sealing free phase CO_2 within the storage formation - this form of hydrogeological trapping is known as structural or stratigraphic trapping [Gunter et al., 2004]. Residual saturation trapping occurs when ganglia of CO_2

are trapped within pore spaces due to capillary forces, or adsorbed onto mineral grains [Chadwick et al., 2008]. Some injected CO_2 may dissolve within the reservoir brine, known as dissolution or solubility trapping. Over long time periods this dissolved CO_2 may react with rock minerals or pore fluid to form other minerals or aqueous complexes resulting in geochemical or mineral trapping [Chadwick et al., 2008].

The importance of each of the above storage mechanisms and the timescales at which they develop will vary considerably between storage sites, being dependent on a number of reservoir properties such as pore size, distribution and connectivity, salinity, aquifer flow regime, temperature, pressure, lithological heterogeneity and mineralogy. Figure 1.1 provides an indication of the typical contribution of each of the four main trapping mechanisms and how this may change over time [Metz et al., 2005]. Mineral trapping is considered the most secure form of CO_2 trapping, as CO_2 becomes immobile and is permanently stored. Thus, if the percentage contribution of mineral trapping increases over time the security of storage is considered to increase. However, initially, the dominant barrier to CO_2 leakage to the surface is structural trapping by low permeability overlying rock layers [Nelson et al., 2005]. Geochemical trapping through mineral reactions is likely to have little effect over a one hundred year timescale, but may start to make an impact on a timescale of hundreds to thousands of years [Chadwick et al., 2008].

Wilkinson et al. [2009] studied a Southern North Sea (UK) gas accumulation with a high natural CO_2 content (~50%), the Fizzy field (Rotliegend Group), as a natural analogue for engineered CO_2 storage to assess the importance of geochemical CO_2-rock reactions over geological timescales. The CO_2 is believed to have been present within the formation for tens of millions of years. Mineralogical assessment and stable isotope analysis concluded that only a small fraction of the CO_2 charge had become locked up by mineral formation, with a similarly small quantity in solution in porewaters. 70-95% of the CO_2 had remained as a free phase. These findings illustrate the importance of physical containment of free-phase CO_2 through structural trapping over both the short and long term for formations similar to the Rotliegend Group.

1.1.2 Leakage risks for structurally trapped CO_2

Assessment of the potential for CO_2 leakage from geological storage is essential prior to large scale implementation of CO_2 storage [Nelson et al., 2005]. Evaluation of the

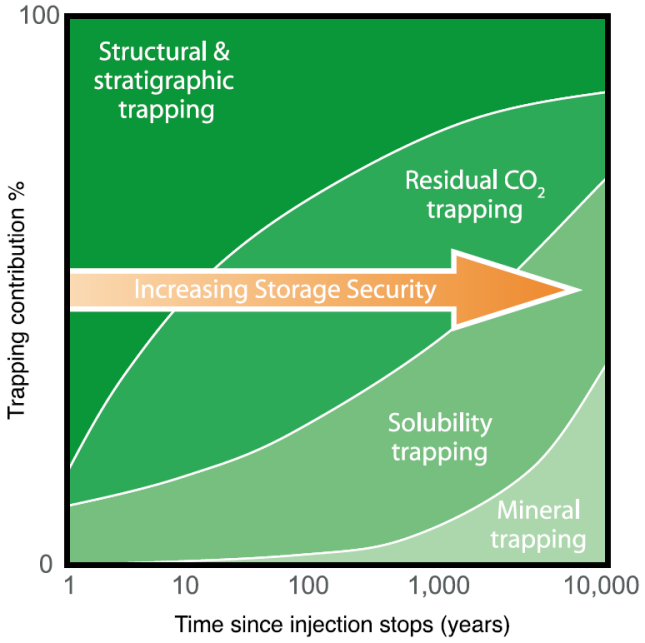

FIGURE 1.1: Importance of CO_2 trapping mechanisms over time [Metz et al., 2005]

integrity of seal rock for CO_2 storage requires an understanding of the geomechanical, geochemical and thermodynamic processes that influence the hydraulic properties of the seal rock. Leakage of structurally trapped CO_2 through the overlying seal rock may occur through three processes: diffusion of CO_2 through brine-saturated caprock, CO_2 breakthrough within the pore network where capillary entry pressures are exceeded, and CO_2 fracture flow [Edlmann et al., 2013].

Diffusive losses through the seal rock have been shown to be negligible under CO_2 storage conditions [Busch et al., 2008, 2010, Wollenweber et al., 2010]. CO_2 breakthrough into water or brine-saturated seal rock pore space is dependent on the wettability of the CO_2/water/rock system as well as the interfacial tension between the fluids [Washburn, 1921]. These vary with both pressure and temperature [Bachu and Bennion, 2009, Broseta et al., 2012, Chalbaud et al., 2009, Chiquet et al., 2007, Hebach et al., 2002]. CO_2 breakthrough pressures have been experimentally investigated within a variety of low permeability rock types including shales, mudrocks, limestone and marlstone under various pressure and temperature conditions [Hildenbrand et al., 2004, Li et al., 2005, Tonnet et al., 2010, Wollenweber et al., 2010]. Repetition of breakthrough tests is observed to result in a reduction in threshold breakthrough pressure [Harrington and Horseman, 1999, Wollenweber et al., 2010]. This indicates the occurrence of

pressure-induced micro-fracturing within the samples. High pressure flow experiments undertaken by Angeli et al. [2009] and Skurtveit et al. [2012], as well as model findings [Jain and Juanes, 2009] provide additional evidence that pressure-induced opening of micro-fractures in shale can be an important mechanism for CO_2 flow. Despite this, effective CO_2 permeabilities in the order of nanoDarcies ($\sim 10^{-21}$ m^2) are observed when breakthrough pressures are exceeded within these typical seal rock samples. Busch et al. [2010] shows that hundreds of thousands of years are required for CO_2 breakthrough to occur through a typical medium to low permeability seal rock with a thickness of 100 m.

Given these findings, CO_2 flow through natural or induced fractures presents the largest risk to storage integrity and requires further investigation [Edlmann et al., 2013]. Fractures can be important conduits for fluid flow and as a result are key potential leakage pathways for structurally trapped CO_2 [Bjørlykke, 1993, Chadwick et al., 2008, Song and Zhang, 2013]. Pre-existing fractures may be present, or overpressure as a result of CO_2 injection may cause hydraulic fracturing or re-activation of fractures within the seal rock [Liu et al., 2012]. During monitoring of the world's first commercial scale on-shore CO_2 storage project, In Salah, evidence for CO_2 migration into the lower, shaley, seal rock layer was observed. This was interpreted to have occurred as a result of tensile opening of a fracture zone in response to pressurisation during CO_2 injection [Shi et al., 2012]. In addition to investigation of failure mechanisms through geomechanical laboratory studies [Hangx et al., 2010, Liang et al., 2007, Ranjith and Perera, 2011], understanding how the behaviour of existing seal rock fractures under a range of typical in-situ conditions affects CO_2 flux is important to assess how site selection or CO_2 injection procedures may enhance or minimise such leakage risk.

1.1.3 Influences on fracture flow

Flow through seal rock fractures is influenced by thermo-hydraulic-mechanical and chemical (THMC) processes. These processes are intrinsically linked such that one process affects the initiation and progress of others [Tsang et al., 2004]. Understanding these coupled THMC processes is of importance in a variety of geoscientific fields: geological nuclear waste disposal; development of geothermal and hot dry/wet rock systems; coal bed gas production and underground coal gasification; petroleum production

and reservoir dynamics; stability of large-scale civil constructions, as well as geological storage of carbon dioxide [Tsang et al., 2004].

There has been significant progress in the last couple of decades within both experimental and theoretical studies regarding the effects of coupling temperature gradient (T), hydrologic flow (H), mechanical deformation (M) and chemical processes (C) in fractured rocks, mainly driven by demands from performance and safety assessment of high-level nuclear waste repositories [Kolditz et al., 2012]. One of the key challenges in the study of THMC coupled processes is the wide difference in characteristic time and spatial scales associated with each of the processes [Tsang et al., 2004]. Thermal effects in rock material have relatively long time and spatial scales. Groundwater flow and transport, spatially, are sensitive to small-scale heterogeneities and fracture system characteristics but have relatively long flow and solute transport times. Conversely, mechanical effects have short time scales as responses can propagate through rock with the speed of elastic waves; deformation can occur on a variety of spatial scales, usually dominated by fracture network distribution and size. Chemical process timescales vary significantly, dependent on the reaction; for reactions associated with CO_2 storage, equilibration times range from a couple of hours to extremely long geological timescales [Gaus et al., 2008].

During flow through natural fractures, dispersion occurs as a result of fracture roughness and aperture variations which can cause flow channelling. Reactive transport processes may also occur during CO_2 flow through brine-saturated media as a result of CO_2 dissolution, which produces carbonic acid (H_2CO_3). The dissociation of carbonic acid into reactive hydrogen ion (H^+) and bicarbonate (HCO_3^-) potentially initiates a complex series of reactions with aquifer fluids and formation rocks to fix CO_2 in mineral phases [Ramajo et al., 2002]. The reactivity is dependent on formation rock mineralogy, formation water properties and thermodynamic conditions. Where CO_2 dissolution into the liquid phase occurs, molecular diffusion of the dissolved CO_2 into the matrix can follow, affecting CO_2 mass transport through retardation. CO_2 transport in fractures is therefore also sensitive to CO_2 solubility, the CO_2 diffusion coefficient and to the surface and volume available for dissolution/diffusion [Ramajo et al., 2002].

1.1.4 Review of previous fracture flow experiments

A number of significant experimental studies have been carried out that relate to dissolution, mechanical deformation and flow channelling along fractures. A selection of these are discussed below. The hydraulic theory associated with fracture flow is presented in Chapter 2.

Of pertinence to CO_2 leakage, Andreani et al. [2008] investigated permeability changes of a fractured claystone due to geochemical activity as a result of seepage of CO_2-enriched brine and water vapour-saturated CO_2. Laboratory experiments were undertaken at 25°C and 0.12 MPa confining and fluid pressures. The rock sample used for investigation was from the Upper Toarcian formation of Tournemire (France) and is compositionally close to the Paris Basin caprocks where a CO_2 pilot project is scheduled. CO_2-saturated brine flow through the fractured sample resulted in porosity increase in the vicinity of the fracture due to dissolution of calcite and quartz over a 280 hour period, although the permeability remained unchanged. However fracture aperture (and as a result permeability) did increase as a result of cyclic flows of CO_2-gas and CO_2-brine flow. It is suggested that the CO_2-brine causes dissolution, while the CO_2-gas flow reduces the cohesion of clay particles. These particles are then flushed out during the next CO_2-brine flow cycle resulting in increased fracture aperture.

Smith et al. [2013] undertook similar experiments to Andreani et al. [2008] on a fractured greywacke sample, at higher pressures and temperature (200°C, 25 MPa confining pressure and $\sim$ 8 MPa fluid pressure). A clear increase in permeability was observed during this 50 day constant CO_2-enriched brine flow experiment, which indicated that wallrock dissolution was the dominant process during this experiment. A study of fracture alteration within limestone by CO_2 acidified brine similarly indicated permeability increase, resulting from calcite dissolution and associated fracture channelisation [Deng et al., 2015]. In contrast, CO_2-rich brine experiments undertaken on fractured cement samples indicate self-healing of fractures as a result of precipitation through cement carbonation, leading to fracture permeability reduction [Huerta et al., 2016, Liteanu and Spiers, 2011, Luquot et al., 2013].

Mineral dissolution along fracture surfaces is not always observed to increase fracture permeability. A flow experiment undertaken with slightly acidic aqueous solution

through a rough fracture in Carrara marble found local dissolution resulted in a reduction of mean aperture and fracture permeability due to closure of the aperture [Durham et al., 2001]. Fracture surfaces were digitized in three dimensions before and after the fluid flow tests. The experiment was undertaken under a confining pressure of 0.2 MPa. At the millimetre scale, mineral dissolution transformed fracture apertures from strongly heterogeneous and tortuous flow channels to a smoother topography. On the sample scale (50 mm x 75 mm), mineral dissolution resulted in creation of a single broad flow channel along the centre of the sample. On both scales there was evidence that there is an inverse relationship between fluid flux and dissolution rate: on the millimetre scale, this is through rapid dissolution near points of asperity contact where fluxes are assumed to be low; and on the sample scale, isolated patches of very high flux and low dissolution were observed in the broad central flow channel. Thus, smoothing of the fracture surface occurred due to dissolution, resulting in closure of the aperture despite the low confining pressure. Although this was not a CO_2 flow experiment, it is possible that in some cases CO_2-saturated brine may cause similar effects on fracture apertures at in-situ pressures, and a reduction in fracture permeability may result from dissolution in deeply buried formations due to mechanical coupling.

There is also evidence from granite fracture flow-through experiments that de-ionised water can result in changes to fracture geometry and apertures as a result of chemical dissolution and precipitation reactions, affecting permeability after hundreds of hours [Yasuhara et al., 2011]. Fracture geometry imaging using x-ray CT scanning during flow-through experiments on naturally-fractured novaculite has enabled the evolution of the fracture geometry to be documented [Yasuhara et al., 2006]. For an experiment undertaken at room temperature and medium confining pressure (1.4 MPa), fracture aperture decreased during the first 1500 hours, but was then subsequently found to increase. This can be explained by the dominant dissolution process switching from prop removal (pressure solution) to etching of the void surfaces [Yasuhara et al., 2006]. For higher confining pressures (5 MPa and 10 MPa), mechanical compaction was found to be more dominant, with dissolution processes resulting in fracture aperture decreasing to a steady state after approximately 400 hours [Yasuhara et al., 2011]. Increasing temperature to 90°C resulted in continued reduction in fracture aperture [Yasuhara et al., 2011].

Mechanical effects on conservative flow and mass transport through fractures have been investigated by Durham [1997] during a detailed study of the shape and hydraulic

behaviour at in-situ stresses (100 MPa) of an undisturbed fracture recovered from a depth of 3800 m during the German Continental Deep Drilling Program (KTB). The fracture was an epidote-filled amphibolite and was found to have a high mechanical stiffness even at high pressure and while conducting water. Permeability measurements confirmed the fracture to be 4-7 orders of magnitude more permeable than the matrix, which helps to explain the anomalously high permeability found at this depth in the borehole. Detailed profiling of the fracture walls allowed both visual inspection and flow simulations of the fracture to be undertaken. These show flow occurring in a distributed array of channels with no apparent linearity – these distributed flow channels are maintained over differing amounts of closure due to the high stiffness of the mineralised fracture. This is in contrast to experiments undertaken on fresh, well-mated granite fractures where permeability changes up to six orders of magnitude with the application of confining pressure. In the fresh granite fractures, uniform flow occurs at more open apertures, with channelling occurring as the aperture decreases. Flow becomes confined to fewer and fewer channels as the confining pressure increases further until the fracture becomes completely closed [Durham, 1997].

The hydro-mechanical behaviour of Kimmeridge shale fractures under normal and shear loading was experimentally investigated by Gutierrez et al. [2000]. The naturally fractured Kimmeridge shale samples were obtained from Kimmeridge Bay in Dorset, UK. Prior to experimentation, the calcite cemented natural fractures were manually split along the fracture plane and the calcite cement dissolved using a strong acid solution. The de-mineralised fracture surfaces were found to be well-matched which suggested that they were extensional fractures not previously subjected to shear deformation. Gutierrez et al. [2000] therefore considered the de-mineralised samples to be representative of the natural fracture prior to cementation, i.e. at the time of creation of the fracture. Initial fracture permeabilities, determined using water, were found to be around nine orders of magnitude higher permeability than the intact shale. Increasing the normal stress across the fracture reduced fracture permeability in an exponential manner, however fracture permeability remained around eight orders of magnitude higher than the intact shale permeability even under normal stresses of twice the unconfined compressive strength of the shale (10 MPa). Shearing under constant normal stresses lower than the unconfined compressive strength of the shale resulted in fracture dilation and fracture permeability increase of around one order of magnitude,

while shearing under higher normal stresses resulted in fracture permeability reduction of around six orders of magnitude due to gouge formation. Despite the significant permeability reduction observed following fracture shearing, the fracture permeability remained around three orders of magnitude higher than the intact rock permeability. These experiments suggest that in tight formations like shales, rough fractures cannot be completely hydraulically closed by mechanical loading and remain as conduits for fluid flow in the absence of mineral cementation.

Subsequent experiments undertaken by Nygård et al. [2006] examined the brittle-ductile transition within Kimmeridge Clay shales and mudrocks and the influence of this transition on the creation of shear-induced fractures. It was found that the brittle-to-ductile transition could be related to the overconsolidation ratio - overconsolidated shales and mudrocks (where effective confining stresses are less than pre-consolidation stress) were found to be associated with brittle behaviour, while normally consolidated samples (effective confining stresses greater than pre-consolidation stress) were ductile. Shear failure occurs in brittle mudrocks and results in the formation of distinct shear fractures which can increase the mudrock permeability by providing a path for channelised flow. Post-peak shearing may further dilate such fractures, similar to the fracture dilation observed by Gutierrez et al. [2000]. These experiments highlight the importance of stress-history in determining mechanical and thus hydraulic behaviour.

Gas flow experiments undertaken using Helium on kaolinite fault gouge indicated significant differences in fracture flow behaviour to that observed during water flow experiments [Cuss et al., 2015, Sathar et al., 2012]. Fluid flow reduced with normal load for both water and gas as expected due to reduced fracture permeability during the experiments of Sathar et al. [2012]. However, water flow experiments showed only partial recovery of fluid flow rate on unloading, while gas flow rate was observed to increase considerably relative to initial flow rates during unloading. It is possible that this may be a result of desiccation of fault gouge during the gas experiments, leading to enhanced gas flow rates on unloading.

Widely varying, non-repeatable gas breakthrough pressures were observed during repeated gas flow experiments undertaken by Cuss et al. [2015] on kaolinite fault gouge. This suggests that gas flow pathways may be dependent on subtle variations in gouge properties, with fault gouge desiccation also potentially playing a role. Experiments

were undertaken with faults oriented at a variety of angles relative to maximum horizontal stress [Cuss et al., 2015]. Gas flow was observed during all experiments, regardless of fault orientation. This finding suggests that critical stress theory, which predicts that faults oriented at an angle close to parallel with respect to the maximum horizontal stress orientation will be conductive while faults oriented close to perpendicular to the maximum horizontal stress orientation will be effectively sealed, may be invalid for gases. In addition, shearing was observed to enhance gas movement both by reduction of gas entry pressure and increased fracture permeability once gas was mobile in all cases. Thus, shearing in kaolinite gouge-filled faults is not observed to be an effective self-sealing mechanism for gas flow. This is in contrast to the findings of Gutierrez et al. [2000] who found that fracture permeability (to water) reduced due to gouge formation during shearing under significant normal loads. The differences in fracture flow behaviour observed between water and Helium gas during the above experiments indicate that further work is required to gain an improved understanding of fracture flow behaviour to a range of fluids.

The above experimental studies have been successful in gaining improved understanding of a number of geochemical and mechanical processes associated with fracture flow. However, very little experimental work has been carried out on the hydraulic and mechanical processes associated with the flow of supercritical CO_2 through natural fractures under reservoir conditions of stress, fluid pressure, and temperature. The work presented within this thesis aims to contribute to addressing this research need. Where limited experimental observations are available numerical models are not well constrained due to lack of available data for calibration purposes. Laboratory investigations therefore not only improve understanding of key mechanisms that influence the conductivity of fractures to CO_2, but also provide valuable data for coupled process model calibration, enabling development of our understanding of CO_2 leakage risks.

1.2 Thesis motivation and objectives

CO_2 flow through natural or induced seal rock fractures is a key leakage risk for geological storage of CO_2. In order to understand the behaviour of fractured rock masses, the behaviour of single fractures must first be thoroughly understood [Jaeger et al., 2009]. The motivation for this study is therefore to improve understanding of the hydraulic

and mechanical processes relevant to supercritical CO_2 flow through discrete seal rock fractures under a range of typical in-situ pressure and temperature conditions.

In order to study hydraulic and mechanical processes in isolation, single phase CO_2 has been used during experiments on dry fractured seal rock samples. Experimental studies suggest that mineral reactivity does not occur between typical caprock minerals and anhydrous supercritical CO_2, except in the special case of water-containing minerals (swelling clays) [Credoz et al., 2009, Loring et al., 2012, Wang et al., 2013]. Thus, use of single phase CO_2 during fracture flow experiments minimises the potential for chemical reactions that may contribute to alteration of fracture geometry. Chemical influences, as well as the influence of multi-phase flow behaviours (i.e. wettability, interfacial tension, etc.) can play an important role and have been considered in previous experimental investigations (see section 1.1). However, removing the coupling of these additional processes is necessary to enable appropriate assessment of hydraulic and mechanical processes.

There is evidence from both natural analogue and field-based CO_2 storage studies that a large proportion of subsurface CO_2 is present as a free phase [Johnson et al., 2011, Wilkinson et al., 2009]. During storage of injected CO_2, the proportion of free phase CO_2 is highest initially (prior to the occurrence of CO_2 dissolution), and leakage risk is greatest. Understanding the behaviour of supercritical CO_2 flow within fractures is therefore particularly pertinent.

Experimental investigation of supercritical CO_2 flow through discretely fractured seal rock is challenging and requires specifically designed equipment. However, assessing how rock fractures respond mechanically to stress and temperature changes under conditions typical of a CO_2 storage site is important for consideration of the resultant fracture conductivity and thus CO_2 leakage rate potential. Supercritical CO_2 density and viscosity varies both with pressure and temperature and this therefore also influences hydraulic behaviour and fracture conductivity. This study aims to gain an improved understanding of the impact of these mechanical and fluid property changes on the hydraulic response of discrete seal rock fractures to free phase CO_2. It is anticipated that the study findings will provide valuable data to enable calibration of hydraulic and mechanical process representation within a range of numerical models, thus improving the accuracy of such models for future use.

The primary objectives of this project were to:

- **Source and prepare fractured seal rock samples**
  Source suitable samples of typical seal rock, from potential storage sites where possible, or from analogues. Prepare appropriate discretely fractured cores from these samples for experiments, ideally from pre-existing discrete fractures, or through inducing discrete fractures within unfractured cores. Undertake sample characterisation, including fracture surface geometry characterisation both pre- and post-experiment where possible, to enable assessment of geometry changes that arise during experiments.

- **Design and build an appropriate experimental rig**
  Design and build an experimental rig to enable assessment of fractured seal rock permeability during CO_2 flow, under a range of typical in-situ pressure and temperature conditions.

- **Undertake CO_2 fracture flow experiments**
  Undertake comprehensive supercritical CO_2 flow experiments on the prepared fractured samples that allow for analysis of the hydraulic behaviour under a variety of temperature and stress conditions. Experimental sequences should enable assessment of:

  - Flow regime (linear or non-linear)
  - Hydraulic response to stress changes (both internal and external)
  - Hydraulic response to temperature changes

- **Analyse experimental results**
  Undertake suitable post-processing and presentation of experimental data to enable analysis and discussion of results, comparison between samples, and review of the supercritical CO_2 flow findings within the context of wider general understanding of mechanical and hydraulic behaviour of fractures.

The experimental temperature and stress conditions chosen for this study were selected to be typical of in-situ ranges within potential CO_2 stores. For efficient CO_2 injection into storage it is desirable for CO_2 to be in a supercritical state; thus CO_2 stores are proposed for depths greater than 800 m where CO_2 will be in this state [Haszeldine, 2006]. At these depths CO_2 fluid pressures will be greater than 8 MPa, thus downstream fluid pressures of 10 MPa, 20 MPa and 30 MPa were selected for experimental testing. This range of fluid pressures is typical of the range present within existing CO_2

storage operations [Michael et al., 2010]. Confining pressures acting on fractures in the subsurface are dependent on fracture orientation and resultant in-situ stresses, which arise due to lithostatic, tectonic, structural and residual stresses. Confining pressure ranges adopted during the study (35, 45 and 55 MPa) were chosen to be typical of lithostatic pressure/vertical stresses present within potential storage sites (depth range ~1-3 km) [Michael et al., 2010]. Within the North Sea Basin, where there is potential for significant CO_2 storage, the average geothermal gradient is ~30°C/km [Harper, 1971], therefore experimental temperatures of 38°C and 58°C were selected for study, typical of temperatures within the depth range 1-2 km.

1.3 Thesis structure

This thesis addresses the objectives above and comprises eight chapters.

- Chapter 2 contains background theory relating to fluid flow, CO_2 properties and fracture mechanics.
- Chapter 3 contains details of both the reservoir and analogue seal rock samples sourced for use within this project. Details of sample characterisation undertaken is included within this chapter, which comprises mineralogical analysis, and porosity, permeability and Mohs hardness testing. Obtaining samples of naturally occurring fractures was challenging, with preparation of only one cored pre-existing Zechstein dolomite fracture from the North Sea Wissey field possible. Thus, this chapter also details the method adopted for preparing induced fracture core samples.
- Chapter 4 presents the fracture surface characterisation undertaken during this study, including the methods adopted and analysis and discussion of results.
- Chapter 5 contains full details of the experimental rig that was designed and built during this study. The chapter also discusses testing of the rig system, some of the challenges that were overcome during the design and build process, and recommendations for future improvement to the design.
- Chapter 6 contains a method overview of the five fractured sample flow experiments undertaken, including presentation of the experimental sequence adopted

for each sample. Operational methods and procedures used during each of the experiments are also detailed, and methods adopted for post-processing of the logged experimental data series are discussed. A review of the various sources of experimental error is included, and the approach adopted for estimating resultant error from these is discussed.

- Chapter 7 presents and discusses the experimental results obtained from each of the five sample experiments. An initial sample overview and comparison section is followed by:
  - Flow regime analysis for each of the samples using a modified Forchheimer Plot method where appropriate.
  - A discussion and illustration of the impact of CO_2 property variation both across the sample during experiments, and between experimental scenarios.
  - A review of the elastic response to stress change observed during each of the sample experiments.
  - A review of the inelastic response to stress change observed during each of the sample experiments.
  - Presentation of the hydraulic aperture, permeability and hydraulic conductivity parameters estimated during each of the sample experiments.
  - A discussion of the coupled effects of hydraulic and mechanical changes to fracture conductivity observed during experiments.
  - A summary of the key experimental findings discussed within this chapter.
- Chapter 8 summarises the main conclusions of this study. It also contains a discussion of the importance of the work and applications for use of the experimental results. Recommendations for further work are also highlighted.

Chapter 2

Background Theory

2.1 Introduction

The flow of fluids through porous and fractured media is governed by three principles: the conservation of mass, the conservation of momentum and the equation of state of the fluid(s). These principles are discussed within this Chapter in the context of the discrete fracture flow experiments undertaken during this project. Fracture mechanics are closely coupled to hydraulic behaviours, and are also discussed within this Chapter.

2.2 Flow of fluids

This section introduces the conservation of mass and conservation of momentum principles in the general context of fluid flow in the subsurface. The equation of state for CO_2 is discussed within section 2.5.

2.2.1 Conservation of mass

The principle of conservation of mass is that mass can neither be created or destroyed, and is described by the continuity (or mass balance) equation (Equation 2.1) [de Marsily, 1986].

$$\nabla(\rho \mathbf{u}) + \frac{\partial \rho}{\partial t} = 0 \tag{2.1}$$

where ρ is the density of the fluid (kg m^{-3}), and $\mathbf{u}$ is the filtration velocity vector representing the mean macroscopic fluid velocity within the medium (ms^{-1}) at time t (s). The first term represents the resultant mass flux into (or out of) a control volume; the second term is the rate of change of density within the control volume. Thus, the equation states that the rate of change of mass within a fixed volume is determined by the resultant mass flux into/out of the volume.

Within the CO_2 fracture flow experiments undertaken in this study measurements are taken under steady state, or pseudo steady-state conditions. Therefore the rate of change of CO_2 mass contained within the sample is considered to be negligible, and the entering mass flux is equal in magnitude to exiting mass flux i.e. a resultant mass flux of zero. It is acknowledged that there is a small potential for dissolution/diffusion to affect mass flux where residual water is present within the samples, however this influence is considered to be negligible within this study.

2.2.2 Conservation of momentum

Darcy's law is a form of the conservation of momentum equation, valid for laminar flow of Newtonian fluids through porous or fractured media [de Marsily, 1986]. Darcy's law was originally derived empirically but can also be theoretically derived from the Navier-Stokes equations which describe the motion of fluid substances. The general form of Darcy's law is stated in Equation 2.2 [de Marsily, 1986].

$$\mathbf{u} = \frac{Q}{A} = -\frac{k}{\mu}\left(\nabla P + \rho g \nabla z\right) \tag{2.2}$$

where $\mathbf{u}$ is the filtration velocity (or darcy velocity) (ms^{-1}), Q is the volumetric flow rate (m^3/s), A is the cross-sectional area of the flow path (m^2), k is the instrinsic permeability of the media (m^2), μ is dynamic viscosity (Pa s), P is fluid pressure (Pa), ρ is fluid density (kg/m^3), g is acceleration due to gravity (ms^{-2}) and z is elevation (m).

On the right hand side of the equation, the first term is derived from the pressure head and the second term from the elevation head. Darcy's law shows that the filtration velocity, $\mathbf{u}$, is proportional to the hydraulic gradient, where the hydraulic gradient is $\frac{\nabla P}{\rho g} + \nabla z$.

For one-dimensional laminar flow where ∇z is zero (i.e. horizontal subsurface flow or laboratory conditions), Darcy's law can be expressed by Equation 2.3 [Bear, 1972].

$$Q = -\frac{Ak\nabla P}{\mu} = -\frac{Ak}{\mu}\frac{\partial P}{\partial x} \tag{2.3}$$

Where the fluid is incompressible (i.e. fluid density and viscosity do not vary with pressure) and volumetric flow rate therefore remains constant under steady state flow, Equation 2.3 further reduces to Equation 2.4 for flow across a sample length, L (m).

$$Q = -\frac{Ak}{\mu}\frac{\partial P}{\partial x} = A\frac{k}{\mu}\left(\frac{P_{us} - P_{ds}}{L}\right) \tag{2.4}$$

where $\nabla P = \partial P/\partial x = (P_{ds} - P_{us})/L)$ (Pa/m) is the fluid pressure gradient, and P_{us} and P_{ds} are the upstream and downstream pressures respectively. Fluid flows from high pressure to low pressure, therefore the flow direction is opposite to the pressure gradient direction.

Where the incompressible form of Darcy's law (Equation 2.4) is valid, a linear relationship between flow rate and pressure gradient exists. Under extreme hydraulic gradients, which are not frequently encountered in nature, we observe deviations from the linear behaviour described by Darcy's law for laminar flow. Non-linear flow regimes are generally considered to result from increased inertial forces, and the onset of turbulent flow. Non-linear flow regimes are discussed in section 2.4.

For compressible fluids, the significance of changes to density, ρ and viscosity, μ with pressure must also be considered, using the equation of state of the fluid in association with the conservation of mass. This is discussed, in the context of CO_2, in section 2.5.

2.3 Fracture flow

The hydraulic conductivity of rock masses significantly depends upon the hydraulic behaviour of single joints or fractures [Xiao et al., 2013], particularly where the rock matrix is of very low permeability. Thus, it is of importance to understand the hydraulic behaviour of such fractures.

Fluid flow through natural rock fractures is complex. Natural fractures are 'closed' i.e. there are points of contact between the fracture surfaces known as contacting asperities [Witherspoon et al., 1979]. This, along with fracture surface roughness, causes flow through the fracture to be subject to channeling and tortuosity, which affects the hydraulic conductivity of the fracture.

The cubic law, analogous to Darcy's law, may be used to describe flow within a discrete fracture where permeability within the surrounding matrix is negligible. The cubic law is presented and discussed within subsection 2.3.1.

2.3.1 The cubic law

The cubic law [Witherspoon et al., 1979] describes fluid flow, Q (m^3/s), through a parallel plate fracture of width, w (m), and aperture, e (m) (Equation 2.5).

$$Q = -\frac{e^3 w \nabla P}{12\mu} = \frac{e^3 w}{12\mu}\left(\frac{P_{us} - P_{ds}}{L}\right) \tag{2.5}$$

where μ is the fluid viscosity (Pa s), ∇P (Pa/m) is the fluid pressure gradient along the fracture, and L (m) is the length of the fracture. The cubic law is derived from the Navier-Stokes equations and is valid for laminar flow of incompressible viscous fluid where the effects of external forces (including gravity) are negligible. Comparison of Equation 2.4 and 2.5 indicates that the cubic law is analogous to Darcy's law.

Although originally derived for describing fluid flow through parallel planar fractures, the cubic law is widely used to describe flow through real rock fractures, where e is replaced by e_h, the hydraulic aperture, or equivalent smooth wall (conducting) aperture [Barton et al., 1985, Witherspoon et al., 1979, Zimmerman et al., 2004]. The hydraulic

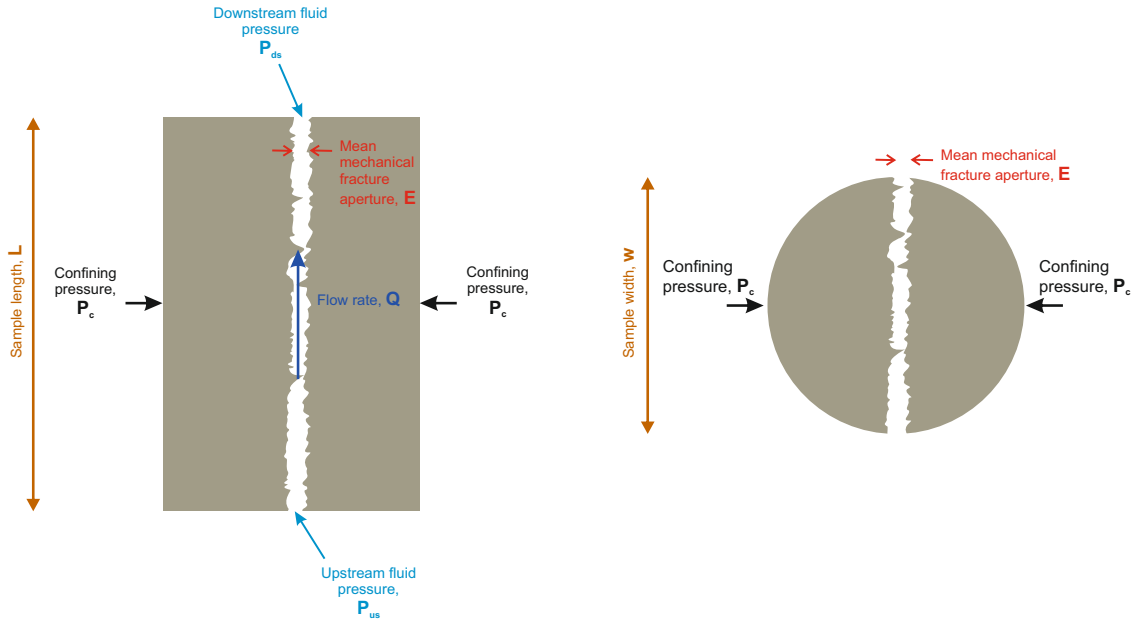

(A) Sample side view (B) Sample top view

FIGURE 2.1: Schematic of the fractured sample geometry used during this experimental study, indicating pressures and flow direction

aperture is generally lower than the mean mechanical aperture, E, of the fracture due to flow losses as a result of tortuosity and surface roughness, and the mismatch between e_h and E has been shown to increase with decreasing fracture aperture [Barton et al., 1985, Renshaw, 1995].

Figure 2.1 is a schematic of the fractured sample geometry and set-up used during this study, indicating the fluid pressures, confining pressure, flow direction and sample dimensions.

During the laboratory fracture flow experiments we measure the sample dimensions (length, L, and diameter, which equates approximately to the fracture width, w, see Figure 2.1). We can control the fluid flow rate, downstream fluid pressure and temperature, as well as the sample temperature and confining pressure (see Chapter 5 for

details). However, we are unable to measure the mean mechanical aperture of the sample and its variation as a result of stress changes during the experiments. We therefore adopt the cubic law to assess hydraulic aperture variation due to stress and temperature changes. Various parameters: transmissivity, hydraulic aperture, fracture permeability and fracture hydraulic conductivity are estimated during analysis. These parameters are defined in subsections 2.3.2 to 2.3.5 for laminar flow of incompressible fluids. Where inertial effects are significant during fluid flow, non-linear deviations from laminar flow behaviour can occur, and if significant, these effects may need to be accounted for. This is discussed within section 2.4. Deviations may also occur for compressible fluids where fluid density and viscosity variation across the sample is significant. Compressibility effects associated with supercritical CO_2 are discussed in section 2.5.

2.3.2 Transmissivity of a fractured sample

During the laboratory flow experiments on discretely fractured cylindrical core samples of low permeability seal rock, the downstream fluid pressure, confining pressure, flow rate and temperature are controlled. The key experimental observation is the differential pressure, $\Delta P = P_{us} - P_{ds}$ (Pa) across the sample, which responds to changes in the controlled parameters. Given knowledge of the sample dimensions, temperature, pressure and flow conditions, the differential pressure can be used to estimate sample transmissivity, T (m^4), as defined in Equation 2.6 [Zimmerman and Bodvarsson, 1996].

$$T = \frac{Q\mu L}{\Delta P} \tag{2.6}$$

where Q (m^3/s) is the flow rate through the sample; μ (Pa s) is fluid viscosity and L (m) is the sample length.

Sample transmissivity is a useful parameter for analysis during fracture flow experiments, as although it assumes laminar flow, the parameter does not assume any particular fracture geometry, and therefore can be used for comparison between samples of different composition or fracture geometry. In fact, sample transmissivity, T, simply defines the transmissivity of the sample as a whole, and could therefore be used for comparison of a variety of 38 mm diameter fractured and non-fractured samples. Reviewing

Darcy's law (Equation 2.4), we can see that $T = kA$, where k is the permeability of the sample, and A is the cross-sectional flow area. For fractures, the cross-sectional flow area is defined by the fracture aperture and k becomes the fracture permeability.

Differential pressure is inversely proportional to transmissivity, therefore an increase in differential pressure correlates to a decrease in transmissivity for a given fluid pressure and flow rate scenario.

2.3.3 Hydraulic aperture estimation

For analysis of fractured seal rock samples, the porosity and permeability of the sample matrix is extremely low (Chapter 3). Consequently, flow through samples can be considered to occur within transmissive fractures only, with negligible transport through the sample matrix. Thus the cubic law (Equation 2.5) may be used to estimate a hydraulic aperture, e_h (m) for the fracture [Zimmerman and Bodvarsson, 1996]. As discussed in subsection 2.3.1, the hydraulic aperture, e_h, gives the equivalent smooth wall aperture associated with a rough-walled fracture, and variation in this parameter can be used to monitor the mechanical impact on fractured samples of any applied stress changes, where mechanical aperture measurement is not possible (see section 2.6 for fracture mechanics discussion).

Hydraulic aperture can be estimated from Equation 2.7 (a rearrangement of Equation 2.5).

$$e_h = \left(\frac{12Q\mu L}{\Delta P w}\right)^{\frac{1}{3}} = \left(\frac{12T}{w}\right)^{\frac{1}{3}} \tag{2.7}$$

From Equation 2.7 we see that hydraulic aperture is proportional to the cube root of transmissivity.

As stated in subsection 2.3.1, the hydraulic aperture will not be equivalent to the mean mechanical aperture, E, of the fracture due to flow losses as a result of tortuosity and surface roughness within the rough rock fracture. The mismatch between e_h and E is likely to increase as the aperture decreases. However, the hydraulic aperture can be considered to be indicative of the equivalent parallel planar fracture aperture and is

therefore an extremely useful parameter in evaluating fracture closure and deformation during the flow experiments.

2.3.4 Fracture permeability

It can be seen, by comparison of Equation 2.4 and 2.5, that the cubic law is analogous to Darcy's law. For flow within a parallel plate fracture of width, w and aperture, e, the cross-sectional flow area, $A = we$. Thus the intrinsic fracture permeability, k_{frac} (m^2), may be estimated by Equation 2.8.

$$k_{frac} = \frac{e_h^2}{12} \tag{2.8}$$

where e_h is the hydraulic aperture of the fracture, which takes account of rough fracture surfaces and contacting asperities that affect the permeability as discussed earlier. Permeability is a widely used parameter so presentation of this parameter is important for comparison between studies.

Transmissivity (T), hydraulic aperture (e_h), and fracture permeability (k_{frac}) are closely-linked parameters and can be directly estimated from each other. All can be estimated from experimental observations (ΔP), to analyse the fracture response to the differing flow, pressure, and temperature conditions considered during the experiments. These three parameters are intrinsic parameters relating to the sample, and are in theory independent of the fluid properties (density and viscosity). Unanticipated changes in these values (not related to mechanical changes) may suggest that deviations from the cubic law are occurring during the flow experiments. Non-linear flow is the most likely cause of such deviations, and is discussed in section 2.4. Deviations due to CO_2 compressibility effects are discussed within section 2.5.

2.3.5 Hydraulic conductivity

Hydraulic conductivity describes the ease with which a fluid can move through the material/fracture, and therefore takes into account the density and viscosity of the

fluid as well as the intrinsic properties of (in this case) the fractured sample. Hydraulic conductivity, K, is related to permeability, k, by Equation 2.9.

$$K = \frac{k\rho g}{\mu} \tag{2.9}$$

We can see from this equation that hydraulic conductivity increases with an increase in density or a reduction in viscosity of the fluid, assuming permeability, k, remains constant. The hydraulic conductivity of a fracture, K_{frac}, can be estimated using Equation 2.10, as the fracture permeability is estimated to be $e_h^2/12$ (Equation 2.8).

$$K_{frac} = \frac{e_h^2 \rho g}{12\mu} \tag{2.10}$$

2.4 Non-linear flow regime

Where Darcy's law or the analogous cubic law is valid, a linear relationship between flow rate and pressure gradient exists. Darcy's law and the cubic law are not valid for turbulent flow regimes due to the significance of inertial effects.

For flow between two smooth parallel plates, the transition from laminar to turbulent flow will typically occur when the Reynolds number, a measure of the ratio of inertial to viscous forces, exceeds 1150, for the Reynolds number as defined in Equation 2.11 [de Marsily, 1986, Zimmerman and Bodvarsson, 1996].

$$Re = \frac{\rho v e}{\mu} = \frac{\rho Q}{\mu w} \tag{2.11}$$

where ρ is density (kg/m^3), μ is viscosity (Pa s), v is velocity (m/s), e is fracture aperture (m) and w is fracture width (m).

However, within rough rock fractures the rough surfaces and contacting asperities lead to tortuous flow paths. The resulting microscopic inertial and viscous forces associated

with these tortuous flow paths can lead to non-linear deviations much earlier (i.e. at notably lower Reynolds numbers) [Ma and Ruth, 1993, Ruth and Ma, 1992, Zimmerman and Bodvarsson, 1996]. Several experimental studies have found that non-Darcy inertial effects become significant above a Reynolds number of around 20 during laboratory measurements on a variety of rough-walled fractures [Ji et al., 2008, Ranjith and Darlington, 2007, Zimmerman et al., 2004].

Microfluidic flow tests undertaken by Zhang et al. [2013] provide evidence for flow deviation and eddy formation where micro-cavities exist within flow channels. These effects contribute to non-linear deviations resulting from associated pressure losses. Thus, the onset of non-linear flow within rough rock fractures is dependent on both the Reynolds number and the relative roughness of the fracture.

The onset of non-linear flow observed prior to the onset of 'true' turbulence, and described above, is due to convective acceleration as a result of e.g. channelling in fractures, and can be described as *non-linear laminar flow*. *Turbulent flow*, which occurs at higher Reynolds numbers, is when the flow pattern becomes transient due to velocity fluctuations, and not due to the geometry of the media [Kolditz, 2001].

Dupuit [1863] and Forchheimer [1901] used a quadratic equation (Equation 2.12) to characterise the non-linear flow phenomenon, known as the 'strong inertia regime', observed at high fluid velocities [Huang and Ayoub, 2006]. This equation may be applicable to both *non-linear laminar flow* and/or *turbulent flow*.

$$-\nabla P = \frac{\mu}{k}V + \beta\rho V^2 = \frac{\mu}{kA}Q + \frac{\beta\rho}{A^2}Q^2 \tag{2.12}$$

where β is a factor describing the significance of inertial forces. The Forchheimer equation (Equation 2.12) consists of a viscous linear term and a quadratic inertial term. Equation 2.12 reduces to Equation 2.4 when inertial effects are negligible ($\beta \to 0$).

Where a non-linear flow regime is observed, a Forchheimer Plot can be used to assess the suitability of the Forchheimer equation for describing the flow regime [Batenburg and Milton-Taylor, 2005, Huang and Ayoub, 2006]. Within this study (Chapter 7), we have adopted a modified Forchheimer Plot method. This method involves application of linear regression to experimental data plots of $Y = -\nabla P/\mu Q$ against $X = \rho Q/\mu$.

With reference to Equation 2.12, we can see that linear regression will take the form of $Y = a' + b'X$, where $a' = 1/kA$ and $b' = \beta/A^2$. The viscosity and density values used for the sample within this analysis have been calculated using the Huang et al. [1984] and Jossi et al. [1944] equations respectively for the mean sample pressure, $\bar{P}_{sample} = (P_{us} + P_{ds})/2$ (see section 2.5). The sample mean volumetric flow rate, Q, has similarly been estimated as the flow rate for the mean sample pressure, $\bar{P}_{sample}$, from the pump flow rate and ratio of densities (mass conservation under steady state flow).

Where the Forchheimer equation is found to suitably describe an observed flow regime the 'true transmissivity' of the sample, $T_0 = kA$, can be estimated from the modified Forchheimer Plot as it is the inverse of the y-axis intercept, a'. The true transmissivity estimates reflect the transmissivity that would be observed were a linear flow regime to be present (i.e. where $\beta \to 0$). T_0 does not vary with flow rate under constant stress conditions. Apparent transmissivity, T_{app}, on the other hand, is the transmissivity estimate derived using a Darcy-type law (Equation 2.13), and decreases with increasing flow rate where a Forchheimer non-linear flow regime is present, as inertial effects increase [Zhang and Nemcik, 2013, Zimmerman et al., 2004].

$$T_{app} = -\frac{\mu Q}{\nabla P} \tag{2.13}$$

In the context of the discrete fracture flow experiments, within Equation 2.13, the fluid pressure gradient, $\nabla P = \frac{P_{ds} - P_{us}}{L}$. Q is the mean volumetric flow rate within the sample, and μ is the mean viscosity within each experimental scenario.

The above modified Forchheimer Plot method differs from the traditional Forchheimer Plots or Graphs used in Batenburg and Milton-Taylor [2005] and Huang and Ayoub [2006], for example, as the volumetric flow rate, Q, has been used in place of the flow velocity, V, within both the x and y-axis. The result is that the y value is equal to $1/T_{app}$ rather than $1/k_{app}$ (see Equation 2.13). Transmissivity in this context refers to the transmissivity of the fractured sample as a whole, rather than the fracture alone. For fractured samples, the cross-sectional flow area, A, is related to the fracture geometry and differs both between samples and with stress changes for a given sample.

This leads to high variability of fracture permeability both within and between experiments. Transmissivity estimates, however, can be derived without knowledge of A from $T_0 = 1/a'$ for each pressure/temperature scenario using the modified Forchheimer Plot method described above, and enable comparison between different stress scenarios and also between samples.

In section 2.3 it is shown that, for a linear flow regime where the cubic law is applicable, the hydraulic aperture, e_h, and fracture permeability, k_{frac} can be directly estimated from transmissivity, T, using the fracture width, w (Equation 2.7). By analogy, we can therefore estimate the true hydraulic aperture, and true fracture permeability using the same relationships, but with the true transmissivity, T_0, derived from the Forchheimer equation, where such a non-linear flow regime is present. We have adopted this method in Chapter 7, during result analysis.

The significance of non-Darcian or non-linear flow can be assessed for each pressure/temperature scenario using the dimensionless Forchheimer number, F_0, defined by Ruth and Ma [1992].

$$F_0 = \frac{k_0 \beta \rho v}{\mu} = \frac{b'}{a'} \frac{\rho Q}{\mu} \tag{2.14}$$

As discussed above, non-linear flow within rock fractures can result from microscopic inertial effects arising from flow along rough fracture surfaces, in addition to the onset of true turbulence at high velocity (high Reynolds number). Consequently, non-Darcian flow has been observed experimentally at relatively low Reynolds numbers [Ji et al., 2008, Ranjith and Darlington, 2007, Zimmerman et al., 2004]. The Forchheimer number (Equation 2.14) accounts for both fluid velocity and rock structure, as $\beta = b'A^2$ is structure dependent [Ruth and Ma, 1992]. The ratio b'/a', therefore, is the component of the Forchheimer number that gives an indication of the relative contribution to non-linearity of the sample geometry.

Incorporating the Forchheimer number, F_0, and the apparent transmissivity (Equation 2.13) into the Forchheimer equation (Equation 2.12), gives the following relationship (Equation 2.15).

$$\frac{1}{T_{app}} = \frac{1}{T_0}(1 + F_0) \tag{2.15}$$

Thus, non-linearity can be considered notable when the Forchheimer number becomes experimentally significant with respect to one, indicating the relative importance of inertial effects. Where inertial effects are negligible, the Forchheimer number tends to zero (and $T_{app} \approx T_0$).

2.5 CO_2 properties and fluid compressibility

Darcy's law as defined in Equation 2.4 is valid for laminar flow of incompressible fluids, as discussed in section 2.2. The analogous cubic law describing flow within a discrete fracture (Equation 2.5) and the associated hydraulic parameters: transmissivity (T), hydraulic aperture (e_h), fracture permeability (k_{frac}) and fracture hydraulic conductivity (K_{frac}) defined in section 2.3 are similarly valid for laminar flow of incompressible fluids. Where inertial effects become significant, deviations from these equations occur due to non-linear flow, as described in section 2.4. Deviations may also occur due to fluid compressibility, if fluid density and fluid viscosity vary significantly with pressure. This section presents details of CO_2 density and viscosity variations under the pressure and temperature conditions utilised within experiments. Density and viscosity variation is reviewed across the full range of experimental scenarios and the implications for use of the incompressible equations is considered.

2.5.1 CO_2 density and viscosity variation

Under reservoir conditions carbon dioxide is a supercritical fluid (Figure 2.2). In the supercritical phase, which occurs when pressures and temperatures exceed those of the critical point (P=7.38 MPa, θ=31.1°C), carbon dioxide behaves like a gas and expands to fill the available space; however it has a liquid-like density, which ranges from 200-900 kg/m^3 depending on pressure and temperature [Bachu, 2000]. This arises due to the convergence of gas and liquid densities under these conditions, thus the removal of any distinction between these two fluid phases.

Carbon dioxide is soluble in water: its solubility increases with pressure and decreases with temperature and water salinity [Bachu, 2000]. In its supercritical phase, carbon dioxide is immiscible with water [Holloway and Savage, 1993].

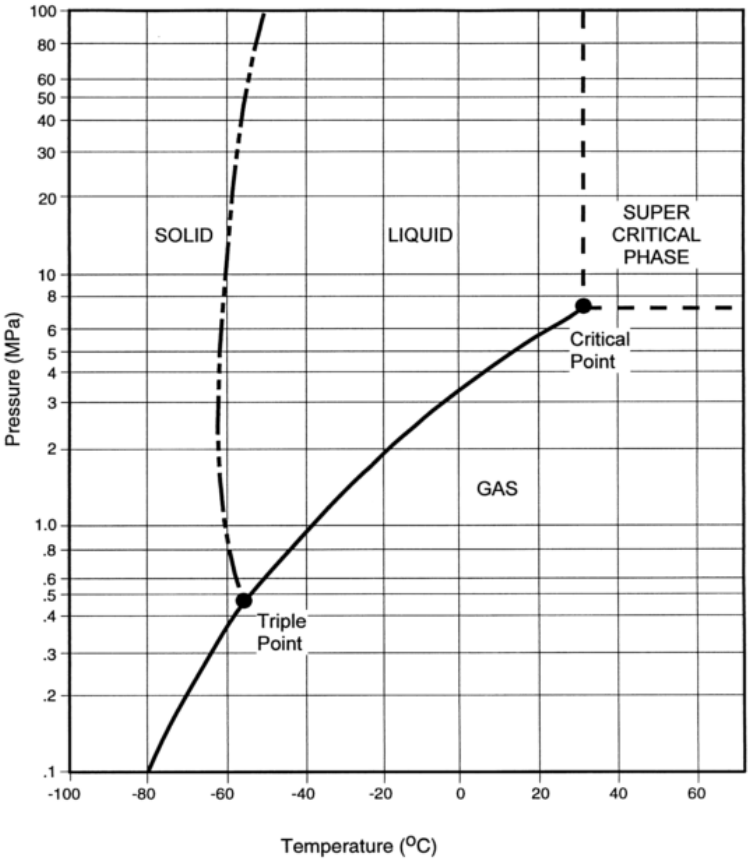

FIGURE 2.2: CO_2 Phase Diagram [Bachu, 2000]

The fluid regime of CO_2 cannot be described analytically by a simple equation of state. The literature therefore contains a large number of semi-analytical or empirical equations of state for carbon dioxide, that describe its thermo-physical properties i.e. [Huang et al., 1984, Peng and Robinson, 1976, Redlich and Kwong, 1949, Span and Wagner, 1996].

The Huang et al. [1984] equation of state has been used within this study to calculate CO_2 density for the wide range of pressure and temperature conditions tested during the experiments. The Huang et al. [1984] relationship is reported to be particularly suited to providing accurate density estimates around the critical region, and is accurate for supercritical CO_2 within the full experimental pressure and temperature ranges.

Density calculations are reliable to within 1% near the critical point, and to within 0.1-0.2% outside this region. The viscosity has been calculated using the Jossi et al. [1944] viscosity relationship for carbon dioxide. Both density and viscosity have been calculated using the above relationships with an in-house R program written by Mark Naylor. This allows rapid estimation of these parameters for the large number of experimental events assessed.

Figure 2.3 shows, on a log-linear plot, how the density of CO_2 varies with pressure within the experimental range tested using the Huang et al. [1984] equation of state. Downstream fluid pressure scenarios of 10, 20 and 30 MPa were adopted during the fracture flow experiments - these are indicated by vertical lines within the plot. Values are displayed for temperature cases of 40°C and 60°C respectively, close to the two experimental temperatures adopted (see Chapter 6). Water density has also been included within the figure for comparison. While water can be considered effectively incompressible, the supercritical CO_2 fluid is clearly compressible, with density variation most significant at the lower end of the pressure range displayed, closest to the critical pressure (7.38 MPa). Density is higher at the lower temperature (40°C) for both fluids. While the density difference between 40°C and 60°C is very small (within 1%) for water, it is significant for supercritical CO_2, particularly at the lowest fluid pressure tested (10 MPa).

Figure 2.4 shows how the viscosity of CO_2 varies with pressure at 40°C and 60°C, on a log-linear plot [Jossi et al., 1944]. As with the density figure, water viscosity has been included for comparison. The figure indicates that, whilst there is a difference in water viscosity between the two temperatures, there is negligible change to water viscosity with fluid pressure change. In contrast, CO_2 viscosity varies notably with both temperature and pressure. As with density, the viscosity variations with pressure are most significant around the low fluid pressure (10 MPa), where the viscosity difference due to temperature is also largest.

Across the experimental pressure and temperature conditions tested, both CO_2 density and viscosity increase with pressure and decrease with temperature. Supercritical CO_2 is of significantly lower density and lower viscosity than water.

Figure 2.5 illustrates how the fluid density/viscosity ratio varies with pressure at both the experimental temperatures tested. This is of particular importance as the hydraulic

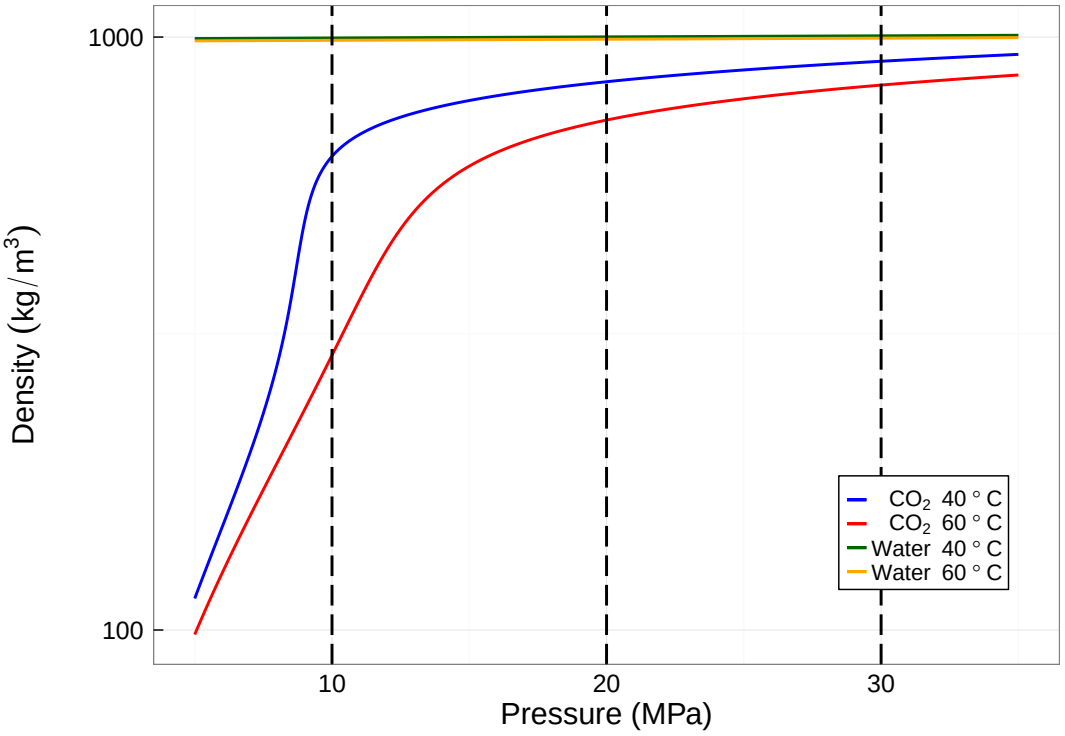

FIGURE 2.3: CO_2 density as a function of pressure (log-linear scale) [Huang et al., 1984]

conductivity, K, is a function of the fluid density/viscosity ratio, as well as of permeability, k (Equation 2.9). Thus, whilst permeability, k, is an intrinsic property of the rock sample (under given stress conditions), the hydraulic conductivity is influenced by fluid properties. The Reynolds number, a measure of the ratio of inertial to viscous forces, is also a function of the ratio of fluid density/viscosity, in addition to flow rate, and thus is similarly affected by fluid property changes (Equation 2.11).

Figure 2.5 shows that, for CO_2 at both 40°C and 60°C, the density/viscosity ratio decreases as the pressure increases within the experimental range. This indicates that, for a given fracture geometry (fixed permeability) and a given flow rate through the sample, the fluid property changes that occur as CO_2 pressure is increased (from 10 MPa to 30 MPa) contribute to a reduction of both hydraulic conductivity and Reynolds number. The figure also indicates that the density/viscosity ratio (and thus Reynolds number and hydraulic conductivity) are greater at the higher temperature (60°C) within the pressure range of interest.

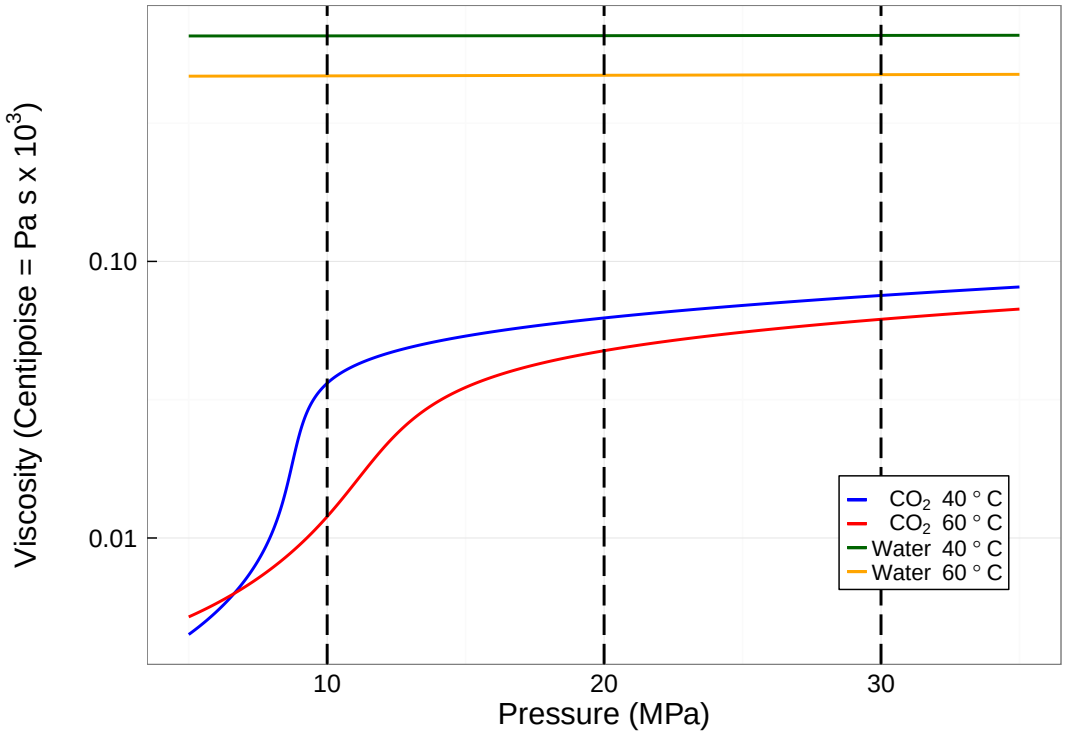

FIGURE 2.4: CO_2 viscosity as a function of pressure (log-linear scale) [Jossi et al., 1944]

The reduction of density/viscosity with increasing pressure, and increase of density/viscosity with increasing temperature indicate that, between experimental pressure scenarios, the viscosity changes are more significant than the density changes for CO_2 under the experimental pressure and temperature ranges. Thus fluid viscosity, rather than fluid density, is the influential or controlling parameter. Where mechanical influences on fracture conductivity are negligible (i.e. constant stress conditions, see section 2.6), higher CO_2 fluid pressures (higher viscosities) are therefore associated with lower hydraulic conductivities, while higher temperatures (lower viscosities) are associated with higher hydraulic conductivities.

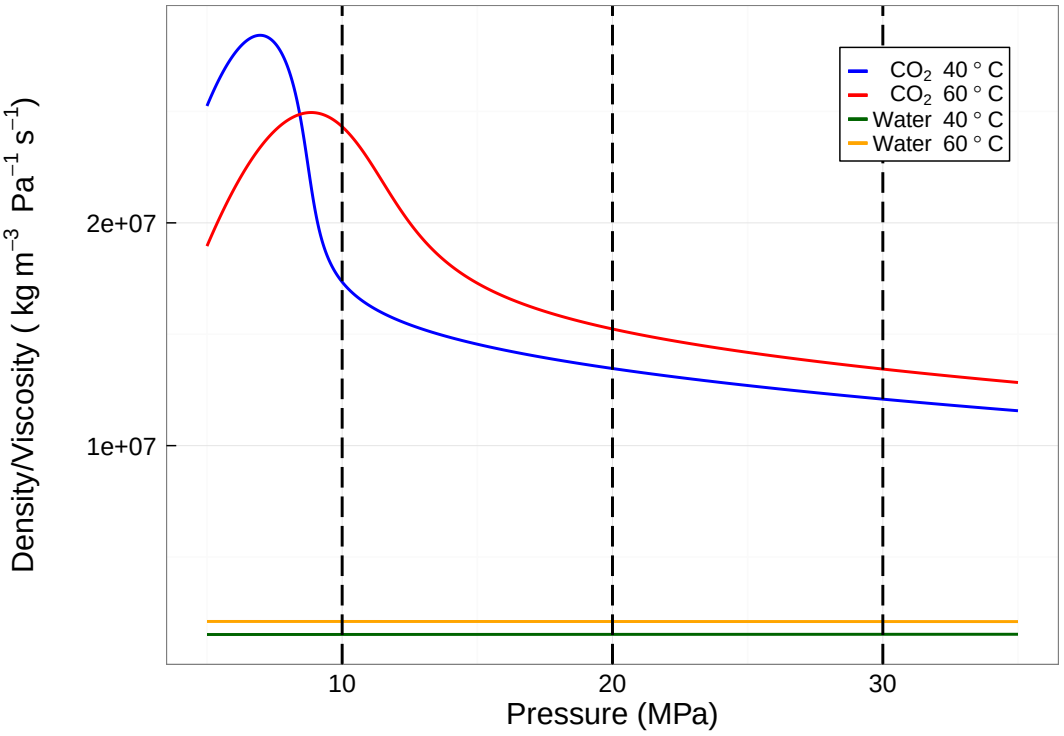

FIGURE 2.5: Fluid density/viscosity ratio as a function of pressure (linear scale)

2.5.2 Implications of CO_2 density and viscosity variation during experiments

We can see from subsection 2.5.1 that both density and viscosity variation is significant between the fluid pressure and temperature scenarios tested within experiments (see Chapter 6 for details), due to large step changes in both downstream fluid pressure, P_{ds} (10 MPa step change, typically) and temperature (20°C step change). Density and viscosity variations are most significant close to the critical point, therefore parameter variation is much greater between the P_{ds} = 10 MPa and P_{ds} = 20 MPa scenarios than between the P_{ds} =20 MPa and P_{ds} = 30 MPa scenarios. This has consequences for both hydraulic conductivity and Reynolds number variation between scenarios, as these are both a function of density/viscosity. Under constant effective stress, hydraulic conductivities and Reynolds numbers are highest during the low fluid pressure, high temperature scenarios, and are lowest during the high fluid pressure, low temperature scenarios.

In addition to density and viscosity changes between experimental scenarios, density and viscosity also varies across experimental samples during each steady state flow experiment, due to the fluid pressure gradient. If density and viscosity variation across the sample is significant, use of the incompressible form of Darcy's law (Equation 2.4) may not be appropriate.

Darcy's law for incompressible laminar flow (Equation 2.4) states that the volumetric flow rate is directly proportional to the pressure gradient causing the flow. During steady flow of incompressible fluids, the mass flow rate and the volumetric flow rate remain constant from point to point along the flow system, as the density remains constant. During steady flow of compressible fluids, however, the mass rate of flow, $G = \rho \mathrm{u}$, remains constant from point to point due to mass conservation (i.e. $\rho_1 \mathrm{u}_1 = \rho_2 \mathrm{u}_2$), but the volumetric flow rate changes as a consequence of density variation. Thus, during one dimensional steady state flow, combining mass conservation with Darcy's law (Equation 2.3) results in Equation 2.16 [Carman, 1956].

$$G = \rho_1 \mathrm{u}_1 = \rho_2 \mathrm{u}_2 = -\frac{k\rho}{\mu}\frac{\partial P}{\partial x} = constant \tag{2.16}$$

For isothermal flow of an ideal gas (where $P = \rho RT$), $P_1 u_1 = P_2 u_2 = Pu = constant$ as $P \propto \rho$, leading to Equation 2.17 [Carman, 1956].

$$P_1 u_1 = P_2 u_2 = Pu = -\frac{kP}{\mu}\frac{\partial P}{\partial x} \tag{2.17}$$

On integration, this leads to Equation 2.18 [Carman, 1956], which is a compressible form of Darcy's law valid for an ideal gas where viscosity, μ, is independent of P.

$$P_1 u_1 = P_2 u_2 = \frac{k}{\mu}\frac{(P_1^2 - P_2^2)}{2x} \tag{2.18}$$

A review of Figures 2.3 and 2.4 illustrate that supercritical CO_2 within the ranges of interest cannot be approximated as an ideal gas: density is not directly proportional to pressure within this range, and viscosity varies with pressure. For these reasons the

Carman [1956] equation (Equation 2.18) is not suitable for use during this supercritical CO_2 study.

In order to account for both CO_2 density and viscosity variation across the experimental sample when calculating sample transmissivity/permeability using Darcy's law, it would be necessary to integrate Equation 2.16, ensuring that both density and viscosity are expressed as a function of pressure, P:

$$G\int_0^L dx = \rho_1 u_1 \int_0^L dx = -k\int_{P_{us}}^{P_{ds}} \frac{\rho}{\mu}\, dP = k\int_{P_{ds}}^{P_{us}} \frac{\rho}{\mu}\, dP \tag{2.19}$$

Under isothermal conditions, Equation 2.19 reduces to:

$$\rho_1 u_1 L = k\int_{P_{ds}}^{P_{us}} \frac{\rho}{\mu}\, dP \tag{2.20}$$

where $\int_{P_{ds}}^{P_{us}} \frac{\rho}{\mu}\, dP$ is the area under the relevant temperature curve in the ρ/μ versus P plot, as illustrated using green shading in Figure 2.6 (a 60°C example).

As there is no analytical solution to this integral, solving Equation 2.20 for k is not straightforward. An approximation to this integral can be made by using the incompressible form of Darcy's law (Equation 2.4) for the mean fluid pressure, $\bar{P} = (P_{us} + P_{ds})/2$. This integral area approximation is illustrated in pink shading within Figure 2.6, and is determined by using the density (ρ), viscosity (μ) and volumetric flow rate (Q) associated with the mean pressure, $\bar{P}$, within Equation 2.4.

A review of density and viscosity variation across the experimental samples during the various temperature, pressure and flow rate scenarios undertaken within this study indicated that, in most cases, the fluid property variation across the sample resulting from compressibility was within the measurement uncertainty of the parameter (both density and viscosity). In these cases, compressibility effects did not require explicit consideration and use of the incompressible form of Darcy's law (Equation 2.4), or the analagous cubic law (Equation 2.5), as described above was appropriate for estimation of hydraulic parameters under a linear flow regime (with Forchheimer adaptation for non-linear flow regimes as described in section 2.4).

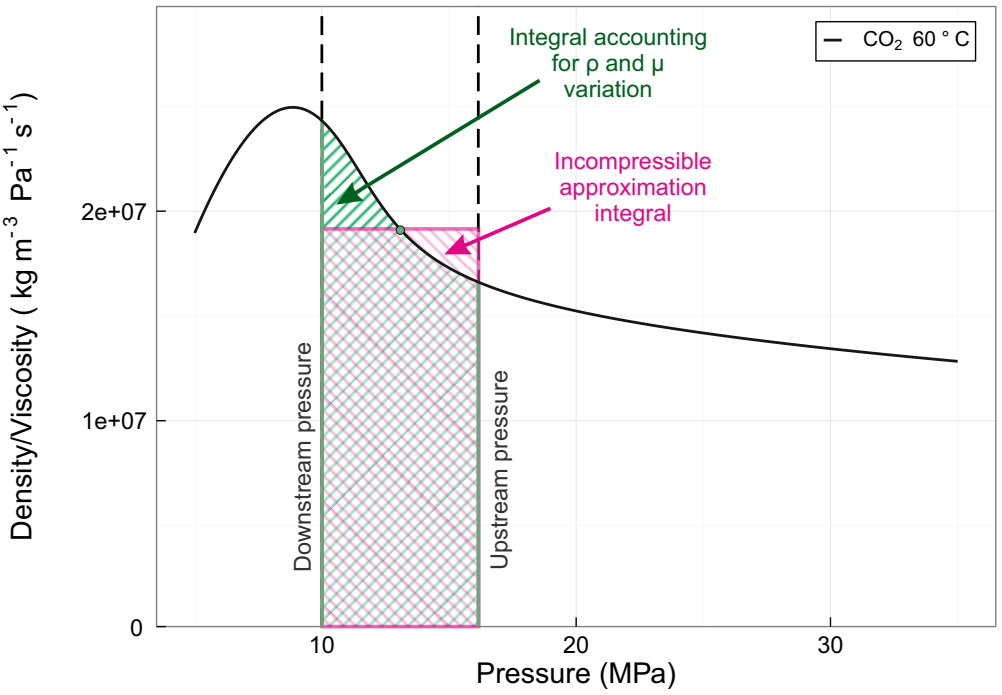

FIGURE 2.6: Example illustration of integral of ρ/μ from $P = P_{ds}$ to $P = P_{us}$ for θ = 60°C case.

For the lower permeability samples, differential pressures are relatively high and density and viscosity variation between the upstream and downstream ends of the sample was therefore sometimes found to be considerably greater than the measurement uncertainty in the parameter, particularly for the high temperature and low fluid pressure scenarios due to the sensitivity of fluid properties under these circumstances (Figure 2.5). In these cases, numerical integration was used to assess the error introduced by use of the incompressible approximation rather than the exact integral as illustrated in Figure 2.6. Across the range of experimental scenarios, the errors associated with using the Darcy approximation instead of numerical integration were found to be within 4% in all cases. As a result of these relatively small errors, and in the context of relatively high uncertainties (both measurement and calculation) elsewhere, it was considered that use of the incompressible approximation integral was appropriate across all experiments. This avoided the requirement for more complex numerical integration during result analysis, and justified use of the incompressible form of Darcy's law (Equation 2.4), or the analagous cubic law (Equation 2.5) for estimation of hydraulic parameters as

appropriate (with incorporation of Forchheimer non-linear adjustments as required, see section 2.4).

The use of incompressible Darcy's law as an approximation for estimation of hydraulic parameters is discussed further in the context of result analysis within section 7.4, where implications for the hydraulic parameter estimates where density and viscosity variations are most notable are discussed.

2.5.3 Klinkenberg effect

The Klinkenberg effect, or 'slip phenomenon' arises during the flow of low density fluids (usually gases) within extremely small flow conduits, and results in higher observed permeabilities than those predicted using Darcy's law [Klinkenberg, 1941]. The Klinkenberg effect occurs when the mean free path of the fluid molecules approaches the dimensions of the flow conduit. In this scenario, the fluid velocity profile is not parabolic with zero velocity at the conduit walls (as in laminar flow theory); there is in fact notable velocity at the interface which contributes additional flux. The Klinkenberg relationship defines the resultant apparent permeability, k_a, observed as a function of the true permeability of the rock system (Equation 2.21).

$$k_a = k\left(1 + \frac{4c\bar{\lambda}}{r}\right) = k\left(1 + \frac{b}{\bar{P}}\right) \tag{2.21}$$

where $\bar{\lambda}$ is the mean free path of the fluid molecules, c is a proportionality constant, r is the pore or flow conduit radius, $\bar{P}$ is the mean fluid pressure and b is a constant that is inversely proportional to the pore or flow conduit radius. The Klinkenberg effect is therefore greatest for small pore sizes or fluid pathways and relatively low fluid densities/pressures. It is negligible where $\bar{\lambda} \ll r$.

Klinkenberg's slip flow effect is suggested to be evident during the flow of sub- and supercritical CO_2 through both porous media [Nasvi et al., 2013] and naturally fractured black coal [Perera et al., 2011] within previous studies, with a more significant effect evident for subcritical or gaseous CO_2, as expected due to the lower density.

However, within this study, the discrete fractures examined are high permeability conduits within low permeability media, and as supercritical CO_2 is dense relative to

gaseous CO_2, it is not anticipated that the Klinkenberg effect will be significant under the conditions examined. The mean free path, $\bar{\lambda}$, of carbon dioxide under the experimental conditions examined ranges from 1×10^{-10} m to 7×10^{-10} m while analysis of results (see Figure 7.50, Chapter 7) indicates that the hydraulic apertures, e_h, of the fractures are within the range 7×10^{-7} m to 3×10^{-5} m. Thus, as $\bar{\lambda} \ll e_h$ during this study, the Klinkenberg effect is likely to be negligible and does not require explicit consideration.

2.5.4 CO_2 in the presence of swelling clays

Swelling clays are a group of clay minerals which are prone to large volume changes as a result of expandability (swelling or shrinking) in the presence of water. An example are the smectite group of clay minerals [Deer et al., 1992]. Seal rocks can commonly contain small quantities of swelling clays, which can nevertheless have a significant impact on seal rock properties. The behaviour of such swelling clays in the presence of CO_2 fluid could therefore be important.

A variety of experimental techniques have been adopted to investigate the response of smectites to supercritical CO_2 [Alotaibi et al., 2012, De Jong et al., 2014, Giesting et al., 2012, Loring et al., 2012, Schaef et al., 2012]. Results were found to be highly dependent on the initial hydration state of the clays [Giesting et al., 2012]. Clay expansion was observed in the presence of supercritical CO_2 for low initial hydration states (less than one layer of hydration), indicating the uptake of CO_2 via intercalation in a similar manner to water uptake [De Jong et al., 2014, Giesting et al., 2012, Loring et al., 2012, Schaef et al., 2012]. Little or no expansion was observed where clays were not initially hydrated [Giesting et al., 2012], while high initial hydration state clays (2 or more layers of hydration) were observed to dehydrate in the presence of supercritical CO_2 [Alotaibi et al., 2012, Schaef et al., 2012].

These findings imply that in the presence of swelling clays, where low hydration states exist within the subsurface, supercritical CO_2 could help to self-heal fractures. Conversely, where initial hydration of swelling clays is high, supercritical CO_2 could cause dehydration which could increase fracture apertures, or even result in additional micro-fracturing. Where extensive swelling effects occur, this could have wider implications for the resultant stress state of the seal rock layer, with the potential for induced faulting which could increase migration pathways for CO_2 leakage [Haszeldine, 2006].

Results from mineralogical analysis of the seal rock samples utilised within this study indicate that swelling clays are not present within the samples used within this study (section 3.4.1). It is therefore assumed that, despite a small degree of uncertainty in the results of the x-ray diffraction (XRD) analysis, that no swelling clay effects will be present during the experiments undertaken during this study.

2.6 Fracture mechanics

2.6.1 Analysis of stresses

Stress, σ (Pa), is defined as applied force per unit area (F/A). Stresses normal to a plane are defined as positive when compressive, and negative when tensile. The application of stress to a solid results in deformation, known as strain, ϵ (dimensionless), defined as the ratio of the change in length as a result of deformation, Δl, against the original length, l: $\epsilon = \frac{\Delta l}{l}$.

The stress/strain relationship is linear for most intact rocks (known as linear elasticity) and can be represented by $\sigma = E\epsilon$, where E is the Young's modulus, a constant describing the modulus of elasticity, or 'stiffness', for a particular rock type. High E values indicate high stiffness materials, while low E values imply high deformability.

Where fractures are present within rock, the observed strain resulting from an applied stress will deviate from that suggested by the Young's modulus due to additional deformation associated with the rock fracture. Potential fracture changes are presented in section 2.6.2.

Figure 2.7 shows the principal stresses acting on the fractured core sample geometry adopted during this study. Normal stress, σ_n, refers to the resultant stress acting normal to a plane and is defined in Equation 2.22 [Jaeger and Cook, 1979].

$$\sigma_n = l^2\sigma_1 + m^2\sigma_2 + n^2\sigma_3 \tag{2.22}$$

where l, m, and n are directional cosines relating to the angle between the direction of the normal stress and the principal axes. With reference to Figure 2.7, we can see

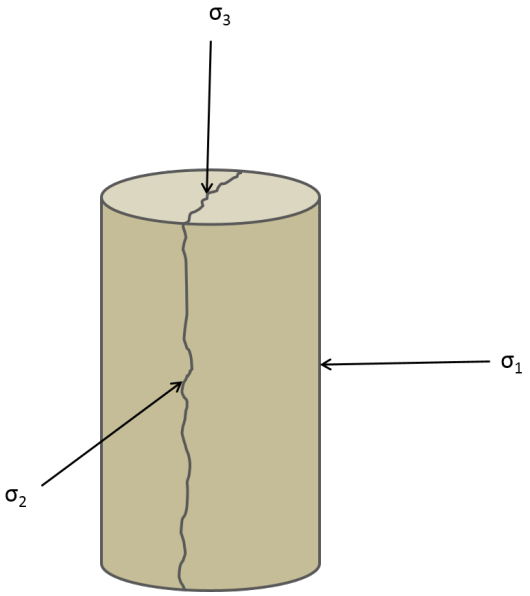

FIGURE 2.7: Principal stresses acting on fractured core sample geometry adopted during this study

that for the case of our discretely fractured core samples where σ_n is defined as acting normal to the fracture plane, $l = \cos 0^\circ = 1$, $m = \cos 90^\circ = 0$ and $n = \cos 90^\circ = 0$. Thus, $\sigma_n = \sigma_1$.

During the experiments within this study, the uniaxial pressure cell (see Chapter 5, section 5.3.2.1) enables the radial confining stress, σ_c, which acts externally on the sample and contributes equally to σ_1 and σ_2 to be controlled. The applied fluid pressure provides an internal stress contribution which acts equally in all directions but is opposite in sign to the confining stress, acting outwards rather than inwards. The fluid pressure within the sample fracture is controlled during this study (see Figure 2.1 and Chapter 5 for details). The design of the cell is such that stainless steel end platens are fixed in place at the core ends when the system is not under stress and no mechanical axial load is applied. Thus, σ_3 is determined by the fluid pressure acting on the core, assuming that the axial stress induced in response to any resultant radial strain is negligible. Therefore, for the loading geometry adopted within this study, the axial stress is smaller than the radial stress. In cases where the axial stress is significantly greater than the radial stress, the axial stress could impact the fracture aperture. However, this is not the case during this experimental study.

Terzaghi [1923] experimentally demonstrated the relationship between confining stress, σ_c, and pore pressure, P_p, for porous media which led to the effective stress law presented in Equation 2.23. This suggests an equal and opposite contribution to the bulk effective stress, $\sigma_{eff_{bulk}}$ from the confining stress, σ_c, and pore pressure, P_p, respectively.

$$\sigma_{eff_{bulk}} = \sigma_c - P_p \tag{2.23}$$

The effective stress law is widely used within porous media [Jaeger and Cook, 1979]. However, a number of studies find that, under certain circumstances, the confining stress and pore pressure do not contribute equally. This generally occurs when the grain compressibility is significant [Biot, 1941, Nur and Byerlee, 1971]. Under these circumstances, the effective stress law is modified to Equation 2.24, where α is the Biot coefficient and is dependent on both the effective bulk modulus of the porous media and the grain bulk modulus. The factor α should be constant for materials which are linearly elastic, and is generally less than or equal to 1. Where grain compressibility is small, $\alpha \approx 1$. The α factor can be estimated from experimental data where permeability has been assessed for a range of confining and pore pressures.

$$\sigma_{eff_{bulk}} = \sigma_c - \alpha P_p \tag{2.24}$$

An equivalent effective stress law to Equation 2.23 is also commonly used for fractured media [Cho et al., 2013, Harpalani and Chen, 1997, Ranjith and Perera, 2011, Zhang and Nemcik, 2013] (Equation 2.25), where σ_{eff} is the effective stress acting on the fracture, and P_f is the mean fluid pressure within the fracture.

$$\sigma_{eff} = \sigma_c - P_f \tag{2.25}$$

Application of this effective stress law (Equation 2.25) to the fractured sample (Figure 2.7) suggests that the resultant stress acting normal to the fracture plane, $\sigma_n = \sigma_1 =$

$\sigma_{eff} = \sigma_c - P_f$. Thus, increasing the confining stress increases the normal stress across the fracture, while increasing the fluid pressure, P_f, reduces the normal stress.

Similarly to porous media, confining pressure and fluid pressure are not always found to contribute equally, giving rise to Equation 2.26 (equivalent to Equation 2.24 for fractures) [Walsh, 1981]. Within Equation 2.26, α is found to be dependent on fracture surface topography as well as the bulk moduli.

$$\sigma_{eff} = \sigma_c - \alpha P_f \tag{2.26}$$

α is found to be close to unity for fractures comprising of smooth, ground surfaces, while α <1 where fracture surface topography is rough and jagged [Kranz et al., 1979, Walsh, 1981]. A minimum α of 0.5-0.6 was observed during the experiments of Kranz et al. [1979] where fluid pressures within the range 20-160 MPa and confining pressures within the range 100-180 MPa were tested on Barre granite fractures.

Fluid pressure contributions were reportedly found to be more significant than confining stress (α>1) in a few sandstone fracture cases [Walsh, 1981], with α values as high as five observed. It was suggested that this was due to the presence of clays within the fracture space. Pore pressure contributing more significantly than confining pressure to sample transmissivity (α>1) has also previously been observed within porous media (Equation 2.24); this was similarly thought to be related to the presence of highly compressible clay material within the pore space [Zoback and Byerlee, 1975]. In the context of fractures, the confining pressure is an external stress acting to close the fracture aperture. This stress will be focussed on the contacting asperities, a relatively small proportion of the fracture dimensions, with relatively low compressibility/high stiffness. However, the pore pressure is an internal stress that acts on the whole fracture surface. It is possible that deformation of higher compressibility surface material between contacting asperities may occur due to an increase in pore pressure, or internal stress, which could not occur as a result of a similar magnitude change in external confining pressure. This is a similar explanation as that offered by Zoback and Byerlee [1975] on the pore scale. Under such circumstances mechanical deformation may not be linearly elastic, and α may not remain constant for a given sample.

The above analysis of stresses, of relevance to the experimental geometry utilised during this study, focuses on normal compressive loading of fractures resulting in minimal induced shear stress. Within the subsurface, fractures commonly also experience a component of shear stress, σ_s, which acts tangentially to the fracture plane (Figure 2.8).

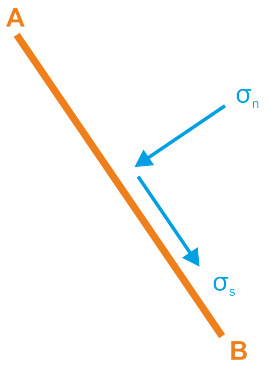

FIGURE 2.8: Normal stress and shear stress acting on fracture plane AB

Shear stresses can result in slip or displacement between fracture surfaces, which can have significant implications for fracture surface geometry, fracture aperture, and thus fracture transport properties [Cuss et al., 2011, Gentier et al., 1997, Guglielmi et al., 2015, Javadi et al., 2014, Olsson and Barton, 2001]. Breakage of asperities, clay smearing and generation of fault gouge are some of the fracture alterations that may result from shear slip. Offsetting of fracture surfaces has been undertaken during this experimental study (see section 6.2 and section 7.2) which was found to significantly increase fracture transmissivity. However the response of fracture transmissivity to active shearing is complex due to potential fracture alterations mentioned above and has not been considered within this study.

2.6.2 Mechanical response of fracture to stress changes

An increase in normal stress acting on a fracture results in fracture aperture closure or deformation. This can result from:

1. elastic compression of the contacting fracture asperities;
2. elastic compression of the fracture wall between contacting asperities;

3. plastic deformation of the contacting asperities and/or fracture wall.

A decrease in normal stress acting on a fracture conversely results in fracture aperture opening, generally due to elastic expansion of the contacting asperities and/or the fracture wall between the contacting asperities. The magnitude of aperture change with stress variation is dependent on both the rock and fracture properties [Duan et al., 2013].

As discussed in section 2.6.1, normal stress can be increased through an increase in the external confining pressure, σ_c, or a decrease in the fluid pressure, P_p, and vice versa. The contribution of each is determined by Equation 2.24, where α is dependent on the fracture geometry, the effective bulk modulus, and the grain modulus. In many cases $\alpha \approx 1$ is found to be a suitable approximation.

A number of studies have examined normal stress loading or stress cycling on real rock fractures while assessing the resultant closure or displacement of rock fractures from deformation [Bandis et al., 1983, Duan et al., 2013, Goodman, 1976]. The relationship between normal stress and rock fracture closure was found to be highly non-linear resembling a hyperbola, with the rate of change of displacement (or fracture aperture closure) reducing as the normal stress increases. This is due to the increased stiffness of the fracture as normal stress increases [Jaeger et al., 2009]. Bandis et al. [1983] and Duan et al. [2013] also found that the loading/unloading process was hysteretic with a component of inelasticity and permanent set/closure also observed. These experiments were undertaken on fractures within a range of rock types: limestone, dolomite, dolerite, siltstone, slate and tight sandstone. The inelastic or plastic component was however very limited during experiments on tight sandstone, due to the high indentation hardness of the rock [Duan et al., 2013].

Figure 2.9 is taken from Bandis et al. [1983], and illustrates the non-linear asymptotic relationship between normal stress and fracture displacement/closure; the hysteresis between loading/unloading; and the resultant inelastic permanent set, observed for a range of samples. Bandis et al. [1983] also found subsequent stress cycles showed similar behaviour but for each subsequent cycle a smaller magnitude of closure, and less hysteresis and inelasticity was observed - this can also be seen clearly within Figure 2.9. Barton et al. [1985] suggested that the hysteresis and inelasticity could be a

laboratory artefact, and that the fourth loading cycle may approximate undisturbed in-situ conditions.

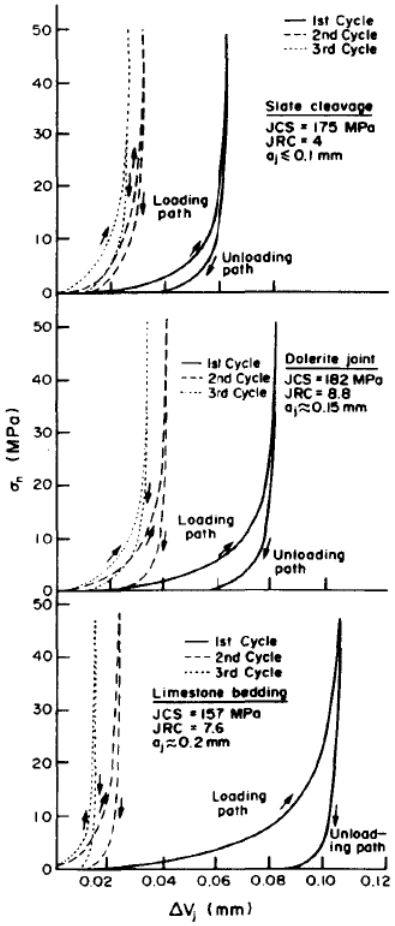

Fig. 3. Normal stress (σ_n) vs closure (ΔV_j) curves for a range of *fresh* joints in different rock types, under repeated loading cycles.

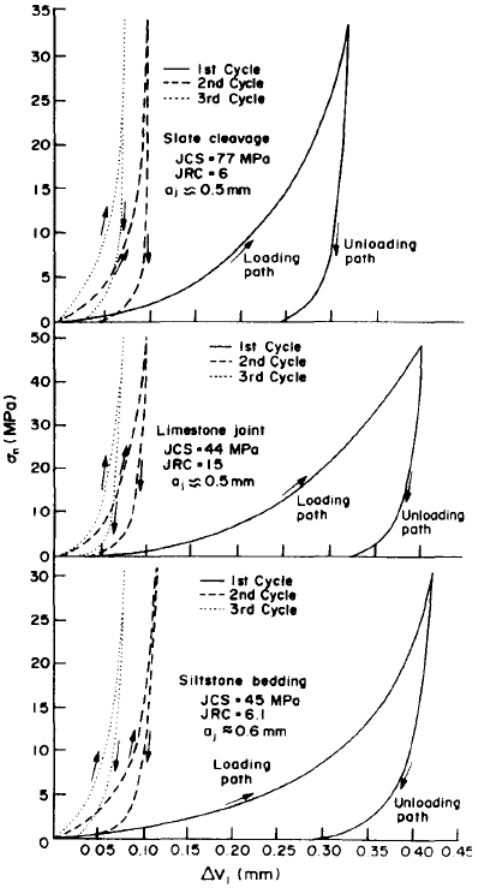

Fig. 4. normal stress (σ_n) vs closure (ΔV_j) curves for a range of *weathered* joints in different rock types under repeated loading cycles.

FIGURE 2.9: Normal stress versus closure curves, taken from Bandis et al. [1983]

Empirical relationships describing fracture closure as a function of normal stress were developed from the experimental observations described above [Bandis et al., 1983, Goodman, 1976]. Use of such empirical relationships, along with statistical properties of fracture surfaces and conceptual models, has enabled a variety of fracture deformation models to be developed which represent both the elastic and plastic deformation processes observed, for example Brown and Scholz [1986], Greenwood and Williamson [1966], McCraw et al. [2016].

The magnitude of mechanical response is dependent on fracture surface geometry, fracture surface and rock stiffness, and the elastic modulus of the fracture. Temperature can influence fracture surface and intact rock stiffness, as well as the elastic modulus of the fracture. Thus, in addition to alteration of fluid properties (section 2.5), temperature change may also affect the mechanical behaviour of fractures during experiments and assessment of temperature effects is considered during this study (Chapter 7).

2.6.3 Hydromechanical behaviour

We see from section 2.3 that fluid flow behaviour within fractures is determined by fracture surface geometry and mean fracture aperture. The mechanical response of a fracture to stress changes (section 2.6.2) therefore affects the fluid flow through the fracture, as fracture geometry and aperture vary. Within this study, we use the fracture flow theory within sections 2.3 and 2.4 to estimate hydraulic parameters (i.e. transmissivity and hydraulic aperture) during the fracture flow experiments. Observed variation in these hydraulic parameters can be used as a proxy for assessing mechanical fracture changes that result from stress changes (both external and internal). Due to roughness and asperity contact hydraulic aperture reduction is not equivalent to mechanical joint closure [Jaeger et al., 2009, Tsang and Witherspoon, 1981, Zimmerman and Bodvarsson, 1996]. However, it provides a valuable qualitative indication of mechanical change. We are primarily interested in the influence of mechanical and fluid property changes on the hydraulic behaviour (transmissivity and conductivity) of fractures, therefore the response of hydraulic parameters is key, and a qualitative assessment of fracture closure is sufficient. Pre- and post-experiment characterisation of fracture surface geometry has also been undertaken (Chapter 4), and provides some additional evidence for plastic deformation of fracture surfaces.

Chapter 3

Sample sourcing, preparation and characterisation

3.1 Introduction

Successful sample sourcing and preparation was essential to enable an experimental study of fracture flow mechanisms to be undertaken. Significant problem solving and method development was required during this stage of the project. Suitable representative rock samples of adequate size had to be identified, located and obtained. The sample preparation process had to be developed, which involved significant trial and error due to the original nature of the research. A range of sample characterisation techniques were adopted to gain information about the mineralogy, matrix porosity and permeability and sample hardness. Fracture surface characterisation was also undertaken (see Chapter 4. While some of these characterisation techniques were carried out within the University of Edinburgh, using readily available equipment and established techniques, liaison with other departments and Universities was required to identify and test equipment and/or develop and adapt techniques to solve non-standard problems, in particular that of undertaking fracture surface characterisation.

This chapter describes the sourcing of suitable analogue rock material (section 3.2); sample coring and preparation of a subset of this material for use within flow experiments (section 3.3); and associated sample characterisation undertaken (section 3.4).

3.2 Identifying and obtaining suitable samples

Cored seal rock samples, both shale and carbonate, that are representative of those at potential future geological storage sites were required to carry out the flow experiments. For use within the experimental rig, the samples must be cylindrical cores of 38 mm diameter no longer than 70mm. In addition, as we are specifically studying fracture mechanisms, the samples must contain discrete longitudinal fractures. The sample dimensions are constrained by the core holder, and are relatively large in comparison to typical samples used in flow and mechanics tests (see Andreani et al. [2008], Smith et al. [2013], Wollenweber et al. [2010], for example).

Sampling naturally occurring fractures within seal rock samples from potential storage sites is challenging as seal rock is seldom cored and discrete natural fractures are relatively rare. In addition, there are challenges in coring discretely fractured rock without inducing further mechanical damage. One of the first major challenges of the project was identifying and negotiating use of well core samples suitable for the experimental work.

Natural CO_2 reservoirs exist in the subsurface, and studying these natural CO_2 reservoirs as analogues for CO_2 storage sites is extremely valuable to gain understanding of the long term behaviour of CO_2 within the subsurface. Ideally experimental core samples would be taken directly from key natural analogues sites, for example the Fizzy Field, Southern North Sea [Miocic et al., 2014]. However no suitable seal rock well core samples were available from natural CO_2 reservoirs. Alternative sources of typical seal rock were therefore identified and investigated.

The subsections below discuss the samples sourced during this project: these comprise core samples (both fractured and unfractured) from both well core and outcrop analogues. Where natural fractures within core samples were not available, cored samples were artificially fractured during the sample preparation stage. This process is discussed within section 3.3.2.

A wide range of rock samples were collected. These are detailed in the subsections below, and consist of:

1. Cambrian shale (seal rock analogue, sourced from quarry, Warwickshire, UK)

2. Kimmeridge Clay (seal rock sampled from East Brae field, North Sea)
3. Zechstein Dolomite (seal rock sampled from Wissey and Wildcat fields, Southern North Sea)
4. Heletz Shale (seal rock sampled from Heletz pilot-scale CO_2 injection experiment, Israel)

Due to both the complexity of the rig design and build phase of the project, and the comprehensive nature of the flow experiments carried out on each experimental sample, a limited selection from this collection were used for the main CO_2 fracture flow experiments (see Chapters 6 and 7 for details). These consisted of:

- an artificially fractured Cambrian shale sample (source: quarry, Warwickshire, UK),
- two artificially fractured Kimmeridge Clay samples (source: East Brae Field, North Sea),
- a naturally fractured Zechstein Dolomite sample (source: Wissey Field, Southern North Sea).

In addition, preliminary CO_2 flow experiments were also undertaken on a second artificially fractured Cambrian shale sample (referred to within section 3.3.3).

The East Brae samples were found to be of very low permeability when the artificially fractured surfaces were matched, relative to the other fractured samples tested. This made comprehensive testing within the rig design described in Chapter 5 difficult. A $\sim$1 mm offset was therefore created between fracture surfaces of one of the samples to assess the impact of fracture offsetting, and an additional set of experiments was undertaken on this offset sample (see section 6.2). There was some variation in the sample preparation and characterisation undertaken on each of the samples. This is discussed within sections 3.3 and 3.4. Unused sample material is available for future research studies.

3.2.1 Shale sourced from UK quarries - Cambrian Stockingford Shale

The Stockingford Shale Group consists of Cambrian muds that were deposited on a deep sea floor in a gently subsiding craton [Brenchley and Rawson, 2006]. A sample block of this dark grey, relatively homogeneous, low permeability Cambrian shale was kindly provided to us by a local masonry supplier, Forth Stone Ltd. Despite being sourced from a near surface location (Warwickshire quarry), this low permeability shale has hydraulic properties that would be desirable within the seal rock of a potential CO_2 storage location. It can therefore be considered to be representative for the purposes of laboratory experiments. Use of outcrop and near surface analogues is common practise within research studies due to the typically very limited availability of well core, and can be of great value providing that any limitations of the analysis are considered and evaluated [Alexander, 1992]. Core material from this block sample was used within flow experiments undertaken during this project. The shale block is shown, after coring has been carried out, in Figure 3.1.

FIGURE 3.1: Cambrian shale block provided by Forth Stone Ltd. Pictured here after coring

3.2.2 Kimmeridge Clay (East Brae)

The basinal mudstones of the Kimmeridge Clay Formation are extensive across the North Sea, and commonly act as a seal [Glennie, 1984]. Permission was granted by Marathon Oil UK Ltd to sample Kimmeridge Clay from several East Brae well cores for use within this project.

The East Brae field is a gas condensate field located within the South Viking Graben of the North Sea. The thick, massive, predominantly medium-grained reservoir sandstones were deposited via high density turbidity currents within a marine environment during the Late Jurassic period. The field is enclosed by the Kimmeridge Clay Formation, which acts as both source and seal rock for the field [Branter, 2003].

A study of the nearby Miller field, which is also vertically sealed by Kimmeridge Clay, suggests that naturally occurring CO_2 has been retained within the field for around 120 million years [Haszeldine et al., 2006]. This suggests the Kimmeridge Clay could be an effective seal for CO_2 storage sites. There has been industry interest in developing storage sites within this geological province [Haszeldine et al., 2006]. This makes our laboratory studies on Kimmeridge Clay particularly relevant.

Core viewing and sampling of Kimmeridge Clay seal rock from the following wells was undertaken: 16/3a-E1; 16/3a-E5; 16/3a-E10. Eight samples were selected from 16/3a-E5, with associated depths ranging from 17357' to 17389' (5290.4 m to 5300.2 m). In addition, four samples were selected from 16/3a-E10, with associated depths ranging from 14929' to 14934' (4550.4 m to 4551.9 m). Unfortunately there were no natural fractures available for sampling within the core available. Samples were therefore selected to be representative of the full lithological variety of seal rock present and ranged from relatively homogeneous shale to samples containing layering and marbling of coarser grained lighter coloured material. There was evidence of organic matter within thin layers in two of the samples (AA and A). A summary of sample information is provided in Table 3.1. The core samples were all 100 mm wide and had a maximum depth of approximately 70 mm.

Core material from sample B and D from well 16/3a-E10 was used within flow experiments undertaken during this project. For these samples (recovery depth:$\sim$4551 m) the associated in-situ temperature is 160°C [Harper, 1971]; pore pressure is 18-29 MPa [Branter, 2003]; and vertical stress is $\sim$103 MPa (using 1 psi/ft rule of thumb for siliclastic lithostatic pressure gradient).

3.2.3 Zechstein Dolomite (Wissey and Wildcat)

The Zechstein formation is the regional seal rock/caprock for the Permian Rotliegend formation, which is the main reservoir for gas fields in the Southern North Sea, including

Table 3.1: East Brae collected samples

Sample ID	Photo	Well	Depth	Sample length (mm)
AA		16/3a-E5	17357'/5290.4 m	255
AB	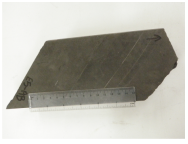	16/3a-E5	17362'/5291.9 m	210
AC		16/3a-E5	17365'/5292.9 m	160
AD	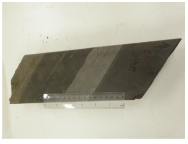	16/3a-E5	17338'/5284.6 m	285
AE	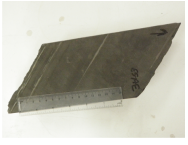	16/3a-E5	17340'/5285.2 m	205
AF	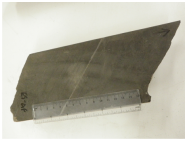	16/3a-E5	17344'/5286.5 m	215
AG		16/3a-E5	17378'/5296.8 m	250
AH	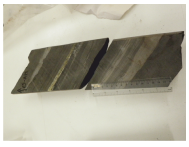	16/3a-E5	17388'/5299.9 m	325
A		16/3a-E10	14929'/4550.4 m	248
B		16/3a-E10	14931'/4551.0 m	170
C	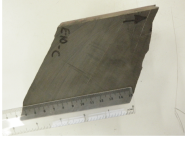	16/3a-E10	14932'/4551.3 m	110
D	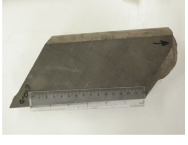	16/3a-E10	14933'/4551.6 m	180

the Fizzy Field natural analogue site [Glennie, 1984]. The Fizzy Field is a natural CO_2 field which has held CO_2 in the Rotleigend formation for several 10s of millions of years without any observed indication of leakage [Wilkinson et al., 2009, Yielding et al., 2011]. In addition to the Fizzy Field, there are a number of other CO_2 rich gas fields in the Southern North Sea which suggests that the Zechstein is in general a good CO_2 seal.

The Zechstein formation represents evaporitic cycles in a landlocked depression which was periodically catastrophically flooded by saline sea waters and in which shales, carbonates, anhydrites and salts up to several 100s of meters thickness were deposited [Legler and Schneider, 2008, Ziegler, 1990].

Digital well logs within the vicinity of the Fizzy Field were interrogated using the Oil and Gas UK CDA (Common Data Access Limited) Datastore (`http://www.oilandgasuk.co.uk/common_data_access.cfm`), to identify any wells where seal rock core was sampled and recovered, in the hope that representative Zechstein core from a nearby well could be obtained for use in experiments. The BGS UK Continental Shelf (offshore) hydrocarbon well collection has a comprehensive online database including core photographs, which was also utilised for identification of suitable potential samples. While the BGS have an extensive well core collection, it is not possible to sample pieces of core of sufficient size for use within our experiments. It was therefore necessary to approach well operators directly for sample sourcing. Figure 3.2 indicates the location of wells within the vicinity of Fizzy Field whose well logs suggested Zechstein core sampling was undertaken. Of these, core viewing and sampling permission was granted by Tullow Oil plc for Zechstein core from the Wissey field 53/04a-9 well and the Wildcat field 53/04-1 well. These wells are located approximately 25 km south-west of the Fizzy field (Figure 3.2). Core viewing and sampling was undertaken at the Kirk Petrophysics core store, Guildford.

Nine pieces of Zechstein core were sampled from the Wissey field 53/04a-9 well. The well core available was a half core, of 109 mm in diameter, with maximum sample depth ranging from 50-70 mm. The sample lengths selected vary from 103 mm to 253 mm, and were from in-situ depths of 5472' to 5642' (1667.9 m to 1719.7 m). The core material varied significantly with depth, with variations to the rock type, homogeneity, brecciation, colour, strength and fracture networks present. The core varied from mudstone to dolomite, and some contained significant halite veins or marbling. Fractures

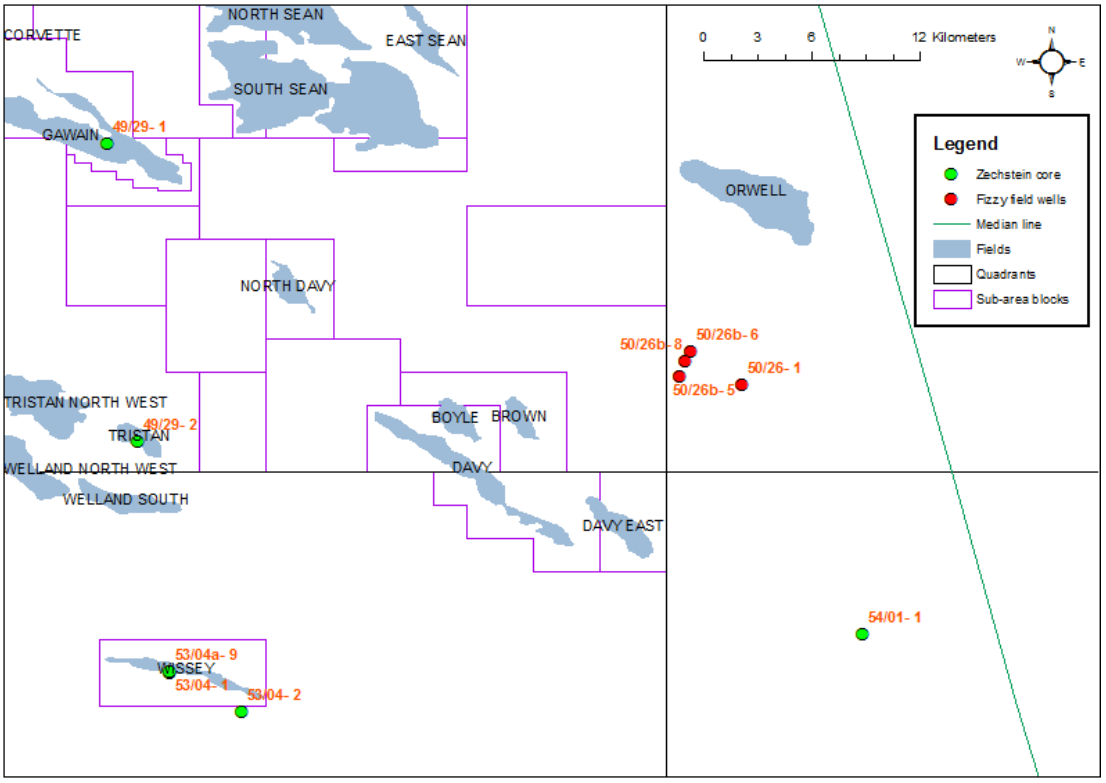

FIGURE 3.2: Locations of Zechstein core samples documented in well logs, relative to Fizzy Field wells

were present in a number of the samples selected - two pieces contained discrete longitudinal fractures, while two others contained complex fracture networks. Fractures along bedding planes were also present within other selected samples.

The Wildcat field 53/04-1 well core available was a 31 mm slice rather than a half core. This limited depth was not ideal for creating experimental samples. In addition, associated depth information was not available with the core. One 150 mm length Dolomite sample was obtained from this well, from a depth within the range 5618' to 5663' (1712.4 m to 1726.1 m).

A summary of the selected samples from Wissey and Wildcat core is provided in Table 3.2. Core material from Wissey sample 5 was used within flow experiments undertaken during this project. For this sample (recovery depth: 1684 m), the associated in-situ temperature is ~47°C [Harper, 1971]; pore pressure is 18.5 MPa [Noy et al., 2012]; and vertical stress is 38 MPa [Noy et al., 2012].

TABLE 3.2: Wissey and Wildcat collected samples

Sample ID	Photo	Well	Depth	Sample length (mm)
1		53/04a-9	5472'/1667.9 m	200
2	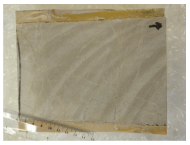	53/04a-9	5476'/1669.1 m	165
3	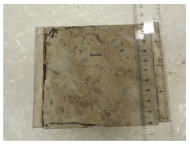	53/04a-9	5506'/1678.2 m	103
4	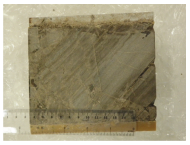	53/04a-9	5512'/1680.1 m	141
5		53/04a-9	5525'/1684.0 m	201
6		53/04a-9	5540'/1688.6 m	173
7	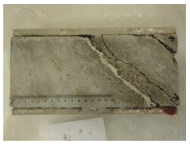	53/04a-9	5549'/1691.3 m	253
8	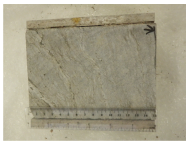	53/04a-9	5552'/1692.2 m	151
9	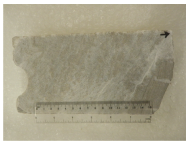	53/04a-9	5641'/1719.4 m	213
10	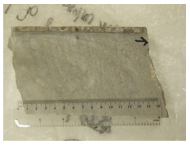	53/04-1	Unknown (within range 5618-5663'/ 1712.4-1726.1 m)	150

3.2.4 Heletz Shale

The Heletz deep injection experiment is a pilot-scale CO_2 injection experiment, undertaken within the MUSTANG and PANACEA EU research and development projects. The site is in Israel, located approximately 10 kilometres east of the city of Ashkelon in a rural area. The Heletz structure is a depleted oil field, and thus is well characterised. The reservoir, comprising of Heletz Sands sandstone, is located at a depth of 1650 m, with the structure encompassing an area of 10 km^2. Baseline pore pressure and temperature for the reservoir are 14.3 MPa and 64°C respectively [Niemi et al., 2016]. The seal rock is a claystone layer 40 m thick [Bensabat, 2013]. The seal rock is Lower Cretaceous encompassing: alluvial braidplain, tidal flat, tidal marsh-coastal swamp, inner shelf and meandering river. The rock consists of repeated regressive – transgressive (fluvial – marine) depositional sequences [McDermott et al., 2012, Steinberg et al., 2008].

Core samples were drilled during development of the pilot-scale project, therefore seal rock material was available for use within lab studies. The seal rock core sample was extremely heterogeneous: it contained significant sand lenses and pebbles. The seal rock core available was drilled from a depth of 1596 - 1596.5 m (5236.2'-5237.9'). Whole core sections were available for use. The core had been preserved in cling film and encased in resin within a metal box, as can be seen in Figure 3.7.

3.3 Sample preparation

Following the initial sample sourcing and collection stage of the project (section 3.2) it was necessary to review the collected samples and select a suitable subset from which to prepare discretely fractured 38 mm diameter cores for flow testing. In addition, unfractured 38 mm diameter core samples were required for matrix porosity and permeability testing, and further material preparation was required for mineralogical analysis (section 3.4).

A long, discrete fracture orientated approximately perpendicular to bedding within sample 5 of the Wissey 53/04a-9 samples (Zechstein Dolomite) was identified as an appropriate pre-existing fracture for flow testing. No other pre-existing discretely fractured samples appropriate for sample coring (and thus flow testing) were available

within the sample collection, therefore sample coring of a selection of unfractured rock samples from each of the three shale groups (Cambrian, East Brae, Heletz) was undertaken, and a method for artificially inducing discrete fractures within the cores was developed (section 3.3.2).

A number of stages are required to prepare samples for use within the flow rig. Due to the original nature of this research the sample preparation techniques have developed and evolved throughout the project. Reviews of initial experimental tests have suggested improvements and these findings are fed back into the sample preparation stage. This section outlines the sample preparation methods adopted and discusses the evolution of the methods where appropriate.

3.3.1 Sample coring and trimming

Sample coring was carried out at the University of Edinburgh using a rock coring pedestal drill with a 38 mm diameter diamond impregnated multi-cut cylindrical core drill bit (manufacturer: DK Holdings Ltd). Wet drilling was carried out with water supplied via the drill chuck.

Samples drilled from well core material (East Brae, Wissey, Heletz) were drilled perpendicular to the well core drill direction. This can be seen in Figure 3.3. This method was adopted to ensure the well core sample could be secured stably on the drilling table. Multiple 38 mm diameter sample cores were drilled from each large well core sample for both East Brae and Wissey. Due to the orientation of the well core, the 38 mm core samples acquired using this method are necessarily drilled parallel with the bedding planes such that the bedding planes run axially within the 38 mm sample.

A large block of **Cambrian** Stockingford shale was supplied by Forth Stone Ltd, Midlothian. Seven 38 mm diameter core samples were drilled from this block with an orientation perpendicular to the bedding plane, as this was practical given the available block sample. In addition, two samples were cored parallel to the bedding plane. The cored block and a sample cored perpendicular to the bedding plane are shown in Figure 3.4.

Samples were drilled from two pieces of **East Brae** well core resulting in three complete 38 mm diameter cores from each piece (four were attempted from sample D but the last

(A) Core drill

(B) Coring samples

(C) Coring East Brae samples

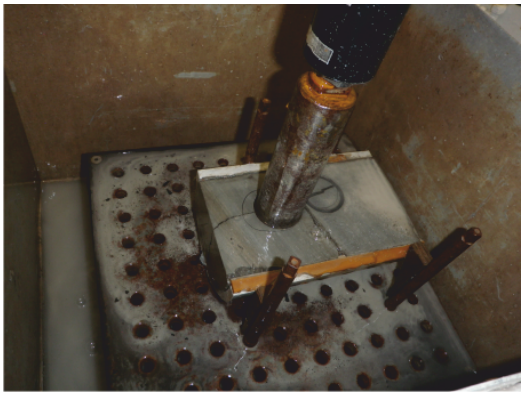

(D) Coring fractured Wissey samples

FIGURE 3.3: Coring 38 mm diameter samples

was of insufficient length). The samples selected for coring were relatively homogeneous in composition and structure (Figure 3.5). The samples were both from well 16/3a-E10, and were samples B (depth 14931'-14931'7"/4551.0-4551.1 m) and D (depth 14933'-14933'7"/4551.6-4551.8 m).

Four samples were drilled from the discretely fractured **Wissey** sample (sample 5, depth 5525'-5525'8"/1684.0-1684.2 m), as seen in Figure 3.6. The Wissey well core was seated within a metal casing and sealed in with resin - this helped stabilise the fractured well

(A) Cambrian vertical (perpendicular to bedding plane) core locations (V1-V7)

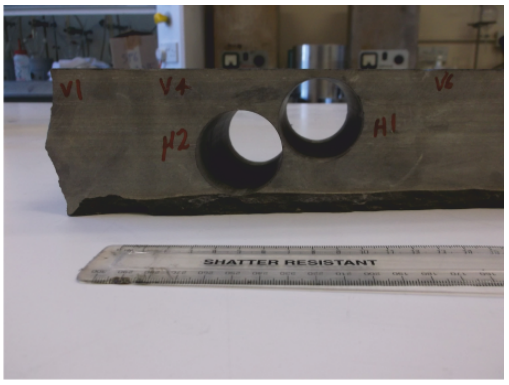

(B) Cambrian horizontal (parallel to bedding plane) core locations (H1-H2)

(C) Cambrian vertically cored sample

FIGURE 3.4: Cambrian shale core locations and cored sample

core during drilling, however it made sample core removal more difficult. The drilling action caused the fracture to open up during coring. Thus each of the samples cored consisted of two discrete pieces. This enabled surface geometry measurement to be undertaken on the exposed fracture surfaces (Chapter 4). However there is a risk that some mismatch may result when recombining fracture surfaces for the flow experiments.

The **Heletz** samples were full core samples, wrapped in cling film and encased in resin and a metal box. Six samples were cored from two well core pieces. Coring was undertaken through the resin, as can be seen in Figure 3.7.

Once cored, all 38 mm diameter samples required core ends to be trimmed and smoothed.

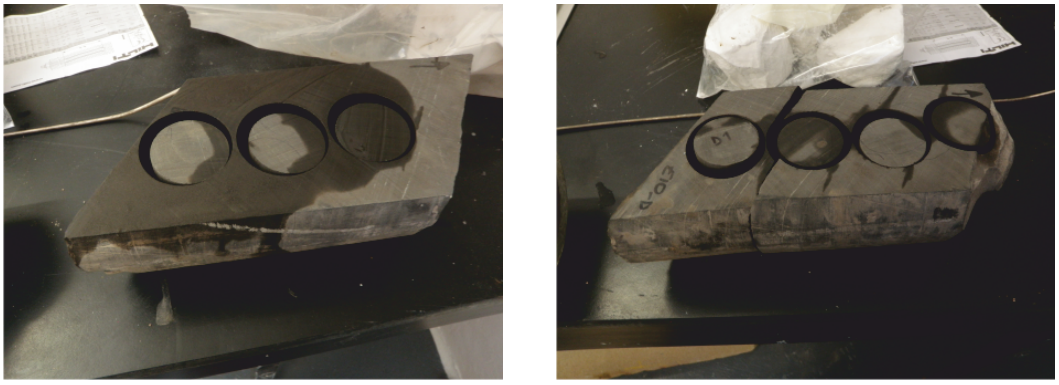

(A) East Brae sample B (core B1-B3, L-R) (B) East Brae sample D (core D1-D3, L-R)

FIGURE 3.5: East Brae cored samples

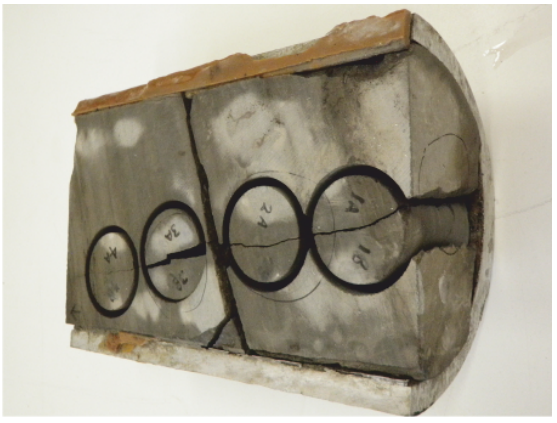

FIGURE 3.6: Wissey sample 5 - fractured core samples (cores W1-W4, located R-L)

(A) Heletz cored samples H1-H3 (B) Heletz cored samples H4-H6

FIGURE 3.7: Heletz cored samples

For successful loading into the experimental rig coreholder the core ends must be exactly orthogonal to the core axis. End trimming was carried out using a rock cutting circular saw (Figure 3.8). Subsequently, smoothing of the ends to ensure orthogonality was carried out using a lapping plate with the core placed within a custom-made cylindrical steel core holder (Figure 3.9). For the Wissey fractured samples, the two fractured core pieces were held tightly together with PTFE tape and an even pressure was applied to the sample from above using a 38 mm diameter cylindrical perspex core to ensure simultaneous and even smoothing of the two rock core pieces.

FIGURE 3.8: Circular saw used to trim core samples

(A) Steel core holder on lapping plate (B) Core inserted into steel holder

FIGURE 3.9: Lapping plate method used for end smoothing

3.3.2 Sample fracturing

Due to the lack of pre-existing discrete fractures within the Cambrian, East Brae and Heletz shale samples, it was necessary to develop a method of artificially creating discrete fractures.

The resultant discretely fractured core must contain a continuous discrete fracture lengthways along the cylindrical core to ensure that CO_2 can flow end-to-end along the core. Other than the presence of the discrete fracture, the core ends must be otherwise smooth and undamaged with no missing rock chips, to ensure adequate sealing and operation of the pressure cell end platens. There must be minimal damage to the core side surface to maintain the integrity of the core holder rubber sleeve liner at high confining pressures, specifically to avoid liner rupture. The fracturing technique should be repeatable, straightforward and reliable.

Various methods were considered and attempted. The successfully adopted method was developed in collaboration with Heriot Watt University. The fracturing method involves applying a sharp short direct force to the unfractured sample using a suitably sized chisel and hammer. A core support was required, which was custom built by the University of Edinburgh Geosciences mechanical workshop. This steel, semi-circular core support was built with an internal diameter of 40 mm, to allow some room for core movement during splitting while ensuring sufficient support for the core. A shallow groove was cut into the side of the core using a hacksaw to provide a placement location for the chisel (Figure 3.10). The chisel was then steadily held vertically in the placement groove as shown in Figure 3.10, while a hammer was used to apply a sharp blow to the chisel, resulting in the fracturing of the core sample.

Due to rock heterogeneity, creation of a clean fracture with minimal additional core damage did not occur every time, and thus some core samples had to be discarded. For successful lengthways fracturing, it was necessary to fracture the sample along the bedding plane for both East Brae and Heletz. Attempts to fracture these samples across the bedding resulted in significant core damage and oblique fracturing. Two Cambrian shale samples (V1 and V2) and two East Brae shale samples (B2 and D2) were successfully fractured, along with two Heletz samples (H2 and H6). Damage to the core side through chipped material at the chisel contact point was notable for the two Heletz samples, with sample H2 particularly damaged. The damage observed in

(A) Cutting a chisel placement groove

(B) Fracture creation

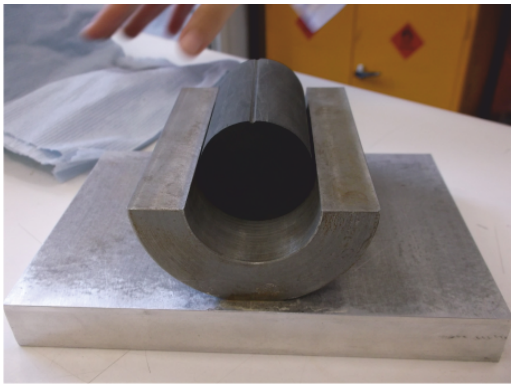

(C) The placement groove

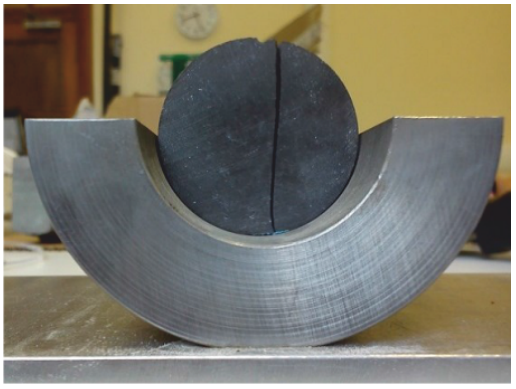

(D) The induced fracture

FIGURE 3.10: Creation of discretely fractured core sample

the Heletz cores is thought to be more significant than in the other cores due to the heterogeneous nature of the rock: this heterogeneity results in strength and cohesion variation throughout the core, therefore preferential fracture paths exist along weaker planes, which reduces the likelihood of a single discrete fracture occurring. As a result, the Heletz samples were not selected for CO_2 fracture flow experiments.

3.3.3 Post fracturing preparation

This stage of sample preparation has developed and evolved throughout the project due both to: (i) our treatment of the discrete fracture, and (ii) to issues with CO_2 reaction with the pressure cell rubber sleeve liner (see section 5.4.2 for further details). Figure 3.11 is a summary timeline of the method development options trialled during the project. The development of these preparation methods are discussed within the subsections below.

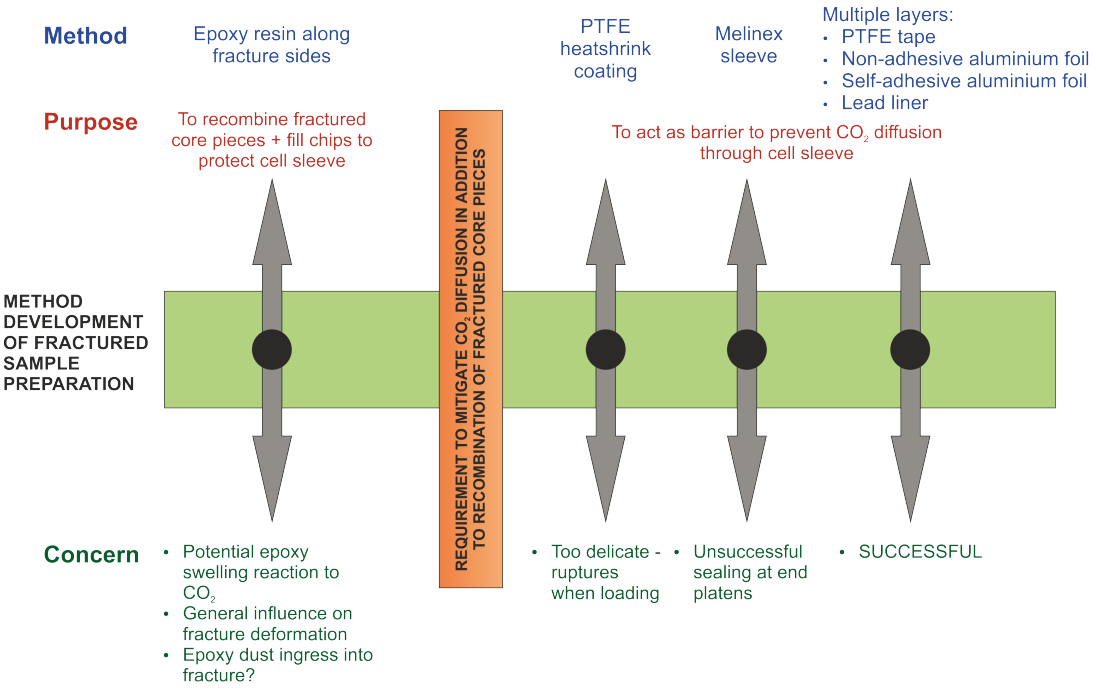

FIGURE 3.11: Timeline of method development associated with fracture sample preparation techniques

3.3.3.1 Recombining fractured parts

As outlined in section 3.3.2, the core sample sides must be smooth to avoid damage to the pressure cell rubber sleeve. In addition, the core ends must be smooth, exactly orthogonal to the core axis, and undamaged to ensure adequate closure and sealing of the pressure cell end platens. As the core sample is loose and unconfined during sample loading, it is also necessary to rejoin the two fractured core pieces prior to loading to ensure that the fracture surfaces are correctly mated within the pressure cell.

3.3.3.1.1 Epoxy resin method

The initial method adopted to ensure the above conditions were met was to recombine the two fractured core pieces using epoxy resin. This method was adopted for the Cambrian shale fractured samples. 2-part, rapid setting epoxy resin was applied sparingly lengthways along the two fracture sides while the fracture surfaces were held firmly together by hand. In addition, epoxy was used to fill any chips or damage along the sides or around the core end edges.

The pressure cell used within the experiments is designed for a 38 mm diameter core, and there is limited tolerance on the allowable size due to the loading design. Therefore, once dry, excess epoxy resin used to seal the fracture sides and edges was carefully removed and smoothed using coarse sandpaper, to ensure the core sample would fit into the cell. Re-trimming of the core ends using the lapping plate was also necessary to remove any epoxy resin present along the core edges that may inhibit sealing of the core end platens.

The epoxy resin fracture closure method was used on two fractured Cambrian shale samples. The first sample (V2) was used within cyclic water/CO_2 tests (not part of this study, but undertaken for an MSc project [Hinchcliffe, 2014]) prior to being used within this study for single phase CO_2 hydraulic tests undertaken at 40°C, with a downstream fluid pressure of 10 MPa and an approximate confining pressure of 25 MPa. The second sample (V1) was used within comprehensive CO_2 flow experiments (see section 6.2).

During the single phase CO_2 fracture flow experiments on the first Cambrian shale fractured sample prepared as above (sample V2), an increase in fracture permeability was observed during the experiment. This was identified through a reduction in the differential pressure to flow rate ratio during the four hour experiment, as shown in Figure 3.12.

There were a number of possible reasons for this permeability increase. As mentioned, the sample had previously been used within cyclic water and CO_2 experiments, and therefore the permeability increase could have been due to drainage of water (the wetting fluid) from the fracture during this time period; or chemical influences (i.e. dissolution) due to the presence of water within the sample. However, there was also

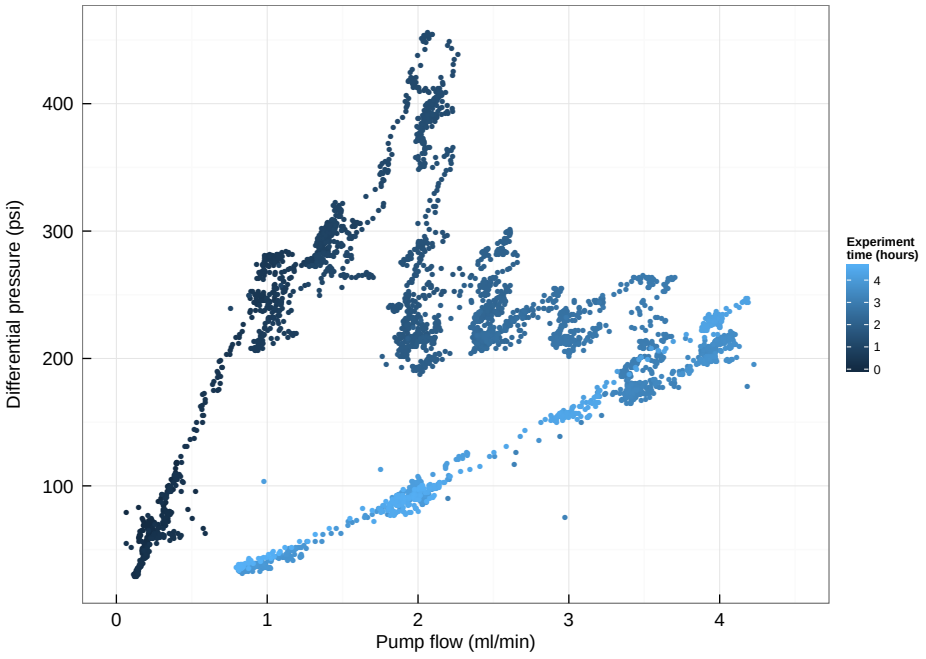

FIGURE 3.12: Reduction in differential pressure (increase in permeability) observed during Cambrian shale fracture flow tests (40°C, 24.5 MPa confining pressure, 10 MPa fluid pressure, sample V2)

concern that the sample preparation method may also potentially influence these results. Firstly, it was possible that epoxy dust or other loose material may have found its way into the fracture during sample preparation, and the increase in permeability observed may have been a result of 'flushing out' of epoxy dust or other loose material from within the fracture during CO_2 flow. In addition, there was concern that epoxy resin swelling may occur during the experiment due to contact with supercritical CO_2 [Paul et al., 2010], and that this epoxy swelling may force the fracture aperture to increase, resulting in increased fracture permeability. This would occur if the epoxy strength was greater than the confining pressure.

More generally, if the epoxy resin compressive strength joining the fractured core together is of similar, or greater magnitude than the confining pressure, the presence of the epoxy is likely to inhibit fracture deformation under confining stress (up to 55 MPa). This would have an associated impact on the hydraulic response. The compression shear strength of the epoxy resin used (Loctite Epoxy Quick Set) is understood to

be within the range 5-15 MPa (www.loctiteproducts.com). However, some manufacturers quote compressive strengths of up to 190 MPa (http://www.epoxyworktops.com/epoxy-resin/mech-properties.html). It was therefore decided that for subsequent flow experiments (East Brae and Wissey samples), epoxy resin should not be used.

In order to minimise the risk of epoxy dust or other loose material clogging up the fracture for the second Cambrian shale experiment the epoxy-sealed fractured core sample (V1) was ultrasonically cleaned in water and then left to dry for several days prior to the flow experiments.

For subsequent experiments (East Brae and Wissey samples) the fractured core sample was recombined with PTFE tape and other flexible external coatings prior to loading into the pressure cell. The sample coatings are discussed in the section below (section 3.3.3.2).

3.3.3.2 Sample coatings

During experimental rig development, significant equipment issues were experienced due to the reaction of polymers in contact with supercritical CO_2 (section 5.4.2). Swelling of polymers, in particular elastomers, in the presence of CO_2 has previously been observed, and is due to absorption of the CO_2 into the polymer material [Paul et al., 2010]. The process of absorption consists firstly of adsorption of the CO_2 onto the polymer material, followed by diffusion through the material. In this way CO_2 can pass through the polymer material, and is generally associated with weakening of the material. The CO_2 diffusion through the material renders the use of the material as a seal ineffective. In addition, rapid depressurisation of the CO_2 can cause rapid, catastrophic damage to the polymers as CO_2 cannot diffuse out quickly enough during depressurisation, resulting in the formation of bubbles or fissures in the polymer material [Davies et al., 1999].

In order to attempt to mitigate CO_2 diffusion into the pressure cell rubber sleeve, observed within initial experiments, multiple barriers were used between the rock sample and the pressure cell sleeve during the three main sets of flow experiments. Various materials were trialled as barriers around the rock sample, including PTFE heat-shrink tubing, Melinex film, copper and aluminium self-adhesive film, and lead.

Use of PTFE heat-shrink tubing was unsuccessful due to the delicate nature of the heat-shrink resulting in tearing of material while loading the sample into the cell due to the low tolerance cell opening.

Melinex also proved unsuccessful, in this case due to unsuccessful sealing around the sample and end-platens, resulting in CO_2 leaking from the cell.

The most successful method of isolating the sample from the pressure cell sleeve was found to be a combination firstly of PTFE tape; a non-adhesive aluminium foil coating held on with PTFE; a self-adhesive foil layer; and finally a lead layer, created to include a small (2-4 mm) overlap onto the end platen on either side of the core sample, to attempt to ensure isolation of CO_2 from the sleeve at the core end/cell platen join. These sample coatings were applied at the sample preparation stage. The self-adhesive foil layer has a < 1 mm overlap that is folded down onto the core ends to ensure an even thickness of coating around the core ends for effective sealing between the end platen and the core end within the pressure cell. Figure 3.13 shows the sample coating after each stage discussed above.

Variations on this method of sample coating were adopted for all fracture flow experiments presented within this thesis (Chapter 6 and 7), as detailed in Table 3.3. The lead layer was found to rupture at the core end/platen joints, and at the core marker notch (see section 4.2, Figure 4.3). However, the inner coatings did not rupture and as there was no evidence of CO_2 diffusion through the pressure cell sleeve with this multi-layered sample coating approach this sample coating method was considered successful.

3.4 Sample characterisation

A range of techniques have been adopted for characterisation of the rock samples obtained during the sample sourcing stage of the project (section 3.2). The mineralogy of the samples has been analysed using x-ray diffraction. The matrix porosity of the samples has been measured using a Boyle's law helium porosimeter and the liquid equivalent matrix permeability (Klinkenberg) has been measured using a nitrogen gas permeameter. An adapted Mohs hardness test has been adopted to provide a qualitative and relative assessment of rock matrix hardness between samples. The techniques and

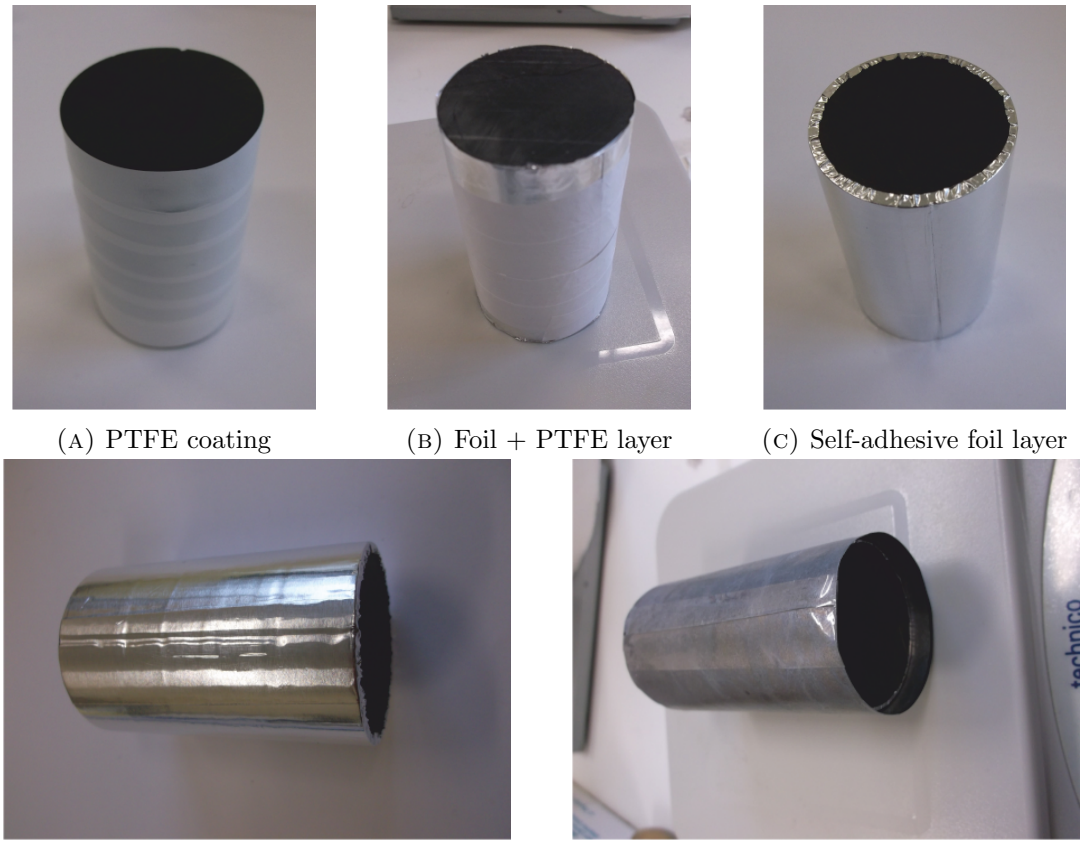

(A) PTFE coating (B) Foil + PTFE layer (C) Self-adhesive foil layer

(D) Self-adhesive foil layer (side view) (E) Lead layer

FIGURE 3.13: Sample coatings: layer by layer

methods used for these characterisation techniques are discussed within the subsections below, along with presentation of the characterisation results.

In addition to sample characterisation, fracture characterisation has been undertaken, and is presented within Chapter 4. Fracture surface topography measurement was undertaken on several samples using a laser profile sensor, with both pre- and post-experiment measurements taken. In addition, computerised tomography was undertaken on the Cambrian shale core (V1) post-experiment to analyse the resultant fracture network within the core sample.

3.4.1 Mineralogical analysis - X-ray Diffraction

X-ray diffraction (XRD) is a sophisticated technique used for both quantitative and qualitative identification of crystalline materials within a powdered rock sample (<

TABLE 3.3: Fractured core sample - preparation and coating details

Core details	Experiment date	Epoxy resin applied?	Sample coating details			
			Layer 1	Layer 2	Layer 3	Layer 4
Cambrian V2*	Jul 2013	Yes	-	-	-	-
Cambrian V1	Mar/Apr 2014	Yes	PTFE (partial cover only)	SAF	SAF	LEAD
East Brae B2	May 2014	No	PTFE	SAF	SAF	LEAD
East Brae D2	Jun 2014	No	PTFE	NAF	SAF	LEAD
East Brae B2b	Jun 2014	No	PTFE	NAF	SAF	LEAD
Wissey W3	Jul 2014	No	PTFE	NAF	SAF	LEAD
PTFE	PTFE tape (full lateral surface area cover)					
NAF	Non-adhesive aluminium foil, held with PTFE					
SAF	Self-adhesive aluminium foil					
LEAD	Lead foil layer, includes platen overlap					

* *Used within initial CO_2 fracture flow tests only*

1 g required). Incident x-rays are diffracted by the lattice structure of the crystals present within the powdered rock sample and the diffraction pattern produced can be decoded to determine the crystals present within the sample, and their relative percentage quantities.

The XRD facility at the University of Edinburgh was utilised for semi-quantitative analysis of our seal rock samples. This facility consists of a Bruker D8 Advance with a Sol-X Energy Dispersive detector. Analysis of the diffraction signal was undertaken by Nic Odling using Bruker Diffrac.EVA software in conjunction with the latest available International Centre for Diffraction Data (ICDD) database. Quantitative analysis is undertaken using TOPAS 3.0 Rietveld analysis software. The XRD result accuracy is ± 1 wt% absolute.

Powdered samples were required for the XRD analysis. Rock cuttings were taken from locations adjacent to where the 38 mm diameter core samples were drilled, to ensure the samples were representative of the cores. The rock cuttings were powdered using the rock crushing and grinding facilities available within the University of Edinburgh (tungsten carbide crushing mill followed by Tema orbital mill).

The XRD results are presented below for each rock type.

3.4.1.1 Cambrian shale

XRD was undertaken on one sample of Cambrian shale during this project. The mineralogy results are presented in Table 3.4 and Figure 3.14.

TABLE 3.4: Cambrian shale XRD results

	Mineral percentages (%)
Core	*Cambrian shale*
Quartz	24.1
Calcite	0.5
Dolomite	8.2
Plagioclase feldspar (Albite)	31.2
Plagioclase feldspar (Anorthite)	5.2
Illite	1.9
Kaolinite	1.8
Chlorite	1.9
Siderite	0.0
K-feldspar (Microcline)	5.8
K-feldspar (Orthoclase)	6.5
Muscovite	5.0
Ankerite	7.9

The dominant mineralogy comprises 36% plagioclase feldspar (31% albite and 5% anorthite) and 24% quartz, with notable dolomite and ankerite also present (both 8%).

Cambrian shale XRD analysis was also undertaken separately during an undergraduate study of cyclic CO_2/water flow [Hinchcliffe, 2014]. This separate sample analysis (taken from the same material block) indicated a higher proportion of illite (9%). Pre and post experiment XRD analysis undertaken during this cyclic flow analysis project presented no evidence of geochemical changes to the rock material as a result of the cyclic flow experiments.

3.4.1.2 East Brae

XRD was undertaken on four powdered samples from East Brae 16/3a-E10. One adjacent to each of the B1, B2, D1 and D2 cores. The XRD mineralogy results are presented

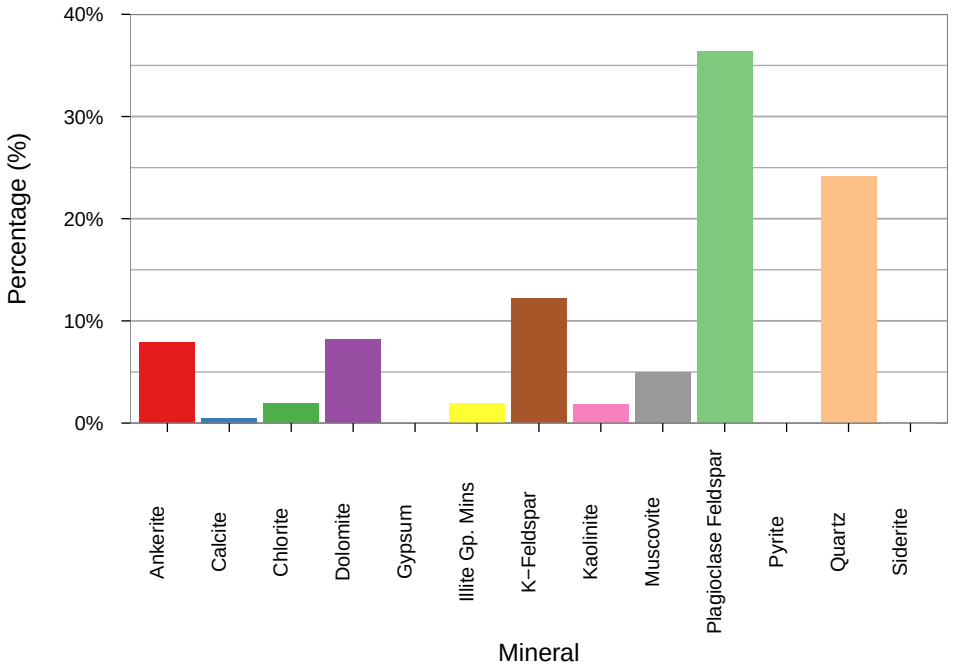

FIGURE 3.14: Cambrian shale mineralogy (from XRD analysis)

in Table 3.5, along with average data from the four samples. The East Brae Kimmeridge Clay samples contained a high quartz content (average of 66%), and also contained a significant illite content (average of 10%). Figure 3.15 presents the average mineralogy data from the four XRD samples. There was no significant variation between samples, as can be seen from Table 3.5.

3.4.1.3 Wissey

XRD was undertaken on four powdered samples from Wissey 53/04a-9. These were all taken from the discretely fractured core sample, sample 5 (5525'-5525'8"/1684.0-1684.2 m). Two of the samples were taken adjacent to core plug W1, and were taken from the matrix and fracture respectively. The other two samples were taken adjacent to core plug W4, and similarly were taken from the matrix and along the fracture respectively.

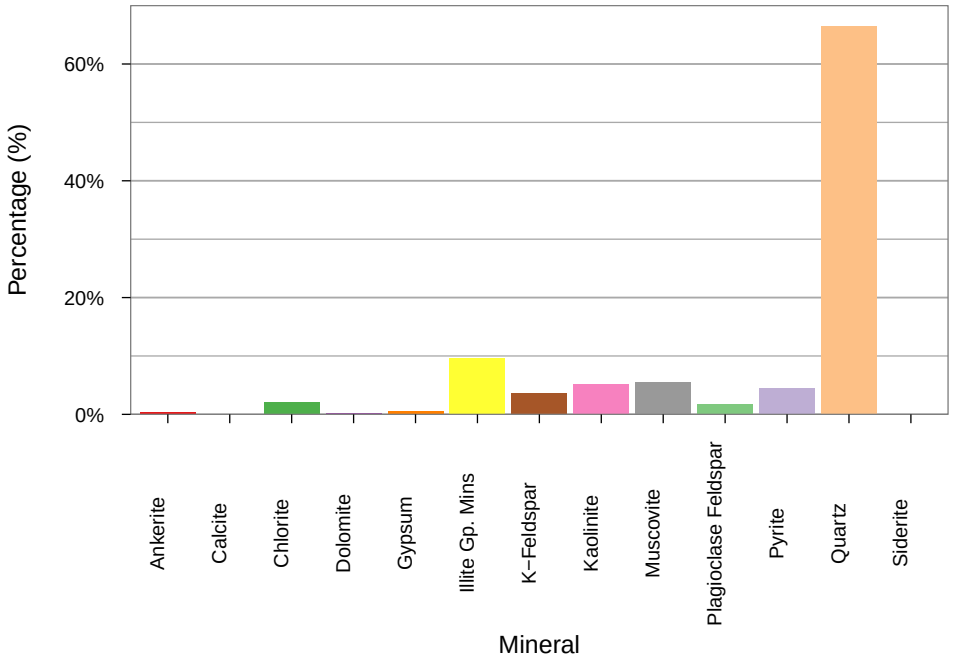

FIGURE 3.15: East Brae mineralogy (averaged from 4 x XRD analysis)

TABLE 3.5: East Brae XRD results

	Mineral percentages (%)				
East Brae core	*B1*	*B2*	*D1*	*D2*	*Average*
Quartz	68.2	64.6	68.3	64.6	66.4
Calcite	0.1	0.0	0.0	0.0	0.0
Dolomite	0.2	0.1	0.3	0.0	0.2
Pyrite	5.0	6.4	2.7	3.9	4.5
Plagioclase Feldspar	1.7	1.6	1.9	1.8	1.7
Gypsum	0.7	0.6	0.4	0.6	0.6
Illite Gp. Mins	8.3	10.2	9.7	10.6	9.7
Kaolinite	5.1	5.0	4.6	5.8	5.1
Chlorite	1.8	2.1	2.0	2.3	2.1
Siderite	0.1	0.1	0.1	0.1	0.1
K-feldspar	3.9	3.9	3.8	3.2	3.7
Muscovite	4.6	5.2	5.9	6.6	5.6
Ankerite	0.3	0.2	0.3	0.4	0.3

The XRD mineralogy results from each of the four samples are presented in Table 3.6, along with the averaged data. The Wissey XRD average mineralogy from the four samples is also displayed in Figure 3.16. The Wissey Zechstein samples are predominantly composed of dolomite (average of 81%).

There was no significant variation in mineralogy between samples, either between the core W1 and W4 samples or between the fracture and matrix samples, as can be seen from (Table 3.6).

TABLE 3.6: Wissey XRD results

	Mineral percentages (%)				
Wissey core	*W1 - fracture*	*W1 - matrix*	*W4 - matrix*	*W4 - fracture*	*Average*
Quartz	3.5	4.0	4.8	4.4	4.2
Calcite	0.0	0.0	0.0	0.0	0.0
Dolomite	78.8	84.2	79.3	80.9	80.8
Pyrite	0.4	0.5	0.6	0.6	0.5
Plagioclase Feldspar	2.5	2.0	2.7	2.4	2.4
Gypsum	1.3	0.8	1.0	1.3	1.1
Illite Gp. Mins	2.2	1.7	2.7	2.4	2.3
Kaolinite	0.6	0.3	0.6	0.4	0.5
Chlorite	1.5	1.7	2.0	1.4	1.6
Siderite	0.5	0.4	0.5	0.3	0.5
K-feldspar	2.4	1.6	1.9	2.1	2.0
Muscovite	3.0	2.7	2.6	2.7	2.7
Ankerite	3.2	0.0	1.3	1.1	1.4

3.4.1.4 Heletz

XRD was undertaken on six powdered samples from the Heletz seal rock, where material was taken adjacent to the core plugs H1 to H6 respectively. The results from these six XRD analyses, along with the averaged data are presented in Table 3.7, with the averaged data also displayed in Figure 3.17.

The dominant mineralogy within the Heletz seal rock is K-feldspar, with an average of 41% present across all six samples. Plagioclase feldspar and kaolinite were also present in significant amounts (15% and 11% respectively). Due to the heterogeneous nature of

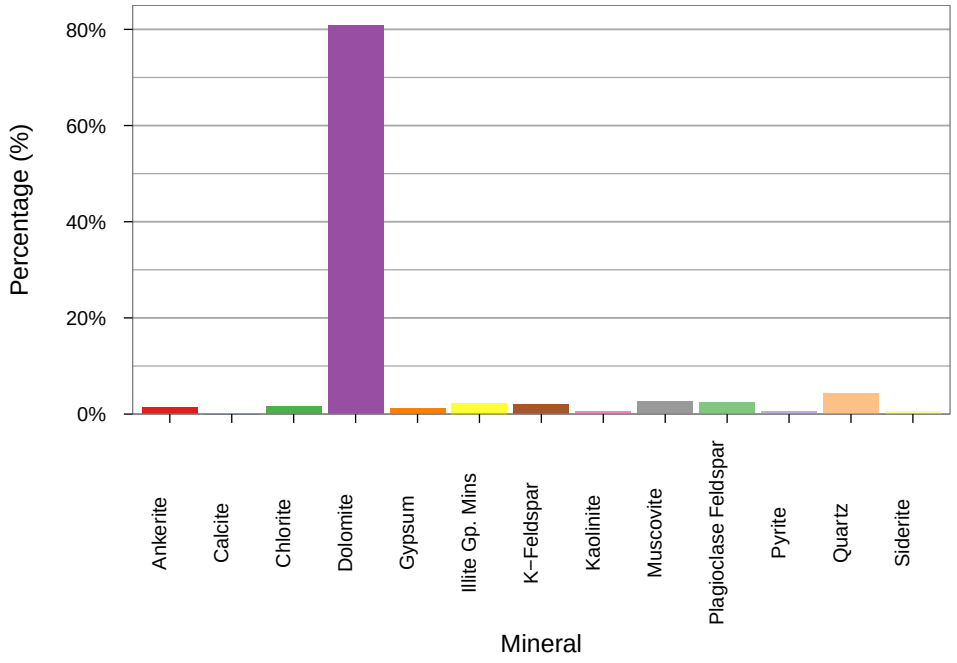

FIGURE 3.16: Wissey mineralogy (averaged from 4 x XRD analysis)

the Heletz seal rock, there is slightly more variation in mineralogy between samples than was observed for East Brae and Wissey. Most notably, there is a higher K-feldspar and plagioclase feldspar content in H1-H3 than in H4-6. Samples H4 and H6 contained beige pebbles that were not present in samples H1-H3, therefore suggesting that the nature of the rock material changed between these two seal rock samples (Figure 3.18). The XRD data may therefore reflect this change through an observed variation in mineralogy.

3.4.1.5 Seal rock mineralogy comparison

The results from XRD mineralogy analysis illustrate the wide variety of seal rock samples sourced during this project. The mineralogy variation between the seal rock types is illustrated in Figure 3.19.

This significant variation in mineralogy between samples will affect the nature of fracturing within the samples and the resultant fracture geometry. In addition, the mineralogy is likely to affect the mechanical behaviour of the fracture (as will temperature), and this will consequently influence the hydraulic behaviour.

TABLE 3.7: Heletz XRD results

	Mineral percentages (%)						
	H1	*H2*	*H3*	*H4*	*H5*	*H6*	*Average*
Quartz	3.6	3.2	0.3	1.6	1.9	5.1	2.6
Calcite	0.6	0.0	0.0	19.1	3.6	4.9	4.7
Dolomite	1.6	0.0	0.0	0.3	2.0	1.9	1.0
Pyrite	3.2	1.4	2.2	2.2	2.3	3.0	2.4
Plagioclase Feldspar	17.8	17.4	16.1	11.2	12.2	12.6	14.6
Gypsum	0.6	0.7	0.3	1.4	0.0	2.6	0.9
Illite Gp. Mins	2.5	4.4	6.7	5.1	11.6	10.0	6.7
Kaolinite	7.3	11.6	12.1	8.7	14.3	12.2	11.0
Chlorite	2.3	6.7	4.9	3.2	5.3	6.1	4.8
Siderite	0.2	0.3	0.6	0.4	0.4	0.1	0.3
K-feldspar	54.8	48.2	46.1	35.7	33.8	29.0	41.3
Muscovite	2.1	4.9	9.9	8.9	10.9	10.0	7.8
Ankerite	3.3	1.1	0.8	2.3	1.7	2.4	1.9

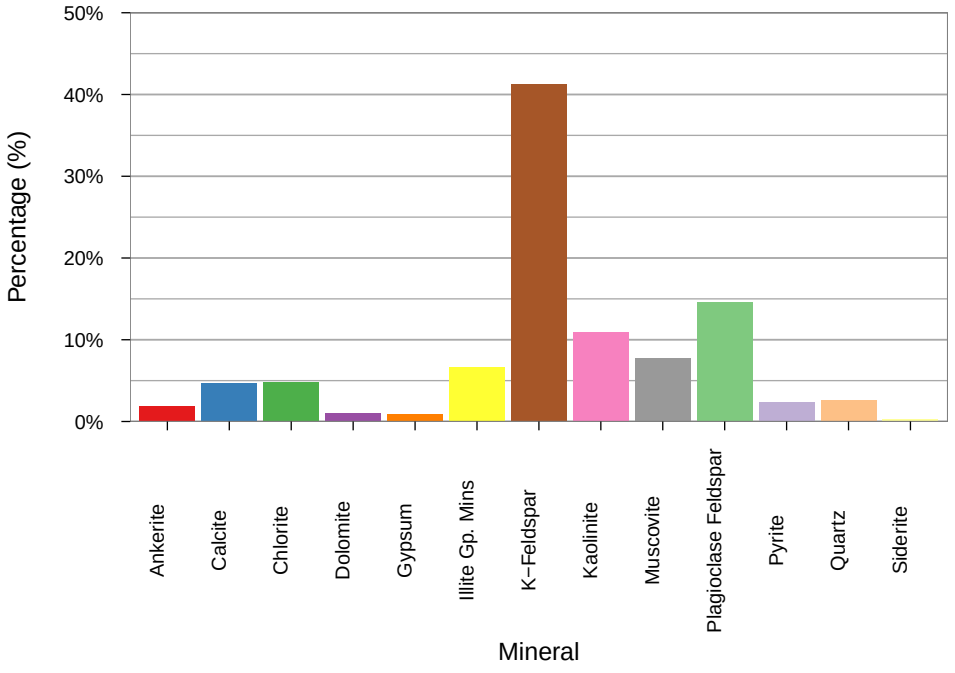

FIGURE 3.17: Heletz seal rock mineralogy (averaged from 6 x XRD analysis)

(A) H1 core sample

(B) H6 core sample (N.B. Contains pebbles)

FIGURE 3.18: Heterogeneity within and between Heletz seal rock samples

The potential for mineral reactions to occur during experiments is minimised as core samples are not saturated prior to flow experiments, and single phase CO_2 flow is studied. While significant geochemical reactivity has been observed during interaction between supercritical CO_2 and both clayey caprock [Credoz et al., 2009] and dolomite [Wang et al., 2013], the presence of water is found to be important for such reactions. Interaction of anhydrous supercritical CO_2 with the same minerals does not result in mineral reactivity, except in the special case of water-containing minerals (swelling clays) [Credoz et al., 2009, Loring et al., 2012, Wang et al., 2013]. As our samples do not contain swelling clays, use of anhydrous conditions during our experiments allows us to more effectively analyse the hydraulic response to thermal and mechanical changes in the coupled system.

3.4.1.6 Clashach

In addition to mineralogical analysis of seal rock samples, XRD analysis has also been undertaken on a powdered sample of Clashach sandstone. Clashach sandstone was used for permeability testing during the rig commissioning (section 5.5.6). Clashach sandstone is a fairly homogeneous sandstone, quarried from the Clashach Quarry in Birnie, Elgin. The results of the Clashach sandstone XRD analysis are presented in Table 3.8 and Figure 3.20. The Clashach mineralogy comprises approximately 90%

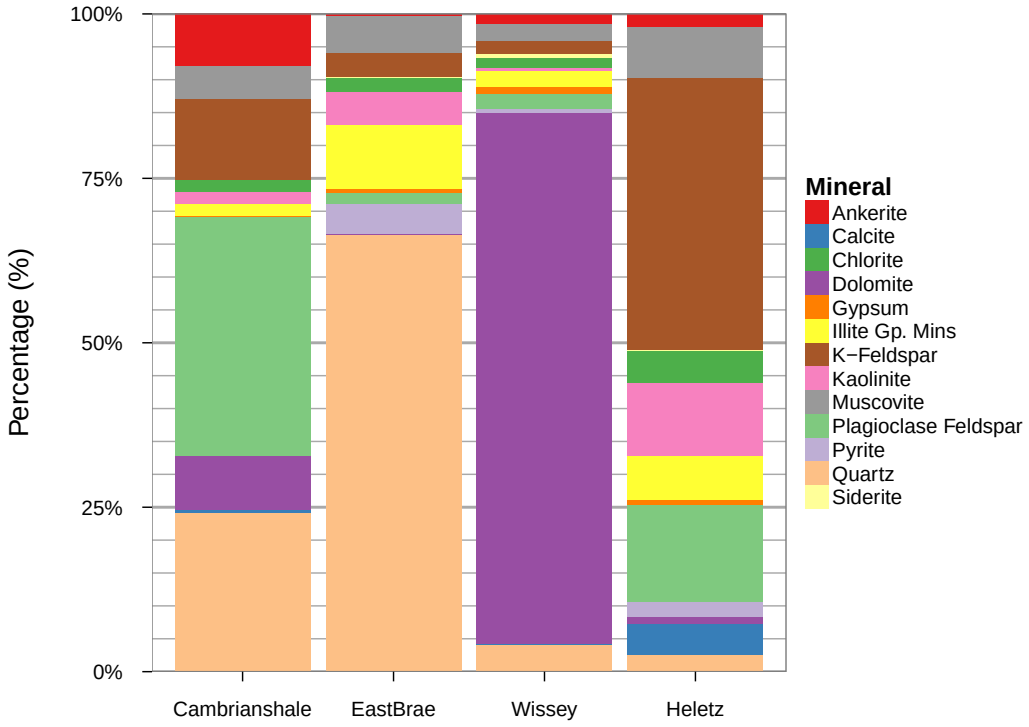

FIGURE 3.19: Comparison of seal rock mineralogy data

quartz, with some K-feldspar and plagioclase feldspar content, as well as traces of other minerals.

3.4.2 Porosity and permeability testing

Porosity and permeability testing of unfractured core samples was undertaken at Heriot Watt University. This provides valuable data relating to the seal rock matrix. Flow through a low permeability seal rock matrix is likely to be negligible in comparison to flow through a discrete fracture within the matrix (section 2.3). This is presumed to be the case during the lab scale experiments undertaken on typical seal rock samples within this study. The matrix porosity and permeability data presented here enables quantification of this assumption, through comparison between the sample permeabilities observed during the flow experiments for CO_2 flow through a fractured sample and the matrix permeability values. This enables justification of our assumption of negligible matrix flow, where applicable.

TABLE 3.8: Clashach XRD results

	Mineral percentages (%)
Core	*Clashach*
Quartz	89.5
Calcite	0.3
Dolomite	0.1
Pyrite	0.0
Plagioclase Feldspar	2.1
Gypsum	0.2
Illite Gp. Mins	0.9
Kaolinite	0.0
Chlorite	0.2
Siderite	0.0
K-feldspar	5.8
Muscovite	0.7
Ankerite	0.2

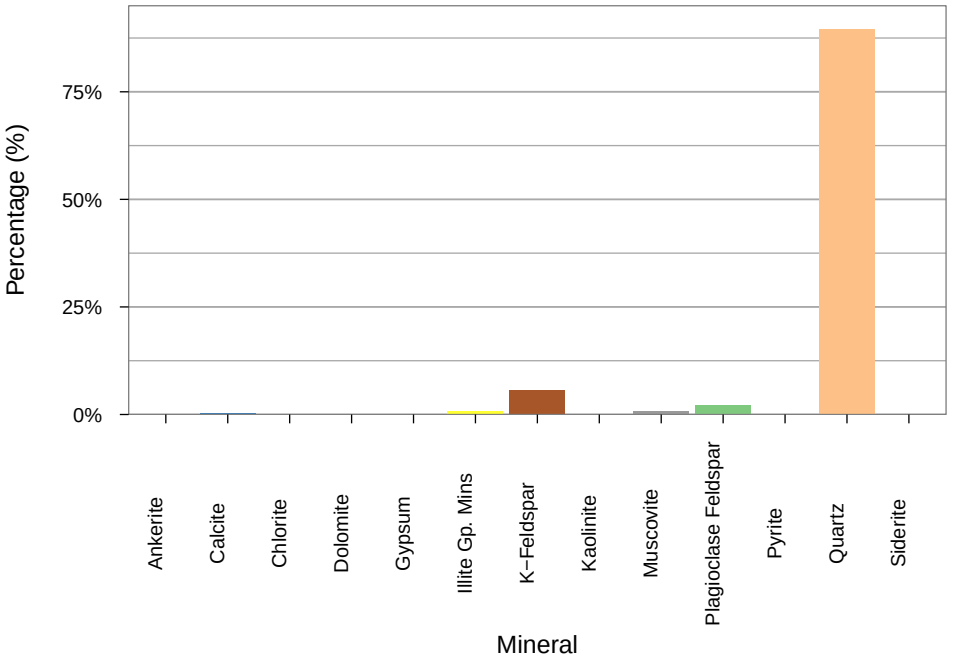

FIGURE 3.20: Clashach sandstone mineralogy

3.4.2.1 Porosity

3.4.2.1.1 Helium porosimeter method

The effective porosity of the seal rock core samples was carried out using a Helium porosimeter (Figure 3.21). This uses a Boyle's Law expansion relationship to calculate the grain volume, and subsequently the effective porosity of a core sample with a non-destructive method. The accuracy of grain volume measurement is considered to be ±0.5% [Jenkins et al., 1960].

FIGURE 3.21: Helium porosimeter

The porosimeter consists of two gas-tight chambers of known volume, connected by a valve. The grain volume of the core sample is determined by placing it in the first chamber under known pressure, P_1, while the second chamber is isolated at a different pressure, P_2. The valve between the two chambers is subsequently opened and, after pressure equalisation, the grain volume is determined from the final equalised pressure value, P_f, using the Boyle's Law relationship shown in Equation 3.1.

$$P_f(V_1 + V_2 - V_g) = P_1(V_1 - V_g) + P_2V_2 \tag{3.1}$$

where V_1 and V_2 are the volumes of the first and second chambers, and V_g is the core sample grain volume.

Once the grain volume, V_g, has been determined the effective porosity of the sample is calculated using this and the bulk volume of the core sample, V_b (Equation 3.2).

$$\phi = (V_b - V_g)/V_b \tag{3.2}$$

The bulk volume of the sample is calculated using length and diameter measurements of the cylindrical sample (linear measurement).

This method calculates effective porosity as gas is unable to enter isolated pores and they are therefore effectively treated as solid. There is a small degree of error due to the sorption of gas on the pore surfaces. Use of the inert gas, Helium, helps to minimise this, however the effective porosity values are generally considered to be slightly high as a result of this effect [Jenkins et al., 1960].

3.4.2.1.2 Results

Effective porosity testing was undertaken on fourteen unfractured core samples: one Cambrian shale sample; five East Brae samples; one Wissey sample; five Heletz samples and two Clashach sandstone samples. Clashach sandstone is used during the experimental rig testing (section 5.5.6), hence it's inclusion for sample characterisation in addition to the representative seal rock samples. Results from the porosity tests are displayed in Table 3.9.

The effective porosity results show extremely low porosities for the Cambrian shale sample (2.5%), all East Brae samples (average of 0.4%), and the Wissey sample (2.5%). The porosities for the Heletz shale samples are higher, with an average of 7.3%. This is likely to be due to the heterogeneous nature of the rock samples, and the presence of notable sand lenses that are likely to be of higher porosity.

3.4.2.2 Permeability

3.4.2.2.1 Nitrogen permeameter method

A steady-state nitrogen permeameter is used for measuring the Klinkenberg (liquid equivalent) permeability of unfractured 38 mm diameter core samples. The apparent permeability of a sample during gas flow may be higher than the liquid equivalent due to

TABLE 3.9: Effective porosity measurements

Source	Sample ID	Sample length (mm)	Bulk Volume (cm^3)	Grain Volume (cm^3)	**Effective Porosity (%)**
Cambrian	V5	66.7	74.5	72.6	**2.5**
East Brae	B1	63.5	72.1	71.8	**0.4**
East Brae	B2	61.0	69.4	69.0	**0.5**
East Brae	B3	62.5	70.8	70.6	**0.2**
East Brae	D1	63.5	72.0	71.7	**0.5**
East Brae	D2	64.4	73.1	72.7	**0.6**
Wissey	W5	22.6	25.6	25.0	**2.5**
Heletz	H2	63.6	71.8	65.5	**8.8**
Heletz	H3	68.5	77.4	73.2	**5.4**
Heletz	H4	71.2	81.0	75.1	**7.3**
Heletz	H5	42.2	47.9	44.4	**7.4**
Heletz	H6	66.3	75.2	69.5	**7.6**
Clashach	A+	56.7	64.5	54.3	**15.8**
Clashach	B++	56.2	64.0	54.3	**15.2**

gas slippage effects [Klinkenberg, 1941] (see also section 2.5.3). However, Klinkenberg [1941] devised a method of calculating the liquid equivalent permeability from multiple gas permeability measurements. The Klinkenberg permeability can be considered to be indicative of the intrinsic permeability of the sample.

Within the nitrogen permeameter the core is held within a Hassler coreholder under a confining pressure of 1 MPa to prevent leakage within the cell. The gas permeability of the core is calculated using the upstream gas pressure, differential pressure, and gas flow rate measured during steady state flow of nitrogen through the core. The ambient temperature is also recorded and used to calculate the viscosity of the nitrogen during the steady state experiments; this is also required for calculations, along with sample dimensions.

Gas permeability measurement is carried out at three different mean gas pressure conditions for each core sample. Klinkenberg analysis is then carried out using this gas permeability data and data extrapolation techniques are used to estimate the Klinkenberg (liquid equivalent) permeability [Klinkenberg, 1941, McPhee and Arthur, 1991].

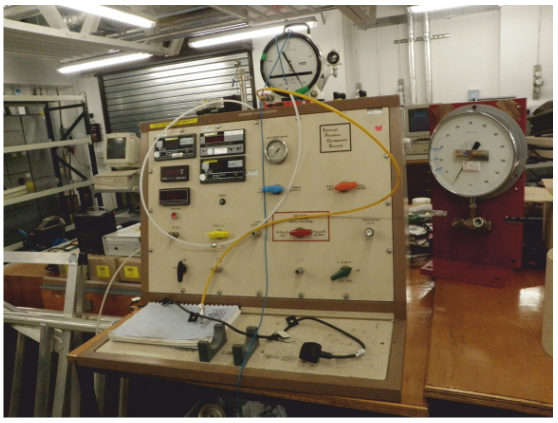

FIGURE 3.22: Nitrogen permeameter

This method of permeability measurement has been carried out on a subset of the samples used for porosity determination. The Wissey sample was of inadequate length for the permeameter and therefore has not been included. In addition, only a subset of the Heletz samples have been tested.

3.4.2.2.2 Results

The permeability results for the samples tested using the Heriot-Watt nitrogen permeameter are shown in Table 3.10.

TABLE 3.10: Klinkenberg permeability measurements (derived using nitrogen permeameter)

Source	Sample ID	Sample length (mm)	**Klinkenberg permeability ($\mathbf{mD/m^2}$)**
Cambrian	V5	66.7	too low for testing
East Brae	B1	63.5	$0.03\ /3.0 \times 10^{-17}$
East Brae	B2	61.0	$0.13\ /1.3 \times 10^{-16}$
East Brae	B3	62.5	$0.04\ /3.9 \times 10^{-17}$
East Brae	D1	63.5	$0.02\ /2.0 \times 10^{-17}$
East Brae	D2	64.4	$1.16\ /1.1 \times 10^{-15}$
Heletz	H3	68.5	$21.90\ /2.2 \times 10^{-14}$
Heletz	H4	71.2	$4.40\ /4.3 \times 10^{-15}$
Clashach	A+	56.7	$286.0\ /2.8 \times 10^{-13}$
Clashach	B++	56.2	$297.9\ /2.9 \times 10^{-13}$

The permeability of the Cambrian shale sample was below the threshold required for testing using the nitrogen permeameter (0.01 mD/1 $\times$ 10^{-17} m^2). The permeability of the East Brae samples was also consistently extremely low. As anticipated, the Heletz samples were of slightly higher permeability and the heterogeneous nature of the rock meant that permeability was not consistent between the two samples tested.

3.4.3 Adapted Mohs hardness test

The Mohs hardness scale [Tabor, 2002] is a mineral hardness scale created in 1812 by Friedrich Mohs and consists of ten minerals from Talc (soft) to Diamond (hard). It is a qualitative, ordinal scale of mineral hardness, based on the relative ability of one natural mineral sample to visibly scratch another. Material hardness is assumed to be key for estimating the potential for fracture surface deformation during CO_2 flow experiments, where samples are subjected to high effective stresses in recreating in-situ storage conditions. The Mohs hardness technique has been adapted for use in this project, to determine the relative hardness of the various fractured samples sourced and tested.

Four samples were tested for hardness, one from each of the rock types sampled and utilised during this study (section 3.2). The samples consisted of small offcuts of sample material, obtained during the sample preparation phase. Hardness testing was undertaken by testing the relative ability of each sample material to visibly scratch the other sample materials. The materials were then ranked with relative hardness ratings from 1 to 4, with 4 being the hardest material tested. The materials have not been placed within the mineral-based Mohs hardness scale. The results of the hardness tests are displayed in Table 3.11.

While the hardness tests are relative tests, and do not provide quantitative information on the hardness of the materials tested, it should be noted that the Heletz and East Brae samples were both found to be relatively soft and easily marked, while the Wissey and Cambrian samples were much harder. This was notable when cutting marker notches into the samples with a hacksaw during sample preparation as the Heletz and East Brae samples were easy to mark, while the Wissey and Cambrian samples required significantly more effort.

TABLE 3.11: Adapted Mohs hardness testing [Relative scale 1-4 (soft to hard)]

Sample	Relative hardness	Comments
Heletz shale (approximate depth: 5237'/1596 m)	1	Matrix material is easily marked - soft
East Brae shale (approximate depth: 14931'/4551 m)	2	Marginally harder than Heletz - still relatively soft
Wissey dolomite (approximate depth: 5525'/1684 m)	3	Significantly harder than East Brae shale
Cambrian shale (quarried)	4	Marginally harder than Wissey

3.5 Sample sourcing, preparation and characterisation summary

During this project a wide variety of representative seal rock samples have been identified, located and sampled from well core and outcrops, thanks to the kind cooperation of a number of industry contacts.

The sample preparation methods adopted have been described, and discussion of associated method development has been included. Sample preparation includes 38 mm diameter core preparation; sample fracturing (where natural fractures are not available); and sample coating, which is required both for recombination of fractured core pieces and to provide a barrier to minimise CO_2 diffusion through the elastomer confining sleeve of the pressure cell.

A range of characterisation techniques have been used to ensure that the mineralogy as well as the matrix hydraulic and hardness properties of the samples are well understood prior to undertaking fracture flow experiments. Fracture characterisation has also been undertaken, and is presented within Chapter 4.

Comprehensive THM (thermo-hydro-mechanical) analysis has been undertaken during controlled supercritical CO_2 flow experiments on four discretely fractured seal rock samples, selected from the range of samples presented within this chapter (see Chapter

6 for experiment details). The results of the THM analysis experiments are presented and discussed within Chapter 7.

Table 3.12 provides a summary details for the samples used within both fracture surface characterisation (Chapter 4) and supercritical CO_2 flow experiments (Chapter 7).

TABLE 3.12: Sample summary table

Sample	Rock type	Recovery depth (m)	Fracture type	Fracture orientation (relative to bedding)	Fracture surface characterisation?	CO_2 flow experiments?	Peak experimental effective stress (MPa)	Peak experimental temperature (°C)
Cambrian V1	Shale (Cambrian Stockingford)	-	Artificial	Perpendicular	✗	✓	45	58
East Brae B2	Shale (Kimmeridge Clay)	4551	Artificial	Parallel	✓	✓	55*	38
East Brae B2b**	Shale (Kimmeridge Clay)	4551	Artificial	Parallel	✓	✓	44	58
East Brae D2	Shale (Kimmeridge Clay)	4552	Artificial	Parallel	✓	✓	30	38
Wissey W3	Dolomite (Zechstein)	1684	Natural	Perpendicular	✓	✓	44	58
Wissey W4	Dolomite (Zechstein)	1684	Natural	Perpendicular	✓	✗	-	-
Heletz H2	Shale (Lower Cretaceous)	1596	Artificial	Parallel	✓	✗	-	-
Heletz H6	Shale (Lower Cretaceous)	1596	Artificial	Parallel/ Oblique	✓	✗	-	-

* *During pre-experiment stress loading*
** *B2b is B2 sample with ∼1 mm offset fracture surfaces (experiments undertaken subsequent to B2)*

Chapter 4

Measurement and analysis of fracture geometry and surface roughness

4.1 Introduction

Fracture surface measurement was undertaken on a number of samples in order to accurately record the surface topography. These data have been used for analysis of fracture surface roughness both at small-scale (submillimetre to millimetre scale), and at a larger scale, incorporating surface topography features. Fracture surface data from six samples were obtained prior to the flow experiments, with post-experiment fracture surface data also gathered for three of these samples. A pre- and post-experiment data comparison has been undertaken for these samples to try to identify geometry changes resulting from the high pressure high temperature CO_2 flow experiments. In addition, the statistical analysis of small-scale surface roughness can be utilised to estimate aperture distributions, for use as geometry input to coupled process models [McCraw et al., 2016, Walsh et al., 2008].

There are a variety of methods available for undertaking fracture surface topography measurement. These include both stylus-based contact methods and optical non-contact methods.

Stylus (mechanical) profilometers measure vertical displacement of a stylus in contact with a surface, as the surface is moved laterally relative to the stylus. Small surface variations can therefore be directly recorded along the line of measurement. This method is not sensitive to surface reflectance or colour, however 2D profiles are obtained and therefore full surface area measurement is difficult and time-consuming. In addition damage to the fresh fracture surfaces may result from the stylus contact. This method was not tested during this project due to the requirement for 3D surface profiles, and concerns over surface damage.

Within the University of Edinburgh a Zygo NewView white light interferometer is available. This is an optical method of undertaking very high resolution 3D surface metrology. Vertical measurements are undertaken interferometrically, while lateral measurements are performed by calculating the pixel size from the field of view of the objective. This high resolution, non-contact method of surface metrology is fast for small objects and is commonly used for micro-electronics and nano-technology applications. The white light interferometer was tested and found to be inadequate for profiling the experimental sample fracture surfaces. This was due to issues with low reflectivity of the surfaces, and high roughness. In addition, the relatively large sample size was problematic.

A Micro-Epsilon ScanCONTROL high resolution laser scanner (model: LLT2700-100) (located at the University of Strathclyde) was found to be the most appropriate tool for undertaking 3D profiling of the experimental sample fracture surfaces. Use of the Micro-Epsilon scanner enabled fast non-contact scanning of the experimental samples with elevations (Z) recorded to a resolution of 5 μm. The x and y resolution of the scan grid was also very high, with resolutions of 0.2 mm and 0.01 mm possible respectively. The low reflectivity of the sample did not cause any issues, and the sample size was ideal for use with this scanner.

In addition to fracture surface measurement, the recently upgraded University of Edinburgh x-ray computed tomography (CT) facility enabled visualisation and measurement of the resultant fracture network within the epoxied Cambrian shale sample post-experiment. This non-destructive method of imaging and measuring fracture networks has huge potential for future experiments. Refining these imaging and associated post-processing techniques could enable the development of fractures and fracture networks to be monitored during future flow experiments.

4.2 Fracture surface scanning method

The Micro-Epsilon ScanCONTROL laser scanner operates using the principle of optical triangulation (Figure 4.1). The scanner projects a laser line onto the target surface. The diffuse light reflected from the target is detected on a high quality optical sensor array which enables the distance of the target from the light source to be determined (z-information). In addition, as a laser line is used, the x-position is also acquired. The scanner at Strathclyde is mounted on a mechanical arm as shown in Figure 4.2a, which allows the scanner to be moved along the y-axis at a constant speed (4mm/s), thus allowing continuous scanning along the length of the sample. In this way, a 3D elevation profile of the fracture surface is obtained (Figure 4.2b). The data is processed and saved as an xyz point data ascii file. The data resolution is 0.2 mm in the x-direction and 0.040-0.045 mm in the y-direction. The y-direction resolution is constrained by the rate of profile acquisition and the length of the sample. The maximum profile acquisition rate is 100 profiles per second, and a maximum of 1600 profiles can be obtained for each completed scan. Thus, fine-tuning is required to ensure that full sample scans are obtained at the highest possible resolution.

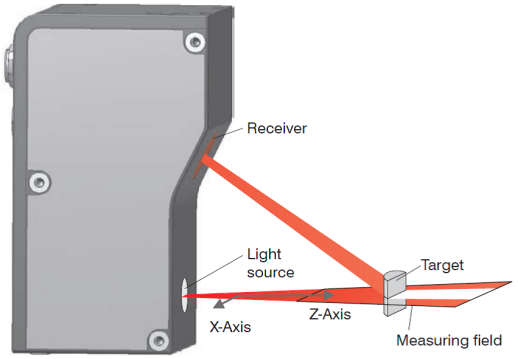

FIGURE 4.1: Micro-Epsilon ScanCONTROL laser scanner set-up [MicroEpsilon Messtechnik, n.d.]

In order to determine the orientation of the sample within the scan, and to relate this to the orientation of the sample during flow experiments, a marker notch was cut into each sample with a hacksaw, as shown in Figure 4.3. This marker notch was sufficiently large that it is visible within the scan images, however it was kept as small as possible to minimise any impact on flow or sample sealing within the core holder during flow experiments.

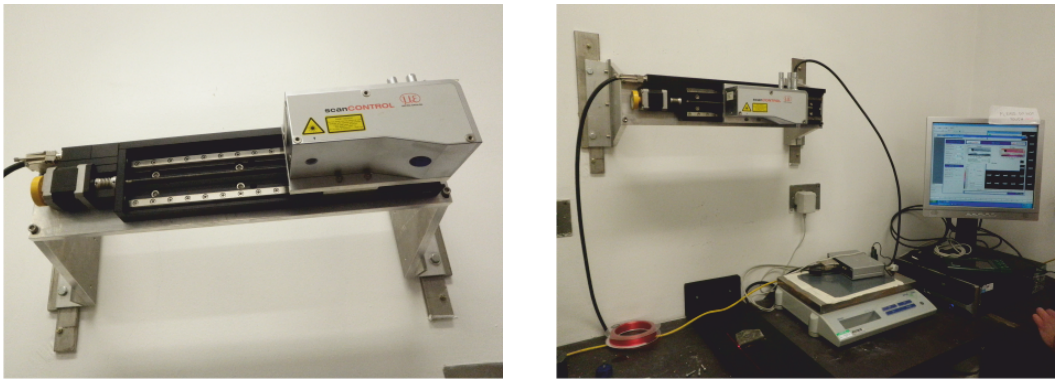

(A) Mounted laser scanner (B) Scanning a sample

FIGURE 4.2: Laser scanner set-up at Strathclyde

FIGURE 4.3: Example of marker notch (East Brae B2)

Table 4.1 lists the six discretely fractured samples for which fracture surface topography measurement was undertaken using the laser scanner. Three of these samples were subsequently used within CO_2 fracture flow experiments and scanned post-experiment to enable comparison of fracture surface characteristics pre- and post-experiment. Of these samples, the Wissey samples were the only ones with pre-existing/natural fractures. Discrete fractures were artificially induced within the East Brae and Heletz samples (section 3.3.2). Due to the differing mineralogy, heterogeneity and bedding between the samples, the large scale fracture surface topography varied significantly between samples. The East Brae samples were both very smooth, while the two Heletz samples differed significantly from each other due to heterogeneity differences. Analysis of both small-scale and large-scale roughness/topography is undertaken using the scan data in sections 4.5 and 4.6 respectively. The analysis method is presented in section 4.4.

TABLE 4.1: Discretely fractured samples for which fracture surface scanning was undertaken

Source	Sample ID	Fracture type	Post-experiment scanning?
Wissey	W3	pre-existing/natural	Yes
Wissey	W4	pre-existing/natural	-
East Brae	B2	artificially induced	Yes
East Brae	D2	artificially induced	Yes
Heletz	H2	artificially induced	-
Heletz	H6	artificially induced	-

4.3 Analysis of fracture scan topography data

Fracture surface geometry plays an important role in determining the hydraulic and mechanical properties of a fracture [Brown et al., 1986, Glover and Hayasbi, 1997, Walsh et al., 2008]. Fracture surface characterisation enables the role of geometry to be considered and assessed as part of this experimental study of discrete fractures.

Fractures are hydraulically conductive due to the mismatch of rough fracture surfaces which creates an aperture between the surfaces [Brown et al., 1986]. Characterisation of natural rough-walled fractures has shown fracture surfaces to be fractal in nature [Brown, 1995, Glover and Hayasbi, 1997]. Fracture surfaces are typically observed to be well matched above a scale of a few millimetres, but mismatched or uncorrelated on the small sub-millimetre to millimetre length scale [Brown, 1995, Brown et al., 1986, Glover et al., 1998]. It is this small scale topography or roughness that therefore determines the aperture distribution of the fracture, which is commonly observed to be symmetric and easily approximated by a Gaussian distribution [Brown et al., 1986, Walsh et al., 2008]. As the small-scale uncorrelated roughness is considered to be responsible for the aperture distribution, this suggests that the aperture distribution is statistically stationary (i.e. not scale dependent) for samples larger than a few centimetres [Brown, 1995].

The fracture surface topography data obtained during this project have been used for

analysis of surface roughness at two different length scales, with the small-scale roughness particularly relevant for consideration of associated aperture distributions. Inclusion of both pre- and post-experiment characterisation has enabled geometry changes resulting from the high pressure, high temperature CO_2 flow experiments to be assessed for three of the samples (Table 4.1).

There is significant potential for further geostatistical analysis of the fracture surface data within future studies, including analysis of spatial correlation. The fracture surface data is also extremely valuable for estimation of geometry input data to numerical models of flow and mechanical deformation within discrete fractures [McCraw et al., 2016, Walsh et al., 2008].

McCraw et al. [2016] used a hybrid numerical-analytical approach to model the hydro-mechanical behaviour of the Wissey fractured sample, through simulation of the experiments presented within this study. The model utilises the fracture surface scan data presented within this Chapter for estimation of fracture geometry. It is anticipated that the fracture surface data presented within this Chapter, along with the experimental results (Chapter 7) will be of further value within future modelling studies.

4.4 Method for fracture surface geometry data processing

Fracture surface geometry data was obtained for six samples using the University of Strathclyde laser scanner as detailed in section 4.2. Three of these samples were utilised within CO_2 fracture flow experiments and were scanned both pre- and post-experiment (see Table 4.1 for details). The resolution of the fracture scan data was 0.2 mm in the x-direction and 0.04-0.045 mm in the y direction (see section 4.2 for details).

As discussed in 4.3, natural fractures have previously been found to be well-matched at long wavelengths (on the order of a few mm length scale), but are unmatched at the small wavelengths (sub-millimetre scale) [Brown, 1995]. It is therefore considered that the small scale roughness defines the fracture aperture distribution. The surface scan data have been used during this project to analyse the roughness of the topography on two separate length scales for comparison purposes. The results may then be used in conjunction with hydraulic behaviour findings (Chapter 7) to assess the relative importance of roughness at the two different length scales during the flow experiments.

In order to analyse the fracture surface small scale roughness, the method described in McCraw et al. [2016] is adopted. Using this method, a 'reference surface' is created where the larger scale topography of the surface is removed. To create the reference surface, a smoothed surface grid is first created through linear interpolation of fracture surface data at a coarser resolution than the detailed surface scan data, but still at a higher resolution than the large scale topography details. The smoothed surface therefore represents the large scale topography of the surface. This smoothed surface is subsequently subtracted from the high resolution (raw) surface scan data thus removing the large scale topography details to create a high resolution reference surface suitable for direct analysis of the small scale roughness.

Two high resolution reference surfaces were created using this technique for each fracture surface: the first was created using a 2 mm scale smoothed surface grid, and the second was created using a 10 mm scale smoothed surface grid. The reference surface created using the 2 mm scale smoothed surface grid enabled assessment of the surface roughness at a sub-millimetre to millimetre scale; while the reference surface associated with the 10 mm scale smoothed surface enabled assessment of the surface roughness at larger scales, up to 10 mm.

The creation of the 2mm and 10 mm reference surfaces for analysis of roughness were carried out within Tecplot 360 software using the following method:

1. Load the ascii xyz laser scan data file into Tecplot (Tecplot Data Loader).
2. Create a high resolution triangulated mesh from the ascii point data (Triangulate).
3. Create a coarse grid within the fracture surface extent with cell size corresponding to the resolution desired for the smoothed surface linear interpolation and interpolate data into the coarse grid directly from the triangulated mesh.
4. Create three identical high resolution grids at a similar resolution to the fracture surface data (0.2 x 0.05 mm), using the same grid extent as the coarse grid.
5. Interpolate data into the first high resolution grid directly from the triangulated mesh - this is therefore representative of the raw surface scan data.
6. Interpolate data into the second high resolution grid from the coarse grid - this creates a smoothed surface as data is linearly interpolated at the coarse grid scale.

7. Calculate grid values for the final high resolution grid from the difference between the first and the second high resolution grids (i.e. raw data - smoothed data). This produces the reference surface which can be used for roughness analysis.

The sub 2 mm scale roughness reference surface is assumed to be indicative of the unmatched asperities between the upper and lower fracture surfaces that determine the fracture aperture distribution [Brown, 1995, Glover et al., 1998]. The asperity distributions associated with these surfaces are analysed by creation of frequency polygons calculated from the reference surface z values. This allows comparison of small scale roughness between samples, as well as pre and post experiment (section 4.5).

The 10 mm reference surfaces include some of the larger scale fracture topography. These larger scale features would play an important role in altering the fracture aperture distribution in the event of significant offset between the two fracture surfaces. Production of these 10 mm reference surfaces enable a comparative assessment of the significance of these features between samples, as well as pre and post experiment, in a similar manner to that undertaken for the 2 mm reference surfaces (section 4.6).

A 10 mm smoothing resolution was chosen for the larger scale assessment to enable consistent analysis across the variety of sample surface sizes - a larger smoothing grid resolution would have limited the analysis to only the large fracture surfaces. Frequency polygons were used for comparison of sub 10 mm topography/roughness between surfaces in the same way as for the sub 2 mm roughness.

For illustration, a 3D visualisation of the raw surface scan data for the Wissey W3A surface (sample W3, surface A) is provided in Figure 4.4a. The 2 mm grid scale is superimposed onto the 3D surface to illustrate the smoothing scale used for analysis of small scale roughness. A photo of the Wissey W3A surface is provided in Figure 4.4b for comparison.

Figure 4.5 illustrates the 2 mm and 10 mm grids used for linearly interpolated smoothing of the Wissey W3A scan data (sample W3, surface A). The 2 mm grid extent contains all but the edges of the surface scan data, as can be seen in Figure 4.4a. The 10 mm grid is smaller due to limitations on the whole number of grid cells that could be included within the surface extent. Despite this, a reasonably high proportion (>60%)of the surface area is included within the 10 mm grid extent, thus the resultant reference surface is considered representative of the sub 10 mm scale roughness of the surface.

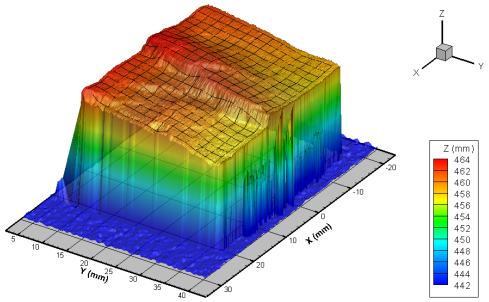

(A) 3D rendering of Wissey W3A scan data with 2 mm grid included

(B) Photo of Wissey W3A surface

FIGURE 4.4: Example of fracture surface, and associated surface scan data, displayed using 3D rendering (Wissey W3A)

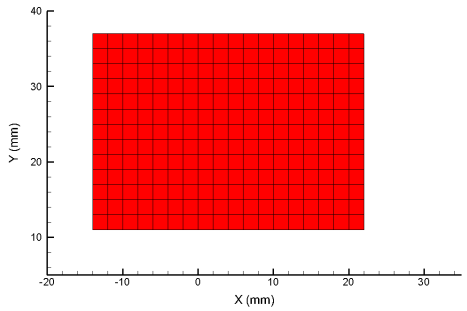

(A) 2 mm smoothing grid for small scale roughness analysis

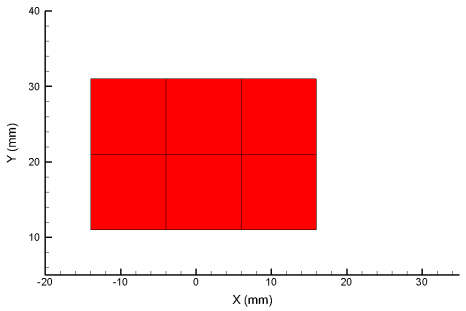

(B) 10 mm smoothing grid for large scale roughness analysis

FIGURE 4.5: Example of grids created for linearly interpolated smoothing of the Wissey W3 sample, surface A scan data

This Wissey sample (sample W3) is the smallest sample analysed. Surface areas for all other samples were therefore of adequate dimensions for both 2mm and 10 mm smoothing and associated roughness analysis.

Small scale (2 mm) roughness grids have been created for all twelve pre-experiment fracture surfaces (two surfaces from each of six samples) and all six post-experiment surfaces (two surfaces from each of three samples). The raw and smoothed surfaces are shown, along with the associated small scale (2 mm) roughness reference surface (raw surface - smooth surface) in Figure 4.6 for the Wissey W3A surface (all are 0.2 mm x

0.05 mm resolution grids), as an example. The small scale (2 mm) roughness surface grids for all eighteen sample surfaces are provided in Appendix A.

It can be seen from Figure 4.6 and Appendix A that the large scale topography features are largely absent from the sub 2 mm roughness reference surface, as intended. However, the centrally-located sharp, linear discontinuity parallel with the y-axis is still visible. This is picked up due to the sharpness of the discontinuity and therefore the significant differences between the smoothed and raw data in this area. However, this is a small proportion of the fracture surface area, and therefore should not significantly skew the small scale roughness frequency polygon.

The larger scale (10 mm) roughness grids are shown for the Wissey W3A surface in Figure 4.7. These utilise the 10 mm smoothing grid for analysis. 10 mm roughness grids have been created in a similar manner for each of the scanned samples (6 pre-experiment and 3 post-experiment), with surface A assessed for each sample. The 10 mm roughness surface grids associated with each of these nine surfaces are provided in Appendix A, in addition to the 2 mm roughness grids.

The main surface topography features are clearly visible within the 10 mm roughness reference surface (Figure 4.7). The 10 mm smoothed surface identifies the surface tilt in the positive y direction for this surface, which is therefore excluded within the reference surface. This ensures the stationarity of the large scale roughness reference surfaces thus enabling data comparison between samples.

Three dimensional images of the two reference surfaces (2 mm and 10 mm) derived for the Wissey sample are shown in Figure 4.8, to complement the two dimensional figures presented in Figures 4.6 and 4.7. These visually emphasise the topographical difference between the two scales of reference surface studied within these assessments.

4.5 Small scale roughness analysis (2 mm)

As discussed in section 4.4, small scale (2 mm) roughness analysis was undertaken on all six pre-experiment and three post-experiment fracture surfaces. The surfaces included artificially fractured East Brae shale, artificially fractured Heletz shale, and naturally fractured Wissey dolomite (Table 4.1).

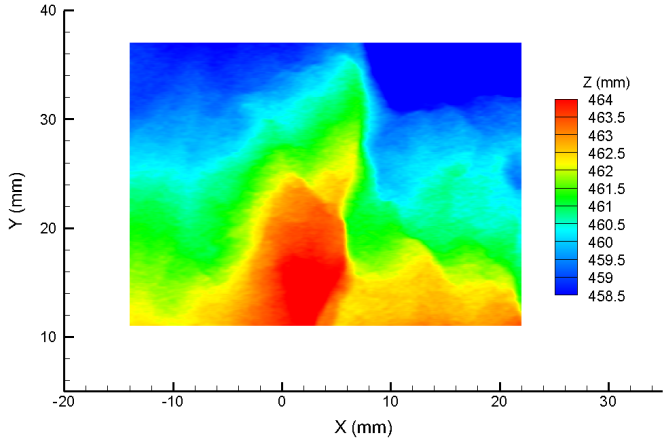

(A) Raw fracture surface data

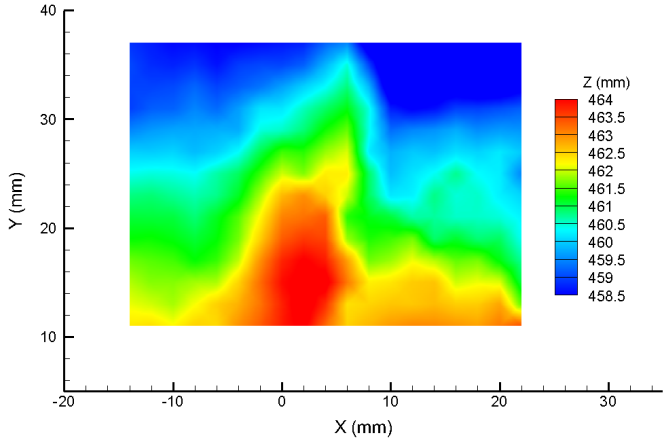

(B) Smoothed fracture surface data (2 mm interpolation)

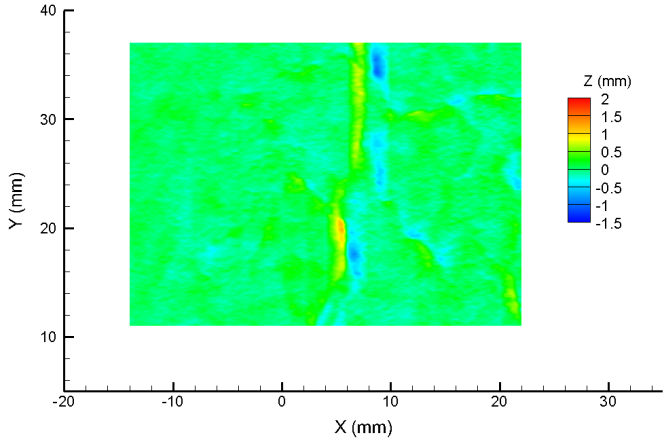

(C) Small scale (2 mm) roughness reference surface (difference between raw and smoothed surfaces)

FIGURE 4.6: Creation of a small scale roughness grid using a 2 mm smoothing technique (Wissey W3A). All datasets are 0.2 mm x 0.05 mm grids.

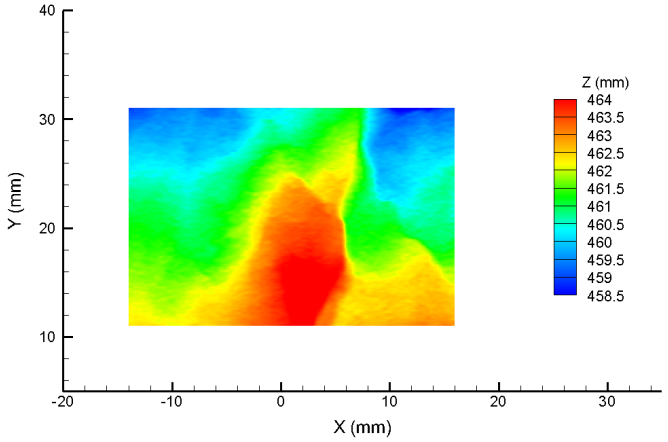

(A) Raw fracture surface data

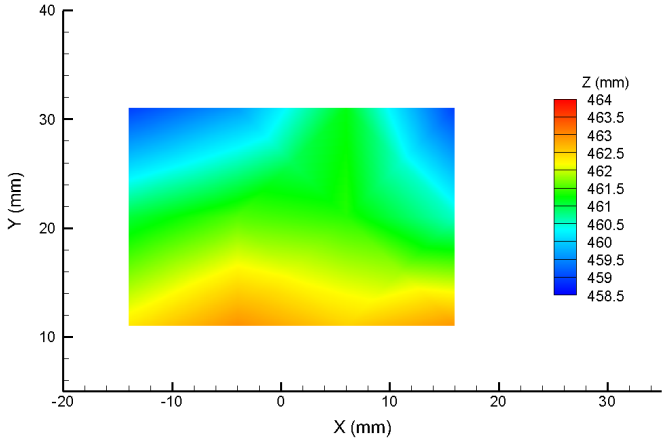

(B) Smoothed fracture surface data (10 mm interpolation)

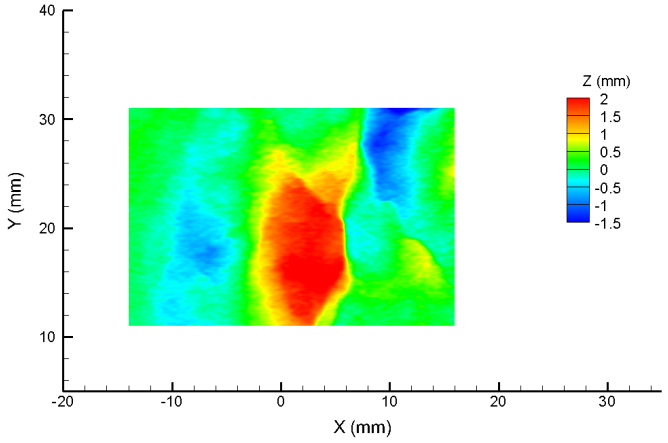

(C) Large scale (10 mm) roughness reference surface (difference between raw and smoothed surfaces)

FIGURE 4.7: Creation of a large scale roughness grid using a 10 mm smoothing technique (Wissey W3A). All datasets are 0.2 mm x 0.05 mm grids.

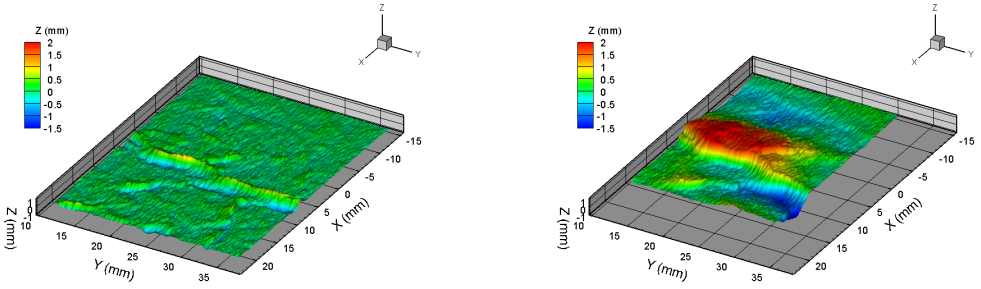

(A) 2 mm reference surface

(B) 10 mm reference surface

FIGURE 4.8: 2 mm and 10 mm reference surfaces created from Wissey W3 sample, surface A scan data

The small scale roughness reference surfaces are used to compare roughness at a sub 2 mm scale between samples. Frequency polygons are plotted for each reference surface. The frequency polygons use the z data points (in metres), and plot a density profile (similar to a histogram) with a bin width of 0.01 mm, that provides information on the distribution profile of z values within the reference surface. As the y-axis is the density of points within each bin rather than the count, the surfaces can be easily compared as each frequency polygon is scaled to integrate to 1, regardless of the number of z points within the surface profile. Thus the area under each graph is the same, and the shapes can be easily compared. In addition, the frequency polygons have all been centred on zero, by subtracting the mean z value from each of the z data points, as it is the z distribution rather than the magnitude that is of interest.

The shape of the frequency polygon provides information about the small scale roughness. A very smooth reference surface will have all z data points extremely close in value (i.e. low standard deviation), thus the associated density profile would be very narrow with a very high peak. If there is significant small scale roughness, the z variation will be high (i.e. high standard deviation), and thus the density profile will be wider (more distributed), and will have a much lower peak value.

The profiles produced from the small scale roughness reference surfaces are discussed within this section.

4.5.1 Pre-experiment fracture surface data analysis

Figure 4.9 shows the frequency polygons produced from each of the pre-experiment samples. From this figure we can see that the frequency polygons all have a relatively symmetrical shape, similar to that of a Gaussian distribution. This is in agreement with the findings of Brown [1995]. There is notable variation in roughness between the surfaces, which is identifiable from the variation in the distribution peaks between profiles (which results from differences in standard deviation between samples). This is expected given the variety in lithology, mineralogy and grain size of the rock types represented (see Chapter 3 for details).

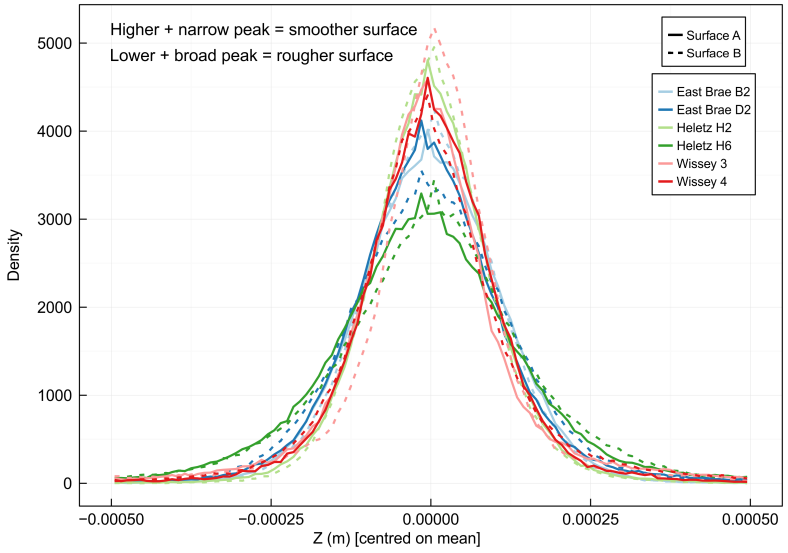

FIGURE 4.9: All pre-experiment surfaces (small scale roughness)

If we compare the Wissey (dolomite) and East Brae (mudrock) profiles (Figure 4.10), we can see that all the Wissey profiles have higher peaks (lower standard deviation) than the East Brae samples. This implies that the small scale roughness of the Wissey surfaces is lower than the East Brae surfaces. Thus, at the small scale, the Wissey surfaces are smoother than the East Brae surfaces. This is in agreement with a visual analysis of the small scale roughness, as the grain structure is better defined in the East Brae mudrock surfaces which suggests higher small scale roughness. The results are as expected given the more crystalline nature of the dolomite (Wissey) mineralogy in comparison to the granular structure of the Kimmeridge Clay mudrock (East Brae).

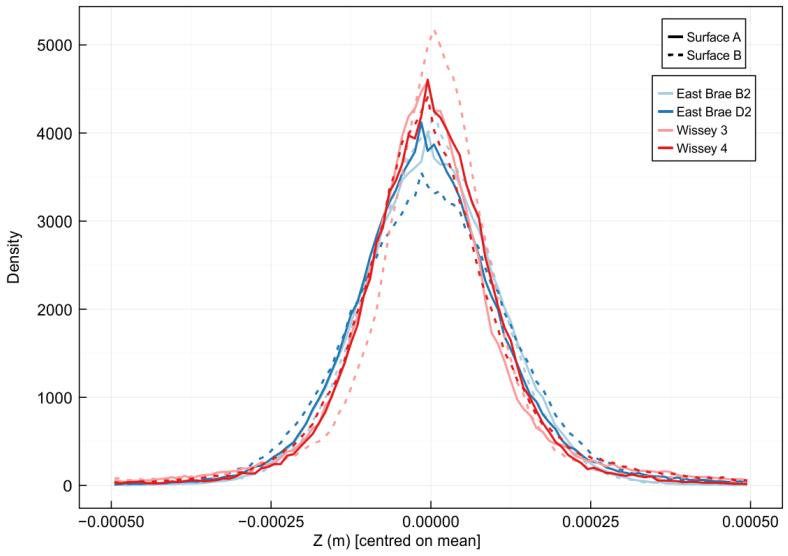

FIGURE 4.10: Wissey and East Brae pre-experiment surfaces (small scale roughness)

It can be seen that the small scale roughness profiles of East Brae samples B2 and D2 are similar to each other, as are the small scale roughness profiles of Wissey samples W3 and W4 (Figure 4.10). However, the two Heletz shale sample profiles (H2 and H6) are very different from each other (Figure 4.11). This is due to the heterogeneous nature of the Heletz shale rock, which consists of silt, mud and pebbles. The difference in the surfaces can clearly be seen visually (Figure 4.12). Sample H2 contains a very smooth fracture surface, parallel to a bedding plane. This fracture appears to be smooth both in terms of large scale and small scale roughness. Heletz sample H6, however, has been fractured close to a pebble, which has remained intact and resulted in significant large scale topographical features within the fracture. The small scale roughness is also greater for H6 due to the fracture crossing bedding planes rather than running parallel to bedding. The roughness profiles for the Heletz samples clearly show the higher small scale roughness of the H6 sample - the H6 profiles have much wider distributions and notably lower peaks. In fact, of all surfaces assessed (including Wissey and East Brae), the H2 surface is the smoothest, while the H6 surface is one of the roughest at this small scale, which emphasises the magnitude of the variation between the two samples. The findings from the small scale roughness profiles are in agreement with visual indicators.

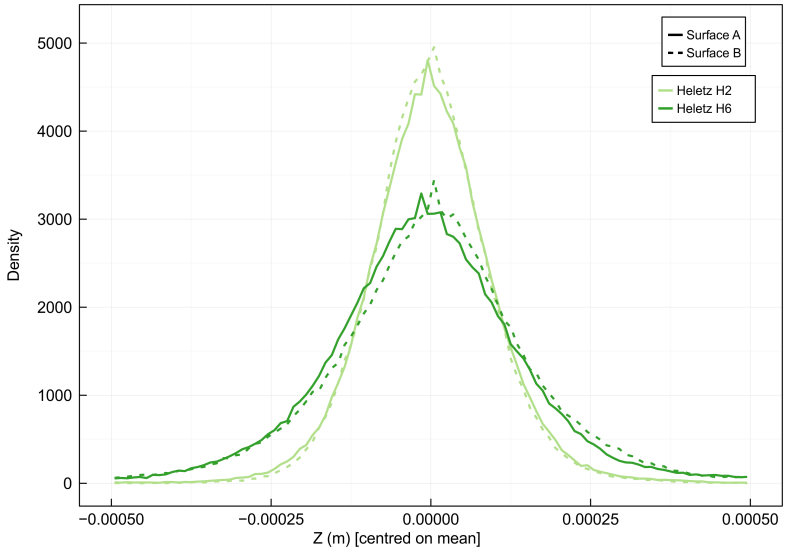

FIGURE 4.11: Heletz surfaces (small scale roughness)

(A) Heletz fracture (H2) (B) Heletz fracture (H6)

FIGURE 4.12: Visual comparison of Heletz fracture surfaces

4.5.2 Post-experiment fracture surface data analysis

Of the six samples scanned pre-experiment, three of these samples were subjected to high pressure, high temperature CO_2 flow experiments during the project. Scanning of these three samples (B2, D2 and W3) was repeated post-experiment. This has enabled comparison of roughness profiles pre- and post-experiment, which has helped to provide insight into the degree of plastic deformation that occurs to surface asperities during the experiments. As the CO_2 flow experiments are undertaken on dry samples it has been assumed that due to the absence of water, mineralogical reactions do not occur, and that any deformation observed results from mechanical stresses applied during the experiments.

Figures 4.13, 4.14 and 4.15 show the change in small scale roughness that has resulted from the high pressure, high temperature CO_2 flow experiments undertaken on East Brae D2, B2 and Wissey W3 respectively. All three samples show a reduction in small scale roughness post experiment.

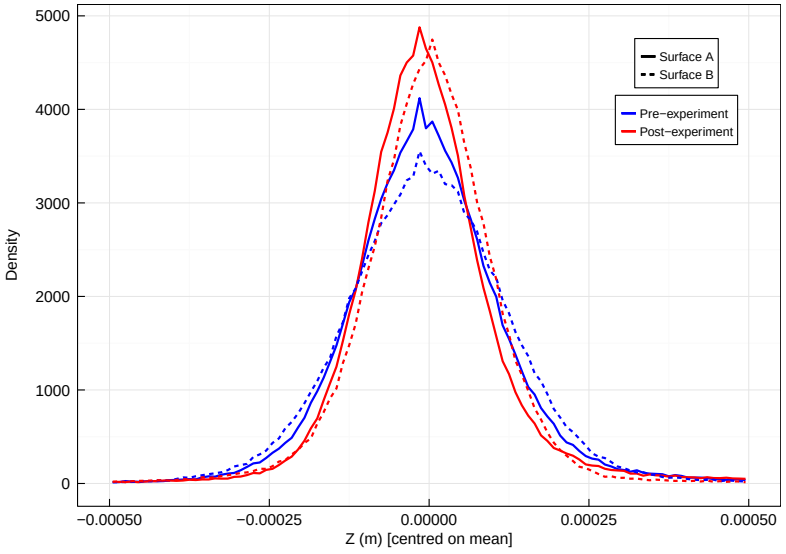

FIGURE 4.13: East Brae D2 small scale roughness change

The East Brae D2 flow experiments were undertaken within a relatively short time period, with the sample held under confining pressure (35-55 MPa) in the coreholder for 13 days. This was as a result of the limited number of scenarios that could be tested due to the low permeability of the fractured sample. Despite this, the post-experiment

small scale roughness profiles indicate a clear reduction in roughness both for fracture surfaces A and B (Figure 4.13).

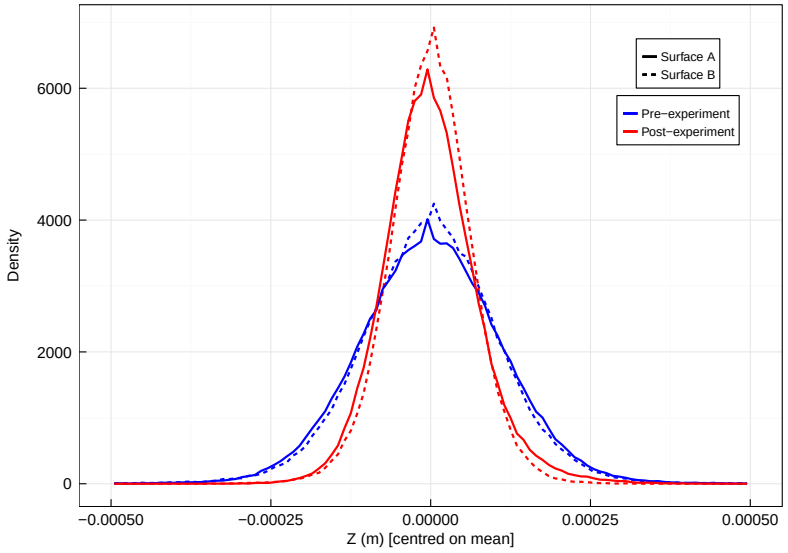

FIGURE 4.14: East Brae B2 small scale roughness change

The East Brae B2 sample was subjected initially to seven days confined within the coreholder during initial flow experiments. Due to low permeability, the sample was then removed and the fracture was manually offset (using sample trimming techniques, section 3.3.1), before further flow testing within the coreholder. The offset fracture experiments were carried out over the period of a further 13 days (see section 6.2). The post-experiment reduction in small scale roughness associated with the fracture surfaces of this sample (Figure 4.14) is significantly more pronounced than that of sample D2. Enhanced deformation of the fracture surfaces may have occurred as a result of the forced offsetting of the fracture, as offsetting is likely to reduce the initial contact area between surfaces thus increasing the force acting on the asperities for a given confining pressure. In addition, the B2 sample was held under maximum confining pressure for a notably longer total duration than sample D2. The maximum confining pressures adopted for both the D2 and offset B2 (B2b) samples were the same, however due to the higher mean fluid pressures within the D2 sample during experiments the maximum effective stress experienced by the offset B2 (B2b) sample was greater which may also contribute to the more significant surface changes observed.

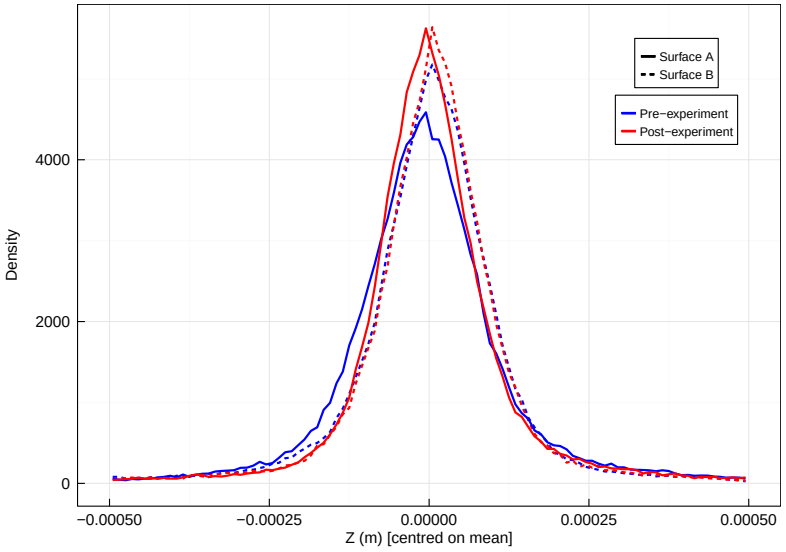

FIGURE 4.15: Wissey W3 small scale roughness change

The Wissey flow experiments were undertaken with the Wissey fractured sample held under confining pressure within the core holder for a 35 day period. Following the experiments, the sample remained within the core holder under more than 20 MPa confining pressure for an additional four months before being released and removed from the rig system. The post-experiment small scale roughness profiles (Figure 4.15) indicate a small reduction in roughness following this extensive period. However, the roughness change is not as significant as that observed for both the East Brae samples, despite the much longer experiment duration. This is considered to be due to the hardness of the Wissey dolomite material, compared with the relatively soft East Brae Kimmeridge clay shale, as demonstrated within the hardness tests (section 3.4.3). Mechanical deformation of the Wissey dolomite fracture surfaces is likely to be proportionally lower than mechanical deformation of the East Brae Kimmeridge clay surfaces under similar experimental conditions due to the higher material hardness. In addition, previous loading of the Wissey natural fracture in situ may have already led to significant inelastic deformation prior to undertaking these experiments, thus limiting the capacity for further deformation.

4.6 Large scale roughness analysis (10 mm)

As discussed in section 4.4, a 10 mm x 10 mm smoothing grid was used to create reference surfaces for analysis of the larger-scale (sub 10 mm) roughness of the fracture surfaces. This has been undertaken to enable a comparative assessment of the large scale fracture surface features between samples, as well as to assess if any changes or deformation to the large scale surface features are evident subsequent to the high pressure high temperature CO_2 flow experiments.

4.6.1 Pre-experiment fracture surface data analysis

Figure 4.16 shows the frequency polygons associated with the 10 mm reference surfaces for each of the six pre-experiment surfaces assessed. These represent the large scale (sub 10 mm) roughness of the surfaces. As with the 2 mm roughness profiles, those with higher peaks and narrower distributions are smoother at the sub 10 mm scale, while the wider lower-peaked profiles indicate rougher surfaces at this scale.

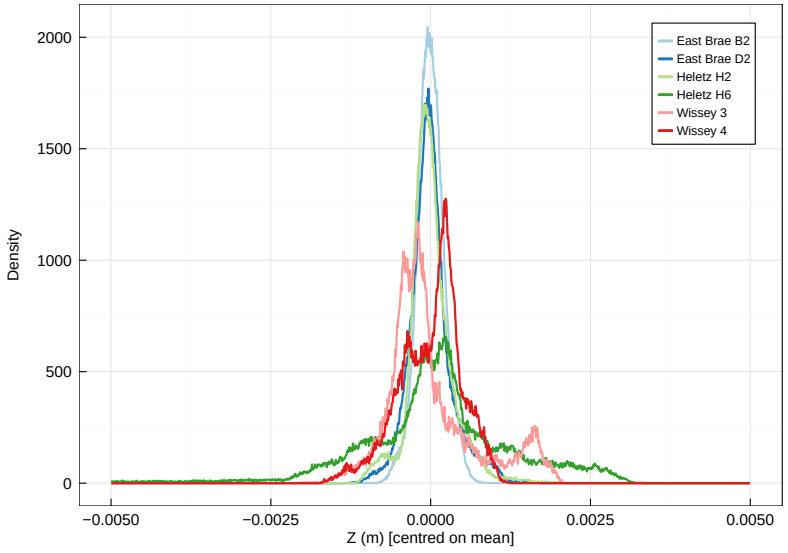

FIGURE 4.16: All pre-experiment surfaces (large scale roughness)

The profiles associated with both East Brae samples and the Heletz H2 sample are almost symmetrical, and similar in shape to a Gaussian distribution, with relatively high peaks. This indicates the smoothness of the fracture surfaces at this larger scale.

Thus, while the East Brae samples are relatively rough at the small scale (Figure 4.9), the large scale topography is very smooth. The Heletz H2 sample, on the other hand, is relatively smooth both at small and large scales.

The large scale roughness profiles associated with the Wissey samples have different shapes, as expected, due to the different topographies of the fracture surfaces. However, they both have similar magnitude density peaks, with both peaks off-centre. The profiles also both contain small secondary peaks. This indicates that the topographical nature of the surfaces is similar, which is expected as both samples are cored from the same pre-existing fracture. The wider profile distribution and lower peaks of the Wissey profiles over the East Brae and Heletz H2 samples indicates the greater topographical prominence seen within the Wissey fracture surfaces.

The Heletz H6 profile has the widest distribution and lowest density peak of the samples tested. This is due to the significant topographical variance associated with the fracture surface of this heterogeneous sample. This sample is very different in nature to the Heletz H2 sample, in that both small and large scale fracture surface roughness is significant, while with H2, both small and large scale roughness is relatively low. This highlights the heterogeneity of the Heletz shale and its potential fracture characteristics, which makes conceptual understanding and representative modelling of this seal rock layer a challenge.

4.6.2 Post-experiment fracture surface data analysis

While analysis of pre- and post-experiment small scale roughness profiles indicate a consistent reduction in small scale surface roughness as a result of the high pressure, high temperature CO_2 flow experiments for all samples, a similar comparison undertaken with large scale roughness profiles does not produce consistent results. A small increase in large-scale roughness can be observed for both of the East Brae samples (Figures 4.17 and 4.18), through a reduction in the density profile peak, and a slightly wider distribution post-experiment. However, while there is some variance between the Wissey pre- and post-experiment density profiles, there is no clear evidence for an increase or decrease in large-scale roughness (Figure 4.19). Some variance in profile shape would be expected due to repeat sampling errors, even if no material change in large-scale roughness had occurred, and this may be the reason for the profile variation observed.

Due to the relative softness of the East Brae Kimmeridge clay material (see section 3.4.3), the increase in large-scale roughness observed within the East Brae samples may be a result of compressional folding of the sample material under the high stresses applied during the CO_2 flow experiments. If this is the reason for the change, the same would not be expected for the Wissey sample due to the much harder dolomite material, which would explain the inconsistent findings between the samples.

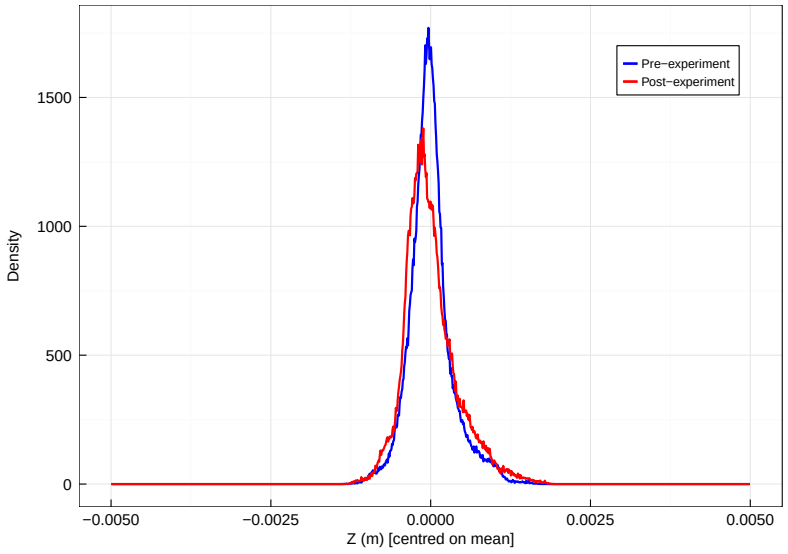

FIGURE 4.17: East Brae D2 large scale roughness change

4.7 Comparative review of fracture surface roughness findings

Analysis of fracture surface roughness has been discussed in the above sections for three of the four samples used within CO_2 experiments: East Brae D2, East Brae B2(b) and Wissey W3. Only qualitative surface information is available for the Cambrian shale fracture. The fracture surface analysis is indicatively illustrated in Figure 4.20 for these four samples for clarity. The analysis indicates that at the larger scale, the Wissey W3 sample is the roughest of the three samples tested during flow experiments, with both East Brae B2b and D2 observed to be significantly smoother. However, consideration of small-scale roughness (thought to be a key influence on fracture aperture for mated fractures) indicates that pre-experiment the East Brae samples (both B2 and D2) are

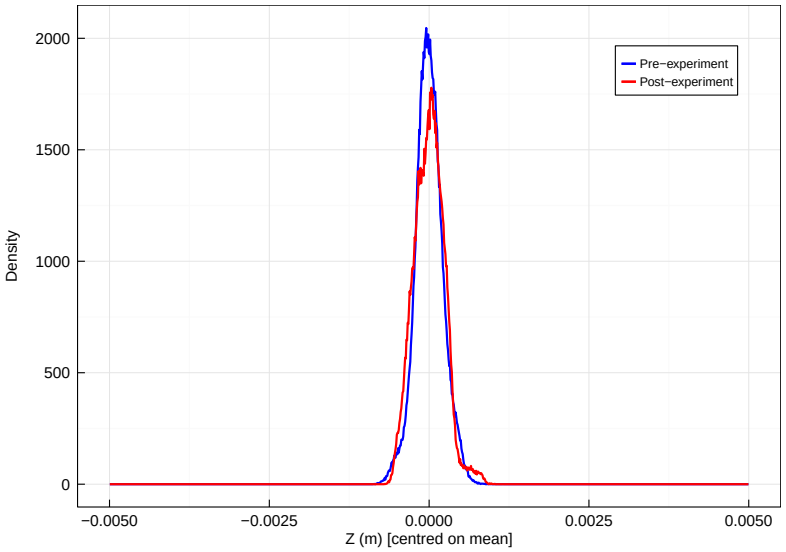

FIGURE 4.18: East Brae B2 large scale roughness change

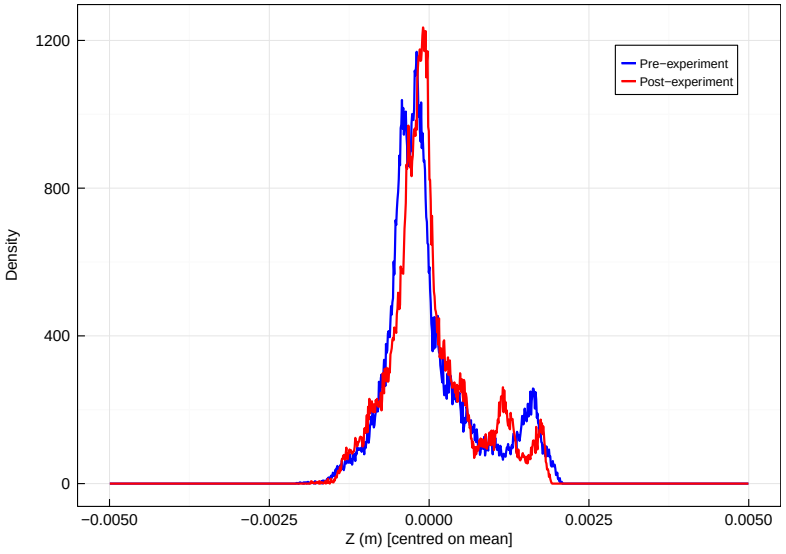

FIGURE 4.19: Wissey W3 large scale roughness change

notably rougher than the Wissey W3 sample. Post-experiment, the small-scale roughness is observed to have reduced to some degree for all samples, which is believed to be due to plastic deformation (section 7.6). The changes are most significant within the East Brae samples. Post-experiment, the D2 sample maintains the highest small-scale roughness despite some roughness reduction during the experiments. East Brae B2 small-scale roughness is however significantly reduced during the experiments such that, post-experiment, it is smoother than the Wissey W3 sample. Qualitatively, the Cambrian shale surfaces are considered to have a large scale roughness similar to East Brae D2. The small scale roughness is considered to be lower than the pre-experiment East Brae samples, but higher than Wissey W3.

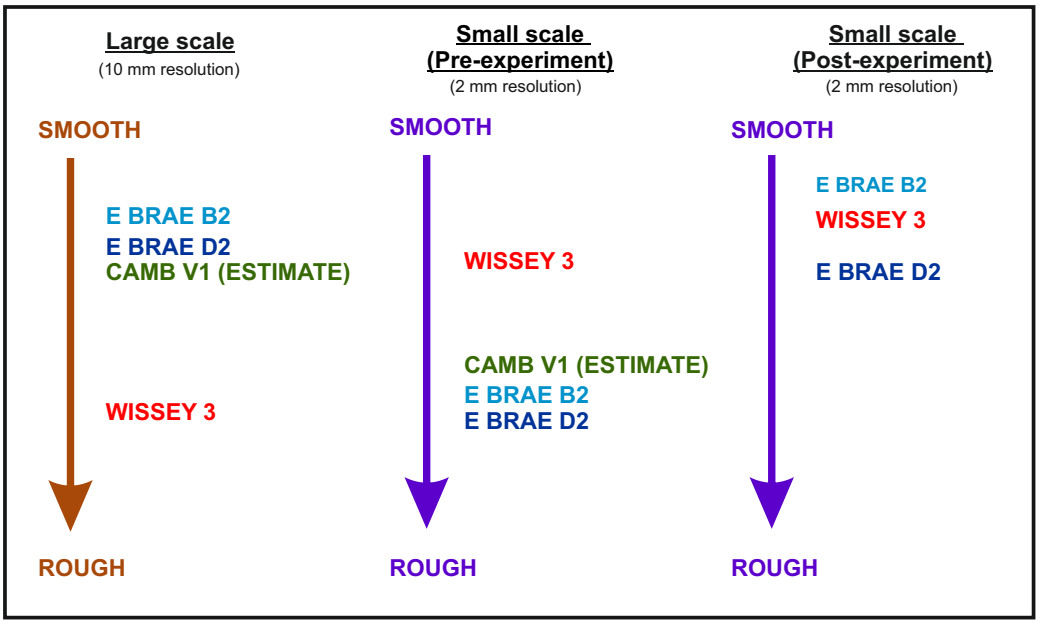

FIGURE 4.20: Indicative roughness scale drawn from fracture surface analysis results

4.8 Applications for fracture surface geometry data

While the roughness analyses presented in sections 4.5 and 4.6 are useful for analytical comparison of fracture surfaces, both between surfaces and for pre- and post-experiment assessment of the same surfaces, the fracture surface data can also be utilised for estimation of fracture aperture distributions. This is of great value as geometry input data into coupled flow and mechanical models of the discrete fractures [Walsh et al., 2008].

Methods have been developed for reconstructing aperture distributions directly from fracture surface topography data [Ameli et al., 2013, Neuville et al., 2012]. However, there are challenges associated with correlating precisely the horizontal positioning of the upper and lower surfaces to ensure the aperture calculation is accurate. Significant aperture errors may be introduced as a result of small misalignment errors between the surfaces. An alternative approach is to use the statistical distribution profiles of small scale roughness, as presented in section 4.5 to create a statistically representative aperture distribution for use within numerical models.

One method for generation of statistically representative aperture data is detailed in McCraw et al. [2016]. This method involves fitting a Gaussian (normal) distribution to the small scale roughness profile generated from the fracture surface data (section 4.5). Two synthetically generated asperity datasets, X_1 and X_2, are then generated that are mathematically described by this fitted Gaussian (normal) distribution, $N(\mu, \sigma^2)$. The aperture data, e, are generated using Equation 4.1, where e_0 and m are calibration parameters that describe the vertical separation and mismatch of the asperity distributions respectively. This aperture dataset is generated at a resolution appropriate for use within the discrete fracture coupled flow and mechanical models, and the parameters e_0 and m are determined during model calibration, using the results from the laboratory fracture flow experiments, and taking consideration of the resulting percentage contact area between the surfaces. The resultant aperture distribution is expected to be approximately Gaussian [Brown et al., 1986, Walsh et al., 2008].

$$e = e_0 + m(X_1 - X_2) \tag{4.1}$$

The effect of parameters e_0 and m are illustrated in Figure 4.21, taken from McCraw et al. [2016].

McCraw et al. [2016] uses the above statistical method for generation of aperture data within a modelling study of Wissey sample W3. The model was calibrated using results from the fracture flow laboratory experiments. A series of fluid back pressure cycles (10 MPa to 30 MPa) and fluid flow rate cycles (~1-13 ml/min, that is 1.7×10^{-8} - 2.2×10^{-7} m^3/s) were simulated at different confining pressures (35 MPa to 55 MPa).

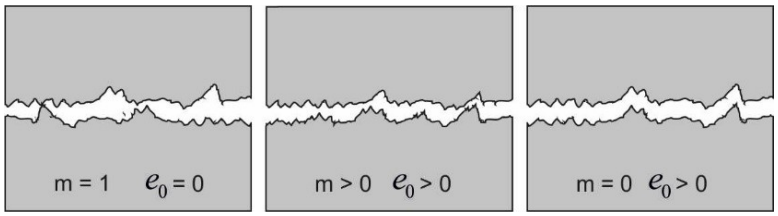

FIGURE 4.21: Generating aperture distribution using Equation 4.1: illustration of effects of e_0 and m [McCraw et al., 2016]

Despite a number of model simplifications, including adoption of the statistically generated aperture distribution and use of constant density and viscosity fluid functions, the model results were found to follow experimental trends reasonably well. This indicates that adoption of statistically representative aperture distributions may be suitable for coupled process (flow and mechanical) modelling. This emphasises the benefits of acquisition of fracture surface topography data and associated statistical analysis undertaken during this project.

As contact area between fracture surfaces increases, the effects of flow path tortuosity increases and connectivity within the fracture is reduced. When the contact area between surfaces is greater than 30%, tortuosity effects can depress the fluid flow rate by two to three orders of magnitude Tsang [1984]. Tsang [1984] found contact areas to be between 10% and 20% for granite and basalt fractures under a maximum applied stress of 20 MPa, while Pyrak-Nolte et al. [1987] found contact areas up to 30-40% for a natural granite fracture under 85 MPa maximum normal stress. Modelling of the Wissey W3 sample within McCraw et al. [2016] suggested that contact area during these experiments remained below 15%, under effective normal stresses of up to 45 MPa. Contact areas during experiments on the relatively soft East Brae Kimmeridge Clay samples under similar stress conditions would be expected to be higher, due to plastic deformation (section 4.5).

4.9 X-ray computed tomography scanning

A high resolution x-ray computed tomography (CT) facility has been built within the experimental geoscience laboratories at the University of Edinburgh. X-ray CT scanning is a non-destructive technique for high resolution visualisation of the interior of opaque solid objects. It can be used to obtain digital information on 3D geometries

and properties (http://www.ctlab.geo.utexas.edu/overview/index.php). The recently upgraded facility at the University of Edinburgh is capable of scanning a full 38 mm diameter core, up to 70 mm in length at 85 μm resolution. Higher resolution (40 μm) scans of core sections are also possible.

The x-ray CT scanner has been used within this project to undertake post experiment scanning of the Cambrian shale fractured sample used during comprehensive CO_2 fracture flow experiments. Post-experiment scanning was undertaken on this sample due to external evidence of an induced micro-fracture network within the core sample post-experiment, which was of particular interest (see Figure 4.22). The x-ray CT scanner was particularly suited to post experiment fracture geometry analysis on this sample as the core remained held together post-experiment by the epoxy resin applied during sample preparation (see section 3.3).

Figure 4.22 contains photos taken of the sample post-experiment, following removal of the adhesive aluminium coating. Evidence for stress-induced fracturing, mainly radial and parallel to the bedding, is clear towards the downstream end of the sample.

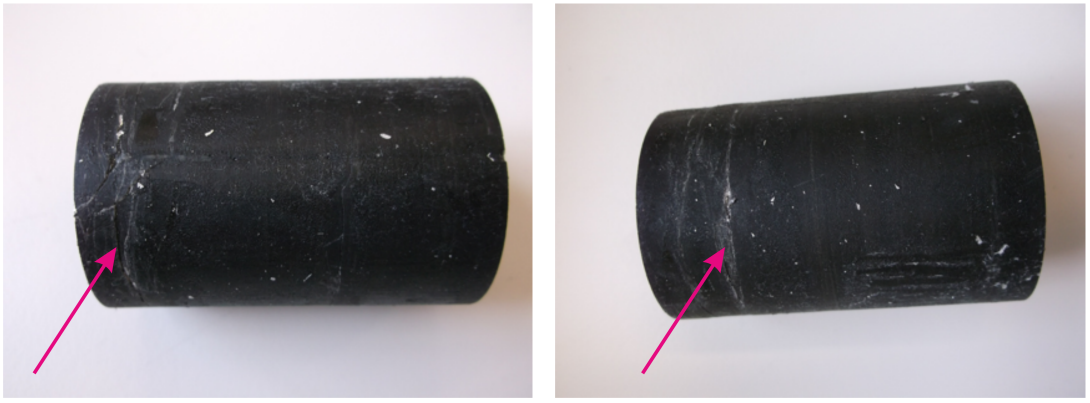

FIGURE 4.22: Images of the Cambrian V1 sample post-experiment showing radial stress-induced fracturing concentrated towards the downstream end of the sample (indicated by arrows).

Figure 4.23 is a CT image slice from a high resolution (40 μm) scan of the post-experiment Cambrian V1 sample. Four micro-fractures can be seen within this image, emanating from the main fracture at the outer ends. These micro-fractures can be seen throughout the CT image stack of the high resolution scan, suggesting that the micro-fractures are axially continuous throughout this section of the sample. As

with the external evidence of radial fracturing in Figure 4.22, these internal, axially-continuous micro-fractures (perpendicular to bedding planes) may also have been induced by stress-loading during the experiments, and could contribute to changes to the hydraulic properties of the sample (Chapter 7).

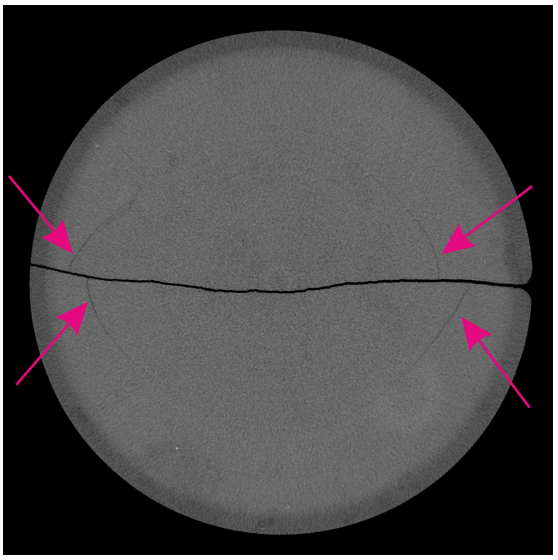

FIGURE 4.23: CT image slice from Cambrian V1 sample post-experiment. This shows evidence of micro-fracturing within the sample, emanating from the main longitudinal fracture (indicated by arrows). Micro-fracturing may have resulted from stress-loading during experiments.

4.10 Summary of fracture surface analysis

This chapter contains an analysis of the fracture surface characterisation data acquired using the laser scanner at the University of Strathclyde. Simple data processing and statistical analysis methods have been adopted to review both small scale and large scale roughness associated with six fractured samples. The acquisition of both pre- and post-experiment data has enabled roughness changes resulting from the high pressure, high temperature CO_2 fracture flow experiments to be assessed.

The analysis indicates that the artificially fractured East Brae surfaces have a higher small scale roughness than the naturally fractured Wissey surfaces, while the opposite is true of the large scale roughness, due to the smooth topography of the East Brae surfaces, which were fractured parallel to bedding.

Two Heletz samples have also been analysed, however the fracture surfaces associated with these are very different in nature, highlighting the heterogeneity of the Heletz shale. Sample H2 has smooth topography and therefore low large scale roughness, similar to that of the East Brae samples, but also has low small scale roughness, in line with that of the Wissey samples. However the H6 fracture surfaces have extreme topographical variation, in part due to the presence of a hard, pebbly feature within the sample which influenced the fracturing process. This has resulted in significant large scale roughness, more notable than for any of the other samples. The associated cross-bedding fracturing has also produced high small scale roughness for this sample, again the most significant of all samples analysed.

Analysis of post-experiment fracture scan data for both East Brae samples and the Wissey W3 sample shows that the small scale roughness is reduced following the high pressure, high temperature CO_2 fracture flow experiments for all samples. This suggests that permanent deformation of the surface asperities may have occurred during the experiments, most likely due to the high effective normal stresses applied. The roughness change is more significant within the East Brae samples, which is thought to be due to the lower material hardness of the East Brae shale in comparison to the Wissey dolomite (section 3.4.3). The post-experiment data suggests that the large scale roughness of the East Brae samples has increased marginally. This may potentially be due to subtle deformation and folding of the whole core sample in response to the high stresses applied to this relatively soft material. There is no clear alteration to the Wissey large scale roughness.

The small scale roughness profiles derived for the fracture surfaces during this project may be used for estimation of associated fracture aperture distributions, as a result of the relationship identified by Brown [1995]. A simple technique for generation of statistically representative aperture data has been successfully tested during coupled process modelling of the Wissey sample [McCraw et al., 2016]. This demonstrates that there are significant potential applications for further use of the fracture surface characterisation data acquired during this project in future modelling studies.

The simple statistical analysis undertaken within this chapter has provided valuable comparative information on the surface roughness of the scanned samples. Findings suggesting a reduction in small scale roughness of all samples post-experiment are significant and imply permanent deformation of surface asperities occurs. However,

there is potential for much more comprehensive and sophisticated geostatistical analysis to be carried out using the surface scan data, including studies of spatial correlation and scale analysis. The valuable surface characterisation data gathered during this project therefore has the potential to form the basis of significant future statistical analysis studies, as well as being of benefit within modelling studies.

The value of fracture surface scanning has been shown within this Chapter, however where a non-destructive method of fracture characterisation is required, use of x-ray CT scanning has been shown to have great potential for future studies. An x-ray CT scan of the Cambrian shale sample identified the presence of longitudinal micro-fractures originating from the main induced fracture. These may have been induced during experimental stress-loading and could contribute to changes in hydraulic properties of the sample. Use of this scanning technique has highlighted great potential for more significant use of x-ray CT scans within future fracture flow experimental studies.

Chapter 5

Rig design and build

5.1 Introduction

An experimental rig was designed and built to meet the requirements of original experimental investigation of CO_2 flow through fractured low permeability geological media under controlled in-situ pressure and temperature conditions. This chapter details the final rig design, and component details. It also includes discussion of the design development process and rig commissioning tests undertaken.

The principal requirements of the rig are the ability to control, measure and log key parameters while enabling supercritical CO_2 flow through a discretely fractured core sample.

In order to assess thermal and mechanical controls on the hydraulic behaviour of the fractured core samples to supercritical CO_2 flow, it is necessary to be able to control:

- the radial confining pressure acting on the sample;
- the downstream fluid pressure;
- the CO_2 fluid flow rate through the sample;
- and the sample and fluid temperature.

Hydraulic behaviour of the fractured sample to CO_2 flow is analysed through measurement and logging of:

- the radial confining pressure acting on the sample;
- the fluid pressure at both the upstream and downstream ends of the sample;
- the differential fluid pressure across the sample;
- the fluid flow rate through the sample (indirect measurement);
- and the sample and fluid temperature.

The rig design (section 5.2) is based on an earlier rig built during the MUSTANG EU FP7 project [Edlmann et al., 2013], and utilises the same core holder, confining oil pump and heat exchanger. It also utilises the same continuous pressure logging equipment. The new rig design, developed during this project, incorporates improved pressure, flow rate and temperature control; differential pressure measurement; and continuous temperature and flow rate logging capabilities.

The rig design has developed and evolved over a two year period, as a number of design issues have been identified and resolved to enable successful experimental analysis. This iterative, problem-solving approach to rig development was necessary due to the original and unique nature of the experimental research, with no established design or method procedures to draw from. The main design and equipment challenges have been: effective operation of the Isco syringe pumps with supercritical CO_2; temperature control; differential pressure measurement; and material selection for use with supercritical CO_2. During the project several pieces of equipment were found to contain material unsuitable for use with supercritical CO_2. This issue is discussed further in section 5.4. Discussion of the other design developments and adaptations is included within section 5.3.

Rig commissioning tests were undertaken to ensure the correct operation and suitability of the system equipment under experimental conditions. Details of the rig commissioning procedures and tests are included in section 5.5.

A timeline of rig design, build, development and testing is provided in Figure 5.1 for reference and to provide context. It was found that resolution or testing of one design issue often led to identification of another, which goes some way to explain the order of rig development actions.

An example of this is that stabilisation of the core holder temperature through containment in an oven (Sep 2013) reduced fluctuations in confining pressure that were a result of the temperature sensitivity of the confining oil. As a result it was then possible to detect the effects of CO_2 diffusion through the elastomer sleeve into the confining oil (Dec 2013), which caused an increase in confining pressure during experiments, as discussed in section 5.4. This materials issue was subsequently mitigated through use of sample coatings and sleeve liners to minimise CO_2 contact with the core holder liner. Details of the associated sample preparation requirements were discussed in Chapter 3. This example demonstrates the complexities and interdependencies of the rig development and sample preparation processes.

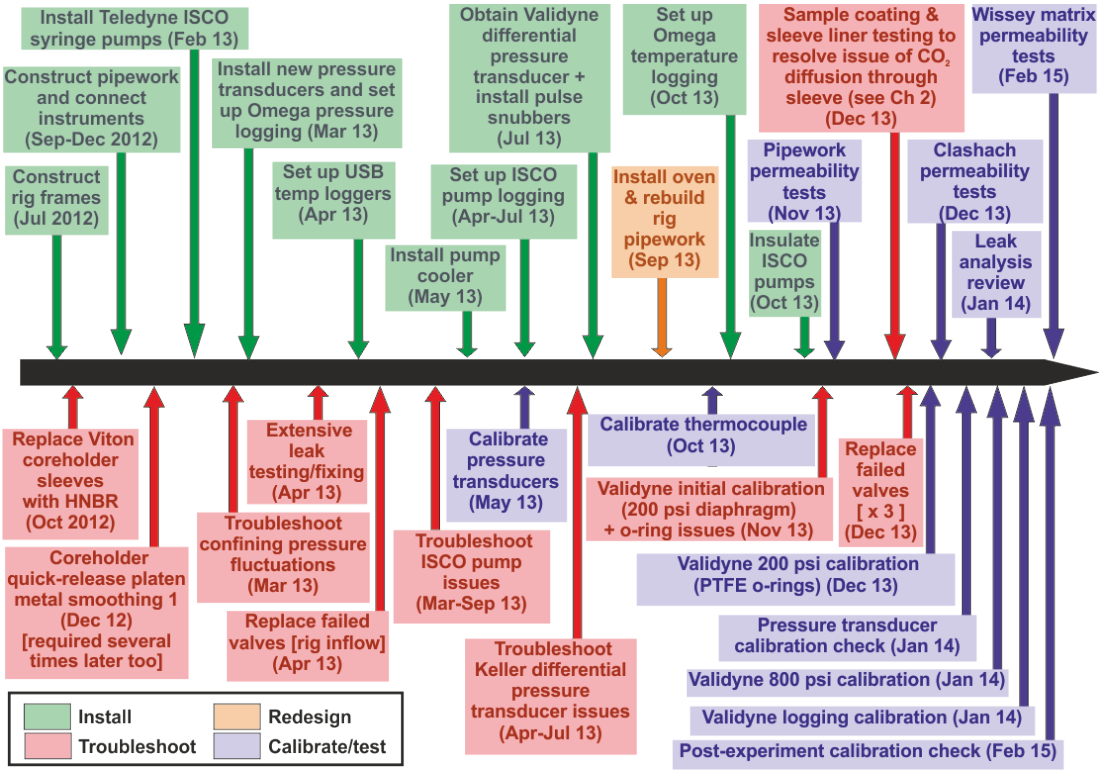

FIGURE 5.1: Experimental design, build, development and testing timeline

The final section of this chapter, section 5.6, discusses recommendations for potential further improvements to rig design for future studies.

5.2 Final rig design

This section provides a summary of the final rig design. Detailed information on the rig control and measurement equipment is contained within section 5.3. A schematic of the rig is provided in Figure 5.2.

The rig is rated for temperatures up to 80°C and confining and fluid pressures up to 68.9 MPa (10,000 psi).

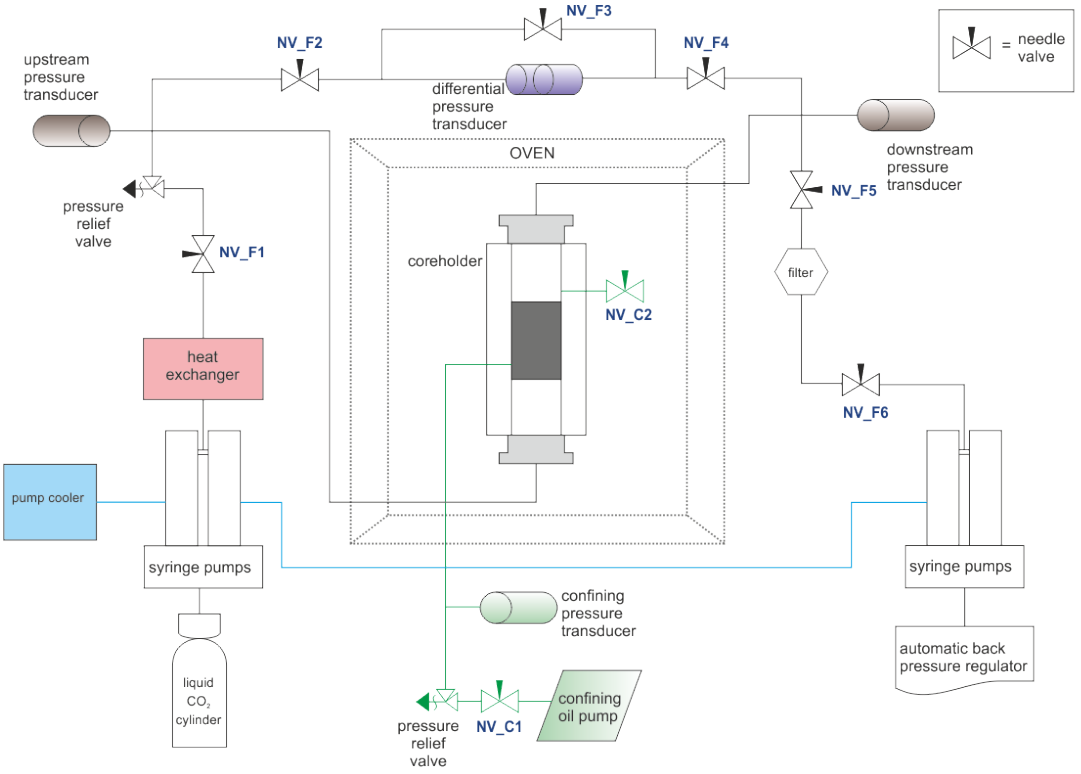

FIGURE 5.2: Experimental rig schematic (excluding temperature measurement and instrument logging details)

As discussed in section 5.1, the principle requirements of the rig are to control and measure key parameters while enabling CO_2 flow through the fractured core sample.

The fractured core sample (38mm diameter) is held vertically within a Hassler-type core holder. Fluid entry/exit ports on both the upstream and downstream end platens allow CO_2 to be pumped into the bottom of the sample and out of the top. Injection of CO_2 is at the bottom of the sample in order to minimise slug flow and maximise the effects of buoyancy of the CO_2 in relation to any residual brine/water within the

sample. This set-up also ensures the rig is versatile for use with other applications i.e. study of multiphase flow, etc. The core holder is contained within an oven, allowing the temperature of the sample to be controlled. Within the core holder the sample is contained within an elastomer sleeve, and radial pressure is applied to the sample by pressurising confining oil on the outside of the elastomer sleeve using a high pressure hydraulic hand pump (see section 5.3.2 for details).

A pair of high pressure syringe pumps at the upstream end of the fluid system control the flow rate of CO_2 through the sample, while a second pair of high pressure syringe pumps on the downstream end of the fluid system work in constant pressure mode to control the fluid pressure on the downstream end of the core by receiving flow into the syringe pumps (out of the rig) as required in order to maintain a set pressure. To ensure fluid bypass around the outside of the core sample does not occur during experiments, the fluid pressures must be kept below the radial confining pressure acting on the sample at all times.

Carbon dioxide is supplied to the upstream pumps via a liquid withdrawal CO_2 cylinder (max pressure 5 MPa). In order to facilitate the filling of the syringe pumps with liquid CO_2, the syringe pumps cylinders must be cooled. A circulating temperature-controlled bath provides cold water/ethylene glycol solution to temperature control jackets that surround the syringe pumps, thus maintaining the pumps (as well as the fluid inside the pumps) at a constant temperature (approximately 2.5°C).

As the flow experiments take place at around 40°C and 60°C, it is necessary to heat up the CO_2 within the system, downstream of the cooled syringe pumps. The CO_2 is therefore pumped through a heat exchanger set to the desired experimental temperature (40°C or 60°C) before the CO_2 pipework enters the core holder oven. Heating tape (set to the same temperature) and pipe insulation are used on the pipework between the heat exchanger and the oven to try to maintain the fluid temperature within this section.

Due to adiabatic expansion of carbon dioxide released from the downstream syringe pumps during their emptying process, and resultant Joule-Thomson cooling effects, there is a danger of the disposal pipework downstream of the pumps freezing and blockages occurring. In order to minimise this risk, an automatic back pressure regulator is fitted downstream of the syringe pumps to step down the pressure in the syringe

pumps to 5 MPa (725 psi) before release to the atmosphere. Downstream of the automatic back pressure regulator heating tape is used to prevent the risk of pipe freezing occurring as the CO_2 expands on release to atmosphere.

Measurement and logging of pressures and temperature is of great importance during the flow experiments. The rig has been designed to enable measurement and logging of: confining pressure; fluid pressure upstream and downstream of the sample; differential pressure across the sample; and temperature of the sample. In addition, standalone temperature loggers are used to monitor the upstream syringe pump temperatures, and syringe pump logging software continuously records pressure and flow data from each of the pump controllers (upstream and downstream). Flow rate through the sample is calculated using the pump flow rate, pump temperature and sample temperature (see section 5.3.3).

Table 5.1 details the instruments used for both measurement and logging of the above parameters. Further information is provided in sections 5.3.3 and 5.3.4 respectively.

To prevent unsafe pressure build up within the system, pressure relief valves are fitted to both the confining oil line and the CO_2 pipework. In addition a CO_2 safety monitor is installed within the laboratory, designed to alert users in the event of excess CO_2 concentrations. Details of this safety equipment is included in section 5.3.5.

5.3 Details of rig components

Details of equipment used within the final rig design is provided within this section. Where components or designs have replaced earlier versions, discussion of the process leading to and justification of their use is also provided.

5.3.1 Rig framework structure and pipework

Initial rig construction required two framework structures to be designed and built. The frames were designed to accommodate the main rig equipment, as shown in Figure 5.3. Construction of the framework was carried out using Dexion Speedframe materials. The shelving and backpanel were made from marine plywood and varnished with polyurethane varnish for durability.

Table 5.1: Measurement and logging instruments

Parameter	**Measuring instrument**	**Instrument accuracy**	**Logging device**	**Log frequency (s)**
Confining pressure	Omega PX302 0-10,000psi (0-68.9 MPa) pressure transducer	±0.25% BFSL	Omega OM-CP current data logger	5
Upstream fluid pressure	Omega PX302 0-10,000psi (0-68.9 MPa) pressure transducer	±0.25% BFSL	Omega OM-CP current data logger	5
Downstream fluid pressure	Omega PX302 0-10,000psi (0-68.9 MPa) pressure transducer	±0.25% BFSL	Omega OM-CP current data logger	5
Differential pressure	Validyne DP360 Differential pressure transducer (0-800 psi/0-5.5 MPa)	±0.5% FS	Omega OM-CP current data logger	5
Cell temperature	Omega JMTSS-010U-12-120 thermocouple	±2.2°C	Omega OM-CP current data logger	5
Pump temperature (for Pump 1A, 1B)	Omega K thermocouple	±2.2°C	Omega OM-EL-USB-TC	10
Pump flow rate (for Pump 1A, 1B, 2A, 2B)	Teledyne Isco Pump	±0.3%	Isco Pump log system	5
Pump pressure (for Pump 1A, 1B, 2A, 2B)	Teledyne Isco Pump	±0.1% of full scale (±20psi/138 kPa)	Isco Pump log system	5
Pump operation status (for Pump 1A, 1B, 2A, 2B)	Teledyne Isco Pump	-	Isco Pump log system	5

FIGURE 5.3: Rig frames (as used prior to acquiring core holder oven)

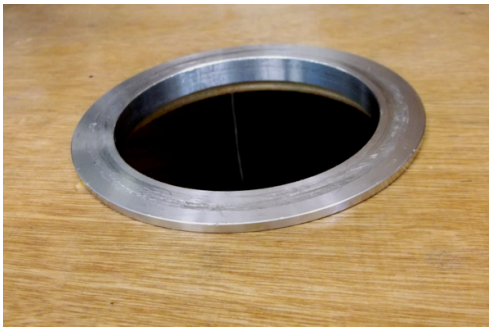

(A) Core holder stand in rig frame

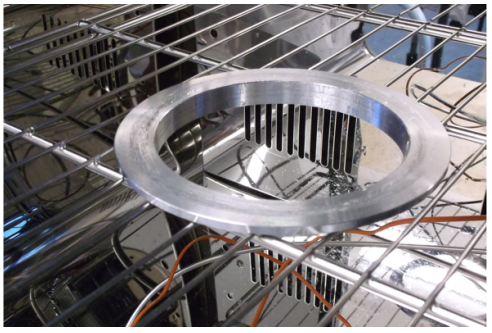

(B) Core holder stand in oven

FIGURE 5.4: Ring stand for securing core holder within rig system

The left frame incorporated a rigid backpanel and single shelf, and was designed to accommodate the core holder, pressure transducers and associated pipework and control valves. The right frame contained several shelves for accommodation of temperature and pressure control, and monitoring and logging equipment. Although the experiments undertaken during this project involved single phase CO_2 flow, the rig was designed to be easily adaptable for multiphase flow experiments, and thus a brine pump was also located within the right frame.

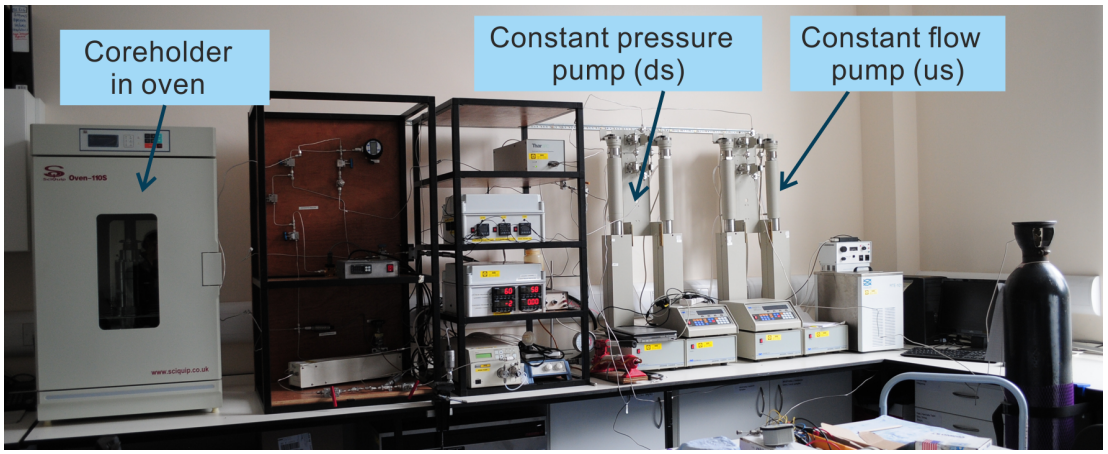

FIGURE 5.5: Final rig layout (with oven)

The University of Edinburgh workshop technicians assisted with incorporation of a stainless steel ring core holder stand within the left frame. Later redesign involved relocation of the core holder and stainless steel stand to a dedicated oven for improved temperature control (see section 5.3.2.3 for details). The core holder stand is shown in Figure 5.4, both within the original frame location, and in the redesigned oven location. The ring stand allowed the core holder to be held securely within the rig system while ensuring easy access to both the top and bottom of the core holder. The layout of the final rig design, which includes containment of the core holder within the oven can be seen in Figure 5.5.

Swagelok tubing and fittings were used to construct the CO_2 fluid system and the confining oil line. All tubing and fittings used were made from the corrosion resistant alloy, Type 316 austenitic stainless steel; the tubing was 1/8" (3.2 mm) outside diameter, with 0.035" (0.9 mm) tube walls and a working pressure of 75.2 MPa (10,900 psi). The fittings all have pressure ratings up to 75.8 MPa (11,000 psi).

As can be seen from Figure 5.2, a number of valves are incorporated into the rig pipework at strategic locations to enable the required fluid control. Within the final rig design all valves are Top Industrie needle valves (910.10.00) except NV_F1, which is a larger Swagelok needle valve (SS-410-FP), and NV_F6, which is a SITEC needle valve (610.3310). All valves are also made from Type 316 austenitic stainless steel and are rated to 10,000 psi (68.9 MPa). Needle valve failure due to corrosion occurred four times during the project (see section 5.4 for details).

The number of joint fittings within the rig pipework were minimised to control the number of locations susceptible to leaks. However, the final number of pipe joints located within the CO_2 pipework was still relatively high to enable connection of all required instruments:

- Single connectors: 32
- Double connectors: 4
- T pieces: 3
- Four way connectors: 3

Leak testing of the rig pipework was undertaken as part of rig commissioning (section 5.5).

5.3.2 Pressure, flow and temperature control

This section describes the equipment used to ensure stable control of pressure, temperatures and flow rate within the rig system.

5.3.2.1 Core holder and confining pressure control

The prepared 38 mm diameter fractured sample is contained within a QRCH 200 Series Coreholder during flow experiments. This is a Hassler-type uniaxial core holder (see Figure 5.6). The core is held vertically in place within an elastomer sleeve in the main body of the cell by two 316 stainless steel end platens. A fixed end-platen on the lower (upstream) end of the core-holder is locked in place through a clover-leaf locking mechanism once the core is loaded. The upper (downstream) adjustable end-platen is then locked down onto the core sample using a screw mechanism. Both the end platens contain a 1/8" (3.2 mm) fluid entry port in the centre of the platen, to allow fluid (in this case CO_2) to enter and exit the core sample. A spider-web grooved pattern within the end plates is used to distribute fluid evenly across the core ends (Figure 5.7).

A radial confining pressure is applied to the core sample through pressurisation of a confining fluid reservoir on the outside of the elastomer sleeve. This ensures an even

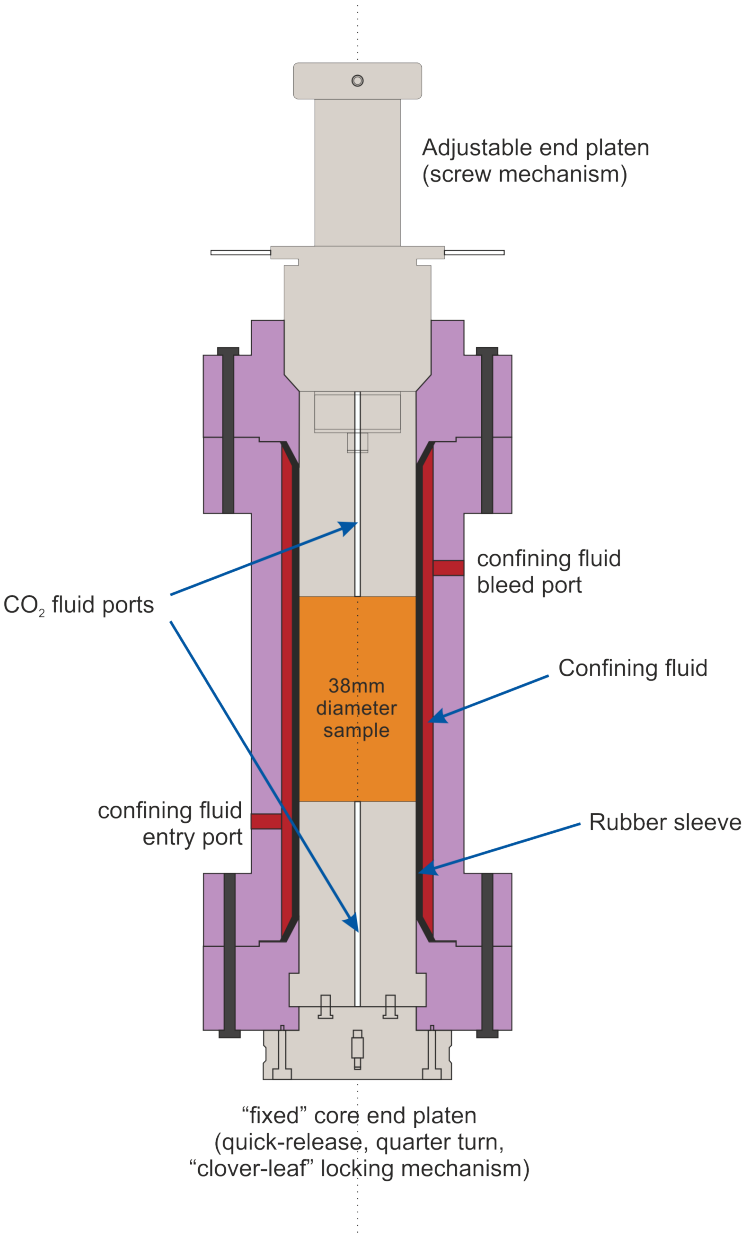

FIGURE 5.6: Core holder (pressure cell) schematic

radial confining pressure across the whole sample. The elastomer sleeve acts as a barrier between the core sample and the confining oil. Issues with CO_2 diffusion through the sleeve were detected during the project, and are discussed within section 5.4. There are two confining fluid ports on the cell: the lower one is used for confining fluid entry, and confining fluid release is controlled through a needle valve tap on the upper port. The fluid ports can be seen in Figure 5.8a.

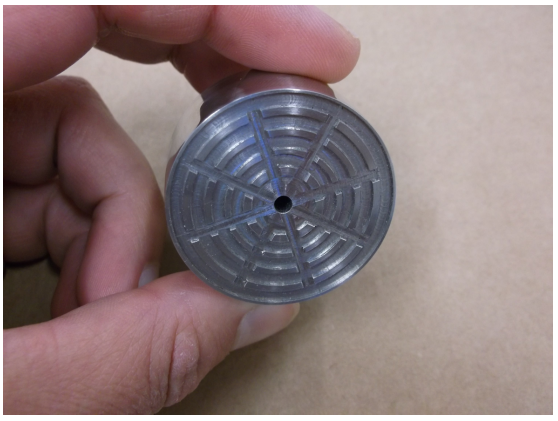

FIGURE 5.7: Platen flow distribution end plate (spider-web)

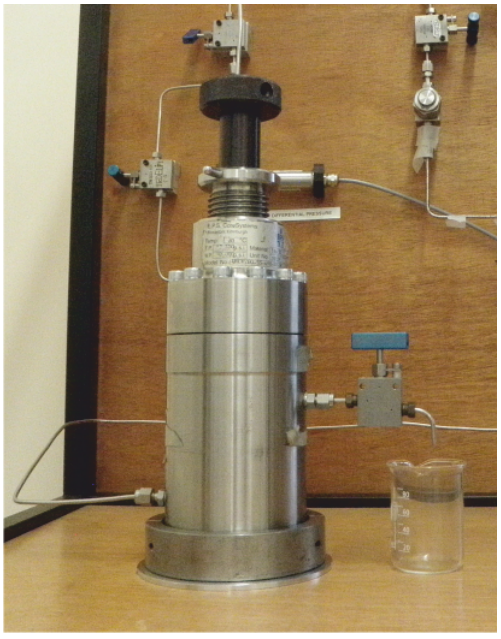

(A) Main body of core holder

(B) Bottom of core holder

FIGURE 5.8: Core holder placed in rig frame

The confining fluid used is Shell Tellus T15 hydraulic oil, and a Sunex 4 Ton hydraulic hand pump is used to apply the confining pressure. The confining fluid is locked into the confining line and core holder through closure of a needle valve upstream of the rig (Figure 5.2). As the confining pressure is controlled through locking in a set volume of confining fluid using a needle valve, it is difficult to set precise confining pressures, particularly as the pressure tends to take a little while to settle following lock-in. Subsequent pressure reduction can be carried out through release via the needle

valve tap on the core holder, but precise control is not possible.

Temperature increase of the locked-in confining oil results in fluid expansion and an associated confining pressure increase; conversely a temperature reduction is associated with a drop in confining pressure. Thus stable temperature control was found to be vital for stable confining pressures during experiments (see section 5.3.2.3 for details).

5.3.2.2 CO_2 fluid control (Isco syringe pumps)

New Teledyne Isco 100DX High Pressure Syringe Pumps were installed for CO_2 fluid control. These 100 ml high precision syringe pumps were installed in pairs to enable continuous operation: the pumps operate alternately, with a smooth, gradual changeover between pumps controlled precisely through an electric valve pump controller system. The pairs of syringe pumps can be operated via the pump controller system to ensure either continuous constant flow or continuous constant pressure in the system, and can be set to either deliver or receive fluid.

Within our rig design one pair of syringe pumps is used to control the flow rate of CO_2 delivered upstream of the sample. The pumps can operate within a flow rate range of 0.01 µl/min (1.7×10^{-13} m^3/s) to 25 ml/min (4.2×10^{-7} m^3/s) with a flow rate accuracy of ±0.3% [Teledyne Isco, 2012*c*]. A second pair of syringe pumps is used on the downstream end of the rig to ensure a constant, controlled CO_2 fluid pressure downstream of the sample - these downstream pumps operate by receiving CO_2 fluid at a rate that ensures constant pressure in the pipework downstream of the sample, thus effectively operating as a back-pressure regulator. The pressure range capability of the pumps is 0.069 MPa to 69 MPa, with a pressure accuracy of ±0.5% of full scale at constant temperature [Teledyne Isco, 2012*c*].

Teledyne Isco syringe pumps were chosen for CO_2 fluid control as they are known to be accurate and reliable for use with high pressure CO_2, having previously been used with CO_2 for a variety of R&D and production applications [Teledyne Isco, 2012*b*]. To ensure effective pump operation with CO_2 fluid, the syringe pumps must be filled with liquid phase CO_2, thus a liquid withdrawal CO_2 cylinder must be used. In addition, the CO_2 within the pumps must be kept at a stable low temperature for effective pump operation. Specially designed Isco temperature control jackets are fitted to both the upstream and downstream pumps. A circulating temperature-controlled bath ensures

continuous circulation of a cold water/ethylene-glycol solution within the temperature control jackets which in turn ensures a stable, constant temperature of the syringe pumps and CO_2 fluid within. In addition, fibreglass insulation jackets are fitted externally to the temperature control jackets to help maintain the stable temperature across all four syringe pumps and for energy efficiency purposes. The syringe pumps are typically maintained at a temperature of 2.5±2.2°C. The temperature is continuously monitored (section 5.3.3.4).

For successful operation of the CO_2 pumps, all pipework connections must be set-up correctly and pump controller settings require careful consideration. In addition, key initial set-up of the syringe pump states is required prior to commencing operation. The liquid withdrawal CO_2 cylinder supplies CO_2 to the pumps at a maximum pressure of 5 MPa (this pressure decreases as the CO_2 cylinder empties). As we require operation of the pumps at pressures in excess of 10 MPa, the syringes must compress the CO_2 after filling, and before commencing pump operation. Prior to initial start-up, the upstream, flow control pumps must both be fully refilled to ensure that there is a sufficient volume of CO_2 within the syringes for appropriate pressurisation prior to commencing operation. In addition, the downstream pumps must also be primed for operation at high pressure prior to inital start-up. This requires pre-compression of CO_2 within the syringes, therefore a connection from the CO_2 cylinder to the downstream pumps is also required for priming purposes only. As the downstream pumps are operated in receive mode, these pumps must not be completely full before operation commences, however the pumps must contain sufficient CO_2 to enable compression to the desired operating pressure. When working with CO_2 at high pressures, finding the appropriate refill volume requires some practice and is dependent on the system operating pressure, pump temperature and CO_2 supply cylinder fill level.

When the upstream syringe pumps begin operating in continuous constant flow mode during the experiments, an initial equilibriation phase occurs whereby both pumps run simultaneously to deliver fluid to the system. Thus both pumps must be full and pressurised. Following equilibriation, the pump controller gradually transfers delivery to a single pump, pump A. While pump A is running, the other pump (pump B) is refilled from the CO_2 cylinder. Once full, the fluid within the pump B syringe is compressed to ensure pressure-matching with pump A. Pressure-matching is then monitored and controlled continuously so that when the fluid volume in pump A drops to a specified lower fill limit, the pump controller can gradually and seamlessly transfer operation

to pump B. This process repeats itself throughout the duration of the experiment. The flow rate can be altered at any time during pump operation, with higher flow rates necessarily reducing the time between pump changeovers. Therefore the flow rate possible under continuous operation mode is limited by the length of time required for refilling and pressurisation of the individual pumps, which increases as the system pressure increases, and also to a lesser extent as the CO_2 cylinder empties.

As the downstream pumps are run in continuous constant pressure receive mode, it was found to be most effective to commence operating these pumps while disconnected from the main upstream rig system via a valve closure (NV_F6, Figure 5.2) to enable the pumps to equilibriate to the correct pressure and begin running with a limited upstream volume. After the system pressure downstream of the sample and upstream of the pumps approaches the desired pressure, the valve (NV_F6) is opened to allow the pumps to take control of the pressure regulation downstream of the sample through receiving fluid. As with the upstream pumps, the initial equilibriation phase for the downstream pumps involves both pumps running simultaneously prior to operation control being gradually handed to a single pump. Operational control then alternates between pumps in a similar manner to the upstream pumps, with changeover initiated when the operational pump reaches a specified upper fill limit, and pressure-matching occurring between pumps prior to changeover.

Once the operational pump changeover of the downstream pumps has taken place, the full downstream pump is emptied at a user-specified flow rate to waste, until a specified fill level is reached. It is important that the downstream pumps are not completely emptied during operational use, as a sufficient volume of CO_2 is required to allow pressure equilibriation to take place in advance of the next changeover to ensure stable pressure control. Due to the Joule-Thomson cooling effect associated with adiabatic expansion of CO_2 during depressurisation, the emptying flow rate is kept relatively low (5-10 ml/min) and a secondary automatic back-pressure regulator has been connected in series downstream of the pumps to step-down the pressure to 5 MPa prior to release. Use of the secondary back-pressure regulator protects the Isco valve system through reduction and transfer of the extreme cooling effect due to rapid depressurisation. Silicone rubber electrical heating tape (Omega HTWAT) is used along the waste pipework, particularly downstream of the secondary back-pressure regulator, to prevent fluid and pipework freezing with associated disruption. CO_2 is vented from the waste pipe into the laboratory fume cupboard.

Effective operation of the two pairs of syringe pumps is fairly complex, and a number of factors must be considered during pump initialisation, set-up and operation. As well as upstream flow rate and downstream pressure, the key control settings to consider during initialisation are:

- The min and max flow rate and pressure limits - these are important safety limits to prevent damage to the sample and rig equipment as pumps will stop operating if these limits are exceeded.
- The fill limits (upper and lower, for multi-pump mode only). These are important in ensuring that pump changeover takes place at an appropriate fill level and that refill/emptying occurs to an appropriate level for both upstream and downstream pumps.
- Emptying flow rate for downstream pumps - this limits the rate of rapid gas depressurisation occurring if kept low, but must be a sufficient rate to allow subsequent pressure-matching between pumps prior to the next pump changeover.

It is also important to ensure that sufficient CO_2 is available within the supply cylinder for the experiment duration. As the liquid withdrawal CO_2 cylinder is used without a regulator, a record of approximate CO_2 usage must be manually logged to ensure CO_2 cylinders are replaced as appropriate.

The installation of these sophisticated high pressure syringe pumps was initially completed in February 2013. Further to this a number of problems occurred while using the Isco pumps with CO_2 during this project, which resulted in the requirement for extensive pump testing, software updates and time-consuming component replacement, which further delayed successful completion of the flow experiments. Details of these issues are discussed in section 5.5.

While the precision and control of these high pressure syringe pumps are a significant improvement on the pump and back pressure control set up used in the MUSTANG experimental rig [Edlmann et al., 2013], the initial installation, testing and associated rig redesign required for commissioning these syringe pumps was extensive. Unanticipated operational problems further delayed successful commissioning. As a result, the experimental scope of the project required adjustment. However, significant detailed knowledge of the pump operation, controls and limitations has been gained during this

project, and the extensive operational testing and review will be of value during future use of these sophisticated syringe pumps.

5.3.2.3 Temperature control

Both the sample and fluid temperature are controlled during flow experiments. Experiments are carried out at two discrete temperatures: 40°C and 60°C (although measurement logging indicated that actual temperatures were lower at 38°C and 58°C, see section 6.2). The CO_2 is heated to the desired temperature through a Thar SCF heat exchanger (CPVC 20' 10KPSI) located between the upstream, flow-control syringe pumps and the sample core holder. The heat exchanger assembly is designed specifically for use with supercritical fluids and is compatible with the flow rate range of the upstream syringe pumps. The temperature setting is controlled via a Tecnologic TL39 temperature controller unit.

The sample core holder is contained within a SciQuip 110S oven which is set to the desired temperature (the same as the heat exchanger). The oven ensures stable, even temperature control of the sample within the core holder, as well as stable control of the confining fluid temperature. CO_2 and confining fluid pipework enters the oven through a small port in the back of the oven. The CO_2 is pre-heated via the heat exchanger, and approximately one metre of CO_2 pipework directly upstream of the cell is contained within the oven, which ensures that the CO_2 temperature is in equilibrium with the sample during fracture flow. In addition, silicone rubber electrical heating tape (Omega SRT051-120) set to the same temperature as the oven and controlled using an Omega temperature controller (CN740) with associated thermocouple sensor is used on the pipework between the heat exchanger and the oven (approximately three metres) to maintain the fluid temperature within this section. Pipe insulation is also used around the pipe and heating tape to help stabilise the temperature.

As mentioned in section 5.3.1 an oven was not used in the initial rig design, but a redesign to incorporate the oven was carried out in September 2013. Silicone rubber electrical heating tapes (both Omega SRT and HTWAT series) were used to heat both the core holder and pipework within the original design, with rockwool insulation used externally to try to maintain the core holder temperature. However, the heating tape temperature was found to fluctuate considerably during experiments through periodical

temperature boosts. This temperature instability had the knock on effect of causing significant fluctuations in confining pressure due to the temperature sensitivity of the confining fluid. The fixed volume of confining fluid expands upon heating, thus resulting in a radial confining pressure increase. The effect of these periodical temperature spikes on the confining pressure can be seen in Figure 5.9, which contains data from a preliminary flow experiment undertaken on a fractured Cambrian shale sample (sample V2) in July 2013. During these preliminary experiments, some manual confining pressure adjustments were undertaken, but it was not possible to control the confining pressure adequately for effective analysis of mechanical control on fracture flow behaviour. Thus an improved temperature control set-up was required for successful completion of the fracture flow experiments.

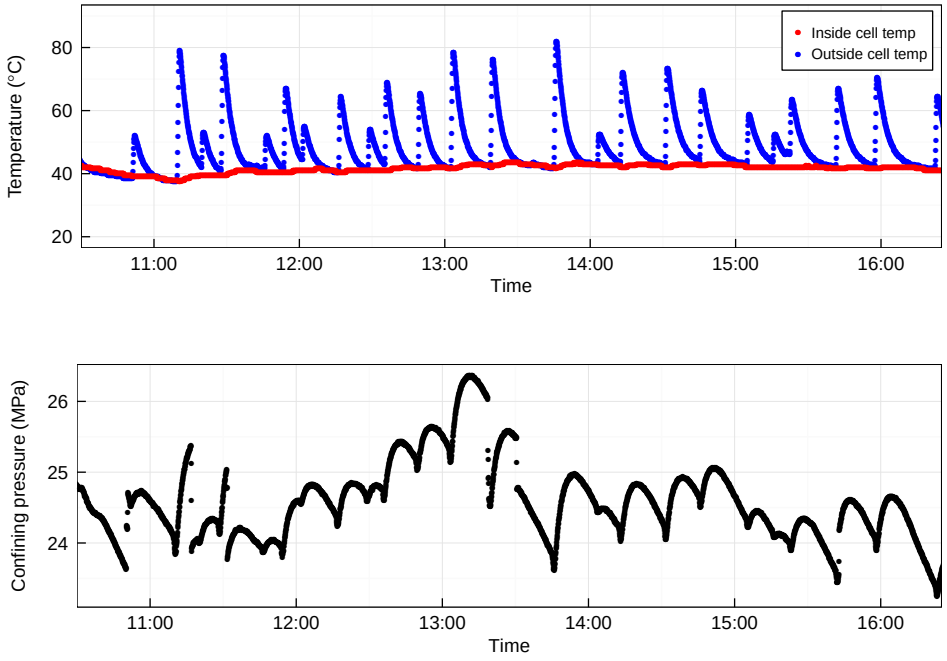

FIGURE 5.9: Temperature fluctuations and resultant confining pressure instability during preliminary flow experiment (fractured Cambrian shale sample V2, Jul 2013)

Both temperature and confining pressure stability were much improved during later experiments undertaken with the core holder contained within an oven (Figure 5.10).

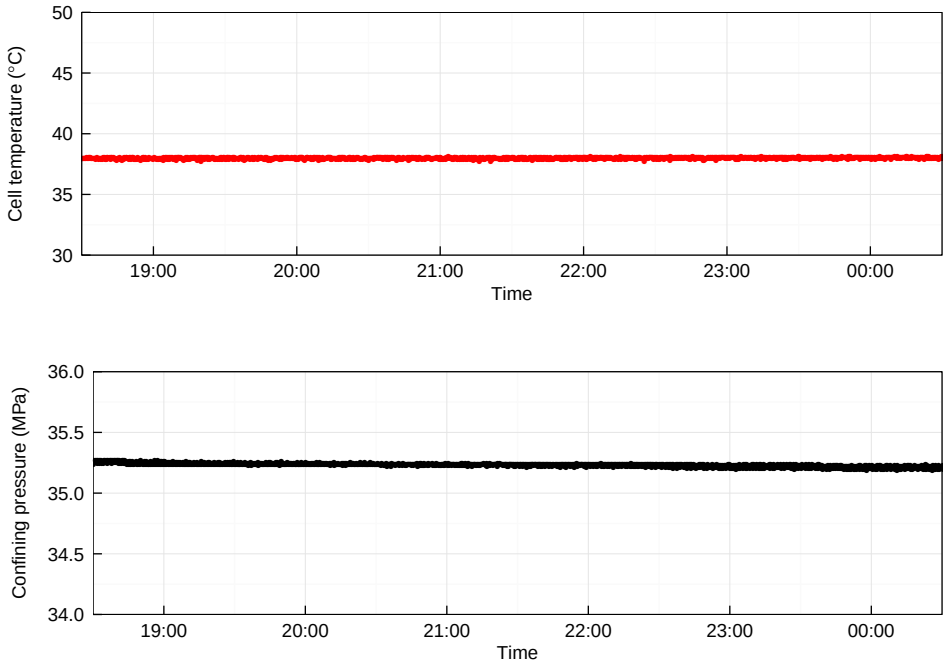

FIGURE 5.10: Temperature and confining pressure fluctuations resolved (fractured Cambrian shale sample V1, April 2014)

5.3.3 Pressure, flow and temperature measurement

As well as parameter control during experiments, effective continual measurement of key parameters is essential. This section describes the measurement equipment utilised within the rig system.

5.3.3.1 Pressure sensors

Omega General Purpose 100 millivolt output pressure sensors (PX302) are used to measure: the confining pressure; the upstream fluid pressure; and the downstream fluid pressure within the system. The transducers measure gauge pressure within the range 0-10,000 psi (0-68.9 MPa), with an output voltage of 0-100 mV linearly correlated to pressures of 0-10,000 psi respectively. The manufacturer quotes the instrument accuracy to be ±0.25% BFSL (Best Fit Straight Line), which accounts for linearity, hysteresis and repeatability errors.

In order to allow continuous (5 or 15 s frequency) measurement and recording of pressure during the experiments, the output signals from the three pressure transducers are logged to a PC, first via separate Omega strain gauge meters which output current signals, and subsequently through an eight channel current data logger (see section 5.3.4 for further details). Calibration of the line pressure to the resultant logging data is required and the calibration procedure, along with the associated error is discussed in section 5.5.4.

5.3.3.1.1 Pressure snubbers

In order to protect the pressure transducers from any pressure surges that may occur during the experiments, Omega pressure pulse snubbers (PS-4G for the CO_2 transducers, and PS-4D for the confining oil (higher viscosity) transducer) were connected in series with the transducers when connecting to the rig. The pressure pulse snubbers contain Stainless Steel 316 porous metal elements that restrict flow and therefore dampen the effects of any pressure surges, thus protecting the pressure sensors.

5.3.3.2 Differential pressure transducer

Within the rig system a differential pressure transducer is used to measure the CO_2 fluid pressure difference across the sample. This is a key parameter for estimation of sample/fracture transmissivity and permeability. The differential pressure magnitude can vary significantly, as some fractures are relatively conductive to fluids, whilst others are not. In addition, differential pressure varies significantly during sample experiments due to mechanical and fluid controls on the fracture conductivity. Therefore, identification of the correct pressure range for a high accuracy differential pressure transducer is a challenge. In addition, transducers must be suitable for use with high pressure CO_2. Two differential pressure transducers were tested within the rig system during this project; the first was found to be unsuitable for use within this set-up.

The differential pressure transducer used within the final rig design is a Validyne DP360 high pressure differential pressure transducer. This transducer design is capable of measuring small differential pressures at high static line pressures (up to 12,500 psi (86.2 MPa)), and has a replaceable sensing diaphragm set-up which allows the differential pressure range to be varied by exchanging diaphragms if required. This versatile set-up

is appropriate for the nature of the experimental work undertaken using the rig system. A 200 psi (1.4 MPa) differential pressure range diaphragm was used during Clashach permeability tests (section 5.5.6), while an 800 psi (5.5 MPa) differential pressure range diaphragm was used during the fractured sample flow experiments.

The differential pressure transducer is operated through a Validyne CP15 Sine Wave Carrier Demodulator which provides a DC output signal with a range of 0-10 V, which, once calibrated, provides a voltage of 0-10 V that is linearly correlated with the differential pressure diaphragm range (i.e. a 10 V output relates to an 800 psi differential pressure for the 800 psi range diaphragm). The transducer is connected to the carrier demodulator using shielded cable.

The Validyne DP360 differential pressure transducer has a stated instrument accuracy of ±0.5% FS (i.e. ±0.5% of the full scale reading). Given the output voltage range of 0-10 V, this equates to an instrument error of ±0.05 V, or ±4 psi/28 kPa for the 800 psi diaphragm used during the fracture flow experiments (±1 psi/7 kPa for the 200 psi diaphragm).

In order to allow continuous measurement of differential pressure during the experiments, the output signal from the differential pressure transducer is logged to a PC, via an Omega strain gauge meter, and the same eight channel Omega data logger used for logging of line pressures and cell temperature (see section 5.3.4 for details).

Calibration of the differential pressure transducer was carried out prior to use. Discussion of the calibration method and results for the 800 psi diaphragm is included in Appendix B, which incorporates calibration of the logging system data transformation. The data transformation process required to enable continuous logging of the differential pressure results was found to introduce additional error, resulting in an overall system error of ±9.6 psi/66 kPa for the 800 psi diaphragm logged data.

Calibration is required each time the diaphragm is exchanged and was also carried out for the 200 psi diaphragm prior to undertaking the Clashach permeability tests. The logging system was not utilised during the Clashach permeability tests, therefore error additional to the instrument error of ±1 psi/7 kPa introduced during differential pressure measurement within these experiments was due to reading error.

Voltage drift was found to occur as a result of significant line pressure change during experiments. The voltage was re-zeroed while maintaining a zero differential pressure to correct for this during experiments, as discussed within Appendix B.

During initial testing of the Validyne transducer, leakage issues were identified and traced to incompatibility of the HNBR o-rings with high pressure CO_2. CO_2 diffusion through the o-rings was occurring, and resulted in voltage drift errors. This was resolved by replacement with PTFE o-rings and is discussed further in section 5.4. Note that PTFE o-rings require replacement each time the transducer is dismantled and the diaphragm is adjusted or exchanged, due to the non-elastic nature of the solid PTFE o-rings.

A Keller PD33X differential pressure transmitter was originally obtained for use within the rig system. This instrument is specified to measure a 0-3 MPa differential pressure range at line pressures of up to 60 MPa, with a stated instrument accuracy of ±0.1% FS (i.e. ±0.1% of the full scale reading, ±3 kPa, or ±0.4 psi). Unfortunately the instrument was found to not function correctly for differential pressures greater than 0.3 MPa within the rig system. Extensive testing and troubleshooting, as well as a manufacturer's service test did not resolve the issue, therefore the Validyne transducer was obtained as an alternative. There was limited scope for identification of the problem with the Keller transmitter during testing due to the instrument consisting of a single sealed unit. The Validyne DP360 instrument was preferred to the Keller instrument for troubleshooting purposes due to the ability for the user to dismantle, clean, check the diaphragm, and replace components (o-rings and diaphragms).

5.3.3.3 Flow rate measurement

During CO_2 flow experiments the flow rate of CO_2 through the sample is controlled by the upstream pair of Isco syringe pumps as discussed in section 5.3.2.2. The flow rate range of the syringe pumps is 0.01 µl/min (1.7×10^{-13} m^3/s) to 25 ml/min (4.2×10^{-7} m^3/s), and the flow rate accuracy is specified to be ±0.3% of the setpoint. Continuous (5 s frequency) logging of the Isco syringe pump flow rate occurs during experiments (see section 5.3.4).

The volumetric flow rate of CO_2 through the sample differs from the pump flow rate due to the density difference between the fluid within the syringe pump and the fluid

within the sample. As CO_2 is a compressible fluid, the fluid temperature increase that occurs within the heat exchanger (located between the pump and sample) results in expansion of the fluid, a reduction in density and consequently an increase in the volumetric flow rate (the mass flow rate remains constant). Flow rate through the sample is not directly measured, therefore it is estimated, using mass conservation, from the pump flow rate multiplied by the density ratio of syringe pump CO_2 over sample CO_2. As density is a function of pressure and temperature, this calculation therefore requires pressure and temperature measurement at both locations, as well as the pump flow rate measurements. Details of experimental data post-processing, which includes calculation of sample flow rates, are discussed in Chapter 6 (section 6.5.4).

5.3.3.4 Temperature measurement

As discussed within section 5.3.2, the temperature of the sample is controlled using an oven. The sample fluid is pre-heated via a heat exchanger prior to entering the oven. Both the oven and heat exchanger are set to the same temperature. There is also approximately one metre of pipework within the oven upstream of the core holder. Therefore it is assumed that the sample and fluid temperatures are equal by the time the fluid passes through the sample.

Our experimental set-up does not allow for direct measurement of the sample temperature. However an Omega transition junction style thermocouple (J-type) with a 0.01" (0.3 mm) diameter probe (JMTSS-010U-12-120) is used to measure the temperature of the core holder that encapsulates the sample. As the core holder is conductive, the temperature of the sample and the fluid within are assumed to be the same as that of the core holder during the experiment. Thus this thermocouple is assumed to monitor the temperature of the sample/fluid system within the oven. The thermocouple probe has a tolerance of $\pm 2.2°C$ within our range of interest ($<80°C$) and is rated to 260°C. Continuous (5 or 15 s frequency) logging of this thermocouple output is set up via a thermocouple input signal conditioner which is connected to the same eight channel current data logger used for logging pressure measurements (section 5.3.4).

In addition to measurement of the temperature of the sample, the temperature of the upstream Isco syringe pumps are also continuously monitored to enable flow calculation, as discussed in section 5.3.3.3. Two type-K insulated beaded wire thermocouples (Omega SC-GG-K-30-36) are used in conjunction with individual battery-operated

thermocouple data loggers with USB interfaces (OM-EL-USB-TC) to measure the temperature of each of the upstream pump syringes. The thermocouple probes are placed in contact with the external surface of the syringe, beneath the insulation layer, and are therefore considered to be representative of the fluid temperature within the syringe itself. As with the sample thermocouple, these thermocouple probes also have a tolerance of ±2.2°C within our range of interest (<80°C) and are rated to 480°C.

Calibration testing of the thermocouples was undertaken, see section 5.5.5 for details.

5.3.4 Measurement logging system

This section describes the logging systems used during the flow experiments. Discussion of methods for post-processing and analysis of the logged data files is included in Chapter 6.

5.3.4.1 Omega logger

The Omega OM-CP logging device is used to record data at 5 second frequency from the following instruments: confining pressure transducer; upstream pressure transducer; downstream pressure transducer; differential pressure transducer; and core holder thermocouple.

The four pressure transducers within the rig (confining, upstream, downstream and differential) are connected to the Omega OM-CP logging device via panel meter gauges (Omega DP25-S), which convert the output voltage from the pressure transducer into a current signal, with specified instrument accuracies of ±0.03%. The panel gauges then send the current signal to an Omega OM-CP-OCTPROCESS, an eight channel current data logger, which is controlled and read from the lab computer via the Omega OM-CP-IFC200 logging software and interface cable. The timing accuracy specified for the OM-CP-OCTPROCESS data logger is ±1 minute per month.

The core holder thermocouple is also logged through the same Omega OM-CP-OCTPROCESS current data logger, however it is connected via a thermocouple signal conditioner (Omega DRF-TC), with an instrument accuracy of ±0.3%, rather than via a panel meter.

Calibration of the logged data against the direct instrument measurement was required for each of the above devices. This procedure is detailed in section 5.5.4 for the gauge pressure transducers (confining, upstream and downstream), section 5.5.5 for the thermocouple, and Appendix B for the Validyne differential pressure transducer. The calibration procedure enabled determination of calibration parameters used to convert logged data into appropriate units. An error is associated with this, which encompasses errors in the data logger, panel meters and signal conditioner as well as data transmission and timing errors. This logging error is of similar, and in some cases greater magnitude than the instrumental error, and therefore must be taken into account during result analysis.

The Omega OM-CP-OCTPROCESS current data logger operates by storing data on internal memory, as directed by the settings selected within its associated software. The device memory is capable of storing 16,383 readings/channel, which allows the device to run for 22 hours, 45 minutes with a reading frequency of 5 s; and 2 days, 20 hours and 15 minutes with a reading frequency of 15 s.

It is also possible to run the OM-CP-OCTPROCESS in "real time chart recording" mode, however in this mode the data are not stored on the logger but pulled straight across to the software. Unfortunately the software does not record data to file in real time, therefore if the software crashes for any reason, all the data since the last manual save are lost. This mode of data recording was not used due to the lack of robustness.

The method used during flow experiments was to set the data logger to run at 5 s frequency during the day while running the flow experiments, and then stop and save the data at the end of each day, before re-starting the logger to run at 15 s frequency overnight, or over the weekend while a minimal flow is maintained to ensure depressurisation of the system does not occur. To stop, download and save the data can take a significant length of time, typically half an hour. Therefore, there are gaps of this length in the time series each morning and night.

5.3.4.2 Pump logging

Each pair of Isco syringe pumps (upstream, flow control pumps; and downstream, pressure control pumps) is connected to a dedicated pump controller. The pump controller is used for setting the mode of operation; settings such as flow rate or fluid pressure;

and operational procedures and safety limits for pump changeovers and general pump operations. The pump controllers are also used to control refilling or emptying of pumps before or after flow experiments.

The pump controller is connected to a PC via an RS-232-C serial interface. The Teledyne Isco Labview toolkit software is used to log pressure and flow data, as well as pump status data, from the pump controller via this interface. The data frequency can be specified - a 5 s data frequency was chosen for the flow experiments, consistent with the omega logger data frequency. Data are exported from the controller in real-time as an ASCII text string of comma-separated values, and can be continuously recorded for the full duration of the flow experiments.

It is not possible to run two instances of the Teledyne Isco Labview toolkit software on one PC, therefore the two pump controllers are logged on separate PCs.

The upstream pumps are used in continuous constant flow mode, therefore the flow rate is specified manually using the upstream pump controller. The pressure is controlled by the downstream rig system.

The downstream pumps are used in continuous constant pressure receive mode, in order to control the fluid pressure in the upstream rig system. Thus, the downstream pumps work as pressure regulators, by accepting CO_2 from the system at a rate that maintains the specified fluid pressure directly upstream.

5.3.4.3 USB temperature logging

As discussed in section 5.3.3, the temperature of the upstream syringe pumps is required during the experiments in order to enable calculation of the CO_2 flow rate through the sample from the known CO_2 pump flow rate.

Two standalone USB thermocouple temperature data loggers (Omega OM-EL-USB-TC) are used to log the temperature of the upstream syringe pumps, 1A and 1B. The pump cylinders are cooled via temperature control jackets that contain circulating cooled fluid. The thermocouples are connected to the temperature control jacket, beneath the jacket insulation, and therefore are indicative of the CO_2 temperature within the syringe pump.

The USB data loggers are set to record temperature every 10 s. The logger memory can hold 32,000 readings, therefore at 10 s frequency the logger can run without interruption for 3 days, 16 hours, and 53 minutes. The logger data was downloaded and the loggers restarted within that timeframe to ensure continuous data during the flow experiments. As the two syringe pumps are cooled using the same method from the same circulating water bath the temperatures are expected to be very similar. Results indicate that this is the case, and an average temperature can therefore be calculated from the Pump 1A and Pump 1B datasets that is representative of the temperature within both upstream syringe pumps.

5.3.5 Safety requirements

The rig incorporates safety features to prevent overpressuring of the system, which could result in damage to instruments and/or a safety hazard to lab users. Pressure relief valves are connected to both the confining pressure line and the CO_2 fluid line, as shown in Figure 5.2. The relief valves used in both instances are Haskel Relief Valves, Model 27741-4, which are suitable for use with gas or liquid fluids. The valves are set to 10,000 psi (68.9 MPa), thus ensuring that this pressure cannot be exceeded within either fluid line.

In addition to the pressure relief valves incorporated into the rig system, the syringe pumps are set up to shut down if a user-specified maximum pressure threshold is exceeded. The maximum pressure threshold set on the syringe pumps is always less than 10,000 psi (68.9 MPa), therefore during pump operation the CO_2 pressure relief valve acts as a back-up safety feature only.

High concentrations of CO_2 can result in asphyxiation. This is a particular hazard in an enclosed space such as a laboratory as CO_2 is denser than air and will therefore drive out the oxygen in the atmosphere if excessive CO_2 leakage occurs. To mitigate against increased CO_2 concentrations in the lab, CO_2 released at the downstream end of the rig system is vented directly to the fume cupboard. In addition, a CellarSafe Carbon Dioxide Safety Monitor is installed within the laboratory. The alarm continuously monitors levels of CO_2 within the lab, and low level and high level alarm signals are set to trigger if concentrations exceed 1.5% and 3% respectively.

5.4 Material selection

The integrity of component materials in the presence of supercritical CO_2 is important for successful operation of the experimental rig. Although significant testing of materials in low pressure CO_2 has been undertaken, limited material testing in the presence of supercritical CO_2 has been carried out [Paul et al., 2010].

Corrosion of metals and degradation of polymers were both found to be significant issues during experimental rig development. This section discusses the operational issues that occurred during the project as a result of material degradation in the presence of supercritical CO_2.

5.4.1 Metals

While pure or dry supercritical CO_2 does not result in corrosion of metals, the presence of supercritical CO_2 in wet environments results in formation of carbonic acid and is known to cause steel corrosion [IEAGHG, 2010, Paul et al., 2010, Russick et al., 1996, Zhang et al., 2011]. However, corrosion of Type 316 austenitic stainless steel was not found to occur during experiments with both pure and water-saturated supercritical CO_2 [Russick et al., 1996, Zhang et al., 2011]. This material is typically used for construction of CO_2 injection wells, and is recommended for use in wet CO_2 environments [IEAGHG, 2010, Parker et al., 2009]. For this reason, Type 316 austenitic stainless steel was used for all pipework and fittings within the rig system (section 5.3.1).

The valves used within the rig were also made from Type 316 austenitic stainless steel. Despite use of this corrosion resistant alloy, valve failures were identified four times during the period of the project. Evidence suggests that valve failures were due to corrosion of valve stems, which is likely to be associated with the presence of supercritical CO_2. An example of a corroded Tedelfi valve replaced during the project with a Top Industrie valve is shown in Figure 5.11. Rust can be seen on the needle stem, and there was evidence of corrosion on the needle valve point too, which as a consequence is blunt and therefore ineffective for valve closure. While some of the valves utilised within the rig system were pre-used during earlier CO_2 and water experiments, failures also occurred for valves purchased specifically for this project, and thus used solely for supercritical CO_2 flow. The experiments were however not undertaken in a completely

dry lab environment, and the evidence of corrosion suggests that the presence of residual water within the core sample and pipework was sufficient for corrosion of the needle valve stem to occur.

FIGURE 5.11: Corroded Tedelfi needle valve

While no other failures were identified within the rig system as a result of metal corrosion, it is considered that Type 316 austenitic stainless steel may not be resistant to corrosion from supercritical CO_2 contact under high stress conditions for prolonged periods of time. This is in contrast to the findings of Russick et al. [1996] and Zhang et al. [2011]. However, the exposure periods were much longer during this project (a maximum of 96 hours was tested within the corrosion tests of Zhang et al. [2011]). In addition, conditions were not static during this project, with a continual supply of flowing supercritical CO_2, and regularly varying pressure and temperature conditions potentially contributing to the onset of corrosion. Indeed, the IEAGHG report on materials selection for CCS systems [IEAGHG, 2010] suggests corrosion risks in a wet CO_2 environment are increased during depressurisation and at valves due to the reduction in water solubility in CO_2 with pressure reduction. The needle valves are therefore considered to be particularly vulnerable and alternative corrosion resistant alloys, or use of titanium or silicon coating should be considered for valves during future experiments to minimise experimental downtime. In addition, confirmation of the needle valve stem material should be specifically sought from manufacturers in case it differs from the needle valve body material quoted within the technical specification sheets.

The core holder used within the rig is made from Type 316 stainless steel. While no corrosion issues were identified in association with the core holder during the project,

bulging or swelling of the quick release end platen material did occur on several occasions during the project whereby permanent expansion or shape alteration of the relatively soft stainless steel platen occurred. This resulted in difficulties opening and closing the quick-release platen on the upstream end of the cell, due to the low tolerance associated with this closure mechanism. This platen bulging was particularly significant following long term high pressure, high temperature experiments. Metalwork smoothing and polishing was required to resolve the issue on these occasions. This ongoing issue with the core holder made loading and unloading the cell complex and time-consuming, with intervention from the metalwork technicians frequently required. Due to the necessity for removal of stainless steel material from the core holder on a regular basis the core holder has a limited lifespan for use in this set-up. For this reason a harder steel alloy, with similar or superior corrosion resistant properties to Type 316 austenitic stainless steel would be recommended for any subsequent core holders used within the rig. Alternatively, an improved closure mechanism, similar to that on the downstream end of the cell, is recommended if adaptation of the existing core holder is to be carried out.

The Teledyne Isco syringe pump cylinders within the rig system were specially ordered in Hastelloy C-276, a particularly corrosion resistant alloy. No corrosion issues were associated with these.

5.4.2 Polymers

Degradation of polymeric materials in the presence of supercritical CO_2 can occur due to material swelling as a result of CO_2 absorption, which consists of adsorption of the CO_2 onto the polymer material followed by diffusion of the CO_2 molecules through the material [Paul et al., 2010]. In addition, rapid gas decompression (or explosive decompression) can occur when pressures are rapidly reduced and CO_2 absorbed within the polymer rapidly expands causing potentially highly destructive blistering or tearing of the material [Davies et al., 1999, IEAGHG, 2010, Paul et al., 2010]. It is recognised that CO_2 dissolves readily in a variety of commercial elastomers, and degradation of these materials does occur [Davies et al., 1999, Paul et al., 2010]. However there has been limited research undertaken on the performance of polymers under supercritical CO_2 conditions [Davies et al., 1999, Paul et al., 2010]. Rapid gas depressurisation can be limited by ensuring decompression rates are kept low, allowing CO_2 diffusion out

of the material to occur. The severity of decompression damage is understood to be greatest where high solubility and low diffusion rates exist [Davies et al., 1999]. Material stiffness also influences the damage severity, with high stiffness materials found to be more resistant to decompression damage [Davies et al., 1999].

Polymer materials are present within the rig system: both the core holder sleeve used to radially confine and seal the core sample and the o-rings within the Validyne differential pressure transducer are made from polymers. During rig development, issues were identified with both. These are discussed within the subsections below.

5.4.2.1 Core holder sleeve

The original sleeves produced for the rig core holder were made of FKM-B (Viton). Sleeve degradation and rupturing occurred on several occasions during the initial experimental testing period, suggesting elastomer degradation, possibly associated with rapid gas depressurisation. The unsuitability of Viton for use in supercritical CO_2 applications was confirmed through discussions with Suzanne Hangx of Shell/Utrecht University, who suggested from experience that HNBR or EPDM would be more robust for supercritical CO_2 conditions.

CO_2 solubility in EPDM is relatively low, thus limiting swelling potential for this elastomer [IEAGHG, 2010]. However, due to the poor resistance of EPDM to hydrocarbons, this material was not appropriate within our core holder, as Shell Tellus T15 is used as the confining fluid. HNBR, on the other hand, is optimised for resistance to hydrocarbons, but CO_2 solubility has the potential to be high [IEAGHG, 2010]. Due to the incompatibility of EPDM with our confining fluid, relatively high hardness (85 IRHD) HNBR sleeves were custom made for testing within our core holder (Figure 5.12) by Elastomer Engineering.

Use of the HNBR sleeves within the core holder resolved the sleeve rupture issues experienced with the FKM-B (Viton) sleeves. However, CO_2 absorption and diffusion through the sleeve was found to be an issue.

During CO_2 flow tests on a piece of uncoated Clashach sandstone core using an HNBR core holder sleeve (December 2013), an unexpected continual increase in confining pressure was observed under stable temperature conditions, as soon as CO_2 flow through

FIGURE 5.12: HNBR sleeve for core holder

the core commenced (Figure 5.13). As can be seen in Figure 5.13, the confining pressure was stable prior to the introduction of CO_2, and following introduction of CO_2 fluid, the CO_2 downstream pressure was held stable at 10 MPa. A constant CO_2 flow rate of 1 ml/min (1.7×10^{-8} m^3/s) was set at the upstream pump as soon as the 10 MPa CO_2 fluid pressure was attained. The continual increase in confining pressure during this 21.5 hour flow experiment was therefore presumed to result from CO_2 diffusion into the fixed volume of confining oil through the core holder sleeve. This was confirmed through significant gas release from the confining oil post-experiment (Figure 5.14).

In addition, there was evidence of elastomer swelling of the HNBR sleeve through inspection of the sleeve following removal of the Clashach core post-experiment (Figure 5.15). The swelling was observed to significantly reduce over time following core removal, which is thought to be due to gradual diffusion of CO_2 out of the sleeve.

Degasification of confining oil was also observed following similar flow tests on uncoated fractured low permeability core samples, however gas bubble volumes were considerably lower. The porous Clashach sandstone core is considered a 'worst-case scenario', due to the much higher sleeve area exposed to supercritical CO_2. During fracture flow

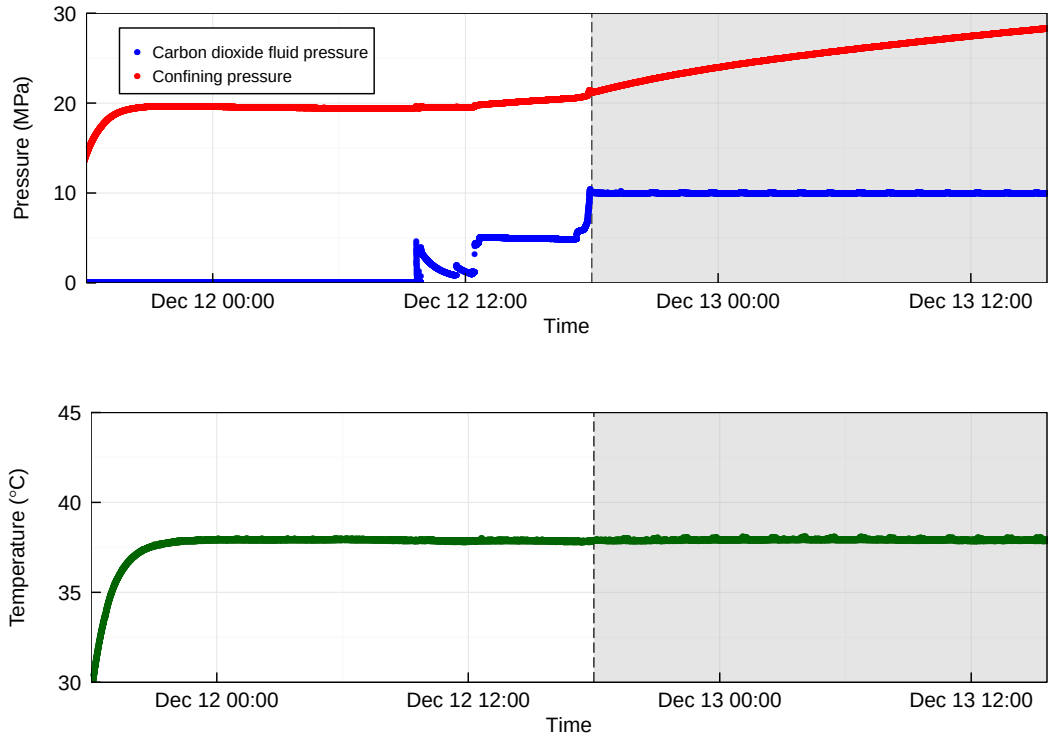

FIGURE 5.13: Confining pressure increase observed during constant CO_2 flow tests on Clashach sandstone core under stable temperature and CO_2 fluid pressure conditions. Evidence for CO_2 diffusion into confining oil (Dec 13).

FIGURE 5.14: CO_2 degasification of confining oil upon release from core holder after uncoated Clashach CO_2 flow tests (Dec 13)

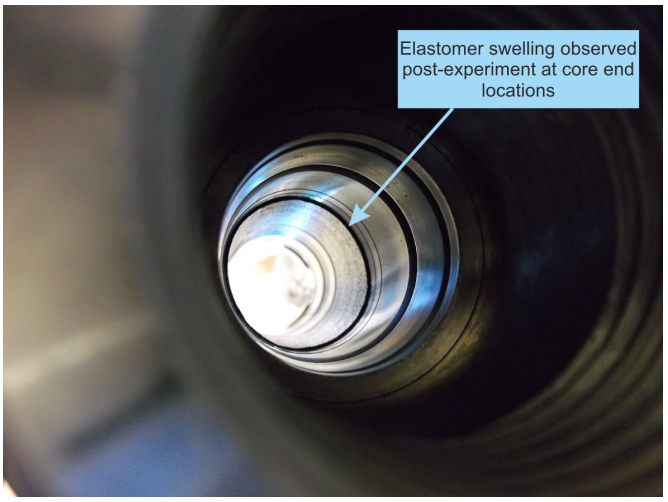

FIGURE 5.15: HNBR sleeve swelling at core ends post-experiment (uncoated Clashach core, Dec 13)

through low permeability core, the sleeve area exposed to CO_2 is limited to core ends and along the fracture line, whereas the full sleeve area is exposed to CO_2 during tests on a permeable sample.

To mitigate CO_2 diffusion into the confining oil, sample coatings and sleeve liners were used as additional barriers between the core sample and the HNBR sleeve as discussed in Chapter 3, section 3.3.3.2. Alternative materials for sleeve liners were considered, and Elastomer Engineering suggested trialling alternative grades of HNBR and FKM (Viton). However, due to time and cost constraints, as well as considerable uncertainties and risks associated with trialling further new materials, the sample coating method was agreed upon as an alternative during this project. Sample coating has been found to be successful in previous CO_2 experimental research [Hangx et al., 2013].

As stated in section 3.3.3.2, the adoption of sample coating was considered to be a success in resolving CO_2 diffusion issues during this project. No evidence of CO_2 diffusion was observed through either confining pressure increases or through evidence of CO_2 in confining oil released post-experiment. Evidence of sleeve swelling was significantly reduced, although some limited swelling/intrusion of the sleeve was still observed at core ends where lead liner ruptures occurred during experiments (Figure 5.16). This is likely to be at least partly a consequence of intrusion due to the high confining pressures applied during the experiments, and highlights the importance for precision in trimming the core ends. As no other evidence of CO_2 diffusion or sleeve damage was

observed, this limited sleeve swelling/intrusion was not considered to be significant, and did not affect the operational use of the core holder sleeve.

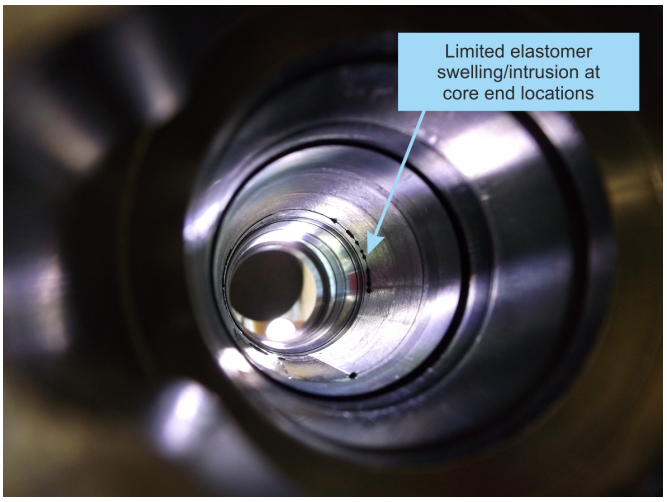

FIGURE 5.16: Limited HNBR sleeve swelling at core ends post-experiment with sample coating adopted (Cambrian core sample V1, May 2014)

5.4.2.2 Validyne O-rings

Within the Validyne differential pressure transducer two o-rings are used to ensure a seal around the diaphragm. HNBR o-rings were originally utilised within the instrument. During initial testing of the Validyne transducer with CO_2, the output voltage was observed to slowly drop under stable pressure conditions (Nov 2013). After troubleshooting potential issues, the o-rings were identified as the source of the problem. During one test, one of the o-rings was observed to extrude from the instrument and on dismantling of the transducer, the o-rings were both observed to be enlarged, swollen, and contain small blisters, typical of rapid gas decompression [Paul et al., 2010].

An available alternative nitrile elastomer, Buna-N, was also tested within the instrument, however similar problems were observed.

A variety of alternative materials were considered for the o-rings. High performance elastomers such as Kalrez and Ekraz were considered as alternative elastomer o-ring solutions, as these are reported to have virtually universal chemical resistance and are also reported to be resistant to swelling. However, these materials are costly and the manufacture and delivery time-scales were considerable. PTFE-encapsulated FKM

(Viton) o-rings were also considered, due to the chemical inertness of PTFE. However, it was not possible to manufacture PTFE-encapsulated o-rings with a sufficiently small cross-section, which ruled out this option. As a result, solid PTFE o-rings were ordered for testing, despite concerns regarding potential sealing issues.

During testing, the PTFE o-rings were found to seal well, and these were successfully used within the transducer. As the o-rings are solid rather than elastic, it was necessary to replace the o-rings each time the transducer was dismantled, to ensure a seal was maintained on reconstruction of the transducer. Thus, each time the diaphragm is switched or replaced, new PTFE o-rings are required. This was found to be a reasonably successful solution to the problem for the purposes of this project, but may not suit all applications. Figure 5.17 illustrates the o-ring placement within the instrument body. The diaphragm is sandwiched between each side of the transducer body with the o-rings ensuring a seal on either side.

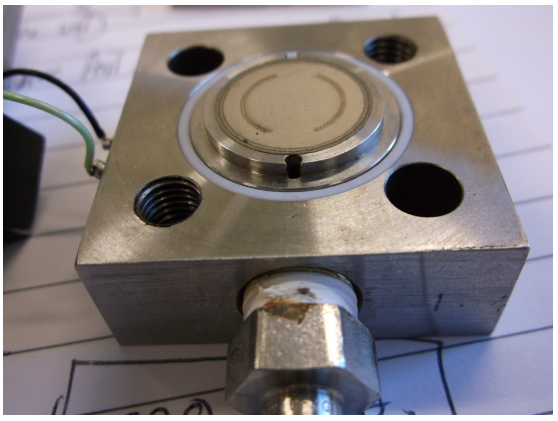

FIGURE 5.17: Inserting PTFE o-rings into the Validyne differential pressure transducer

5.5 Rig commissioning and testing

This section includes details of instrument calibrations, and rig validation checks and tests undertaken as part of the rig commissioning process.

5.5.1 Pump testing

As discussed in section 5.3.2.2, the high precision Isco syringe pumps installed within the rig system are versatile and have a track record of suitability for supercritical CO_2 applications [Teledyne Isco, 2012*b*]. However, due to the unique nature of the experimental research application, significant initial pump commissioning and testing was required to establish the most appropriate pump settings and operational methods for use of the pumps within the rig system.

As the syringe pumps require liquid CO_2 for effective operation, it was necessary to use a liquid withdrawal CO_2 cylinder and maintain a low temperature within the syringes using the syringe pump temperature control jackets to avoid issues with fluid phase change within the pumps. The CO_2 cylinder supplies CO_2 at a pressure of up to 5 MPa, which corresponds to gaseous CO_2 at 20°C, hence the requirement for pump cooling. Initially, tap water was used within the temperature control jackets as a coolant, however pressure fluctuations and instability observed during initial testing indicated that the temperature needed to be further reduced, and a circulating temperature-controlled bath was introduced to circulate aqueous ethylene-glycol solution at 2.5°C around the temperature control jackets. Ethylene-glycol solution was used rather than tap water to lower the freezing point of the coolant and prevent potential localised freezing.

Due to the requirement for liquid phase CO_2 within both the upstream and downstream pumps, it was found to be problematic to test gaseous phase CO_2 flow through the core samples, particularly prior to introduction of the lower temperature control. This is due to the relatively narrow pressure range for which syringe temperature CO_2 is liquid simultaneously with sample temperature CO_2 being purely gaseous within the core sample. In addition, issues were encountered with setting the fill levels and rates as pressures within the syringes required reduction through fluid expansion following refill as opposed to pressure increase through compression, the more usual pressure adjustment. It was therefore decided to carry out all main flow experiments within the supercritical phase, with a variety of supercritical phase CO_2 pressures tested.

During initial flow experiment tests, a further pump problem was identified within the upstream pair of syringe pumps. The problem was first detected through observation of a significant pressure drop within the logging data following continuous constant flow of CO_2 overnight. This was observed during flow of gaseous CO_2 through an

artificially fractured St Ninian's shale (Fife Quarry) core sample (Figure 5.18). Prior to the pressure loss episode CO_2 had been flowing relatively stably for over 12 hours at a pump flow rate of 2 ml/min (3.3×10^{-8} m^3/s) with no intervention. The small pressure spikes that can be seen within the logged data prior to the pressure loss incident occur at pump changeovers and are due to errors associated with pressure matching between pumps during multi-pump mode. These were minimised for later experiments through adjustment of refill rate and fill settings. Determining control settings was more complex for gaseous CO_2 flow, as mentioned above.

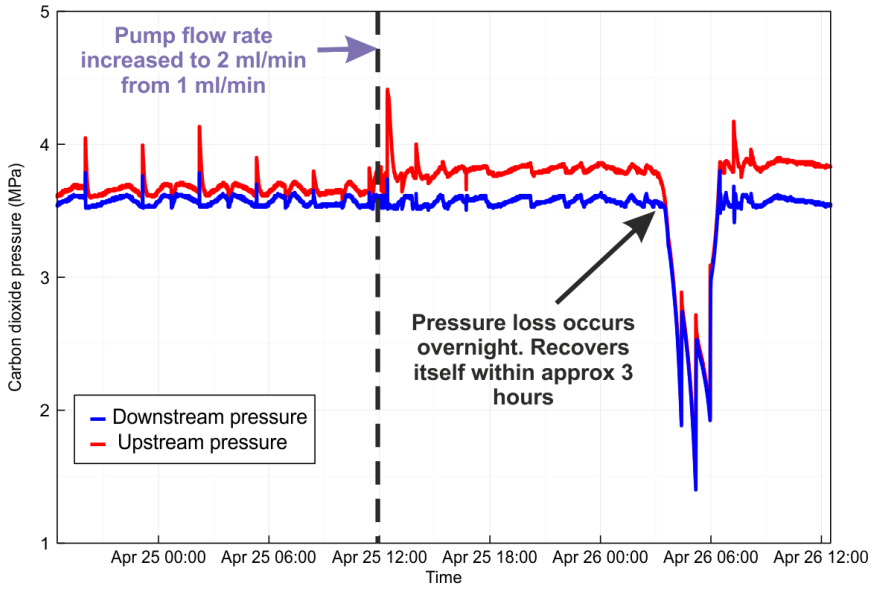

FIGURE 5.18: Overnight pressure loss and recovery during gaseous CO_2 flow through fractured St Ninian's shale core sample (April 2013)

The significant pressure loss event that can be seen in Figure 5.18 occurred at around 3 am. The pumps continued operating despite this pressure loss, and pressure recovery occurred within a few hours, after several syringe pump cycles. The reason for this pressure loss was not obvious, and it was considered possible that it was related to the low operating fluid pressures, although it seemed unusual that this had occurred after a significant period of stable flow with no problems.

Similar pressure loss episodes were observed several more times subsequent to this first recorded episode, during higher pressure liquid CO_2 flow tests, which indicated that the issue was not related to low fluid pressures within the pumps. An example of a

pressure loss episode that occurred during liquid CO_2 flow through the same fractured St Ninian's shale core sample can be seen in Figure 5.19.

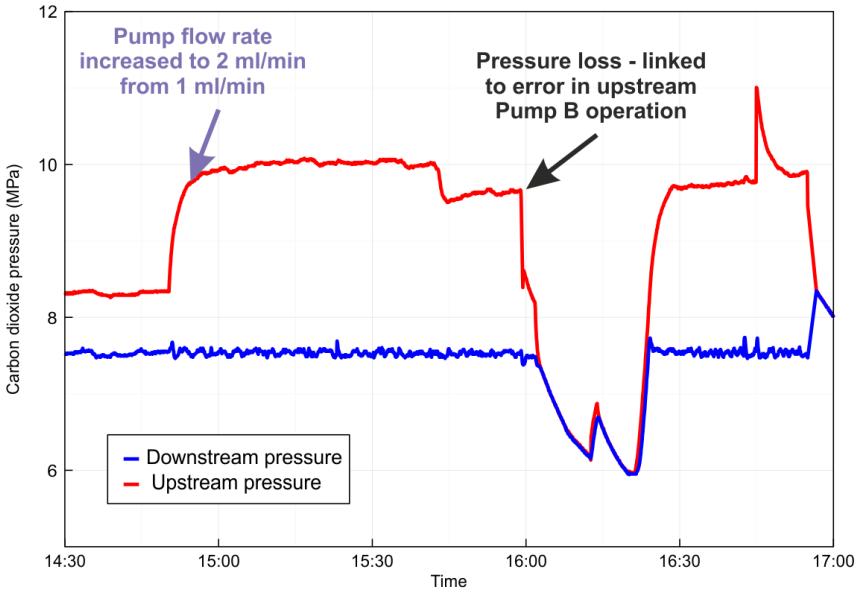

FIGURE 5.19: Pressure loss and recovery during liquid CO_2 flow through fractured St Ninian's shale core sample (May 2013)

During the pressure loss incident shown in Figure 5.19 the pump controller display was monitored, and it was observed that the pump controller pressure readings for Pump B during refill were much lower than expected from the CO_2 liquid withdrawal cylinder. The pressure reading during refill was 1.4 MPa (200 psi) rather than around 5 MPa.

As a result of these intermittent pressure loss incidents, a lengthy pump testing exercise was undertaken with some liaison with Presearch (now ARC Sciences), the pump suppliers. Testing included CO_2 supply cylinder replacement, pump inflow valve checks and testing of alterations to pump control settings over long durations. Extensive testing established that pressure loss or pressure spike incidents occur as a result of an intermittent error in the pressure reading on the upstream pump controller for Pump B. When Pump B pressure reading errors on the controller do occur, the pressure displayed is always significantly lower than the actual pressure in the syringe, which can be deduced from upstream rig pressure transducer measurements. The discrepancy magnitude varies but has been observed in the range of a few, to over ten MPa. Negative pressure readings have been displayed during Pump B refills on several occasions. If the error initiates itself during Pump A operation, pressure matching of Pump B

to Pump A that occurs during multi-pump mode results in overpressuring of Pump B by the discrepancy magnitude, as the controller readings are utilised during pressure matching. This Pump B overpressure causes a high pressure spike during Pump A to B changeover. If the discrepancy is present during Pump B operation, pressure matching of Pump A to the erroneous low Pump B reading results in underpressuring of Pump A, and a pressure drop occurs at the Pump B to A changeover.

Liaison with Teledyne Isco manufacturers suggested that the problem was likely to be associated with the Pump B pressure transducer. This was therefore replaced with an alternative pressure transducer unit to enable flow experiments to proceed. However, despite the pressure transducer replacement, similar pressure surge and loss incidents continued to occur on an intermittent basis throughout the project duration, indicating that this did not resolve the pump error.

Figure 5.20 illustrates a pressure spike followed by a pressure loss as a result of a pump error incident during the fractured Cambrian shale core V1 flow experiments. The effects of these pressure errors on the differential pressure across the core sample can be seen in Figure 5.21. The pressure discrepancy between the upstream pump controller reading and the upstream rig pressure measurement (actual upstream pressure) can be seen in Figure 5.22. On this occasion the pump controller reading is 10 MPa lower than the observed pressure. The resulting pressure spike that occurs during the Pump A to B changeover is mitigated by reaction of the downstream pump controller, which increases the receiving flow rate correspondingly to absorb the excess pressure, thus minimising the pressure surge period. However, the pressure dip lasts for a longer period than the spike, as the downstream pumps can only receive excess pressure and cannot deliver CO_2 (unidirectional control), so the pressure loss is rectified over a longer period through unenhanced CO_2 delivery from the upstream end. The downstream pump flow rate spike and the subsequent period of no flow that are responses to the upstream pressure spike and dip respectively can be seen in Figure 5.23.

Pressure surge and loss effects such as these could result in significant damage to both rig equipment and experimental core samples. This could lead to serious complications with experimental results and findings. In addition, there are obvious safety issues that result from the syringe pressure being higher than the controller thinks it is, as maximum thresholds can be exceeded, potentially resulting in serious damage or failure of equipment.

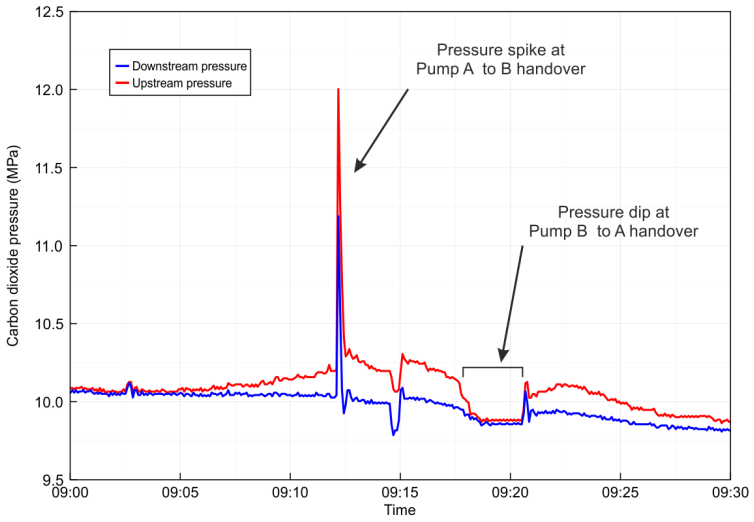

FIGURE 5.20: Upstream pressure spike and pressure dip resulting from pump error [Fractured Cambrian shale core flow experiments (Mar 2014)]

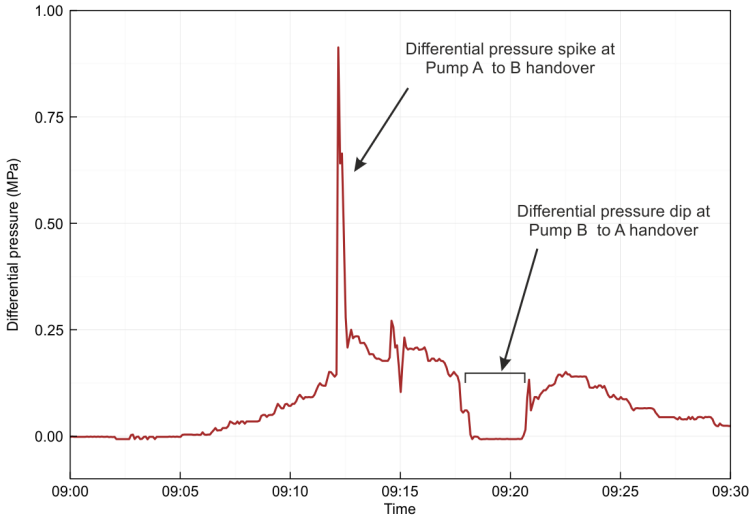

FIGURE 5.21: Effects of pressure spike and dip on differential pressure [Fractured Cambrian shale core (Mar 2014)]

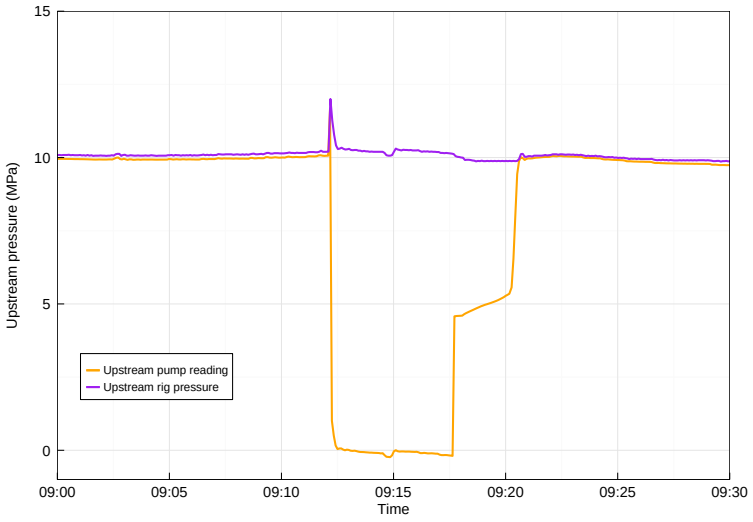

FIGURE 5.22: Pressure discrepancy during upstream pump error [Fractured Cambrian shale core (Mar 2014)]

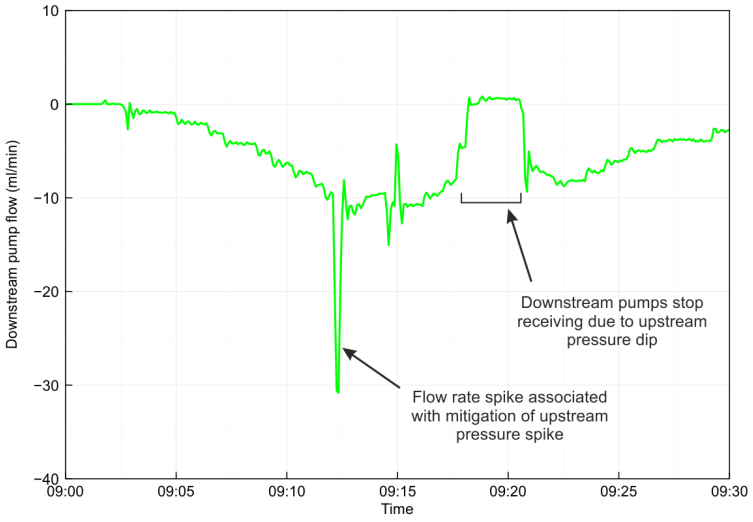

FIGURE 5.23: Response of downstream flow rate to upstream pump error [Fractured Cambrian shale core (Mar 2014)]

As a result of the hazards outlined above, the experimental rig required close monitoring throughout the duration of the flow experiments. In addition, experimental results had to be carefully assessed to ensure that pump errors had not influenced the findings, with some sections of data discarded where pump error influence was significant.

While the error within the pump system has been identified and assessed during this project, the source of the error has not been found and the issue has not yet been resolved. Despite this, we have been able to carry out successful supercritical CO_2 flow experiments during this project, but recommend that the pump error is addressed in collaboration with the suppliers, ARC Sciences (formerly Aquilant Scientific/Presearch), prior to commencement of future projects, as this will reduce the risk of equipment and sample damage. ARC Sciences (formerly Aquilant Scientific/Presearch) have agreed to replace the upstream Pump B syringe pump, as advised by the manufacturers (Teledyne Isco), in the hope that this will resolve the issue. This was not carried out during the project due to the further time delay and disruption to flow experiments that would have resulted. Teledyne Isco have no record of any similar pump errors occurring to date, which has made troubleshooting particularly challenging during this project.

5.5.2 Pipework permeability

Pipework permeability tests were undertaken to ensure that the resistance of the rig pipework to supercritical CO_2 did not influence sample core flow results under typical experimental conditions. To enable this, a stainless steel 38 mm diameter core plug containing a central hole of the same diameter as the pipework internal diameter (0.055”/1.4 mm) was created by the University of Edinburgh workshop (Figure 5.24).

The stainless steel ‘pipe core’ was loaded into the core holder and confined under a radial pressure of 27 MPa. Use of this set-up is equivalent to having continuous pipework through the core holder and allows the ‘permeability’ of the rig pipework to be measured by monitoring the differential pressure across the pipework system over a range of flow rates. The pipework system was expected to be of very high permeability, with negligible differential pressure induced. During pipework permeability testing the temperature of the system was set to 40°C and the downstream CO_2 pressure control was set to 10 MPa, typical of experimental conditions.

FIGURE 5.24: Stainless steel 'pipe core', used for pipework permeability tests

The Validyne 200 psi (1.4 MPa) differential pressure transducer (section 5.3.3.2) was used to monitor any fluctuations in the differential pressure resulting from changes in CO_2 flow rate through the system. Upstream pump flow rates within the range 0 to 10 ml/min (0 - 1.7×10^{-7} m^3/s) were tested, with maximum differential pressure variations of ±0.08 psi/0.6 kPa observed throughout the testing period. The differential pressure variations observed are significantly below the instrument accuracy (±1 psi/7 kPa), and are therefore negligible. Thus, these pipework permeability tests show that the pipework resistance does not influence differential pressure readings taken across core samples during flow experiments, validating the use of the rig for estimation of sample permeability and transmissivity.

5.5.3 Leak analysis tests

Leak detection and reduction required ongoing attention throughout the duration of the project. Leaks within the rig system can occur at any pipework joint or instrument connection, and due to regular revisions to the rig set-up and equipment, as well as the requirement to disconnect and reconnect three joints during sample loading and unloading (confining oil input, and CO_2 input and output core holder connections), regular leakage monitoring was required.

To minimise the occurrence of leaks, the creation of joints was undertaken very carefully, using a rotary drill with a cutting disk to ensure clean straight cuts to the swagelok tubing. Tube fittings were fitted with care, ensuring that they were not overtightened resulting in damage to the seal.

A number of methods were used to identify the location of any leaks within the rig system. Large leaks were audible under high pressure CO_2. In addition, CO_2 leaks resulted in localised cooling of pipework due to the adiabatic cooling effect (Joule-Thomson) associated with leakage and the resultant expansion of high pressure CO_2. Leak detector spray was used to detect very small leaks within the system. When used, fluid escaping from leaking joints creates visible bubbles, which enables identification of leaks undetected by other methods. Leaks were fixed through tightening/adjustment of fittings, or realignment/straightening of associated pipework.

Despite resolving all detectable leaks within the system, a small residual level of CO_2 leakage remained throughout the project. The leakage level is expected to increase with increasing fluid pressure, and is also anticipated to vary with temperature. Leakage levels were tested using a number of methods at various stages throughout the rig development project. Of most relevance are the leakage tests undertaken immediately prior to commencement of the main flow experiments, in Feb 2014. These were undertaken with the fractured Cambrian shale sample (see section 6.2) within the core holder, and the rig system (core and fluid) at 38°C, and are therefore most representative of the leakage levels present during the main flow experiments.

Leakage level quantification was undertaken by setting a very low CO_2 flow rate input to the 'closed' rig system at the upstream end and recording the steady state CO_2 pressure that resulted from this input. In a leak-free system, the pressure would continue rising indefinitely. However, with low-level leakage the CO_2 pressure will plateau at a steady value if left to settle - this occurs when the flow rate input is equal to the leakage rate. If a number of flow rates are tested, this helps create an understanding of the leakage rate variation with pressure (Figure 5.25).

Figure 5.25 presents the results of the Feb 2014 leakage tests undertaken on the rig system with the core holder containing the fractured Cambrian shale core at 40°C. It was found that the resultant pressures associated with the various input flow rates were also dependent on the operating pump. As can be seen from the figure, the pressures are higher during Pump B operation, suggesting lower leakage levels during Pump B

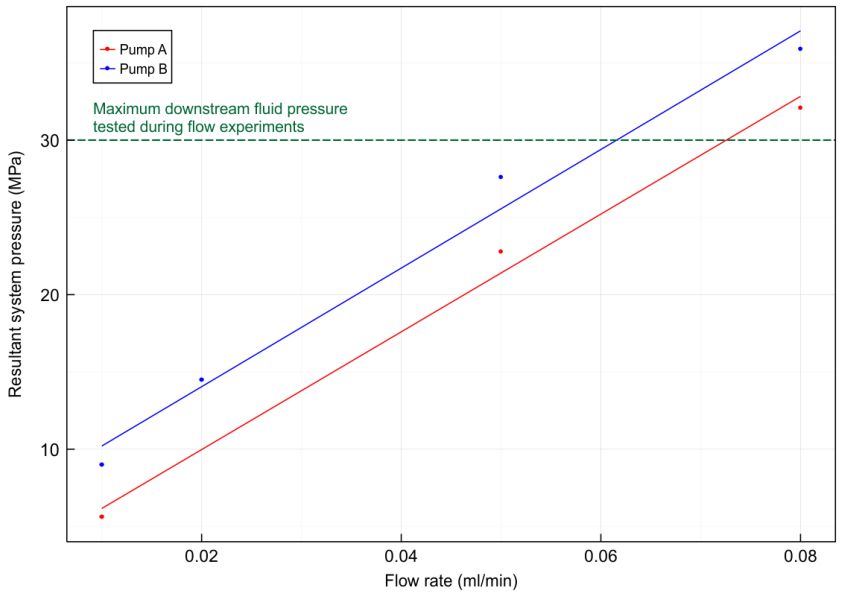

FIGURE 5.25: Results from leakage analysis undertaken at 40°C in Feb 2014 immediately prior to the fractured Cambrian shale flow experiments

operation than Pump A operation. This implies that a proportion of the CO_2 leakage occurs within the syringe pump system.

The maximum downstream fluid pressure control adopted during the main flow experiments is 30 MPa. The leakage rate data in Figure 5.25 therefore indicates that leakage levels during the 40°C experiments are likely to remain below 0.075 ml/min (1.3×10^{-9} m^3/s) during 40°C flow experiments. It should be noted that these leakage tests are indicative, and may vary throughout the various flow experiments due to changes that occur during sample exchange, as well as through regular leakage monitoring and reduction measures. It is also possible that leakage rates may differ during the higher temperature (60°C) experiments.

The residual leakage level contributes to the flow error in a systematic manner, as the error contribution is always negative. This is taken into consideration during result analysis.

5.5.4 Pressure sensor calibration

This section describes the calibration of the recorded logging data from the three gauge pressure transducers using an accurate digital pressure gauge. Calibration of the Validyne differential pressure transducer is slightly more complex than the pressure transducer calibration, and is described in detail in Appendix B.

Calibration testing of the three gauge pressure transducers (confining, upstream fluid and downstream fluid) is undertaken by connecting a digital pressure gauge (Omega DPG8001, 0-10,000 psi (0-68.9 MPa) gauge pressure) with 0.25% full scale terminal point accuracy into the pipework adjacent to the pressure transducer of interest. For the fluid pressure transducers, the CO_2 line pressure is controlled and varied using the Isco syringe pumps. The hand pump is used to control the confining oil pressure line for testing of the confining pressure transducer. Digital pressure gauge readings are taken across the full pressure range of interest and these readings are recorded alongside the corresponding logged data reading (mA). A simple linear regression model is used to define the relationship between the logging data and the pressure data (as defined by the digital gauge readings) for each of the pressure transducers. This linear calibration model is used to convert the logged data recorded during the subsequent flow experiments to pressure data.

During calibration, pressures were recorded with the system both at lab temperature and at 40°C, to check that temperature did not significantly influence the readings. Temperature was not found to have an observable effect on pressure measurement within this range.

The calibration data are presented along with the linear regression model for each of the three pressure transducers in Figure 5.26.

There is an error associated with the data transformation and transmission that occurs between the pressure sensor and the PC. This is incorporated into the error in the calibration models shown in Figure 5.26. Uncertainty limits for the linear model fits have been calculated from 95% prediction intervals. The limits result in an uncertainty of ±5.5 psi/38 kPa;±2.4 psi/17 kPa and ±11.1 psi/77 kPa respectively for the upstream, downstream and confining pressure sensors.

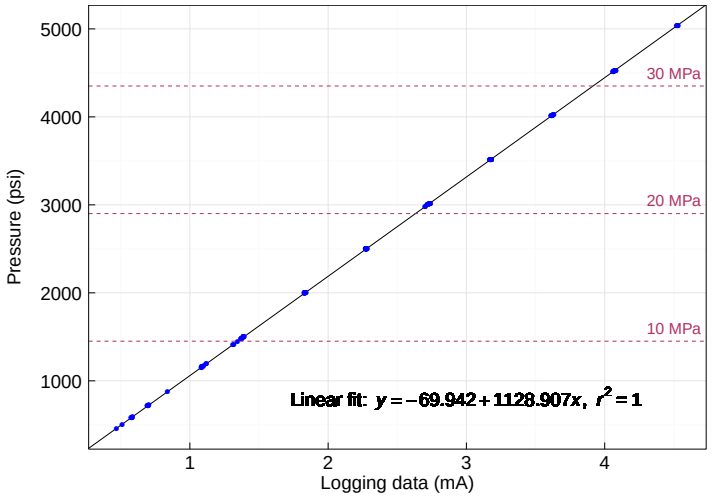

(A) Upstream fluid pressure transducer calibration (147 calibration points)

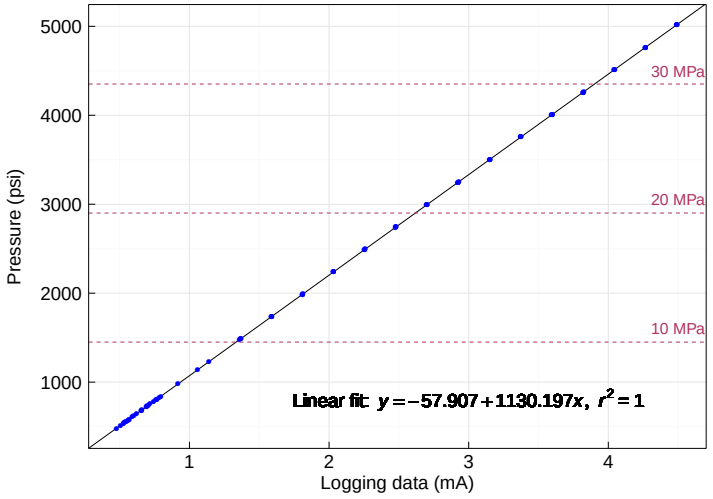

(B) Downstream fluid pressure transducer calibration (88 calibration points)

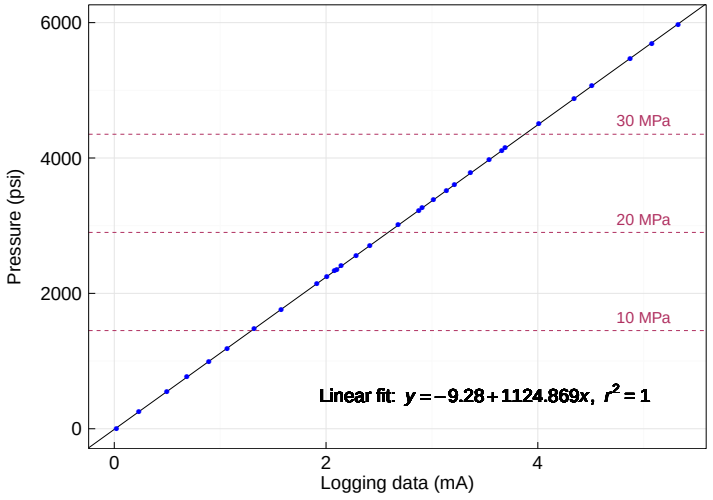

(C) Confining pressure transducer calibration (31 calibration points)

FIGURE 5.26: Calibrating pressure logging data against gauge pressure

As mentioned previously, the instrument accuracy is ±0.25% BFSL which, within the pressure ranges of interest (∼1000-8000 psi/6.9-55.2 MPa), gives an accuracy of between ±2.5 psi/17 kPa and ±20 psi/138 kPa. Thus, the additional error associated with continuous recording of the pressure sensor data is of a similar order of magnitude to the instrumental error.

5.5.5 Thermocouple calibration

Calibration of the logged data output from the omega thermocouple used for monitoring the sample/core holder temperature (J-type sensor) was carried out using a K-type thermocouple with USB temperature logger, with an associated instrument error of ±2.2°C. This is the same accuracy as quoted for the J-type thermocouple being tested. In addition, an alcohol thermometer (with an associated reading error of ±0.5°C) and an RS thermocouple connected directly to a digital meter (instrument error ±2.2°C) were used for validation checking.

Calibration was carried out by placing the thermocouple probe in a beaker of water, along with the calibration K-type thermocouple, the alcohol thermometer, and the RS thermocouple. The beaker of water was slowly heated (using a hot plate) from lab temperature (20°C) to around 85°C, thereby covering the full range of temperatures of interest. A magnetic stirrer was used through the duration of the calibration testing to ensure the water was well mixed and thus temperature variation within the fluid was minimised.

The thermocouple log data were continuously recorded at 5 s intervals throughout the experiment, as were the calibration thermocouple data (via it's standalone USB logger). In addition, readings were taken from the alcohol thermometer and RS thermocouple digital meter on average every two minutes during the experiments, for comparison purposes. The calibration data from the USB thermocouple logger and the validation data from the alcohol thermometer and RS thermocouple digital meter are plotted against the corresponding thermocouple logging data in Figure 5.27.

The USB logger data used for calibration were found to match the alcohol thermometer temperature data (within expected uncertainty levels), which was reassuring for validation purposes. However, as can be seen from Figure 5.27, the RS thermocouple data were found to give higher temperature estimates. As the alcohol thermometer is

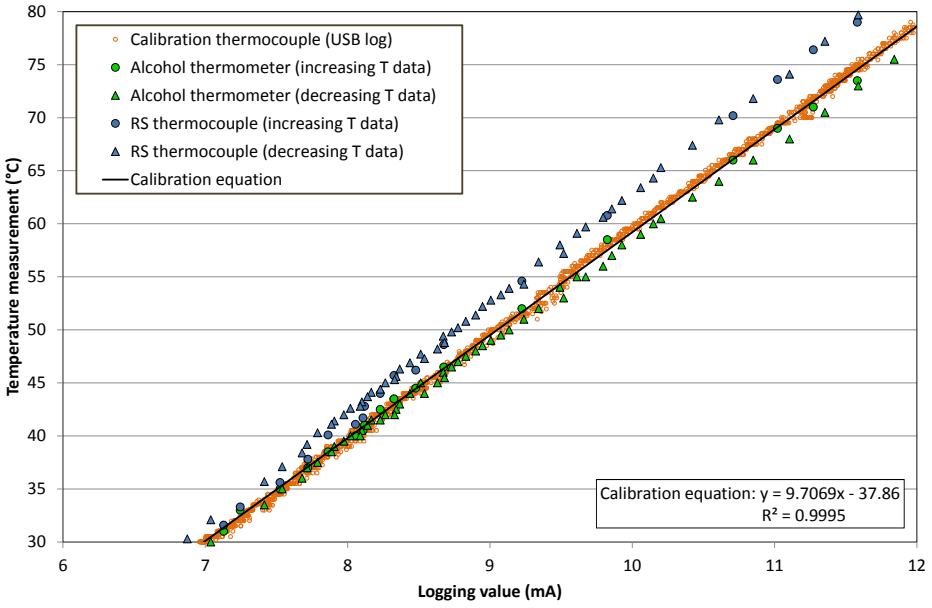

FIGURE 5.27: Thermocouple calibration data

expected to be of higher accuracy than the RS thermocouple, the RS thermocouple data were considered to be overestimating, and was thus neglected.

A simple linear regression model is used to define the relationship between the thermocouple logging data and the USB logged temperature data. This linear calibration model is used to convert the logged data recorded during the subsequent flow experiments to temperature data, and is shown in Figure 5.27. Uncertainty limits for the linear model fit have been calculated from the 95% prediction intervals. The limits result in an uncertainty of ± 0.83°C. Thus the uncertainty in the linear fit is lower than the expected instrument uncertainty, indicating a good calibration model fit. Error due to data transformation and transmission of the thermocouple signal through the logging system is accounted for within the calibration process as it is the final logged data signal that is calibrated against 'known' temperature data.

5.5.6 Clashach permeability test

After commissioning was largely complete (December 2013), the rig was used to undertake permeability testing of a Clashach sandstone core sample using CO_2 fluid. Prior to these permeability tests the Clashach core (sample B++) had been subjected to independent porosity and permeability testing using a helium porosimeter and nitrogen permeameter at Heriot Watt University (see Chapter 3, section 3.4). The rig permeability tests were carried out as validation checks for the rig, with results compared against the independent permeability test.

5.5.6.1 Sample

Figure 5.28 shows the cored Clashach sample used within the permeability tests. Sample details are provided in Table 5.2. The porosity and permeability values provided in the table are those obtained from testing undertaken at Heriot Watt university.

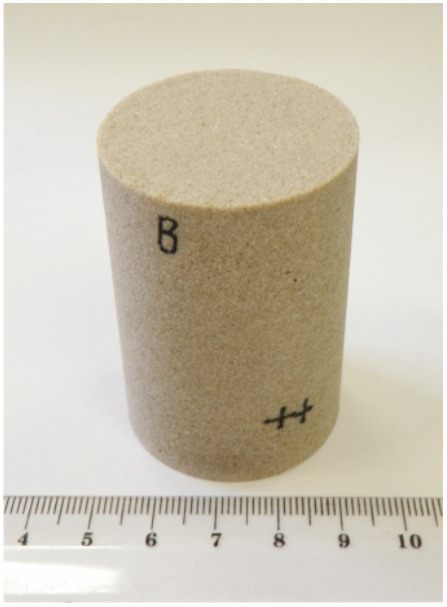

FIGURE 5.28: Clashach sandstone core sample used within permeability tests

As discussed in section 3.3.3.2, to minimise CO_2 diffusion through the core holder sleeve, rock core samples used within the rig's core holder were coated around the curved surface area of the core prior to loading. Sample coating was particularly important during the Clashach permeability tests as CO_2 exposure was expected along the full

TABLE 5.2: Clashach sample details (with porosity and permeability values obtained through independent testing undertaken at Heriot Watt university

Sample ID	Clashach B++
Sample length (mm)	56.2
Sample diameter (mm)	38.1
Sample weight (g)	141.2
Effective porosity (%)	15.2
Klinkenberg permeability (mD/m^2)	$297.7/2.93 \times 10^{-13}$

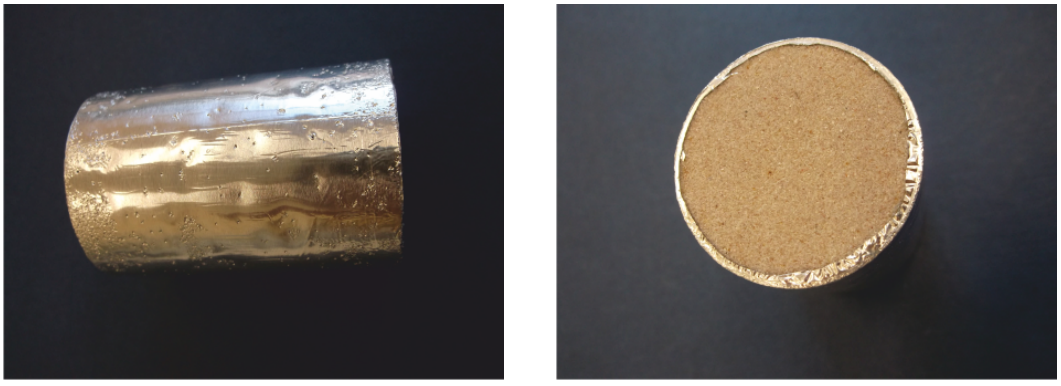

(A) Side view of core

(B) End view of core

FIGURE 5.29: Sample coating post-experiment, showing piercing of foil coating due to coarse-grained sample

surface area of the core due to the relatively high sample permeability. The Clashach sample was coated with self-adhesive aluminium foil prior to these permeability tests, which was overlapped slightly onto the core ends to help ensure an even end seal between the core end and the core holder platen. This technique also helped minimise the sleeve exposure to CO_2 at the core ends.

Figure 5.29 shows the sample coating post experiment. It is evident from this figure that the coarse-grained nature of the sample has resulted in extensive piercing of the sample coating during the flow experiment when a high radial confining pressure is applied. Despite this, no evidence of CO_2 diffusion into the confining oil was detected during this experiment. This is thought to be in part due to the short timescale of the experiment. However, as a consequence of the piercing of the coating observed during this experiment, lead foil layers were introduced as an additional barrier during the subsequent discretely fractured sample experiments (see Chapter 3, section 3.3.3.2 for details).

5.5.6.2 Method

In order to undertake permeability tests, the coated Clashach sample was loaded into the core holder. The sample temperature was brought up to 40°C and a high confining pressure of approximately 30 MPa was applied. The confining pressure must be higher than the fluid pressure to ensure that CO_2 cannot bypass the sample during testing. Thus a high confining pressure allows for relatively high fluid pressure testing of the sample.

Eight different differential pressure readings were taken during permeability testing. The flow rate through the sample and the downstream fluid pressure were varied during testing. The differential pressure readings were taken periodically when the system was in steady state (i.e. the pressure readings were relatively stable and flow was constant). The measurement logging system was not fully functional at this stage of the project, therefore logging and checking of the flow and fluid pressures during experiments was carried out via videos of the digital pressure displays.

As discussed in section 5.3.3.2, the diaphragms within the Validyne differential pressure transducer can be interchanged to enable the transducer to be used for different differential pressure ranges. However, due to the requirement for PTFE o-rings within the transducer when using supercritical CO_2 fluid, changing the diaphragm requires replacement of the o-rings (due to their inelasticity), and full recalibration of the system, therefore diaphragm changes were kept to a minimum. The diaphragm used within the Validyne differential pressure transducer during the Clashach permeability experiments was a 0-200 psi (0-1.4 MPa) range diaphragm. The instrument accuracy is ±1 psi/7 kPa with this diaphragm in use (±0.5 % FS). As the Clashach permeability is relatively high, and differential pressures are therefore correspondingly low (can be <1 psi), this means that there is a high degree of error within the differential pressure readings recorded, and therefore the permeability values calculated. As a result, these tests are indicative only, but are still of value as a rig commissioning check. A lower permeability rock, or lower range diaphragm, would have been more suitable for this rig validation check, and is recommended for any future validation tests.

The results of the permeability tests are shown in Table 5.3. The confining pressure was approximately 30 MPa throughout the duration of the permeability testing. In addition, both the CO_2 fluid and sample temperature were set to 40°C via control of

the fluid heat exchanger and oven temperature respectively. Temperature logging of the core holder indicated that the actual sample temperature was 38°C throughout the permeability testing (as with main flow experiments, Chapter 6). Thus 38°C has been used rather than 40°C for density and viscosity calculations for the fluid as it is assumed that the core holder temperature is representative of both the sample and fluid temperature during the experiments.

TABLE 5.3: Clashach permeability test data

Test	Downstream fluid pressure, P_{ds} (MPa)	Viscosity μ (Pa s)	Flow rate, Q (ml/min)	Differential pressure, ΔP (kPa)	**Permeability, k** (mD/m^2)
1	10.39	3.89×10^{-5}	13.7	1.2	354 /3.49×10^{-13}
2	11.06	4.23×10^{-5}	26.6	4.3	213 /2.10×10^{-13}
3	17.97	5.93×10^{-5}	34.9	10.1	169 /1.67×10^{-13}
4	13.20	4.95×10^{-5}	25.1	5.1	200 /1.97×10^{-13}
5	10.94	4.17×10^{-5}	13.4	1.7	273 /2.69×10^{-13}
6	10.07	3.68×10^{-5}	14.0	1.4	308 /3.04×10^{-13}
7	10.11	3.71×10^{-5}	28.0	4.8	177 /1.75×10^{-13}
8	10.11	3.71×10^{-5}	14.0	1.4	309 /3.05×10^{-13}

The downstream fluid pressure, P_{ds}, and differential fluid pressure across the sample, ΔP, are measured during the experiments. The flow rate through the sample is calculated from the pump flow rate and ratio of densities between the pump and sample, as discussed in section 5.3.2.2. The CO_2 densities at the pump (7°C) and the sample (38°C) have been calculated using the Huang et al. [1984] equation of state (see section 2.5.1).

The permeability, k, estimates have been calculated using Darcy's law (Equation 2.4), with CO_2 viscosities estimated using Jossi et al. [1944] (see section 2.5.1).

The Klinkenberg effect (section 2.5.3) has not been considered for these permeability tests. The Clashach sandstone sample has a relatively high permeability and therefore the Klinkenberg effect is expected to be small. In addition there is considerable error in the permeability estimates, predominantly due to the large ($> 100\%$) error associated with the differential pressure readings. The Klinkenberg effect is therefore considered to be relatively insignificant at this level of accuracy.

Taking the mean permeability and sample standard error calculated from the eight tests presented in Table 5.3, the Clashach permeability tests undertaken on the rig suggest

the permeability of the Clashach sample is **250 ± 75 mD** ($2.47 \times 10^{-13} \pm 0.74 \times 10^{-13}$ m^2). Given the low accuracy of the differential pressure readings, and therefore the subsequent large uncertainty associated with the permeability estimates, this result is remarkably close to the Klinkenberg permeability of 298 mD (2.94×10^{-13} m^2) calculated during the nitrogen permeameter tests undertaken on the same sample. The permeability magnitude is also within published Clashach permeability ranges [Ojala et al., 2004]. These permeability tests undertaken on the Clashach sample therefore help to establish confidence in the suitability of the experimental rig, particularly as the measurement error is proportionally much lower for lower permeability samples, such as the discretely fractured samples studied within this project.

5.5.7 Wissey permeability check

In addition to the permeability testing of the high permeability Clashach sandstone sample, the experimental rig was also used to test the permeability of a short sample of unfractured Wissey (dolomite) seal rock (Figure 5.30). The permeability of this sample could not be determined using the nitrogen permeameter (section 3.4) due to the sample being of insufficient length (22.6 mm). As the Wissey core is of low permeability, the permeability test methodology adopted for the Clashach sandstone (section 5.5.6) could not be directly followed and required adaptation. Two separate permeability tests were undertaken on the Wissey sample, and are discussed in the subsections below.

The sample used within the permeability tests is the same sample used for porosity testing (section 3.4), and was found to have a porosity of 2.5%. Vugular pores can be seen within the sample (Figure 5.30) which, particularly considering the short sample length, may potentially lead to a higher sample permeability than is generally representative of the matrix at a larger scale, if connectivity of large pores is present within the sample. In addition, heterogeneity can be seen within the short sample in Figure 5.30. The Wissey permeability testing is therefore intended as a tool for illustrating an indicative permeability magnitude for the Wissey seal rock matrix rather than for obtaining a conclusive matrix permeability result.

Prior to loading the sample into the core holder the Wissey sample was coated with: PTFE tape; non-adhesive aluminium foil; self-adhesive aluminium foil; and a lead liner, as described in section 3.3.3.2. Sample coating was undertaken to mitigate the risk of CO_2 diffusion through the core holder elastomer sleeve.

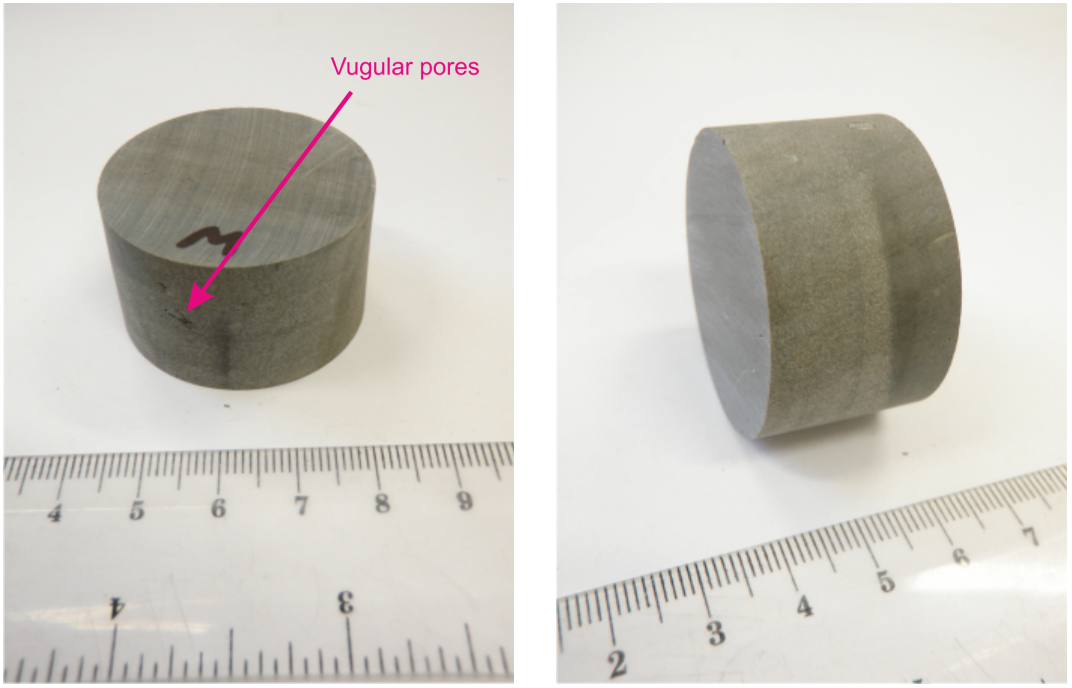

FIGURE 5.30: Wissey matrix core sample for permeability testing. Vugular pores can be seen on the side of the core in the left image and heterogeneity can be seen in the right image (colour variation).

5.5.7.1 Constant differential pressure test

The first permeability test carried out on the Wissey sample involved setting constant CO_2 fluid pressures of different values both upstream and downstream of the sample. The flow rates at the upstream and downstream pumps were monitored and used to estimate a flow rate through the sample once steady state conditions were achieved. These parameters were then used to estimate a transmissivity and permeability for the sample using Darcy's law (Equation 2.4). The transmissivity magnitude can then be compared with the transmissivity range for the fractured Wissey sample (Chapter 7) to assess the relative transmissivity of the Wissey matrix.

The upstream fluid pressure was set to 20 MPa and the downstream fluid pressure was set to 10 MPa during this permeability test. The sample was under a confining pressure of 54.6 MPa and the sample temperature was 38°C. The pump temperature during the permeability test was 4°C.

Pump flow rates (both upstream and downstream) were monitored continuously throughout the duration of the experiment and were used to estimate the flow rate through the

sample during steady state conditions, using mass conservation (see section 5.3.3.3). The fluid pressures and upstream pump flow rate are shown for the experiment duration in Figure 5.31. The steady state period used for calculation of transmissivity and permeability estimates is indicated.

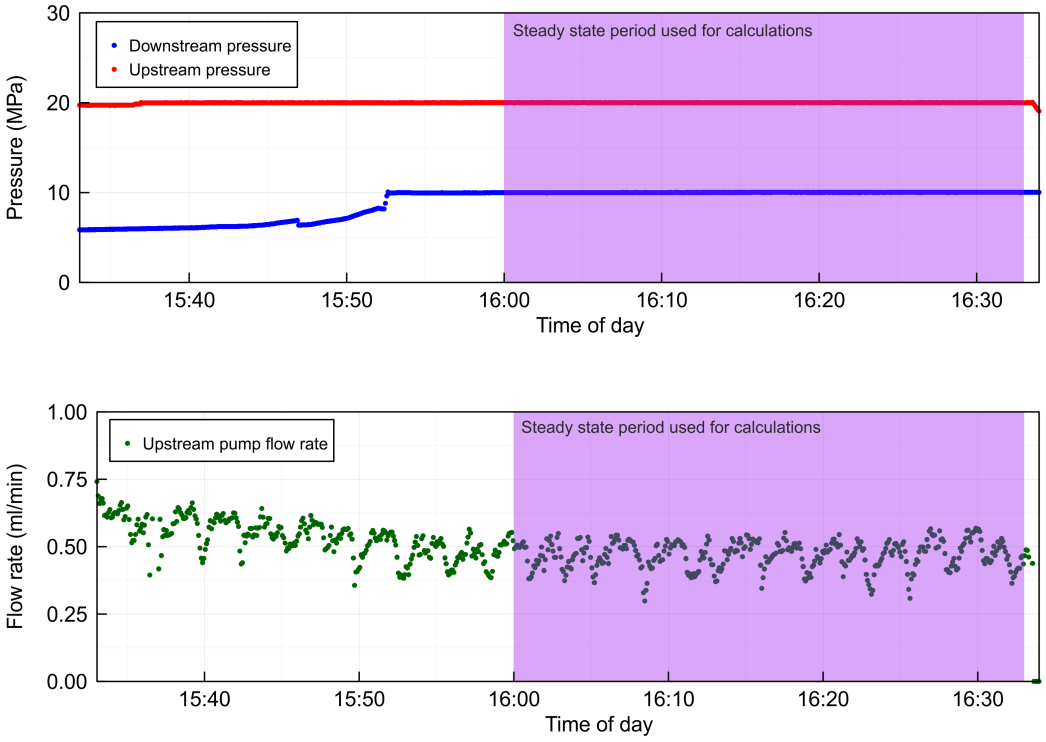

FIGURE 5.31: Fluid pressures on either side of Wissey core, and upstream pump flow rate during constant differential pressure permeability test

For the steady state duration (approximately half an hour), the mean upstream pump flow rate was multiplied by the ratio of fluid densities between the upstream pump and the upstream side of the sample to estimate a flow rate for the upstream end of the sample. Similarly, the mean downstream pump flow rate for the same duration was multiplied by the ratio of densities between the pump and the downstream side of the sample to obtain an estimate for the flow rate for the downstream end of the sample. The density and viscosity values used in calculations during this permeability test were obtained from the NIST Chemistry Webbook [Lemmon et al., 2011]. The full list of parameter values during this experiment are provided for the four key locations within the rig system (upstream and downstream pumps and sample upstream and downstream ends) in Table 5.4.

TABLE 5.4: Parameter values at key locations during constant differential pressure permeability test

Location	Upstream pump	Downstream pump	Sample upstream	Sample downstream
Fluid pressure (MPa)	20	10	20	10
Temperature (°C)	3.5	3.5	37.5	37.5
Flow rate (ml/min) *	0.470	0.416	0.554	0.590
Fluid density (kg/m^3) **	1006.7	956.18	852.91	675.28
Fluid viscosity (Pa s) **	12.55×10^{-5}	10.78×10^{-5}	8.09×10^{-5}	5.30×10^{-5}

* *Flow rates are measured at pumps and estimated using density ratios at sample ends*
** *Density and viscosity values sourced from NIST* [Lemmon et al., 2011]

A sample permeability estimate was calculated using Darcy's law (Equation 2.4). Transmissivity was also calculated, where transmissivity is defined as the product of permeability and the cross-sectional area of the sample (section 2.3.2). This transmissivity definition is useful for comparison between matrix samples and fractured samples, as it describes transmissivity through the sample as a whole, for either unfractured or fractured samples. In contrast, fracture permeability describes the permeability of the fracture channel only, rather than the permeability of the whole sample due to the presence of the fracture. Thus fracture permeability estimates from flow experiments cannot be directly compared to matrix permeability estimates such as this.

A mean flow rate and viscosity estimate for the sample was calculated from the average of the sample upstream and sample downstream estimates, and these values were used in transmissivity and permeability calculations. Table 5.5 presents the parameters used for transmissivity and permeability estimation, as well as the estimates themselves.

From Chapter 7 we see that the transmissivity values for low flows through the naturally fractured Wissey sample at 38°C are in the order of 10^{-19} to 10^{-18} m^4. The transmissivity estimate calculated here for the unfractured Wissey sample, and therefore indicative of Wissey matrix transmissivity is 1.4×10^{-21} m^4, more than two orders of magnitude smaller than that of the fractured sample. This suggests that matrix permeability is likely to be negligible in comparison to fracture permeability for the fractured core sample.

TABLE 5.5: Wissey matrix transmissivity and permeability estimates and associated input parameters (first test)

Sample parameters	Value
Sample length (m)	0.02256
Cross-sectional area (m^2)	0.00113
Confining pressure (MPa)	54.6
Upstream CO_2 pressure (MPa)	20
Downstream CO_2 pressure (MPa)	10
Mean fluid viscosity (Pa s) *	6.70×10^{-5}
Mean flow rate (ml/min) *	0.572
Transmissivity estimate (m^4)	1.4×10^{-21}
Permeability estimate (m^2)	1.3×10^{-18}
Permeability estimate (mD)	**0.0013**

* Mean of sample upstream and sample downstream values

5.5.7.2 Constant flow rate test

The second permeability test undertaken on the Wissey sample comprised of setting the downstream fluid pressure to a constant pressure (10 MPa), and setting the pump flow rate of the upstream CO_2 pumps to a constant rate of 1 ml/min (1.7×10^{-8} m^3/s). The system was left to attain steady state conditions, with the resultant steady state upstream fluid pressure used in estimation of sample permeability and transmissivity in the same way as the constant differential pressure test. Thus, while in the first test the upstream fluid pressure was controlled and the flow rate measured, in this alternative test the flow rate is controlled and the upstream fluid pressure is measured.

Figure 5.32 shows the upstream pressure increasing to steady state conditions during the experiment, and identifies the four minute data period used for calculation of transmissivity and permeability estimates. The reduction of upstream pressure at the end of the data period was a result of upstream pump shutdown due to an overpressure threshold trigger. The data period immediately prior to this was considered sufficiently stable for use in permeability calculations.

Flow rates, pressures and temperatures were monitored continuously during this experiment, as with the previous experiment. Table 5.6 provides data on parameter values at the four key rig locations during the steady state period of this constant flow rate experiment.

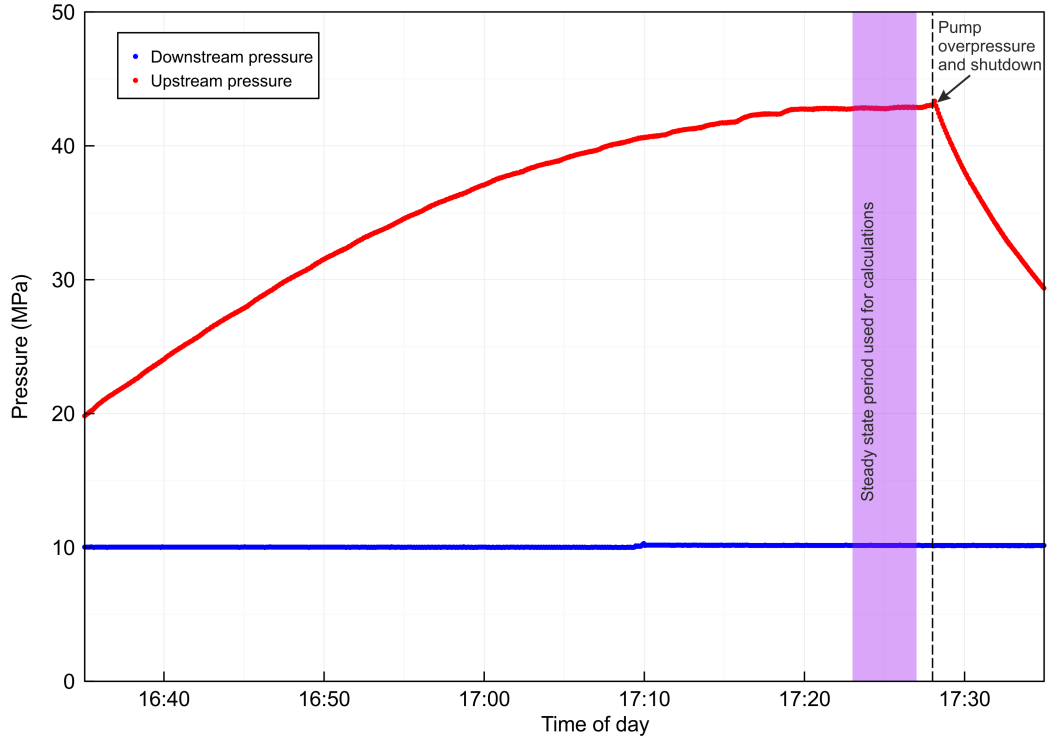

FIGURE 5.32: Fluid pressures on either side of Wissey core during constant flow rate permeability test

TABLE 5.6: Parameter values at key locations during constant flow rate permeability test

Location	Upstream pump	Downstream pump	Sample upstream	Sample downstream
Fluid pressure (MPa)	42.82	10.14	42.82	10.14
Temperature (°C)	3.5	3.5	37.5	37.5
Flow rate (ml/min) *	1.000	0.974	1.106	1.580
Fluid density (kg/m^3) **	1078	957.07	974.66	682.21
Fluid viscosity (Pa s) **	1.57×10^{-4}	1.08×10^{-4}	1.12×10^{-4}	0.54×10^{-4}

* *Flow rates are measured at pumps and estimated using density ratios at sample ends*
** *Density and viscosity values sourced from NIST* [Lemmon et al., 2011]

Transmissivity and permeability estimates were calculated for the Wissey core sample from experimental data during this constant flow rate test in a similar manner to the constant differential pressure test. Mean flow rate and fluid viscosity parameters (calculated from upstream and downstream sample parameters) were used in calculations. The parameters used in the calculations, as well as the resulting estimates are included in Table 5.7.

TABLE 5.7: Wissey matrix transmissivity and permeability estimates and associated input parameters (second test)

Sample parameters	Value
Sample length (m)	0.02256
Cross-sectional area (m^2)	0.00113
Confining pressure (MPa)	55.43
Upstream CO_2 pressure (MPa)	42.82
Downstream CO_2 pressure (MPa)	10.14
Mean fluid viscosity (Pa s) *	8.31×10^{-5}
Mean flow rate (ml/min) *	1.34
Transmissivity estimate (m^4)	1.3×10^{-21}
Permeability estimate (m^2)	1.1×10^{-18}
Permeability estimate (mD)	**0.0011**

* Mean of sample upstream and sample downstream values

The transmissivity and permeability estimates calculated during the constant flow rate permeability test on the Wissey matrix core are very similar to those from the constant differential pressure estimate, which validates our methods and provides confidence in the rig performance. The two tests undertaken on the short Wissey core sample both indicate that the Wissey matrix transmissivity is more than two orders of magnitude smaller than the fractured core transmissivity ($\sim 10^{-19}$ to 10^{-18} m^4, Chapter 7). This suggests that the matrix permeability will be negligible during testing of the fractured sample. In addition, these Wissey permeability estimates suggest that the Wissey dolomite matrix is at least as low permeability as the shale samples (East Brae, Heletz) tested using the nitrogen permeameter (Chapter 3).

5.6 Summary and recommendations for future improvement in rig design

This chapter details the final rig design used for supercritical CO_2 flow experiments undertaken during this project and discusses the design development processes that led to construction of the final rig design. Material selection for both metals and polymers is discussed in the context of suitability for use with supercritical CO_2 fluid. The chapter also includes details of instrument calibrations and rig validation checks undertaken as part of the rig commissioning process.

Rig design and build was a significant component of this project. A rig design suitable for undertaking supercritical CO_2 flow experiments has been built, and successful use of the rig has been demonstrated. The rig has been designed to enable good temperature, pressure and flow control during experiments. In addition, the rig has been designed so that it can be easily adapted for multiphase fluid experiments, and is suitable for a variety of core samples. The versatile differential pressure transducer utilised within the rig allows diaphragm exchange which enables potential measurement of a wide range of differential pressures. Care has been taken to limit corrosion and chemically resistant materials have been used within all components of the rig system.

While commissioning tests validate the suitability of the rig (section 5.5), a number of recommendations for future improvement are listed that would improve the user-friendliness of the rig system, as well as accuracy and flexibility:

Adopt a universal logging system

Three separate logging systems were used to continuously record pressure measurements, pump data and temperature measurements. Operation of the three separate logging systems increased the potential for user errors during experiments and complicated post-processing of data (Chapter 6). A universal logging system to incorporate logging of all data would improve the usability of the rig and reduce the errors associated with merging multiple datasets during post-processing.

Core holder platen upgrade

As described in section 5.4, opening and closing of the upstream 'quick-release' platen was problematic throughout the duration of the project, due to bulging

of the cylindrical platen during high pressure, high temperature experiments. Smoothing and polishing of the relatively soft Type 316 stainless steel platen was undertaken by workshop technicians on several occasions, but due to the low tolerance associated with the closure mechanism, the problem was recurring. This could be resolved by redesigning the closure mechanism to match the screw design of the downstream platen, or by use of a harder material that would be less prone to swelling/bulging under the experimental pressure and temperature conditions.

Upgrade core holder sleeve material

While replacement of Viton sleeves with HNBR sleeves during this project has mitigated earlier sleeve rupture problems, extensive sample coating is required to limit CO_2 diffusion through the core holder sleeve during experiments. If an appropriate sleeve material can be identified that does not degrade and is not susceptible to CO_2 diffusion, this would substantially simplify the sample preparation and loading stage of the experiments.

Resolve pump error

The intermittent pump error detailed in section 5.5.1 has not yet been resolved. It is highly recommended that the source of this error is identified and addressed, in collaboration with the pump suppliers (ARC Sciences) prior to use of the rig for future experiments. An additional pressure relief valve should also be incorporated into the rig system downstream of the core holder to address safety concerns associated with the potential development of overpressure within the downstream pumps, as experienced during this study.

In addition to the above recommendations for improvement to the rig design, measurement accuracy could be enhanced by incorporation of:

- a flow meter within the CO_2 pipework system close to the sample, to measure accurately the CO_2 flow rate under the experimental pressure and temperature conditions;
- a more direct temperature measurement system i.e. a thermocouple internal to the core holder; and

- replacement of the single differential pressure transducer with a series of parallel differential pressure transducers covering a wide range of differential pressure ranges to allow accurate measurement of a wide range of differential pressures during a single experiment.

Chapter 6

Experimental methods and techniques

6.1 Introduction

CO_2 flow experiments were undertaken on four fractured core samples from three sources: a Cambrian shale outcrop and the East Brae and Wissey North Sea fields. This chapter describes the methods adopted to undertake CO_2 flow experiments on each of the samples. Section 6.2 presents the experimental scenarios assessed for each sample and discusses the reasoning for both the experimental scenarios and the order of testing. Experimental start-up and shut-down procedures are discussed in section 6.3 and operational procedure during the flow experiments is presented in section 6.4.

Methods developed for processing data post-experiment are also included within this chapter, in section 6.5. Data collation, conversion and merging are required due to the logging methods utilised. Further to this, sampling of representative data from the logged time series is required to enable meaningful result analysis. Sampling representative data for experimental scenarios is complex and requires automated processing of logged time series datasets due to the large number of scenarios assessed for each sample. This is further complicated for the Wissey sample experiments by timing discrepancies identified between the omega logging system and the upstream ISCO pump logging system.

Extraction of representative data from the logged parameters enables calculation of various hydraulic parameters used for analysis and review of the hydraulic characteristics of the fractured sample during CO_2 flow under the various experimental scenarios tested. The processed data are categorised and error analysis is undertaken to enable successful result analysis and discussion. An overview of error analysis is included within section 6.6.

6.2 An overview of sample experiments

6.2.1 General

The purpose of the CO_2 flow experiments is to assess the hydraulic behaviour and response of the fractured samples during supercritical CO_2 flow under a variety of pressure and temperature scenarios. Hydraulic responses to changes in stress (by means of both fluid and confining pressure changes) and CO_2 flow rate were undertaken at two temperatures where possible. The confining pressures, fluid pressures and temperatures assessed are typical of in-situ conditions at proposed CO_2 storage sites. The results are therefore pertinent for developing understanding of the coupled process behaviour of fractures in a CO_2 storage setting.

The CO_2 flow experiments have been undertaken on dry, fractured samples in order that the hydraulic behaviour of single phase supercritical CO_2 within fractures can be assessed under changing stress and temperature conditions. The use of dry samples avoids the issues of drainage and imbibition that arise from the presence of multiphase fluids, thus allowing the fracture conductivity to supercritical CO_2 to be examined in isolation. This is important for consideration of the validity of fluid flow theories to supercritical CO_2. The issues of CO_2 dissolution and production of carbonic acid are also avoided, as is the associated mineral reactivity, thus ensuring that permeability changes observed result from the controlled mechanical and temperature changes applied.

To assess the hydraulic behaviour of the fractured samples to multiple temperature, confining pressure, fluid pressure and flow rate scenarios, a sequence of testing was developed to ensure all variable combinations were tested in a suitable order, with each scenario tested for an appropriate duration. In addition, the experimental scenario sequence was developed to enable assessment of the presence of hysteretic effects, or

irreversible changes to fractured samples that may result from stress or thermal loading. The standard values tested for each of the four controlled variables are stated in Table 6.1. The temperature settings used on the core holder oven and heat exchanger were 40°C and 60°C, however the observed temperatures were found to be approximately 2°C lower than the temperatures set.

TABLE 6.1: Standard values tested for controlled variables during CO_2 flow experiments

Variable	**Standard values tested**
Temperature (°C)	38, 58
Confining pressure (MPa)	35, 45, 55
Downstream fluid pressure (MPa)	10, 20, 30
Upstream pump flow rate (ml/min)	1-10 [1.7×10^{-8} - 1.7×10^{-7} m^3/s]

As mentioned within Chapter 5, volumetric flow rates through the fractured sample are higher than the upstream pump flow rates due to the fluid temperature increase (and associated density decrease) between the pump and the sample. The volumetric flow rate increase is determined by the ratio of fluid densities ($\rho_{pump}/\rho_{sample}$). Thus, for the higher temperature experiments, the flow rates through the sample are greater than those occurring for the same pump flow rate during the lower temperature experiments, due to the higher density ratio. In the same way, for a given temperature, the density ratio is slightly higher for the low fluid pressure scenarios than the high fluid pressure scenarios, which consequently means that for a given pump flow rate, the flow rate through the sample is higher during the low fluid pressure scenario. It is therefore important that when analysing results we ensure that result comparisons are undertaken against sample flow rate, rather than pump flow rate. Sample flow rates can be up to 85% higher than pump flow rates during the high temperature experiments.

The upstream flow rate and downstream fluid pressure are controlled by the upstream and downstream syringe pump controllers respectively (see Chapter 5, section 5.3.2). These enable rapid and well-controlled changes to the variable values, and variable changes can therefore be carried out at relatively high frequency. In contrast, the confining pressure is manually controlled through use of a hydraulic hand pump and needle valve. Fine adjustment of confining pressure is therefore difficult, and a significant stabilisation period (in the order of hours) is required following confining pressure changes due to the temperature sensitivity of the confining fluid. Temperature changes are

instigated through adjustment of the core holder oven temperature, as well as adjustment of the upstream fluid heat exchanger and pipework heating tape temperatures. Temperature changes require several hours for stabilisation (even longer than confining pressure changes), and are therefore undertaken overnight. Due to this hierarchy of change response times, it was determined that variable changes should be undertaken from high frequency to low frequency in the following order: flow rate, downstream fluid pressure, confining pressure, temperature.

The naming convention used for describing subsets of experimental scenarios for each sample, are as follows:

- A constant **flow rate** subdivision during experimental testing is described as an experimental **event**.
- A constant **downstream fluid pressure** subdivision is described as an experimental **step**.
- A constant **confining pressure** subdivision is described as an experimental **stage**.
- A constant **temperature** subdivision is described as an **experiment**.

Thus, each sample experiment (undertaken at a constant temperature) consists of multiple experimental stages, each of which is undertaken at a given confining pressure. Within each confining pressure stage, multiple experimental steps are undertaken to test variation of the downstream fluid pressure. Lastly, within each experimental step, multiple flow rate events are tested. Variable values are stepped up from low to high, and then returned to low again within each experimental subset, to enable assessment of the presence of hysteresis or inelastic changes. In this way both stress loading and temperature loading cycles may be assessed. The experimental scenarios assessed for each sample tested are detailed within the following subsections.

An artificially fractured Cambrian shale sample was the first sample subjected to comprehensive CO_2 flow testing, followed by experiments on two artificially fractured East Brae samples (one of which was tested twice, initially with matched fracture surfaces and subsequently with $\approx$1 mm fracture surface offset). A naturally fractured Wissey sample was the final sample subjected to CO_2 flow testing. The experimental approach

was adapted for each of the samples tested, in response to the wide range of sample permeabilities observed. In addition, improvements to the experimental method were instigated for the later samples in response to findings from the first sample experiments.

The application of epoxy resin during sample preparation was not undertaken for the East Brae and Wissey experiments due to concerns that the presence of epoxy resin may influence the response of the fracture aperture to stress changes (see Chapter 3 for details). In addition, repeat stress loading cycles were undertaken within the first two experiments on the Wissey sample following observations from earlier experiments that inelastic closure can be significant within the first stress loading cycle. Where inelastic changes are observed during experiments, direct comparison between experiments becomes challenging. Inelastic effects were observed to be less significant within repeat cycles, which helped with assessment of the elastic responses. The stress loading effects observed are discussed within the results chapter (Chapter 7).

6.2.2 Cambrian shale experiments

An artificially fractured Cambrian shale sample (V1) was the first discretely fractured sample subject to supercritical CO_2 flow testing over a comprehensive set of experimental scenarios. The Cambrian shale sample was obtained through a local stonemason, and is of low permeability and porosity (Chapter 3). A 38 mm core was sampled and artificially fractured for use within the flow experiments. After fracturing, the sample halves were recombined using epoxy resin lengthways along the sample. This was carried out due to concern that small chips in the sample resulting from the fracturing process would pierce and rupture the core holder sleeve under high confining pressures. Excess epoxy was smoothed off with sandpaper, and the recombined sample was ultrasonically cleaned in distilled water to remove any potential rock and epoxy dust from the fracture. The sample was dried at lab temperature over several days. It was then coated with two layers of self-adhesive foil and a lead liner prior to loading into the core holder to minimise CO_2 diffusion through the core holder sleeve, as discussed in Chapter 3. Table 6.2 contains a summary of the Cambrian shale sample details.

The sequence or order of experimental scenarios undertaken for the Cambrian shale sample is presented in Figure 6.1. This shows the confining pressure, downstream

Table 6.2: Cambrian shale V1 sample details

Sample	**Cambrian shale V1**
Location	Outcrop/quarry (sourced from masonry supplier)
Fracture type	Artifically induced
Rock type	Shale (Cambrian Stockingford) [Mineralogy: albite (27%), quartz (21%) with lesser proportions of illite, carbonates and potassium feldspars]
Sample length	58.6 mm
Sample diameter	38.0 mm
Sample weight	178.7 g
Matrix porosity	2.5 %
Matrix permeability	<0.01 mD/1 $\times 10^{-17}$ m^2 (below permeameter limit.)

fluid pressure and temperatures tested within each experimental step of the Cambrian shale experiments, which is in line with the proposed variable values stated in Table 6.1. Multiple upstream pump flow rates within the range 1-10 ml/min (1.7×10^{-8} - 1.7×10^{-7} m^3/s) were tested within each experimental step, with flow rates increased from 1 ml/min to 10 ml/min and back to 1 ml/min on each occasion. For most steps, increments of 1 ml/min were used within the flow rate testing cycles.

The duration of each confining pressure stage was approximately one day, with each stage consisting of a fluid pressure loading cycle from 10 MPa to 30 MPa, and returning to 10 MPa in increments of 10 MPa. Three experiments were undertaken for this sample, with Experiments A and C undertaken at the lower temperature (38°C) and Experiment B undertaken at the high temperature (58°C). Experiment A was carried out during the period 11-17 March 2014. Between Experiment A and B, the sample was held at 58°C under a confining pressure of ∼35 MPa for 13 days. Experiment B was undertaken between 31 March and 4 April, while Experiment C was undertaken on 7 April.

The sample was held within the core holder at 38°C for 19 days prior to the commencement of the flow experiments. During this time, leak testing of the rig was undertaken with CO_2 fluid pressure varied throughout the period. Flow bypassing of the fractured sample was set-up during this period, thus no differential pressure was applied across the core. The sample was subjected to a mean confining pressure of 35 MPa during this pre-experiment period.

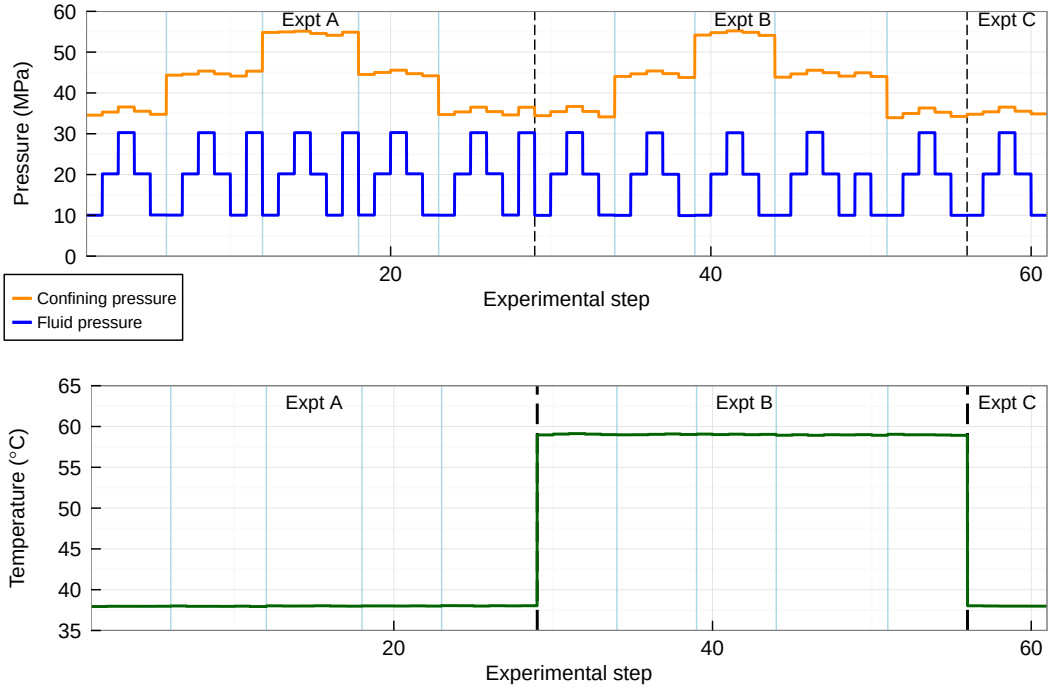

FIGURE 6.1: Sequence of pressure and temperature scenarios tested during flow experiments (Cambrian V1)

The effective stress approximation of Terzaghi [1923] as applied to fractures (Equation 2.25) is provided for the Cambrian shale experimental steps in Figure 6.2. Consideration of the effective stress acting on the fracture is important for assessment of the coupling between mechanical stress and the hydraulic behaviour of the fractured sample.

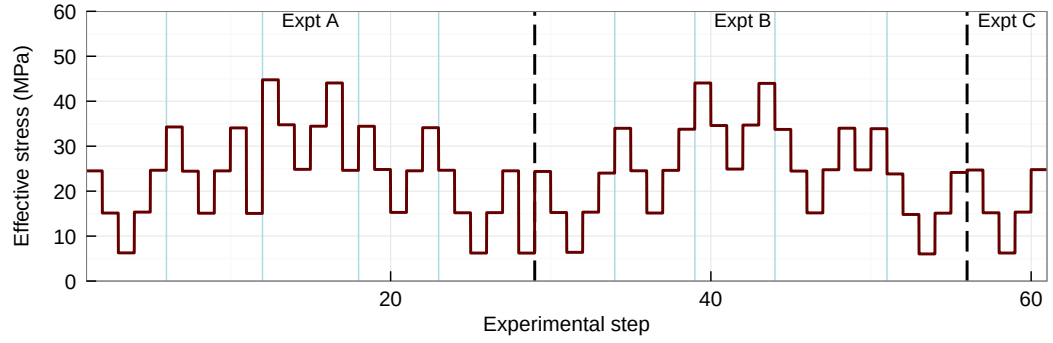

FIGURE 6.2: Effective stress scenarios during flow experiments (Cambrian V1)

During the CO_2 flow experiments the permeability of the fractured Cambrian shale sample was found to be relatively high. Thus, the differential pressures induced across the core sample were small, and at the lower limit of the differential pressure transducer measurement range. As a result, the errors associated with the differential pressure measurement (and thus the calculated hydraulic parameters, see section 6.5.4) are relatively high. As discussed within Chapter 5, the incorporation of an additional, more sensitive, differential pressure transducer in parallel with the existing differential pressure transducer would enable more precise measurement of a wider range of differential pressures by allowing selection of the most appropriate differential pressure range for each experiment. This is recommended for future development of the rig design.

6.2.3 East Brae Kimmeridge Clay experiments

Kimmeridge clay core was obtained from the East Brae North Sea field (Chapter 3). No natural fractures were found within the core samples, therefore 38 mm cores were sampled and artificially fractured to enable CO_2 fracture flow experiments to be undertaken. Testing of two artificially fractured East Brae samples, B2 and D2, demonstrated extremely low permeability during the CO_2 flow experiments, such that full comprehensive flow testing was not possible. An offset fracture was created ($\sim$1 mm offset) by trimming opposite ends of one of these fractured samples (B2), with a view to increasing the fracture permeability to allow analysis to be undertaken. The result of offsetting the fractured sample was creation of a very high permeability fracture (sample B2b), which resulted in differential pressure measurements at the extreme low end of the possible measurement range. Thus, the fractured sample was subject to 'strain hardening' by subjecting the sample to a temperature of 58°C and a confining pressure of $\sim$54.5 MPa overnight. This resulted in deformation of the fracture with a resultant $\sim$10 fold reduction in permeability.

Table 6.3 contains a summary of the sample details for each of the East Brae samples. The table includes estimates of the in-situ pressure and temperature conditions associated with the core samples. While the fluid pressures used within the lab CO_2 flow experiments are typical of the pore pressures within the East Brae Kimmeridge Clay, it should be noted that simulation of the extremely high lithological stresses and in-situ temperatures associated with these samples is outwith the capabilities of the experimental rig design. The confining pressures and temperatures tested during the

CO_2 flow experiments are typical of shallower subsurface conditions, such as that of the Wissey field (section 6.2.4).

TABLE 6.3: East Brae sample details

Samples	**East Brae**		
Location	East Brae field, North Sea		
Rock type	Shale (Kimmeridge Clay) [Mineralogy: ∼65% quartz, ∼10% illite group minerals]		
Sample	**B2**	**D2**	**B2b**
Sample length (mm)	60.6	64.0	58.0
Sample diameter (mm)	37.7	37.7	37.7
Sample weight (g)	172.9	178.0	165.4
Matrix porosity (%)	0.5	0.6	0.5
Matrix permeability (mD/m^2)	0.13 / 1.3×10^{-16}	1.16 / 1.1×10^{-15}	0.13 / 1.3×10^{-16}
Fracture type	artificially induced	artificially induced	artificially induced + offset
In-situ depth	14931'/4551m	14933'/4552 m	14931'/4551 m
In-situ pore pressure	17.9-29.0 MPa [Branter, 2003]		
In-situ temperature	∼160°C MPa [Harper, 1971]		
In-situ vertical stress	Estimate of ∼103 MPa (1 psi/ft rule of thumb for siliciclastic lithostatic pressure gradient)		

Subsequent to fracturing and core sample preparation, sample coating was undertaken for each of the East Brae samples as detailed in Chapter 3 (Table 3.3). Note that no epoxy resin was used on the East Brae samples, and all samples were coated in PTFE, aluminium foil and lead during the experiments.

The stress and temperature conditions assessed for each of the East Brae samples was dependent on the permeability of the fractured sample to CO_2. The experimental scenarios tested for each of the East Brae samples are described within the subsections below.

6.2.3.1 East Brae B2

The first East Brae sample tested within the experimental rig was the artificially fractured East Brae B2 sample. Following loading of the sample into the core holder, the sample was subjected to initial external stress loading through application of a 54.5

MPa confining pressure overnight. This was undertaken due to observation of fracture permeability reduction as a result of stress loading during the Cambrian shale experiments, and in response to discussion within Barton et al. [1985] which suggests that initial hysteresis under stress loading is considered a laboratory artefact and that representative in-situ conditions are likely to be observed subsequent to initial stress loading cycles.

In contrast to the Cambrian shale fractured sample, the East Brae B2 fractured sample was found to have a very low permeability to supercritical CO_2. Due to this, extremely high differential pressures were observed across the sample, with very limited CO_2 flow rates observed. To obtain stable observations, CO_2 flow testing of this sample had to be undertaken using constant pressure control at both the upstream and downstream ends of the sample, with the flow rate observed through logging of the upstream pump flow rate. Testing was undertaken in May 2014 under only a single scenario, due to difficulties associated with the low permeability of the sample within our rig system. Testing was undertaken with a sample temperature of 38°C, a confining pressure of 35.3 MPa, and upstream and downstream fluid pressures of 31.7 MPa and 9.7 MPa respectively. Stable results were recorded over a 5 hour period which included two syringe pump changeovers. Between pump changeovers the fluid pressures were observed to be stable to within ±0.06 MPa, however step changes of up to 1.3 MPa are observed during pump changeovers. This is likely to be due to pressure equalisation errors between the paired syringe pumps (see Chapter 5, section 5.5.1).

6.2.3.2 East Brae D2

The artificially fractured East Brae D2 sample was tested within the experimental rig subsequent to the East Brae B2 sample. Initial stress loading of the East Brae D2 sample was not undertaken, due to the expected initial low permeability of the fractured sample following tests on the similar East Brae B2 sample.

Although still very low permeability, the permeability to supercritical CO_2 of the East Brae D2 sample was found to be considerably higher than that of the B2 sample. As such, it was possible to subject the sample to the standard matrix of confining and fluid pressure conditions detailed in section 6.2.1, but under upstream pump flow rates of up to 2 ml/min (3.3×10^{-8} m^3/s) only for each scenario. The differential fluid pressures

observed across the sample were in excess of the differential pressure transducer range (0-800 psi/0-5.52 MPa), and were therefore recorded using the upstream and downstream gauge pressure transducers only. The differential pressure response time to flow rate, fluid pressure and confining pressure changes was slow due to the low permeability of the sample, therefore experiments were limited to a single confining pressure loading cycle at a single temperature (37°C). Fluid pressure loading cycles were undertaken at each confining pressure, as shown in Figure 6.3, with multiple flow rates (0.5 to 2 ml/min only [8.3×10^{-9} to 3.3×10^{-8} m^3/s]) tested for each fluid pressure step. The duration for which each flow rate was tested was dependent on the differential pressure response to change, but was typically around 20 minutes. The D2 experiments were carried out over 6 days within an 11 day period (June 2014).

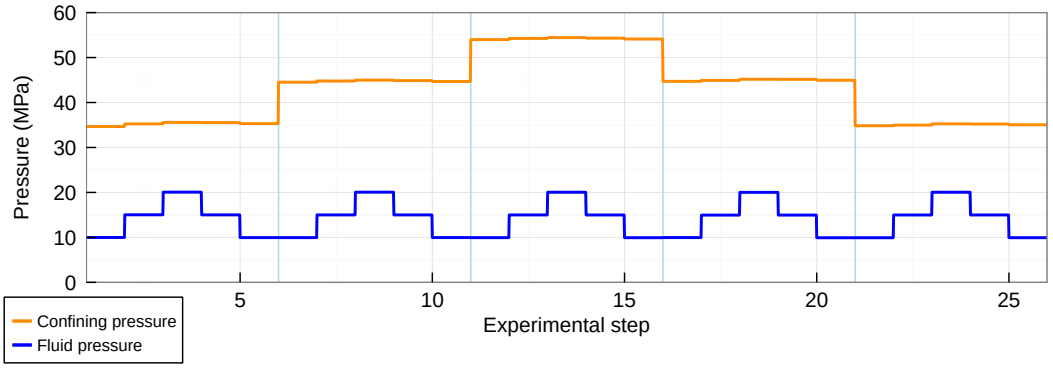

FIGURE 6.3: Pressure scenario sequence during flow experiments (East Brae D2)

The effective stress associated with the experimental pressure scenarios for D2, estimated using the effective stress law of Terzaghi [1923] (Equation 2.25), are plotted in Figure 6.4.

6.2.3.3 East Brae B2b - the offset fracture

The final East Brae sample tested was the artificially fractured and manually offset East Brae B2b sample. The fracture surfaces of this sample were manually offset by 1 mm in the vertical direction during the flow experiments. Fracture offsetting results in a significant increase to the fracture aperture, as the large scale surface topography becomes unmated, thus influencing the resultant aperture. The East Brae B2 sample was used to create the offset sample (B2b), subsequent to the B2 flow experiments.

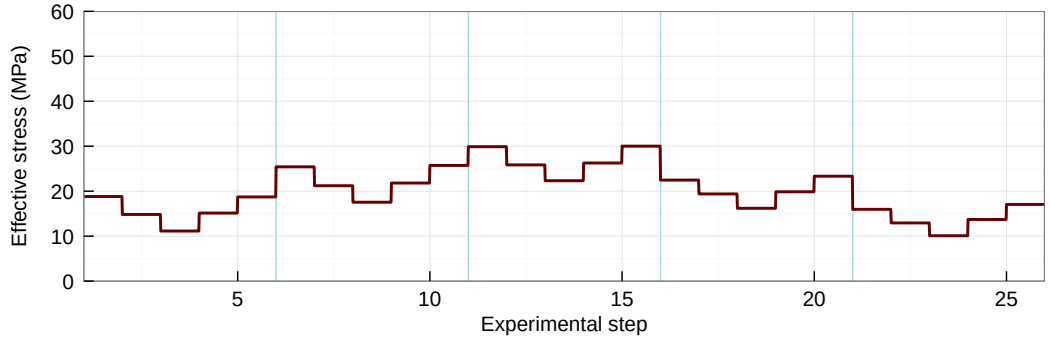

FIGURE 6.4: Effective stress scenarios during flow experiments (East Brae D2)

The core ends were trimmed following surface offset, to ensure the offset was fixed at 1 mm under closure of the end platens within the coreholder.

As a result of the fracture offsetting, and associated increase in fracture aperture, the East Brae B2b sample was found to have a very high permeability. The differential pressures observed across the sample were at the extreme low end of the possible measurement range. Thus, the sample was subjected to 'strain hardening' under a temperature of 59°C and a confining pressure of 55 MPa overnight, prior to commencing CO_2 flow experiments. It was estimated by comparison of observed differential pressures before and after the strain hardening that this resulted in an approximate ten-fold inelastic reduction in sample permeability, which is thought to be mainly due to fracture surface deformation.

The standard temperature and pressure scenarios (Table 6.1) were tested within the B2b experiments, as shown in Figure 6.5. For each experimental step (fluid pressure scenario) within the East Brae B2b sample experiments, upstream pump flow rates within the range 1-10 ml/min (1.7×10^{-8} - 1.7×10^{-7} m^3/s) were tested as shown in Figure 6.6.

The confining pressure was changed two times daily within these experiments, due to the rapid response of the high permeability fractured sample to flow rate and fluid pressure changes. Therefore in Experiments A to C, the fluid pressure cycles were undertaken at ∼half day frequency, with confining pressure cycles having a duration of ∼3 days. The whole sequence of experiments was undertaken between 20 June and 1 July 2014 with strain hardening undertaken prior to this (18-19 June).

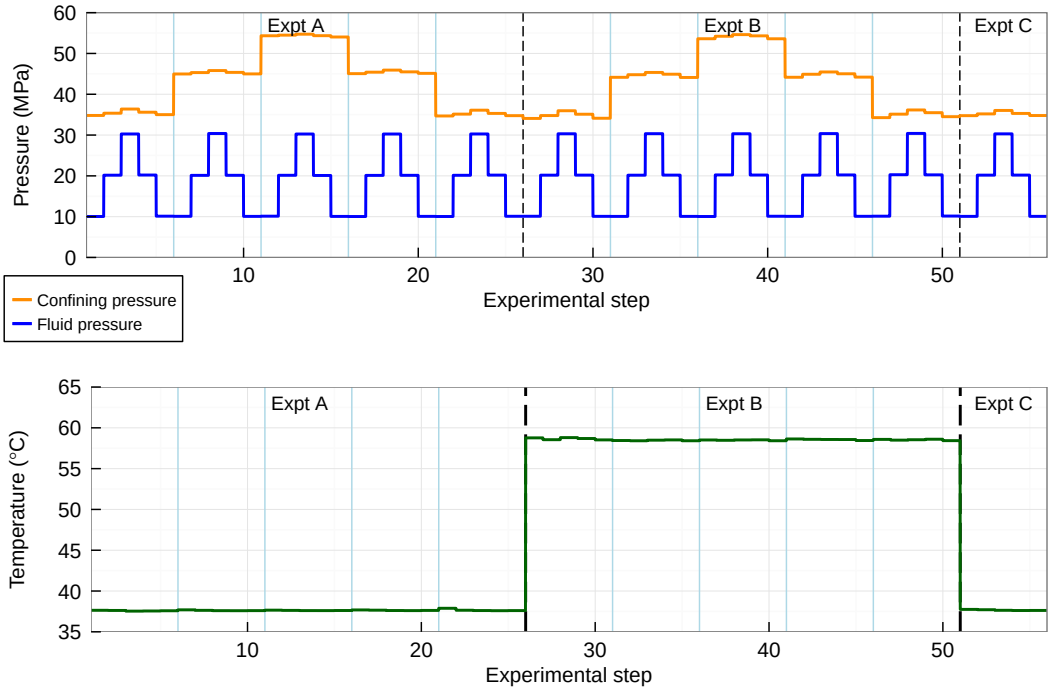

FIGURE 6.5: Sequence of pressure and temperature scenarios tested during flow experiments (East Brae B2b)

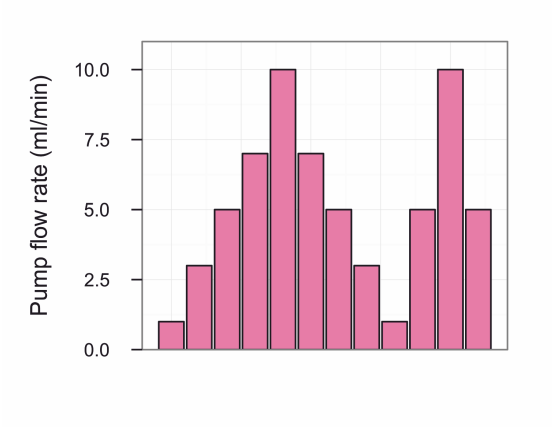

FIGURE 6.6: Flow sequences tested within each experimental step shown in Figure 6.5 (East Brae B2b).

The effective stress approximation of Terzaghi [1923] (Equation 2.25) associated with the East Brae B2b experimental steps is provided in Figure 6.7.

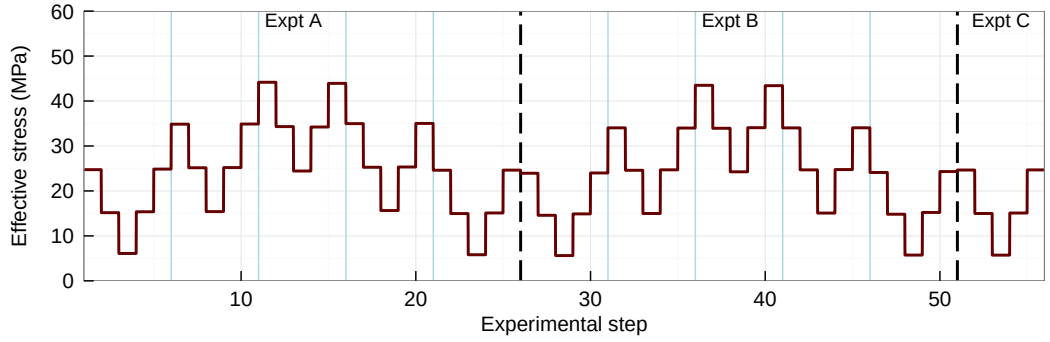

FIGURE 6.7: Effective stress scenarios during flow experiments (East Brae B2b)

6.2.4 Wissey Zechstein dolomite experiments

A natural fracture within the Zechstein dolomite of the Southern North Sea field, Wissey, was sampled and cored. A single core sample was used for CO_2 flow experiments (Wissey W3). Details of the sample preparation are included in Chapter 3. Note that, as with the East Brae samples, no epoxy resin was used on this natural fracture sample. Table 6.4 contains a summary of the Wissey fractured sample details.

TABLE 6.4: Wissey sample details

Sample	**Wissey W3**
Location	Wissey field, Southern North Sea
Fracture type	Natural
Rock type	Dolomite (Zechstein) [Mineralogy: 80% dolomite]
Sample length	27.6 mm
Sample diameter	37.6 mm
Sample weight	87.3 g
Matrix porosity	2.5 %
Matrix permeability	~0.001 mD /1×10^{-18} m^2 (see Chapter 5)
In-situ depth	5525'/1684 m
In-situ pore pressure	18.5 MPa [Noy et al., 2012]
In-situ temperature	~47°C MPa [Harper, 1971]
In-situ vertical stress	38 MPa [Noy et al., 2012]

The Wissey naturally fractured sample was the final sample used within the experimental rig for CO_2 flow experiments. The experimental sequence undertaken on this sample was the most comprehensive undertaken during this project, consisting of nine confining pressure cycles and two temperature cycles as detailed within Figure 6.8. This enabled a comprehensive analysis of the effects of repeat stress loading cycles on fracture behaviour, and the impact of temperature change on fracture conductivity to CO_2. The standard temperature and pressure scenarios (Table 6.1) were adopted within the experiments. In a similar manner to prior experiments, fluid pressure cycles were undertaken within each confining pressure stage for the first two confining pressure loading cycles of Experiment A, and within Experiments B and C1. Experiments C2, D and E consisted of confining pressure loading cycles undertaken at a constant downstream fluid pressure (10 MPa).

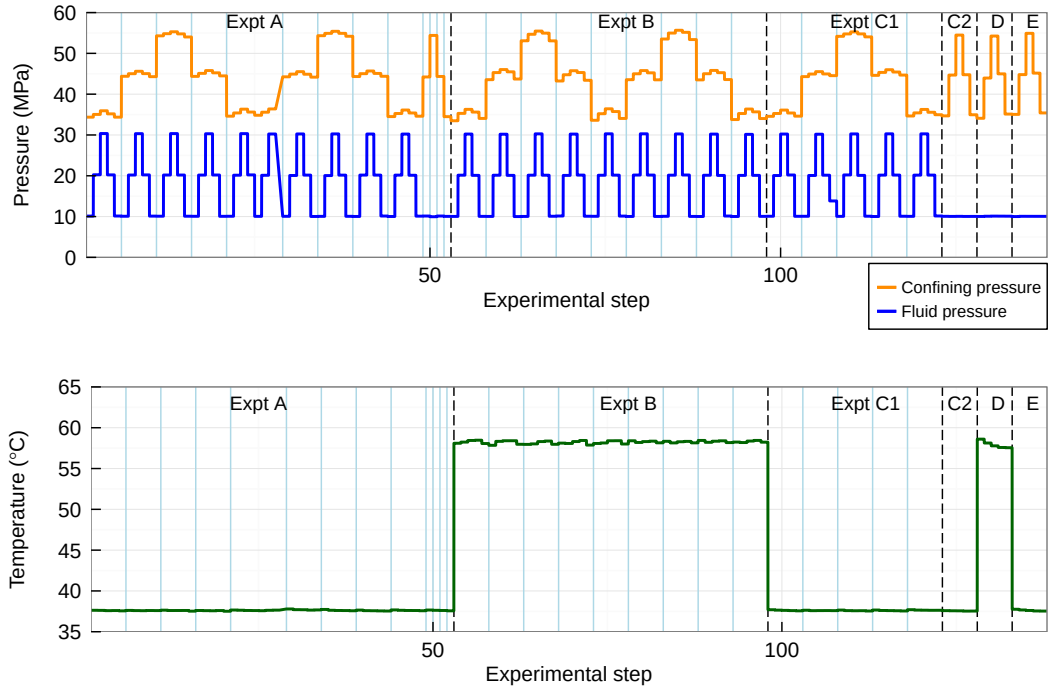

FIGURE 6.8: Sequence of pressure and temperature scenarios tested during flow experiments (Wissey W3)

For each experimental step (fluid pressure scenario) within Experiments A, B and C1, pump flow rates within the range 1-10 ml/min (1.7×10^{-8} - 1.7×10^{-7} m^3/s) were tested as detailed in Figure 6.9. Experiments C2, D and E were undertaken with a

constant upstream pump flow rate of 5 ml/min (as well as constant downstream fluid pressure).

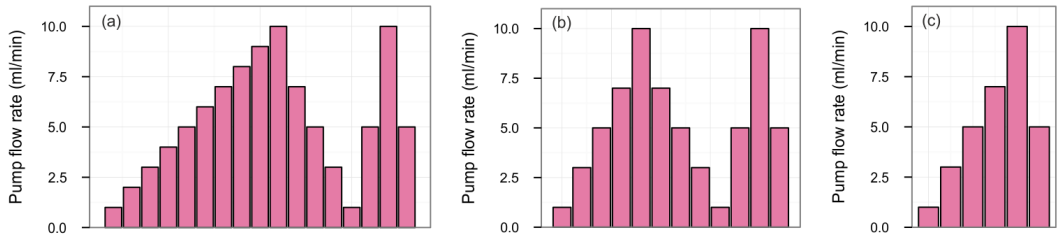

FIGURE 6.9: Flow sequences tested within each experimental step shown in Figure 6.8 for Expt A-C1 where: (a) applies to Expt A, first confining pressure cycle; (b) applies to Expt B, first confining pressure cycle; and (c) applies to all other Expt A-C1 steps.

The confining pressure was changed approximately daily, therefore in Experiments A to C1, the fluid pressure cycles were completed at ∼daily frequency, with confining pressure cycles having a frequency of ∼5 days. The whole sequence of experiments was undertaken between 3 July and 5 August (>1 month duration).

The effective stress approximation of Terzaghi [1923] (Equation 2.25) associated with the Wissey W3 experimental steps is provided in Figure 6.10.

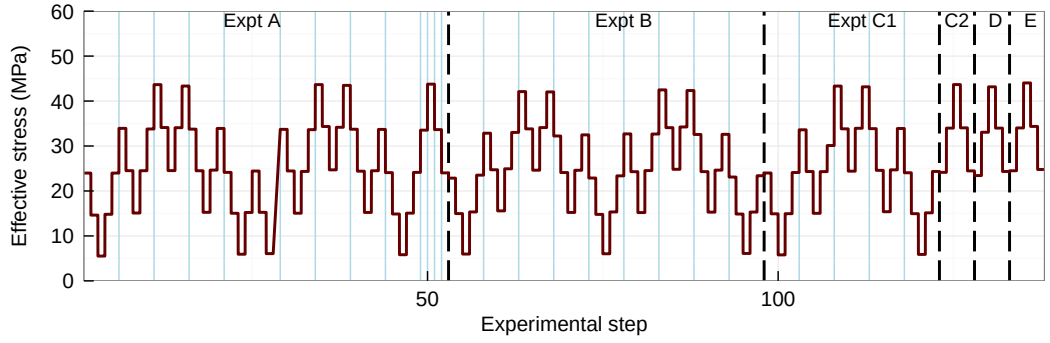

FIGURE 6.10: Effective stress scenarios during flow experiments (Wissey W3)

The permeability range of the naturally fractured Wissey sample was found to be notably lower than that of the Cambrian shale and offset East Brae (B2b) samples. However, the permeability was significantly higher than that observed for the artificially fractured East Brae shale samples with no fracture surface offset applied. The

permeability range of the Wissey fractured sample was well suited to the experimental rig set-up, allowing the differential pressure transducer to be used throughout the experiments to record accurate differential pressure data.

6.3 Experiment start-up and shut-down procedures

Prior to commencing flow experiments a number of procedures and checks need to be carried out to prepare for the CO_2 flow experiments. Similarly, on completion of the CO_2 experiments the rig must be shut down in an appropriate manner prior to removal of the samples. This section details methods developed for loading and unloading the core holder, preparing the rig system prior to CO_2 flow experiments on each sample, and shutting down the rig system subsequent to completion of sample experiments.

6.3.1 Loading and unloading the core holder

During the flow experiments, the fractured sample is held within a Hassler-type core holder in a benchtop oven (see Chapter 5 for details). The core holder is connected to the rig pipework via standard swagelok fittings. There are three connections to the core holder: the upstream CO_2 fluid connection, the downstream CO_2 fluid connection, and the confining oil fluid entry port.

To load a sample into the core holder the following steps are followed:

1. The core holder is disconnected from the rig pipework at the three locations.
2. End caps are connected to the disconnected confining oil pipe ends, to minimise oil leakage.
3. The core holder is then carefully removed from its mount within the oven and placed on its side on a clear lab bench. [*Caution: The core holder is very heavy - care must be taken when lifting and moving this item*]
4. The top (downstream) end platen is unscrewed and removed from the core holder.
5. The bottom (upstream) end platen is removed from the core holder by releasing the clover-leaf locking mechanism. [*Note. This can become stiff and/or jammed*

following prolonged high temperature/high pressure experiments (see Chapter 5 for details), and may require workshop intervention.]

6. Check the inside of the core holder is clean and the sleeve is undamaged.

7. Place the prepared and coated sample within its lead liner sleeve, and insert as one into the core holder from the bottom end. Note there is very little tolerance in the sample diameter, so the coatings and liner must be carefully and smoothly prepared.

8. Position the sample and liner carefully into the correct position within the core holder, using the end platens to guide the location. Ensure that both the liner and sample are positioned correctly and that there is a small lead overlap with the platen on either end of the sample. The liner may have to be moved separate to the sample to ensure this - a rubber grip on the end of a long metal rod was found to be appropriate for moving the liner within the coreholder.

9. Once the sample and liner are positioned correctly, close the bottom (upstream) end platen followed by the top (downstream) end platen.

10. Lift the core holder back into its mount within the oven and reconnect the two CO_2 fluid connections and the confining oil entry port to the rig pipework.

If the core holder already has a sample in it, this must be removed between steps 5 and 6. Removal of a core sample can be tricky due to potential cohesion of the core holder sleeve to the sample that may result from application of high external stresses during the experiments. To release the sample from the sleeve, use a syringe attached to the confining oil exit port to suction out any remaining confining oil and pull the sleeve away from the sample allowing it to be gently pushed out using the top (downstream) end platen.

Following removal of a sample post-experiment, the sleeve is checked for any damage and the sleeve and end platens are thoroughly cleaned using acetone.

6.3.2 Initial rig preparation and checks

Once the fractured sample is loaded into the core holder, a number of rig start-up steps are undertaken to enable the commencement of flow experiments. These include checks

on the measuring instruments; a purge followed by pressurisation of the confining oil system; configuring the syringe pumps; switching on temperature control and logging systems; and pressurising the CO_2 fluid system. The steps are detailed below. Refer to Figure 5.2 (Chapter 5) for details of the rig set-up.

1. **Check pressure transducers.** While the rig pipework is open to atmospheric pressure, check that the three pressure transducer readings are valid.

2. **Commence omega logging.** Commence logging at 5 s frequency. Omega logging records data from all pressure transducers (including differential pressure) and sample temperature.

3. **Purge and pressurise confining oil system.** Open both confining fluid needle valves (NV_C1 and NV_C2) and use the hydraulic hand pump to flush confining oil through the confining fluid system to bleed it, collecting the flushed out oil in a beaker downstream of NV_C2. Once the oil is running smoothly through the system with no air bubbles present, shut off valve NV_C2 and continue to use the hand pump to pressurise the confining fluid. Once the confining fluid is at the desired pressure, close NV_C1 to lock the pressurised oil in, and release the pressure in the hand pump. After an hour or so, bleed any remaining air from the system through valve NV_C2 and top up the confining pressure as required. [*N.B. The confining pressure increases significantly as the temperature increases, so make sure confining pressure at lab temperature is approximately half the pressure desired at the initial experimental temperature (∼ 40 °C).*]

4. **Set sample temperature.** Switch on the oven and leave overnight for confining pressure to settle. In the morning, make minor adjustments to confining pressure as necessary [*N.B. Fine control is not possible, so within ±100 psi (0.69 MPa) is adequate.*]

5. **Initiate pump cooling.** Switch on the low temperature fluid bath circulator. This will take several hours to cool the syringe pumps to the desired temperature (∼ 2.5°C).

6. **Commence upstream pump temperature logging.** 10 s frequency.

7. **Initiate CO_2 fluid heating.** Switch on the heat exchanger and the fluid pipework heating tape to the experimental temperature required (should be the

same as the oven, 40°C or 60°C). This requires ∼ an hour to reach temperature after turning on.

8. **Prepare CO_2 pipework for pressurisation.** Ensure that needle valves NV_F1 and NV_F6 are closed, and all other needle valves on the CO_2 fluid pipework system are open. (Keep confining oil valves NV_C1 and NV_C2 closed.)

9. **Set up pumps and pump logging.**

   a. Switch on syringe pumps and pump controllers and commence pump logging, ensuring that the logging commencement times are recorded to 1 s precision using the lab computer. This is required to merge pump logging and omega logging post-experiment (section 6.5).

   b. Switch on the freeze protection heating tape downstream of the pressure control (downstream) syringe pumps before running the pumps and check that the CO_2 outflow is safely contained within the fume cupboard.

   c. Refill both upstream and downstream syringe pumps from the liquid withdrawal CO_2 cylinder as required - both upstream syringes should be full, and downstream syringes should be ∼ 50-70% full to allow for pressurisation of the fluid.

10. **Pressurise CO_2 fluid system.**

    a. Set the upstream pumps to start flowing CO_2 using "continuous constant flow" mode, at a flow rate of 1 ml/min until fluid pressure builds up to around 1000 psi (6.89 MPa).

    b. Open the upstream rig valve, NV_F1, slowly, to allow the fluid pressure in the whole rig system to build up. Note that the pump pressure will initially drop significantly as the increased pipework volume of the rig is connected.

    c. Set downstream pumps to "continuous constant pressure (RECEIVE)" mode, and start running to maintain a pressure of 1450 psi (10 MPa).

    d. Once fluid pressure in the rig is approximately 1450 psi (10 MPa), open the downstream rig valve, NV_F6. Now the fluid system is open between the upstream and downstream pumps, so the downstream pumps should be receiving CO_2 at the same steady state flow rate that the upstream pumps are running at in order to maintain a pressure of 1450 psi in the rig system.

11. **Zero differential pressure transducer.** Reduce the flow rate to a very small value i.e. 0.1 ml/min, to minimise disturbance around the differential pressure transducer. With valve NV_F3 open, adjust the ZERO setting on the differential pressure transducer carrier demodulator, to account for the voltage drift as a result of the line pressure increase. There should be no differential pressure across the diaphragm as the two sides are connected via the differential pressure bypass loop.

12. **Start flow through the sample.** Close valve NV_F3. This will force flow through the sample as the bypass loop is now closed, so a differential pressure across the sample will be induced. Increase the flow rate to 1 ml/min to commence the flow experiments.

The steps above ensure that the rig system is correctly set-up prior to undertaking the flow experiments. As the temperature and associated confining pressure response takes several hours to stabilise, the rig preparation must commence at least one day prior to starting the flow experiments.

6.3.3 Rig shut-down

Subsequent to completion of the experiments, the rig system must be shut down correctly to avoid damage to instruments and equipment. The steps required are detailed within this section. While the order of steps is reasonably flexible, it is very important to ensure that the CO_2 pressure is released slowly to minimise rapid gas decompression, which could damage equipment such as the sleeve liner and pressure transducers. In addition, it is important that the CO_2 pressure is released prior to releasing the confining pressure, to ensure the core holder sleeve liner remains sealed against the sample.

The steps required for shutting down the rig system are as follows:

1. Stop both CO_2 pumps (upstream and downstream), switch off the pump cooling system and close the CO_2 cylinder.

2. Open the differential pressure bypass loop (valve NV_F3) to equalise the pressure upstream and downstream of the sample.

3. Switch off the heating system (oven, heating tapes,heat exchanger). Slow reduction of temperature reduces the fluid pressures (CO_2 and confining oil), so it is recommended to wait until temperature reduction has occurred before forcing further depressurisation (i.e. overnight).

4. Very slowly vent CO_2 from the rig pipework at the upstream end (a manual pressure release valve is located adjacent to valve NV_F1) to avoid damage to equipment.

5. Depressurise the confining fluid system by releasing oil from confining fluid bleed port (valve NV_C2).

6. Stop all logging systems (omega, pump, pump temperature) and ensure all log files are saved and backed up.

6.4 Experimental methods and operational procedure

During the sample CO_2 flow experiments a number of operational procedures and monitoring must be undertaken for the experiments to be successful. This section describes the methods developed for undertaking these processes.

A large number of scenarios are assessed within each set of sample experiments (see section 6.2), thus requiring multiple changes to each of the following parameters: pump flow rate, downstream fluid pressure, confining pressure and temperature. Due to the uniqueness of each sample, the response times to parameter changes can vary considerably across experiments, and continual monitoring of parameters is required to ensure that the frequency of changes is appropriate during the experiments. Changes to confining pressure and temperature in particular require long stabilisation periods, while fluid pressure changes must be made steadily and smoothly to prevent damage to measuring instruments and equipment. The methods developed and adopted for varying parameter values are detailed within the following subsections.

In addition to parameter changes, continual monitoring of the system is required to respond to any unexpected changes, such as the occurrence of the upstream pump problems detailed in Chapter 5, section 5.5.1. Detailed lab notes and manual data logging was undertaken to assist with monitoring and post experiment analysis. This

proved essential for identification of log timing discrepancies during the Wissey experiments (section 6.5.2.2). Both continual monitoring and parameter changes make undertaking the experiments a very intensive process. Experiments are undertaken over multiple days. The overnight and weekend procedure adopted was to leave all equipment running to ensure stable conditions. The CO_2 flow rate was reduced to a minimal value (around 0.1 ml/min) and the differential pressure bypass valve was opened to equalise the CO_2 pressures across the sample, thus ensuring that although experimental pressures and temperatures were maintained, CO_2 flow through the sample did not occur.

While the pump logging system saves data to file in real time during the experiments, and can be left running for the duration of each set of sample experiments, both the omega logging system and pump temperature logging systems require to be stopped, data to be downloaded, and the loggers to be restarted on a regular basis. Details of this operational process are contained within Chapter 5, section 5.3.4.

6.4.1 Changing flow rate

Changing the flow rate of fluid within the system is straightforward and is carried out via the upstream pump controller. The response of the differential pressure across the sample to changing the flow rate is dependent on the permeability of the fractured sample and the pressure and flow rate conditions applied, but was observed to vary from <1 minute within the Cambrian shale and offset East Brae sample (B2b) experiments, to approximately half an hour for the very low permeability East Brae D2 sample. This is illustrated in Figure 6.11. For the more permeable samples (Cambrian shale, East Brae B2b and Wissey), stabilisation periods of around a minute were common, with periods of a few minutes generally adequate to determine the steady state differential pressure conditions associated with each flow rate tested. Thus, for all but the very low permeability East Brae samples (B2 and D2), the flow rate change frequency was in the order of a few minutes.

6.4.2 Changing fluid pressure

Following completion of all flow rate tests within each fluid pressure experimental step, the downstream fluid pressure within the system must be changed. The differential

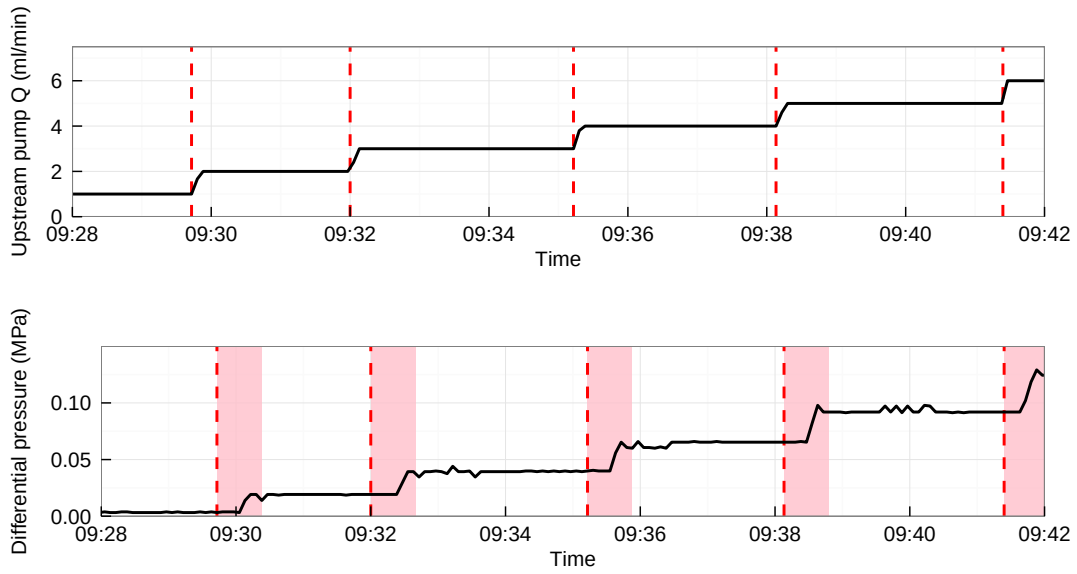

(A) Cambrian V1 (<40 s ΔP response)

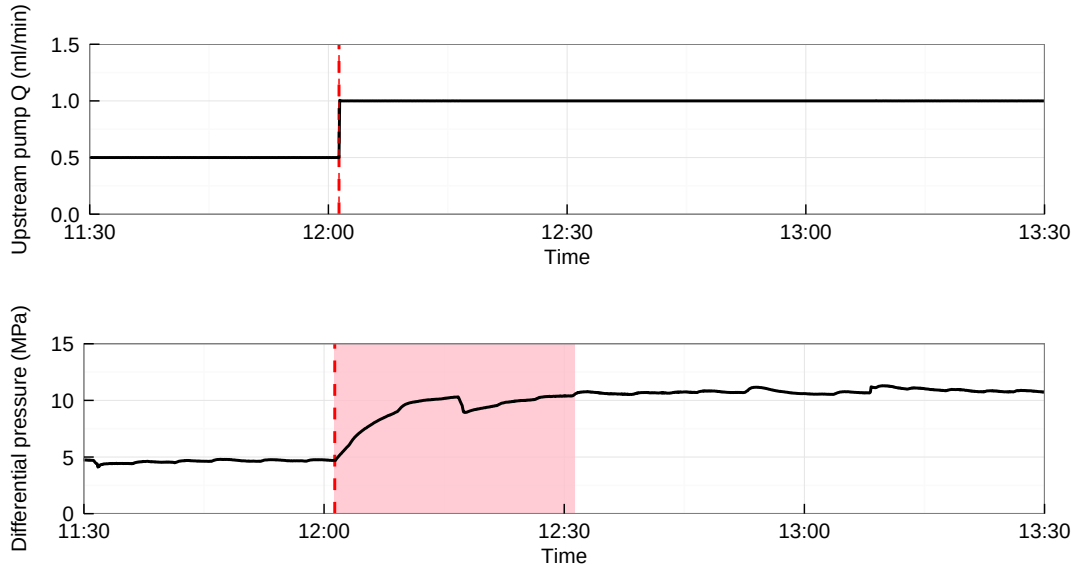

(B) East Brae D2 (∼ 30 min ΔP response)

FIGURE 6.11: Contrast in differential pressure response rate to flow rate change between samples

pressure transducer output voltage can be affected by significant changes to the line pressure, therefore each time the downstream fluid pressure is changed the differential pressure transducer carrier demodulator is also re-zeroed. This is undertaken with a very low flow rate (0.1 ml/min) and the differential pressure loop bypass valve (NV_F3) open to ensure that there is no differential pressure across the transducer. This section describes the method developed for changing the downstream fluid pressure within the rig system, and the associated differential pressure transducer checks and adjustments undertaken during the CO_2 flow experiments.

The procedure for **increasing** the fluid pressure is provided in the following steps:

1. Initially set flow rate to 0.1 ml/min and open the differential pressure loop bypass valve (NV_F3) to check the differential pressure output voltage is negligible at the current line pressure and to protect the differential pressure transducer during fluid pressurisation.
2. Close the downstream rig valve (NV_F6) and set the flow rate to 1-1.5 ml/min to allow the system fluid pressure to gradually increase as CO_2 flows in from the upstream pumps.
3. Set the downstream pumps to the desired fluid pressure. As valve NV_F6 is closed, this will pressurise the pipework downstream of this valve to the desired pressure while disconnected from the rig.
4. When the rig pipework upstream of NV_F6 reaches the desired fluid pressure, slowly reopen valve NV_F6. The downstream pumps will respond by receiving CO_2 at the appropriate flow rate to maintain a stable downstream pressure.
5. Set flow rate to low value (i.e. 0.1 ml/min) and rezero the differential pressure transducer output voltage to account for the increased line pressure.
6. Close the differential pressure loop bypass valve (NV_F3) and reset the flow rate to 1 ml/min to recommence flow experiments at the new downstream fluid pressure.

The procedure to **reduce** the fluid pressure within the system is slightly different:

1. Set flow rate to 0.1 ml/min and open the differential pressure loop bypass valve (NV_F3) to check the differential pressure output voltage is negligible at the

current line pressure and to protect the differential pressure transducer during fluid depressurisation.

2. Close the downstream rig valve (NV_F6) to isolate the rig system from the downstream pressure control pumps.

3. Set the downstream pumps to the desired fluid pressure (i.e. 10 MPa). As valve NV_F6 is closed, this will lower the pressure in the pipework downstream of the valve to the desired pressure.

4. Open the system bleed valve (adjacent to NV_F1) a tiny amount to allow the fluid within the rig system to very slowly depressurise, so as not to damage any of the instruments. N.B. The valve will become very cold due to adiabatic expansion as CO_2 is released.

5. When the rig pipework upstream of NV_F6 gets close to the desired fluid pressure, shut off the system bleed valve, and slowly reopen valve NV_F6. The downstream pumps should ensure the fluid pressure settles to the correct value and is maintained.

6. Re-zero the differential pressure transducer output voltage to account for the reduced line pressure.

7. Close the differential pressure loop bypass valve (NV_F3) and reset the flow rate to 1 ml/min to recommence flow experiments.

Changing the fluid pressure can take up to 20 minutes per 10 MPa change. It is important that this parameter change isn't rushed, as instrument damage can occur as a result of rapid pressurisation/depressurisation.

6.4.3 Changing confining pressure

Confining pressure increase is undertaken using a hydraulic hand pump, with use of a needle valve for control. Confining pressure decrease is undertaken by releasing confining oil pressure using the core holder bleed valve (NV_C2). It is best practise to allow confining pressure to settle for several hours after intervention, preferably overnight, as it has been observed to take long periods of time to settle (Figure 6.12).

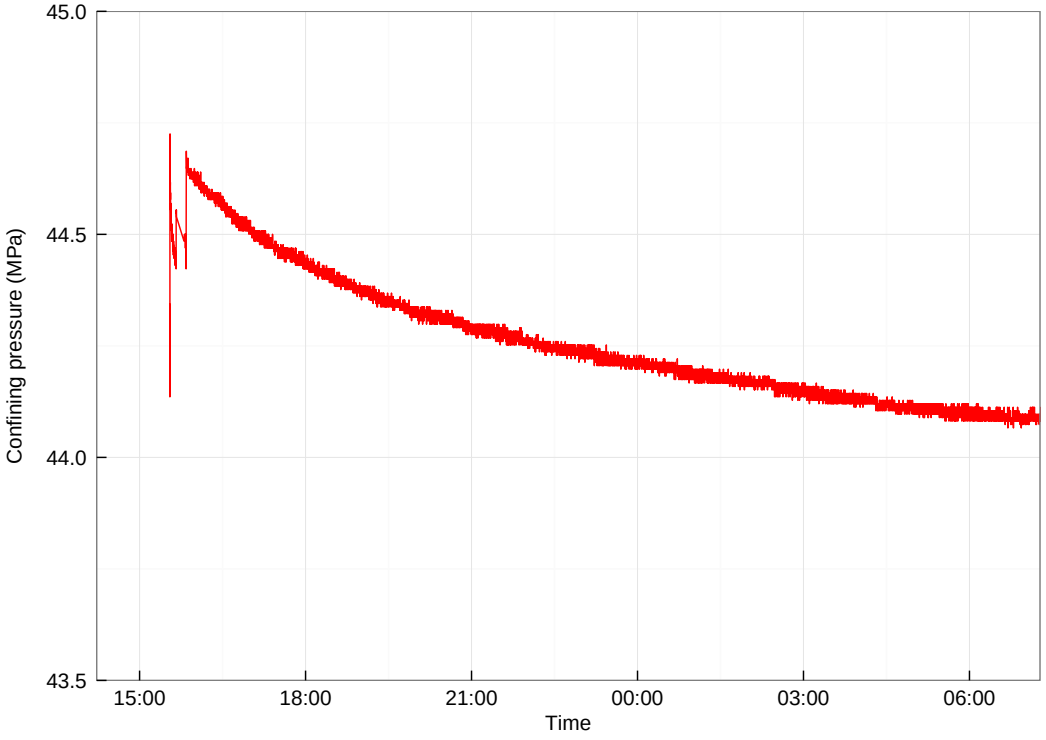

FIGURE 6.12: Confining pressure settling overnight

Increasing confining pressure is best done with an assistant, and is carried out as follows:

1. Engage the hand pump and pump until pressure is greater than current rig system fluid pressure while disconnected from the rig.
2. Continue pumping while valve NV_C1 is opened (easier with 2 people).
3. Pump until confining pressure is approximately the confining pressure required.
4. Close valve NV_C1.
5. Leave several hours to settle - the pressure usually drops slightly, so it may be better to set at a pressure slightly higher than desired.

To **decrease** the confining pressure, simply open the oven door and bleed some confining oil carefully by slowly opening needle valve NV_C2 a tiny amount. Be careful

not to bleed too much oil out of the system. Note that opening the door creates a temporary temperature decrease and the oven can respond to this by ramping up the heating power, resulting in over temperature of the oven. If this occurs it then takes a while for the temperature, and consequently the confining pressure, to stabilise. The confining pressure is very sensitive to temperature change.

It should be noted that, in addition to manual changes to the confining pressure, the confining pressure does vary slightly in response to changes in fluid pressure. As fluid pressure is increased, confining pressure is observed to increase slightly - it is believed that this results from the fracture aperture increase associated with the fluid pressure increase. This increases the bulk volume of the sample, thus reducing the volume of the confining oil reservoir, resulting in a confining pressure increase. The magnitude of change is relatively small (within ±1 MPa) and should therefore not significantly affect experimental findings.

6.4.4 Changing temperature

To change the experimental temperature the core holder oven temperature must be adjusted. In addition, the upstream fluid heat exchanger and electrical heating tapes used to heat and maintain fluid temperature must also be adjusted to the same temperature. The temperature response has been observed to take up to 6 hours to reach stabilisation at the new temperature, therefore temperature changes were all undertaken overnight. As discussed in section 6.4.3, confining pressure is sensitive to temperature change, therefore confining pressure adjustments are always required in conjunction with a temperature change.

6.5 Data post-processing

Following completion of the flow experiments, the data logged requires post-processing to allow analysis to be undertaken. This includes conversion of data to meaningful units using calibration data and conversion factors, merging and interpolation of data recorded by the various data loggers (Omega; ISCO pump loggers x 2; USB temperature loggers); and appropriate sampling, averaging and classification of data for parameter calculation, presentation and analysis.

R software, an open source statistical computing and graphics programming language, has been used to undertake the data processing, analysis and presentation. This software has been used as it enables the adoption of effective and repeatable methods for processing and sampling the large experimental log datasets collected for each sample. The functionality to graphically analyse the datasets within the same software package is useful during result analysis, and for data presentation.

Experimental data have been grouped together by sample for processing. This section details the procedure that has been developed and executed for each experimental sample.

6.5.1 Data collation, conversion, and merging

The first stage of data processing required post-experiment is collation and merging of the various logged data files into one combined logged dataset for analysis. This is carried out once per sample, and thus includes collation of data covering the time period from commencement of the first experiment on the sample to the end of the last experiment on the sample.

Data files are collated from each of the three laboratory logging systems:

- the Omega data logger (all pressure and differential pressure data and core holder thermocouple data);
- the ISCO pump loggers (all pump data including pressure and flow); and
- the USB temperature loggers (pump temperature data).

The first data collation stage involves production of a single dataset associated with each data logger. As two pump loggers and two USB temperature loggers are used during experiments, five datasets are produced from this stage of processing. During this data processing stage, each logged data field is also converted to units appropriate for further analysis. Conversion is carried out where required using calibration data or conversion factors as appropriate.

Following production of converted datasets for each of the logging systems, relevant data from the two pump log and two pump temperature log datasets are merged into

the Omega log dataset to produce a single consistent logged dataset for analysis (section 6.5.1.4). This is carried out using linear interpolation between data points to estimate pump and temperature data for the omega data timestamps. The error introduced to the pump datasets through this method of data syncing is expected to be small due to the high frequency (5 s) of both the Omega and pump data logging systems, which means that data interpolation is carried out within a 5 second window for the pump log data. The pump temperature log data are collected at a lower 10 s frequency, however the pumps are maintained at a stable temperature throughout the experiments using temperature control jackets and a low temperature fluid circulation system (Chapter 5), so errors associated with linear interpolation of these pump temperature datasets are expected to be negligible.

The subsections below detail the data collation and unit conversions carried out for each data logging system during the first data processing stage. The R programs used for data collation, conversion and merging of the East Brae B2b datasets, are provided in Appendix C, as an example. The same processing steps were adopted for data from all sample experiments.

6.5.1.1 Omega logger

The Omega logger records data for the following five instruments: confining pressure transducer; upstream fluid pressure transducer; downstream fluid pressure transducer; differential pressure transducer and core holder thermocouple. As described in Chapter 5, section 5.3.4, to ensure robust and reliable data logging, the Omega data logger is stopped, downloaded and restarted at the start and end of each day while experiments are ongoing. This ensures that data are regularly saved and backed up, but results in the creation of a significant number of omega log data files for each sample. Data are logged at a 5 s frequency during the day, and a 15 s frequency overnight. Times are recorded to ± 1 s precision.

The first data processing step is to load all Omega data files and collate into a single dataset. The data are then sorted into chronological order and checked for duplicates (in case the same data file is stored multiple times within the source folder). The collated dataset is then saved as a csv file for further processing. The R program associated with this data processing step is called 'omegacollate.R' and is included in Appendix C.

The next step is to convert the data within the omega log data table to correct units. Data associated with the three pressure transducers and the core holder thermocouple are converted to psi pressure units and degrees Celsius respectively using linear models derived during the calibration process (Chapter 5, section 5.5). The differential pressure transducer data are converted to psi pressure units using the second order polynomial model derived during calibration (Appendix B). In addition to the converted data, upper and lower 95% prediction intervals are calculated for each data point, based on the accuracy of the calibration model fit. The pressure data are also converted into MPa for calculation and display purposes. The converted datasets are saved to a csv file for subsequent analysis. The R program associated with this data conversion step is called 'omegaconvert.R' and is included in Appendix C.

6.5.1.2 ISCO Pump loggers

Pump data are logged separately for the upstream and downstream pump controllers. The data files stored by the logging software for each pump controller include data for the combined pump system as well as data relating to the individual pumps (A and B), as detailed in Table 6.5. In addition, status flags are used to record the operational status or problem status of the individual pumps during the logging period, which can assist with troubleshooting issues if required [Teledyne Isco, 2012*a*]. Data are recorded at 5 s frequency during the experiments and are saved in real time into a csv file. This real time recording means that the pump logging does not need to be restarted frequently in the same way as the Omega logging data.

TABLE 6.5: ISCO logging: data fields recorded for each controller

	Parameter	Units	Resolution
Pump system	Flow rate	litres/min $\times 10^{10}$	0.1 nanolitre/min
	Pressure	psi $\times$ 5	0.2 psi
	Volume Total	litres $\times 10^{6}$	1 microlitre
Individual pumps (A and B)	Flow rate	litres/min $\times 10^{10}$	0.1 nanolitre/min
	Pressure	psi $\times$ 5	0.2 psi
	Volume	litres $\times 10^{9}$	1 nanolitre

As discussed in Chapter 5, section 5.3.4, the pump data logs record data according to time in milliseconds since start of recording, therefore the logging start time must be recorded precisely ($\pm$1 second) using the lab computer timestamp, and saved manually

in a separate datafile to enable syncing of the pump data to the Omega log data during data processing.

A single R program file has been written to process the logged pump datasets prior to merging with the Omega data. The procedure for merging, sorting and converting units of data fields for the pump log data files is similar to that used for the Omega log files, although conversion factors rather than calibration models make unit conversion simpler. As the pump loggers do not need to be restarted with the same frequency that the Omega logger does, there are also fewer files to merge than for the Omega data, and in some cases there may be just a single file. The main additional step is referencing of a timestamp table to assign the correct date/time stamp data to the logged dataset and associated conversion of the time field from milliseconds since logging start time to a date/time value. The R program, 'iscoload.R' (Appendix C) is used for separate processing of both the upstream and downstream pump controllers. The processed log dataset contains pressure data in psi, flow rate data in ml/min and volume data in ml.

During continuous constant flow and continuous constant pressure modes, the pump system data (Table 6.5) provide information about the resultant fluid delivered to or received from the experimental rig without concern over which pump is delivering or receiving the fluid. These data are generally used for result analysis unless specific information relating to individual pumps is required.

6.5.1.3 Pump temperature loggers

The data file output from the USB thermocouple temperature data loggers is a simple csv file that includes a date/time column (to ±1 s) and a temperature (°C) column. Thus, processing of the log files is relatively straightforward. The data files are loaded into the R program, and the date format is confirmed. Any NA/missing values are omitted, and then all the log data files are merged into one continuous temperature record. This process is carried out separately for each of the USB temperature data loggers, associated with Pump 1A and Pump 1B respectively. The two resulting continuous temperature data files are both sorted chronologically and any duplicate records are removed. The files are saved as csv files for future use. The R program associated with processing of this pump temperature data, 'USBtempload.R', is contained within Appendix C.

6.5.1.4 Merging and organisation of logged data sets

Once the log data files from each of the five logging devices have been processed as described above, relevant pump log and pump temperature log data fields are merged into the Omega log data file, using linear interpolation to estimate data values at the Omega log timestamps. As discussed earlier in this section, the error that arises from this data merging method is considered to be small, and negligible relative to errors arising from the measurement, logging and sampling processes. The merging process is carried out within the first part of the R program, 'logmerge_eventextraction.R', which is included within Appendix C.

The data fields merged into the Omega log dataset are:

- Upstream pump system flow rate (ml/min);
- Upstream pump system temperature (°C);
- Downstream pump system pressure (psi).

The upstream pump temperature was measured separately at Pump 1A and Pump 1B during experiments, using two separate USB temperature loggers. However, analysis of the recorded data indicate that there is negligible difference in temperature between the two pumps, due to the effective temperature control system in place. Thus, the pump temperature used within the merged log dataset (after satisfactory quality checking of the two datasets) is the mean of the two pump temperature readings.

For both the East Brae B2 and the Wissey W3 sample experiments, errors were observed within the Pump 1A temperature logger data on occasions during the experimental period. As the temperature difference is observed to be negligible between Pump 1A and 1B at all other times, the Pump 1B temperature data alone were used to represent the pump temperature during these two sets of experiments.

6.5.2 Extraction of representative parameter results from the logged data series

Once all the relevant logger data have been merged into a single dataset, categorisation and data extraction procedures are carried out to assist with subsequent data analysis.

The merged logging dataset is a time series containing data from a large number of experimental scenarios, with temperature, confining pressure, fluid pressure and flow rate all varied at different frequencies.

Flow rate is the parameter changed at the highest frequency, with multiple flow rates tested for each temperature, confining pressure and fluid pressure combination. Thus, the logging dataset can be subdivided up into 'events', where each 'event' is associated with a particular flow rate test. By extracting single, representative, steady-state values for each of the logged parameters for each event, a manageable and representative database of results can be extracted from the large logging dataset time series. This section describes how such data have been identified and extracted for each of the sample datasets. Table 6.6 specifies the size of the log dataset for each of the sample experiments, as well as the number of events extracted using the methods described within this section.

TABLE 6.6: Event data extraction

Sample	Log dataset size (timesteps)	Number of events
Cambrian V1	213198	791
East Brae B2	42802	3
East Brae D2	106946	93
East Brae B2b	125229	665
Wissey W3	337673	1182

Section 6.5.2.1 outlines the general methodology adopted for extraction of the event data, used for the East Brae (sample D2 and B2b) and Cambrian shale (sample V1) datasets. Unfortunately, pump log timing discrepancies were identified within the Wissey logging dataset during this stage of post-processing. The pump log timing errors were inconsistent and non-systematic, and created timing discrepancies between the pump flow data and the resultant pressure response. This created a more complex challenge for extraction of representative event parameters within this dataset, as correction of these timing discrepancies was also required as part of the process. The methodology adopted for processing of the Wissey log dataset is therefore discussed separately in section 6.5.2.2. Due to the extremely low permeability, and therefore limited data available for the East Brae B2 sample, the three event data points associated with this dataset have been processed manually rather than using the automated procedures described in this section.

6.5.2.1 General method

An automated approach was required for event data extraction due to the large number of flow rate events tested within each set of sample experiments. The main steps involved with extraction of representative event data from the logged data time series are outlined in Table 6.7. The method has been written and executed within an R program. The event extraction code for East Brae B2b can be found within the second part of the R program, 'logmerge_eventextraction.R', which is included within Appendix C. The same method has been used for extraction of event data for East Brae D2 and Cambrian V1 as well as East Brae B2b.

Identification of the experimental flow rate events is the first procedure. Changes to upstream pump flow rate are used to identify the event boundaries (Step 1). While differential pressure response to flow rate change is relatively rapid, a brief time period is required following flow rate change to allow the differential pressure across the sample to approach steady state. This 'settling' period varies from sample to sample, and with experimental pressure conditions. During calculation of representative means of logged parameters for each of the events, this settling period should be excluded so that the parameter values are representative of steady state pressure conditions. For this reason, short events are completely excluded from further analysis where insufficient time has been allowed to achieve steady state pressure conditions (Step 2). Mean logged parameter values are then calculated for all remaining events (Step 4), using data within the event duration period (defined in Step 3), which aims to exclude the initial pressure settling period following flow rate change. Finally the transition events, where one or more of the controlled parameters is being varied between experimental steps, are removed from the event means dataset (Step 5).

The minimum event duration, as well as other thresholds used for defining the event start time, vary from sample to sample as a result of the variation in pressure response observed. The thresholds used for each sample were defined using an iterative trial and error procedure, and are provided in Table 6.8. The resulting event durations are reviewed using time series plots to assess suitability. Figure 6.13 is an example of one such time series plot, which is extracted from the East Brae B2b flow experiments dataset, from Experiment A, Stage 3 with 10 MPa fluid pressure.

TABLE 6.7: General method for automated extraction of representative event data from log datasets

STEP 1: Identify pump Q change times	• Calculate difference between consecutive upstream pump Q values within the log dataset time series • Identify timesteps where the difference magnitude is >0.1 ml/min AND take only the first occurrence of adjacent timesteps identified
STEP 2: Remove short events	• To ensure flow rate event length is sufficient for provision of representative data, discard event data where the event duration (defined within this step as the period between pump Q changes) is less than or equal to the threshold, **D**.
STEP 3: Define event duration	• For each event, initially define the event start time to be **x** timesteps after the flow rate change time identified in step 1. • While the event duration is >12 timesteps (∼60 s) long and EITHER: 1. the rate of change of the 5 step moving average differential fluid pressure parameter at the event start time is above a threshold, $\mathbf{C}_1$, OR 2. the mean rate of change of the 5 step moving average differential fluid pressure parameter for the duration of the event is greater than $\mathbf{C}_2$, continue to delay the event start time on a timestep-by-timestep basis. The 5 step moving average parameter has been used as an alternative to the raw differential pressure data to minimise the effects of noise within the dataset. • Set the event end time to be a single timestep prior to the subsequent flow rate change time.
STEP 4: Calculate event means	• For each of the parameters within the log dataset, calculate a mean value for each event using the data contained within the event duration.
STEP 4: Remove non-stationary events	• Identify and remove pressure transition events i.e. where fluid or confining pressure is being changed. These are identified by pressure standard deviations in excess of defined thresholds: 100 psi (0.69 MPa) for fluid pressure and 500 psi (3.45 MPa) for confining pressure. • Also remove events where pump flow rate is either <0.6 ml/min or >10.5 ml/min (this removes temperature transition and events and any other erroneous data).

TABLE 6.8: Threshold parameters (defined in Table 6.7)

Sample	**D** (s)	**x** (timesteps)	**C_1** (Pa/s)	**C_2** (Pa/s)
Cambrian V1	65	6	500	70
East Brae D2	480	96	2500	1500
East Brae B2b	65	6	1000	500

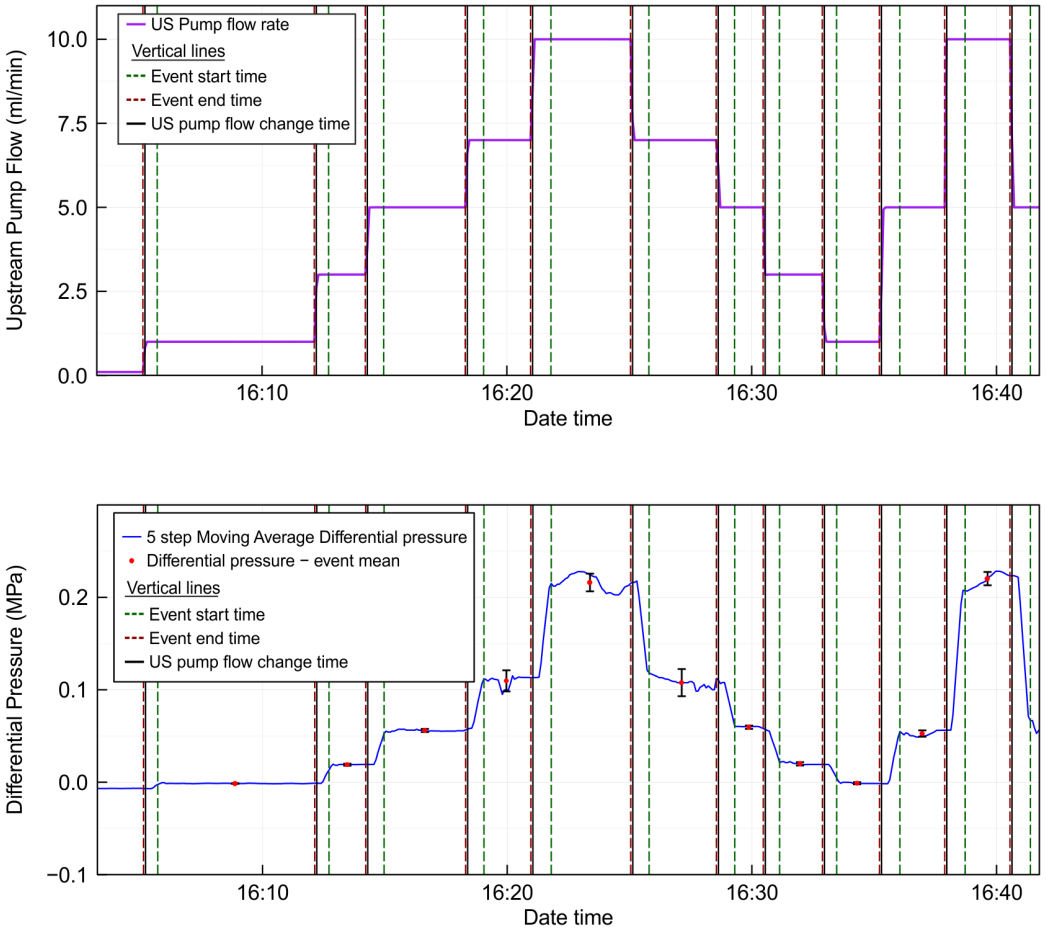

FIGURE 6.13: Example time series figure of upstream pump flow rate and differential pressure results from automated event data extraction for East Brae B2b sample (Expt A, Stage 3, 10 MPa fluid pressure)

Figure 6.13 illustrates the representative event data that have been derived using the method detailed (Table 6.7), and helps to justify the steps used within the event extraction method. The top plot of Figure 6.13 shows the upstream pump flow rate time series, while the bottom plot includes a line graph of the 5 step moving average differential pressure data. The differential pressure is the key result parameter during the flow experiments. Other pressure, temperature and flow rate parameters logged during experiments are controlled parameters. The stability of the differential pressure value during the events is therefore key for assessing the suitability of the event duration selected. In order to minimise the effects of noise within the differential pressure log dataset, a 5 step moving average differential pressure dataset has been utilised for identification of appropriate event start times, as specified within Step 3 of Table 6.7. This moving average dataset simply smooths out any high frequency oscillations (noise) within the dataset, as shown in Figure 6.14. Vertical lines in Figure 6.13 indicate the event start and end times derived within Step 3 of the event data extraction method, as well as the pump flow rate change times, identified within Step 1 of the method. The mean parameter values for each event duration are used as representative event data within result analysis. The mean differential pressure values are plotted as points within the lower plot of Figure 6.13, with associated error bars indicating the standard deviation associated with this mean value.

Within Figure 6.13, the start and end times for event durations determined using the event data extraction method (Table 6.7) appear suitable for determination of representative event mean data for the logged parameters. The figure indicates that the automated method used for determining event durations is appropriate, and adequately takes account of the differential pressure response to flow rate change during the experiments. Time series have been reviewed extensively for each of the sample experiments, with snapshots viewed across all confining pressure stages and fluid pressure steps. The standard deviation values associated with the differential pressure parameters are, in general, observed to be reasonably consistent. Higher standard deviation (or variance) is found within high flow rate events. However, the magnitude of standard deviation for most events is still smaller than the difference in mean differential pressure observed due to flow rate change, therefore indicating that the event means are meaningful and valid for use during result analysis. The standard deviation values are considered to be representative for use as error bars within this dataset.

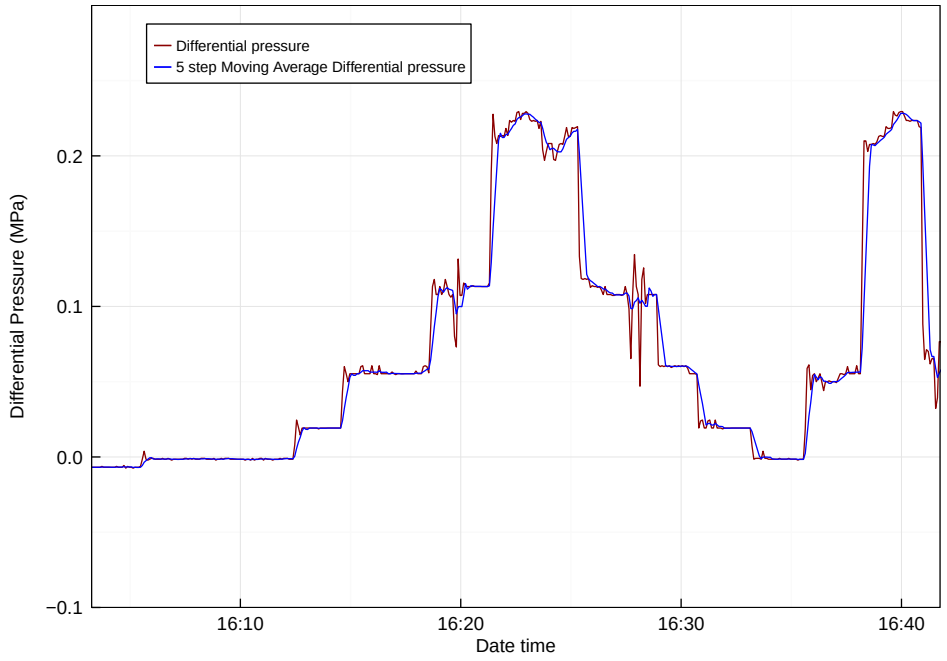

FIGURE 6.14: Illustration of difference between the raw differential fluid pressure log data and the 5 step moving average differential pressure dataset for East Brae B2b sample (Expt A, Stage 3, 10 MPa fluid pressure).

Figure 6.15 plots all of the differential pressure event data for the East Brae B2b, Experiment A, Stage 3 experimental steps against upstream pump flow rate. These data have all been extracted using the method described in Table 6.7, and standard deviation error bars are plotted for the differential pressure data. The data include the 10 MPa fluid pressure subset presented within Figure 6.13 (dataset (i) in Figure 6.15). As with Figure 6.13, Figure 6.15 indicates that, while there is some variability in the errors (standard deviation) associated with event data, the errors are generally much smaller than the difference in differential pressure results for differing flow rates. The standard deviation errors are largest for the low fluid pressure (10 MPa) results, and for the higher flow rates.

A database is created for the event data associated with each sample, which contains the event start and end times, as defined within step 3 (Table 6.7), as well as all the mean log parameters values, that are considered to be representative values for the events. The standard deviation associated with the differential pressure, fluid pressure

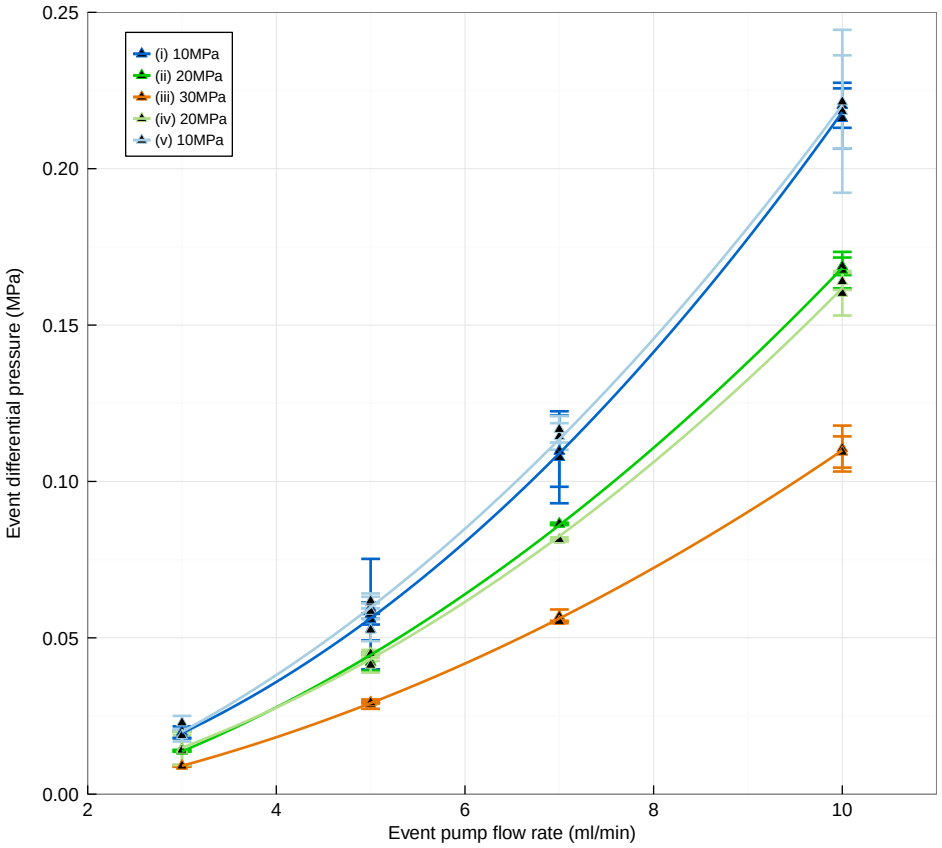

FIGURE 6.15: Event data plot of differential pressure against upstream pump flow rate for East Brae B2b sample (Expt A, Stage 3). Standard deviation error bars are included for the differential pressure data values. The legend sequence (i) to (v) indicates the experimental sequence.

and confining pressure values are also included. This event dataset is used for result analysis in Chapter 7.

The maximum standard deviations associated with the differential pressure event data for the East Brae B2b and Cambrian V1 samples are 6.6 psi (0.046 MPa) and 4.5 psi (0.031 MPa) respectively. Mean standard deviations for all events within the sample experiments are 0.5 psi (0.003 MPa) and 0.3 psi (0.002 MPa) respectively. Given that the differential pressure transducer instrument accuracy is ±4.8 psi (0.033 MPa), the standard deviations (representative of event averaging or sampling errors) are considered to be very reasonable for these experiments. The maximum and mean standard deviations associated with automatically extracted event data for East Brae D2 are higher, with values of 113.4 psi (0.782 MPa) and 24.4 psi (0.168 MPa) respectively.

This is due to the very low permeability of this sample, which resulted in much more significant time required to achieve steady state differential pressure conditions. The associated differential pressures were high, and outwith the range (0-800 psi/0-5.52 MPa) of the differential pressure transducer diaphragm in use. The differences between the upstream and downstream fluid pressure measurements were therefore used to calculate differential pressure data. This method has a much higher measurement error associated with it, which will also have contributed to the increased variance within the differential pressure dataset.

The method of automated event data extraction presented within this section has been adopted to extract representative event data from flow experiments on the following fractured samples: Cambrian V1, East Brae D2 and East Brae B2b. An automated approach is required due to the large number of event scenarios assessed for each sample. The method parameters have been manually tweaked for each sample (Table 6.8) to account for the differences in differential pressure response observed between samples. A review of event data suitability, presented within this section, indicates that the automated approach adopted for extraction of representative event data from the time series logs is valid and appropriate for result analysis purposes.

6.5.2.2 Wissey flow rate events

During the quality assurance checking of the merged log dataset associated with the Wissey flow experiments, a timing discrepancy between the pump and Omega log data series was identified. Further assessment of the Wissey log data, including checks against detailed lab book notes, identified that the timing error was associated with the upstream pump log data. The timing discrepancy was found to be an issue for the duration of the Wissey experiment. Spot checks undertaken between pump log data and manually recorded lab book data indicated that the error was not a consistent fixed magnitude error, or a systematic cumulative error, but that the timing discrepancy varied throughout the experiment duration, with both positive and negative timing errors identified. Figure 6.16 plots the pump log timing error associated with all 43 spot checks undertaken through the duration of the experiment. The figure shows a trend from negative timing errors during the first half of the sample experiments, to positive timing errors during the second half of the sample experiments. However, the significant scatter and variance within the dataset indicated that a systematic correction

was not possible. The maximum discrepancies identified within the spot checks were +53 seconds and -63 seconds. The mean magnitude of error calculated from the spot checks was 23 seconds. Figure 6.17 illustrates one example of a positive timing error in the pump log dataset (Event A), where the pump log data time is later than the observed time of flow rate change; and one example of a negative timing error (Event B), where the pump log dataset flow rate change time is earlier than the observed flow rate change time.

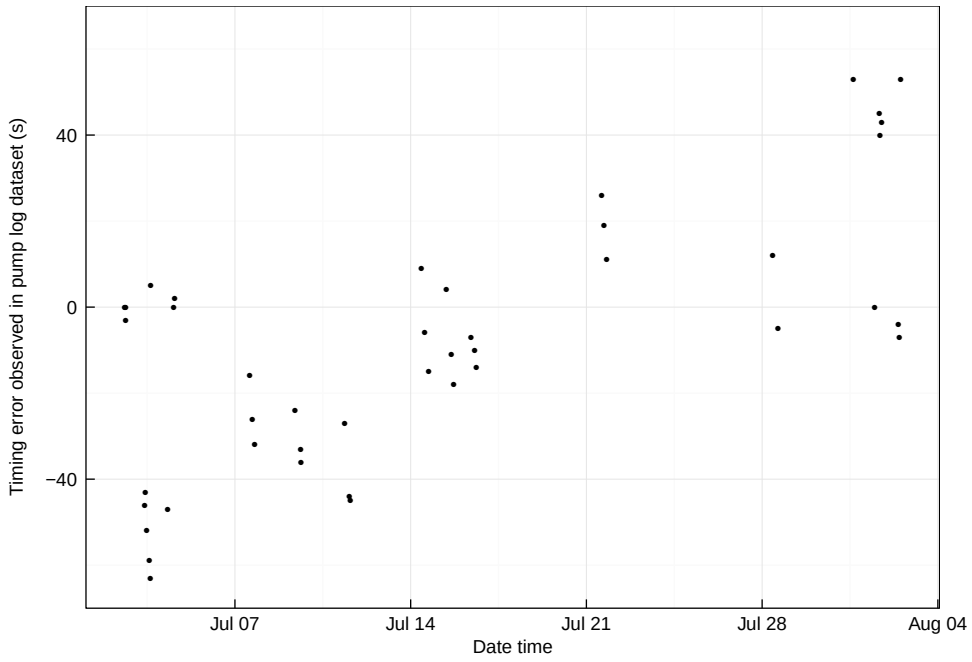

FIGURE 6.16: Pump log timing errors observed throughout duration of Wissey flow experiments

Errors were accounted for within the full logging time series using an automated approach on an event-by-event basis, due to the large number of events tested during the Wissey sample experiments (1182 events). Identification of the presence and magnitude of the pump log timing discrepancy was challenging given the non-systematic nature of the error, and had to be carried out by comparison and matching of the relative timing of pump flow rate changes (pump log data) and the associated differential pressure response (omega log data). The event data extraction process described in section 6.5.2.1, Table 6.7 was modified to incorporate corrections to event times for parameter averaging that would account for these pump timing discrepancies. The

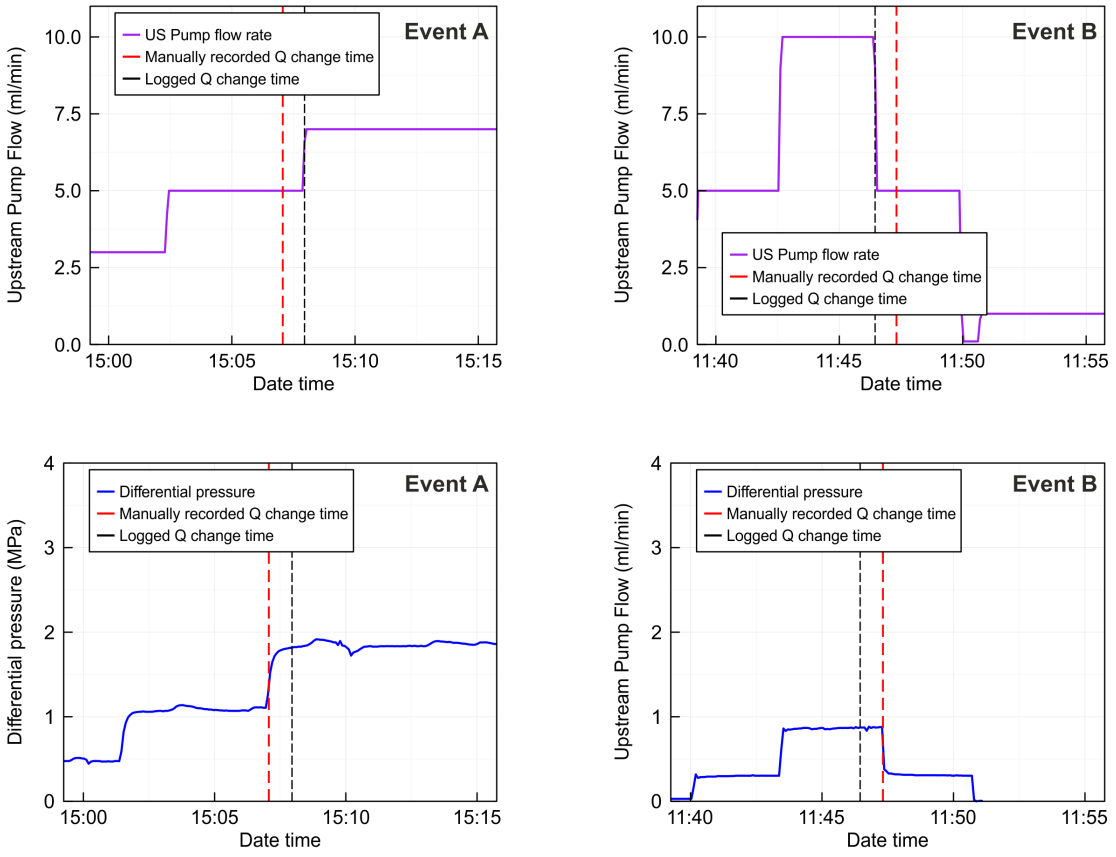

(A) Positive timing discrepancy - logged time is later than observed (and manually recorded) time (31 Jul 2014)

(B) Negative timing discrepancy - logged time is earlier than observed (and manually recorded) time (3 Jul 2014)

FIGURE 6.17: Example of both positive (Event A) and negative (Event B) timing discrepancies observed within the pump log dataset for the Wissey sample

method adopted was developed using an iterative approach, with regular assessment of the event durations and parameter averages against the log time series dataset used to tweak threshold parameters required within the automated method. Although not all events could be assessed in detail, a relatively comprehensive review of time series data across the full range of temperatures, confining pressure stages and fluid pressure steps was undertaken during the iterative review process in order to determine the most appropriate threshold parameters for defining the representative event times.

The steps involved in the extraction of representative event data for the Wissey sample experiments, using an automated approach which accounts for both differential

pressure response and pump log timing errors, are detailed in Table 6.9. Within this procedure, a 5 step moving average differential pressure value has been used rather than the raw logged differential pressure data to minimise the influence of noise. Figure 6.18 illustrates the difference between the raw data and the moving average data for an extract of the Wissey data. The raw data have however been used for the final calculation of event mean and standard deviation data. The code associated with the data extraction procedure can be found within the second part of the R program 'logmerge_wisseyeventextraction.R', which is included within Appendix C.

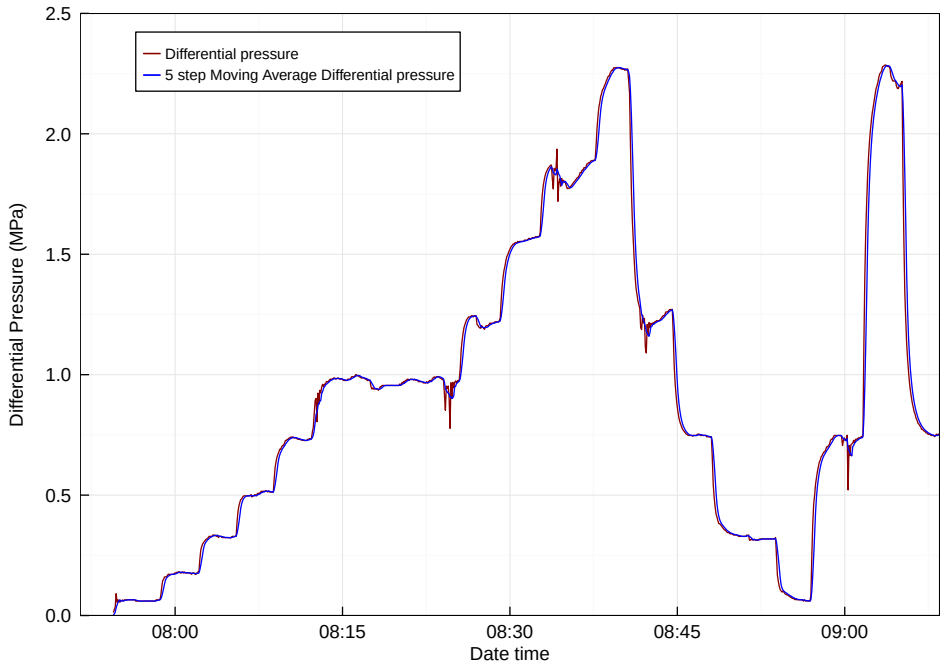

FIGURE 6.18: Illustration of difference between the raw differential fluid pressure log data and the 5 step moving average differential pressure dataset for Wissey sample (Expt A, Stage 2, 10 MPa fluid pressure).

Steps 1 and 2 of the revised automated event data extraction method used for Wissey are the same as those within the general procedure: identification of initial event durations based on pump flow rate changes followed by removal of short events. Steps 3 & 4 of the revised method consist of calculation of a few key event statistics using initial event durations (defined by pump flow rate change times), and removal of non-stationary events i.e. events where temperature, fluid or confining pressure are being changed. The revision of event start and end times (Step 5) is carried out using a more complex method than that defined in section 6.5.2.1. The event end time as well as the start

TABLE 6.9: Method for automated extraction of representative event data from log datasets whilst accounting for pump log timing errors (applied to Wissey sample results)

STEP 1: Identify pump Q change times	• Calculate difference between consecutive upstream pump Q values within the log dataset time series. • Identify timesteps where the difference magnitude is >0.1 ml/min AND take only the first occurrence of adjacent timesteps identified.
STEP 2: Remove short events	• To ensure flow rate event length is sufficient for provision of representative data, discard event data where the initial event duration (defined within this step as the period between pump Q changes) is less than or equal to the threshold, **D**=60 s.
STEP 3: Calculate initial statistics	• Use initial event durations to calculate mean pump Q and 5 step moving average differential pressure as well as standard deviations for downstream fluid pressure, differential pressure and confining pressure. These values are used in STEPS 4 & 5.
STEP 4: Remove non-stationary events	• Identify and remove pressure transition events i.e. where fluid or confining pressure is being changed. These are identified by pressure standard deviations in excess of defined thresholds: 100 psi (0.69 MPa) for fluid pressure and 500 psi (3.45 MPa) for confining pressure. • Also remove events where pump flow rate is either <0.5 ml/min or >10.5 ml/min.
STEP 5: Define event duration	• This is a multi-step procedure used to shift both start and end times of the event duration to account for pump log errors and differential pressure response. The revised event duration enables representative event means to be calculated for logged parameters. Details of the sub-steps are contained within Table 6.10.
STEP 6: Quality checks	• Check there are no negative event durations. • Manually check data where event overlaps >15 s occur. • Remove any other erroneous events (documented in lab book during experiment operations).
STEP 7: Calculate event means	• For each of the parameters within the log dataset (excluding pump Q), calculate a mean value for each event using the revised event durations from Step 5. Also calculate standard deviations for the differential pressure data. • Maintain the pump Q means calculated in Step 3 within the final dataset.

time must be assessed by review of the magnitude and rate of change of differential pressure, as both times may be either prior to or after the logged pump flow rate change time due to the pump logging timing errors. Due to the complexity of this step, the associated sub-steps are detailed separately in Table 6.10. It should be noted that at the commencement of Step 5 the initial event start and end times are defined by the pump flow rate change times, according to the pump log data. Following revision to the event start and end times to ensure representative event durations, erroneous event data are removed through quality checking (Step 6), and event data means of all log parameters are calculated for the finalised event durations (Step 7). The upstream pump flow rate value is retained from the initial event duration periods for each of the events, due to the timing discrepancy associated with this parameter.

The resultant event durations for the Wissey sample experiments are reviewed using time series plots to assess suitability, in the same way as illustrated in section 6.5.2.1. Figure 6.19 is an example plot, using data extracted from Wissey Experiment A, Stage 2, with 10 MPa fluid pressure. The figure is in the same format as Figure 6.13, with the pump data within the top plot, and the associated differential pressure response within the lower plot. A negative discrepancy in the pump log data is observed throughout the data period presented in Figure 6.19 - the flow rate change times are earlier than indicated by the response of the observed differential pressure. Review of the figure indicates that the mean differential pressure derived using the revised event durations are representative of steady state conditions, with reasonable event start and end times defined that correct for the pump log timing error and the differential pressure response. The standard deviations (error bars) associated with mean differential pressure values are reasonably small, and a reasonably stable differential pressure has been attained within the event duration for the majority of events. The high flow rates appear to take longer to reach steady state, and where large flow rate changes are made pressure conditions within the subsequent event are slightly less stable. Despite this, the differential pressure event means are considered to be a reasonable estimate of steady state conditions for all events, and thus the automated event extraction procedure is considered to be successful in extracting representative event means for use within result analysis. A review of similar time plots across the full range of temperatures, confining pressure and fluid pressures assessed has been carried out for the duration of the Wissey experiments, to ensure the extraction procedure and associated thresholds are valid for the full experiment duration.

TABLE 6.10: Sub-steps involved with defining revised event start and end times to account for pump log errors and differential pressure response (STEP 5 of Table 6.9).

STEP	ACTION	PURPOSE
5a	While the event duration is >6 timesteps (∼ 30 s), delay the event start time on a timestep-by-timestep basis if the differential pressure at the start is outwith 1 standard deviation of the mean differential pressure.	This ensures that the defined start time is not prior to the associated differential pressure response.
5b	Commencing with the start time from 5a, find the maximum rate of change of differential pressure within a ±10 timestep window, and readjust the start to this time if the event duration remains >5 timesteps (i.e. a minimum of 30 s).	This places the start time at the maximum differential pressure response time, and allows for a negative shift, if required, due to pump log errors.
5c	Work out the overall start time shift resulting from steps 5a and 5b and then shift the end time for events by the same amount.	This assumes that the start time shift is solely due to the pump log error and thus the end time will be equally affected.
5d	Delay the revised start time on a timestep-by-timestep basis while: 1. the rate of change of differential pressure is above a threshold $\mathbf{C}_1$=0.3 MPas, AND 2. the differential pressure at the mid-point of the event is within 2 standard deviations of the mean, AND 3. the event duration is >5 timesteps (i.e. a minimum of 30 s).	This adjusts the shifted event duration start time to account for the rate of differential pressure response.
5e	Shift the end time backwards on a timestep-by-timestep basis using the same conditions as sub-step 5d.	This ensures the event end time is also representative of steady state conditions.
N.B. Within this procedure the 5 step moving average differential pressure parameter has been used rather than the raw logged differential pressure value to reduce the effects of noise (high frequency oscillations).		

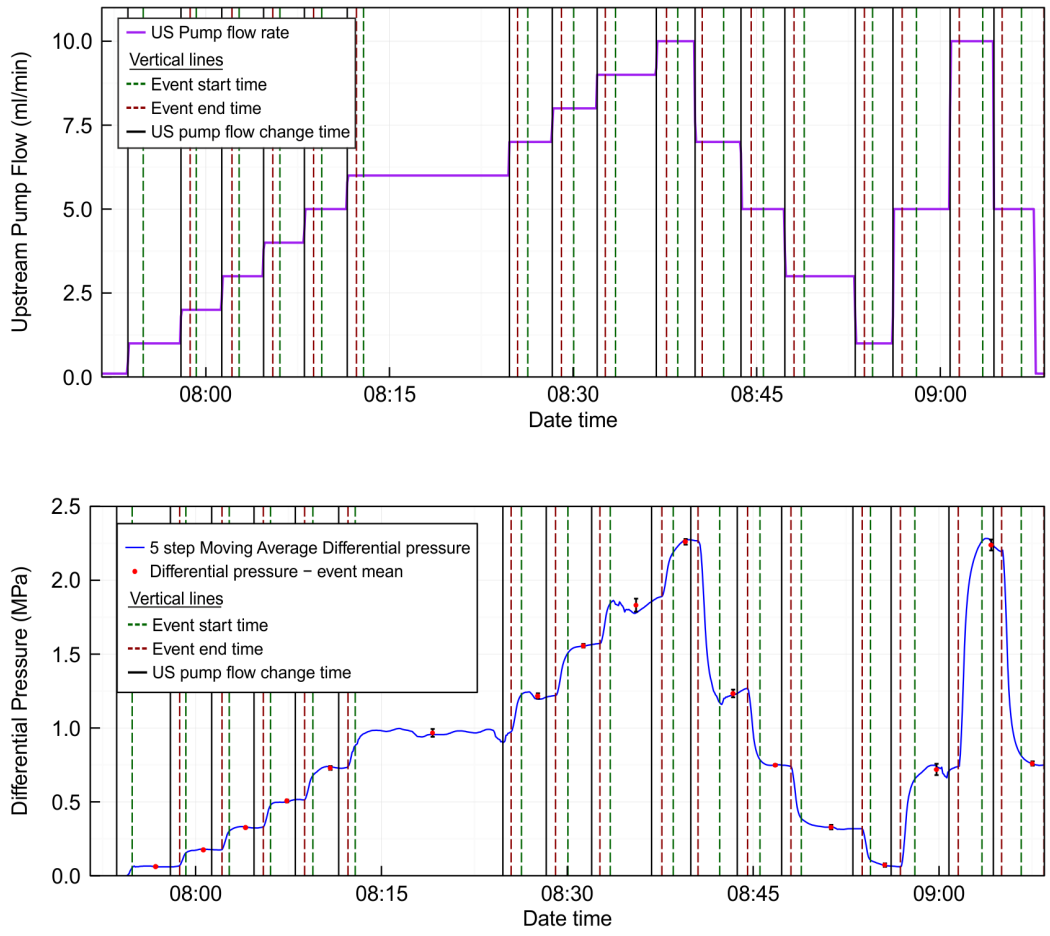

FIGURE 6.19: Example time series figure of results from automated event data extraction for Wissey W3 sample (Expt A, Stage 2, 10 MPa fluid pressure)

Figure 6.20 plots all the differential pressure event data for Wissey Experiment A, Stage 2 experimental steps against upstream pump flow rate. These data have all been extracted using the method in Table 6.9, and standard deviation error bars are plotted for the differential pressure data. The data include the 10 MPa fluid pressure subset presented within Figure 6.19 (dataset (i) in Figure 6.20). As with Figure 6.19, Figure 6.20 indicates that, while there is some variability in the means and errors (standard deviation) associated with event data and a couple of outliers exist, the errors are generally much smaller than the difference in differential pressure results for differing flow rates. As with Figure 6.15, the standard deviation errors appear to be largest for the low fluid pressure (10 MPa) results, and for the higher flow rates.

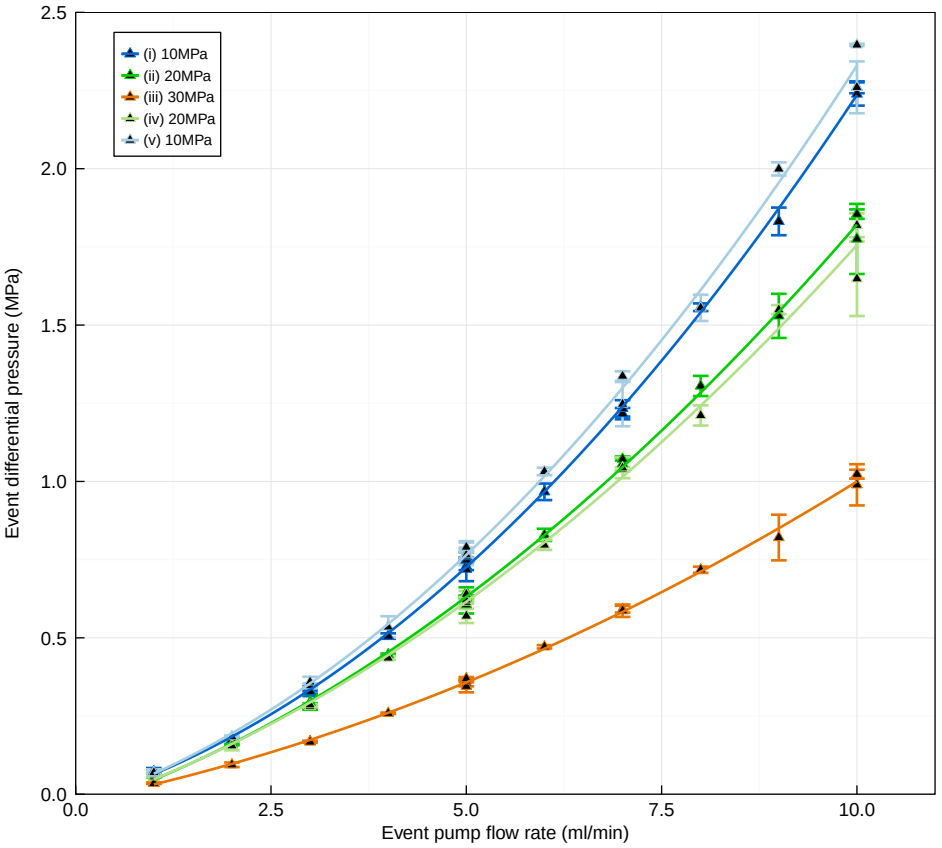

FIGURE 6.20: Event data plot of differential pressure against upstream pump flow rate for Wissey sample W3 (Expt A, Stage 2). Standard deviation error bars are included for the differential pressure data values. The legend sequence (i) to (v) indicates the experimental sequence.

A database is created for the event data associated with each sample, which contains the event start and end times, as defined within step 5 (Table 6.10), as well as all the mean log parameter values that are considered to be representative values for the events (with the pump flow rate assigned based on the initial event duration). This event dataset is used for result analysis in Chapter 7.

An assessment of the differential pressure (ΔP) standard deviation (or sampling error) as a percentage of the event ΔP value, indicates that the mean sampling error resulting from ΔP variance during the Wissey events is 4.5%, with the frequency distribution indicating that most event data sampling errors lie within this value (Figure 6.21). The mean sampling error (standard deviation) magnitude associated with the differential pressure event data for the Wissey samples (Experiments A-C1) is 4.0 psi (0.028 MPa).

Given that the differential pressure transducer instrument accuracy is ±4.8 psi (0.033 MPa), this suggests that the additional sampling error introduced due to the event data extraction process is, on average, a similar magnitude as the instrument error. This is encouraging given the variability and occasional instability observed within the differential pressure response, as well as the automated nature of the data extraction procedure. The error could be further reduced within future experiments of this nature by reducing the frequency at which the flow rate is changed within the experiments, thus increasing the duration for which steady state pressure conditions exist, and thus the reliability of the event data.

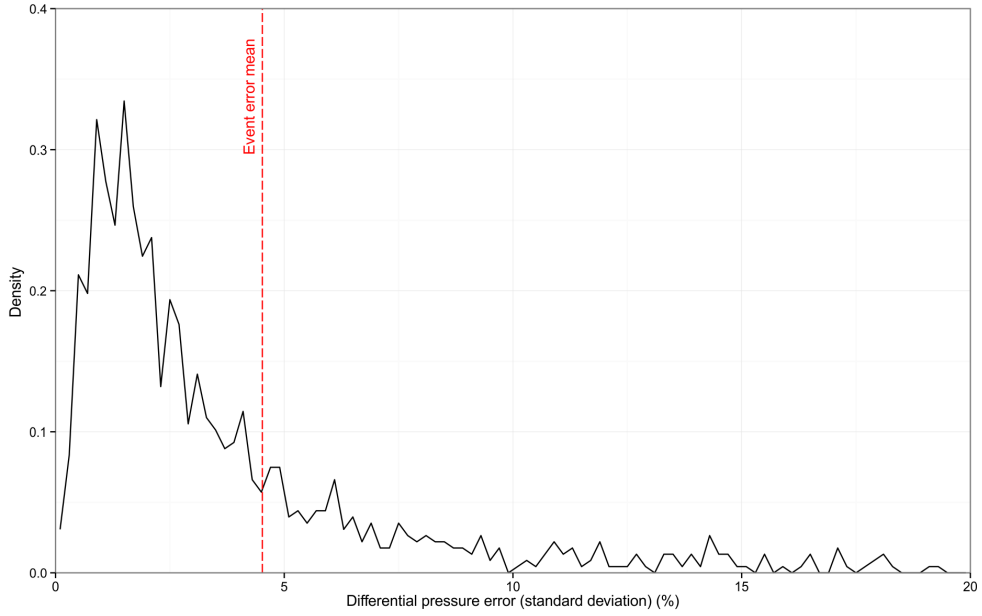

FIGURE 6.21: Frequency distribution of the differential pressure error resulting from variance within the event data extraction period for Wissey event data (Experiments A-C1).

The method of automated event data extraction developed to account for both pump log timing errors and differential pressure response during the Wissey flow experiments has been shown to produce representative event data from the experimental data logs, despite the challenges associated with accounting for the wide range of flow rates and pressures (both fluid and confining) tested. Despite the relatively high frequency of flow rate changes undertaken during the experiments (required for assessment of the large number of experimental scenarios), the system pressure response was relatively rapid, which ensured that event data were considered representative of steady state or near steady state conditions throughout the experiments. The threshold parameters used

within the event data extraction procedure (Table 6.9 and 6.10) have been set using an iterative test and review procedure. A review of event data suitability, presented within this section, indicates that the automated approach adopted for extraction of representative event data from the Wissey time series logs is valid and appropriate for result analysis purposes.

6.5.2.3 Wissey confining pressure events

The approach described in section 6.5.2.2 was suitable for event data extraction for Wissey experiments A, B and C1, where flow rate change was the highest frequency parameter change and thus events were defined by flow rate change. As detailed in section 6.2, Experiments C2, D and E were undertaken with a constant flow rate of 5 ml/min (8.3×10^{-8} m^3/s) and a constant downstream fluid pressure of 10 MPa. These experiments were undertaken to assess the effects of changing confining pressure and temperature only, with confining pressure being the highest frequency parameter change. Thus an additional automated event data extraction program was required to calculate event means for these final experiments, where an event was redefined as a steady state confining pressure time period. The event data extraction steps associated with data extraction for these latter experiments are summarised in Table 6.11. The associated R program, 'log_wissey_extract_Pc_events.R', is contained within Appendix C.

Due to the longer event durations for Experiments C2 to E, a simpler approach to defining event start and end times was adopted, by assigning a set time delay (90 s) to allow for pressure response at the start of the event, and a set time (30 s) for any event boundary issues (i.e. event boundary timing error) at the end of the event too. As the upstream pump flow rate was constant for the duration of these experiments, there were no issues with log timing discrepancies, as with the earlier Wissey experiments.

Figure 6.22 contains time series plots that illustrate the differential pressure response observed to changes in confining pressure during Experiment D. The 5 step moving average differential pressure parameter is utilised within the differential plot, thus smoothing out high frequency noise/variations within the differential pressure log dataset. However, lower frequency variations can still be observed within the data series, which may be sourced from noise within the instrument and logging set-up, but also may be due to

TABLE 6.11: Method for automated extraction of representative event data from confining pressure events (Wissey experiments C2, D & E)

STEP 1: Create subset of logging data	• A subset of the logging data time series was created for the time period from the commencement of Expt C2 to the end of Expt E.
STEP 2: Remove data records	• Remove data records from time series where upstream pump Q is NOT 5.0±0.3 ml/min. • Remove data records from time series where confining pressure gradient is >0.01 MPa/s.
STEP 3: Identify events	• Identify event boundaries by searching for: 1. times when confining pressure changes occur, and 2. large time gaps within the dataset.
STEP 4: Remove short events	• Remove events with a duration of less than 120 seconds.
STEP 5: Define event duration	• Set start time to 90 s after the event boundary for all events. • Set end time to 6 timesteps (30 s) before subsequent event start time
STEP 6: Calculate event means	• Calculate event means for all log parameters using the event duration periods, and standard deviation for the differential pressure parameter.

variations in the hydraulic response of the fracture. The mean and standard deviation error bars for the raw differential pressure log data are also included within the plot for each confining pressure event. As the long-term differential pressure response is stable, it is considered appropriate to use the means calculated using the method in Table 6.11 for result analysis (Chapter 7). The standard deviation values are helpful for providing an indication of the error associated with the event data extraction process.

Figure 6.23 plots differential pressure event data against confining pressure for Experiments C2, D and E. Standard deviation error bars are included within the plot. These illustrate that the effects of both confining pressure and temperature on differential pressure are greater than the differential pressure error magnitude, thus validating the experimental results.

In addition, both the mean and maximum differential pressure standard deviations from C2 events, 0.052 MPa (7.3 psi) and 0.074 MPa (10.7 psi), are slightly larger

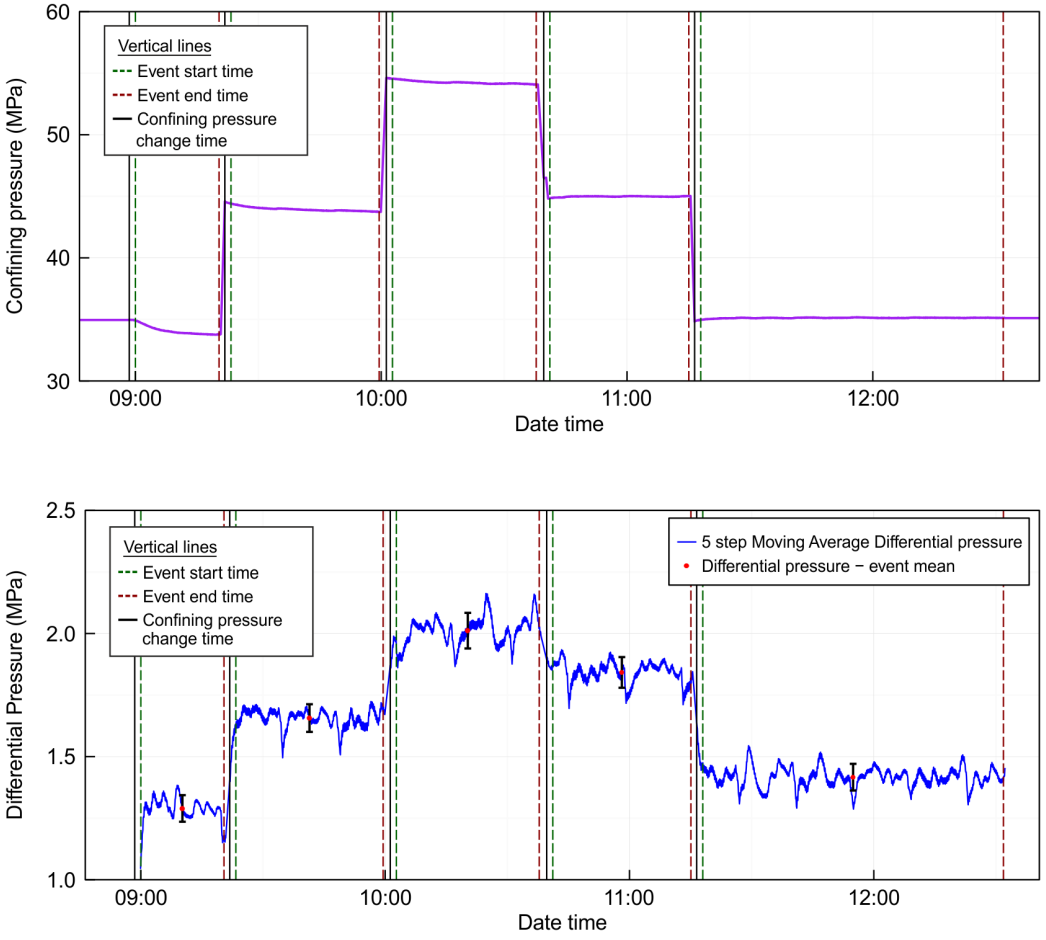

FIGURE 6.22: Example time series figure of results from automated confining presure event data extraction for Wissey W3 sample Expt D (Upstream pump Q = 5 ml/min, Downstream fluid pressure = 10 MPa)

(although a similar order of magnitude) as the mean and maximum from C1 events for equivalent flow rate and fluid pressure scenarios, 0.035 MPa (5.1 psi) and 0.065 MPa (9.4 psi) respectively. Both experiments were undertaken at the same temperature (38°C). The similar magnitude of the standard deviations improves confidence that the C1 experimental results are representative of steady state conditions despite the short event durations, as the variance within the event duration is of a similar magnitude as that found over a much longer duration. The results from the flow experiments are discussed within Chapter 7.

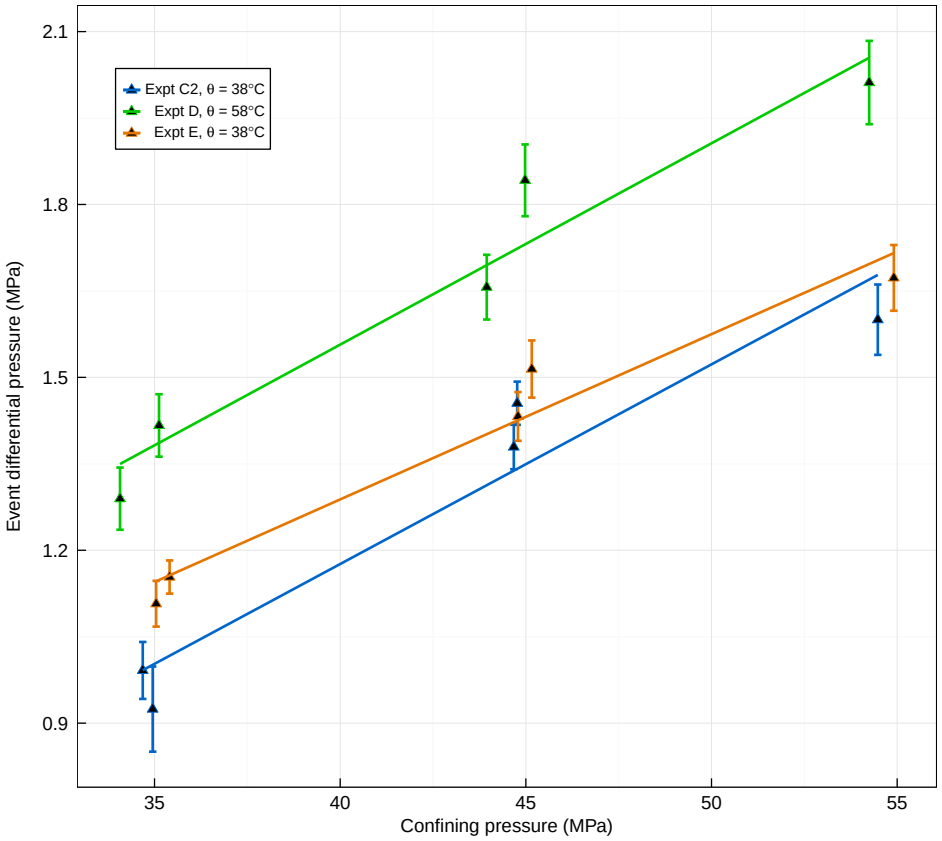

FIGURE 6.23: Event data plot of differential pressure against confining pressure for Wissey sample W3, Experiments C2, D and E. Standard deviation error bars are included for the differential pressure data values. (Upstream pump Q = 5 ml/min, Downstream fluid pressure = 10 MPa, for all experiments)

6.5.3 Categorisation of data

Section 6.5.2 discusses how representative event values of logged data parameters have been calculated and incorporated into an event data table, where an 'event' is a steady state constant flow rate period within the experimental dataset. As discussed within section 6.2, as well as varying flow rate during the experiments, a comprehensive sequence of experimental scenarios has been assessed for each sample with a variety of fluid pressures and confining pressures assessed at two temperatures. The experimental event data have therefore been subsequently categorised into 'experiments', 'stages', 'steps' and 'events', using the approach detailed in section 6.2, to enable analysis of subsets of the experimental event data for each sample.

Figures within section 6.2 show the experimental steps, stages and experiments undertaken for each sample. The event datasets for each sample were categorised using an R program, which searched for significant changes in fluid pressure, confining pressure and temperature between events to define the step, stage and experiment boundaries respectively. The boundaries were then used to allocate categorisation data to the event data. The experimental steps were numbered continuously from the start of the sample experiments to the end for each sample, while the stage numbering commenced from 1 at the start of each temperature experiment. The experiments were labelled as indicated within the associated figures in section 6.2.

In addition to step, stage and experiment categorisation, the events within each confining pressure stage were flagged according to whether they were before or after the maximum fluid pressure step. This enables the effect of fluid pressure hysteresis to be examined within experimental stages during result analysis. Confining pressure hysteresis can be easily assessed by comparison of stage data prior to and subsequent to the maximum confining pressure stages within each experiment.

Categorisation of the event data in accordance with the experimental subset criteria set out within section 6.2 enables the large event datasets to be analysed and plotted more easily, making use of data subsets for comparative purposes (Chapter 7).

6.5.4 Parameter calculation

Further to event data extraction and categorisation, the experimental event data are used to calculate key parameters required for assessment of the hydraulic characteristics of the fracture throughout the flow experiments. The parameters calculated are detailed in Table 6.12, along with units, location and the estimation method adopted. Parameters were calculated for each experimental event within each of the sample experimental sets. Calculated parameters consist of density (ρ), viscosity (μ), and CO_2 flow rate (Q) at several locations within the rig system. Sample transmissivity (T), fracture hydraulic aperture (e_h), fracture permeability (k_{frac}) and fracture hydraulic conductivity (K_{frac}) were also estimated, with different approaches depending on the significance of non-linearity observed (section 2.4). The theory associated with the parameter calculation methods adopted is discussed in Chapter 2.

Sample transmissivity, T, has been calculated using the relationship defined within Zimmerman and Bodvarsson [1996] (Equation 2.6) where a linear flow regime exists. Linear regression is used for estimation where multiple measurements are available for a given pressure/temperature scenario (see section 7.3.2 for details). Where significant non-linearity is observed within the flow regime, the Zimmerman and Bodvarsson [1996] relationship provides an estimate of apparent transmissivity, T_{app} (Equation 2.13), and true transmissivity, T_0, may be estimated using the modified Forchheimer plot method detailed in section 2.4. Fracture hydraulic aperture, fracture permeability and fracture hydraulic conductivity have been calculated from the appropriate transmissivity estimate (T or T_0 depending on flow regime) using the cubic law [Witherspoon et al., 1979].

The cubic law assumes laminar flow of incompressible fluid and therefore is a simplistic approximation for the CO_2 fluid behaviour within the sample fractures during the high pressure high temperature flow experiments. However, turbulent or non-linear flow is accounted for prior to use of the cubic law where applicable, by adoption of the Forchheimer equation for transmissivity estimation as stated above (see section 7.3 for details). Compressibility effects have been assessed for CO_2 in the context of this particular experimental study (section 2.5.2 and 7.4.2), and it was concluded that use of an incompressible approximation was appropriate. Use of the above method for hydraulic parameter estimation therefore enables meaningful result analysis, comparison and discussion (Chapter 7).

6.6 Error analysis and discussion

Due to the complex nature of the experimental work and the data post processing, a variety of sources of error or uncertainty are introduced to the experimental results analysed within this chapter.

For the parameters logged directly during the experiments, such as differential pressure (ΔP), upstream fluid pressure (P_{us}), downstream fluid pressure (P_{ds}), confining pressure (P_c), temperature (θ) and pump flow rate (Q_{pump}), the main sources of error are from instrumental errors, logging errors, and sampling errors. The instrumental and logging errors are presented within Chapter 5. The main experimental observation is the differential pressure, with the other parameters controlled within the rig system.

TABLE 6.12: Calculated event parameters

Parameter	Units	Location	Method
ρ_{pump}	kg/m^3	Upstream pump	(Huang, 1984) Inputs: P_{pump},θ_{pump}
ρ_{us}	kg/m^3	Upstream sample	(Huang, 1984) Inputs: P_{us},θ_{sample}
ρ_{ds}	kg/m^3	Downstream sample	(Huang, 1984) Inputs: P_{ds},θ_{sample}
ρ_{sample}	kg/m^3	Mean for sample	(Huang, 1984) Inputs: $\bar{P}$,θ_{sample} where $\bar{P} = (P_{us} + P_{ds})/2$
μ_{pump}	Centipoise	Upstream pump	(Jossi, 1944) Inputs: ρ_{pump},θ_{pump}
μ_{us}	Centipoise	Upstream sample	(Jossi, 1944) Inputs: ρ_{us},θ_{sample}
μ_{ds}	Centipoise	Downstream sample	(Jossi, 1944) Inputs: ρ_{ds},θ_{sample}
μ_{sample}	Centipoise	Mean for sample	(Jossi, 1944) Inputs: ρ_{sample},θ_{sample}
Q_{us}	ml/min	Upstream sample	$Q_{pump} * (\rho_{pump}/\rho_{us})$ (mass conservation)
Q_{ds}	ml/min	Downstream sample	$Q_{pump} * (\rho_{pump}/\rho_{ds})$ (mass conservation)
Q_{sample}	ml/min	Mean for sample	$Q_{pump} * (\rho_{pump}/\rho_{sample})$ (mass conservation)
T	m^4	Sample	$\frac{Q_{sample}\mu_{sample}L}{\Delta P}$ (for linear flow)
T_0	m^4	Sample	$\frac{Q_{sample}\mu_{sample}L}{\Delta P}\left(1 + \frac{b'}{a'}\frac{\rho_{sample}Q}{\mu}\right)$ (for Forchheimer flow)
e_h	m	Sample fracture	$\left(\frac{12T}{w}\right)^{\frac{1}{3}}$ or $\left(\frac{12T_0}{w}\right)^{\frac{1}{3}}$ (dependent on flow regime)
k_{frac}	m^2	Sample fracture	$e_h^2/12$
K_{frac}	m/s	Sample fracture	$(k_{frac}\rho_{sample}g)/\mu_{sample}$

However, there are notable measurement (instrumental and logging) errors associated with the controlled parameters as well as the differential pressure.

As discussed within section 6.5.2, event data have been extracted for each constant flow rate event within the flow experiment durations, by calculating mean parameter values within a determined event window duration. A review of the time series logging data suggests that the sampling error associated with this data processing stage is considered to be small for most of the event parameters in comparison to the instrumental and logging errors, and can therefore be neglected. However, the sampling error may be more significant for the differential pressure observation, as this key parameter is directly affected by flow rate change, and therefore not only takes a short period of time to respond and thus reach steady state conditions after a flow rate change, but once steady state conditions are reached, small scale fluctuations are still observed within the differential pressure time series. Representative differential pressure data values for each event are taken as the mean value within an event window, where the event window is selected to be representative of steady state pressure conditions. The standard deviation associated with the differential pressure event data is a good estimate of the sampling error associated with the event data, and the magnitude of this error has been discussed within section 6.5.2.

For parameters calculated directly from the logged parameter values: viscosity (μ), density (ρ), flow rate through the sample (Q_{sample})(Table 6.12), the errors or uncertainties associated with the input variables must be considered in order to understand the uncertainty in the calculated parameters. An uncertainty/error estimate for these parameters may be calculated using the following rule [Peters, 2001]:

For a variable, z, that is the product of powers of N independent variables (Equation 6.1),

$$z = \prod_{i=1}^{N} x_i^{a_i} \tag{6.1}$$

the relative variance in z is given by Equation 6.2, where σ_x is the variance or error associated with variable, x.

$$\frac{\sigma_z^2}{z^2} = \sum a_i^2 \frac{\sigma_{x_i}^2}{x_i^2} \tag{6.2}$$

When considering instrumental errors contributing to the calculated parameter values, the most significant ones are found to be that of the differential pressure (±4.8 psi), which has a very large impact on calculations using low differential pressure readings; and the temperature error ±2.2 °C, which is significant for calculation of density and viscosity parameters.

As discussed in section 2.5, due to the compressible nature of the CO_2 fluid, the density, ρ, and viscosity, μ, vary within the sample due to the pressure differential across the sample. A higher density and viscosity exists at the upstream end of the sample where the pressure is higher. To assess the significance of these density and viscosity changes (compressibility effects) within the sample, parameter estimates have been calculated for both the upstream and downstream ends of the sample, using the associated pressure and temperature measurements taken during the experiments. The variance between upstream and downstream parameter estimates can then be compared to measurement error estimates for both density and viscosity to assess the significance of the compressibility effects (see section 7.4.2).

Density and viscosity estimates are calculated using the Huang et al. [1984] equation of state for CO_2 and the viscosity relationship of Jossi et al. [1944] (section 2.5). These use fluid pressure and temperature experimental event data for parameter estimation. The relative magnitude of the temperature errors are significantly higher than the fluid pressure errors, therefore the fluid pressure errors can be neglected when estimating density and viscosity measurement errors. To estimate the magnitude of density and viscosity measurement errors, the effect of the temperature uncertainty on density and viscosity estimates has been calculated for each of the three downstream fluid pressure scenarios tested, at both experiment sample temperatures. These six relative error magnitudes (2 temperature x 3 fluid pressure scenarios) have been applied to all sample density and viscosity values according to their associated experimental pressure and temperature scenario. This is an approximate, simplified approach that is considered adequate for error estimation purposes and has been used to prevent the requirement for individual calculation of density and viscosity error calculation for all density and

viscosity estimates within each event data record, which would be challenging given the large datasets.

The magnitude of both the density and viscosity measurement error (due to temperature uncertainty) and the compressibility error vary with pressure and temperature conditions tested, however the relative measurement error and the relative variance due to compressibility are both largest during the low fluid pressure tests (10 MPa), where the sensitivity of the density and viscosity values is greatest. As the measurement error source is a fixed magnitude uncertainty in the temperature inputs ($\pm 2.2°C$) for the density and viscosity estimates, the relative measurement errors are therefore highest at low temperatures, where the relative uncertainty is highest. In contrast, both densities and viscosities are lower at high temperatures and the compressibility effects are proportionally larger. Thus, the compressibility effects are of most significance for the high temperature scenarios, and can also be significant for high flow rates within the low temperature experiments, where the pressure differentials across the sample are high. The significance of the compressibility effects are considered for all samples within result analysis (section 7.4).

The uncertainty or variance in the density parameter affects the estimate of volumetric flow rate through the sample, as this is obtained through using a ratio of densities between the fluid at the upstream pump and at the sample, to convert the upstream pump volumetric flow rate to a sample flow rate, as discussed in Chapter 5. A volumetric flow rate is calculated for both the upstream and downstream ends of the sample, as well as for the mid-pressure point within the sample (see Table 6.12). Although a ratio of densities is used to calculate the sample flow rate, the relative errors associated with the flow rate measurements are the same as the relative errors associated with the density estimates. This is due to the much lower uncertainty associated with the liquid CO_2 density at the upstream pump, which can thus be neglected within the flow rate estimation.

The errors calculated for the above parameters were of great value for use within flow regime analysis (section 7.3), and for assessment of the significance of fluid property variations (section 7.4).

As mentioned in section 6.5.4, flow regime and the significance of non-linearity has been considered prior to estimation of sample transmissivities. Where a linear flow regime is observed, Darcy's law can be used to estimate a single transmissivity value, T, for

each pressure/temperature scenario using linear regression where multiple points are available (see section 7.3.2 for details). Where a non-linear flow regime is observed, use of a modified Forchheimer plot method has been used to estimate true transmissivity, T_0, using regression analysis where possible (section 2.4 and 7.3). The use of regression analysis for transmissivity estimation makes quantification of uncertainties or errors in transmissivity estimates challenging as goodness-of-fit must be accounted for in addition to uncertainties associated with input data points. Error quantification has therefore not been undertaken for this parameter. As transmissivity estimates are primarily used within result analysis (Chapter 7) for assessment of relative behaviour in response to i.e. stress or temperature changes, the absolute magnitudes are not considered as important and error quantification was not a priority. An indication of the uncertainty associated with transmissivity estimates can be gained qualitatively through review of the associated regression figures (section 7.3), and visual assessment both of the goodness-of-fit of the regression, as well the uncertainty associated with the data points (included as error bars).

As transmissivity estimates (T or T_0 respectively) have been used to calculate hydraulic aperture (e_h), fracture permeability (k_{frac}) and fracture hydraulic conductivity (K_{frac}) estimates (section 6.5.4), errors have not been quantified for these parameters either. In a similar manner to transmissivity, it is the relative behaviour of these parameters rather than the absolute magnitude that is most important during result analysis, therefore the data estimates are still of great value.

6.7 Summary

This chapter presents details of the CO_2 flow experiments undertaken on four fractured samples, sourced from a Cambrian shale outcrop, the East Brae North Sea field (Kimmeridge Clay) and the Wissey North Sea field (Zechstein Dolomite). While details of the rig design are presented within Chapter 5, this chapter details the methods developed for operational use of the rig during the CO_2 flow experiments. The chapter also presents pre and post experiment rig procedures, and includes details of the techniques used for loading and unloading samples into the core holder.

As well as experimental methods, this chapter provides comprehensive details of the processing of experimental data undertaken subsequent to completion of the experiments.

Pump log timing discrepancies identified within the Wissey experimental results led to the requirement for modifications and additions to the general event data extraction post-processing procedures developed, and thus the Wissey event data extraction procedures are presented separately. Parameter calculation details are summarised within the data post-processing section. The associated theory is discussed within Chapter 2. This chapter acknowledges the presence of both measurement and sampling errors in experimental results, and includes a discussion of how error propagation has been undertaken for calculated parameters. It is also acknowledged that, where model fits have been used to estimate hydraulic parameters (i.e. T_0 using the Forchheimer model fit, see section 7.3), additional uncertainty is associated with the goodness-of-fit of the model, which may be significant and is not easily quantifiable. Error bars have been included within result analysis plots where appropriate within Chapter 7, based on the error estimation methods detailed within this chapter.

All methods for undertaking the experiments and post-processing of experimental data presented within this chapter were personally developed during the PhD project, due to the unique nature of the experimental research. The methods developed will be of great value for future users of this particular experimental rig, and could also inform external experimentalists undertaking related research. The methods will also help to inform priorities for further rig development.

Chapter 7

Experimental Results

7.1 Introduction

This chapter contains results and discussion from CO_2 flow experiments undertaken on four discretely fractured low permeability rock samples. The samples consisted of one artificially fractured Cambrian shale outcrop sample; one Wissey field Zechstein dolomite sample containing a pre-existing fracture; and two artificially fractured East Brae field Kimmeridge Clay samples. The two East Brae 'mated fracture' samples (B2 and D2) were found to be of extremely low permeability, therefore a higher permeability 'offset fracture' sample (B2b) was created by introducing a manual ~1 mm longitudinal fracture surface offset to the B2 sample subsequent to initial testing. This enabled an additional set of flow experiments to be undertaken.

Sample testing was undertaken at multiple controlled flow rates, downstream fluid pressures, confining pressures and temperatures where possible, with the experimental sequence described for each sample in Chapter 6, section 6.2. Due to very low sample permeability, the East Brae D2 tests were undertaken at low temperature (38°C) only, under a limited range of flow rates. The East Brae B2 sample permeability was even lower, allowing only a single low confining pressure, low flow rate CO_2 permeability test to be undertaken at 38°C. Table 7.1 summarises the tests undertaken on each of the samples. This chapter discusses the results from these experiments.

TABLE 7.1: Experiment summary table

Sample	Prior stress-loading	CO_2 flow test	Flow regime analysis	External stress loading	Internal stress loading	38°C	58°C
Cambrian V1	-	✓	✓	✓	✓	✓	✓
East Brae B2	✓	✓	-	-	-	✓	-
East Brae D2	-	✓	✓	✓	✓	✓	-
East Brae B2b	✓	✓	✓	✓	✓	✓	✓
Wissey W3	-	✓	✓	✓	✓	✓	✓

While flow rate, downstream fluid pressure, confining pressure and temperature were imposed (controlled) and monitored during experiments the key experimental observations were the differential pressure response measurements. As detailed in section 6.5.4, a variety of parameters have been calculated from the experimental measurements to enable assessment and analysis of the fracture hydraulic response during the experiments. Figure 7.1 details the experimental measurements of both imposed and dependent parameters used to calculate each of these parameters and indicates which flow theories or laws have been assumed in calculating each parameter. As can be seen from the Figure, the differential pressure response measurement is key for calculation of all hydraulic response parameters: sample transmissivity, fracture hydraulic aperture, fracture permeability and fracture hydraulic conductivity.

Complex coupling between thermal, hydraulic and mechanical processes during the experiments makes presentation of isolated behaviours challenging. Figure 7.2 illustrates how thermal, hydraulic and mechanical processes influence each of the hydromechanical mechanisms studied within this chapter.

The results of the supercritical CO_2 flow experiments have been used to assess a number of important behaviours and mechanisms relating to hydraulic, mechanical and thermal processes within this Chapter. Table 7.2 outlines the purpose of each of the analysis sections within this chapter, and summarises which samples and parameters were used within the section analysis in each case.

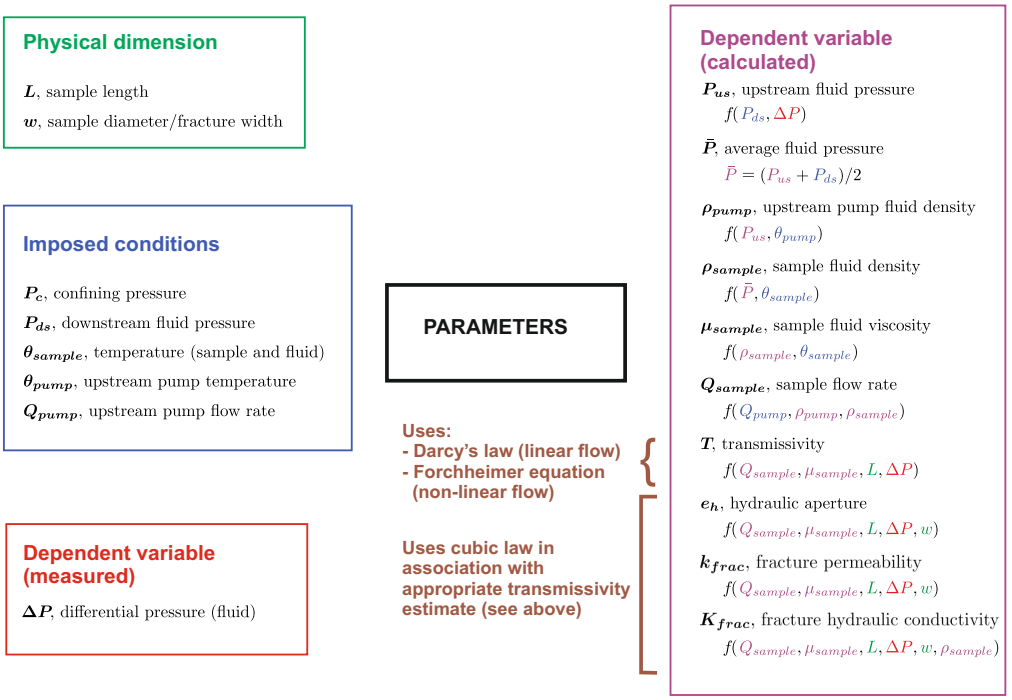

FIGURE 7.1: Imposed and dependent (measured and calculated) parameters during experiments

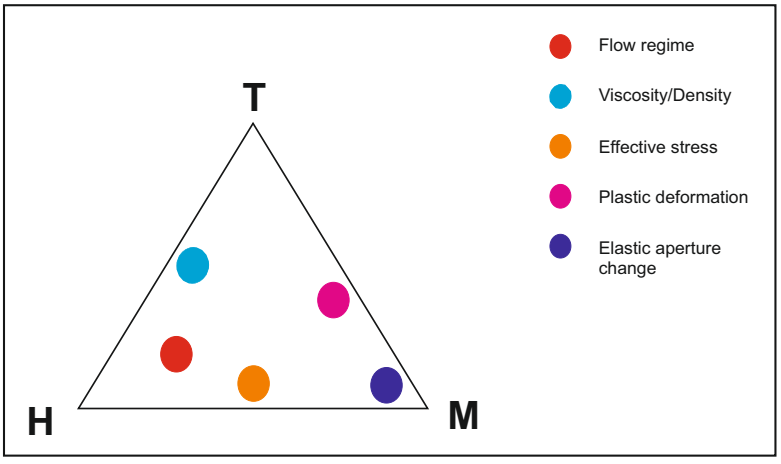

FIGURE 7.2: Map of mechanisms studied experimentally as a function of thermal (T), hydraulic (H) and mechanical (M) processes

TABLE 7.2: Chapter outline

Section	Purpose	Samples assessed	Parameter comments
7.2	Initial overview and comparison of samples	ALL	ΔP, T_{app} *[Prior to comprehensive transmissivity assessment (section 7.3), T_{app} values were used for initial comparison between samples.]*
7.3	Flow regime analysis and transmissivity estimation	V1 D2 B2b W3	Derives: T/T_0 for linear/non-linear flow regime experiments respectively, where possible. Utilises: ΔP, Q, μ, T_{app} for assessment
7.4	Assesses CO_2 fluid property variation and implications	ALL	Utilises: ρ, μ
7.5	Assesses elastic mechanical response to stress change*	W3 V1 D2	Utilises: T/T_0 for *[D2]/[W3,V1]* samples respectively
7.6	Assesses inelastic mechanical response to stress change**	W3 V1 D2	Utilises: $T/T_{app}/T_0$ for *D2/V1/W3* sample respectively *[Insufficient data points available for T_0 estimation for V1 within these data subsets]*
7.7	Presents e_h, k_{frac}, and K_{frac} parameters	W3 V1 D2 B2	Derives: e_h, k_{frac}, and K_{frac} Utilises: T/T_0 for *[D2,B2]/[W3,V1]* samples respectively
7.8	Assesses coupled effects of mechanical and hydraulic behaviour on K_{frac}	W3 V1 D2	Utilises: K_{frac}

** utilises latter stages of experiments (to minimise inelastic effects)*
*** utilises initial stages of experiments where inelasticity is most significant*

V1 = Cambrian V1; D2 = East Brae D2; B2 = East Brae B2
B2b = East Brae B2b; W3 = Wissey W3

The Wissey W3 sample underwent the most comprehensive flow testing, with repeat stress loading cycles at both low and high temperature (section 6.2). It therefore provided the largest and most suitable dataset for assessment of mechanical behaviour. Due to uncertainty in the East Brae B2b observations, limited analysis was undertaken on this sample. The influence of temperature is discussed in context within each of the Chapter sections. The main experimental findings are summarised in section 7.9. Note that to simplify notation within this Chapter, Q, μ and ρ refer to the mean sample parameters Q_{sample}, μ_{sample} and ρ_{sample} respectively (Table 6.12), unless otherwise specified.

7.2 Sample overview and comparison

The experimental rig was used to undertake five sets of supercritical CO_2 flow experiments on four fractured samples, as detailed in Chapter 6, section 6.2. The Wissey W3 sample was the only natural or pre-existing fracture sampled; fractures in the other samples were artificially induced as described in Chapter 3. Due to sampling and preparation differences the sample lengths varied (Table 7.3). In particular, the Wissey sample was around half the length of the other samples. Thus, as differential pressure is proportional to sample length and inversely proportional to transmissivity, the variance in differential pressures observed between samples were a result of both sample length and transmissivity differences.

TABLE 7.3: Lengths of fractured samples

Sample	Length (mm)
Cambrian V1	58.6
East Brae B2	60.6
East Brae D2	64.0
East Brae B2b	58.0
Wissey W3	27.6

The differential pressures ranges observed for each sample during the 38°C experiments with pressure conditions $P_c = 35$ MPa and $P_{ds} = 10$ MPa are shown in Figure 7.3, with samples shown in the order in which experiments were undertaken. As can be seen from the figure, the differential pressures were very small for the Cambrian V1 and East Brae B2b samples, indicating relatively high sample transmissivities. These differential

pressure values were at the lower limit of the differential pressure transducer range and therefore have high associated measurement errors. Conversely, the differential pressures were very large for the mated East Brae B2 and D2 samples, indicating very low sample transmissivities. The differential pressures for these two East Brae samples exceeded the range of the differential pressure transducer and were therefore measured using the difference in fluid pressure between the upstream and downstream transducers. The Wissey W3 sample differential pressures were comfortably within the range of the differential pressure transducer due to a combination of a relatively low sample transmissivity and short sample length.

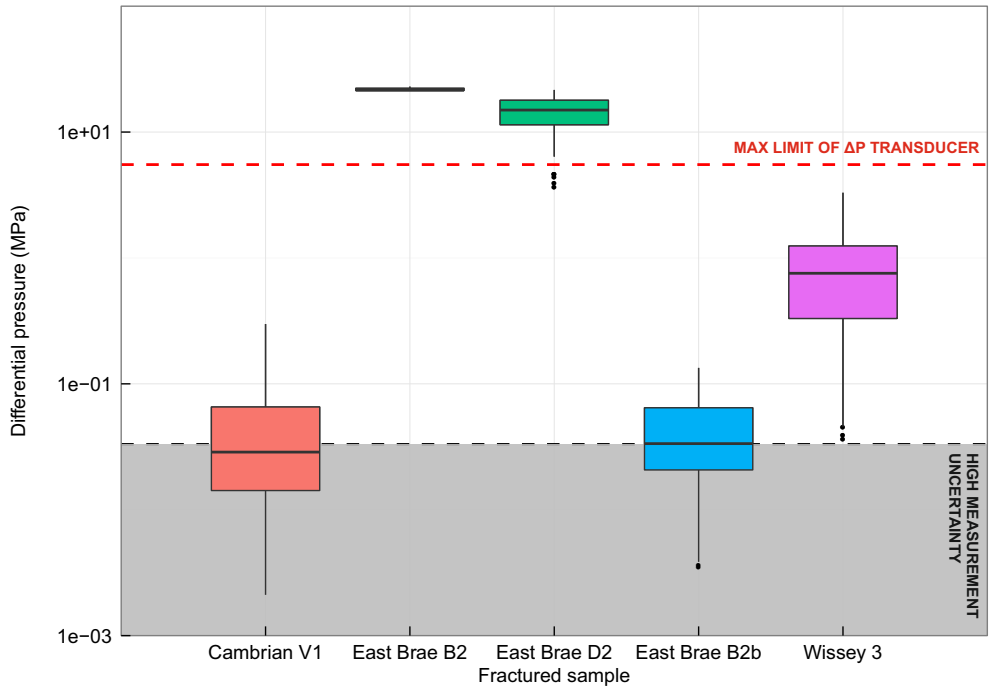

FIGURE 7.3: Differential pressure ranges observed during all 38°C CO_2 flow experiments undertaken with $P_c = 35$ MPa and $P_{ds} = 10$ MPa for all fractured samples

The apparent transmissivities of the samples have been calculated for all experimental scenarios using Equation 2.13 by analogy with linear Darcy's law [Zhang and Nemcik, 2013, Zimmerman et al., 2004] (see Chapter 2 for associated theory). A more in-depth assessment of sample transmissivities (accounting for non-linear flow effects (section 2.4) is contained in section 7.3 in the context of flow-regime analysis.

The apparent transmissivity ranges associated with the respective differential pressures of Figure 7.3 (38°C experiments with pressure conditions $P_c = 35$ MPa and $P_{ds} = 10$ MPa) are shown in Figure 7.4. The apparent transmissivities range from $\sim 10^{-21}$ m^4 for the East Brae B2 sample to $\sim 10^{-17}$ m^4 for both the Cambrian and offset East Brae B2b samples.

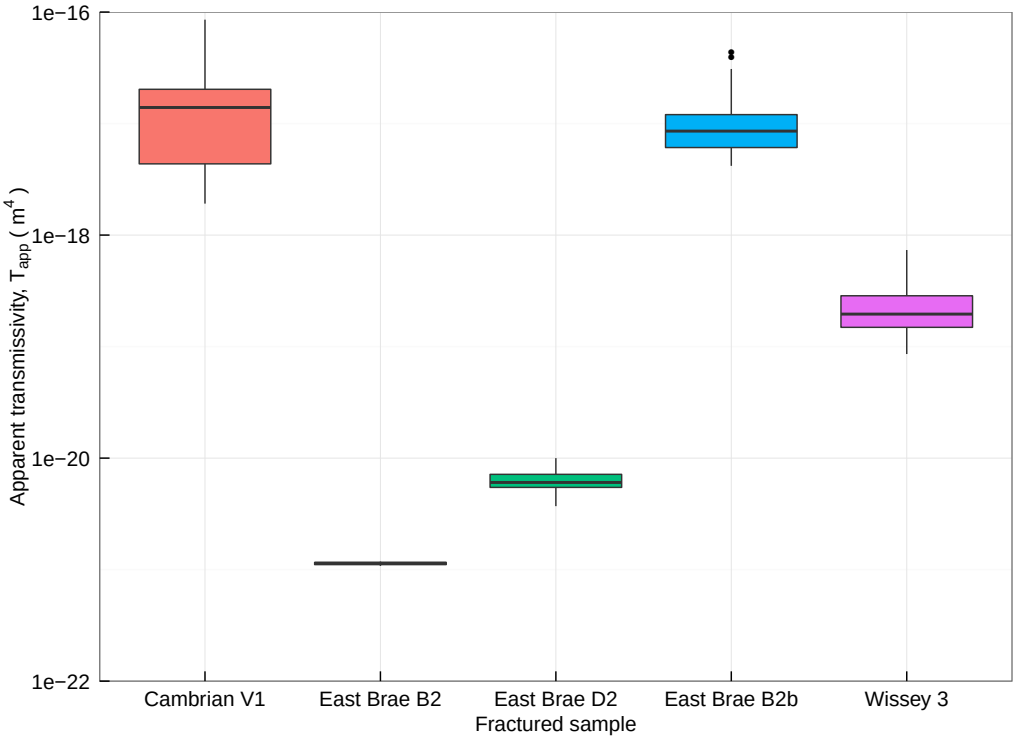

FIGURE 7.4: Apparent transmissivity ranges of samples during all 38°C CO_2 flow experiments undertaken with $P_c = 35$ MPa and $P_{ds} = 10$ MPa

The two mated East Brae fractured samples (B2 and D2) have significantly lower apparent transmissivities than the other three samples. It is thought that this is in part due to the smooth fracture topography (and surface matching) and in part due to the softness of the East Brae sample material within these mated fractured samples (see Chapter 3, section 3.4.3). The softness of the material is likely to be related to the relatively high clay content (section 3.4.1). This gives the potential for significant consolidation and plastic deformation of surface asperities under confining pressure which would minimise the effective fracture aperture and increase fracture surface contact area within the fracture to minimise transmissivity. Evidence for plastic deformation

within the experimental results is examined within section 7.6. It has also been observed through fracture surface topography analysis (Chapter 4).

A significant change in transmissivity is observed as a result of introducing a small longitudinal offset between the two fracture surfaces of an East Brae sample. This can be seen through comparison of the apparent transmissivities of East Brae B2 (mated fracture), and East Brae B2b (the same sample with the fracture surfaces offset by ∼1 mm). By offsetting the fracture surfaces of the lowest transmissivity sample (B2), the apparent sample transmissivity is observed to increase by approximately four orders of magnitude following initial stress-loading, becoming a similar magnitude to the highest transmissivity fractured sample tested (Cambrian V1). This highlights that shear displacement can have a significant influence on fracture transport properties. In addition to physical displacement of fracture surfaces, any offsetting process (e.g. shearing) that occurs within in-situ 'real' fractures is likely to result in significant additional transmissivity effects. Examination of such fracture alterations (see section 2.6.1) was outwith the scope of this study.

The Wissey sample apparent transmissivity range is mid-way between that of the mated East Brae samples and the Cambrian shale sample ($\sim 10^{-19}$ m^4). While the Wissey dolomite was found to be significantly harder than the East Brae shale, the small scale roughness of the fracture surfaces was found to be lower (Chapter 4, section 4.5). The larger scale topography of the fracture (section 4.6) may also play a role in determining the fracture conductivity, particularly if any mismatch is present between the fracture surfaces. As the Wissey fracture is a natural fracture, mismatch between the surfaces may have resulted from mineral reactions or shearing prior to sampling, in addition to the risk of mismatch introduced during sample preparation.

There was evidence of the creation of additional micro-cracks or micro-fractures within the Cambrian shale sample post-experiment (see section 4.9). These are thought to have been induced during stress-loading of the sample and could influence the sample transmissivities observed during the experiments, particularly if the micro-fractures become active flow pathways under certain pressure conditions. Fluid flow pathways within the micro-fracture network are most likely to occur under low effective stress (low confining pressure, high fluid pressure) scenarios [Skurtveit et al., 2012]. Externally, radial micro-fractures were observed, however within CT scan images there was also evidence suggesting longitudinal micro-fractures existed, originating from the main

longitudinal induced rough fracture (Figure 4.23). The potential implications of this additional micro-crack fracture network are discussed further within subsequent sections of this Chapter (sections 7.3 and 7.6). There was no external evidence of induced micro-fractures on any of the other experimental samples.

The significant difference in transmissivity observed between the matched East Brae samples and the Cambrian shale sample demonstrates the capacity for fractures in some shales to be much less transmissive than others. This is likely to be due to differences in mineralogical content and material hardness in addition to any potential micro-fracture influence. In this instance, the East Brae sample had both a higher clay content and lower material hardness than the Cambrian shale (see Chapter 3 for details).

The experimental pressure and temperature conditions used within the experiments were chosen to be typical of those found at potential CO_2 geological storage sites: 35 MPa $< P_c <$ 55 MPa; 10 MPa $< P_{ds} <$ 30 MPa; 37°C $< T <$ 58°C. The Wissey dolomite sample was cored from the Southern North Sea, from a depth of 1.7 km where in-situ pressures and temperatures are within the ranges assessed experimentally (Table 6.4). Thus the CO_2 and rock properties and behaviours experienced in the lab are as close as possible to those that would be experienced in-situ. The East Brae samples were cored from the Northern North Sea from a much greater depth of 4551 m. As a result the experimental pressures and temperatures are lower than the in-situ conditions associated with these cored samples (Table 6.3), and are more representative of conditions at shallower depths. Despite the experimental effective stresses being significantly lower than the in-situ stresses for the East Brae samples, the East Brae mated fractures were observed to be of extremely low apparent permeability, highlighting the effectiveness of the East Brae Kimmeridge Clay as a seal.

As noted in Chapter 1, the CO_2 flow experiments undertaken during this study do not directly simulate in-situ conditions as they are simplified by the use of dry samples and single phase CO_2 fluid. In nature the rocks will initially be saturated with brine, thus multiphase flow, including drainage and imbibition processes that will be influenced by rock-fluid wettability, will affect the CO_2 flow behaviour. CO_2 dissolution, production of carbonic acid and mineral reactivity add to the complexity of hydro-mechanical and chemical processes that occur. The lab experiments enable us to isolate and study the hydro-mechanical behaviour of CO_2 within typical seal rock fractures under in-situ conditions. This is important to enable improved understanding of the contribution

that these hydro-mechanical processes play within the more complex scenario observed in nature, and to ensure accurate representation within models.

7.3 Flow regime - assessing evidence for non-linear flow

7.3.1 Introduction

Flow rate variation was undertaken during each experimental step on all the fractured sample experiments during this study (except East Brae B2 due to extremely low transmissivity). Flow rate variation enabled examination of the flow regime during each of the experiments and assessment of any non-linear deviations. The range of upstream pump flow rates adopted for the experiments was 1 to 10 ml/min (1.7×10^{-8} to 1.7×10^{-7} m^3/s), except for East Brae D2 where upstream pump flow rates were limited to 0.5 to 2 ml/min (0.8×10^{-8} to 3.3×10^{-8} m^3/s) due to low transmissivity.

The mean volumetric flow rates through the samples were up to 1.5 times the pump flow rates at ∼38°C due to the change in temperature between pump and sample (see Chapter 5, section 5.3.3.3), and up to 3.3 times the pump flow rates at ∼58°C (dependent on fluid pressure). The experimental flow rate ranges were constrained by the rig design.

Flow non-linearity can occur at relatively low Reynolds numbers within fractures due to surface roughness and flow tortuosity, as discussed in section 2.4. Fracture surface roughness of the experimental samples was analysed in Chapter 4, with Figure 4.20 providing comparative roughness scales (both large and small scale) drawn from this analysis. Alteration of small scale roughness was observed post-experiment in all three samples assessed.

Evidence for non-linear flow is assessed for each of the four samples within the subsections below by plotting the fluid pressure gradient across the sample as a function of sample flow rate for each pressure/temperature scenario. From Equations 2.4 and 2.12 we can see that a straight line plot would be observed if linear (viscous) flow occurs, while a quadratic function is expected if inertial effects are significant. No evidence for inertial effects was observed for the lowest transmissivity sample, East Brae D2, within the limited flow rates tested, although results suggest fracture dilation may be

occurring. Evidence for a non-linear Forchheimer flow regime was observed for the other three samples: Wissey W3, East Brae B2b (offset) and Cambrian V1, suggesting significant inertial effects during CO_2 flow through these fractured samples. Data presentation and comprehensive analysis and discussion of the flow regime findings for each sample is contained within the following subsections.

In association with the flow regime analysis, appropriate sample transmissivity (T) estimates for linear cases and true transmissivity (T_0) estimates for non-linear cases have been derived for each pressure/temperature scenario, where possible, using regression analysis. As stated within section 7.1, these T and T_0 estimates are utilised within sections 7.5 to 7.8 as indicators to assess fracture response to mechanical and hydraulic processes during experiments.

7.3.2 East Brae D2 sample

The observed differential pressure across the artificially fractured East Brae D2 shale sample during experiments was extremely high (Figure 7.3) due to the very low conductivity of the sample (Figure 7.4). As a result, only a limited number of experimental scenarios could be assessed at a single temperature (37°C) due to the constraints of the rig and the long time period required to achieve steady state conditions for each scenario (Chapter 6). The fluid pressure scenarios adopted were 10, 15 and 20 MPa, with confining pressure scenarios of 35, 45 and 55 MPa.

A very limited range of low flow rates were tested during the East Brae D2 experiments. Therefore the Reynolds numbers remained relatively low, within the range 2 to 13 for low to high flow rates respectively.

Figure 7.5 illustrates the pressure gradients as a function of flow rate for the East Brae D2 experiments (with linear regression lines added for reference). Due to the high differential pressures observed, the differential pressure measurement error (and thus pressure gradient error) during these experiments is low. However, there is significant scatter between measurements during these experiments. This is mainly due to observed inelastic hysteresis, which is thought to be a result of permanent mechanical changes of the fracture resulting from stress loading (see section 7.6 for details). Prior stress loading of the sample to minimise these hysteresis effects was not undertaken for this sample due to the initial very low transmissivity of the sample and concerns that stress

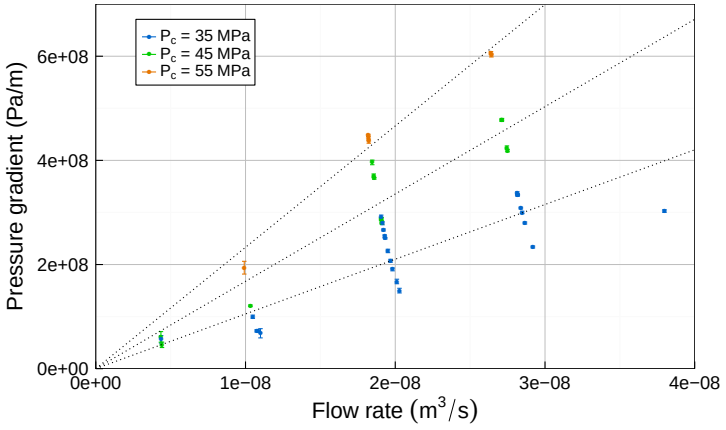

(A) P_{ds} = 10 MPa (LOW)

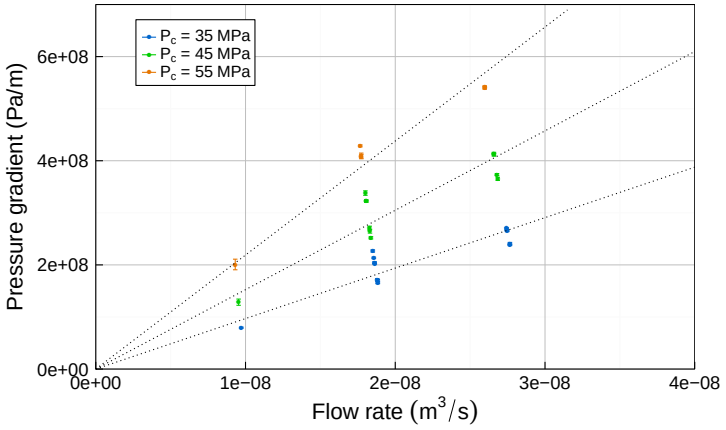

(B) P_{ds} = 15 MPa (MIDDLE)

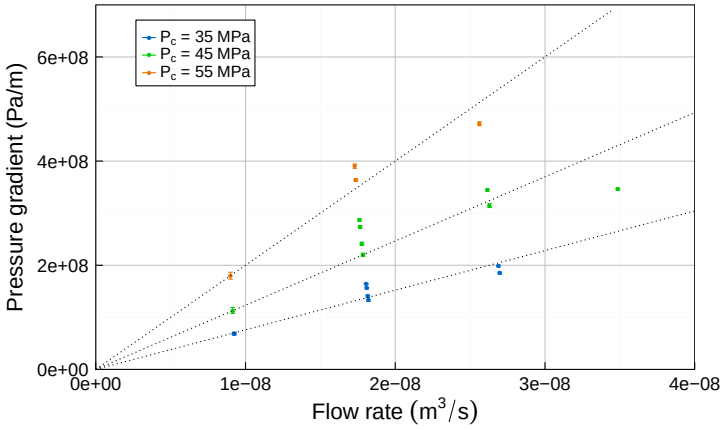

(C) P_{ds} = 20 MPa (HIGH)

FIGURE 7.5: Sample East Brae D2 (37°C): Differential pressure gradient as a function of flow rate

loading would further reduce transmissivity to the extent that no measurements would be possible.

A deviation from linearity can be observed in all D2 sub-plots (Figure 7.5). Rather than an increase in the gradient $\nabla P/Q$, anticipated if inertial effects or frictional losses become significant (as in the Forchheimer equation, Equation 2.12), a decrease in $\nabla P/Q$ is observed. This deviation from linearity may indicate fracture aperture dilation due to excessive pressures upstream of the sample [Quinn et al., 2011]. Alternatively, leakage or bypassing of the sample could result in similar $\nabla P/Q$ gradient deviations. The observed pressure gradients during the East Brae D2 experiments were however extremely high, and it is therefore reasonable to suggest that fracture dilation may be occurring during these experiments. Of the samples tested, this negative deviation from linearity is only observed within the East Brae D2 sample, where the $\nabla P/Q$ gradients are significantly higher than those observed for the other samples.

Despite the deviation from linearity observed within Figure 7.5, Darcy's law (Equation 2.4) has been used to provide an estimate of sample transmissivity for each pressure scenario tested, where transmissivity, $T = kA$ (m^4). To account for the effects of mean viscosity variation with flow rate, discussed in section 7.4, transmissivity estimates have been derived from linear regression model fits (with intercept equal to zero) applied to $\nabla P/\mu$ versus Q plots (Figure 7.6), rather than the ∇P versus Q plots in Figure 7.5. Thus the gradient, a, of the linear model is $1/T$, rather than μ/T, which is unsuitable due to significant μ variation with Q. The model fit parameters associated with the linear regressions in Figure 7.6 are provided within Table 7.4 along with the associated transmissivity estimates.

Both Figure 7.5 and Figure 7.6 include vertical error bars, which indicate measurement errors associated with the experimental parameters. The error bars in Figure 7.6 do not incorporate the viscosity variance between the upstream and downstream ends of the sample which is high due to the large differential pressures observed during experiments. This is most significant for the low fluid pressure scenario (see section 7.4), and is presented using vertical bars in Figure 7.7, for information.

The R^2 values within Table 7.4 indicate that the experimental data closely fit the linear regression models despite the observed deviation from linearity which may be related to fracture dilation or fluid leakage or bypassing within the experimental rig. The deviation from linearity may cause a small underestimation of the linear gradient for each

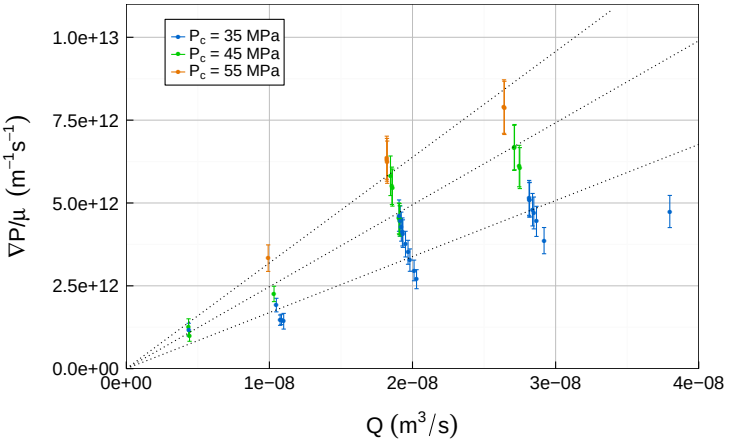

(A) P_{ds} = 10 MPa (LOW)

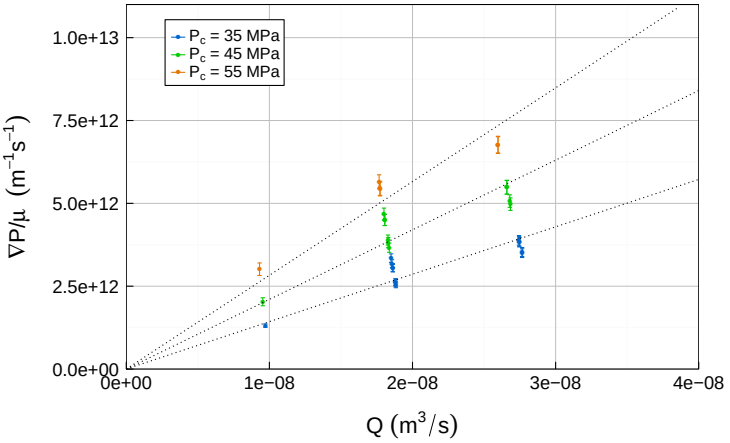

(B) P_{ds} = 15 MPa (MIDDLE)

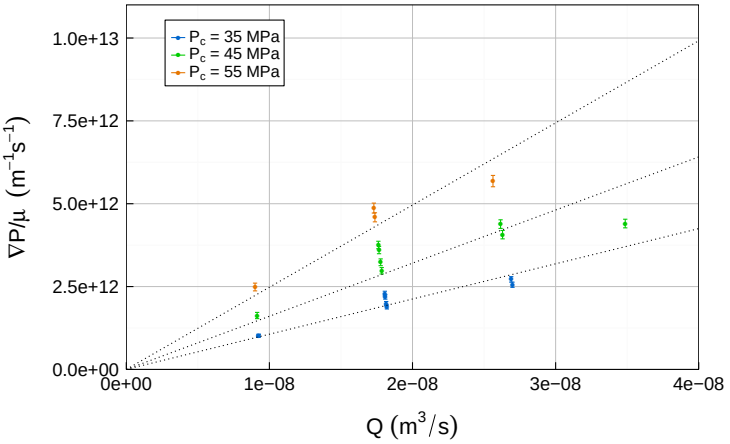

(C) P_{ds} = 20 MPa (HIGH)

FIGURE 7.6: Sample East Brae D2 (37°C): Differential pressure gradient/viscosity as a function of flow rate.

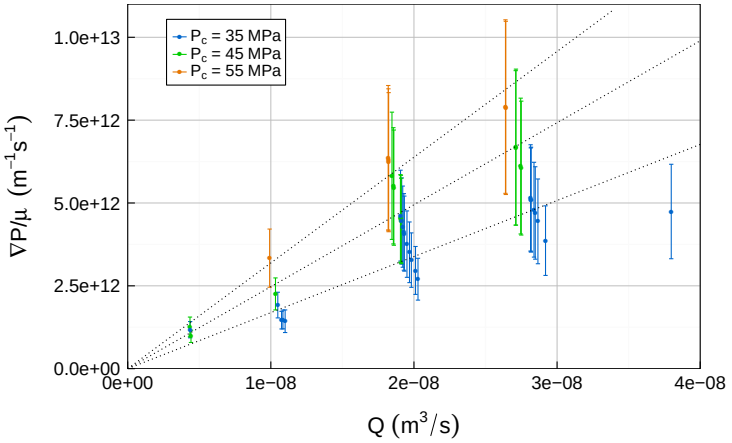

FIGURE 7.7: Sample East Brae D2 (37°C): Differential pressure gradient/viscosity as a function of flow rate for P_{ds} = 10 MPa, with viscosity variance error bars.

TABLE 7.4: East Brae D2 - Linear regression of pressure gradient/viscosity vs. flow rate. [$a = 1/T$ is the gradient of the linear model fits]

P_c (MPa)	P_{ds} (MPa)	a	T (m^4)	R^2
35	10	1.69×10^{20}	5.91×10^{-21}	0.9645
45	10	2.47×10^{20}	4.04×10^{-21}	0.9862
55	10	3.19×10^{20}	3.13×10^{-21}	0.9948
35	15	1.43×10^{20}	6.99×10^{-21}	0.9884
45	15	2.10×10^{20}	4.76×10^{-21}	0.9882
55	15	2.83×10^{20}	3.54×10^{-21}	0.9916
35	20	1.06×10^{20}	9.41×10^{-21}	0.9901
45	20	1.60×10^{20}	6.24×10^{-21}	0.9701
55	20	2.48×10^{20}	4.03×10^{-21}	0.9888

pressure scenario which would result in a fractional overestimation in transmissivity values. However, this effect is likely to be small, and is consistent across all pressure scenarios, therefore the general transmissivity magnitudes are considered reasonably accurate and the relative transmissivities between pressure scenarios are also considered representative. It can be seen from Table 7.4 that transmissivity decreases with increasing confining pressure under constant fluid pressure, and also that transmissivity increases with increasing fluid pressure under constant confining pressure for the East Brae D2 experiments. These observations are discussed further within section 7.5.

7.3.3 Wissey W3 sample

As stated in section 7.3.1, a more comprehensive set of flow experiments was carried out on the Wissey W3 sample than the East Brae D2 sample, with a wider range of flow rates tested, and experiments undertaken at two temperatures. Multiple stress loading cycles were carried out during the experiments (Chapter 6, Figure 6.8). Initial stress loading cycles were observed to result in inelastic changes to sample transmissivity (section 7.6). Inelastic effects were significant during the first experiment (Experiment A) and the first two stages of Experiment B. To ensure that inelastic effects did not impact on flow regime analysis, datasets from stages 3 to 9 of Experiment B, and all of Experiment C1 are therefore used within this section for flow regime analysis.

Due to the higher flow rates tested during the Wissey W3 sample experiments, the Reynolds number ranges were higher than for the East Brae D2 experiments: 5 to 90 for the low temperature (38°C) experiments and 7 to 233 for the high temperature (58°C) experiments.

Figures 7.8 and 7.9 present the observed differential pressure gradient as a function of flow rate at 38°C (Experiment C1) and 58°C (Experiment B) respectively for the Wissey sample.

It is clear from Figures 7.8 and 7.9 that a non-linear flow regime is present for all Wissey W3 pressure and temperature scenarios, within the flow rate ranges tested. To assess the suitability of the Forchheimer equation (Equation 2.12) in describing the observed flow regime, a modified Forchheimer Plot method has been adopted (see Chapter 2, section 2.4 for details).

Figures 7.10 and 7.11 contain the modified Forchheimer Plots for 38°C (Experiment C1) and 58°C (Experiment B) respectively. The error bars illustrate the measurement error associated with the experimental parameters for each measurement data point; they do not incorporate the viscosity variance between the upstream and downstream ends of the sample. The fluid property (viscosity and density) variance with flow rate is accounted for within these linear plots, through incorporation of these variable parameters into both $X = \rho Q/\mu$ and $Y = -\nabla P/\mu Q$.

Linear regression has been applied to the nine pressure scenario subsets for each of the two temperatures assessed. These regression models are displayed as dotted lines

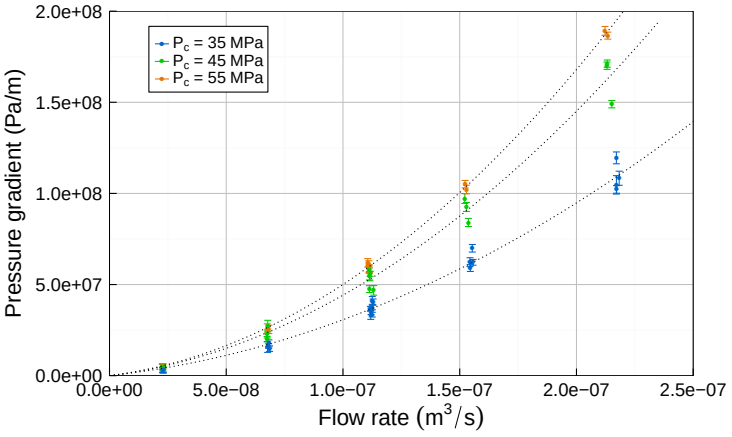

(A) P_{ds} = 10 MPa (LOW)

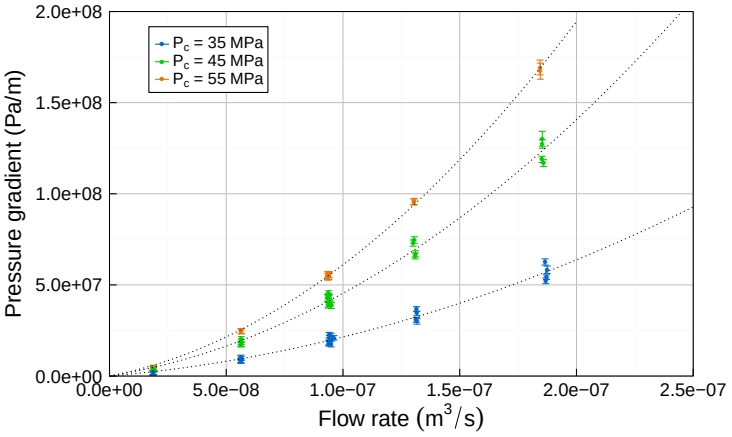

(B) P_{ds} = 20 MPa (MIDDLE)

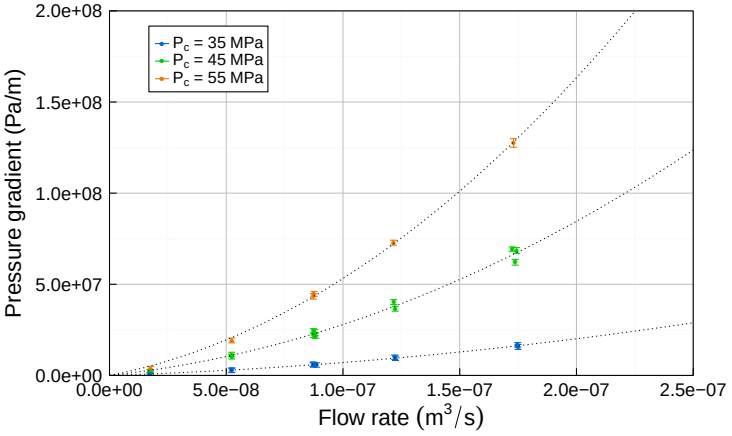

(C) P_{ds} = 30 MPa (HIGH)

FIGURE 7.8: Sample Wissey W3, Expt C1 (38°C): Differential pressure gradient as a function of flow rate

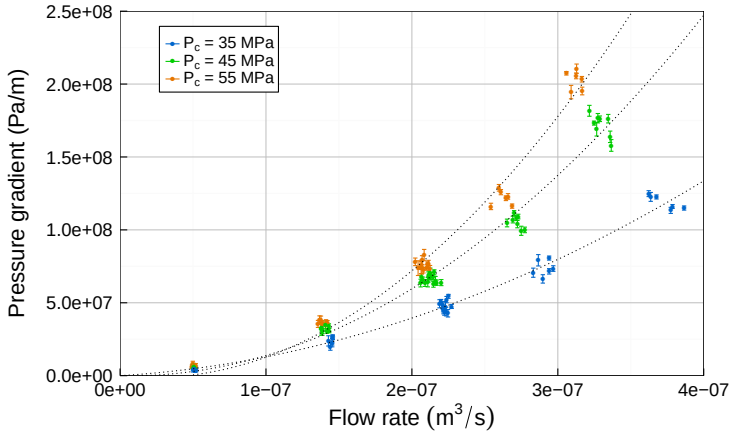

(A) P_{ds} = 10 MPa (LOW)

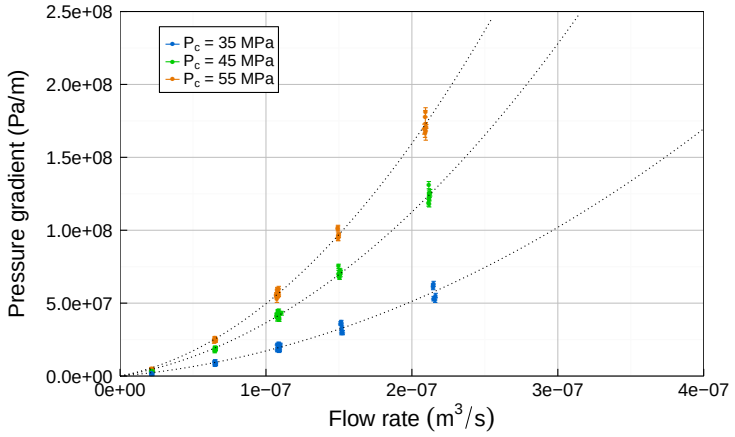

(B) P_{ds} = 20 MPa (MIDDLE)

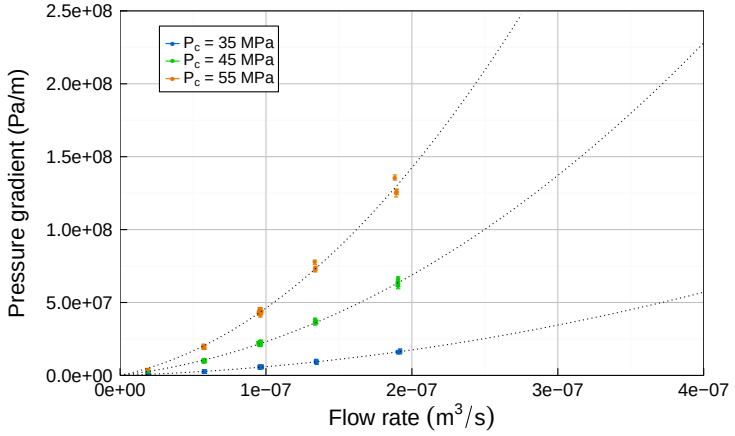

(C) P_{ds} = 30 MPa (HIGH)

FIGURE 7.9: Sample Wissey W3, Expt B (58°C): Differential pressure gradient as a function of flow rate

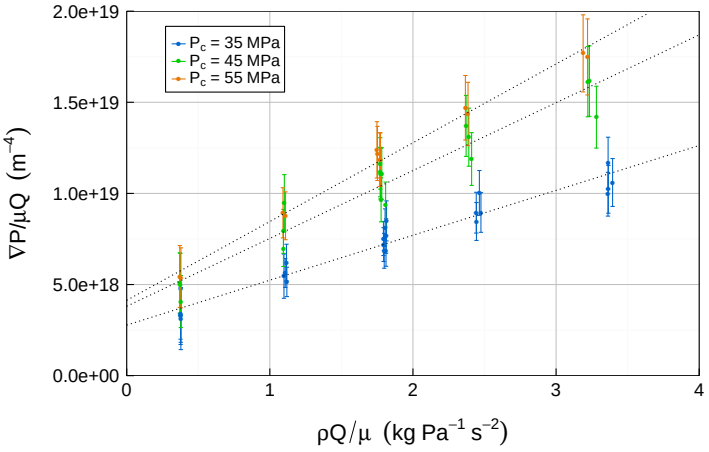

(A) P_{ds} = 10 MPa (LOW)

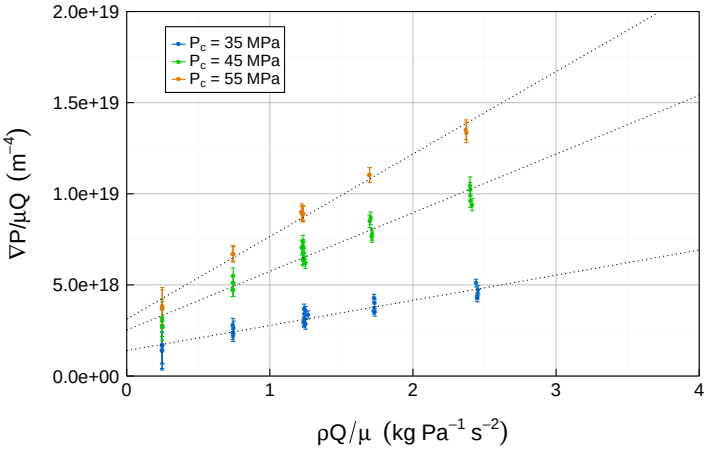

(B) P_{ds} = 20 MPa (MIDDLE)

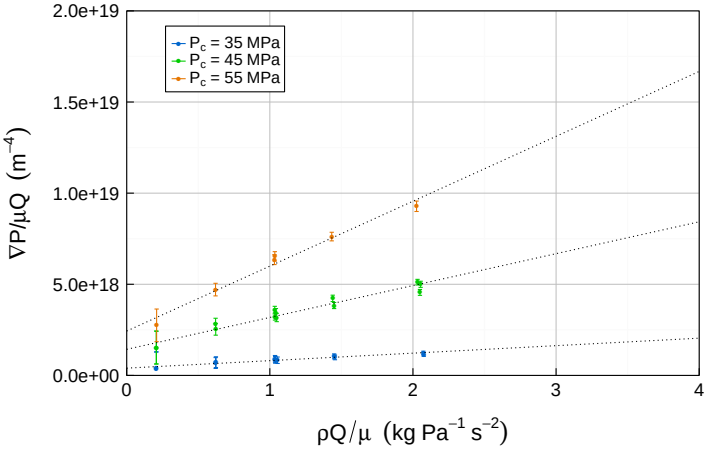

(C) P_{ds} = 30 MPa (HIGH)

FIGURE 7.10: Sample Wissey W3, Expt C1 (38°C): Modified Forchheimer Plots

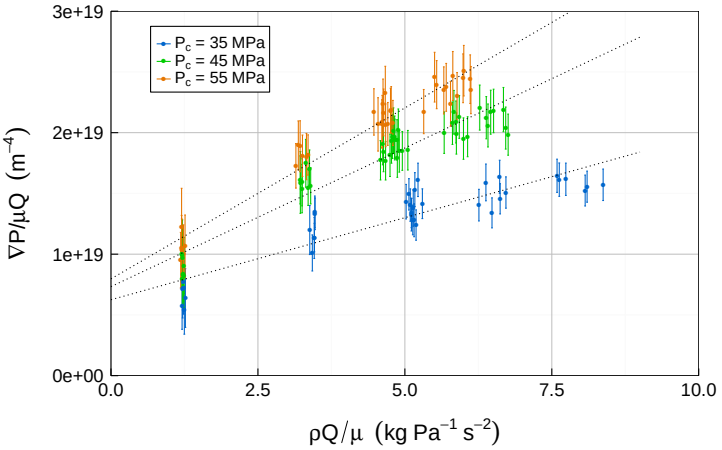

(A) P_{ds} = 10 MPa (LOW)

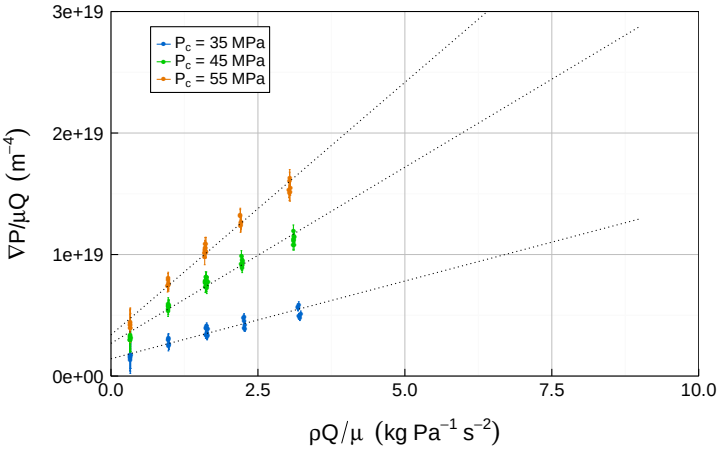

(B) P_{ds} = 20 MPa (MIDDLE)

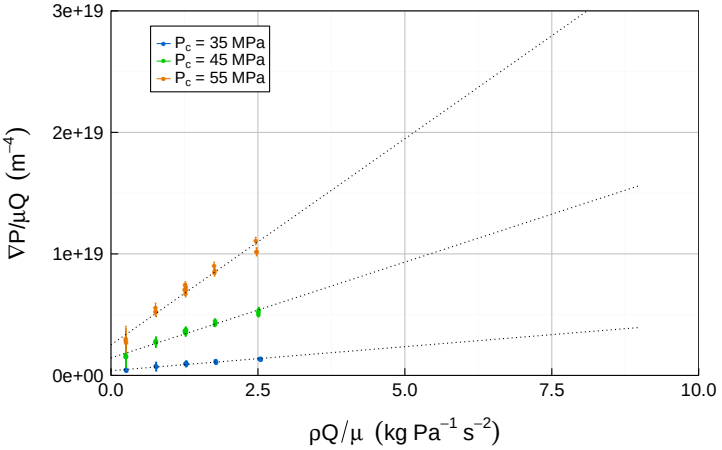

(C) P_{ds} = 30 MPa (HIGH)

FIGURE 7.11: Sample Wissey W3, Expt B (58°C): Modified Forchheimer Plots

within the figures. As described in section 2.4, the model intercept from the regressions determines the true transmissivity, T_0, estimates.

Table 7.5 presents the linear regression parameters, a' and b' for each of the 18 pressure/temperature scenarios, along with the coefficient of determination, R^2, associated with the linear regression fit. The true transmissivity, $T_0 = 1/a'$ is also presented within the table. The ratio b'/a' gives an indication of the relative contribution to non-linearity of the sample geometry (see Equation 2.14), and has therefore also been included within the table.

TABLE 7.5: Wissey W3 - Modified Forchheimer Plot linear regression parameters, and associated T_0 estimates

P_c (MPa)	P_{ds} (MPa)	a'	b'	R^2	T_0 (m^4)	b'/a'
Low Temperature (38 °C)						
35	10	2.78×10^{18}	2.46×10^{18}	0.9392	3.60×10^{-19}	0.89
45	10	3.81×10^{18}	3.72×10^{18}	0.9310	2.63×10^{-19}	0.98
55	10	4.13×10^{18}	4.32×10^{18}	0.9917	2.42×10^{-19}	1.03
35	20	1.40×10^{18}	1.38×10^{18}	0.9093	7.16×10^{-19}	0.99
45	20	2.52×10^{18}	3.22×10^{18}	0.9558	3.96×10^{-19}	1.28
55	20	3.13×10^{18}	4.53×10^{18}	0.9881	3.20×10^{-19}	1.45
35	30	3.99×10^{17}	4.11×10^{17}	0.9390	2.51×10^{-18}	1.03
45	30	1.43×10^{18}	1.75×10^{18}	0.9550	6.99×10^{-19}	1.22
55	30	2.44×10^{18}	3.56×10^{18}	0.9782	4.11×10^{-19}	1.46
High Temperature (58 °C)						
35	10	6.25×10^{18}	1.35×10^{18}	0.8217	1.60×10^{-19}	0.22
45	10	7.33×10^{18}	2.28×10^{18}	0.9139	1.36×10^{-19}	0.31
55	10	7.97×10^{18}	2.81×10^{18}	0.9471	1.25×10^{-19}	0.35
35	20	1.42×10^{18}	1.28×10^{18}	0.9173	7.04×10^{-19}	0.90
45	20	2.69×10^{18}	2.90×10^{18}	0.9723	3.72×10^{-19}	1.08
55	20	3.39×10^{18}	4.16×10^{18}	0.9822	2.95×10^{-19}	1.23
35	30	3.91×10^{17}	3.95×10^{17}	0.9610	2.56×10^{-18}	1.01
45	30	1.44×10^{18}	1.58×10^{18}	0.9683	6.97×10^{-19}	1.10
55	30	2.51×10^{18}	3.39×10^{18}	0.9679	3.98×10^{-19}	1.35

The linear regression models are observed to fit the datasets well (Figures 7.10 and 7.11), which suggests that the Forchheimer equation is appropriate for describing the flow regime during the Wissey CO_2 flow experiments. There is notable scatter within

the high temperature, low fluid pressure (P_{ds} = 10MPa) experiments (Figure 7.11a), which is reflected in the slightly lower associated R^2 values, particularly for the P_c=35 MPa scenario. Scatter is also observed to be highest for the low fluid pressure scenarios during the low temperature experiments (Figure 7.10a). This scatter is likely to be due to measurement errors, which are most significant at low fluid pressures due to the higher sensitivity of viscosity and density, particularly under the high temperature scenario (section 2.5).

Despite the scatter observed during low fluid pressure scenarios, all model fits are good (refer to R^2 values in Table 7.5), and the true transmissivity estimates appear to be of realistic magnitudes. In a similar manner to the East Brae D2 transmissivities, the true transmissivity estimates for Wissey are observed to decrease with increasing confining pressure under constant fluid pressure, and increase with increasing fluid pressure under constant confining pressure. These observations are discussed further within section 7.5.

Considerable variance is observed in b'/a' between scenarios. While the Forchheimer number provides a measure of the significance of inertial flow resulting from both turbulent flow and the physical structure of the flow paths, b'/a' is the component of the Forchheimer number describing the latter (Equation 2.14). Notably, it is observed that b'/a', and thus the significance of non-linearity due to sample geometry, increases with increasing confining pressure. This is in line with expectations for a discrete fracture, as an increase in confining pressure is thought to be associated with a reduction in fracture aperture (see section 7.5). A decrease in fracture aperture, as well as reducing transmissivity, will result in increased flow path tortuosity and increased significance of frictional effects.

For a given temperature and confining pressure, b'/a' values are also, generally (with one exception), observed to increase with fluid pressure for the Wissey sample. The effects on non-linearity of fluid pressure changes are more complex than confining pressure changes as both mechanical and fluid property effects occur, which influence non-linear flow in different ways. An increase in fluid pressure may be expected to increase fracture aperture (see section 7.5), potentially reducing flow tortuosity through contact area reduction; while an increase in fluid pressure is also associated with higher viscosity, and thus increased inertial effects arising from interaction between the fluid and the rock surfaces (friction and other interfacial processes). The increase in b'/a' observed with fluid pressure for the Wissey sample suggests that the increase in inertial/interfacial

effects due to the fluid pressure/viscosity increase may be more significant than the reduction in flow path tortuosity resulting from any associated aperture opening within these experiments.

The b'/a' values are observed to be higher during the low temperature experiments than the high temperature experiments, which suggests that non-linear flow effects are more significant at lower temperatures for this sample, potentially due to the higher associated viscosities.

One method of visually presenting the significance of the non-linearity is to compare true transmissivity, T_0, to apparent transmissivity, T_{app}, where apparent transmissivity (Equation 2.13) is calculated by analogy with linear Darcy's law [Zhang and Nemcik, 2013, Zimmerman et al., 2004].

Apparent transmissivities, T_{app}, have been calculated from observed data for each experimental step (Equation 2.13). These apparent transmissivities have been normalised against associated true transmissivity values, and are plotted as points within Figures 7.12 and 7.13 for low temperature and high temperature experiments respectively. If a linear flow regime was present, the apparent transmissivity would be equal to the true transmissivity, and thus the normalised apparent transmissivities (T_{app}/T_0) would be constant and equal to one at all flow rates. However, where non-linearity does exist, apparent transmissivity, T_{app}, varies with flow rate while true transmissivity, T_0, is a constant for each pressure/temperature scenario. Therefore the deviation of normalised apparent transmissivity from a value of one indicates the significance of non-linearity within the flow regime as a function flow rate.

As well as use of the measured apparent transmissivities calculated from experimental data points, apparent transmissivity may be computed from associated T_0 and F_0 estimates using the Forchheimer equation (Equation 2.15 form).

Computed apparent transmissivity data have been presented as lines within Figures 7.12 and 7.13 alongside the measured point data.

As can be seen from both Figure 7.12 and Figure 7.13, both the measured and computed apparent transmissivities are observed to decrease hyperbolically with increasing flow rate. The decreasing apparent transmissivity trend is similar for all pressure and temperature scenarios indicating that the non-linear term is significant for all scenarios.

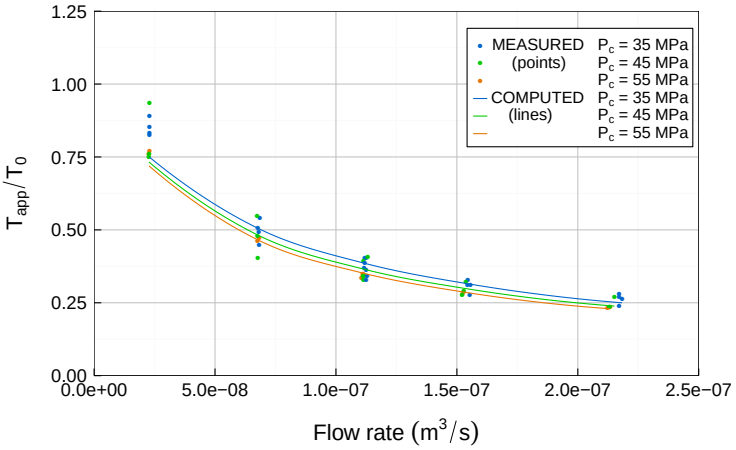

(A) P_{ds} = 10 MPa (LOW)

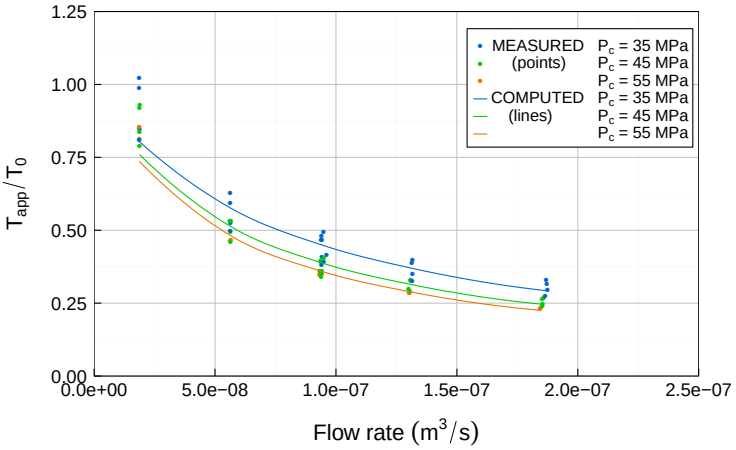

(B) P_{ds} = 20 MPa (MIDDLE)

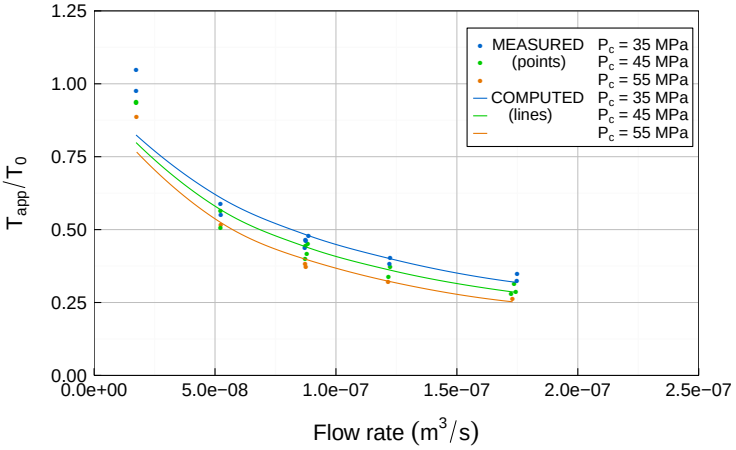

(C) P_{ds} = 30 MPa (HIGH)

FIGURE 7.12: Sample Wissey W3, Expt C1 (38°C): T_{app}/T_0 as a function of flow rate

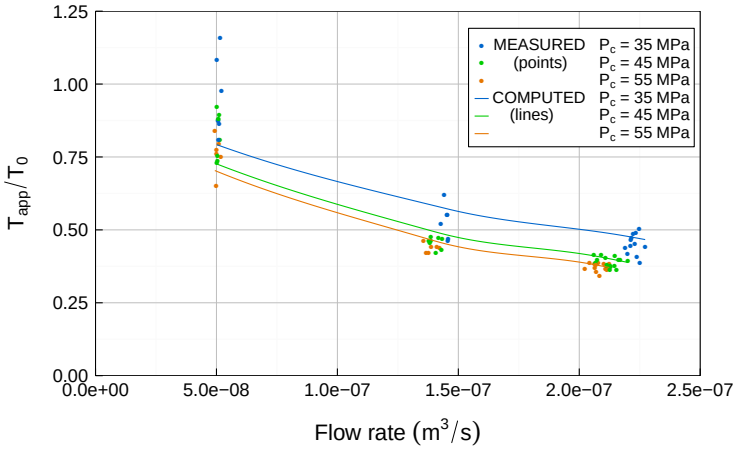

(A) P_{ds} = 10 MPa (LOW)

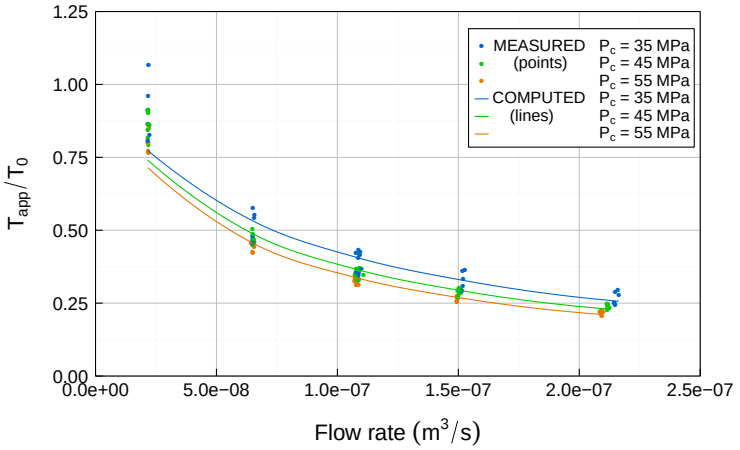

(B) P_{ds} = 20 MPa (MIDDLE)

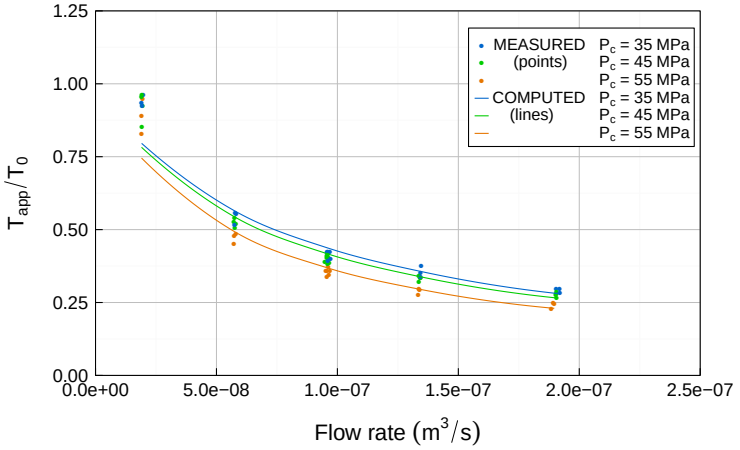

(C) P_{ds} = 30 MPa (HIGH)

FIGURE 7.13: Sample Wissey W3, Expt B (58°C): T_{app}/T_0 as a function of flow rate

At low flow rates the effects of non-linearity are smaller and the apparent transmissivity becomes closer to the true transmissivity value. We would expect that for very low flow rates, where non-linear effects become insignificant ($F_0 \rightarrow 0$), the ratio of T_{app}/T_0 would approach one, as the apparent transmissivity approaches the true transmissivity estimate. This can be seen within the computed apparent transmissivities for all scenarios.

The measured apparent transmissivities closely match the computed values for most scenarios at high flow rates, particularly within the low temperature experiments (Figure 7.12), validating the appropriateness of the Forchheimer model fits. However, at low flow rates, the measured T_{app} values deviate and generally exceed the computed values. This is true for both low and high temperature experiments, although it is slightly more notable within the higher temperature experiments. The measured T_{app}/T_0 values approach 1.05 at the lowest flow rates for the P_{ds}=30 MPa low temperature experiment, while values reach 1.16 within the P_{ds} = 10 MPa high temperature experiments, indicating that the observed T_{app} values at low flow rates are higher than predicted by the Forchheimer model for these scenarios. These deviations are considered most likely to be due to experimental errors. A small overestimation of flow rate could occur if the fluid temperature has not fully equalised with the sample temperature, or if any CO_2 leakage occurs between the upstream pump and the sample. Prior issues with the experimental rig set-up, discussed in Chapter 5, have been minimised during the project, however residual issues are likely to remain towards the lower limits of our measurement range, given the various difficulties discovered in association with supercritical CO_2 use.

The main findings of the flow regime analysis for the Wissey W3 sample still stand despite the T_{app} deviations observed at low flow rates. These findings suggest that a non-linear flow regime exists for all pressure and temperature scenarios tested, within the flow rate ranges adopted. The Forchheimer equation suitably describes the observed flow regime in all cases, although there is higher uncertainty associated with the model fits within the low fluid pressure scenarios due to scatter within the datasets. This is likely to be due to higher measurement uncertainties within these scenarios due to fluid density and viscosity sensitivity at low pressure (section 7.4).

Confidence in the true transmissivity estimates is gained through comparison with apparent transmissivity values, which are calculated from experimental data by analogy

with linear Darcy's law. The true and apparent transmissivity estimates are the same order of magnitude. Apparent transmissivities decrease as flow rate increases, reflecting an increase in the significance of non-linear inertial effects. At high flow rates the apparent transmissivities are significantly lower than the true transmissivities (T_{app}/T_0 approaches 0.2); while at low flow rates the apparent transmissivities are close to the true transmissivity estimates. These findings illustrate the significance of non-linear effects observed during the experiments. Consequently, the true transmissivity estimates (Table 7.5), derived using the Forchheimer equation, will be used within subsequent chapter sections for analysis of hydro-mechanical observations, to minimise the potential interference of non-linearity.

7.3.4 Cambrian V1 sample

As with the Wissey sample, significant inelastic stress loading change was observed during both Experiment A (38°C) and the first two stages of Experiment B (58°C) for the Cambrian V1 experiments (see section 7.6). Due to this these datasets/subsets have not been used within flow regime analysis. Datasets used within this section for flow regime analysis are from stages 3 to 5 of Experiment B (58°C) and Experiment C (38°C). However, as can be seen from Chapter 6, Figure 6.1, a reduced set of scenarios was undertaken for Experiment C, and thus analysis is available at low confining pressures only for the low temperature case.

It is noted that post-experiment, the Cambrian shale sample was observed to contain micro-fractures in addition to the main induced longitudinal fracture (section 4.9). It is thought that these micro-fractures may have been induced during stress-loading and may affect transmissivities observed during the experiments. Transmissivities could be affected through activation of additional flow pathways within the micro-fracture network under certain pressure conditions. There was no external evidence of continuous longitudinal micro-fractures, therefore any additional transmissivity resulting from the micro-fractures is expected to be small relative to the transmissivity associated with the main induced longitudinal fracture. However, if activation of micro-fractures occurs during the CO_2 flow experiments, the significance of non-linearity is likely to increase due to the tortuosity associated with the micro-fracture flow paths.

The Reynolds number range within the low temperature experiment (Experiment C) was 7 to 102, while within the high temperature experiment (Experiment B), the range

was 7 to 335. The low temperature range is similar to that of the Wissey experiments, as expected due to adoption of the same flow rate ranges (section 7.3.1). However, for the high temperature experiments, the Reynolds numbers become much higher for the Cambrian V1 low fluid pressure scenarios than for the Wissey low fluid pressure scenarios. This is due to the notable variance of both CO_2 density and viscosity around this fluid pressure (10 MPa). As discussed in section 7.2, the transmissivity of the Cambrian V1 fractured sample was high which meant the observed differential pressures were much lower than those observed during the Wissey W3 experiments. As a result of the very low differential pressures during the Cambrian V1 experiments, the mean sample pressure was notably lower than during the Wissey experiments. The lower mean fluid pressure within the sample meant the density/viscosity ratio was higher, leading to higher Reynolds numbers (Equation 2.11) than those estimated for the Wissey W3 sample (see section 7.4).

Figures 7.14 and 7.15 present the observed fluid pressure gradient as a function of flow rate at 38°C (Experiment C) and 58°C (Experiment B - stages 3-5 only) respectively for the Cambrian V1 sample. Due to the very low differential pressures the relative errors associated with these measurements were quite high, as can be seen within the figures. Despite this the figures still clearly suggest that a non-linear flow regime exists for all pressure scenarios, as with the Wissey W3 sample, within the flow rate ranges tested. For the high temperature experiments the pressure gradient is observed to increase with confining pressure (see section 7.5), although there is little difference in pressure gradients observed between the $P_c = 45$ MPa and $P_c = 55$ MPa scenarios when $P_{ds} = 10$ MPa.

Modified Forchheimer Plots for the Cambrian V1 sample data are provided in Figures 7.16 and 7.17 for 38°C (Experiment C) and 58°C (Experiment B) respectively. Within these plots it can be observed that the combined measurement errors (illustrated using error bars) are very large at low flow rates due to the significance of the differential pressure error contribution, arising from differential pressure measurements taken towards the lower limit of the instrument range under low flow rates.

Linear regression has been applied to each pressure/temperature scenario for both low and high temperature experiments, displayed as dotted lines within the figures. Table 7.6 provides details of the linear regression model parameters and the associated coefficient of determination, R^2. The table also presents the true transmissivities, T_0,

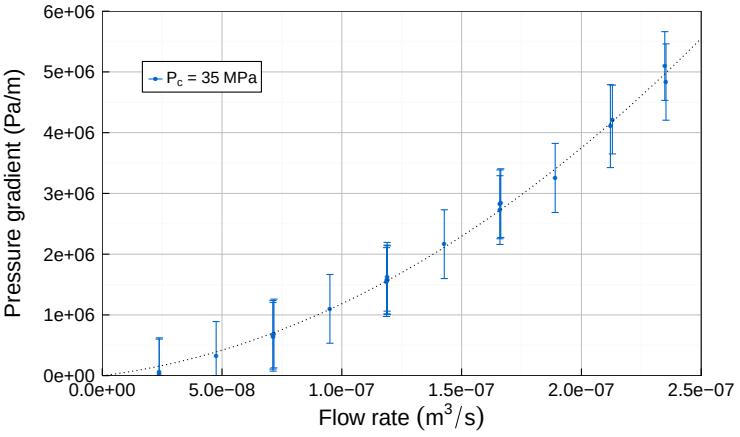

(A) P_{ds} = 10 MPa (LOW)

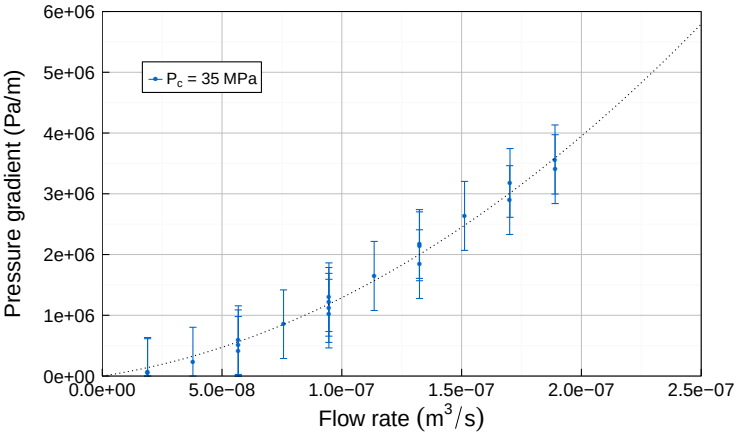

(B) P_{ds} = 20 MPa (MIDDLE)

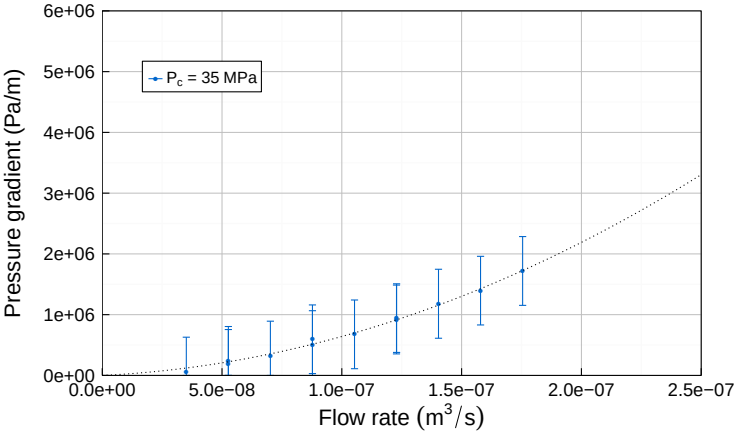

(C) P_{ds} = 30 MPa (HIGH)

FIGURE 7.14: Sample Cambrian V1, Expt C (38°C): Differential pressure gradient as a function of flow rate

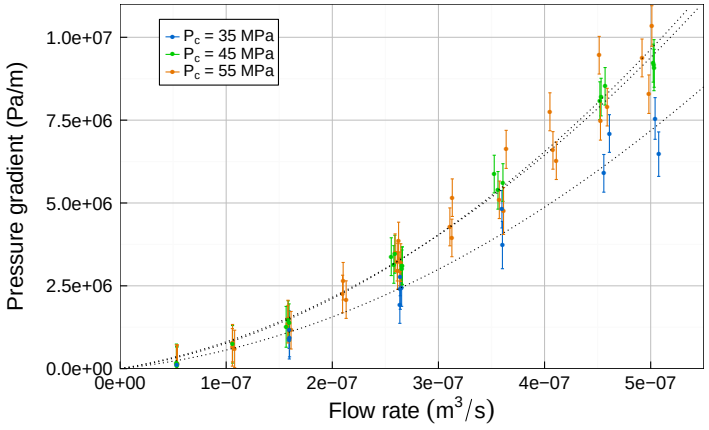

(A) P_{ds} = 10 MPa (LOW)

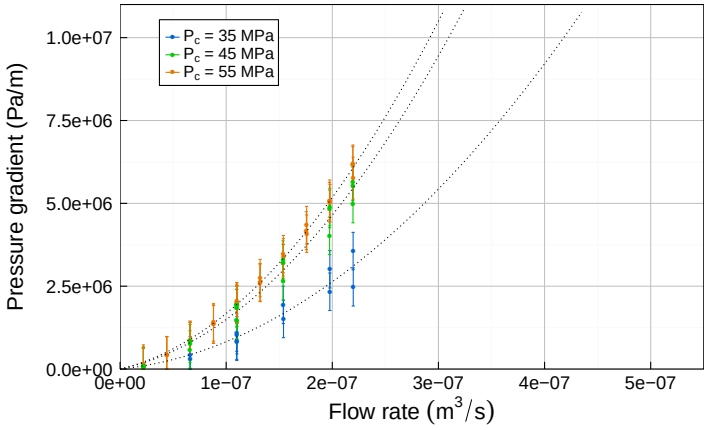

(B) P_{ds} = 20 MPa (MIDDLE)

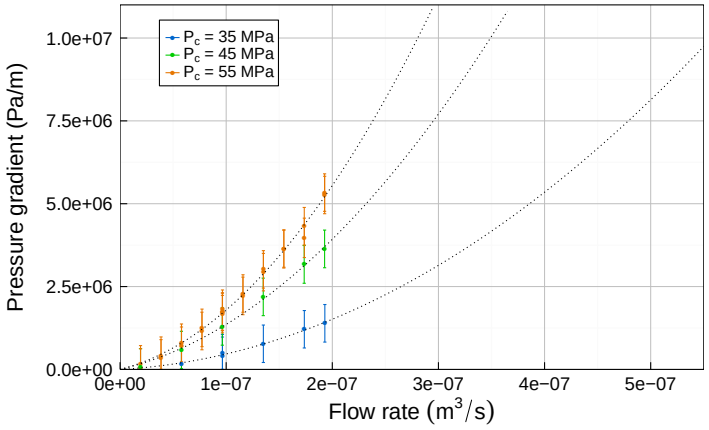

(C) P_{ds} = 30 MPa (HIGH)

FIGURE 7.15: Sample Cambrian V1, Expt B (58°C): Differential pressure gradient as a function of flow rate

estimated from the linear regression coefficients, a'. The value b'/a' has also been included within the table to enable review of the significance of inertial effects/non-linearity resulting from fracture geometry.

TABLE 7.6: Cambrian V1 - Modified Forchheimer Plot linear regression parameters, and associated T_0 estimates

P_c (MPa)	P_{ds} (MPa)	a'	b'	R^2	T_0 (m^4)	b'/a'
Low Temperature (38 °C)						
35	10	6.70×10^{16}	1.21×10^{17}	0.9509	1.49×10^{-17}	1.81
35	20	5.33×10^{16}	1.03×10^{17}	0.9208	1.88×10^{-17}	1.92
35	30	1.50×10^{16}	5.56×10^{16}	0.9416	6.69×10^{-17}	3.72
High Temperature (58 °C)						
35	10	1.89×10^{17}	7.82×10^{16}	0.8674	5.29×10^{-18}	0.41
45	10	2.19×10^{17}	1.06×10^{17}	0.9241	4.56×10^{-18}	0.48
55	10	2.48×10^{17}	1.06×10^{17}	0.8645	4.04×10^{-18}	0.43
35	20	5.15×10^{16}	7.35×10^{16}	0.7718	1.94×10^{-17}	1.43
45	20	7.10×10^{16}	1.39×10^{17}	0.9084	1.41×10^{-17}	1.96
55	20	1.03×10^{17}	1.47×10^{17}	0.9574	9.70×10^{-18}	1.43
35	30	1.98×10^{16}	3.89×10^{16}	0.9418	5.05×10^{-17}	1.96
45	30	5.97×10^{16}	1.02×10^{17}	0.9325	1.67×10^{-17}	1.71
55	30	9.06×10^{16}	1.38×10^{17}	0.9426	1.10×10^{-17}	1.53

Despite the large uncertainties associated with the differential pressure measurements, the linear regressions fit experimental data well within the low temperature experiments (Figure 7.16). There is more notable scatter present within the high temperature datasets (Figure 7.17), particularly within the low fluid pressure $P_{ds} = 10$ MPa scenarios. This is due to the higher fluid density and viscosity sensitivity around this fluid pressure and temperature, and thus there is an associated higher measurement uncertainty. There may also be some scatter due to inelastic change during the experiment, although this has been minimised by removal of severely affected data.

The coefficients of determination, R^2, in Table 7.6, indicate that the data do not fit the linear regression models quite as well within the high temperature, low fluid pressure scenarios, and also the $P_c = 35$ MPa, $P_{ds} = 20$ MPa scenario, due to the observed scatter. Despite this, the true transmissivity estimates are of a realistic magnitude for all pressure and temperature scenarios, and are likely to reflect the mean transmissivity

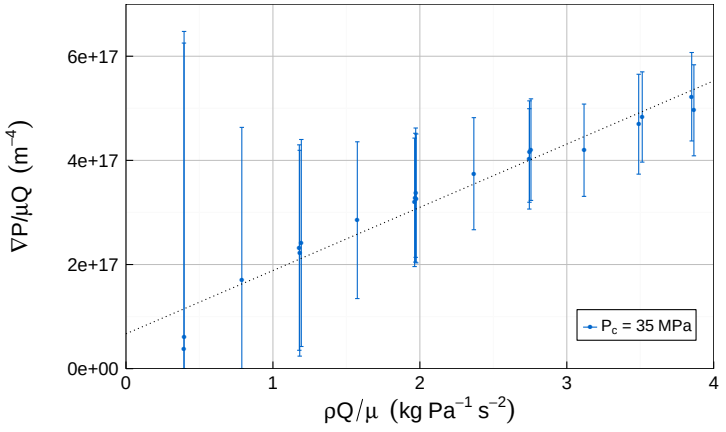

(A) P_{ds} = 10 MPa (LOW)

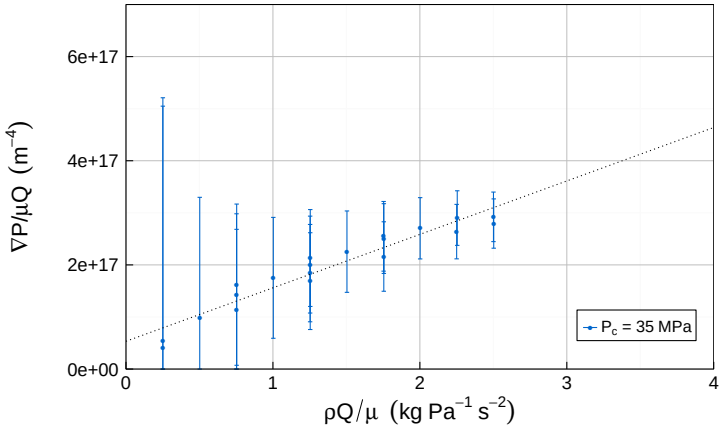

(B) P_{ds} = 20 MPa (MIDDLE)

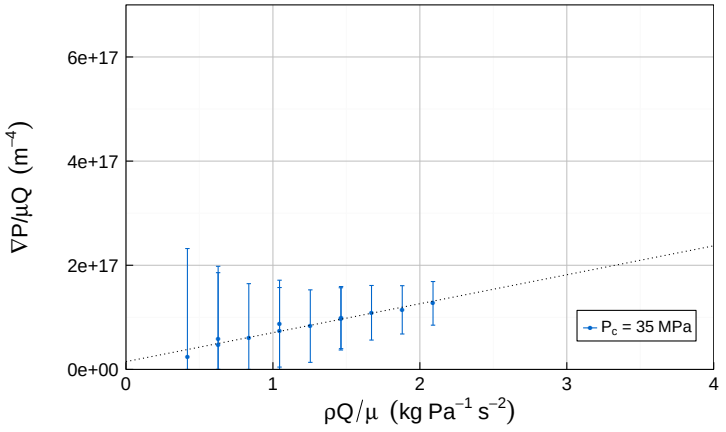

(C) P_{ds} = 30 MPa (HIGH)

FIGURE 7.16: Sample Cambrian V1, Expt C (38°C): Modified Forchheimer Plots

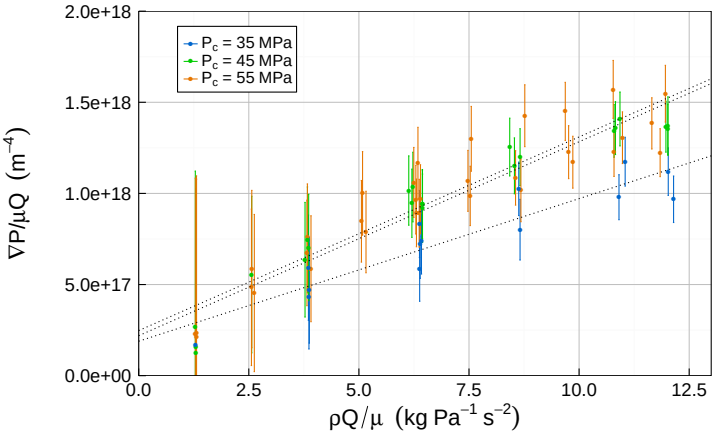

(A) P_{ds} = 10 MPa (LOW)

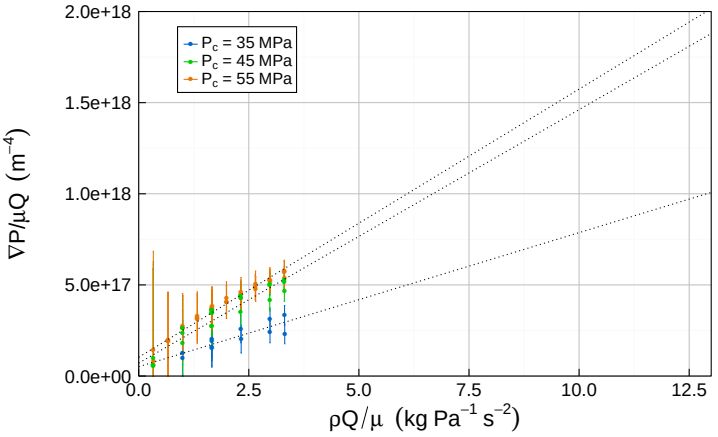

(B) P_{ds} = 20 MPa (MIDDLE)

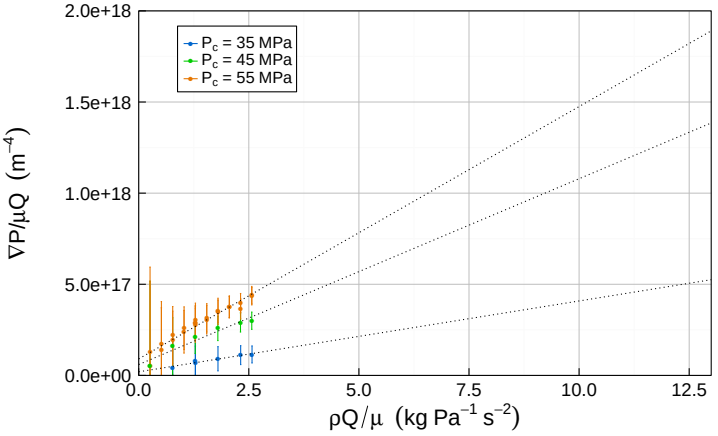

(C) P_{ds} = 30 MPa (HIGH)

FIGURE 7.17: Sample Cambrian V1, Expt B (58°C): Modified Forchheimer Plots

observed within each scenario. The change in true transmissivity observed between pressure and temperature scenarios is consistent with the true transmissivity behaviour of the Wissey W3 sample, as well as the transmissivity behaviour of the East Brae D2 sample, namely an increase in transmissivity with increasing fluid pressure and a decrease in transmissivity with increasing confining pressure. These observations are discussed further in section 7.5.

As expected, the true transmissivity estimates associated with the Cambrian sample are significantly higher than those of the Wissey sample. The b'/a' numbers associated with the Cambrian V1 sample are also notably higher than those estimated for the Wissey sample. This suggests that the significance of non-linearity associated with fluid-rock interactions is greater for the Cambrian V1 sample, in addition to higher transmissivities.

Comparison of b'/a' values between low temperature and high temperature experiments for equivalent pressure scenarios show that b'/a' values are higher at the low temperature (38°C), as observed during the Wissey experiments. This suggests non-linearity effects are greater during the low temperature experiments, which may be due to the higher associated fluid viscosities.

Within the high temperature experiments, where confining pressures were varied, there is not a consistent correlation between b'/a' values and confining pressure change. For high fluid pressures, b'/a' decreases as confining pressure increases, while at the lower fluid pressures, the highest b'/a' value is for the middle confining pressure scenario. This does not align with our observations for the Wissey sample, where b'/a' values consistently increased with confining pressures. As discussed earlier, micro-fractures were observed within the Cambrian sample post-experiment; activation of micro-fractures may therefore occur during some of the flow scenarios. This would be expected to have a notable increase to observed non-linearity due to a significant increase in flow tortuosity and fluid-rock frictional effects. An observed decrease in non-linear significance could therefore result either from: a) closure of micro-fracture channels thus reducing tortuosity of flow paths by channeling flow into fewer, more direct, flow path channels; or b) opening of fracture channels thus reducing tortuosity within the channel itself. This could explain the inconsistencies in b'/a' patterns with changing confining pressure observed between fluid pressure scenarios. Opening of micro-fractures is most likely under low effective stresses (high fluid pressures), however fluid properties

may also impact micro-fracture flow with micro-fractures more likely to be conductive to lower viscosity fluids, i.e. low fluid pressures. The situation is therefore complex, however it may be possible that during the P_{ds} = 30 MPa scenarios, for example, the reduction in b'/a' values observed with increasing confining pressure may be related to closure of micro-fracture channels.

For both the low and high temperature experiments, the b'/a' values (with one exception) are observed to increase with fluid pressure in a similar manner to that observed within the Wissey sample experiments. As discussed in section 7.3.3 this is likely to be due to the increase in inertial effects associated with fluid-rock interaction resulting from viscosity increase. The exception is within the high temperature P_c = 45 MPa experiments, where a decrease in b'/a' is observed between P_{ds} = 20 MPa and P_{ds} = 30 MPa. This may be related to significant coupled mechanical changes (including potential micro-fracture activity discussed above), or may be an anomalous estimate resulting from experimental uncertainty.

The true transmissivities derived from the linear term of the Forchheimer equation are compared to the apparent transmissivities for the low temperature (38°C) and high temperature (58°C) Cambrian V1 experiments in Figures 7.18 and 7.19 respectively. Similarly to the Wissey sample, both the measured and computed apparent transmissivities decrease as flow rate increases, indicating the increase in significance of the non-linear effects. The computed T_{app}/T_0 approaches one when the flow rate becomes very low, while the measured T_{app}/T_0 deviates above the computed values at low flow rates, with a few values exceeding 1.5 within the high temperature experiments. The deviation of measured apparent transmissivities observed at low flow rates may be due to experimental errors in ∇P or Q measurements, as with the Wissey W3 sample results.

For the Cambrian V1 sample, uncertainty in ∇P is particularly high at low flow rates due to the very small differential pressures observed, close to the lower limit of the differential pressure transducer measurement range. However, the computed and measured apparent transmissivities match reasonably well above these lowest flow rates, implying that the non-linear flow regime observed during the Cambrian V1 experiments can be reasonably described by the Forchheimer equation for both the low and high temperature experiments at all pressure conditions tested. Thus the true transmissivity estimates derived and presented within Table 7.6 will be used for assessment of

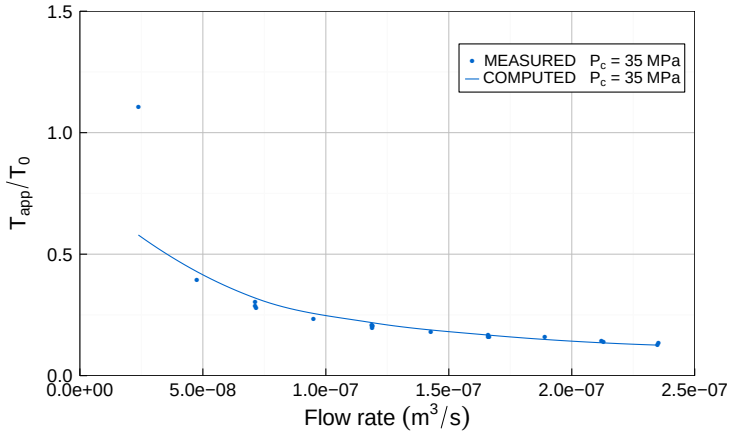

(A) P_{ds} = 10 MPa (LOW)

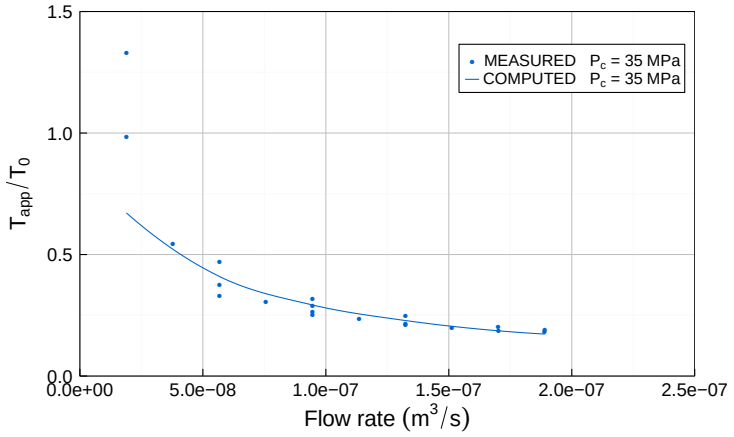

(B) P_{ds} = 20 MPa (MIDDLE)

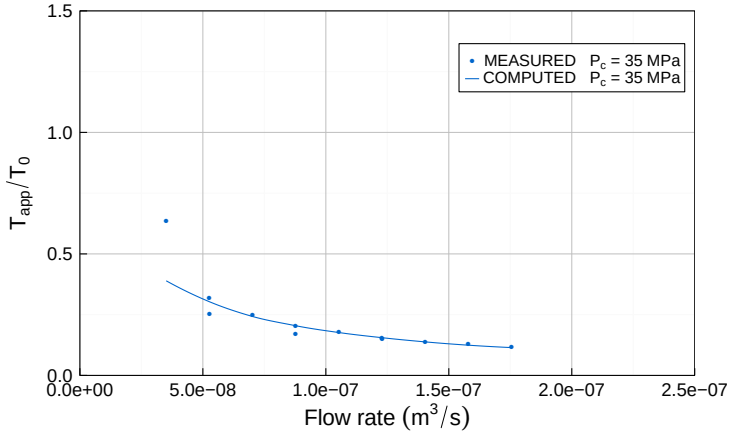

(C) P_{ds} = 30 MPa (HIGH)

FIGURE 7.18: Sample Cambrian V1, Expt C (38°C): T_{app}/T_0 as a function of flow rate

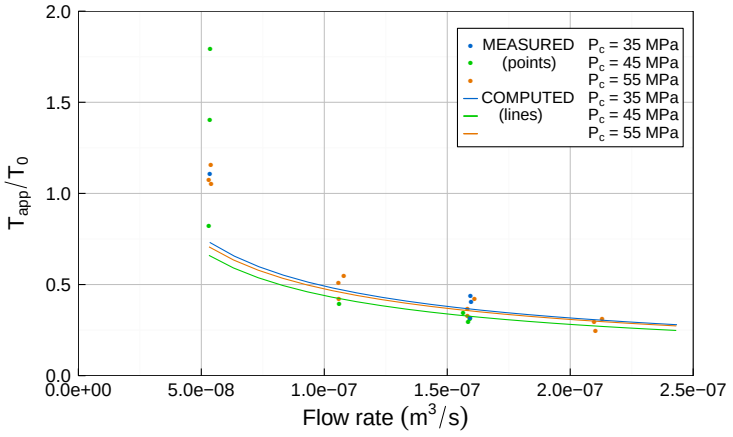

(A) P_{ds} = 10 MPa (LOW)

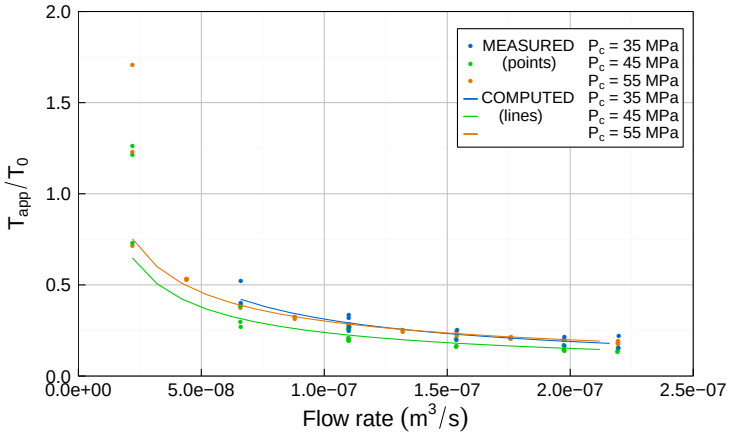

(B) P_{ds} = 20 MPa (MIDDLE)

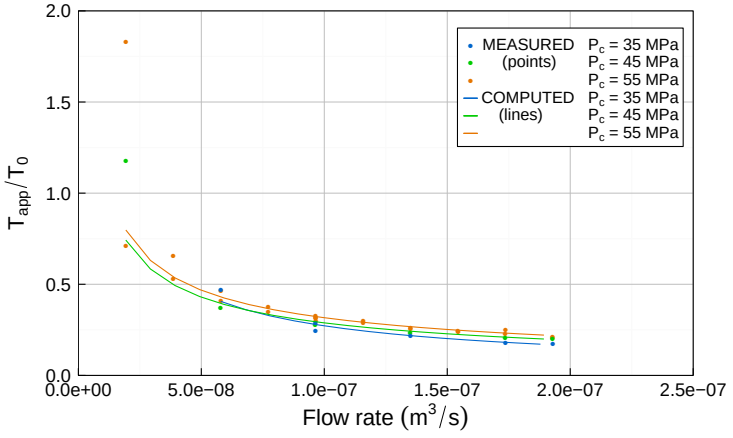

(C) P_{ds} = 30 MPa (HIGH)

FIGURE 7.19: Sample Cambrian V1, Expt B (58°C): T_{app}/T_0 as a function of flow rate

hydro-mechanical observations for Cambrian V1 within later sections of this Chapter, to minimise the interference of non-linearity effects during analysis.

7.3.5 East Brae B2b sample

Experiments undertaken on the East Brae B2b sample were carried out after initial stress loading of the offset fractured sample to minimise the inelastic fracture changes observed during the other sample experiments (section 7.6). Figures 7.20 and 7.21 present the observed differential pressure gradient as a function of flow rate at 38°C and 58°C during Experiments A and B respectively. The Reynolds number range during the low temperature experiments (Experiment A) was between 6 and 102, while for the high temperature experiments the Reynolds number range was between 7 and 326. The Reynolds number ranges are similar to those of the Cambrian shale sample. Both fractured samples were observed to be highly conductive during the CO_2 experiments.

A little hysteresis, likely to be due to continued inelastic change, can be seen within the low fluid pressure, low confining pressure experiment in Figure 7.20 (Experiment A). However, more notable are the extremely large uncertainties associated with the differential pressure gradient measurements. These are due to the very low differential pressures observed across the sample as a result of the high conductivity of the offset fracture. The observed differential pressures are close to the lower limit of the differential pressure transducer range (see Figure 7.3) and therefore high uncertainties are associated with their measurement. Despite this, the measurements demonstrate a similar non-linear trend to that observed for both the Wissey W3 and Cambrian V1 samples, which suggests significant inertial flow effects are occurring during the experiments.

Modified Forchheimer Plots for the East Brae B2b data are provided in Figures 7.22 and 7.23 for 38°C (Experiment A) and 58°C (Experiment B) respectively. The associated linear regression parameters are provided within Table 7.7. Although, from the R^2 values, the quality of the linear regression fits are seen to be reasonably good, more than half of the a' parameters are negative and therefore the models are not suitable for application of the Forchheimer equation. This is likely to be a result of the high associated differential pressure uncertainties. As a result, it was not possible to obtain true transmissivity estimates from the East Brae B2b results.

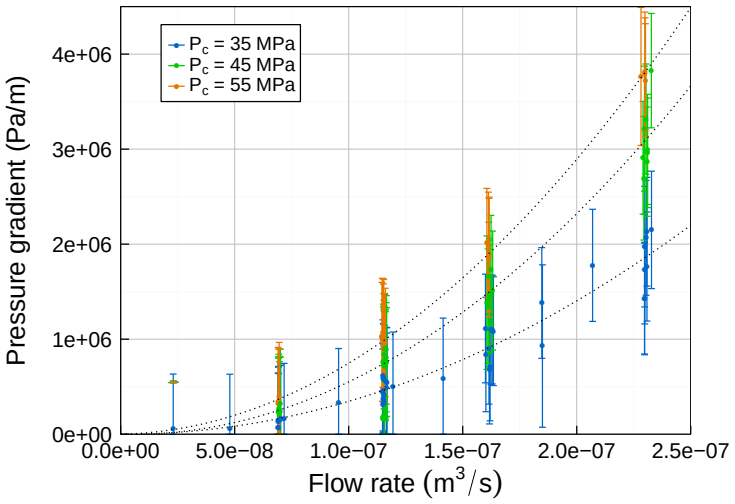

(A) P_{ds} = 10 MPa (LOW)

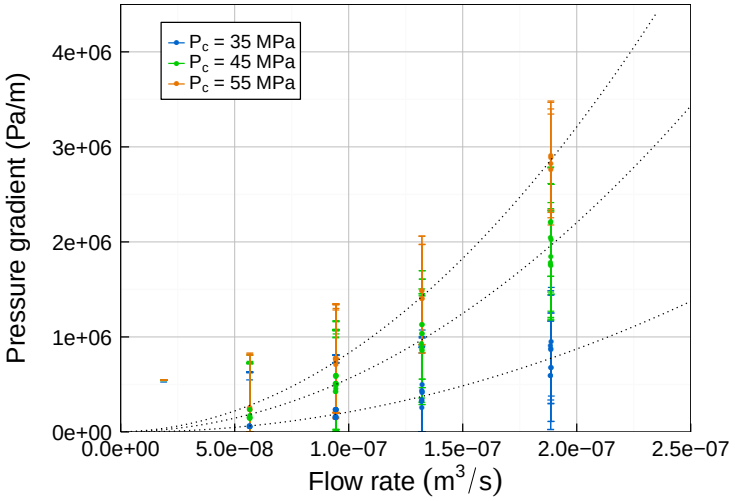

(B) P_{ds} = 20 MPa (MIDDLE)

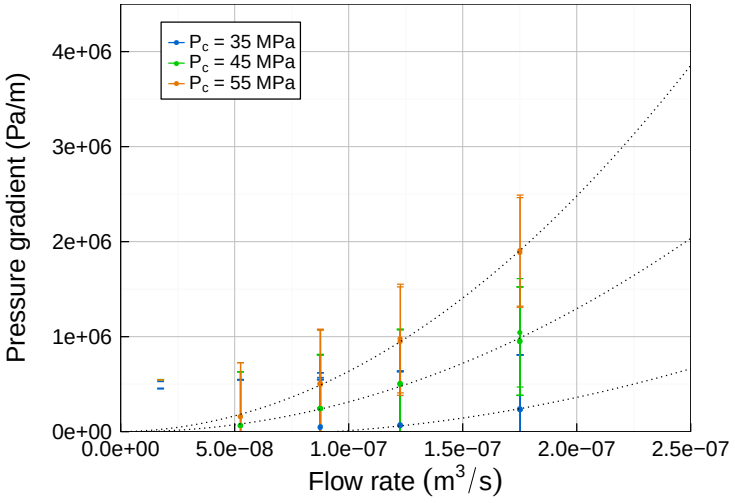

(C) P_{ds} = 30 MPa (HIGH)

FIGURE 7.20: Sample East Brae B2b, Expt A (38°C): Differential pressure gradient as a function of flow rate

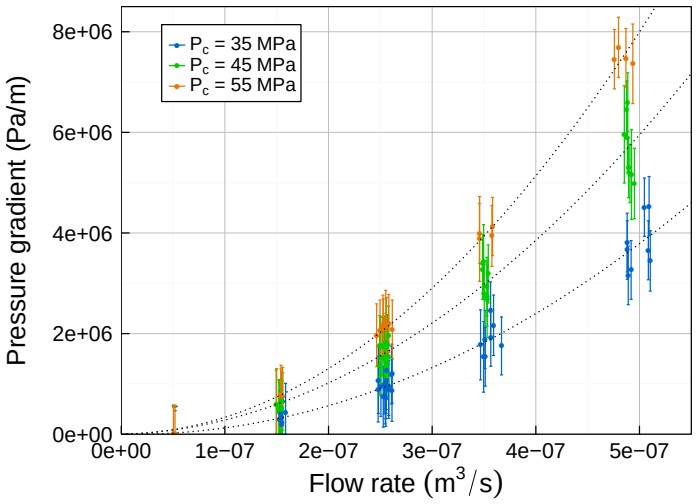

(A) P_{ds} = 10 MPa (LOW)

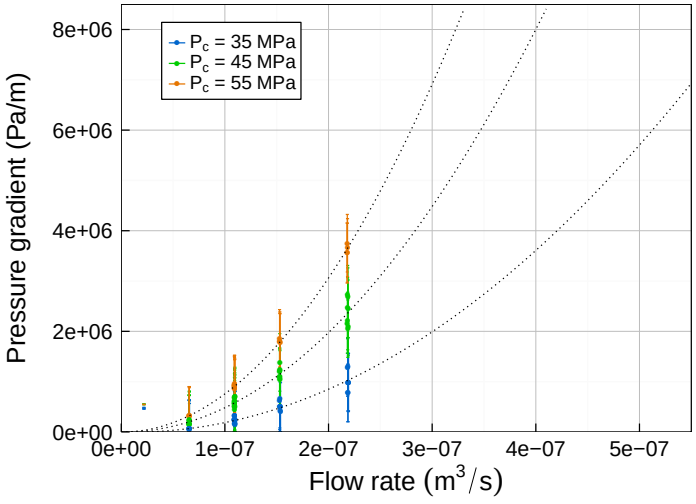

(B) P_{ds} = 20 MPa (MIDDLE)

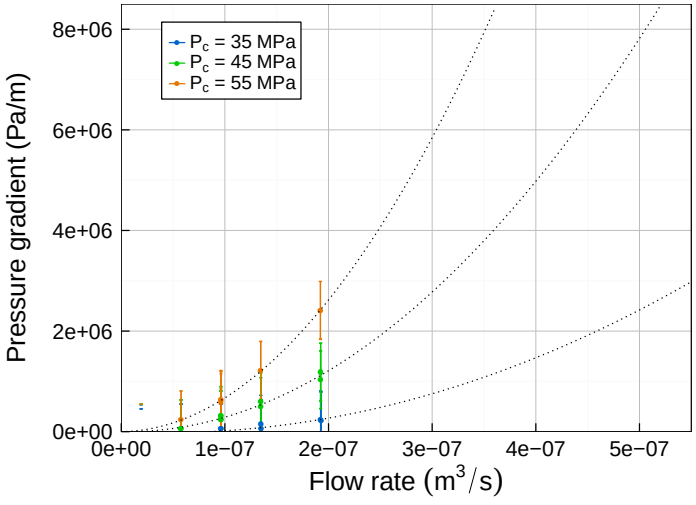

(C) P_{ds} = 30 MPa (HIGH)

FIGURE 7.21: Sample East Brae B2b, Expt B (58°C): Differential pressure gradient as a function of flow rate

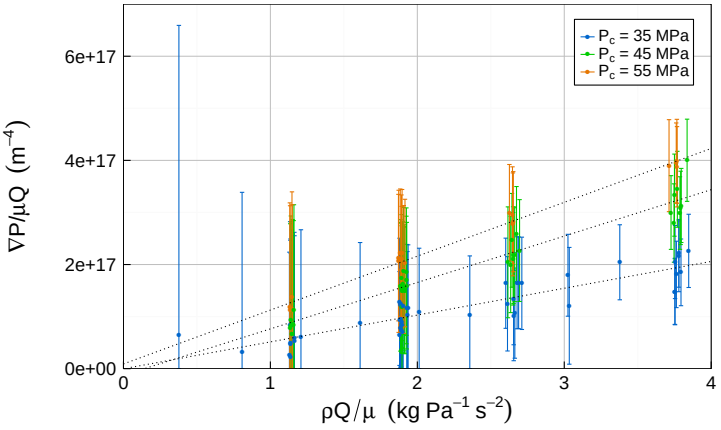

(A) P_{ds} = 10 MPa (LOW)

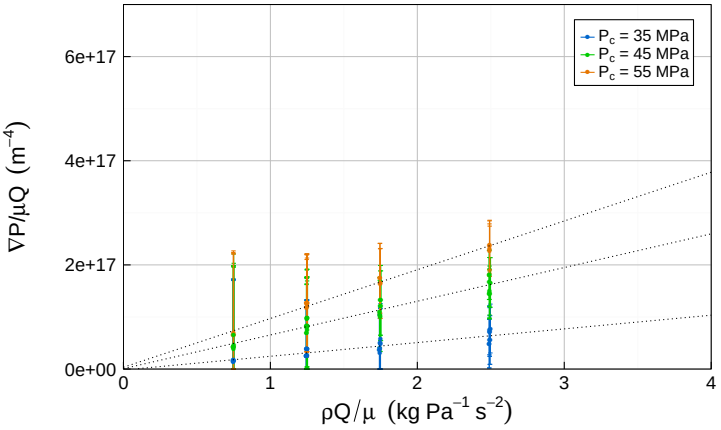

(B) P_{ds} = 20 MPa (MIDDLE)

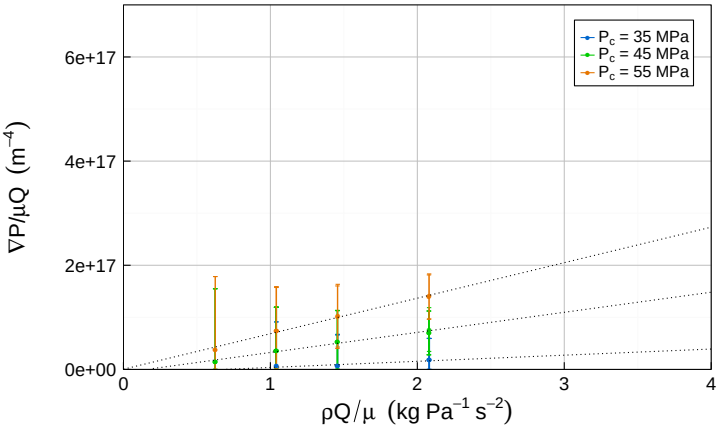

(C) P_{ds} = 30 MPa (HIGH)

FIGURE 7.22: Sample East Brae B2b, Expt A (38°C): Modified Forchheimer Plots

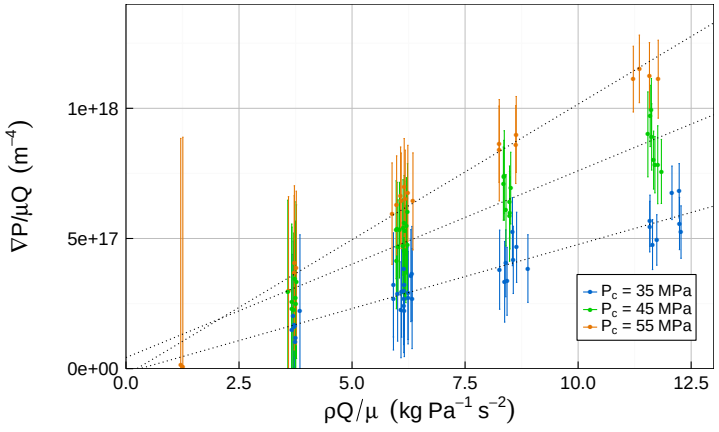

(A) P_{ds} = 10 MPa (LOW)

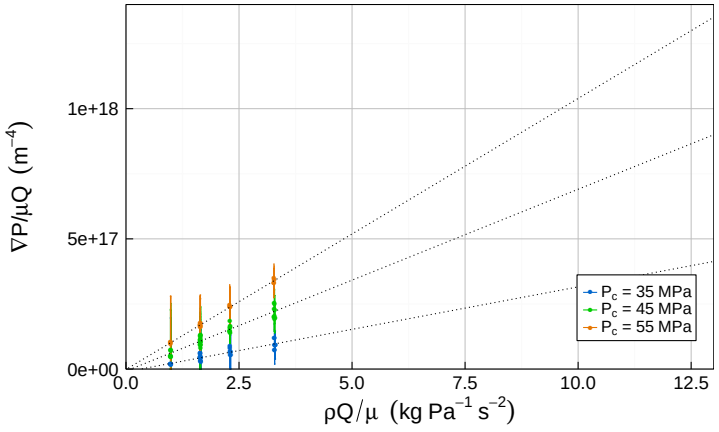

(B) P_{ds} = 20 MPa (MIDDLE)

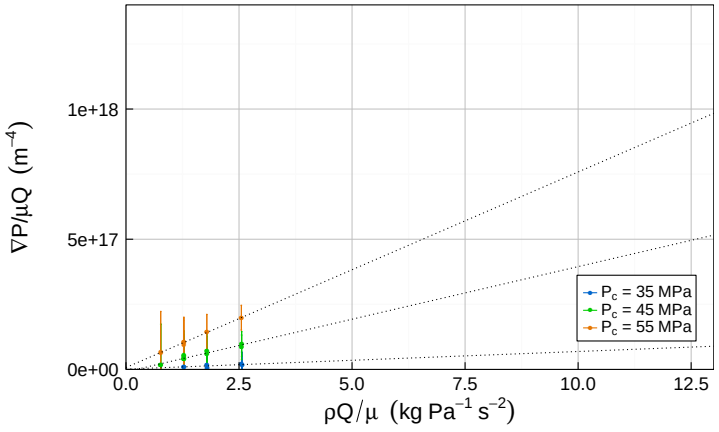

(C) P_{ds} = 30 MPa (HIGH)

FIGURE 7.23: Sample East Brae B2b, Expt B (58°C): Modified Forchheimer Plots

TABLE 7.7: East Brae B2b - Modified Forchheimer Plot linear regression parameters

P_c (MPa)	P_{ds} (MPa)	a'	b'	R^2
Low Temperature (38 °C)				
35	10	-9.37×10^{13}	5.15×10^{16}	0.8013
45	10	-1.27×10^{16}	8.91×10^{16}	0.9380
55	10	9.11×10^{15}	1.03×10^{17}	0.9854
35	20	-1.79×10^{15}	2.63×10^{16}	0.7964
45	20	7.14×10^{14}	6.47×10^{16}	0.9206
55	20	3.47×10^{15}	9.36×10^{16}	0.9878
35	30	-8.02×10^{15}	1.18×10^{16}	0.8374
45	30	-6.07×10^{15}	3.86×10^{16}	0.9808
55	30	3.67×10^{14}	6.82×10^{16}	0.9908
High Temperature (58 °C)				
35	10	-1.50×10^{16}	4.92×10^{16}	0.8750
45	10	4.28×10^{16}	7.17×10^{16}	0.8950
55	10	-2.50×10^{16}	1.04×10^{17}	0.9770
35	20	-1.06×10^{16}	3.26×10^{16}	0.8240
45	20	-7.68×10^{15}	6.98×10^{16}	0.9178
55	20	-1.60×10^{15}	1.04×10^{17}	0.9950
35	30	1.21×10^{15}	6.77×10^{15}	0.5619
45	30	-9.22×10^{15}	4.04×10^{16}	0.9358
55	30	7.29×10^{15}	7.51×10^{16}	0.9956

The apparent transmissivities calculated from the East Brae B2b observations are plotted in Figure 7.24, with the low temperature plots on the left and the high temperature plots on the right. These plots indicate that, despite notable measurement errors, the apparent transmissivities generally decrease with increasing flow rate, in line with other experimental sample observations, which suggests increasing non-linear effects. Apparent transmissivities during the experiment are in the region 10^{-16} to 10^{-15} m^4; the highest of all samples tested.

Due to the high sample conductivity, and thus the associated high measurement error, East Brae B2b experimental results are not used in subsequent sections of this chapter. However, it is notable that a similar Forchheimer-type non-linear flow regime is present during experiments on this high conductivity offset fractured sample to that observed during the Wissey W3 and Cambrian V1 mated fractured sample experiments.

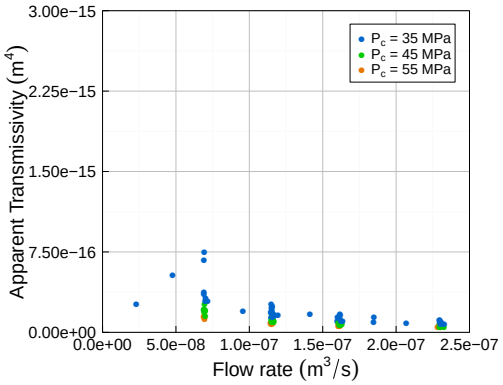

(A) P_{ds} = 10 MPa (38°C)

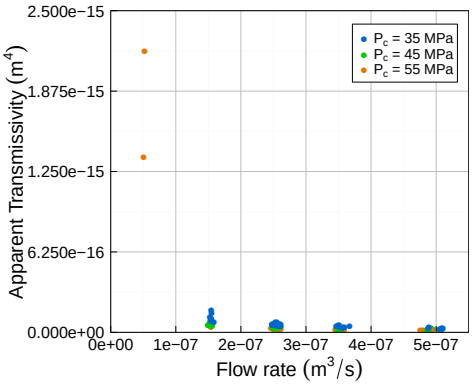

(B) P_{ds} = 10 MPa (58°C)

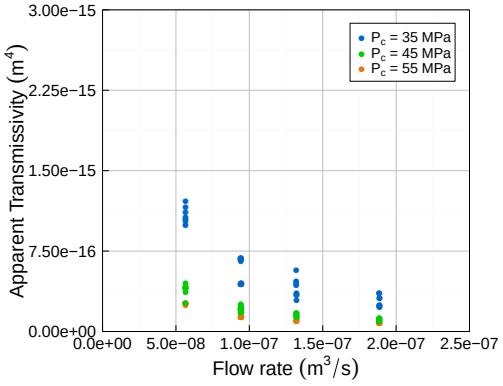

(C) P_{ds} = 20 MPa (38°C)

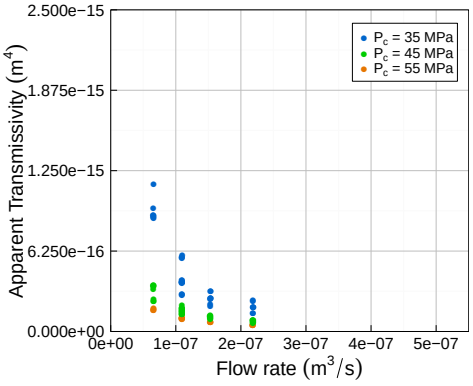

(D) P_{ds} = 20 MPa (58°C)

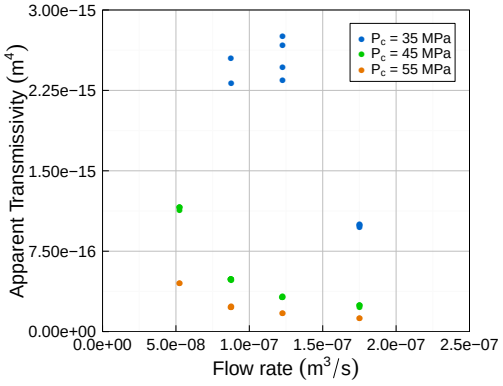

(E) P_{ds} = 30 MPa (38°C)

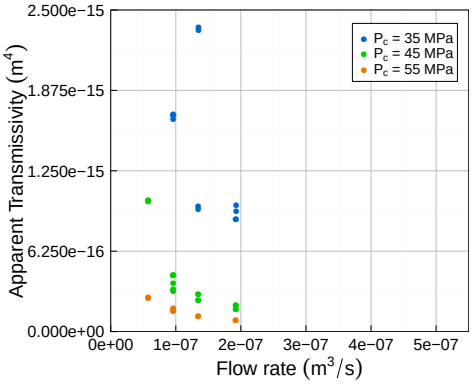

(F) P_{ds} = 30 MPa (58°C)

FIGURE 7.24: Sample East Brae B2b: Apparent transmissivities as a function of flow rate

7.3.6 Significance of non-linearity - comparison between samples and scenarios

The Forchheimer equation has been found to be suitable for describing the non-linear flow regime observed during CO_2 flow experiments carried out across a range of pressure and temperature scenarios on both the Wissey and the Cambrian samples. Thus, a review of the significance of non-linearity with pressure and temperature variations can be carried out for each of the two samples, as well as comparisons between samples, using the associated Forchheimer numbers. This section contains such a review, and builds upon the discussions within section 7.3.3 and 7.3.4.

The Forchheimer number (Equation 2.14), defined by Ruth and Ma [1992], is a dimensionless measure of the significance of non-Darcian or non-linear flow, which can occur due to microscopic inertial effects arising from fluid flow along rough fracture surfaces, or tortuous channels, as well as from true fluid turbulence. The Forchheimer numbers associated with the Wissey W3 and Cambrian V1 flow experiments are presented in Figures 7.25 and 7.26 as a function of Reynolds number, for low and high temperature experiments respectively. Plotting the Forchheimer number as a function of Reynolds number, which describes the significance of inertial forces associated with the fluid flow state alone, allows assessment and comparison of the significance of inertial effects arising from the fluid-rock interactions, due to fracture roughness, flow tortuosity, etc. A number of observations can be drawn from analysis of the variation of Forchheimer number between pressure and temperature scenarios, and between samples, from these figures. These are discussed below.

Within both low and high temperature experiments (Figure 7.25 and 7.26 respectively), it is observed that the Forchheimer numbers associated with the Cambrian shale sample are greater than those of the Wissey sample, when plotted as a function of Reynolds number. This implies that the microscopic inertial effects associated with the fracture surface structure were more significant for the Cambrian sample than for the Wissey sample. The geometry of the flow paths (or fracture(s)) within the Cambrian V1 sample must therefore induce greater inertial forces. One possible reason for this could be higher frictional effects within the main fracture. From Figure 4.20 we see that the small scale roughness was qualitatively found to be higher for the Cambrian V1 sample than the Wissey W3 sample, which may lead to increased frictional effects within the Cambrian sample. In addition, evidence for micro-fractures within the Cambrian

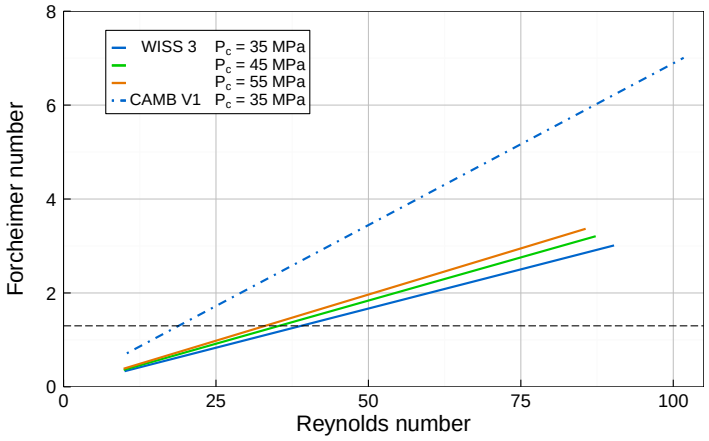

(A) P_{ds} = 10 MPa (LOW)

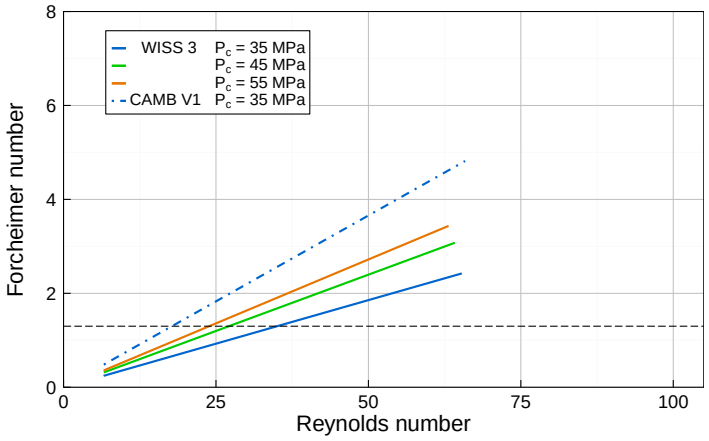

(B) P_{ds} = 20 MPa (MIDDLE)

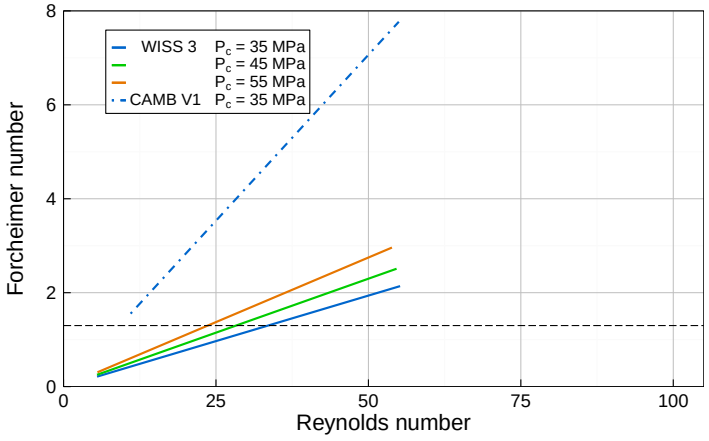

(C) P_{ds} = 30 MPa (HIGH)

FIGURE 7.25: Wissey W3 and Cambrian V1 Forchheimer number against Reynolds number during low temperature experiments (38°C)

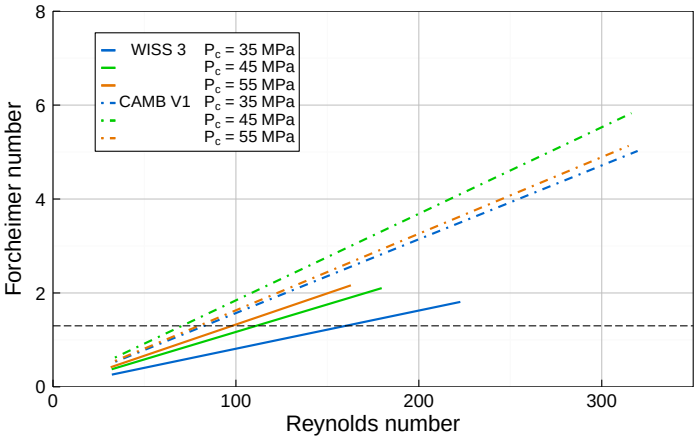

(A) P_{ds} = 10 MPa (LOW)

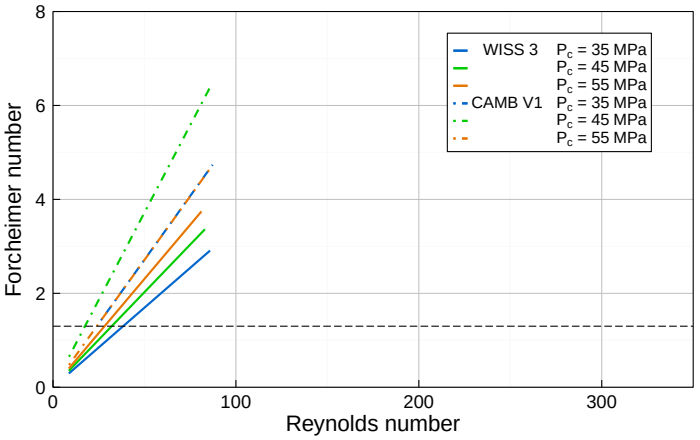

(B) P_{ds} = 20 MPa (MIDDLE)

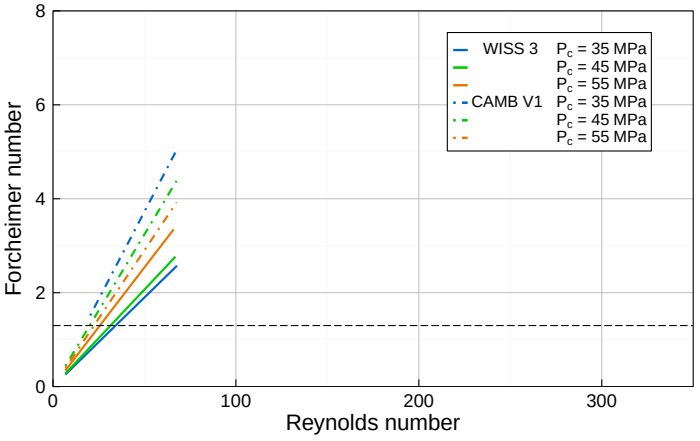

(C) P_{ds} = 30 MPa (HIGH)

FIGURE 7.26: Wissey W3 and Cambrian V1 Forchheimer number against Reynolds number during high temperature experiments (58°C)

sample post-experiment suggests that micro-fracture flow may contribute to sample transmissivity. No evidence for micro-fractures was observed for the Wissey sample. Flow within micro-fractures is likely to be associated with high flow path tortuosity as well as increased frictional effects, both of which would lead to increased non-linearity. Therefore micro-fracture activation is another possible explanation for the greater non-linearity significance of the Cambrian sample.

While an increase in Forchheimer number is observed with confining pressure for the Wissey sample (both low and high temperature scenarios) this is not observed for the Cambrian sample (high temperature scenarios available only). The opposite is observed for the Cambrian shale sample for P_{ds} = 30 MPa, and for both P_{ds} = 10 MPa and P_{ds} = 20 MPa the middle confining pressure (P_c = 45 MPa) scenario has the greatest Forchheimer numbers, while the Forchheimer numbers associated with high and low confining pressures are similar in magnitude in both cases.

As mentioned previously, and discussed in section 7.5, mechanical changes to the fracture aperture result from confining pressure changes, with an increase in confining pressure expected to result in a reduction of fracture aperture, and a reduction in confining pressure corresponding to an increase in fracture aperture. For a single, discrete fracture, an increase in non-linearity would normally be expected from an increase in confining pressure (and resultant reduction in fracture aperture) as flow path tortuosity would increase as would the relative significance of frictional effects within the fracture. This is in line with observations for the Wissey sample.

The inconsistent response observed for the Cambrian shale sample may be explained by the presence of micro-fracture networks, which may be active flow pathways under certain pressure conditions. While flow may occur within both the main fracture and micro-fracture network within the Cambrian shale sample under low confining pressures, with correspondingly high flow path tortuosity and associated inertial effects, an increase in confining pressure may gradually close the micro-fracture network channels, thus reducing the number of tortuous flow paths and confining fluid flow to the more direct, main fracture channels. In this scenario, we could expect to see a reduction in non-linearity with an increase in confining pressure, as observed for the Cambrian shale sample high fluid pressure scenario. Complex changes to the fracture network geometry within the Cambrian shale sample due to pressure changes could also explain

the inconsistent Forchheimer number variation observed for the low and middle fluid pressure scenarios in a similar manner.

The effect of changes in fluid pressure to non-linearity are more complex than changes in confining pressure as fluid pressure changes result in both mechanical aperture alterations (due to effective stress change) and changes to frictional effects (due to viscosity change). Increasing fluid pressure reduces effective stress (section 7.5), thus an increase in aperture would be expected, while increased frictional effects would also be expected as a result of the increased viscosity (section 7.4). The former would be expected to reduce non-linearity within a single discrete fracture while the latter would increase non-linearity. Non-linearity increase may also however be observed as a result of reduced effective stress if activation of micro-fractures occurs, due to the associated increased flow path tortuosity and frictional effects.

In all experiments we observe an increase in Forchheimer number as a function of Reynolds number between $P_{ds} = 10$ MPa and $P_{ds} = 20$ MPa scenarios (both low and high temperatures for both samples), suggesting that the increased frictional effects due to viscosity increase are more significant than any reduction in non-linearity as a result of fracture aperture increase. The same Forchheimer number increase is generally observed between $P_{ds} = 20$ MPa and $P_{ds} = 30$, with a couple of exceptions. The viscosity differences between $P_{ds} = 20$ MPa and $P_{ds} = 30$ MPa, are much less significant than the differences between $P_{ds} = 10$ MPa and $P_{ds} = 20$ MPa at both temperatures (section 7.4). It is therefore reasonable to suggest that non-linearity changes due to mechanical effects may be more significant than non-linearity changes due to viscosity effects in some cases, depending on fracture geometry and structure. This could explain the instances where reduction in Forchheimer number is observed between $P_{ds} = 20$ MPa and $P_{ds} = 30$ MPa scenarios.

Results from both samples indicate that non-linearity due to fluid-rock interaction is generally more significant under the lower temperature (38°C) conditions. This can be observed as higher b'/a' numbers, or higher Forchheimer numbers as a function of Reynolds number (within Figures 7.25 and 7.26). As fluid viscosities are higher at lower temperatures, frictional effects are likely to be greater, which may explain the more significant non-linearity observed.

Forchheimer number estimates for the Wissey experiments ranged from 0.2 to 3.7, and for the Cambrian experiments ranged from 0.4 to 7.8 (Figures 7.25 and 7.26). The

experimental work of Ranjith and Viete [2011] suggests that for non-Darcian fracture flow, inertial effects are modest for Forchheimer numbers less than 1.3, and suggests that valid permeability estimates may be made by neglecting inertial effects under these scenarios. Within our experiments, Forchheimer number estimates are less than 1.3 for only 41% of Wissey scenarios, and 14% of Cambrian scenarios, therefore the effects of non-linearity must be accounted for. True transmissivity estimates calculated within section 7.3.3 and 7.3.4 are therefore utilised for further analysis in subsequent sections of this chapter.

7.3.7 Flow regime analysis summary

Flow regime analysis has been carried out within this section for each of four fractured samples. A broadly linear flow regime was found to exist during the very low conductivity East Brae D2 fractured sample experiments. Due to the low conductivity only low flow rates could be tested and the Reynolds number during these experiments remained below 13. Within the limited East Brae D2 dataset some small deviations from linearity (decrease in $\nabla P/Q$) were observed which may result from fracture dilation under the high fluid pressure gradients observed. Alternatively residual CO_2 leakage within the experimental rig at higher pressures may result in similar observed deviations. As the deviations are not considered to be significant, linear Darcy's law was deemed valid for estimating transmissivities, T, for this sample.

Flow regime analysis has shown that a non-linear flow regime is present during all experiments undertaken on the Wissey W3, Cambrian V1 and East Brae B2b samples. The Reynolds number ranges during the low temperature (38°C) experiments are similar for all three samples, lying within the range 5 to 102. For the high temperature (58°C) experiments, the Reynolds numbers are greater due to the fluid property density and viscosity changes. For the Wissey W3 sample Reynolds numbers reach 233, while for the Cambrian V1 and East Brae B2b samples the Reynolds numbers are higher, reaching up to 335. The higher Reynolds numbers for the Cambrian V1 and East Brae B2b samples are due to their higher conductivities, and therefore the associated lower mean fluid pressures within the samples. The lower mean fluid pressures have higher density/viscosity ratios (see section 7.4) and therefore higher associated Reynolds numbers. The observation of non-linearity for all three samples within the above Reynolds number ranges is consistent with the experimental findings of Ji et al. [2008], Ranjith

and Darlington [2007], Zimmerman et al. [2004], where non-linearity was observed for Reynolds numbers exceeding ∼20. This is an interesting observation, and suggests the validity of these findings for CO_2 fluid as well as water, the fluid used within the referenced studies.

The Forchheimer equation (Equation 2.12) has been found to be suitable for estimation of true transmissivity, T_0, values for the Wissey W3 sample experiments and the Cambrian V1 sample experiments. Due to high measurement errors, the Forchheimer equation regression coefficients were found to be unsuitable for estimation of true transmissivities for the East Brae B2b sample. Where the Forchheimer equation is considered suitable (Wissey W3 and Cambrian V1 experiments), true transmissivity estimates will be adopted within subsequent results sections for hydro-mechanical behaviour analysis. This will enable hydro-mechanical behaviour during fracture flow to be assessed while minimising interference from non-linear flow effects, which makes assessment of observations simpler and clearer.

Transmissivity magnitudes were found to be of the order of 10^{-21} m^4, 10^{-19} m^4 and 10^{-17} m^4 for the East Brae D2, Wissey W3 and Cambrian V1 samples respectively. From apparent transmissivity estimates, the East Brae B2b true transmissivity magnitudes are estimated to be of the order of 10^{-15} m^4. Discussion on transmissivity variation between scenarios will be covered in sections 7.6 and 7.5.

The significance of inertial or non-linear flow is found to be greater for the Cambrian V1 sample than for the Wissey W3 sample across all pressure/temperature scenarios tested (section 7.3.6). We also observe that for both samples non-linearity significance is, in general, higher within the lower temperature and higher fluid pressure scenarios. This is thought to be due to the higher fluid viscosities found at low temperature/fluid pressure respectively, and thus increased frictional effects. The significance of non-linearity was observed to increase with confining pressure for the Wissey W3 sample, however this was not consistently observed for the Cambrian V1 sample. For flow within a discrete fracture, confining pressure increase would be expected to reduce fracture aperture, with an associated increase in flow tortuosity and inertial effects, as observed for the Wissey W3 sample. The observations for the Cambrian V1 sample could indicate the occurrence of micro-fracture network flow, with associated high non-linearity. Complex changes to micro-fracture networks are likely to result from both fluid and confining

pressure changes, which could explain the inconsistent non-linearity trends observed during these experiments.

7.4 CO_2 fluid property variation

The experimental pressure and temperature ranges adopted during this project were chosen to be representative of those within potential CO_2 geological storage sites. All pressures and temperature conditions are in excess of the critical point (7.38 MPa, 31.1°C) therefore CO_2 is a supercritical fluid at all times during the experiments [Bachu, 2000]. However, the supercritical CO_2 fluid properties (both the density and viscosity) vary notably within the experimental pressure and temperature ranges as discussed within section 2.5.1.

This section discusses the two main implications of this density and viscosity variance for the flow experiments undertaken within this study. The first is the implication of variation in the mean sample fluid density and viscosity observed between experimental scenarios, discussed in section 7.4.1. The second is the variance in both fluid density and viscosity across the sample and the implications of this for use of hydraulic equations that assume incompressible fluid (i.e. Darcy's law, and the analogous cubic law). This is discussed in section 7.4.2.

7.4.1 Mean sample fluid property variation between scenarios

Fluid property changes can be significant between downstream fluid pressure scenarios (10, 20 and 30 MPa) and temperature scenarios (38°C and 58°C). In addition, due to the impact of both confining pressure changes and flow rate changes on differential pressure, and thus mean fluid pressure where the downstream fluid pressure is fixed, fluid property variation may also be notable between confining pressure and flow rate scenarios. This is likely to be particularly notable for the lower permeability samples (i.e. East Brae B2, D2 and Wissey W3) where differential pressures and thus differential pressure changes between confining pressure and flow rate scenarios can be significant.

Differential pressure increases with both flow rate and confining pressure under a constant downstream fluid pressure as a result of hydraulic and mechanical responses respectively (see Chapter 2 for associated theory). As the fluid pressure is controlled at

the downstream end of the sample during experiments, differential pressure increase across the sample is associated with mean fluid pressure increase, and therefore also mean density and viscosity increase within the sample.

The density and viscosity changes between experimental scenarios for the Wissey sample experiments are illustrated in Figures 7.27 and 7.28 respectively as an example, with subplots used for each temperature scenario. Within these plots, the data points reflect the density and viscosity values at the mean fluid pressure within the sample, $\bar{P} = (P_{us} + P_{ds})/2$, as used within the incompressible Darcy's law approximation (section 2.5.2). The vertical bars associated with the data points show the density and viscosity range between the upstream and downstream ends of the sample, which is discussed in section 7.4.2. Densities and viscosities plotted within these figures have been calculated using the Huang et al. [1984] equation of state and Jossi et al. [1944] CO_2 viscosity relationship respectively (section 2.5.1).

Figures 7.27 and 7.28 illustrate the step change in density and viscosity that exists between downstream fluid pressure and temperature scenarios, with both density and viscosity increasing with downstream fluid pressure increase and decreasing with temperature increase. In addition, the figures indicate an increase in sample density and viscosity with flow rate within each pressure/temperature scenario due to differential fluid pressure increase (and thus mean fluid pressure increase) under controlled downstream fluid pressure conditions. The observed differential fluid pressures (and thus mean fluid pressures) are also higher for higher confining pressures (see section 7.5 for details) and the figures also illustrate the corresponding increase in sample density and viscosity with confining pressure as a result. The density and viscosity variations in response to both flow rate and confining pressure change are greatest within the low downstream fluid pressure scenarios (10 MPa). Both density and viscosity of CO_2 are particularly sensitive to changes in fluid pressure close to the critical pressure of 7.38 MPa. The density and viscosity sensitivity is also higher during the high temperature experiments, as can be seen by comparison of the subplots within each figure.

During the flow experiments, discrete upstream pump flow rates were tested at each pressure/temperature scenario as defined in section 6.2. Each discrete pump flow rate corresponds to a range of CO_2 flow rates through the sample depending on the pressure/temperature scenario, as seen in Figures 7.27 and 7.28. This is due to variation in the density difference between the upstream pump and the sample that results from the

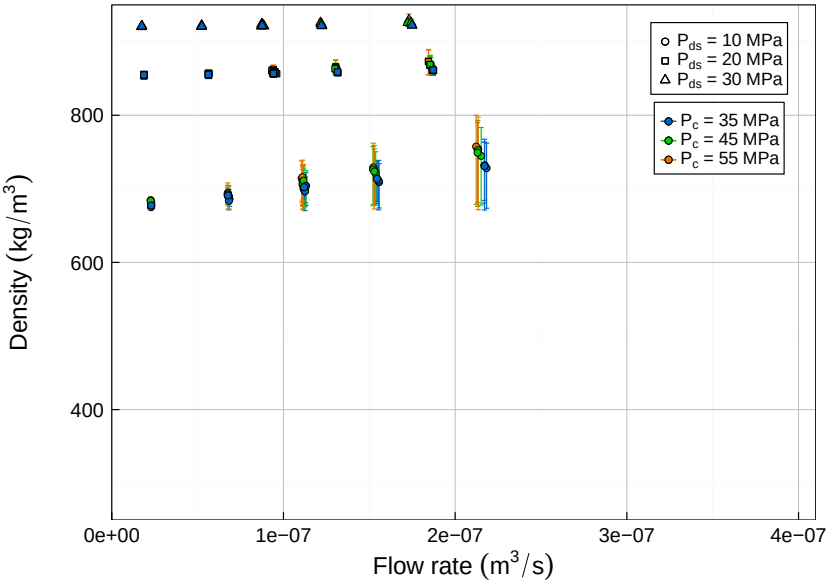

(A) Low Temperature (38°C)

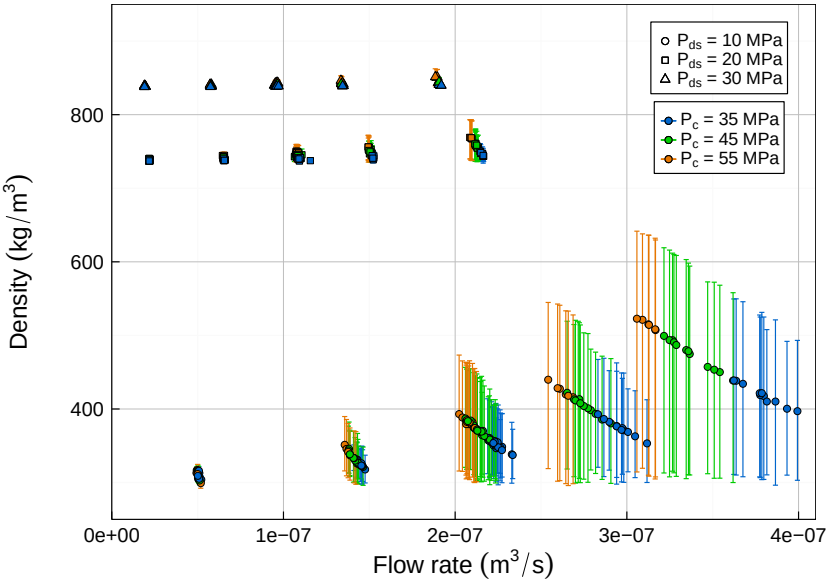

(B) High Temperature (58°C)

FIGURE 7.27: Density variation with flow rate within Wissey sample experimental scenarios. Vertical bars indicate variation of parameter between the upstream and downstream sample ends.

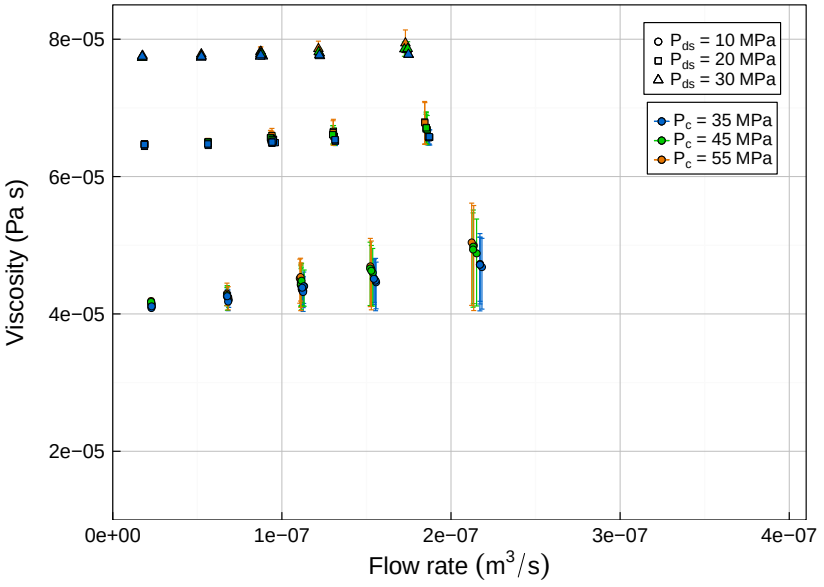

(A) Low Temperature (38°C)

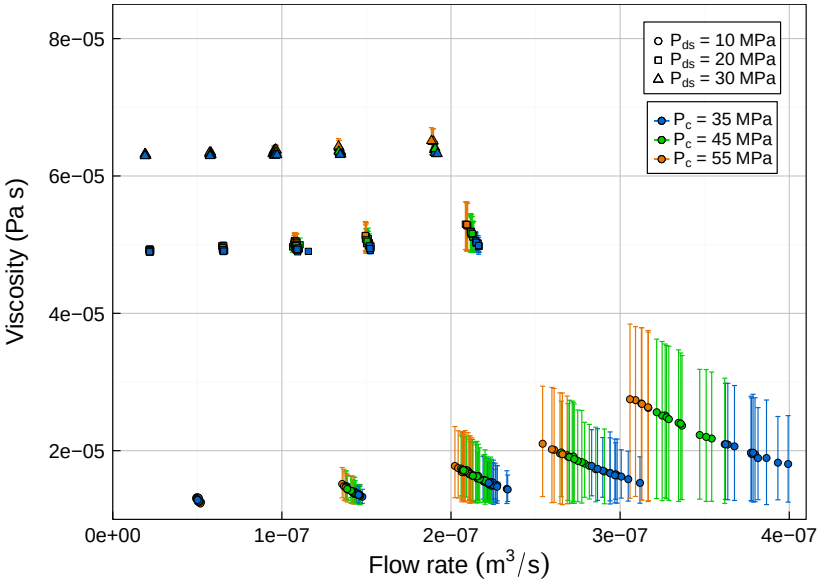

(B) High Temperature (58°C)

FIGURE 7.28: Viscosity variation with flow rate within Wissey sample experimental scenarios. Vertical bars indicate variation of parameter between the upstream and downstream sample ends.

associated temperature and pressure change (section 5.3.3.3). A range of differential pressures are also observed within each pressure/temperature/flow rate scenario due to inelastic changes that occur during the experiments (see section 7.6 for details). As the downstream fluid pressure is fixed within a given pressure scenario, variation in differential pressure also varies the mean flow rate through the sample, hence the flow rate variation even within a given pressure/temperature/pump flow rate scenario.

As discussed in section 2.5.1, the density to viscosity ratio is of particular interest, as it is proportional to the hydraulic conductivity (Equation 2.9) as well as the Reynolds number (Equation 2.11). Figure 7.29 illustrates, again using the Wissey sample data as an example, the variation in density/viscosity between experimental scenarios. As expected, in line with Figure 2.5, the density/viscosity ratio during experiments is highest for low fluid pressure conditions, and high temperatures. A reduction in density/viscosity is observed with flow rate increase due to associated differential pressure increase, and thus also mean fluid pressure increase under controlled downstream fluid pressure conditions. In addition, as high confining pressure scenarios are associated with higher differential pressures, the density/viscosity ratio also decreases with an increase in confining pressure.

As hydraulic conductivity is proportional to the density/viscosity ratio, the observations in Figure 7.29 are directly transferable to fracture hydraulic conductivity if constant effective stress conditions are present (i.e. stable mechanical scenario and constant permeability). The Reynolds number is affected in a similar manner. Thus, under constant effective stress conditions, both hydraulic conductivity and Reynolds numbers are highest under low fluid pressure and high temperature conditions. Hydraulic conductivity also decreases with increasing flow rate in association with differential pressure (and thus mean fluid pressure) increase. This is not the case for the Reynolds number as it is proportional to Q as well as ρ/μ (Equation 2.11). The flow rate effects on hydraulic conductivity can be notable, particularly under low fluid pressures (approaching critical pressure). This shows that CO_2 fluid property changes can influence flow behaviour within fractured low permeability rock under in-situ pressure and temperature conditions, and require due consideration.

Fluid property variation observed within pressure and temperature scenarios due to flow rate variation also has implications for transmissivity estimation. This has been accounted for within section 7.3.

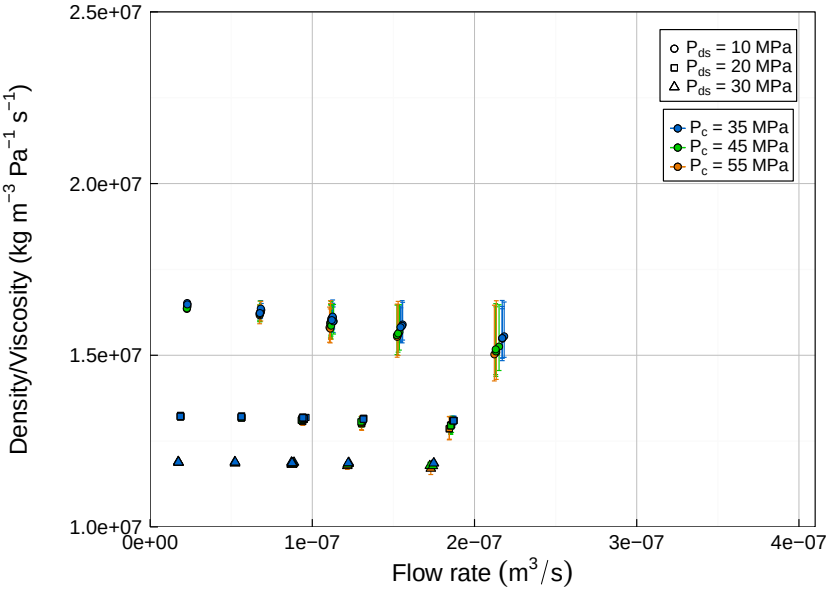

(A) Low Temperature (38°C)

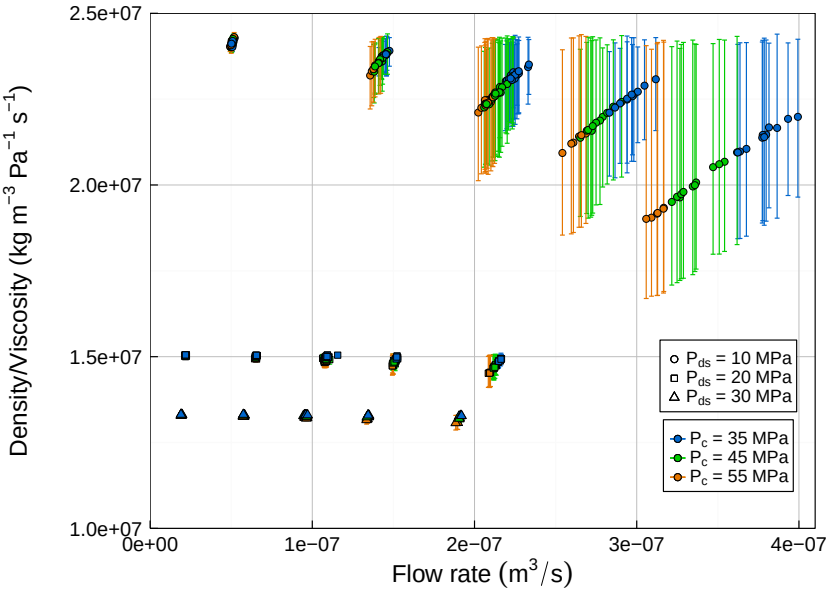

(B) High Temperature (58°C)

FIGURE 7.29: Density/viscosity variation with flow rate within Wissey sample experimental scenarios. Vertical bars indicate variation of parameter between the upstream and downstream sample ends.

7.4.2 Suitability of incompressible flow equations for analysis

Within section 2.5.2, it is stated that for the experiments undertaken within this study, approximation of CO_2 as an incompressible fluid through adoption of Darcy's law (and the analogous cubic law) at the mean fluid pressure, $\bar{P} = (P_{us} + P_{ds})/2$ was found to be suitable despite the variation in both density and viscosity parameters across the experimental samples. This section provides further details on the justification of this for each of the experimental samples.

The magnitude of density and viscosity variation across the sample was compared to the measurement uncertainty/error associated with the density and viscosity estimates respectively for each of the experimental results. Table 7.8 details what percentage of measurements for each sample have fluid property variations across the sample that are greater than the uncertainty associated with the same fluid property parameter. Where fluid property variations are smaller than the associated parameter uncertainty, there is no benefit from explicit consideration of the fluid property variation effects, thus use of the incompressible form of Darcy's law (Equation 2.4), or the analogous cubic law (Equation 2.5) is appropriate as discussed in section 2.5.2.

TABLE 7.8: Fluid property variation magnitude compared to parameter uncertainty

Sample	Number of measurements taken	Measurements where density variation across the sample > density uncertainty	Measurements where viscosity variation across the sample > viscosity uncertainty
Cambrian V1	685	1%	2%
East Brae B2	3	100%	100%
East Brae D2	92	100%	100%
East Brae B2b	535	0%	1%
Wissey W3	1165	17%	18%

From Table 7.8 it can be seen that variations are smaller than parameter uncertainty for almost all of the Cambrian V1 and East Brae B2b sample measurements. This is due to the relatively high permeability/transmissivity of these fractured samples (section 7.2), and thus the small associated differential pressures. Thus, for the Cambrian V1 and East Brae B2b samples, the use of incompressible equations is appropriate (section 2.5.2).

The fluid property variations across the sample were found to be greater than parameter uncertainty for the lower permeability samples: East Brae B2, East Brae D2, and also for a proportion of the Wissey W3 measurements. For this subset of measurements, where fluid property variation was found to be more significant than measurement uncertainty, numerical integration was undertaken to estimate the value of $\int_{P_{ds}}^{P_{us}} \frac{\rho}{\mu}\, dP$ in each case, using a pressure step size of 0.03 MPa and the trapezoidal rule. These estimates were then compared to the respective incompressible approximation estimates, $\frac{\rho\, \Delta P}{\mu}$, where ρ and μ estimates for $\bar{P} = (P_{us} + P_{ds})/2$ were used (see section 2.5.2). Figure 2.6 is an example illustration comparing the integral and the incompressible approximation estimates discussed here. Table 7.9 details the percentage difference range between these two estimates for each of the affected samples. For the Wissey W3 sample, the calculations were only carried out for the 18% of measurements where fluid property variation was greater than parameter uncertainty. The table statistics have also been split into low and high temperature subsets for the Wissey W3 sample (only low temperature experiments were undertaken on East Brae B2 and D2).

TABLE 7.9: Percentage error in integral estimation resulting from use of Darcy's incompressible approximation

Sample	Number of measurements	Percentage error arising from incompressible approximation			Differential pressure range (MPa)
		Max	Min	Mean	
East Brae B2	3	-2.4%	-2.1%	-2.3%	21.3-23.0
East Brae D2	92	-3.5%	+0.1%	-1.4%	2.9-38.8
Wissey W3 (38°C)	45	-1.6%	+0.3%	-0.6%	2.2-5.2
Wissey W3 (58°C)	170	-2.3%	+4.0%	+0.6%	0.5-5.8

Table 7.9 demonstrates that the error associated with use of an incompressible approximation for hydraulic parameter estimation is small when compared to results using numerical integration, within 4% for all measurements. For the East Brae B2 and D2 samples, the errors are mainly negative, which indicates that the incompressible approximation underestimates the value of the integral $\int_{P_{ds}}^{P_{us}} \frac{\rho}{\mu}\, dP$. As permeability/-transmissivity is inversely proportional to this integral, the result is that use of the incompressible approximation slightly overestimates permeability/transmissivity values in these cases. However, the percentage errors are small and are expected to have no significant effects on the hydraulic parameter estimates overall.

For the Wissey W3 sample, where the associated differential pressures are much smaller than those of the East Brae samples, both over- and underestimation of the integral is observed through use of the incompressible approximation. Overestimation of the integral (associated with underestimation of the permeability/transmissivity estimates) is observed more commonly for the lower differential pressure measurements, and within the higher temperature experiments, while integral underestimation (permeability/-transmissivity overestimation) is observed for the higher differential pressures. At low differential pressures (i.e. Wissey W3 high temperature measurements), the error associated with the numerical integration estimate is higher, given the use of a 0.03 MPa pressure step size, and this may contribute to the percentage difference observed between the two calculation methods (numerical integration and incompressible approximation) in these cases. If the magnitude of under/overestimation of the incompressible approximation was more significant, this could impact on observations of non-linearity. However the effects during this study are considered to be reasonably small given the already significant measurement uncertainties present during flow regime analysis (section 7.3).

The above review of errors associated with use of an incompressible approximation within hydraulic parameter estimation demonstrates that the impact of this approximation is small. It is therefore concluded that use of the incompressible form of Darcy's law (Equation 2.4), and the analogous cubic law (Equation 2.5) is appropriate for CO_2 under the experimental conditions assessed during this study, with incorporation of Forchheimer non-linear adjustments as required, see sections 2.4 and 7.3. As stated in section 2.5.2, this incompressible approximation approach has therefore been adopted within this experimental study, thus avoiding the requirement for more complex numerical integration during result analysis.

7.5 Elastic response to stress change

7.5.1 Introduction

This section examines the impact of stress changes on fracture transmissivity, using the transmissivity estimates derived in section 7.3 for the Wissey sample; the Cambrian shale sample; and the East Brae D2 sample. As discussed in Chapter 2, stress change

is expected to result in mechanical changes to the fracture, with a resultant effect on transmissivity. Elastic changes are examined within this section using results from the latter stages of sample experiments where possible, to ensure stable experimental conditions thus minimising inelastic change and associated influences. Section 7.6 discusses inelastic changes observed predominantly during the early stages of sample experiments.

The effects on transmissivity of both confining pressure change and fluid pressure change are examined within this section. Effective stress is also considered, using the transmissivity estimates to assess the suitability of the Terzaghi [1923] effective stress law (Equation 2.25) for describing the stresses acting on discrete fractures. Results from the Wissey W3, Cambrian V1 and East Brae D2 samples are presented in subsections 7.5.2, 7.5.3 and 7.5.4 respectively.

7.5.2 Wissey W3 sample

True transmissivity estimates were calculated for each pressure scenario assessed during Experiments B (58°C) and C1 (38°C) for the Wissey W3 sample in section 7.3, with data from multiple experimental stages with the same pressure and temperature conditions combined to maximise the size of the dataset used for transmissivity estimations (see Chapter 6, section 6.2). Larger datasets minimise the uncertainty associated with model fits, and thus minimise uncertainty associated with the transmissivity estimates, where inelastic effects between experimental stages are considered to be small. Data from Experiment A and the first two stages of Experiment B were however excluded from this analysis due to the significance of inelastic effects observed (see section 7.6 for details). Inelastic effects were considered to be small relative to elastic effects during Experiment C1 and the latter stages of Experiments B.

These true transmissivity estimates are used to assess elastic mechanical changes resulting from stress change, both through confining pressure and fluid pressure change. According to the cubic law (see Equation 2.5 and 2.7), fracture transmissivity is proportional to the cube of the hydraulic aperture of a discrete fracture, and thus is an effective indicator for fracture aperture, where direct measurement is not possible. Three confining pressures and three downstream fluid pressures were tested during both Experiment C1 (38°C) and B (58°C); there are therefore nine pressure scenario combinations, and thus nine true transmissivity estimates for each temperature experiment.

Figure 7.30 plots the true transmissivity estimates as a function of confining pressure for the Wissey sample. From this figure it is clear that, under all temperature and fluid pressure conditions tested, the sample transmissivity decreases as confining pressure increases. In addition we observe that, for all temperature and confining pressure scenarios, sample transmissivity increases with an increase in fluid pressure. These observations are in line with expectations, as normal closure of the fracture aperture is expected to occur as effective stress on the sample (and thus normal stress acting on the fracture plane) increases [Bandis et al., 1983, Barton et al., 1985]. Effective stress on the sample and thus normal stress on the fracture plane increases with increasing confining pressure, and decreases with increasing fluid pressure (see section 2.6).

The relationship between normal stress and fracture aperture closure is highly non-linear and is suggested to follow a hyperbolic function dependent on fracture stiffness [Bandis et al., 1983]. The rate of aperture closure has been found to decrease as normal stress increases [Bandis et al., 1983]. We observe from our experiments (Figure 7.30) that the rate of change of transmissivity to stress change is greatest at low confining pressures and high fluid pressures, i.e. where normal effective stresses are lowest, which is in agreement with the findings of Bandis et al. [1983] and Barton et al. [1985].

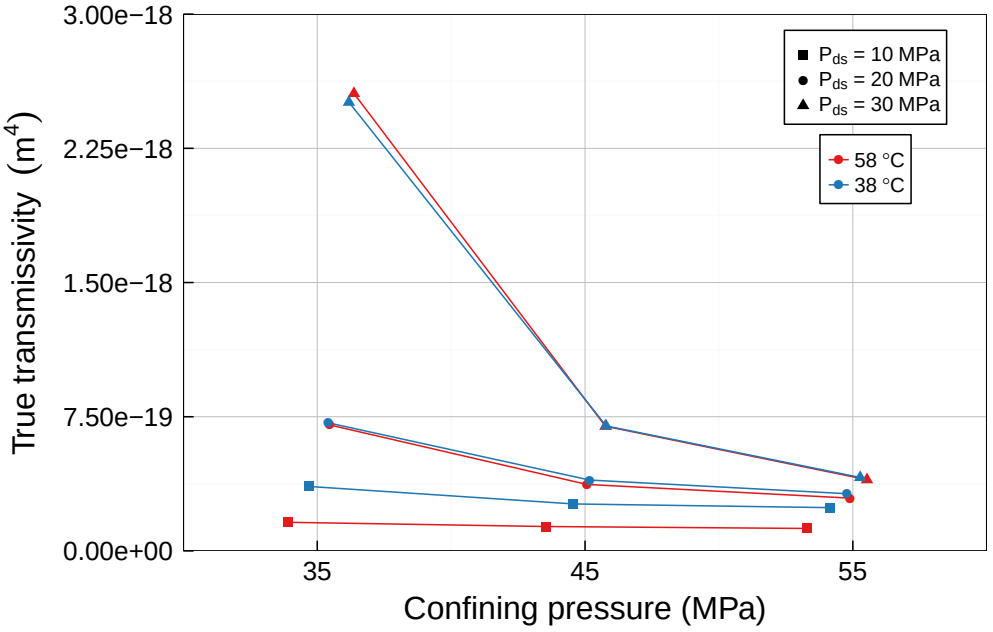

FIGURE 7.30: True transmissivity estimates as a function of confining pressure for the Wissey sample (Expts B & C1)

From Figure 7.30, temperature is observed to have little effect on transmissivity estimates for the higher fluid pressure scenarios (P_{ds} = 20 MPa and P_{ds} = 30 MPa). At low fluid pressure (P_{ds} = 10 MPa), transmissivity estimates are observed to be lower for the high temperature scenarios at all confining pressures.

In theory transmissivity and permeability are intrinsic properties of the rock, and therefore should not be influenced by fluid properties (section 7.4). Transmissivity and permeability are influenced by rock properties such as fracture geometry and surface roughness. Any observed temperature effects on transmissivity are therefore likely to relate to associated changes to rock properties i.e. fracture geometry or stiffness, or alternatively may arise from uncertainty or error in transmissivity estimates. As discussed in section 7.4, uncertainty in transmissivity estimates are greatest for the low fluid pressure, high temperature scenarios due to increased uncertainty associated with fluid properties.

Figure 7.31 displays the same Wissey transmissivity estimates as Figure 7.30, but in this case as a function of effective stress, using the Terzaghi [1923] relationship where effective stress is confining pressure minus mean fluid pressure (Equation 2.25). Figure 7.31 suggests that the Terzaghi [1923] relationship is valid for the experiments, as a clear trend is observed that fits data from almost all scenarios. The low fluid pressure, high temperature results are atypical. A power law model is fitted to all the data in Figure 7.31 to describe the relationship between transmissivity and effective stress. The model is a reasonably good fit ($R^2 = 0.87$) and suggests that the relationship between true transmissivity, T_0 (m^4), and effective stress, σ_{eff} (MPa), for the Wissey sample may be described by $T_0 = 3.2 \times 10^{-17} \times \sigma_{eff}^{-1.4}$.

On a log-log scale (Figure 7.32), it is clear that there is notable deviation of experimental data points from the model at high effective stresses. This is a result of the data outliers from the high temperature, low fluid pressure scenarios. Exclusion of these 3 data points results in an improved power law model fit to the rest of the dataset, as can be observed in Figure 7.33. The revised power law model, adopted in this figure, is $T_0 = 2.1 \times 10^{-17} \times \sigma_{eff}^{-1.2}$, with an associated $R^2 = 0.98$.

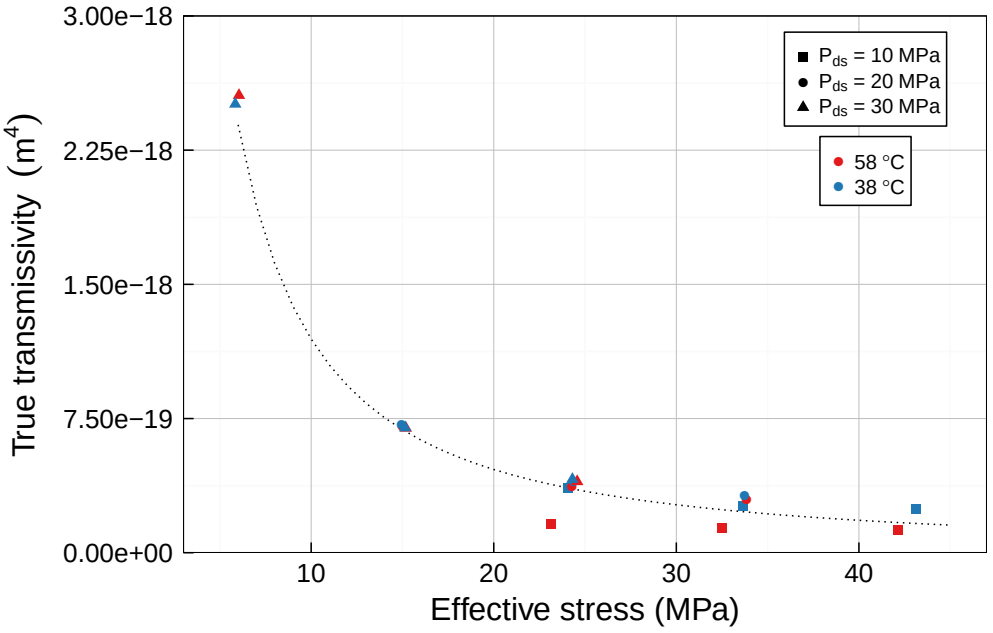

FIGURE 7.31: Power law model fit to true transmissivity as a function of effective stress (Wissey - Expts B & C1)

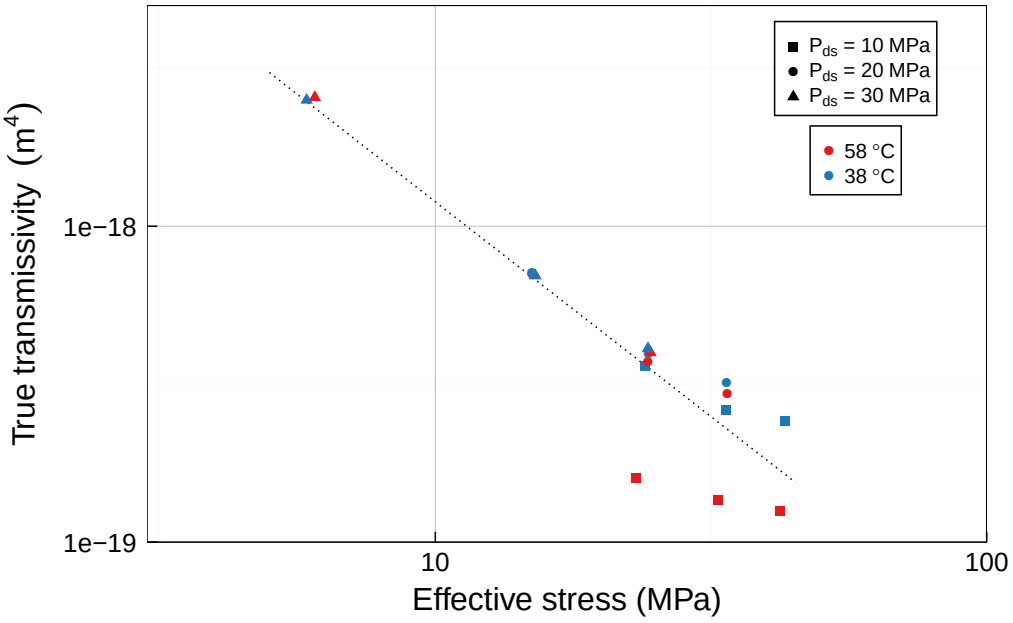

FIGURE 7.32: Power law model fit to true transmissivity as a function of effective stress (Wissey - Expts B & C1) [log-log scale]

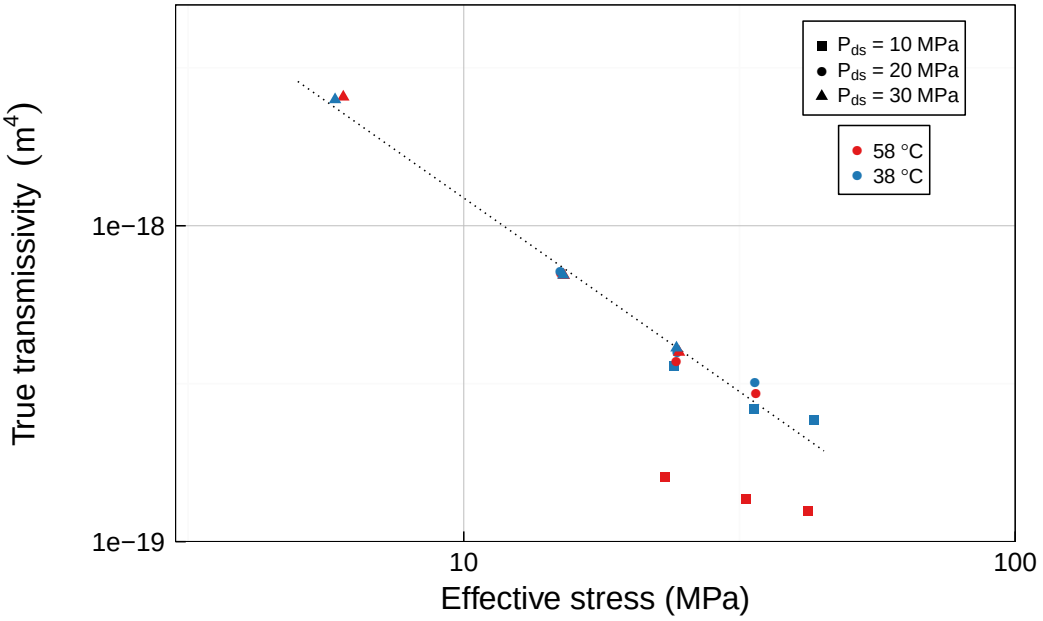

FIGURE 7.33: Power law model fit to true transmissivity as a function of effective stress, excluding the 58°C, P_{ds} = 10 MPa data outliers (Wissey - Expts B & C1) [log-log scale]

7.5.3 Cambrian V1 sample

As with the Wissey sample, data from Experiments C (38°C) and the latter three stages of Experiment B (58°C) have been used for estimation of true transmissivities for each pressure/temperature scenario tested. Data from Experiment A and the first two stages of Experiment B have been excluded from this analysis due to the significance of inelastic effects observed (section 7.6). Nine pressure scenarios were assessed for Experiment B (3 confining pressures, and 3 fluid pressures), while only the low confining pressure (35 MPa) was assessed for Experiment C resulting in transmissivity estimates for the three fluid pressures only.

The transmissivity estimates have been plotted as a function of confining pressures in Figure 7.34. As with the Wissey sample, transmissivities are observed to decrease with an increase in confining pressure, and increase with an increase in fluid pressure at both temperatures, in line with expectations.

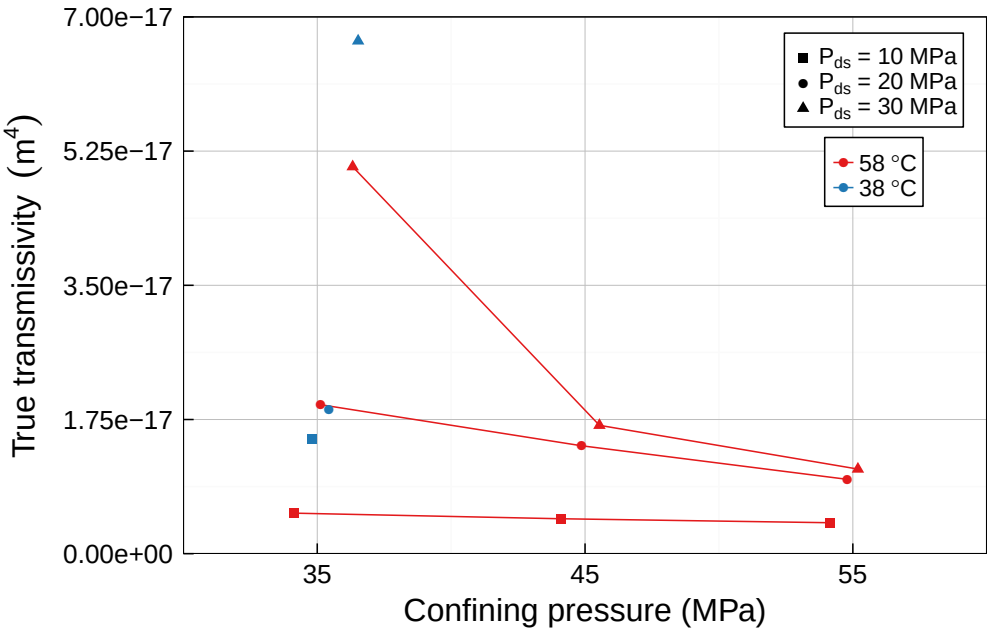

FIGURE 7.34: True transmissivity estimates as a function of confining pressure for the Cambrian shale sample (Expts B & C)

Adopting the Terzaghi [1923] effective stress relationship (Equation 2.25), the transmissivity estimates have been plotted as a function of effective stress in Figure 7.35. Excluding some deviation at high effective stresses for high temperature, low fluid pressure scenarios (similar to that observed for the Wissey sample), the data collapse reasonably well onto a single trend line, indicating the general suitability of the Terzaghi [1923] effective stress law. A power law model, represented by a dotted line, is fitted to all the data in both Figure 7.35 and Figure 7.36 (linear and log-log plots respectively). The model fit (with $R^2 = 0.84$) suggests that transmissivity can be described as function of effective stress by $T_0 = 1.5 \times 10^{-15} \times \sigma_{eff}^{-1.5}$ for the Cambrian shale sample.

As with the Wissey sample, deviation of experimental data points away from the model fit is notable at high effective stresses for the Cambrian shale sample. In a similar manner to the Wissey sample, the three high temperature, low fluid pressure transmissivity estimates are significantly lower than the other data points at similar effective stresses. In Figure 7.37, we have used a revised model fit that excludes these three data points. This results in a significant improvement in model fit to the rest of the dataset. The revised power law model, adopted in this figure, is $T_0 = 3.5 \times 10^{-16} \times \sigma_{eff}^{-1.0}$, with an associated $R^2 = 0.94$.

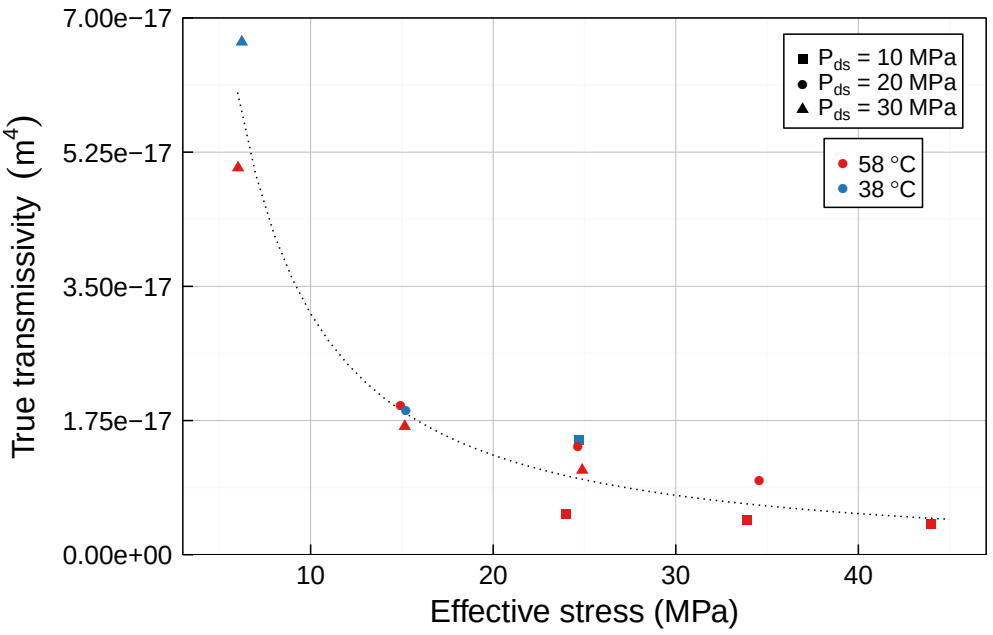

FIGURE 7.35: Power law model fit to true transmissivity as a function of effective stress (Cambrian shale - Expts B & C)

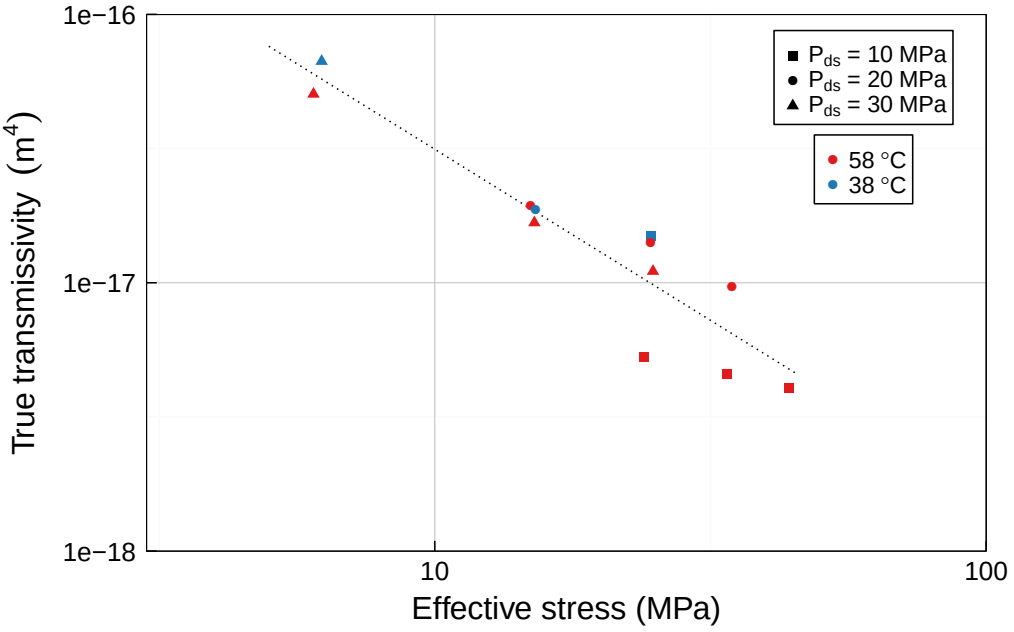

FIGURE 7.36: Power law model fit to true transmissivity as a function of effective stress (Cambrian shale - Expts B & C) [log-log scale]

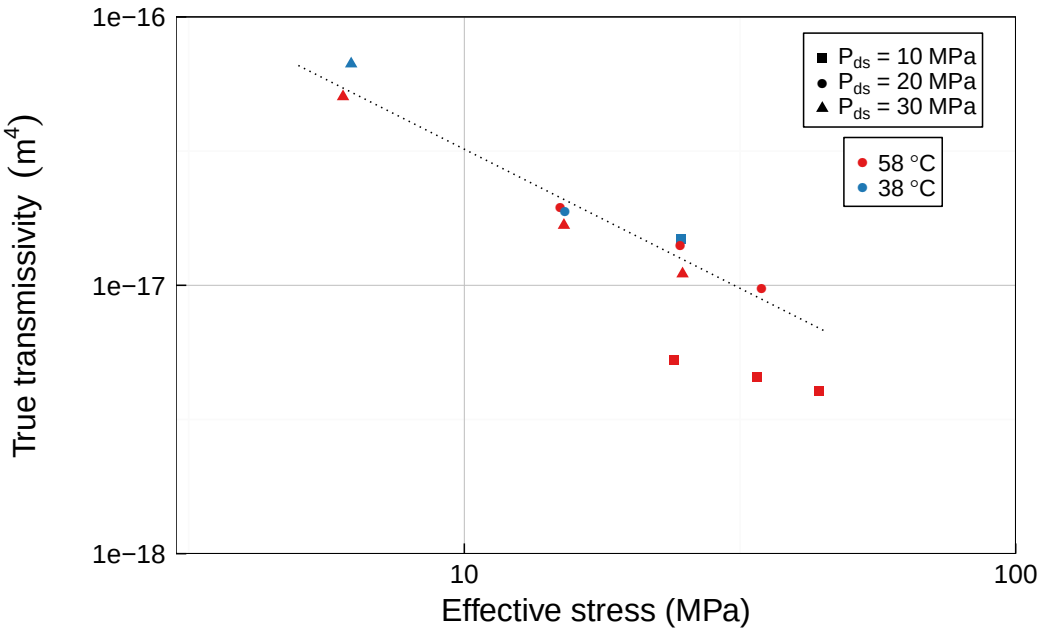

FIGURE 7.37: Power law model fit to true transmissivity as a function of effective stress, excluding the 58°C, P_{ds} = 10 MPa data outliers (Cambrian shale) [log-log scale]

The low transmissivity estimates observed for the 58°C, P_{ds} = 10 MPa scenarios for both the Wissey and Cambrian shale samples suggest that, under high temperature and low CO_2 fluid pressure conditions, fracture aperture closure is greater than under the alternative experimental conditions tested. This could result from either a deviation from the validity of the effective stress law under these conditions, or deviation from the transmissivity versus effective stress relationship. The latter would result from changes to rock properties, such as a reduced fracture stiffness under high temperature conditions, resulting in greater deformation of fracture surface asperities for a given effective stress. Another possibility is that a small degree of thermal expansion of the bulk rock may occur during the higher temperature experiments, which could result in a fractional reduction of the fracture aperture, affecting transmissivities at high effective stresses. However, both of the above scenarios would be expected to affect the P_{ds} = 20 MPa and P_{ds} = 30 MPa high temperature scenarios in addition to the P_{ds} = 10 MPa scenarios at equivalent effective stresses. This is not observed within the experimental data. Review of Figures 2.3 and 2.4 in section 7.4 highlights the particularly low density and viscosity of CO_2 under the high temperature (58°C) and low fluid pressure

(P_{ds} = 10 MPa) experimental conditions in comparison to all other scenarios tested. This could suggest that, under these low density and viscosity conditions, the fluid pressure contribution to effective stress may not be in proportion to the confining stress contribution, implying that the Terzaghi [1923] effective stress law may not be valid for these circumstances. Under these conditions, the modified effective stress law (Equation 2.26) may be applicable, with α being less than unity. It should also be noted that, as discussed in section 7.4, the sensitivity of the density and viscosity parameters are greatest during these high temperature, low fluid pressure scenarios. The uncertainty in transmissivity estimates is therefore also most significant for these values and may contribute to the deviation observed. The cause of these atypical results therefore remains unclear and further experimental investigation is recommended.

7.5.4 East Brae D2 sample

The East Brae D2 sample was only assessed through one series of experiments undertaken at 38°C, due to high differential pressures as a result of low sample transmissivity. Downstream fluid pressures tested also differed from other experiments for this reason, with 10, 15 and 20 MPa used instead of 10, 20 and 30 MPa. Within section 7.3, it was determined that a linear flow regime existed during East Brae D2 experiments. Initial stress-loading of the sample was not undertaken, therefore some inelastic mechanical behaviour was present during the experiments (section 7.6). As only a single confining pressure stress loading cycle was carried out, all data have been used within this analysis, despite the inelastic influence. Use of mean values for transmissivity estimation (see section 7.3), should average out hysteretic effects associated with inelastic processes, and provide indicative results for the elastic response.

Nine pressure scenarios were assessed (3 confining pressures, and 3 fluid pressures). The transmissivity estimates associated with these nine scenarios have been plotted as a function of confining pressures in Figure 7.38. As with the Wissey and Cambrian shale samples, transmissivities are observed to decrease with an increase in confining pressure, and increase with an increase in fluid pressure.

Adopting the Terzaghi [1923] effective stress relationship (Equation 2.25), the transmissivity estimates have been plotted as a function of effective stress in Figures 7.39 and 7.40, linear and log-log plots respectively. A power law model, represented by a dotted

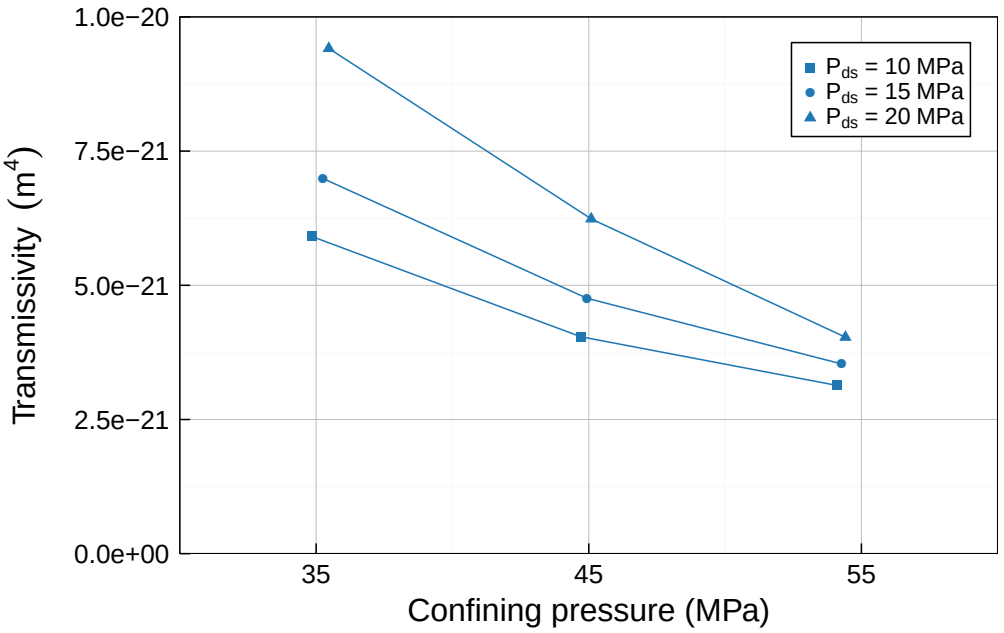

FIGURE 7.38: Transmissivity estimates as a function of confining pressure for the East Brae D2 sample

line, fits the data very well. The model fit (with $R^2 = 0.98$) suggests that transmissivity can be described as function of effective stress by $T_0 = 1.3 \times 10^{-19} \times \sigma_{eff}^{-1.1}$ for the East Brae D2 sample.

7.6 Inelastic response to stress change

7.6.1 Introduction

This section examines the inelastic changes to fracture transmissivity that were observed to result from stress changes. Analysis is undertaken for the Wissey W3 sample, the Cambrian V1 sample and the East Brae D2 sample in subsections 7.6.2, 7.6.3 and 7.6.4 respectively. The effects of both confining pressure (external stress) and fluid pressure (internal stress) cycling are examined for each sample.

To assess inelastic changes to transmissivity as a result of stress loading, transmissivity estimates are compared at various different times during the experiment. Where

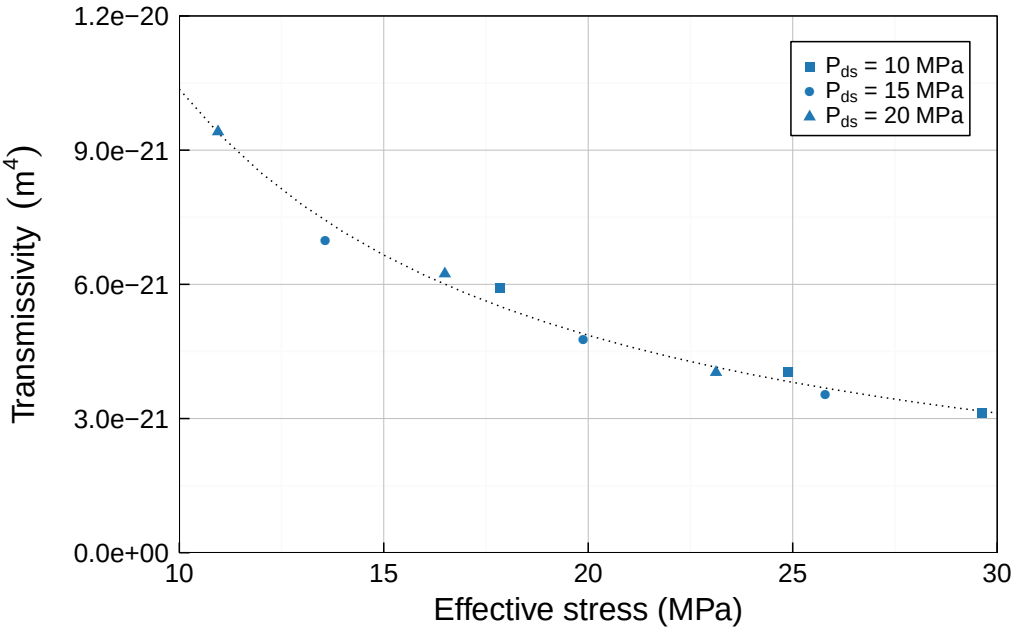

FIGURE 7.39: Power law model fit to transmissivity as a function of effective stress data (East Brae D2)

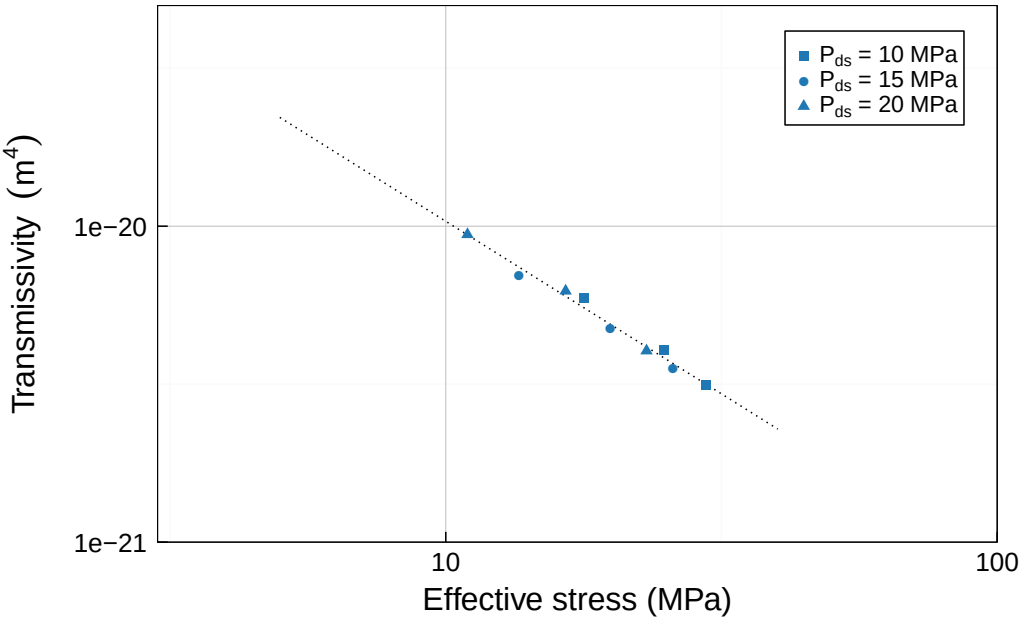

FIGURE 7.40: Power law model fit to transmissivity as a function of effective stress data (East Brae D2) [log-log scale]

pressure conditions are the same, transmissivity estimates are directly comparable and indicate whether change has occurred as a result of inelastic processes.

For assessment of external stress (confining pressure) loading, transmissivity estimates are required for each confining pressure stage of the experiments, using experimental data from that stage only. Separate transmissivity estimates are determined for each fluid pressure scenario within the stage. The data subsets available for estimation of transmissivities are therefore smaller than those used for general transmissivity estimation in section 7.3. For analysis of inelastic behaviour during internal stress (fluid pressure) cycling, transmissivity estimates are required for each fluid pressure step, thus dataset sizes used for transmissivity estimation are even smaller.

Despite the smaller data subsets, the same linear transmissivity estimation technique adopted within section 7.3 has been used for inelastic behaviour analysis of external stress loading for East Brae D2. Similarly, the same non-linear true transmissivity estimation technique adopted within section 7.3 has been used for both external and internal stress loading for the Wissey sample. Model fit checks were undertaken to ensure the suitability of transmissivity estimates, given the smaller number of data points available for model-fitting. Higher uncertainties are associated with these subset transmissivity estimates due to the small datasets, however model fit checks indicated their suitability for use.

There were insufficient points within data subsets to enable model-fitting and true transmissivity estimation for the Cambrian shale sample inelastic behaviour analysis, or for inelastic behaviour analysis of internal stress loading of the East Brae D2 sample. Mean apparent transmissivities were therefore adopted as an alternative to enable analysis in these cases.

7.6.2 Wissey W3 sample

7.6.2.1 External stress loading

Multiple stress loading cycles were carried out during testing of the Wissey sample (Chapter 6 , Figure 6.8). This has enabled transmissivity evolution as a result of repeated external stress loading to be examined at both low (38°C) and high (58°C) temperatures. Figure 7.41 illustrates the evolution of sample transmissivity during the

Wissey experiments using true transmissivity estimates from each low confining pressure (P_c = 35 MPa) stage. A stress loading cycle is undertaken between each low confining pressure stage, therefore the figure illustrates the reduction in true transmissivity observed as a result of each stress loading cycle. Results from the high fluid pressure scenarios (P_{ds} = 30 MPa) have been utilised within this figure due to greater fluid property stability and thus lower measurement uncertainty (section 7.4).

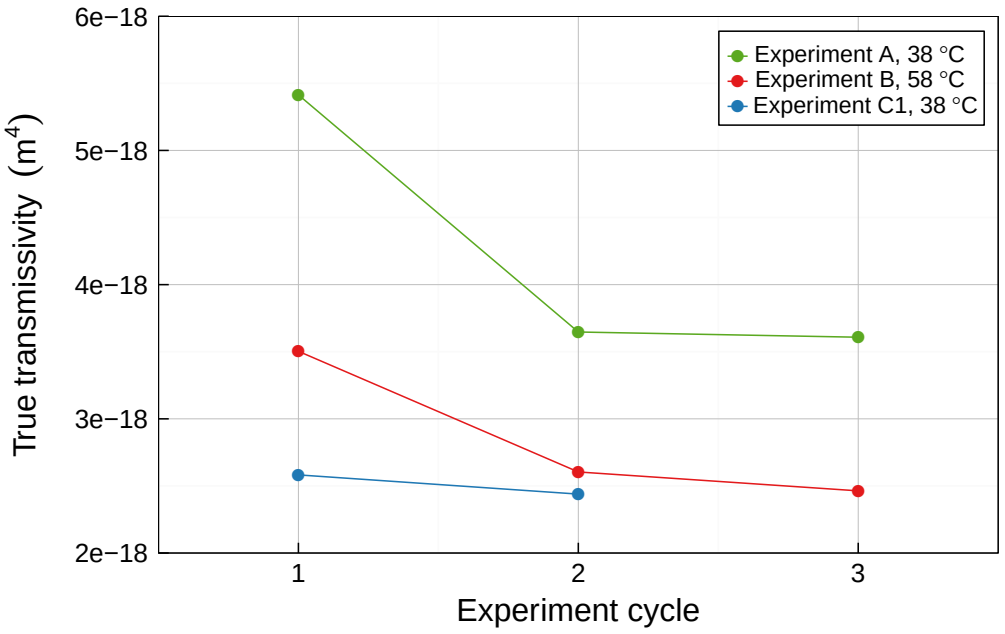

FIGURE 7.41: True transmissivity estimates at each low confining pressure stage (P_c = 35 MPa), illustrating the impact of stress cycling on sample transmissivity for the Wissey W3 sample. [T_0 estimates for P_{ds} = 30 MPa scenario]

Figure 7.41 indicates that during the first experiment (Expt A), undertaken at 38°C, sample transmissivity reduced significantly during the first stress loading cycle (between experiment cycle 1 and 2). This suggests the occurrence of inelastic (plastic) change of the fracture geometry due to the stress loading, with a resultant overall reduction of the fracture aperture. This may be a result of readjustment of the seating position of the two fracture surfaces and/or through plastic deformation of the fracture surfaces. Further transmissivity reduction is observed during the second stress loading cycle (between cycle 2 and 3), however the magnitude of reduction is very small in comparison. These observations are in line with fracture closure measurements undertaken by [Bandis et al., 1983] on a variety of natural fractures (see Chapter 2).

There was little change in estimated transmissivity between the end of Experiment A and the start of Experiment B in association with the temperature increase from 38°C to 58°C. However, during the first stress loading cycle of Experiment B, significant transmissivity reduction was observed. This indicates that the combination of higher temperature in association with repeat stress loading enables the occurrence of additional plastic deformation of the fracture surfaces. As with Experiment A, further transmissivity reduction was observed during the second stress loading cycle of Experiment B, but the magnitude was much smaller than during the first.

Transmissivity estimates were similar between the end of Experiment B and the start of Experiment C1, despite the associated temperature reduction. Only a small reduction in transmissivity was observed during Experiment C1 stress loading. This indicates that inelastic effects become small during repeat stress loading cycles. This is in line with the observations of Bandis et al. [1983], with the additional observation that temperature increase in association with stress loading enhanced inelastic closure for the Wissey fractured sample.

Figure 7.41 indicated the magnitude of transmissivity reduction between external stress loading cycles during the Wissey experiments. By analysing the transmissivity changes observed during stress loading cycles we can also assess the significance of hysteresis during stress loading.

Figure 7.42 illustrates the permanent set (fracture closure) that occurs during external stress (confining pressure) loading within the first stages of both Experiment A and B. This is not observed during Experiment C1. In addition to the permanent set, a small degree of additional 'repeatable', or cyclic hysteresis is observed within the second and third stress loading cycles of Experiment A. This cyclic hysteresis is considered negligible relative to the uncertainty associated with the transmissivity estimates.

7.6.2.2 Internal stress loading

Figure 7.43 illustrates the effect on transmissivity of internal stress (fluid pressure) cycling undertaken during the first stage of each of Experiments A (38°C), B (58°C), and C1 (38°C). Fluid pressure cycling was undertaken during each stage of the experiments (see Chapter 6, Figure 6.8), but presentation of the first stage results was chosen for this analysis as the influence of confining pressure stress loading is minimised at the

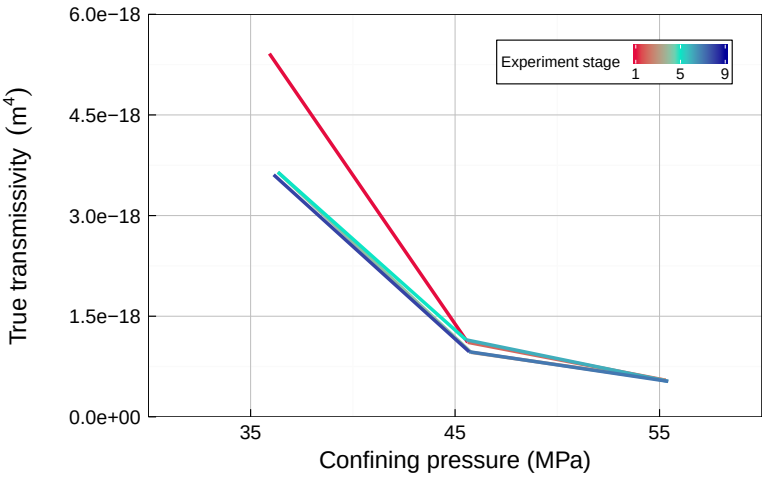

(A) Experiment A (38°C)

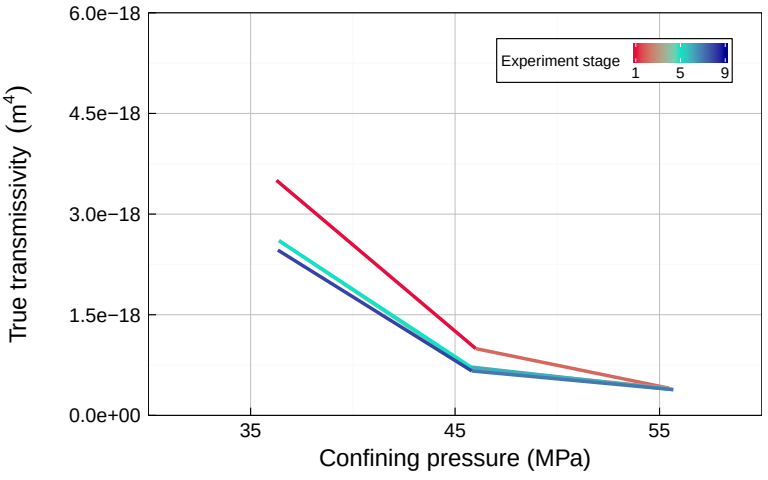

(B) Experiment B (58°C)

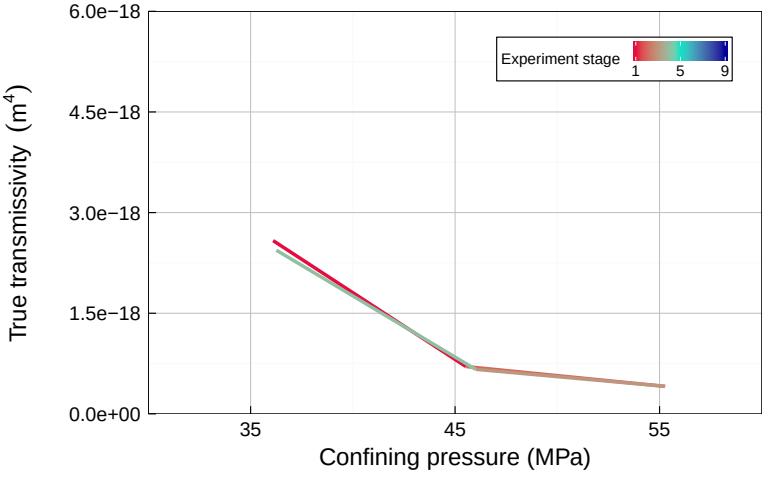

(C) Experiment C1 (38°C)

FIGURE 7.42: True transmissivity plots illustrating hysteresis oberved during the Wissey experiments as a result of confining pressure stress loading (P_{ds} = 30 MPa)

start of the experiments, and fluid pressure effects are most significant at low confining pressure (P_c = 35 MPa).

Figure 7.43 illustrates that transmissivity increases with increasing fluid pressure, under constant confining pressure and temperature, as presented and discussed in section 7.5. The transmissivity differences between Experiment A and C1 in Figure 7.43 are due to the permanent mechanical changes resulting from inelastic external stress loading cycles (Figure 7.41). Unlike the significant inelastic effects observed during external stress loading, no permanent effects on transmissivity are observed as a result of fluid pressure cycling during any of the experiments - the transmissivities at the end of the fluid pressure cycle are the same as the initial transmissivities in all cases. In addition, there is negligible cyclic hysteresis observed during fluid pressure cycling in Experiment A, while only very limited cyclic hysteresis is observed during fluid pressure cycling in Experiments B and C1. Cyclic hysteresis, although still relatively insignificant, is most apparent during Experiment C1, where inelastic fracture changes due to external stress loading are considered negligible. This suggests that external stress loading may have an impact on the fluid pressure cycle observations during Experiments A and B, damping out any hysteresis that could have resulted from fluid pressure cycling.

In all cases, the effects of cyclic hysteresis during fluid pressure cycling are considered to be of the same order of magnitude as transmissivity estimate uncertainty; therefore hysteresis is unlikely to significantly impact results. No cyclic hysteresis is observed during fluid pressure cycling at higher confining pressures.

7.6.3 Cambrian V1 sample

7.6.3.1 External stress loading

External stress (confining pressure) loading cycles were undertaken once during each of Experiments A (38°C) and B (58°C) for the Cambrian shale sample (see Figure 6.1). External stress loading was not undertaken during Experiment C.

Insufficient data points were available within the Cambrian shale experiments to enable true transmissivity estimates to be calculated for each confining pressure stage using the Forchheimer plot method demonstrated in section 7.3, and used for the Wissey sample in section 7.6.2. Mean apparent transmissivities have therefore been used to illustrate

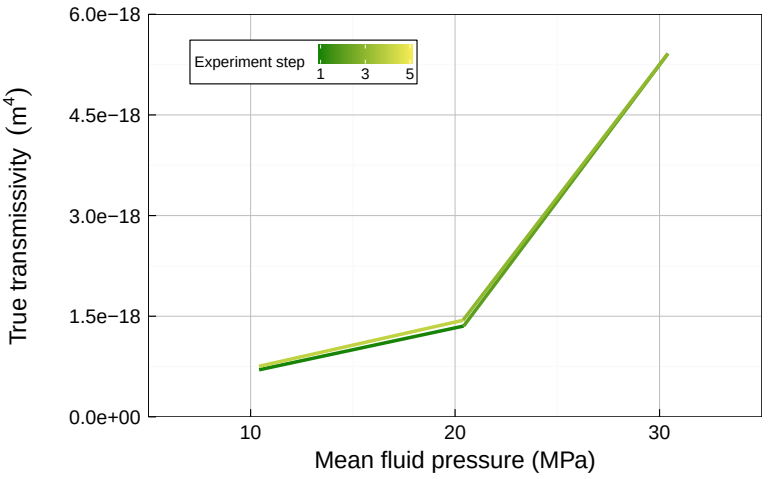

(A) Experiment A (38°C)

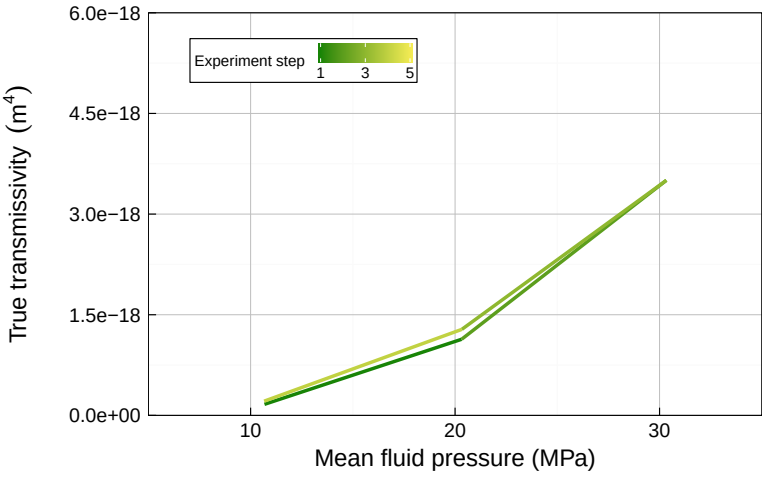

(B) Experiment B (58°C)

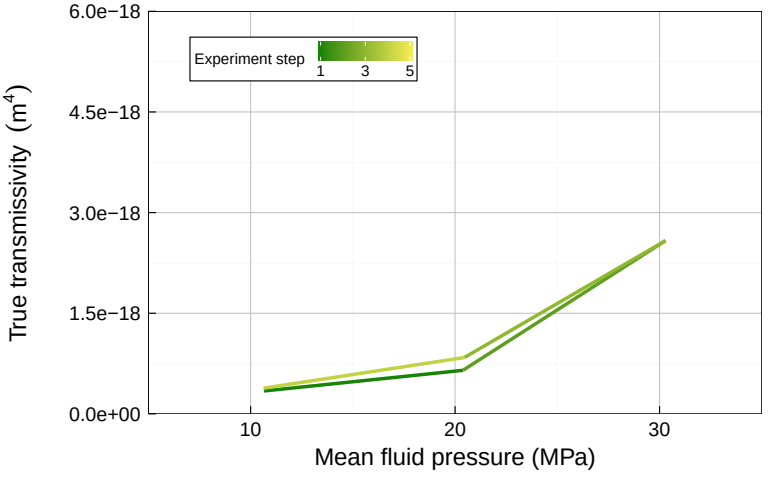

(C) Experiment C1 (38°C)

FIGURE 7.43: True transmissivity plots illustrating hysteresis observed during initial fluid pressure stress cycles of each experiment (Wissey experiments, stage 1, $P_c = 35$ MPa)

the transmissivity changes observed during the external stress loading cycles for the Cambrian shale sample. Mean apparent transmissivities were calculated using Equation 2.13 with the P_{ds} = 30 MPa data subset for each confining pressure stage. Figure 7.44 highlights the significance of inelastic processes during the Cambrian shale external stress loading cycles, through illustration of the impact on apparent transmissivity. The stress loading cycle of Experiment A (38°C) results in a reduction of apparent transmissivity to around one third of the initial value (comparison of stage 1 and stage 5 apparent transmissivities). The hysteretic transmissivity changes during the loading and unloading can also be observed. During Experiment B (58°C), inelastic processes remain significant with apparent transmissivity approximately halved as a result of this subsequent, higher temperature external stress loading cycle.

The apparent transmissivity reductions observed indicate the occurrence of inelastic mechanical processes during stress loading, resulting in reduction of the effective aperture of the fracture (and potentially also microfractures) within the Cambrian sample. These observations are in line with the findings from the Wissey experiments (section 7.6.2), where evidence for inelastic fracture closure was observed during initial external stress loading undertaken at 38°C, with indications for further inelastic closure observed during subsequent high temperature (58°C) stress loading.

7.6.3.2 Internal stress loading

Figure 7.45 uses mean apparent transmissivities to demonstrate the effect of fluid pressure cycling on sample transmissivity during the first stage of each of Experiment A, B and C for the Cambrian shale sample.

Significant hysteresis and permanent set is observed during the initial fluid pressure loading cycle in Experiment A for the Cambrian shale sample. This may be a result of micro-fracturing of the Cambrian shale sample during initial fluid pressure loading. There is evidence of micro-fractures within the sample post-experiment (see section 4.9); these micro-fractures were not visible pre-experiment and are therefore thought to have been created during the experiments. Creation of micro-fractures would be expected to result in an increase in sample transmissivity due to increased flow paths, and micro-fracture generation is most likely to occur as a result of internal stress loading i.e. fluid pressure increase. It is noted that permanent set is not observed in association

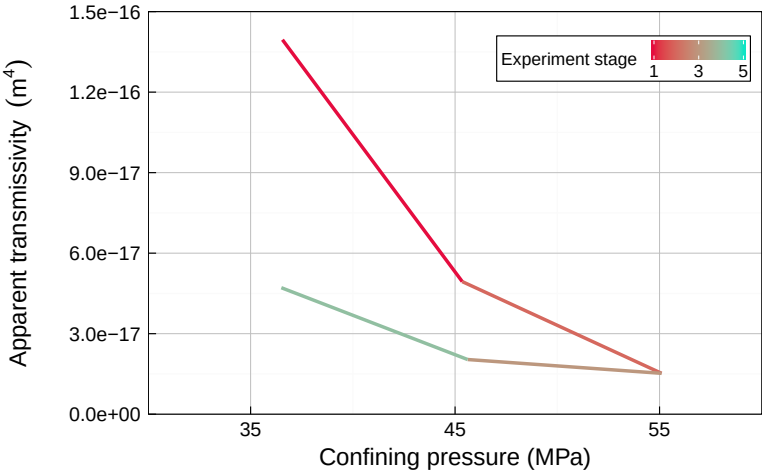

(A) Experiment A (38°C)

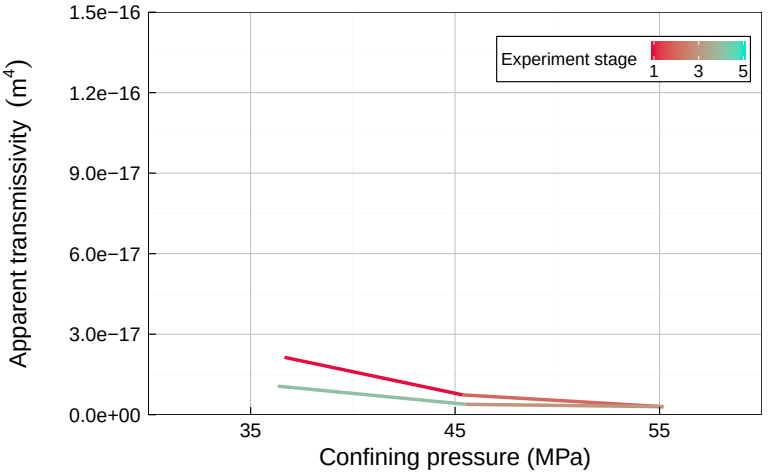

(B) Experiment B (58°C)

FIGURE 7.44: Apparent transmissivity plots illustrating hysteresis observed during confining pressure stress loading (Cambrian shale experiments)

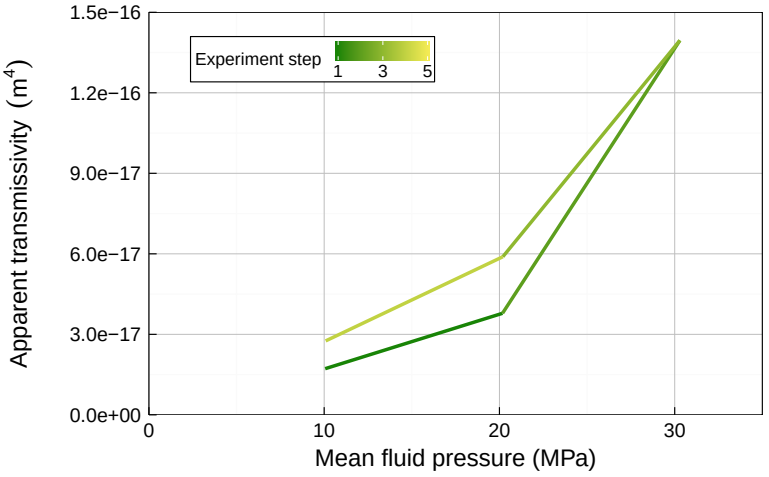

(A) Experiment A (38°C)

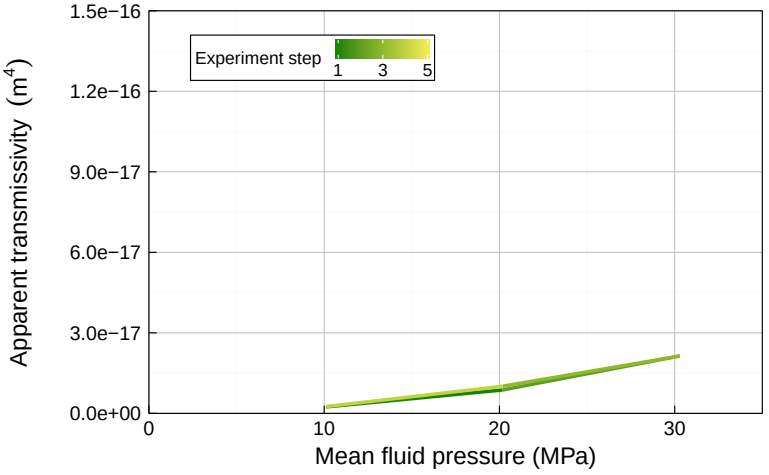

(B) Experiment B (58°C)

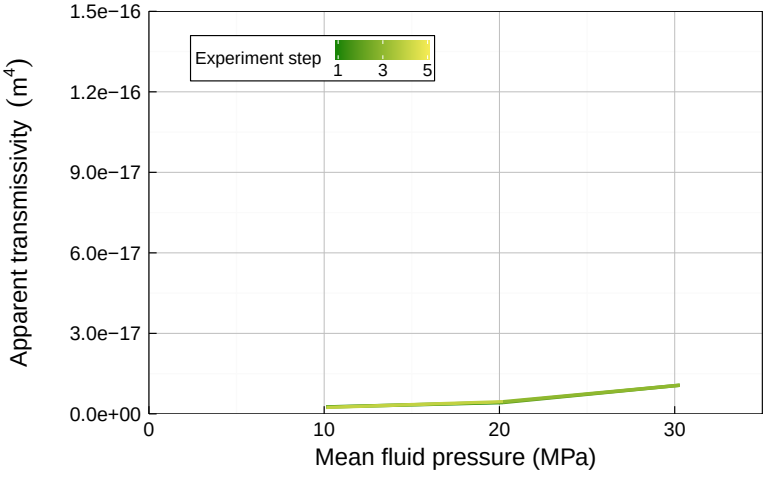

(C) Experiment C (38°C)

FIGURE 7.45: Apparent transmissivity plots illustrating hysteresis observed during the initial fluid pressure stress cycles of each experiment (Cambrian shale V1 experiments, stage 1, $P_c = 35$ MPa)

with internal stress loading for either of the other two fractured samples tested (Wissey and East Brae D2), nor is there evidence of micro-fracturing within these samples post-experiment. This adds weight to the hypothesis that the permanent set observed in Figure 7.45a is associated with the micro-fracturing process.

Negligible cyclic hysteresis and no further permanent set was observed during the subsequent experiments (B and C, Figure 7.45), suggesting that micro-fracturing occurred during the initial stages of the experiment only. Indeed, a general reduction in transmissivity was observed throughout the experiments (see section 7.6.3.1). As micro-fracturing would be expected to result in transmissivity increases, these observations suggest any further micro-fracturing is negligible during the experiments. The observed transmissivity reduction is thought to result from fracture aperture reduction, in association with confining pressure stress loading, in a similar manner to the Wissey sample, as discussed above.

7.6.4 East Brae D2 sample

7.6.4.1 External stress loading

External stress loading during the East Brae D2 experiments is demonstrated within Figure 7.46 for the P_{ds} = 10 MPa scenarios. During these scenarios, sufficient data points were available to estimate transmissivity at each stage of the experiment using Darcy's law (Equation 2.4) and the linear regression technique described in section 7.3.2.

Figure 7.46 shows evidence for inelastic fracture closure through permanent reduction in transmissivity following the external stress (confining pressure) loading undertaken during the East Brae D2 experiments. This is in line with observations from the Wissey and Cambrian shale sample experiments.

7.6.4.2 Internal stress loading

There were insufficient data available for estimation of transmissivities through linear regression within each experimental fluid pressure step for the East Brae D2 sample (Figure 6.3) therefore transmissivity estimates have been calculated for each step by

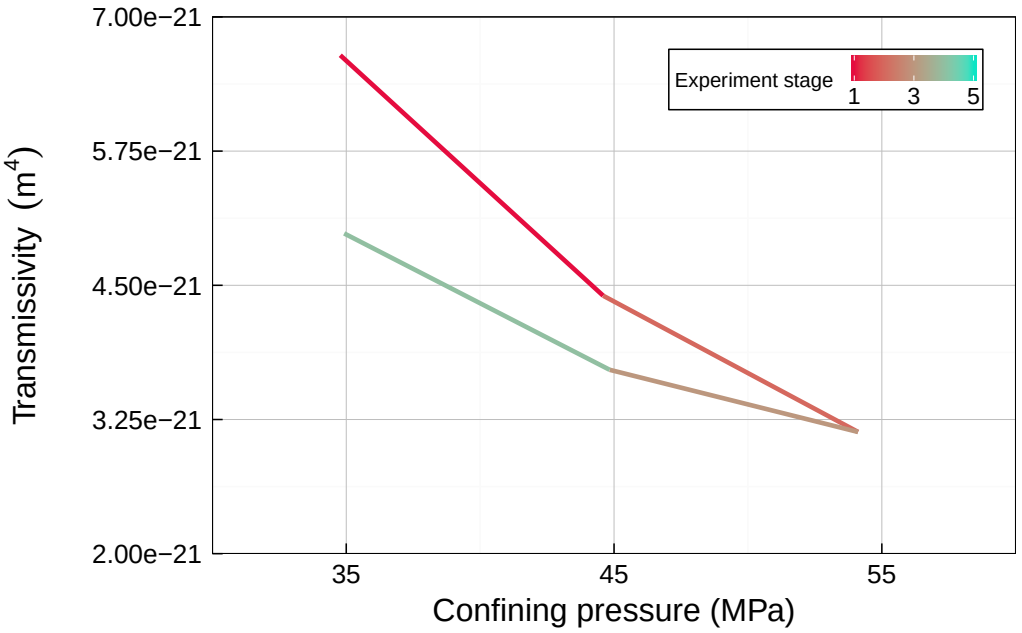

FIGURE 7.46: External (confining pressure) stress loading hysteresis during East Brae D2 experiments. [P_{ds} = 10 MPa]

using Equation 2.6 directly on each of the step data points and calculating the mean from these estimates. They have been labelled as 'apparent transmissivities' in Figure 7.47 to distinguish from the linear regression transmissivity method used in section 7.6.4.1. Stage 5 has been used for this analysis as there were only sufficient data points available during the P_c = 35 MPa experimental stages (1 and 5), and closure due to initial application of external stress during stage 1 was more significant than the internal stress cycling effects. This was due to incomplete stabilisation of the East Brae D2 sample under initial external stress prior to commencement of the flow experiments. The reason for this was the extremely low permeability of the sample, and the associated slow response times of the differential pressure measurement to stress and flow rate changes. This was not an issue during the Wissey and Cambrian shale experiments.

Figure 7.47 shows evidence of cyclic hysteresis during fluid pressure cycling within the East Brae D2 experiments. However, there is no evidence of a permanent change to transmissivity following the fluid pressure cycle. The cyclic hysteresis observed may reflect the slow response of differential pressure to fluid pressure changes for the East

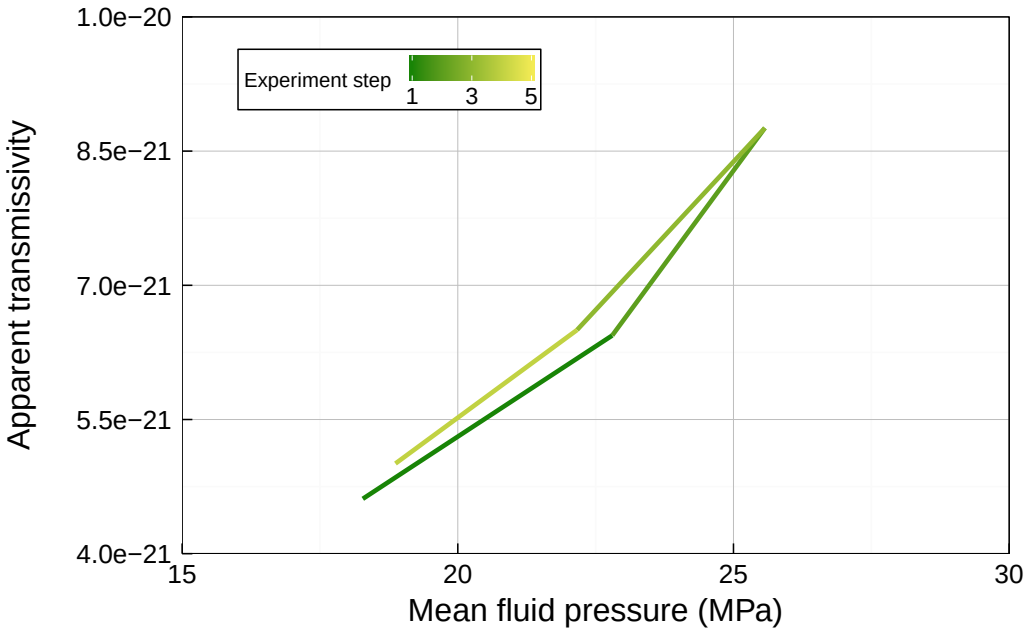

FIGURE 7.47: Internal (fluid pressure) stress loading hysteresis during East Brae D2 experiments. [Stage 5, $P_c = 35$ MPa]

Brae D2 sample, and thus a lag in observed transmissivity change following fluid pressure changes. This effect was minimised as far as possible by ensuring a significant response time between measurements. However, continued small magnitude changes were still observed during some measurement periods within the East Brae D2 sample experiments. A further increase of response time between measurements was not possible for practical reasons.

7.7 Review of hydraulic aperture, fracture permeability and fracture hydraulic conductivity estimates

7.7.1 Introduction

Having derived 'true transmissivity', T_0, estimates using the Forchheimer equation to account for the non-linear flow regime present during the Wissey and Cambrian shale flow experiments (section 7.3), the cubic law (Equation 2.5) for describing flow through

discrete fractures has been used to estimate hydraulic aperture (e_h), fracture permeability (k_{frac}) and fracture hydraulic conductivities (K_{frac}) from these 'true transmissivity' estimates for both samples (Chapter 2). As 'true transmissivity' reflects the transmissivity that would be observed were a linear flow regime to be present (i.e. at very low flow rates), these e_h, k_{frac}, and K_{frac} estimates can be used as reference values for comparison between scenarios and samples. They reflect the e_h, k_{frac}, and K_{frac} values that would be expected under a linear flow regime. The presence of non-linearity during the experiments means that the 'observed' or 'apparent' values are lower than these reference or 'true' values; these apparent values reduce with flow rate as with apparent transmissivity, T_{app} (section 7.3). Due to high measurement uncertainty, it was not possible to undertake similar estimations for the East Brae B2b offset fracture sample.

Hydraulic aperture (e_h), fracture permeability (k_{frac}) and fracture hydraulic conductivities (K_{frac}) associated with the East Brae D2 and B2 samples have also been estimated from transmissivities (T). As a broadly linear flow regime is observed during the East Brae D2 experiments, Darcy's law is valid. Transmissivities for East Brae D2 were therefore estimated using linear regression (section 7.3). It has been assumed, in the absence of available data for flow regime analysis, that Darcy's law is also valid during the single flow test undertaken on the East Brae B2 sample, as the sample flow rate during the flow test was very low (0.4 ml/min or 6.4×10^{-9} m^3/s), and the associated transmissivity estimate (1.1×10^{-21} m^4) calculated using Equation 2.6 is lower, but of a similar magnitude to the D2 estimates (Table 7.4).

This section presents the hydraulic aperture (e_h), fracture permeability (k_{frac}) and fracture hydraulic conductivity (K_{frac}) estimates for each of the four fractured samples for which transmissivity estimates have been derived: Wissey W3, Cambrian shale V1 and East Brae D2 and B2. While the hydraulic aperture and fracture permeability values are simple functions of transmissivity, the hydraulic conductivity estimates are also a function of fluid density and fluid viscosity. Thus, the hydraulic conductivity estimates are utilised within section 7.8 to assess the relative importance of fluid and mechanical changes between experimental scenarios.

A boxplot in Figure 7.48 illustrates the range of transmissivity (or true transmissivity) estimates derived in association with flow regime analysis (section 7.3) for each sample. These transmissivity estimates are used for estimation of hydraulic apertures, fracture

permeabilities and fracture hydraulic conductivities in the following subsections. As discussed above, true transmissivity estimates have been adopted within this plot where non-linear flow effects are significant (Wissey and Cambrian shale samples).

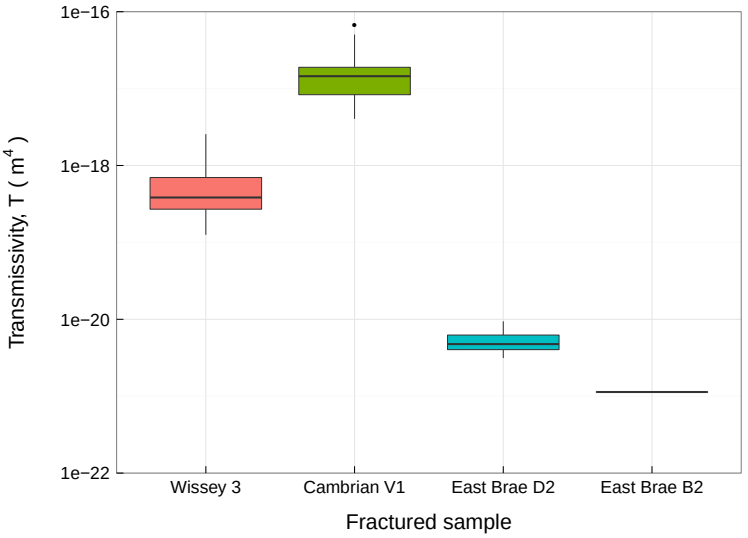

FIGURE 7.48: The transmissivity range associated with all CO_2 flow experiments for each fractured sample, estimated during flow regime analysis. True transmissivities are displayed for the Wissey and Cambrian shale samples as non-linear flow effects are significant.

7.7.2 Hydraulic aperture

Using the true transmissivity (T_0) estimates, the estimated hydraulic apertures range from 3.4×10^{-6} m (3.4 μm) to 9.3×10^{-6} m (9.3 μm) for the Wissey sample, and 1.1×10^{-5} m (11 μm) to 2.8×10^{-5} m (28 μm) for the Cambrian shale sample. The hydraulic apertures associated with the transmissivity estimates for the East Brae D2 sample range from 1.0×10^{-6} m (1.0 μm) to 1.4×10^{-6} m (1.4 μm), and the hydraulic aperture associated with the East Brae B2 test is 7.1×10^{-7} m (0.7 μm). Hydraulic aperture is proportional to the cube root of transmissivity (Equation 2.7). The East Brae samples, which have the lowest transmissivities of the four samples, therefore have the lowest hydraulic aperture estimates, while the hydraulic aperture estimates associated with the relatively high transmissivity Cambrian shale sample are more than 10 times larger. There is no overlap of hydraulic aperture ranges between the three samples.

The hydraulic aperture estimates are presented as a function of effective stress in Figure 7.49, with subplots for each sample, excluding East Brae B2 where effective stress was 14.6 MPa and was not varied. Regression lines using power law models are included within the plots. The regressions are fitted to all data excluding the high temperature (58°C), low fluid pressure (P_{ds} = 10 MPa) data points as, as with the transmissivities (see section 7.5), these points are again observed to be atypical.

A boxplot is used to illustrate a summary comparison of the hydraulic aperture ranges estimated for each of the four samples (Figure 7.50).

7.7.3 Fracture permeability

Using the true transmissivity (T_0) estimates, the estimated fracture permeabilities range from 1.0×10^{-12} m^2 to 7.3×10^{-12} m^2 for the Wissey sample, and 1.0×10^{-11} m^2 to 6.4×10^{-11} m^2 for the Cambrian shale sample. The fracture permeabilities associated with the transmissivity estimates for the East Brae D2 sample range from 8.3×10^{-14} m^2 to 1.7×10^{-13} m^2, and for the East Brae B2 test the fracture permeability was 4.2×10^{-14} m^2. Fracture permeability is proportional to transmissivity to the power of $\frac{2}{3}$ (Equation 2.8). Consequently, as with hydraulic aperture there is no overlap between permeability estimate ranges, with East Brae estimates being the lowest, and Cambrian shale the highest.

The fracture permeability estimates are presented as a function of effective stress in Figure 7.51, with subplots for each sample (except East Brae B2). Regression lines using power law models are included within the plots. As with Figure 7.49, the regressions are fitted to all data excluding the high temperature (58°C), low fluid pressure (P_{ds} = 10 MPa) data points as these points are observed to be outliers when adopting the Terzaghi [1923] effective stress relationship (section 7.5).

A boxplot is used to illustrate a summary comparison of the fracture permeability ranges estimated for each of the four samples (Figure 7.52).

7.7.4 Fracture hydraulic conductivity

Fracture hydraulic conductivity estimates derived from true transmisssivities range from 2.1×10^{-4} m/s to 9.5×10^{-4} m/s for the Wissey sample, and 2.3×10^{-3} m/s to

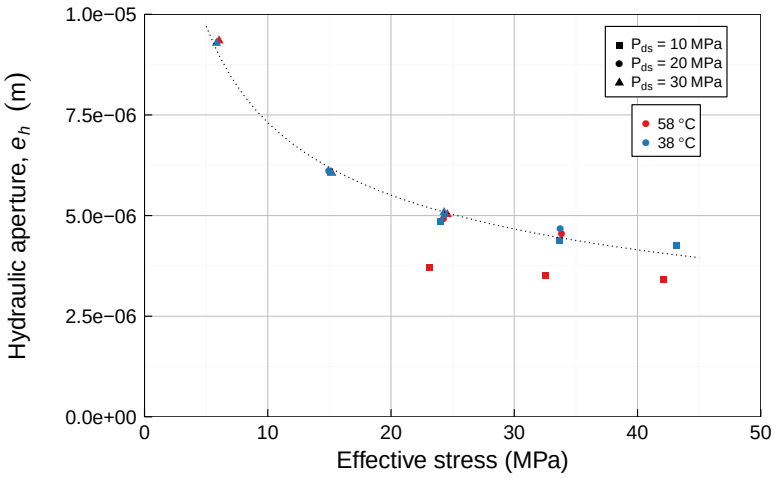

(A) Wissey sample

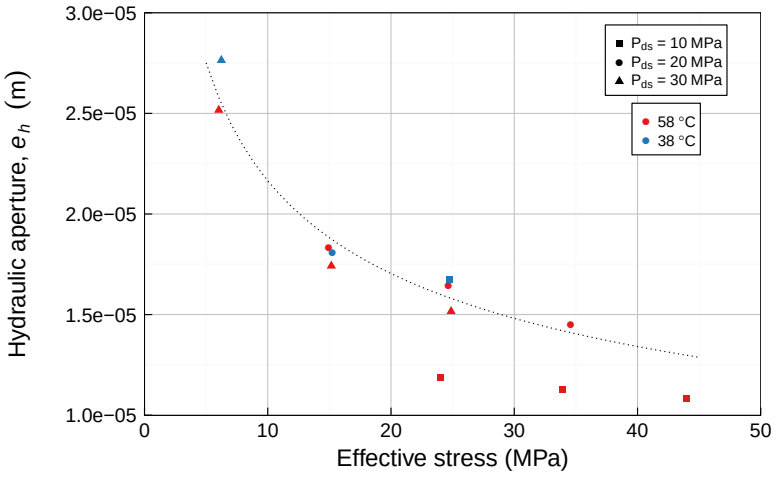

(B) Cambrian shale sample

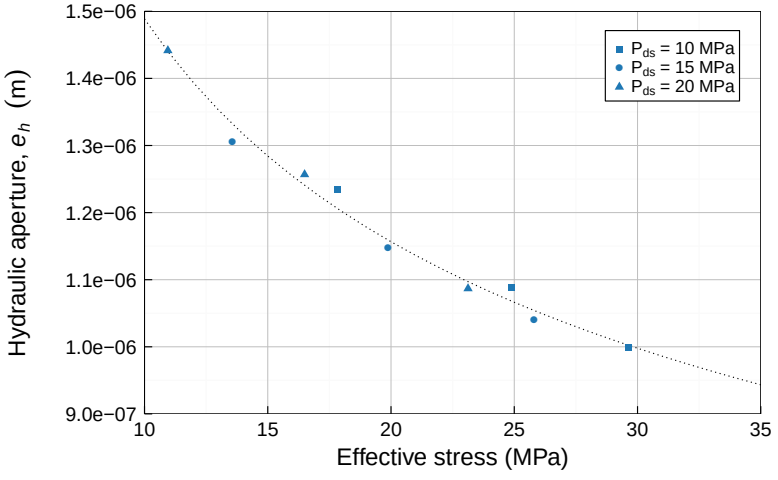

(C) East Brae D2 sample

FIGURE 7.49: Hydraulic aperture as a function of effective stress

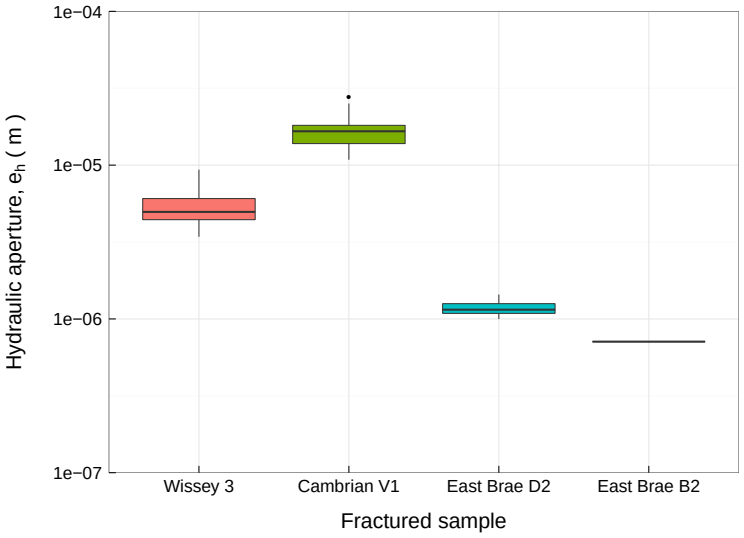

FIGURE 7.50: Hydraulic aperture ranges associated with all CO_2 flow experiments for each fractured sample.

7.4×10^{-3} m/s for the Cambrian shale sample. Fracture hydraulic conductivities associated with the East Brae D2 sample range from 1.0×10^{-5} m/s to 2.1×10^{-5} m/s, and for East Brae B2 the fracture hydraulic conductivity estimate was 5.4×10^{-6} m/s. It is apparent from Figure 7.53, where hydraulic conductivity data are plotted as a function of effective stress, that there is significantly more scatter associated with the hydraulic conductivities than the transmissivities, hydraulic apertures and permeabilities.

While transmissivity, hydraulic aperture and permeability are all intrinsic rock properties, the hydraulic conductivity is also affected by fluid property changes. It is these fluid property changes (variance is discussed in section 7.4), that result in the observed scatter. Vertical bars on the data points within Figure 7.53 represent the range of hydraulic conductivity estimates within each pressure/temperature scenario that arise due to flow rate changes and the associated ρ_{sample} and μ_{sample} variations. These variations result from differential pressure and thus mean fluid pressure responses to flow rate changes. As discussed in section 6.6, quantification of errors has not been undertaken for T, e_h, k_{frac} or K_{frac} due to the challenges associated with estimating uncertainty in Forchheimer/Darcy regression analysis respectively. The relative influence of temperature and fluid pressure on hydraulic conductivity are examined in section 7.8.

A boxplot is used to illustrate a summary comparison of the fracture hydraulic conductivity ranges estimated for each of the four samples (Figure 7.54).

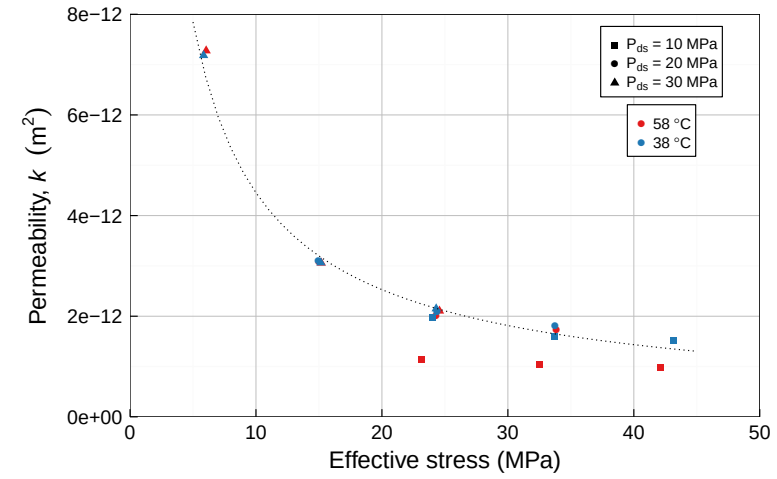

(A) Wissey sample

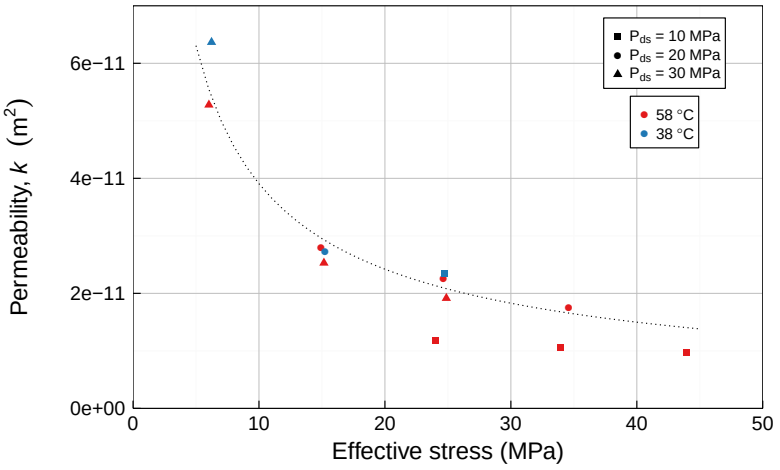

(B) Cambrian shale sample

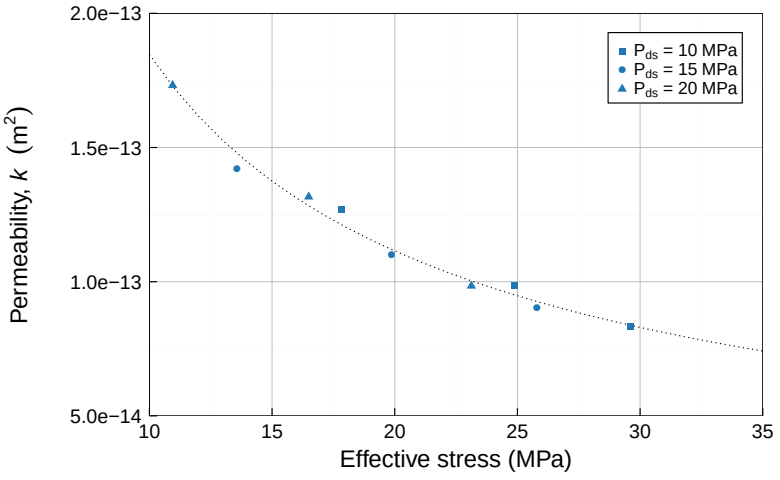

(C) East Brae D2 sample

FIGURE 7.51: Fracture permeability as a function of effective stress

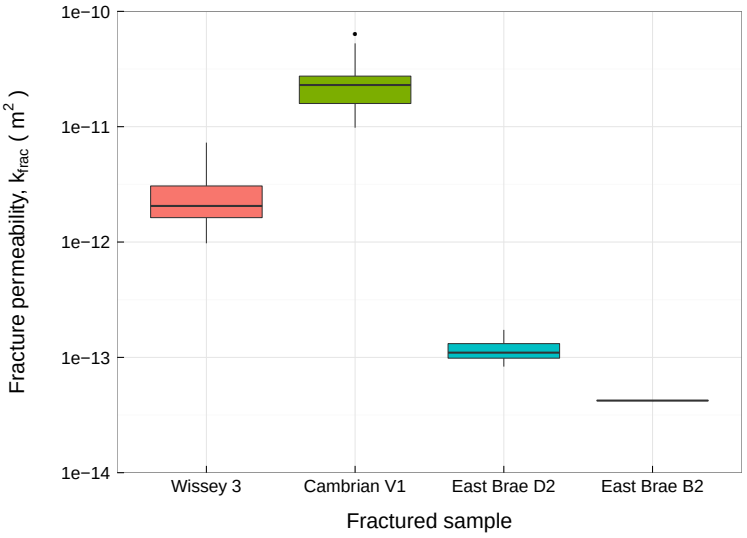

FIGURE 7.52: Fracture permeability ranges associated with all CO_2 flow experiments for each fractured sample.

7.8 Effects of coupled hydraulic and mechanical behaviour on fracture conductivity

7.8.1 Introduction

This section assesses the variation of fracture hydraulic conductivity estimates (section 7.7) between pressure and temperature scenarios where possible for each of three fractured samples: Wissey W3, Cambrian V1 and East Brae D2. Fracture hydraulic conductivity is a function of both rock and fluid properties, therefore conductivity changes may result from changes to either hydraulic or mechanical conditions, or both. A review of the resultant change to conductivity allows an assessment of the relative importance of both hydraulic and mechanical changes between the experimental scenarios. This enables a fuller understanding of the importance of hydraulic and mechanical processes under in-situ conditions.

Mechanical changes are expected to occur in response to stress changes. Therefore under constant effective stress, mechanical changes are expected to be negligible. We observe that there is negligible variation in transmissivity under constant effective stress (section 7.5), which is consistent with expectations. In sections 7.8.2 and 7.8.3 we

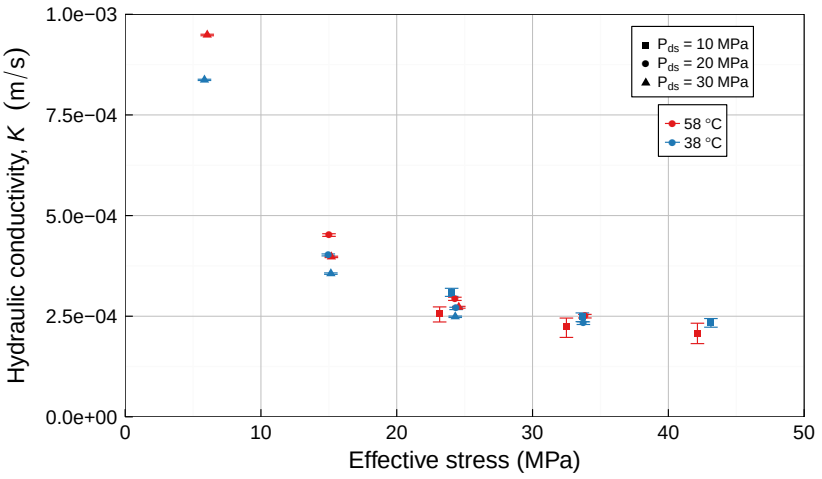

(A) Wissey sample

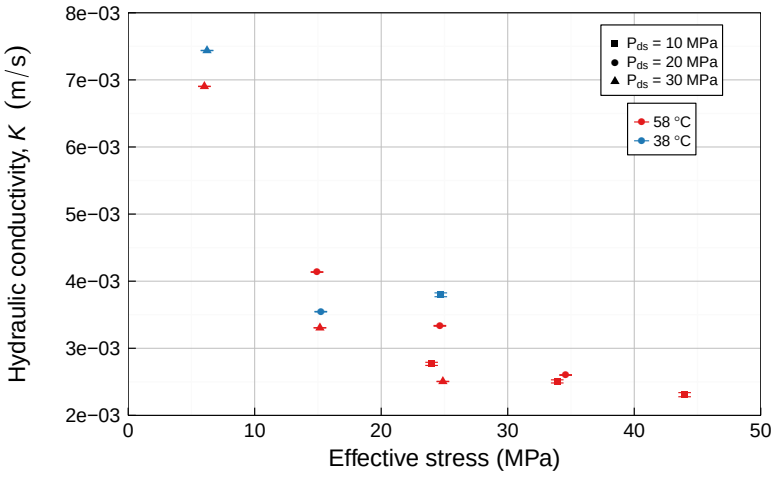

(B) Cambrian shale sample

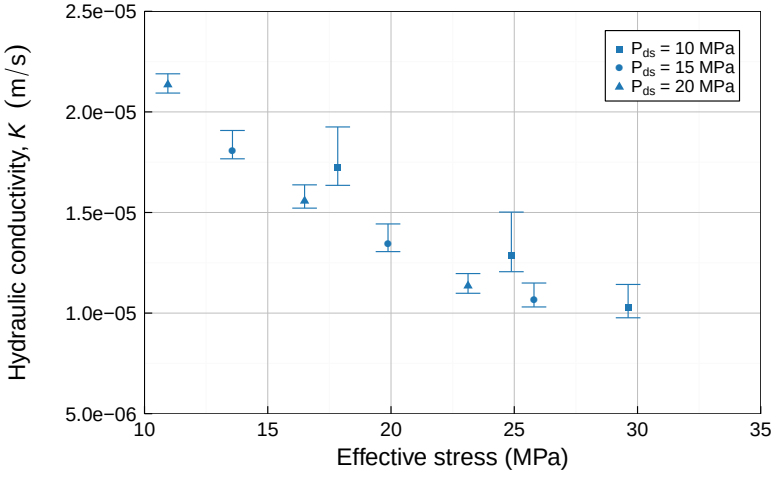

(C) East Brae D2 sample

FIGURE 7.53: Fracture hydraulic conductivity as a function of effective stress. Vertical bars represent the estimate range within each pressure/temperature due to flow rate variation (not the parameter uncertainty).

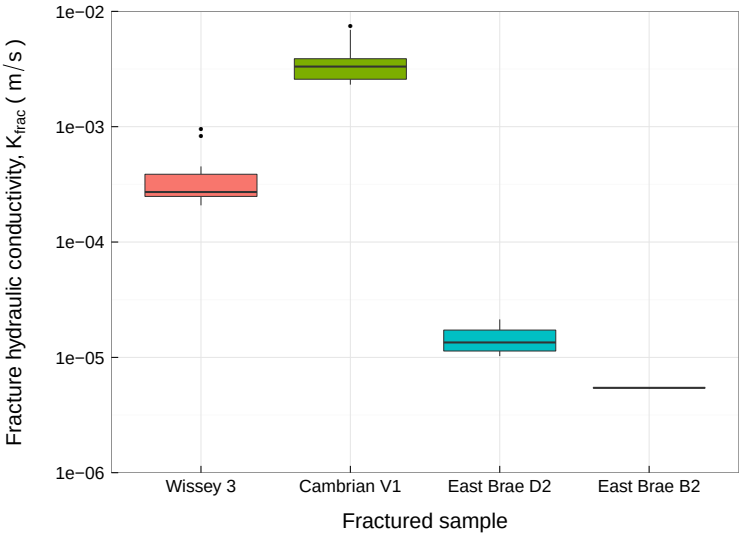

FIGURE 7.54: Fracture hydraulic conductivity ranges associated with all CO_2 flow experiments for each fractured sample.

assess variations to fracture hydraulic conductivity observed under constant effective stress (using the Terzaghi [1923] effective stress law, Equation 2.25), in response to temperature and fluid pressure changes respectively. These observed fracture hydraulic conductivity variations arise due to fluid property (hydraulic) changes.

Within section 7.8.4 the resultant variation to fracture hydraulic conductivity arising from fluid pressure changes under constant confining pressure are examined. Under constant confining pressure, fluid pressure changes result in both effective stress change (and associated mechanical response) as well as fluid property change (and associated hydraulic response). Thus, this section examines the relative significance of mechanical and hydraulic responses respectively, under the range of pressure and temperature scenarios considered.

High temperature (58°C), low fluid pressure (P_{ds} = 10 MPa) data points were excluded from analysis within this section, as they were found to be outliers during effective stress analysis in section 7.5. The cause of these atypical values is as yet unclear.

7.8.2 Temperature variation

In general, transmissivity is not observed to vary with temperature change in the absence of inelastic mechanical processes during these experiments. Transmissivity is

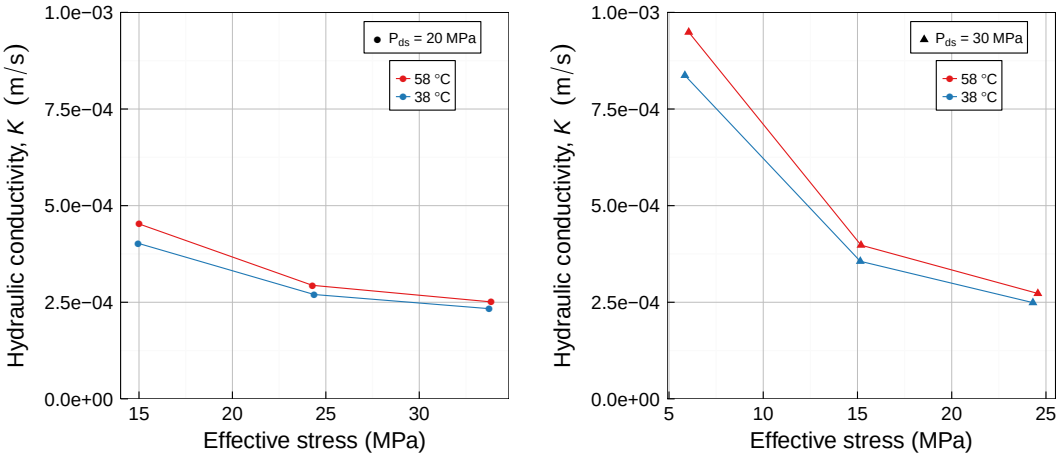

(A) P_{ds} = 20 MPa (B) P_{ds} = 30 MPa

FIGURE 7.55: Temperature effects on fracture hydraulic conductivity (Wissey W3)

a function of rock properties (fracture geometry/surface/stiffness) only (section 7.5) therefore these observations suggest that any thermo-elastic rock effects do not significantly influence fracture transmissivity under the experimental conditions tested. However, hydraulic conductivity, K (Equation 2.9), a function of both mechanical and hydraulic properties, is affected by temperature during CO_2 flow. Temperature increase is associated with fluid density and fluid viscosity reduction. As discussed in section 2.5, viscosity is the controlling fluid property parameter during experiments, and thus an increase in temperature, associated with a viscosity reduction, results in an increase in hydraulic conductivity in the absence of any mechanical changes. This can be observed for fracture hydraulic conductivities within the Wissey experimental results (Figure 7.55) for both the P_{ds} = 20 MPa and P_{ds} = 30 MPa scenarios.

Insufficient data were available for the Cambrian V1 and East Brae D2 experiments to enable similar comparative analysis to be undertaken for these samples.

7.8.3 Fluid pressure variation under constant effective stress

Hydraulic conductivity, K, is affected by fluid pressure change, as well as temperature (Equation 2.9). Figures 7.56 and 7.57 illustrate that, under a constant effective stress, K_{frac} is higher for lower fluid pressures. Under constant effective stress, no mechanical

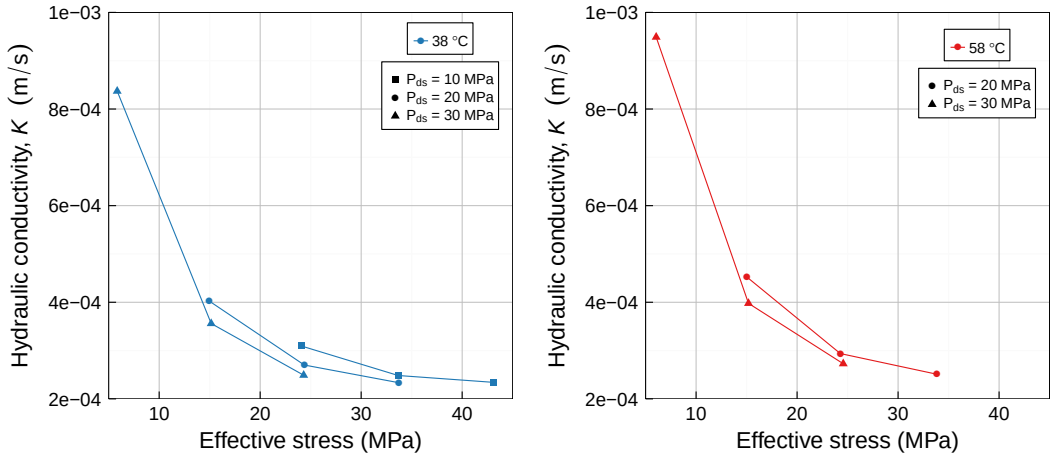

(A) $\theta = 38°C$ (B) $\theta = 58°C$

FIGURE 7.56: Fluid pressure effects on fracture hydraulic conductivity (Wissey W3)

changes are expected, therefore this observation is due to lower fluid viscosities at lower fluid pressures (see section 2.5). The fracture hydraulic conductivity changes with fluid pressure are not significant in comparison to changes resulting from effective stress (mechanical) change, however they can clearly by seen in both figures where the lower fluid pressure points are higher for a given effective stress in all cases.

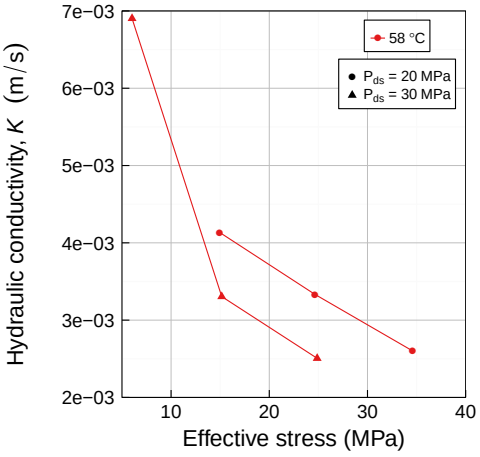

FIGURE 7.57: Fluid pressure effects on fracture hydraulic conductivity (Cambrian V1) [$\theta = 58°C$]

For the East Brae D2 sample (Figure 7.58), smaller fluid pressure increments were adopted during experiments: 5 MPa rather than 10 MPa. For this sample there is

not a clear difference in fracture hydraulic conductivity between P_{ds} = 15 MPa and P_{ds} = 20 MPa, possibly due to the relatively small associated density/viscosity change (Figure 2.5). There is, however, a clear reduction in K_{frac} between the P_{ds} = 10 MPa scenarios and the higher fluid pressure scenarios due to the notably lower associated CO_2 viscosity when P_{ds} = 10 MPa.

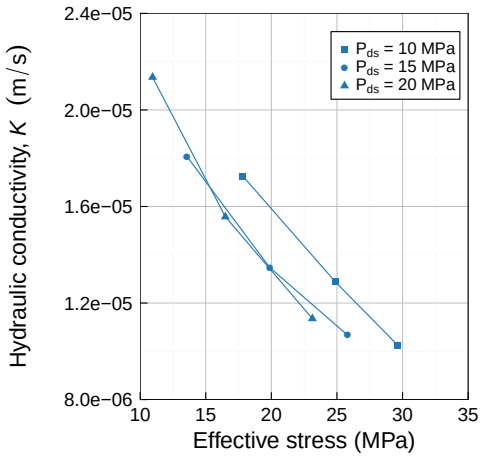

FIGURE 7.58: Fluid pressure effects on fracture hydraulic conductivity (East Brae D2) [θ = 38°C]

7.8.4 Fluid pressure variation under constant confining pressure

Under constant confining pressure, an increase in fluid pressure is associated with a reduction to the effective stress acting on the fractured sample (Equation 2.25). This results in mechanical fracture opening (section 7.5) leading to an increase in transmissivity. The fluid pressure increase also results in an increase in both fluid density and viscosity, with a resultant decrease to the density/viscosity ratio (Figure 7.29). The fracture hydraulic conductivity increases due to the transmissivity increase, and decreases due to the reduction in the density/viscosity ratio. The resultant change to K_{frac} is dependent on the relative significance of the mechanical (transmissivity) and hydraulic (density/viscosity) changes. Fracture hydraulic conductivity, K_{frac}, is proportional to $T^{2/3}$; it is also proportional to ρ/μ (Equation 7.1, see Chapter 2 for further detail). Thus, if we consider the magnitude of the observed increase to T against the magnitude of the decrease to ρ/μ, we are able to calculate the resultant change to K_{frac} as all other values are constant.

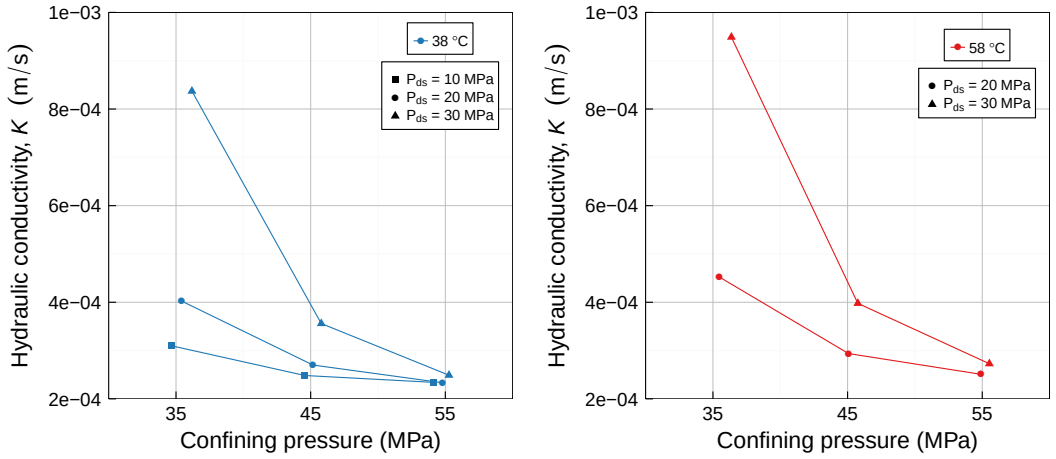

(A) Experiment C1 (38°C)

(B) Experiment B (58°C)

FIGURE 7.59: Fluid pressure effects on fracture hydraulic conductivity under constant confining pressure (Wissey W3)

$$K_{frac} = \frac{k_{frac}\rho g}{\mu} = \frac{e_h^2 \rho g}{12\mu} = \left(\frac{12T}{w}\right)^{\frac{2}{3}} \frac{\rho g}{12\mu} \tag{7.1}$$

Within section 7.5, it is observed that transmissivity changes are least significant under high effective stress conditions: this corresponds to high confining pressure, and low fluid pressure scenarios. Conversely, fluid property changes are most significant at low fluid pressures (section 7.4).

7.8.4.1 Wissey W3 sample

Figure 7.59 shows the estimated fracture hydraulic conductivity change between pressure scenarios for the Wissey sample. By plotting fracture hydraulic conductivity, K_{frac}, as a function of confining pressure it is possible to see that in general (for both low and high temperatures) K_{frac} is higher for the higher fluid pressures under constant confining pressure. At high confining pressures the differences are less significant and for the $P_c = 55$ MPa, low temperature (38°C) scenario, the difference between the $P_{ds} = 10$ MPa and $P_{ds} = 20$ MPa conductivities is negligible.

Figure 7.60 compares the relative change to key parameters as a result of fluid pressure increase for the Wissey experiments. The key parameters are: true transmissivity (T_0); density/viscosity (ρ/μ); and fracture hydraulic conductivity (K_{frac}). Each parameter is normalised against it's initial value (at low fluid pressure), and thus the relative changes of all three parameters can be plotted together for comparison using multipliers to illustrate the parameter change observed between fluid pressure scenarios. K_{frac} is a function of both T_0 and ρ/μ (Equation 7.1, where $T = T_0$ to account for the non-linear flow regime). We can observe the relative influence on K_{frac} of changes in both T_0 and ρ/μ within Figure 7.60 for each confining pressure scenario. The low temperature (Expt C1) plots are on the left hand side, and the high temperature plots (Expt B) are on the right hand side.

It is clear that transmissivity increases with fluid pressure increase, while density/viscosity decreases with fluid pressure increase. At low confining pressure, the magnitude of transmissivity change with fluid pressure is much greater than the magnitude of density/viscosity change, while at high confining pressure the influence of density/viscosity on fracture hydraulic conductivity becomes more important as transmissivity changes become smaller. Thus, despite density/viscosity change always being of less significance than transmissivity change for the Wissey experiments, at high confining pressure it exerts notable influence on hydraulic conductivities. This is relevant to both temperature experiments, but the relative effects are particularly notable within the low temperature experiments, where there is negligible change in K_{frac} between P_{ds} = 10 MPa and P_{ds} = 20 MPa.

7.8.4.2 Cambrian V1 sample

Figure 7.61 presents all valid fracture hydraulic conductivity (K_{frac}) estimates for the Cambrian V1 sample as a function of confining pressure. Results from the high temperature (58°C) experiments indicate that for an increase of fluid pressure from P_{ds} = 20 MPa to P_{ds} = 30 MPa, K_{frac} increases substantially at low confining pressure (P_c = 35 MPa). However, for the same fluid pressure increase at P_c = 45 MPa there is negligible change to K_{frac}, while at P_c = 55 MPa a very small decrease in K_{frac} is observed.

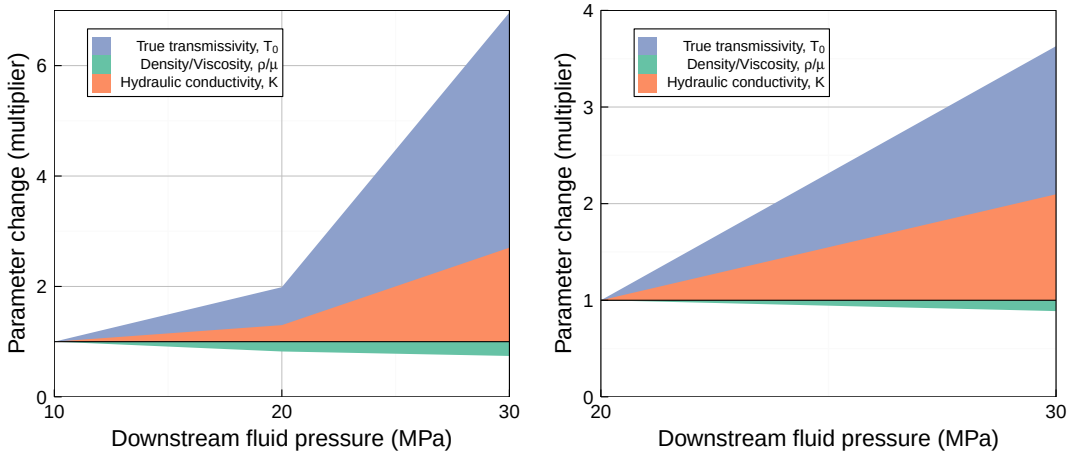

(A) $P_c \approx 35$ MPa, 38°C (Expt C1)

(B) $P_c \approx 35$ MPa, 58°C (Expt B)

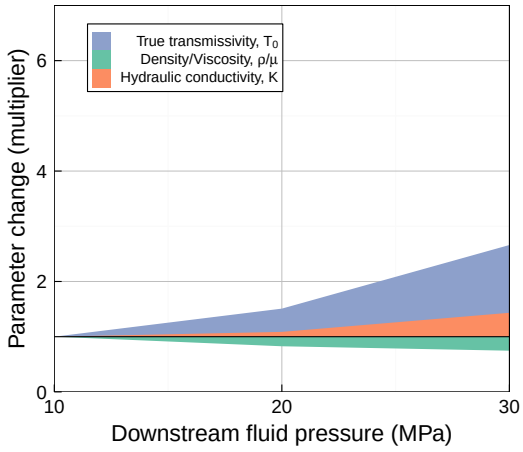

(C) $P_c \approx 45$ MPa, 38°C (Expt C1)

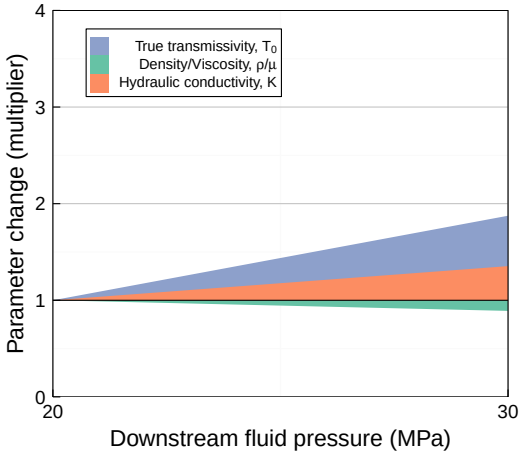

(D) $P_c \approx 45$ MPa, 58°C (Expt B)

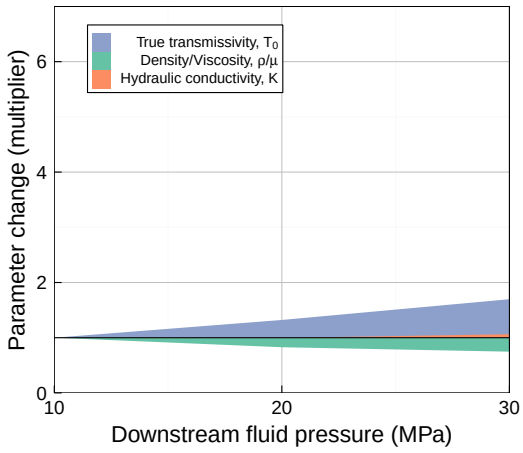

(E) $P_c \approx 55$ MPa, 38°C (Expt C1)

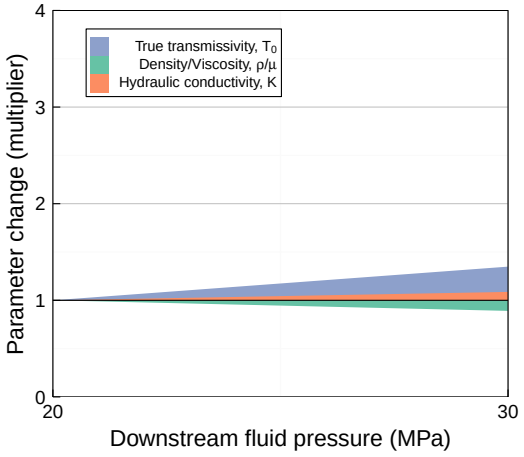

(F) $P_c \approx 55$ MPa, 58°C (Expt B)

FIGURE 7.60: Fluid pressure effects on key parameters under constant confining pressure (Wissey W3). In each subplot, parameters are normalised against their values at the lowest fluid pressure shown.

The P_c = 35 MPa low temperature results (38°C) indicate a large increase in K_{frac} between the P_{ds} = 20 MPa and P_{ds} = 30 MPa scenario, but a small reduction in K_{frac} between the P_{ds} = 10 MPa and P_{ds} = 20 MPa scenario.

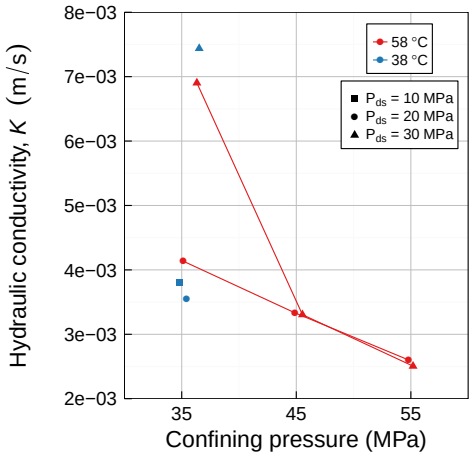

FIGURE 7.61: Fluid pressure effects on fracture hydraulic conductivity under constant confining pressure (Cambrian shale sample)

Parameter change analysis plots in Figure 7.62 present the change to K_{frac} as a result of fluid pressure increase alongside changes to associated key parameters, T_0 and ρ/μ. The three high temperature (Expt B) confining pressure plots are on the left hand side, while the single low temperature (Expt C) confining pressure plot is on the right hand side of the figure. These plots help to provide context for the changes observed in Figure 7.61.

It can be observed that the increase in T_0 has a much more significant effect on K_{frac} than the decrease in ρ/μ in Figure 7.62a and between P_{ds} = 20 MPa and P_{ds} = 30 MPa in Figure 7.62b, reulting in a notable increase in K_{frac} with fluid pressure increase. For both these scenarios $P_c \approx 35$ MPa. However, for the other scenarios within Figure 7.62, the ρ/μ reduction resulting from fluid pressure increase has a comparable or greater influence on K_{frac} than the associated T_0 increase, which results in a negligible change (Figure 7.62c), or reduction (Figures 7.62b and 7.62d) in K_{frac} respectively.

The above findings from the Cambrian shale experiments illustrate that under certain conditions, ρ/μ change can be equally, or more significant than true transmissivity (T_0) change, as a contributor to K_{frac}.

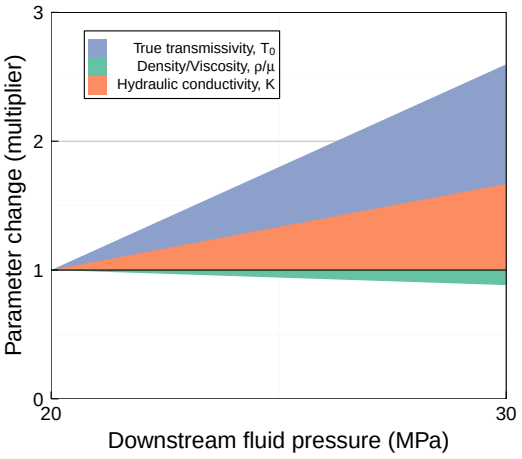

(A) $P_c \approx 35$ MPa, 58°C (Expt B)

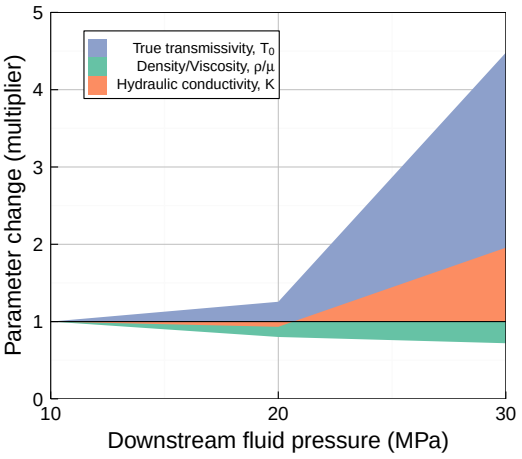

(B) $P_c \approx 35$ MPa, 38°C (Expt C)

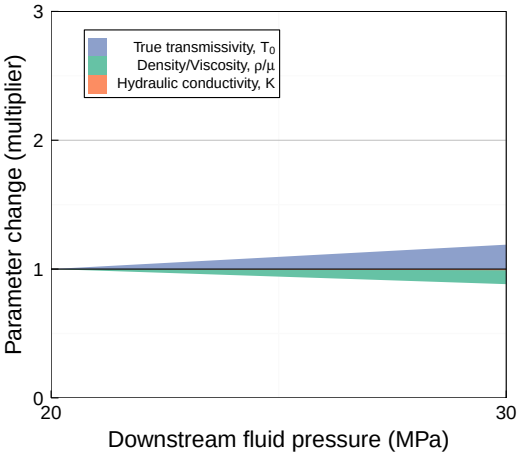

(C) $P_c \approx 45$ MPa, 58°C (Expt B)

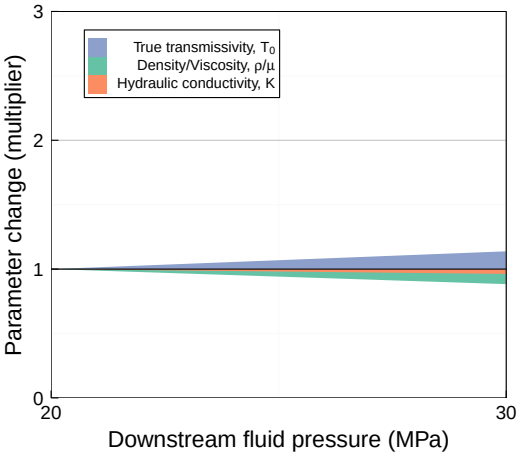

(D) $P_c \approx 55$ MPa, 58°C (Expt B)

FIGURE 7.62: Fluid pressure effects on key parameters under constant confining pressure (Cambrian shale sample). In each subplot, parameters are normalised against their values at the lowest fluid pressure shown.

7.8.4.3 East Brae D2 sample

Figure 7.63 illustrates that during the East Brae D2 experiments (undertaken at 38°C), K_{frac} was observed to increase with fluid pressure at all confining pressures. Figure 7.64 shows the magnitude of K_{frac} change against the magnitude of T_0 and ρ/μ changes. It is clear from this figure that T changes contribute much more significantly than ρ/μ changes to K_{frac} for all scenarios for the East Brae D2 sample, which explains the clear trends observed in Figure 7.63.

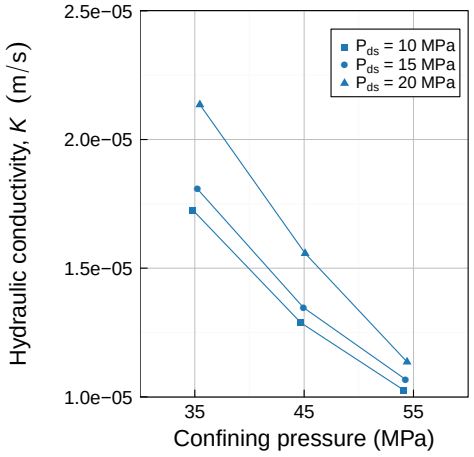

FIGURE 7.63: Fluid pressure effects on fracture hydraulic conductivity under constant confining pressure (East Brae D2 sample, 38°C)

7.8.5 Summary

The significance of fluid property variation has been reviewed by assessing fracture hydraulic conductivity (K_{frac}) variation under varying temperature and fluid pressure conditions.

Under a constant effective stress, transmissivity alterations are not generally observed to occur as a result of temperature change (section 7.5). Thus, changes to K_{frac} observed with temperature variation are most likely a result of fluid property changes only (Equation 7.1). Temperature increase is associated with an increase in ρ/μ for CO_2 under these conditions. There is therefore an associated increase to K_{frac} with temperature increase which is demonstrated in section 7.8.2 using results from the Wissey sample experiments.

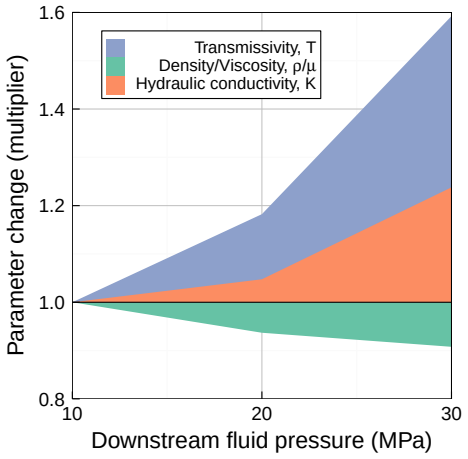

(A) $P_c \approx 35$ MPa

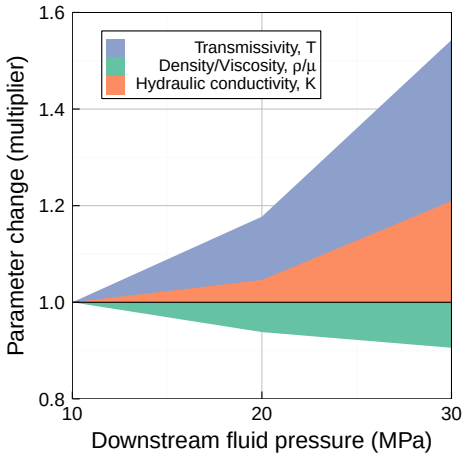

(B) $P_c \approx 45$ MPa

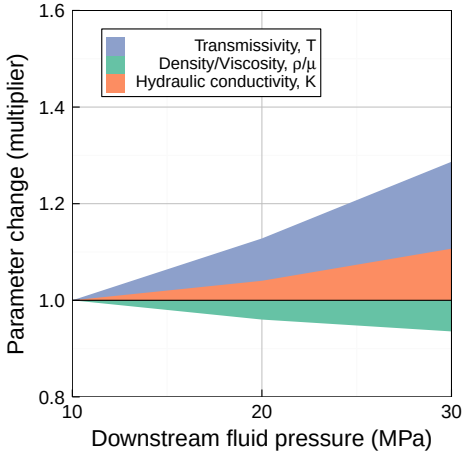

(C) $P_c \approx 55$ MPa

 FIGURE 7.64: Fluid pressure effects on key parameters under constant confining pressure at 38°C (East Brae D2 sample). Parameters are normalised against their values at the lowest fluid pressure shown.

Similarly, fluid pressure change under constant effective stress affects fluid properties, with negligible mechanical change. In general, for significant increases to fluid presssures at constant effective stress, a reduction in K_{frac} is observed due to ρ/μ decrease.

Under constant confining pressure, changes to fluid pressure result in both mechanical change (due to effective stress alteration) and hydraulic changes (due to fluid property changes). Mechanical changes resulting from an increase in fluid pressure are associated with an increase in K_{frac}, while hydraulic changes are associated with a decrease in K_{frac}. The relative significance of mechanical versus hydraulic changes therefore determines the resultant change in fracture hydraulic conductivity (K_{frac}). At low effective stresses, as well as for lower permeability fractured samples (East Brae D2), the mechanical changes resulting from fluid pressure increase are observed to be much more significant than hydraulic changes, with a resultant increase to K_{frac} (transmissivity increase is more significant than ρ/μ decrease). However, at high effective stresses, for the higher permeability fractured samples (Wissey and Cambrian), hydraulic changes have a more significant influence. For the Wissey sample this results in a much smaller increase or negligible change to K_{frac} in association with fluid pressure increase; while for the Cambrian sample, reductions to K_{frac} are observed in some cases which indicates that hydraulic changes are more significant than mechanical changes for these scenarios. These results highlight the importance of considering the influence of fluid property variation on fracture hydraulic conductivity. The implications in the context of CO_2 storage are discussed in section 7.9.

7.9 Summary of experimental findings

7.9.1 Overview and sample comparison

Five sets of supercritical CO_2 flow experiments were undertaken on fractured low permeability samples during this project. The samples consisted of:

- An artificially fractured Cambrian shale quarry sample
- Two artificially fractured East Brae field Kimmeridge Clay samples (B2 and D2)
- An artificially fractured East Brae field Kimmeridge Clay sample with ~1 mm longitudinal offset between fracture surfaces (B2b)

- A Wissey field dolomite sample containing a pre-existing fracture

The offset East Brae sample (B2b) was created from East Brae sample B2 subsequent to initial testing.

Flow experiments were undertaken at 38°C and 58°C with CO_2 fluid pressures in the range 10 to 50 MPa, confining pressures in the range 35 to 55 MPa, and CO_2 flow rates through the fractured samples of up to 32 ml/min (5.3×10^{-7} m^3/s). The pressure and temperature conditions tested are typical of those found at potential CO_2 geological storage sites.

Of the samples tested, the East Brae field Kimmeridge Clay fractured samples (B2 and D2) were found to be of lowest permeability to supercritical CO_2, with fracture permeabilities of the order of 10^{-14} to 10^{-13} m^2, and sample transmissivities of the order 10^{-21} m^4. However, introduction of a ∼1mm longitudinal offset between fracture surfaces (sample B2b) increased apparent sample transmissivity by approximately four orders of magnitude, making the offset sample the highest permeability of all fractured samples tested. In the context of geological storage of CO_2, there is a risk that shear movement of pre-existing fractures could arise from fracture stimulation during CO_2 injection as a result of localised stress changes. The offset experiments undertaken during this project suggest that the mechanical effects associated with such shear movement could be significant, with the potential to notably increase the conductivity of pre-existing seal rock fractures to CO_2, thus increasing leakage risk locally. The findings are also relevant within the field of hydraulic fracturing, where high permeability conduits are a desirable result, enabling shale gas extraction. It should however be noted that, in situ, shear displacement of fractures may result in clay smearing or fault gouge generation, which could conversely act to reduce fracture conductivity.

Aside from the offset East Brae B2b sample, the Cambrian shale V1 fractured sample had the next highest permeability of the samples tested during the supercritical CO_2 flow experiments, with fracture permeabilities of the order of 10^{-11} m^2, and sample transmissivities of the order 10^{-18} to 10^{-17} m^4. The Cambrian shale was found to be hard, and relatively brittle during sample characterisation and preparation, relative to the other samples tested. Post-experiment, the sample was found to contain additional micro-fractures, that must have been induced during experimental investigation. These

were not observed within any of the other tested samples. Uniquely, an inelastic increase to transmissivity was also observed during the initial fluid pressure loading of the Cambrian V1 sample (section 7.6), which is likely to be associated with micro-fracture creation and suggests that this occurred within the first stage of the experiment. There is no evidence for further micro-fracturing later during the experiments. The Cambrian V1 sample was one of the early samples tested within the rig, and as such epoxy resin was used to recombine the two-part fractured core during sample preparation. This technique was not adopted for later experiments due to concern that the resin may impact fracture aperture changes, thus influencing experimental findings. It is possible that the epoxy resin may have contributed to the occurrence of micro-fracturing, in addition to the brittleness of the shale material. Further experiments on fractured Cambrian shale samples (with no epoxy resin) would be required to assess the contribution of epoxy resin, if any, to micro-fracture creation. Micro-fracture creation during fluid or pore pressure loading is another risk that could be associated with CO_2 injection into geological storage sites, increasing the seal rock permeability locally in a similar manner to aperture increase of pre-existing fractures, as discussed above. The experiments undertaken during this project indicate that this could occur, although this is likely to be dependent on seal rock and fracture properties and is most likely within brittle materials.

The Wissey field Zechstein dolomite sample was the only sample containing a pre-existing fracture. Fracture permeabilities were of the order 10^{-12} m^2, with associated sample transmissivities of the order 10^{-19} to 10^{-18} m^4. Thus, this sample is an order of magnitude less permeable than the Cambrian shale V1 sample (and offset East Brae B2b sample), but a couple of orders of magnitude more permeable than the original artificially fractured East Brae field samples. Multiple stress loading cycles were carried out at both 38°C and 58°C for this sample (Figure 6.8), ensuring a very comprehensive dataset for analysis.

7.9.2 Flow regime analysis

Flow regime analysis was undertaken in section 7.3 for all samples except East Brae B2, where the permeability was insufficient to enable multiple flow test scenarios. The East Brae D2 sample was found to have a broadly linear flow regime during CO_2 flow tests, indicating the validity of Darcy's law. The associated Reynolds numbers remained

below 13 during the East Brae D2 experiments. It is expected that a linear flow regime is also present during the East Brae B2 sample flow test.

Non-linearity was notable during CO_2 flow tests on all other samples (offset East Brae B2b, Cambrian shale V1 and Wissey samples). The Reynolds number ranges were similar at 38°C for all three samples, ranging from ∼5 at low flow rates to ∼100 at high flow rates. At 58°C, the Reynolds numbers reached 233 for the Wissey sample experiments, and Reynolds numbers of up to 335 were found during both the Cambrian shale V1 and East Brae B2b experiments. The observance of non-linearity during these CO_2 flow experiments is consistent with the experimental findings of Ji et al. [2008], Ranjith and Darlington [2007], Zimmerman et al. [2004], where non-linearity was observed during water flow through fractures for Reynolds numbers exceeding ∼20. This is interesting, and suggests the validity of this observation for CO_2 fluid as well as water.

The Forchheimer equation was found to be suitable for describing the non-linear flow regime for the Cambrian V1 and Wissey W3 experiments, enabling estimation of true transmissivities for these samples using Forchheimer plots. The significance of inertial or non-linear flow was found to be greater for the Cambrian V1 sample than for the Wissey W3 sample, which may be due to differences in fracture surface geometry, although micro-fracture influence within the Cambrian V1 sample may also play a part. For the Wissey W3 sample, non-linearity significance was observed to increase with increasing confining pressure, which is likely to be due to an increase in flow path tortuosity as contacting asperities and contact areas increase within the fracture. This pattern was not observed for the Cambrian V1 sample, again possibly due to micro-fracture influence on non-linearity.

Measurement uncertainties were large for the East Brae B2b sample due to the very low associated differential pressures. As a result, it was not possible to estimate true transmissivities for this sample using Forchheimer model fits, as with the Cambrian shale and Wissey samples.

7.9.3 Mechanical and hydraulic influences on fracture transmissivity and conductivity

Assessment of the mechanical impact on transmissivity was undertaken using true transmissivities where non-linearity was significant (Wissey W3 and Cambrian V1 experiments) and Darcy transmissivities elsewhere (East Brae D2). Insufficient data were available for East Brae B2 analysis and uncertainties were too significant to enable transmissivity estimation for B2b, thus ruling out consideration of these two samples within the analysis. Both elastic (section 7.5) and inelastic (section 7.6) behaviour was considered during assessments.

During initial external stress loading cycles (and during subsequent high temperature external stress loading), inelastic fracture closure was indicated for all samples through permanent reduction to transmissivities. This is in line with the experimental findings of Bandis et al. [1983] and Barton et al. [1985]. Inelastic observations are associated with mechanical changes to fracture geometry, which could arise from adjustment of sample seating position such as realignment of fracture surfaces, or could arise from plastic deformation of fracture surfaces. Barton et al. [1985] suggests that the permanent set that they observed was likely to be largely due to disturbances caused by sampling i.e. fracture surface misalignment, and as such suggests that this was an experimental artefact, and that in-situ conditions are represented by subsequent experimental stress-loading cycles. Fracture surface characterisation undertaken in association with our experiments (Chapter 4) does however provide post-experiment evidence for plastic deformation of fracture surfaces for both the East Brae and Wissey samples (more significant for East Brae samples). This could be of relevance in-situ, where effective stress increases prior to CO_2 injection could reduce the transmissivity or permeability of any existing fractures. This may occur if, for example, pore pressure is reduced through fluid extraction (brine/oil/gas) prior to CO_2 injection. Any such stress changes are likely to be relatively small within the seal rock due to the lower permeability of this layer relative to the storage rock below, however the effects may be important at the reservoir-seal rock interface. Thus, where effective stress change in seal rock is notable, the risk of CO_2 leakage through fractures may be slightly reduced by the prior depletion (and pore pressure reduction) of storage reservoirs. In addition, this finding implies that certain burial histories will be more favourable for fracture sealing or permeability minimisation.

Inelastic behaviour was not generally observed during internal (fluid pressure) stress loading cycles, with the exception of the initial fluid pressure loading cycle of the Cambrian V1 sample discussed above (section 7.9.1) in the context of micro-fracture creation. Minor hysteresis was observed during some internal stress loading cycles. It is possible that there is an experimental artefact contribution to these observations, resulting from use of quasi-steady state measurements for practical purposes (see Chapter 6 for details). In any event, the observed hysteresis is not considered to be significant.

An elastic transmissivity-stress relationship was found for subsequent stress loading cycles (both external and internal) indicating that inelastic processes such as surface deformation and micro-fracturing were not notably enhanced by repeat stress loading, but are affected by the maximum and minimum stress history (and maximum temperature) only. The Terzaghi [1923] effective stress law (Equation 2.25) was, in general, found to be suitable and was used to describe the elastic transmissivity-effective stress relationship. The only outliers were the data points associated with the lowest density CO_2 (the low fluid pressure, high temperature scenarios). It may be that the Terzaghi [1923] effective stress law does not hold for such low density fluid, and that the fluid pressure contributes less significantly to the effective stress under these conditions. Transmissivity uncertainty due to high density/viscosity sensitivity, or enhanced non-linear flow effects as a result of higher Reynolds numbers may also be factors during these scenarios.

The elastic transmissivity-stress relationship observed is non-linear and hyperbolic in nature, such that transmissivity variations are large at low effective stresses and small at high effective stresses. This is due to fracture stiffness, which increases exponentially as contact area and the number of contacting asperities increases. This means that for a given stress change, aperture variation is relatively large under low effective stresses, and very small under high effective stresses.

Hydraulic aperture, fracture permeability and fracture hydraulic conductivities have been estimated from transmissivity and true transmissivity estimates for linear and non-linear flow regime experiments respectively. Use of true transmissivity estimates for the non-linear cases gives reference values of these parameters for comparison purposes. The values are those that would be expected were viscous/linear flow to occur within the same fracture geometry; observed or apparent values are lower and decrease as flow

rate increases due to energy loss associated with inertial effects, in the same manner observed for apparent transmissivities (section 7.3).

As fracture hydraulic conductivity, K_{frac}, is a function of both transmissivity/permeability (intrinsic to rock properties) and ρ/μ (fluid properties), the coupled impact of mechanical and hydraulic changes have been examined using this parameter. Under constant effective stress, no mechanical changes are expected to occur, and we see that K_{frac} is higher at both higher temperatures and lower fluid pressures due to the lower fluid viscosities.

At constant confining pressure, alteration to fluid pressure changes both fluid properties and effective stress, thus has both hydraulic and mechanical impacts, with opposing effects on K_{frac}. For the lowest transmissivity sample (East Brae D2), and at low confining pressures for the other samples (Wissey W3 and Cambrian V1), the mechanical impacts dominate, thus hydraulic impacts are relatively insignificant and K_{frac} increases with increasing fluid pressure. However, at high confining pressures for the higher permeability samples (Wissey and Cambrian), mechanical impacts become much smaller as a result of the non-linear hyperbolic relationship between transmissivity (or fracture closure) and effective stress. As a result, the hydraulic impacts become relatively significant, and comparable in magnitude to mechanical impacts. The result is a much smaller change in K_{frac}. In some cases, hydraulic impacts are more significant than mechanical impacts, and a reduction in K_{frac} with increased fluid pressure occurs. These findings indicate that (depending on in-situ conditions, rock properties and fracture geometry) hydraulic impacts may become significant where mechanical changes are small. Thus, the significance of changes to hydraulic properties must be considered during CO_2 storage site assessment, particularly as they also impact on the flow regime (section 7.3).

Chapter 8

Conclusions and recommendations for further work

8.1 Conclusions

The motivation for this study was to improve understanding of the hydraulic and mechanical processes that influence supercritical CO_2 flow through discrete seal rock fractures under a range of typical in-situ pressure and temperature conditions. This is of importance as CO_2 flow through natural or induced seal rock fractures is a key leakage risk for geological storage of CO_2 and there are currently limited experimental datasets available on the influence of hydraulic and mechanical processes on CO_2 flow through fractures. The primary objectives of the thesis (section 1.2) were achieved as summarised below.

- A variety of typical seal rock samples were sourced from North Sea reservoir core, a pilot-scale CO_2 injection experiment site (Heletz, Israel), and from UK quarry material. Characterisation of samples included mineralogical analysis, matrix porosity and permeability testing, and an adapted Mohs hardness test (Chapter 3).

- Several 38 mm discretely fractured cores were prepared for experimental analysis from the seal rock samples. These core samples included a natural or pre-existing discrete fracture within Wissey field Zechstein Dolomite. No other pre-existing discrete fractures suitable for coring were available within the remaining sample material, therefore discrete fractures were artificially induced in cored material (Chapter 3). Of these, two East Brae Kimmeridge Clay cores and a Cambrian shale core were prepared for experimental analysis.

- During sample preparation, fracture surface analysis was undertaken on East Brae Kimmeridge Clay, Wissey Zechstein Dolomite and Heletz shale samples using laser scanning. Similar fracture surface analysis was undertaken post-experiment on the East Brae and Wissey samples, while x-ray CT imaging was undertaken on the Cambrian shale fractured core, post-experiment, where evidence of micro-fracture creation was observed. Fracture topography data have been used for assessment of both small and large scale surface roughness/geometry (Chapter 4). The Wissey fracture surface data have also been utilised within numerical simulation analysis outwith this study [McCraw et al., 2016].

- A customised experimental rig was successfully designed and built to enable single phase supercritical CO_2 fracture flow experiments to be undertaken under typical in-situ pressure and temperature conditions. Due to challenges associated with identifying materials and instrumentation suitable for use with supercritical CO_2, design development was a significant component of this study (Chapter 5).

- Experimental methods were developed to ensure a comprehensive dataset suitable for undertaking analysis of a variety of hydraulic and mechanical behaviours was obtained. This included significant post-processing of data to extract key relevant data from experimental data logs (Chapter 6).

- Five sets of supercritical CO_2 fracture flow experiments were undertaken on four discretely fractured core samples: the pre-existing discretely fractured Wissey Zechstein Dolomite sample, and three artificially induced fracture core samples (two East Brae Kimmeridge Clay and one Cambrian shale). A longitudinal fracture surface offset of $\sim$1 mm was introduced to one of the East Brae samples following initial experiments, enabling a second set of experiments to be undertaken on this sample with inclusion of an assessment into the impact of fracture offsetting.

- Experiments were undertaken at two temperatures (38°C and 58°C) with CO_2 fluid pressures in the range 10 to 50 MPa, confining pressures in the range 35 to 55 MPa, and CO_2 flow rates through the fractured samples of up to 32 ml/min (5.3×10^{-7} m^3/s). The pressure and temperature conditions tested are typical of those found at potential CO_2 geological storage sites.

- Of the four 'matched' fracture surface experiments the two East Brae samples were found to be the least permeable, with fracture permeability estimates in the order of 10^{-14} to 10^{-13} m^2 and sample transmissivities of the order 10^{-21} m^4 under experimental conditions. The Cambrian shale fractured sample was the most permeable, with fracture permeabilities of the order of 10^{-11} m^2, and sample transmissivities of the order 10^{-18} to 10^{-17} m^4. Fracture permeabilities in the order of 10^{-12} m^2, with associated sample transmissivities of the order 10^{-19} to 10^{-18} m^4 were measured for the Wissey pre-existing fractured sample. Review of the adapted Mohs hardness test (section 3.4.3) shows that fractures created from harder rock were found to be more permeable. This indicates that rock hardness could be a key influence in determining fracture permeability.

- Manual offsetting of the fracture surfaces of the East Brae B2 sample by ~1 mm increased apparent sample transmissivity by approximately four orders of magnitude under experimental stress conditions. This highlights the importance of fracture surface matching, and the role that fracture surface topography plays in influencing fracture permeability. Within geological storage sites, the risks associated with the activation of fracture shearing therefore require consideration.

- Flow regime analysis was undertaken on the 'matched' East Brae D2 sample, the 'offset' East Brae B2b sample, the Wissey W3 sample and the Cambrian V1 sample. A linear flow regime was observed for the very low permeability East Brae D2 sample, and linear regression using Darcy's law was used to obtain transmissivity, T, estimates for this sample. Non-linearity was observed to be significant within the other three higher permeability fractured samples. The Forchheimer equation was found to be suitable for estimation of true transmissivities, T_0, for the Wissey W3 sample and the Cambrian V1 sample. However, due to high measurement uncertainties associated with the East Brae B2b data, true transmissivity estimation for this sample was not possible. Non-linearity was found to be more significant for the Cambrian V1 sample than the Wissey W3 sample. A review of

the significance of non-linearity during the Wissey W3 sample and the Cambrian V1 sample experiments also indicated that activation of induced micro-fractures may occur for the Cambrian V1 sample under certain stress conditions, resulting in increased non-linearity through the high tortuosity and roughness associated with the additional micro-fracture flow paths.

- Inelastic transmissivity reduction associated with fracture closure was observed during initial external stress loading for all samples tested. Inelastic effects were minimal or negligible during subsequent stress loading cycles carried out at the same temperature. These observations are in line with the experimental findings of Bandis et al. [1983] and Barton et al. [1985]. In addition, it was observed that further inelastic closure occurred during repeat stress loadings undertaken at a higher temperature. Alteration of fracture surfaces in the form of small scale roughness smoothing was also observed for all samples where pre- and post-experiment surface scanning was undertaken (Chapter 4). This suggests that the inelastic closure may be associated with deformation of fracture surface asperities. These observations highlight the importance of understanding the stress and temperature history of potential storage sites to help anticipate mechanical changes that may result from future predicted stress changes. For example, will prior fluid extraction or other localised significant stress change influence the response of seal rock to CO_2 injection?

- Inelastic effects were not generally observed during internal stress loading (fluid pressure) cycles. The exception to this was the initial internal stress loading cycle of the Cambrian V1 sample where inelastic transmissivity increase was observed. The presence of micro-fractures within this sample post-experiment suggested that these inelastic observations were related to induction of micro-fractures. External evidence of micro-fractures was not observed in any of the other samples post-experiment. The Cambrian shale was the most brittle of the samples tested.

- Subsequent to observation of the inelastic behaviour identified above, an elastic response to stress and temperature changes was observed for all samples analysed. The transmissivity-stress relationship observed is non-linear and hyperbolic in nature, such that transmissivity (and thus fracture aperture) variations are large at

low effective stresses and small at high effective stresses. This is due to fracture stiffness, which increases exponentially as contact area and the number of contacting asperities increases.

- The Terzaghi [1923] effective stress law was, in general, found to be suitable to describe the elastic transmissivity-effective stress relationship. The only outliers were the data points associated with the lowest density CO_2 (the low fluid pressure, high temperature scenarios). The cause of these atypical data points is unclear. One suggestion is that the Terzaghi [1923] effective stress law may not hold for low density fluid, with fluid pressure providing a lower contribution to effective stress under these conditions. Alternatively, thermo-elastic expansion of the bulk rock could potentially contribute. As transmissivity uncertainty is relatively high for these scenarios due to high density/viscosity sensitivity and enhanced non-linear flow effects as a result of higher Reynolds numbers, further experimental investigation is recommended.

- While transmissivity and fracture permeability are intrinsic properties of the fractured rock, fracture hydraulic conductivity, K_{frac}, is a function of both rock properties and fluid properties. Thus, this parameter was used to examine the coupled impact of mechanical and hydraulic changes during supercritical CO_2 flow. Under constant effective stress, no mechanical changes are expected to occur and K_{frac} is observed to be higher at both higher temperatures and lower fluid pressures due to higher density/viscosity ratios. Under constant confining pressure, changes to fluid pressure have both mechanical and hydraulic impacts on K_{frac}, with opposite effects observed. Under low confining pressures mechanical impacts are found to dominate, with K_{frac} increasing with fluid pressure due to fracture aperture opening. However, under high confining pressures mechanical impacts are smaller and, particularly for the higher permeability fractures, hydraulic impacts may be similar in magnitude and occasionally greater than the mechanical impacts resulting in a negligible change or a small decrease in K_{frac} in response to fluid pressure increase due to the associated viscosity increase. These findings illustrate that the effect of changes to CO_2 fluid properties in response to pressure and temperature changes can be significant, and should be considered during CO_2 storage site assessment.

The unique experimental results obtained during this study contribute towards improved understanding of the hydraulic and mechanical processes associated with supercritical CO_2 flow through discretely fractured seal rock. Use of single phase supercritical CO_2 has enabled these processes to be analysed in isolation. During geological storage of CO_2, multiphase flow behaviours (i.e. wettability, interfacial tension, relative permeability, diffusion) as well as chemical influences (i.e. mineral dissolution, mineral precipitation) also contribute to the resultant behaviour of the CO_2 and to the permeability of fractures.

To enable comprehensive analyses of potential CO_2 storage sites, coupled process numerical models are required to predict storage security, in conjunction with findings from geological studies of natural CO_2 stores and field experiments. The key value of the experimental results presented within this study is therefore for informing analyses of geological study and field observations and for enabling validation of theoretical processes represented within coupled process models. The experimental results and fracture surface data have already been utilised within a numerical simulation study of supercritical CO_2 through the naturally fractured Wissey sample [McCraw et al., 2016], and it is anticipated that the data will inform a number of future studies.

8.2 Context and implications

This section discusses the main experimental findings from this study within the context of existing fracture flow experimental literature (section 1.1.4). The implications of the findings for CO_2 sequestration as well as other related applications - hydro-fracking and radioactive waste disposal, are also discussed.

8.2.1 Experimental findings in the context of existing fracture flow experimental literature

The experiments undertaken during this study are distinct from other published fracture flow experiments as the single phase fluid under investigation is supercritical CO_2. The absence of water or brine saturation of the matrix material minimises the potential for chemical reactions and multi-phase flow behaviour to influence fracture flow results, thus enabling physical effects on fluid flow and fracture mechanics to be isolated.

Stresses and temperatures adopted are typical of those within existing and potential future CO_2 storage sites [Michael et al., 2010].

Inelastic transmissivity reduction of fractured samples subjected to external stress loading and unloading cycles was observed consistently, but to varying degrees, across all experimental samples during this study. The transmissivity reduction is considered to result from mechanical fracture closure during experiments which could arise as a result of e.g. plastic deformation of asperities. This consistent observation of mechanical fracture closure suggests that this process is also likely to be present to some degree during the dissolution experiments discussed in section 1.1.4 [Andreani et al., 2008, Deng et al., 2015, Durham et al., 2001, Smith et al., 2013, Yasuhara et al., 2011, 2006]. Where fracture aperture reduction is observed during these experiments [Durham et al., 2001, Yasuhara et al., 2011, 2006] mechanical closure due to normal stress loading may contribute towards such aperture reduction and thus the dissolution effects may be less significant than suggested. Conversely, where fracture aperture increase is observed [Andreani et al., 2008, Deng et al., 2015, Smith et al., 2013, Yasuhara et al., 2006] any mechanical closure effects would act to oppose dissolution effects, thus dissolution effects may be greater than suggested by direct observation. The degree of mechanical closure will be dependent on fracture geometry, fracture stiffness and the magnitude of normal stress loading, and thus will vary considerably between experiments. Enhanced mechanical closure effects were observed at higher temperatures (under thermal loading) during this study. Such enhanced mechanical closure due to thermal loading may therefore contribute to the additional fracture aperture reduction observed during the raised temperature (90°C) experiments of Yasuhara et al. [2011], in addition to the enhanced dissolution effects investigated.

The majority of published fracture flow investigations have been undertaken with liquid fluid in the form of a variety of aqueous solutions. Exceptions are the Helium gas flow experiments of Sathar et al. [2012] and Cuss et al. [2015] (section 1.1.4), undertaken with kaolinite fault gouge, which indicate significant differences in fracture flow behaviour to that observed during aqueous flow. Of relevance to the findings of this study Sathar et al. [2012] found that fault gouge fracture permeability during gas flow reduced in response to normal stress loading, but a resultant permeability increase was observed following unloading. This is contrary to the inelastic closure and associated fracture permeability reduction observed within this study of rough rock fractures for

supercritical CO_2 flow. Although there are significant differences in experimental set-up between the two studies (fault gouge versus rough rock fracture), this observation suggests that in this respect supercritical CO_2 does not behave in a similar manner to gas but is more consistent with the behaviour observed for aqueous flow. It is possible that dessication of fault gouge may influence the permeability increase observed for gas flow in Sathar et al. [2012]. As the rock fractures used within this study are not water or brine-saturated, similar dessication would not occur during the supercritical CO_2 experiments undertaken within this study, thus preventing comparison of this effect. Repetition of the Sathar et al. [2012] experiments using supercritical CO_2 would be required to enable direct comparison and thus conclusive findings.

Artificially induced fractures within East Brae Kimmeridge Clay material were found to have the lowest permeability of those tested during this study, with fracture permeabilities in the order of 10^{-14} to 10^{-13} m^2 under the experimental stress and temperature ranges. East Brae matrix permeability estimates, tested at only 1 MPa confining pressure (and thus anticipated to be even lower under the higher experimental stresses) were two orders of magnitude lower, 10^{-16} to 10^{-15} m^2 (Chapter 3). Comparison of these permeability estimates highlights that within the Kimmeridge Clay, fractures are still important conduits for fluid flow, despite their relatively low permeability. Water flow within Kimmeridge shale fractures has previously been studied by Gutierrez et al. [2000] (section 1.1.4). The sample material used by Gutierrez et al. [2000] was naturally fractured shale sourced from outcrops in Dorset, UK. The matrix permeability estimate for this sample material was notably lower than the East Brae shale ($\sim 10^{-19}$ m^2), which may be a result of the significantly higher clay content [Gutierrez et al., 2000]. Fracture permeabilities of 10^{-10} to 10^{-11} m^2 were measured by Gutierrez et al. [2000] under lower normal stresses than those adopted within this study (<10 MPa), thus direct comparison is not possible. These fracture permeabilities reduced to $\sim 10^{-18}$ m^2 following fracture shearing of 6 mm. Despite the wide range of fracture permeabilities measured during the experimental investigations of Gutierrez et al. [2000], they all remain notably higher than the corresponding matrix permeability estimate, which is consistent with the findings of this study.

While shearing of Kimmeridge shale fractures during the Gutierrez et al. [2000] experiments resulted in a significant fracture permeability reduction, introduction of a ~1 mm shear offset without active shearing during this study resulted in an increase in fracture permeability of around four orders of magnitude. These contrasting results highlight

the important influence of fracture geometry change and fault gouge production during the shearing process, which can act to reduce fracture permeability. Direct offsetting without active shearing, on the other hand, is observed to enhance permeability during this study. Further investigation of shearing processes, outwith the scope of this study, would thus be valuable in the future.

8.2.2 Implications for CO_2 sequestration and other related activities

As discussed in Chapter 1, CO_2 flow through natural or induced fractures presents a significant risk to storage integrity at CO_2 sequestration sites. Evidence from existing CO_2 storage sites suggests that CO_2 migration through fractures in overlying seal rock has occurred. At the In Salah CO_2 storage site, where 4 million metric tons of CO_2 were injected between 2004 and 2011, indirect monitoring observations suggest that CO_2 has migrated upwards into the lower portion of the 900 m thick Carboniferous Viséan mudstone. It is hypothesised that this migration has occurred as a result of tensile hydrofracture creation within the seal rock, or via either intrinsically permeable, or reactivated pre-existing fractures [White et al., 2014]. At the Sleipner CO_2 storage site (offshore Norway), where 1 Mt/yr of CO_2 has been injected into the 1 km deep Utsira Formation saline aquifer since 1996, seismic reflections surveys have been used to map the CO_2 plume migration [Cavanagh and Haszeldine, 2014]. These surveys indicate that the CO_2 plume has breached eight shale barriers within the storage site, the thickest of which is 6-7 m thick and geologically similar to the primary seal (Nordland Shale). Numerical simulation of the plume migration suggests that the shales are likely to be fractured. Given the weak overpressure of the CO_2 plume it is not considered that fracturing was caused by CO_2 injection, but that the shale fractures were pre-existing [Cavanagh and Haszeldine, 2014].

Given the above evidence for the importance of fractures as conduits for CO_2 migration through overlying seal rock, the experimental findings of this study are particularly relevant. With respect to fracture mechanics observations, the consistent inelastic transmissivity reduction observed during experiments, following both external stress loading and thermal loading cycles, is encouraging for CO_2 sequestration. It suggests that, following initial creation or reactivation of fractures, temporary increases to in-situ effective stresses and temperatures are likely to act to permanently reduce fracture transmissivity. In general, no permanent (inelastic) effects were observed due to fluid

pressure loading cycles, suggesting that temporary overpressuring during CO_2 injection is unlikely to result in a permanent increase in the permeability of existing fractures. Thus, in the absence of active shearing or a continuous reduction in effective stress, a runaway increase in the permeability of pre-existing fractures due to mechanical response is not likely to occur. Some degree of permanent reduction to fracture permeability, however, would not be unexpected in response to temporary stress or thermal loading.

The inelastic fracture permeability changes observed during this experimental study also highlight that the stress and temperature history of seal rock is important, and therefore requires consideration during site selection for CO_2 storage. Stress and temperature history can affect rock properties e.g. brittleness may be related to consolidation history [Nygård et al., 2006], but as discussed above, it has been shown during this study to also affect the hydraulic properties of pre-existing fractures, e.g. fracture permeability reduction in response to prior stress or thermal loading cycles.

During this study, the degree of fracture surface deformation resulting from mechanical stress loading and thermal loading was observed to be most significant for the East Brae Kimmeridge Clay samples (Chapter 4). This material was the softest of the three tested (section 3.4.3). The ductile nature of the Kimmeridge Clay is likely to be due to the relatively high clay content, and the material's consolidation history. The ductile East Brae Kimmeridge Clay samples were also found to have the lowest fracture permeabilities (prior to offsetting fracture surfaces), while fracture permeabilities were higher within the harder, more brittle, Wissey Zechstein dolomite and Cambrian shale fractures (section 7.7). This is in line with the findings of Angeli et al. [2013] which suggest that faults are less conductive within seal rocks with a ductile rheology than those with a brittle rheology. These experimental findings therefore suggest that the ductility of seal rock may be an important factor to consider during CO_2 storage site selection as fractures within ductile seal rocks are likely to be less conductive to fluids, and may also experience a higher degree of self-sealing under mechanical stress loading or thermal loading. However, it is worth noting that, in line with the findings of Gutierrez et al. [2000] (section 1.1.4), this study also suggests that mechanical loading does not result in complete hydraulic closure of fractures for any of the samples tested. Thus, in the absence of mineral cementation, or potentially the presence of swelling clays, fractures will remain conduits for fluid flow.

While investigation of active fracture shearing was not within the scope of this study, offsetting of the fracture surfaces of an East Brae Kimmeridge Clay sample by ~1 mm was found to increase fracture permeability by approximately four orders of magnitude. This fracture permeability increase is in line with the experimental findings of Yeo et al. [1998]. Published literature contains evidence for both fracture dilation and fracture aperture reduction as a result of active shearing, dependent on rock properties and the degree of fault gouge production [Cuss et al., 2011, Gutierrez et al., 2000, Nygård et al., 2006, Olsson and Brown, 1993, Sathar et al., 2012]. However, it is clear from all these studies that shearing of fracture surfaces is likely to significantly alter fracture permeability. Thus, understanding the stress field regime and therefore the likely mechanisms of fracture creation and mechanical alteration is important during site selection. Further investigation is required to determine the potential consequences of shearing, which may require consideration at a site specific level.

The elastic relationship observed between fracture transmissivity and effective stress subsequent to initial stress loading cycles (section 7.5) suggests that fracture transmissivity will reduce with depth, as effective stress generally increases with depth. The relationship also indicates that imposed increases in fluid pressure due to CO_2 injection (internal stress loading) will result in increased fracture transmissivity as fluid pressure increase reduces effective stress. Deeper storage sites are therefore likely to be more secure due to lower fracture transmissivities within the overlying seal rock, and careful control of fluid pressures within the injection zone may be used to minimise the leakage risk through overlying fractures. However, the optimum depth of proposed storage sites is likely to be limited by economical and technical feasibility, therefore a careful compromise will be required during site selection to ensure leakage risk is minimised as far as possible.

Hydraulic observations from this experimental study suggest that flow non-linearity is likely to occur, even at relatively low Reynolds numbers, for supercritical CO_2 through rough rock fractures. In addition, CO_2 density and viscosity varies significantly with fluid pressure and temperature, and this influences the conductivity of fractures to CO_2 flow. CO_2 fluid is less conductive at high fluid pressures and low temperatures, due to the higher associated fluid viscosity. Although in a large number of scenarios mechanical effects are found to dominate, these findings indicate that fluid properties should be taken into account during CO_2 storage site characterisation.

The experimental findings from this fracture flow study have implications for CO_2 sequestration as discussed above, but there are also implications for other fields such as hydro-fracking and radioactive waste disposal. In contrast to the requirements for CO_2 sequestration, during extraction of shale gas using hydro-fracking techniques it is desirable for fractures created within the shale to be of high permeability to enable a productive gas yield. Thus, in contrast to the recommendations above of identifying ductile shales for CO_2 storage seals, brittle shales would be more desirable for hydro-fracking. Brittle shales are known to fracture more easily [Lee et al., 2011], but this experimental study indicates that resultant fracture permeabilities are also likely to be higher. The inelastic fracture permeability reduction observed during the experimental study in response to stress and thermal loading suggests that shale gas yield is likely to decline with time not only due to depletion of gas at the site, but also due to fracture permeability reduction associated with mechanical closure of fractures. Proppants are utilised to minimise these effects [Lee et al., 2011].

Radioactive waste disposal is another field where fracture flow behaviour is of great importance. The excavation of Geological Disposal Facilities (GDF) is recognised to induce fractures within both crystalline and clay-rich host rocks, with dehydration of host rock close to the disposal site also likely to occur [Cuss et al., 2015, Tsang et al., 2005]. In addition, heat from the decaying waste alters temperature gradients within the subsurface region. Groundwater and gas movement are expected to play a significant role in the transport of radionuclides away from the disposal site. Therefore understanding the conductivity of the fractures within the surrounding host rock is important as these are likely to be conduits for fluid flow. Thus the stress and thermal loading results of this experimental fracture flow study are likely to be of particular interest and relevance to this field, which has notable parallels in research needs to that of CCS.

8.3 Recommendations for further work

Within this study, a number of experimental techniques have been adopted to demonstrate a variety of hydraulic and mechanical processes that influence the permeability of seal rock fractures to CO_2. However there is great potential for future experimental work to be undertaken to confirm and expand on these experimental findings, as well as

to undertake further analyses using the data obtained during this study. Recommendations for future work detailed below relate to: improvements to the experimental rig design, future analyses using experimental samples and datasets from this study, and future experiments.

8.3.1 Improvements to the experimental rig design

The recommendations within this section suggest incremental improvements to the experimental rig designed and built during this study.

- **Adopt a universal logging system**
  Three separate logging systems were used to continuously record pressure measurements, pump data and temperature measurements. Operation of the three separate logging systems increased the potential for user errors during experiments and complicated post-processing of data (Chapter 6). A universal logging system to incorporate logging of all data would improve the usability of the rig and reduce the errors associated with merging multiple datasets during post-processing.

- **Core holder platen upgrade**
  As described in section 5.4, opening and closing of the upstream 'quick-release' platen was problematic throughout the duration of the project, due to bulging of the cylindrical platen during high pressure, high temperature experiments. Smoothing and polishing of the relatively soft Type 316 stainless steel platen was undertaken by workshop technicians on several occasions, but due to the low tolerance associated with the closure mechanism, the problem was recurring. This could be resolved by redesigning the closure mechanism to match the screw design of the downstream platen, or by use of a harder material that would be less prone to swelling/bulging under the experimental pressure and temperature conditions.

- **Upgrade core holder sleeve material**
  While replacement of Viton sleeves with HNBR sleeves during this project has mitigated earlier sleeve rupture problems, extensive sample coating is required to limit CO_2 diffusion through the core holder sleeve during experiments. If an appropriate sleeve material can be identified that does not degrade and is

not susceptible to CO_2 diffusion, this would substantially simplify the sample preparation and loading stage of the experiments.

- **Resolve pump error**
  The intermittent pump error detailed in section 5.5.1 has not yet been resolved. It is highly recommended that the source of this error is identified and addressed, in collaboration with the pump suppliers (Aquilant Scientific) prior to use of the rig for future experiments.

In addition to the above recommendations for improvement to the rig design, measurement accuracy could be enhanced by incorporation of:

- a flow meter within the CO_2 pipework system close to the sample, to measure accurately the CO_2 flow rate under the experimental pressure and temperature conditions;
- a more direct temperature measurement system i.e. a thermocouple internal to the core holder; and
- replacement of the single differential pressure transducer with a series of parallel differential pressure transducers covering a wide range of differential pressure ranges to allow accurate measurement of a wide range of differential pressures during a single experiment.

8.3.2 Future analyses using experimental datasets and samples

- Substantial effort was invested in obtaining North Sea seal rock material for use during this study, of which only a small proportion was used within the supercritical CO_2 flow experiments. Seal rock core material is difficult to obtain as it is seldom cored. The remaining sample material could therefore be of great value for use within future research. Some ideas for future experimental work are detailed within section 8.3.3.
- Fracture surface topography data were obtained both pre- and post-experiment using a high resolution laser scanner. This study presents a simple statistical analysis undertaken using these data to provide indicative and comparative data on

surface roughness at two length scales. However, there is potential for much more comprehensive and sophisticated geostatistical analyses to be carried out using the surface scan data, including studies of spatial correlation and scale analysis. These could provide valuable data to improve our understanding of fracture surface geometry and to inform future fracture modelling and experimental studies.

- An x-ray CT scan of the Cambrian V1 fracture sample was obtained post-experiment, following external observation of the presence of induced micro-fractures. Due to time constraints, little processing of this dataset was undertaken during this study. A more detailed analysis of this CT scan data could provide greater insight into the fracture network present within this sample post-experiment. X-ray CT scanning also has great potential for future studies, and it is recommended that this is incorporated into experimental study scopes to enable both pre- and post-experiment analysis of samples. There is also great potential for incorporating CT scanning into an experimental rig design to enable 'real-time analysis' of fracture apertures and fracture networks during fluid flow experiments (see Deng et al. [2015], for example). This could enable measurement of mechanical fracture apertures which could be assessed in conjunction with hydraulic analysis results.

- As stated in the conclusions (section 8.1), the experimental results presented in this study will be of great value for use in validation and benchmarking of coupled process numerical models. There are numerous software applications that simulate multi-physics subsurface processes (thermal, hydraulic, mechanical, chemical). However there are often relatively few experimental datasets available to enable validation or informative comparison of such models. The experimental data presented within this study provide real observations, which have already been used within initial model validation studies [McCraw et al., 2016]. It is recommended that development of this modelling work is undertaken now that the experimental result analysis contained within this study is complete, and that the experimental data are also used more widely within alternative models for comparison.

8.3.3 Future experimental studies

The experiments undertaken during this study were limited to single phase flow of supercritical CO_2, to enable hydraulic and mechanical processes to be assessed in isolation. Studies were undertaken on single samples of Wissey Zechstein Dolomite and Cambrian shale, with two samples of East Brae Kimmeridge Clay used. It would be of great value to undertake additional fracture flow experiments using the same sample material to help build up a picture of the typical behaviour of fractures within each sample material. This is not possible with examination of single samples as the contribution of the sample material cannot be easily distinguished from the contribution of fracture geometry, for example. If fracture flow experiments were undertaken using multiple samples from a single source, it would also be interesting to examine the influence of fracture orientation, if fractures could be induced within samples both parallel to and across sample bedding. Comparison of the behaviour of natural to artificially induced fractures within the same sample material would also be of interest. These investigations would be valuable in conjunction with comprehensive fracture surface characterisation. During future experiments, consideration of the influence of matrix consolidation would be of value, and additional studies into the impact of fracture offsetting or shearing would also be worthwhile.

Non-linearity was found to be significant during analysis of the CO_2 flow regime during fracture flow experiments. Examination of the microscopic behaviour of CO_2 fluid within such fractures would be beneficial for improving understanding of the processes contributing to this observed non-linearity. Microscopic fluid flow studies have previously been undertaken using water [Zhang et al., 2013].

While the Terzaghi [1923] effective stress law appeared to be valid for most scenarios during experimental result analysis, the lowest density CO_2 results did not fit the transmissivity-stress relationship observed for all other scenarios (section 8). Further experimental investigation to determine the cause of these atypical results is recommended. Potential effects to consider include thermo-elastic expansion of the bulk rock, and investigation of the validity of the Terzaghi [1923] effective stress law for CO_2 fracture flow across a range of experimental pressure and temperature conditions. It is possible that the relative influence of confining pressure and fluid pressure to mechanical changes may not be equal under certain conditions (see section 2.6.1).

Future experimental studies could additionally examine other processes relevant to geological storage of CO_2. It would be particularly interesting to undertake studies of surface-fluid interactions with carbon dioxide and brine to assess the wettability associated with the various seal rock samples used within this study, to inform our understanding of the expected multiphase flow processes when brine is present. Multiphase flow experiments could also be undertaken in conjunction with such studies. Experimental assessment of mineral reactions that occur during brine/CO_2 interaction with the sample material would also be of value for building a more comprehensive understanding of the influence that each of these processes are likely to have in-situ. As significant mineral reactions may only occur over geological timescales, investigations should also be continued into sourcing seal rock material from natural CO_2 stores if possible, to assist with understanding the influence of such reactions to seal rock integrity.

Appendix A

Fracture surface analysis grids

This appendix contains all fracture surface grids created during the fracture surface analysis work (Chapter 4). This includes both small scale (2 mm) roughness and large scale (10 mm) roughness grids. All surface grids are at a resolution of 0.2 mm x 0.05 mm. See section 4.4 for details of methodology. The grids are listed by sample type, with large scale roughness grids available for surface A of each sample only.

Note that the Z scales change between surfaces, as well as between the topography grids (raw, smooth) and difference grids/reference surfaces.

A.1 Wissey surfaces (pre-experiment): samples W3 and W4

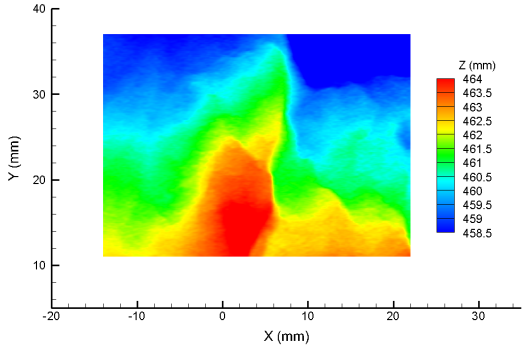

(A) Raw fracture surface data

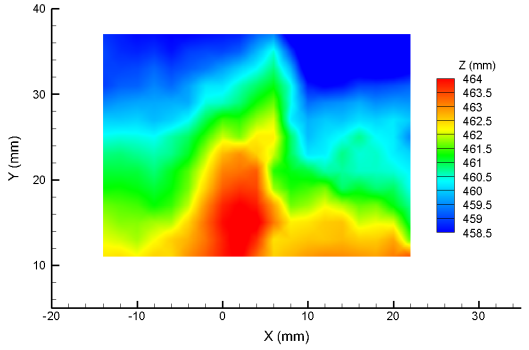

(B) Smoothed fracture surface data (2 mm interpolation)

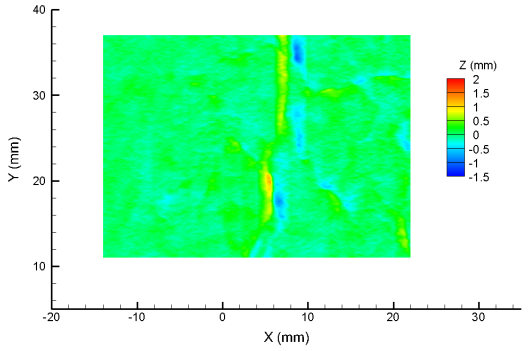

(C) Wissey W3A: Small scale roughness reference surface (raw-smooth)

FIGURE A.1: Wissey surface W3A (sample W3) - creation of a small scale roughness grid using a 2 mm smoothing technique

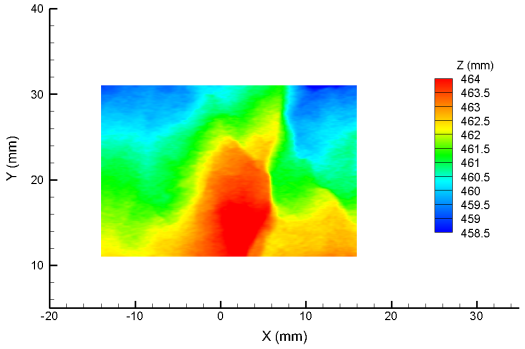

(A) Raw fracture surface data

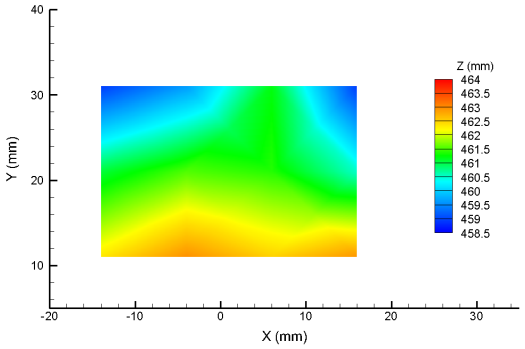

(B) Smoothed fracture surface data (10 mm interpolation)

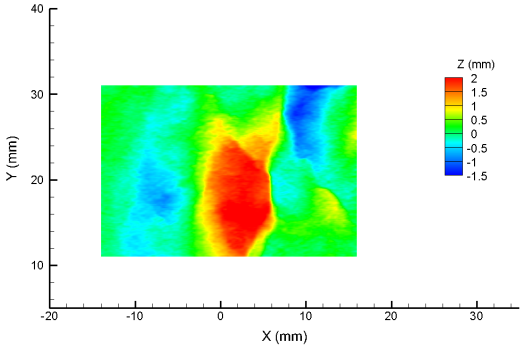

(C) Wissey W3A: Large scale roughness reference surface (raw-smooth)

FIGURE A.2: Wissey surface W3A (sample W3) - creation of a large scale roughness grid using a 10 mm smoothing technique

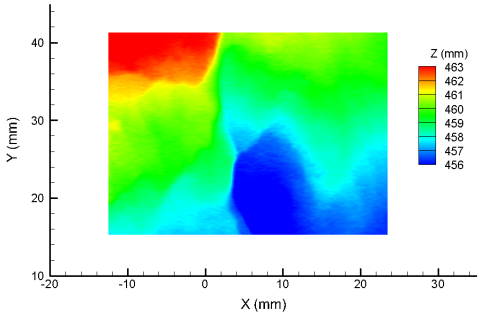

(A) Raw fracture surface data

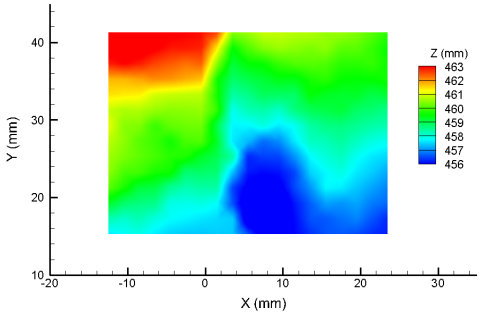

(B) Smoothed fracture surface data (2 mm interpolation)

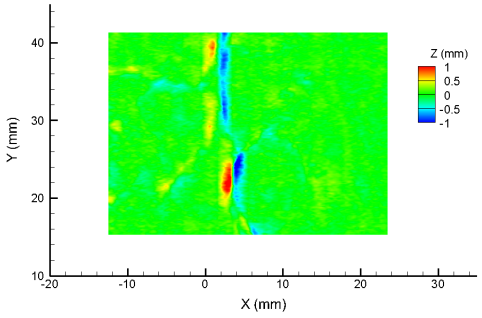

(C) Wissey W3B: Small scale roughness reference surface (raw-smooth)

FIGURE A.3: Wissey surface W3B (sample W3) - creation of a small scale roughness grid using a 2 mm smoothing technique

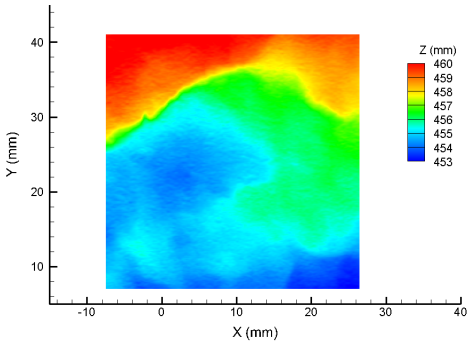

(A) Raw fracture surface data

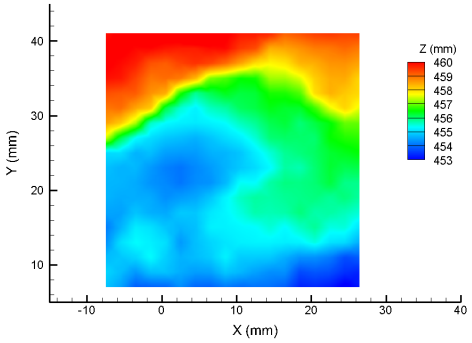

(B) Smoothed fracture surface data (2 mm interpolation)

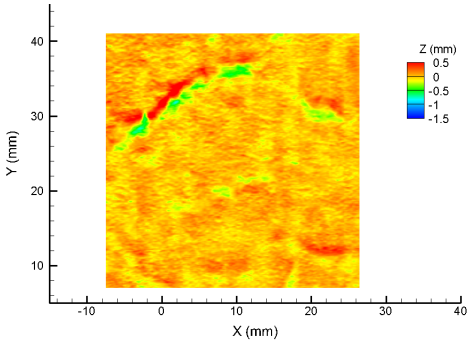

(C) Wissey W4A: Small scale roughness reference surface (raw-smooth)

FIGURE A.4: Wissey surface W4A (sample W4) - creation of a small scale roughness grid using a 2 mm smoothing technique

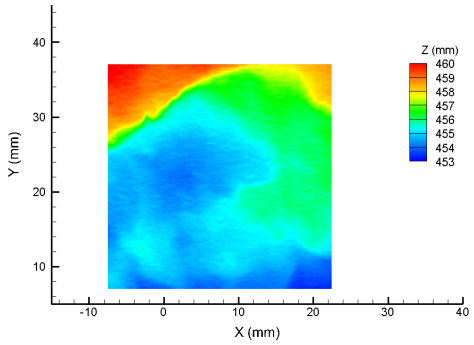

(A) Raw fracture surface data

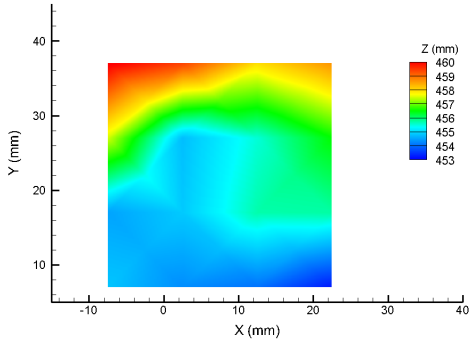

(B) Smoothed fracture surface data (10 mm interpolation)

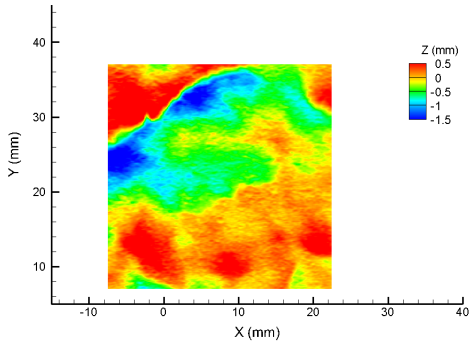

(C) Wissey W4A: Large scale roughness reference surface (raw-smooth)

FIGURE A.5: Wissey surface W4A (sample W4) - creation of a large scale roughness grid using a 10 mm smoothing technique

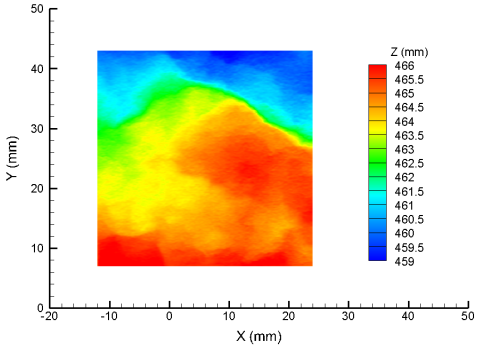

(A) Raw fracture surface data

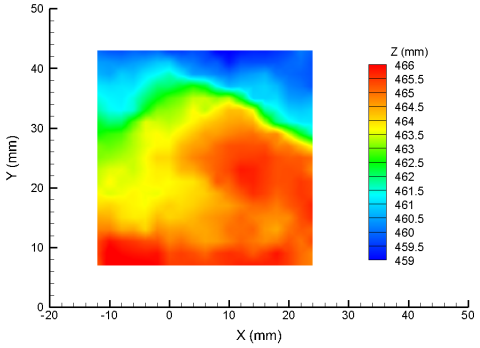

(B) Smoothed fracture surface data (2 mm interpolation)

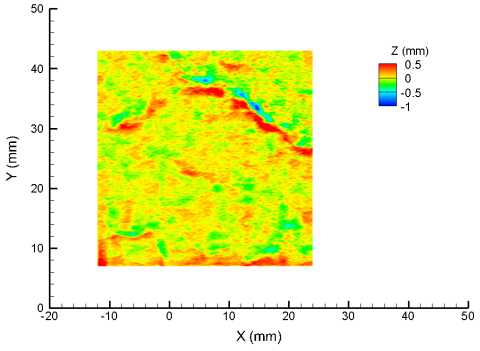

(C) Wissey W4B: Small scale roughness reference surface (raw-smooth)

FIGURE A.6: Wissey surface W4B (sample W4) - creation of a small scale roughness grid using a 2 mm smoothing technique

A.2 Wissey surfaces (post-experiment): sample W3

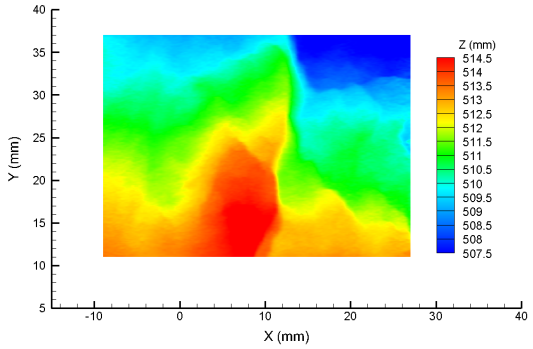

(A) Raw fracture surface data

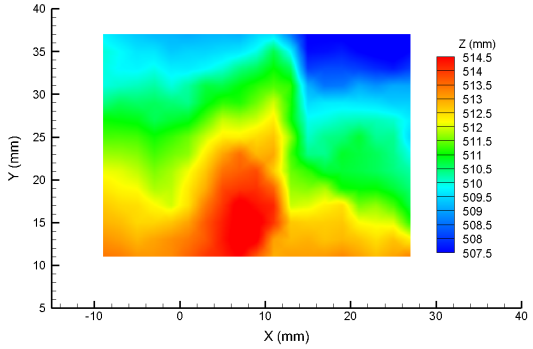

(B) Smoothed fracture surface data (2 mm interpolation)

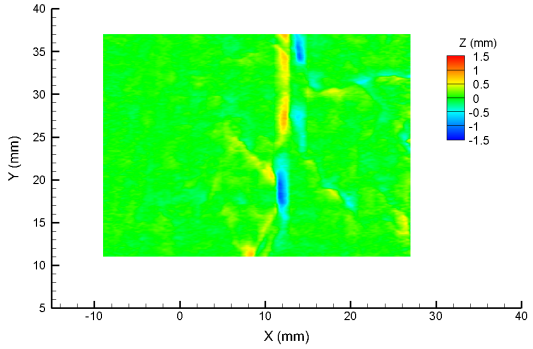

(C) Wissey W3A: Small scale roughness reference surface (raw-smooth)

FIGURE A.7: Wissey surface W3A (sample W3) POST-EXPERIMENT - creation of a small scale roughness grid using a 2 mm smoothing technique

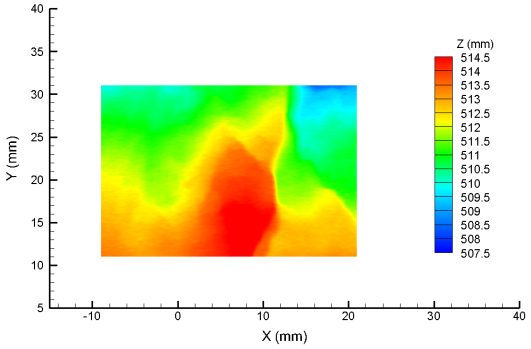

(A) Raw fracture surface data

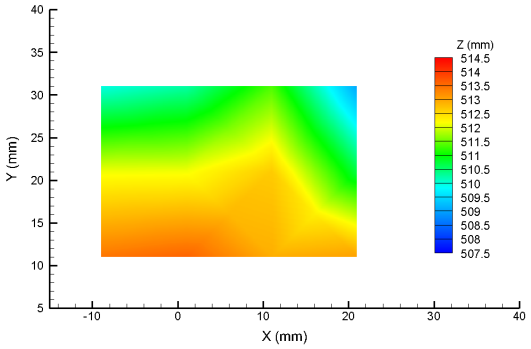

(B) Smoothed fracture surface data (10 mm interpolation)

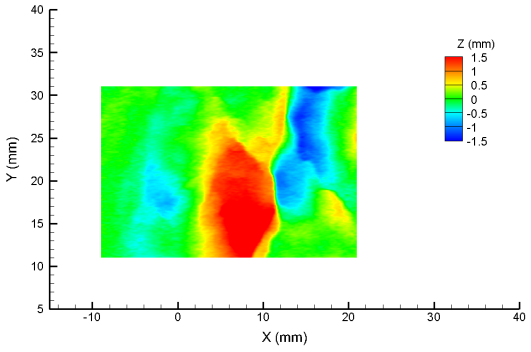

(C) Wissey W3A: Large scale roughness reference surface (raw-smooth)

FIGURE A.8: Wissey surface W3A (sample W3) POST-EXPERIMENT - creation of a large scale roughness grid using a 10 mm smoothing technique

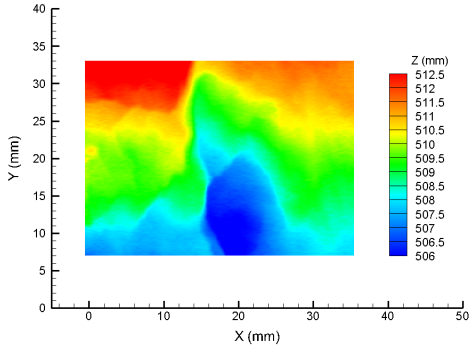

(A) Raw fracture surface data

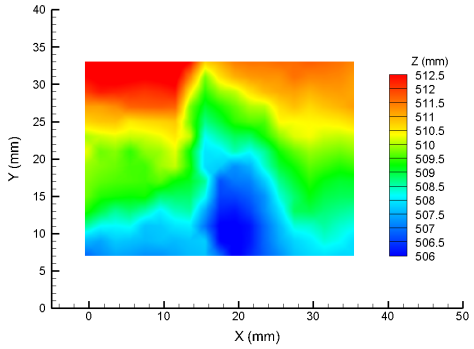

(B) Smoothed fracture surface data (2 mm interpolation)

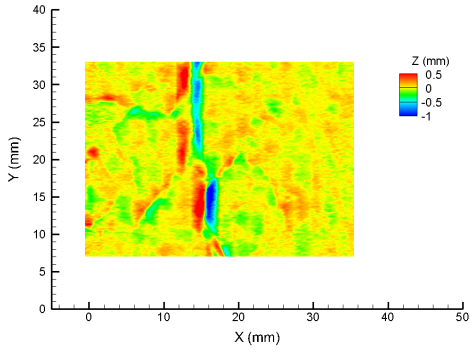

(C) Wissey W3B: Small scale roughness reference surface (raw-smooth)

FIGURE A.9: Wissey surface W3B (sample W3) POST-EXPERIMENT - creation of a small scale roughness grid using a 2 mm smoothing technique

A.3 East Brae surfaces (pre-experiment): samples B2 and D2

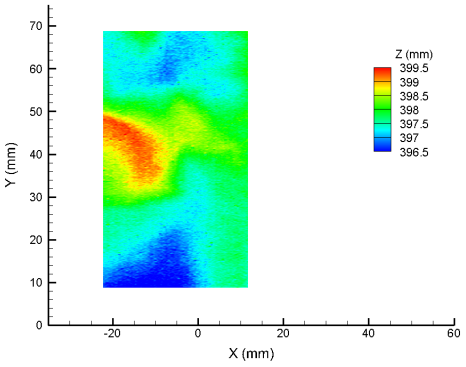

(A) Raw fracture surface data

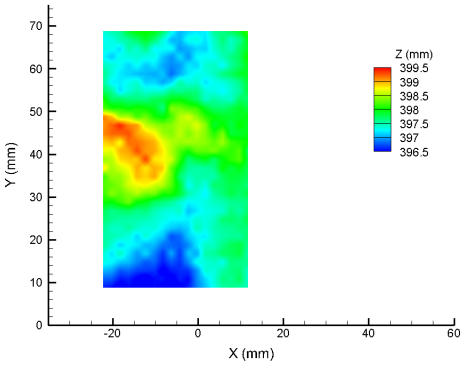

(B) Smoothed fracture surface data (2 mm interpolation)

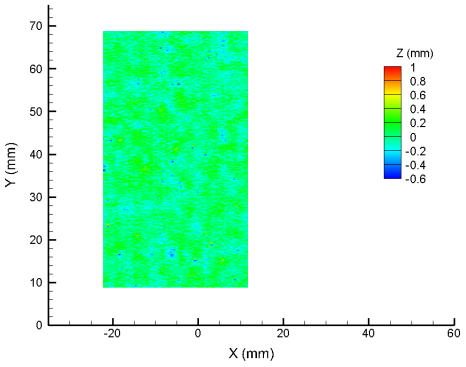

(C) East Brae B2A: Small scale roughness reference surface (raw-smooth)

FIGURE A.10: East Brae surface B2A (sample B2) - creation of a small scale roughness grid using a 2 mm smoothing technique

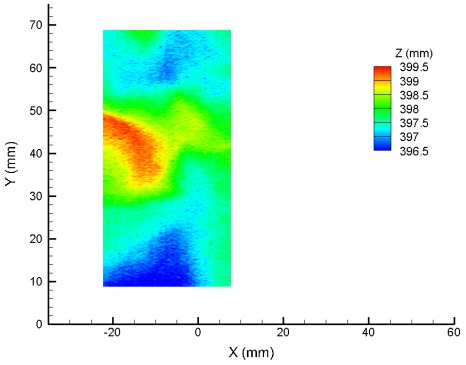

(A) Raw fracture surface data

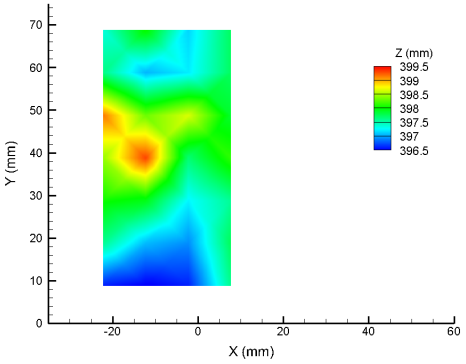

(B) Smoothed fracture surface data (10 mm interpolation)

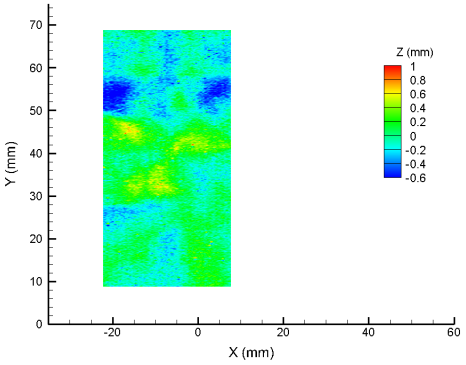

(C) East Brae B2A: Large scale roughness reference surface (raw-smooth)

FIGURE A.11: East Brae surface B2A (sample B2) - creation of a large scale roughness grid using a 10 mm smoothing technique

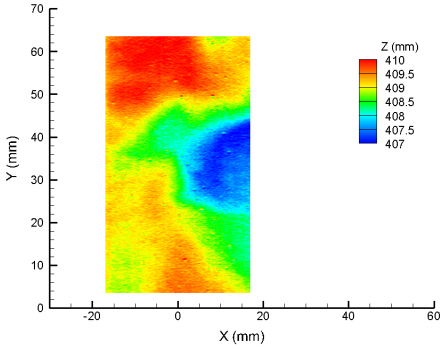

(A) Raw fracture surface data

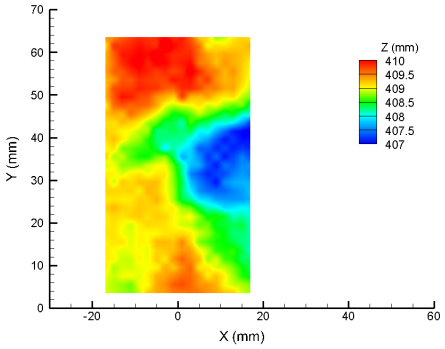

(B) Smoothed fracture surface data (2 mm interpolation)

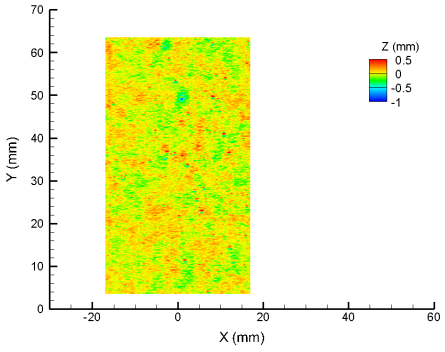

(C) East Brae B2B: Small scale roughness reference surface (raw-smooth)

FIGURE A.12: East Brae surface B2B (sample B2) - creation of a small scale roughness grid using a 2 mm smoothing technique

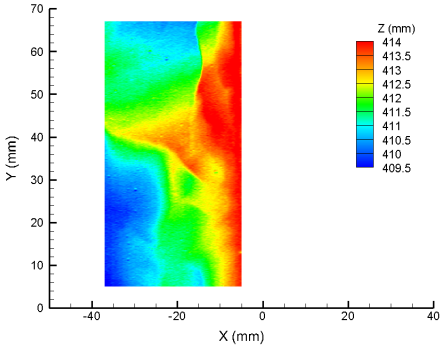

(A) Raw fracture surface data

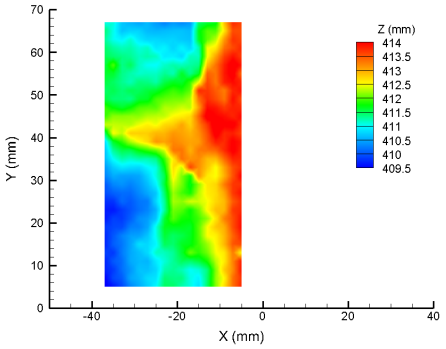

(B) Smoothed fracture surface data (2 mm interpolation)

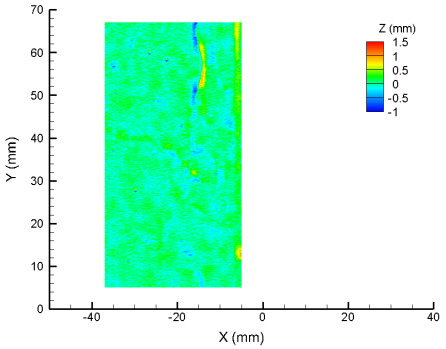

(C) East Brae D2A: Small scale roughness reference surface (raw-smooth)

FIGURE A.13: East Brae surface D2A (sample D2) - creation of a small scale roughness grid using a 2 mm smoothing technique

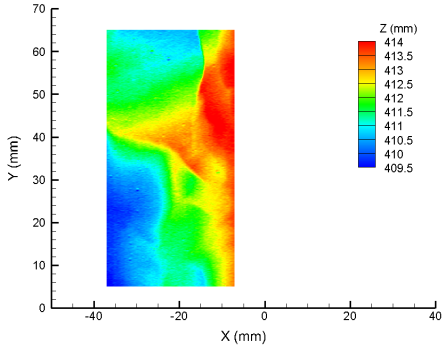

(A) Raw fracture surface data

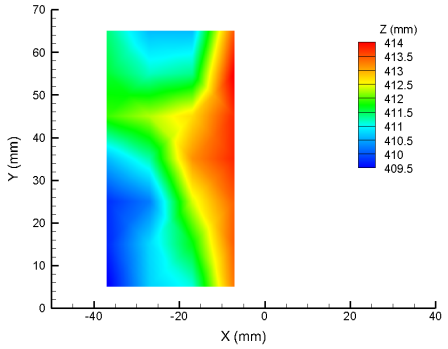

(B) Smoothed fracture surface data (10 mm interpolation)

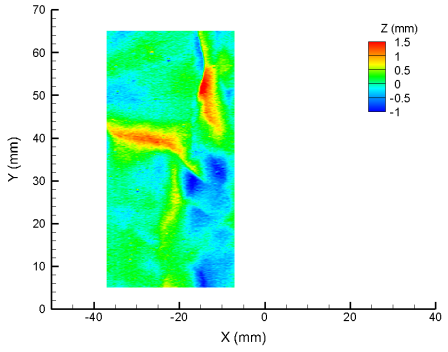

(C) East Brae D2A: Large scale roughness reference surface (raw-smooth)

FIGURE A.14: East Brae surface D2A (sample D2) - creation of a large scale roughness grid using a 10 mm smoothing technique

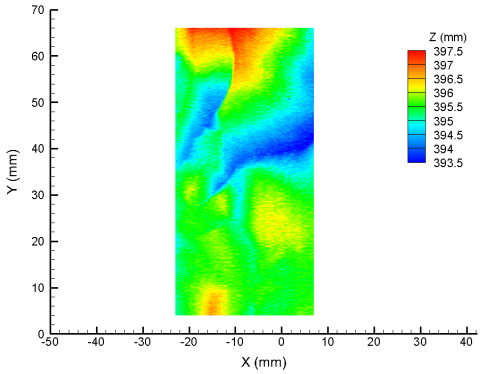

(A) Raw fracture surface data

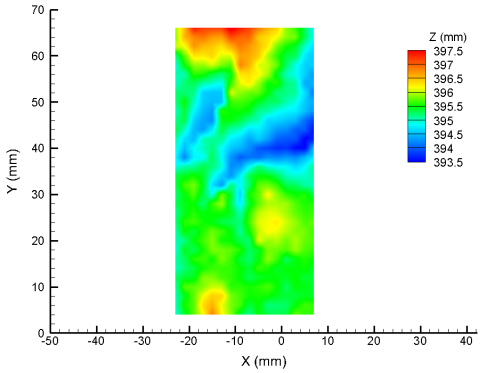

(B) Smoothed fracture surface data (2 mm interpolation)

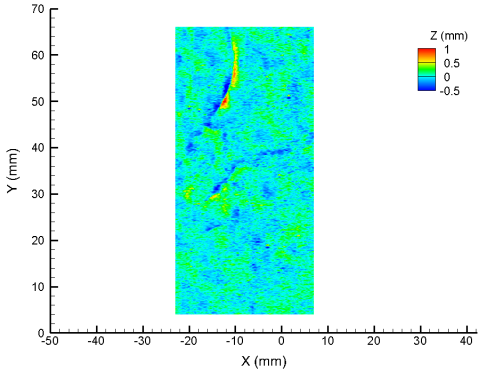

(C) East Brae D2B: Small scale roughness reference surface (raw-smooth)

FIGURE A.15: East Brae surface D2B (sample D2) - creation of a small scale roughness grid using a 2 mm smoothing technique

A.4 East Brae surfaces (post-experiment): samples B2b and D2

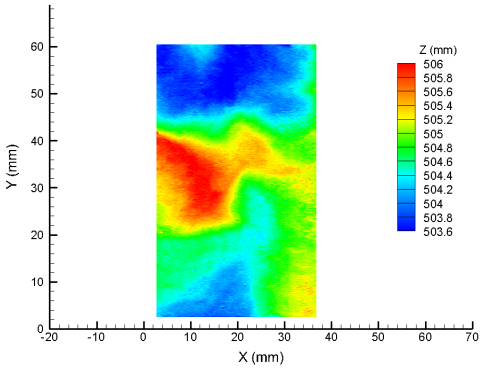

(A) Raw fracture surface data

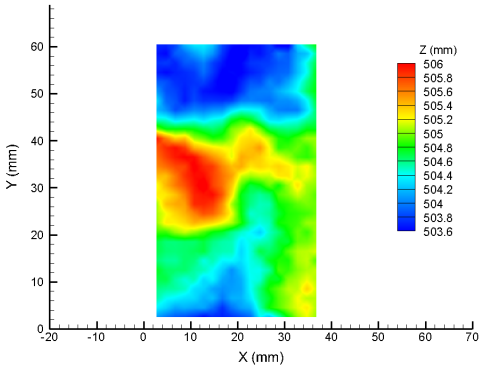

(B) Smoothed fracture surface data (2 mm interpolation)

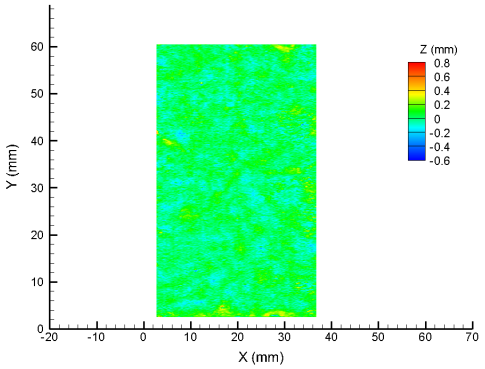

(C) East Brae B2bA: Small scale roughness reference surface (raw-smooth)

FIGURE A.16: East Brae surface B2bA (sample B2b) POST-EXPERIMENT - creation of a small scale roughness grid using a 2 mm smoothing technique

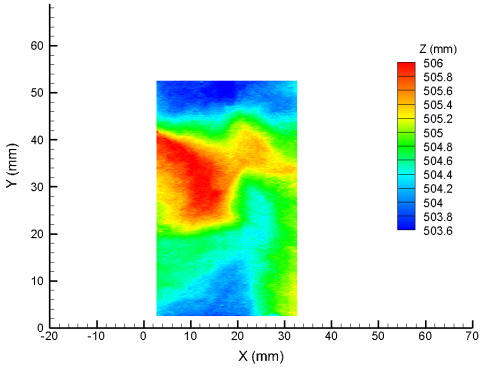

(A) Raw fracture surface data

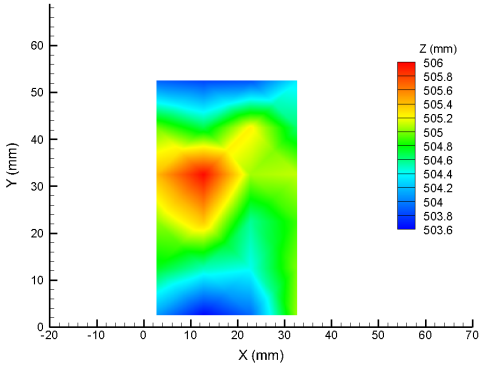

(B) Smoothed fracture surface data (10 mm interpolation)

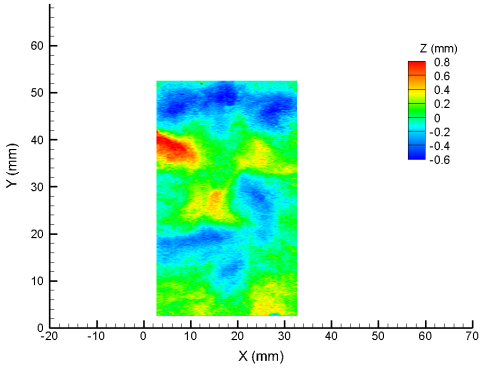

(C) East Brae B2bA: Large scale roughness reference surface (raw-smooth)

FIGURE A.17: East Brae surface B2bA (sample B2b) POST-EXPERIMENT - creation of a large scale roughness grid using a 10 mm smoothing technique

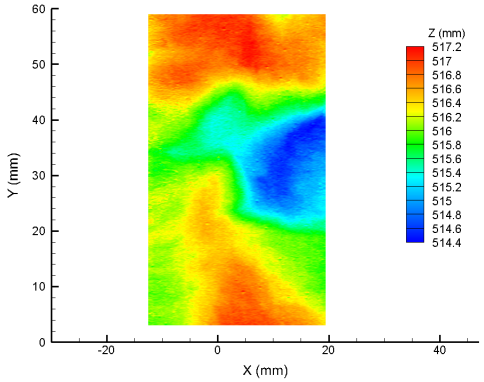

(A) Raw fracture surface data

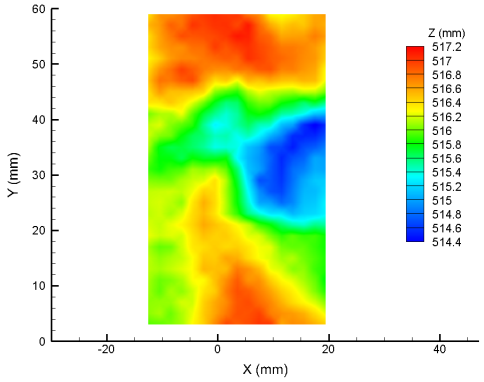

(B) Smoothed fracture surface data (2 mm interpolation)

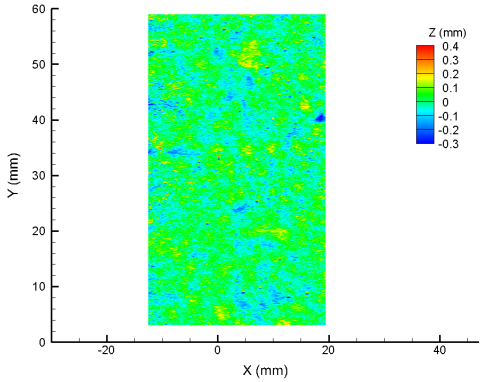

(C) East Brae B2bB: Small scale roughness reference surface (raw-smooth)

FIGURE A.18: East Brae surface B2bB (sample B2b) POST-EXPERIMENT - creation of a small scale roughness grid using a 2 mm smoothing technique

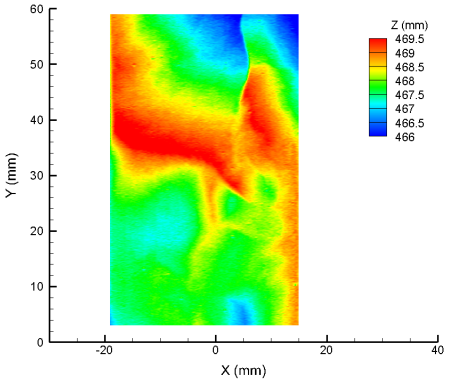

(A) Raw fracture surface data

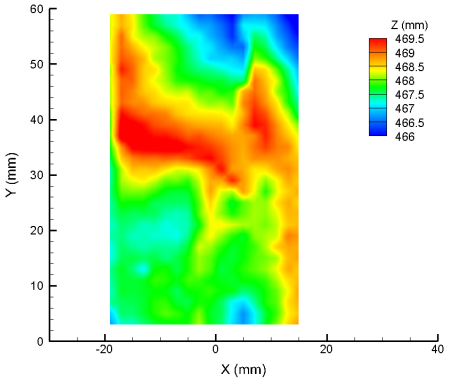

(B) Smoothed fracture surface data (2 mm interpolation)

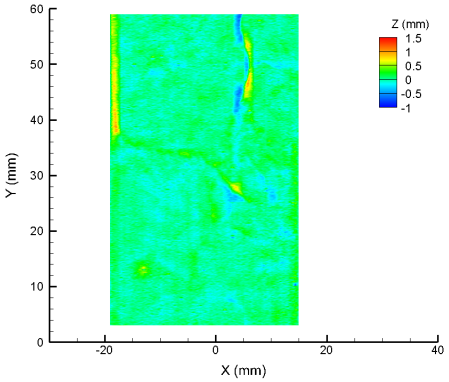

(C) East Brae D2A: Small scale roughness reference surface (raw-smooth)

FIGURE A.19: East Brae surface D2A (sample D2) POST-EXPERIMENT - creation of a small scale roughness grid using a 2 mm smoothing technique

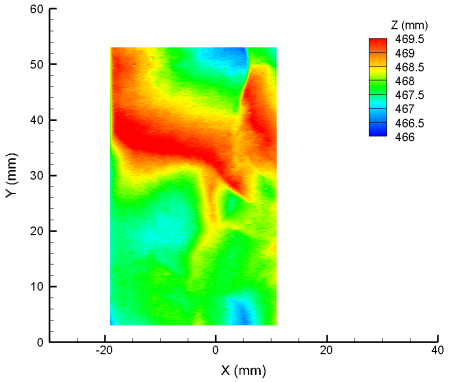

(A) Raw fracture surface data

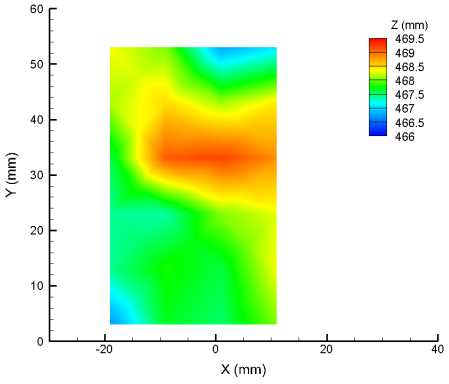

(B) Smoothed fracture surface data (10 mm interpolation)

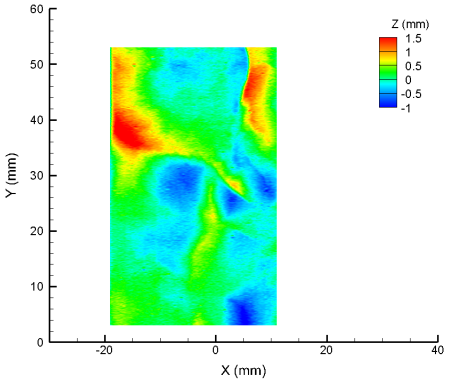

(C) East Brae D2A: Large scale roughness reference surface (raw-smooth)

FIGURE A.20: East Brae surface D2A (sample D2) POST-EXPERIMENT - creation of a large scale roughness grid using a 10 mm smoothing technique

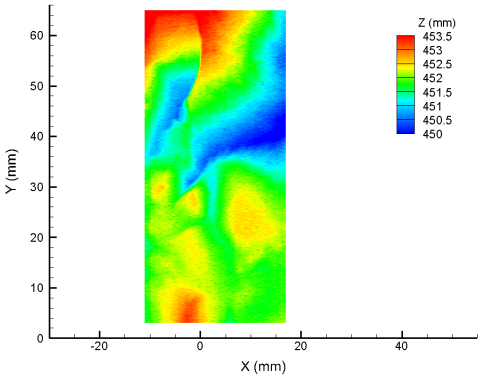

(A) Raw fracture surface data

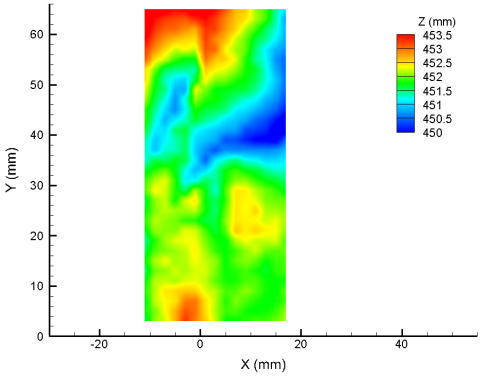

(B) Smoothed fracture surface data (2 mm interpolation)

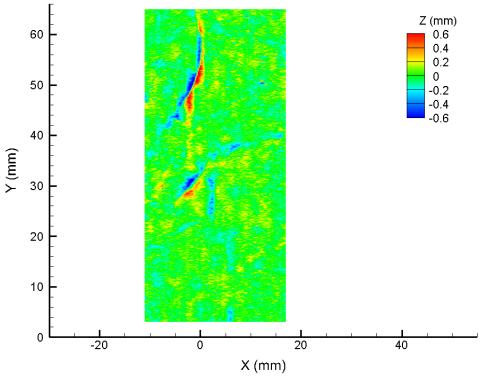

(C) East Brae D2B: Small scale roughness reference surface (raw-smooth)

FIGURE A.21: East Brae surface D2B (sample D2) POST-EXPERIMENT - creation of a small scale roughness grid using a 2 mm smoothing technique

A.5 Heletz surfaces (pre-experiment): samples H2 and H6

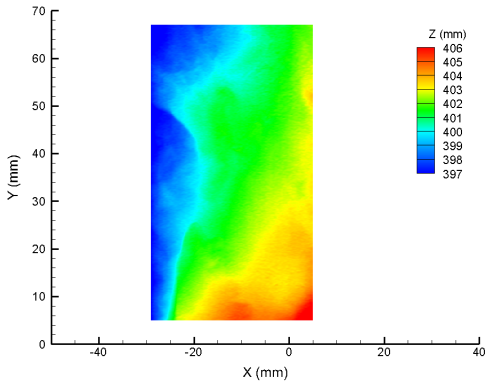

(A) Raw fracture surface data

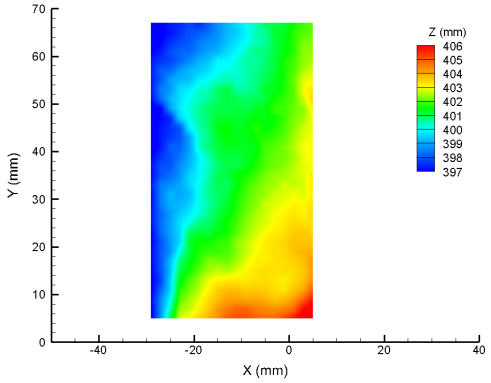

(B) Smoothed fracture surface data (2 mm interpolation)

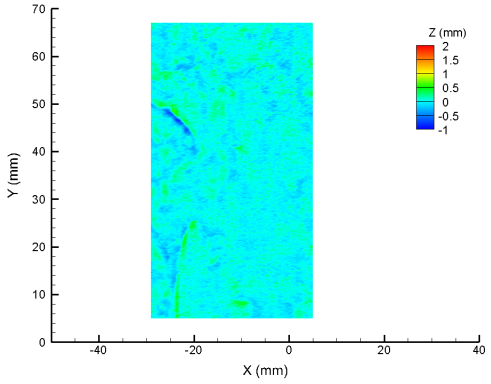

(C) Heletz H2A: Small scale roughness reference surface (raw-smooth)

FIGURE A.22: Heletz surface H2A (sample H2) - creation of a small scale roughness grid using a 2 mm smoothing technique

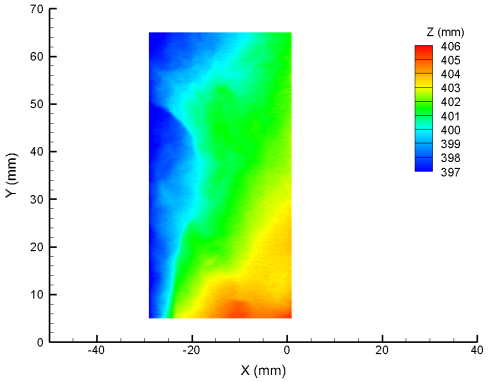

(A) Raw fracture surface data

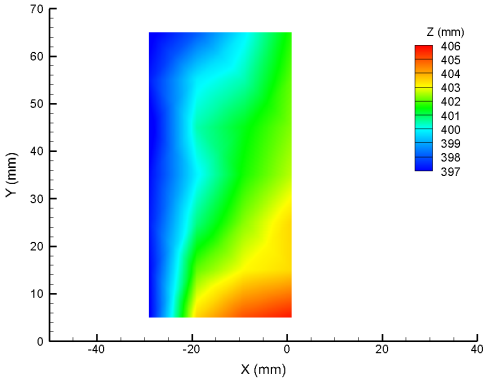

(B) Smoothed fracture surface data (10 mm interpolation)

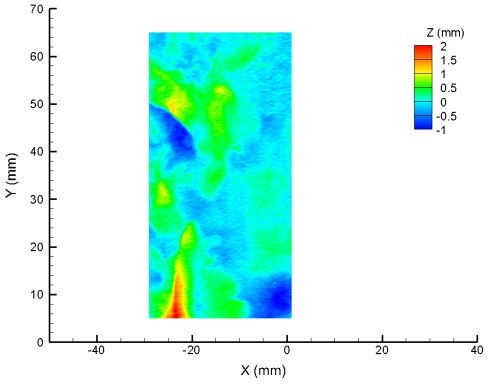

(C) Heletz H2A: Large scale roughness reference surface (raw-smooth)

FIGURE A.23: Heletz surface H2A (sample H2) - creation of a large scale roughness grid using a 10 mm smoothing technique

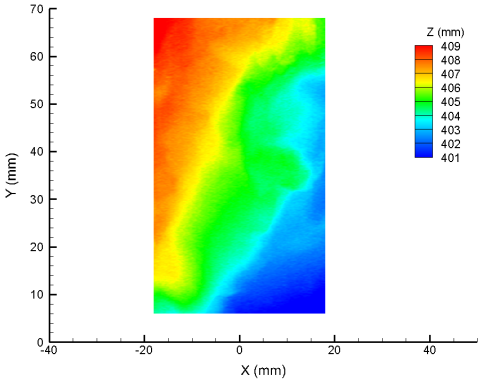

(A) Raw fracture surface data

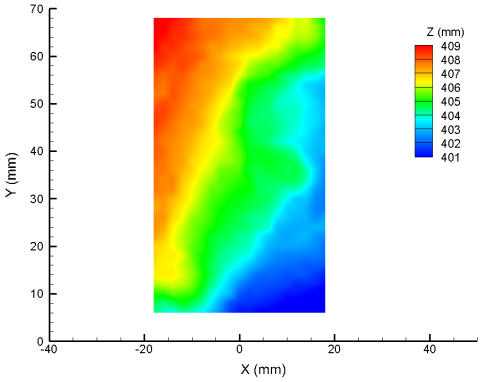

(B) Smoothed fracture surface data (2 mm interpolation)

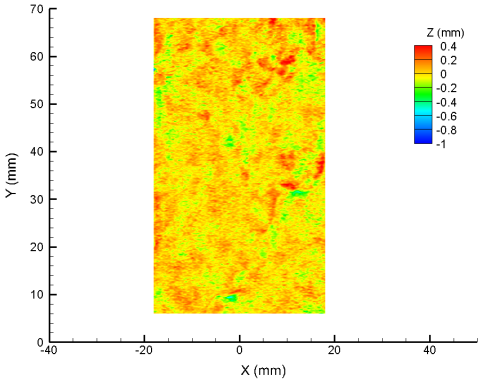

(C) Heletz H2B: Small scale roughness reference surface (raw-smooth)

FIGURE A.24: Heletz surface H2B (sample H2) - creation of a small scale roughness grid using a 2 mm smoothing technique

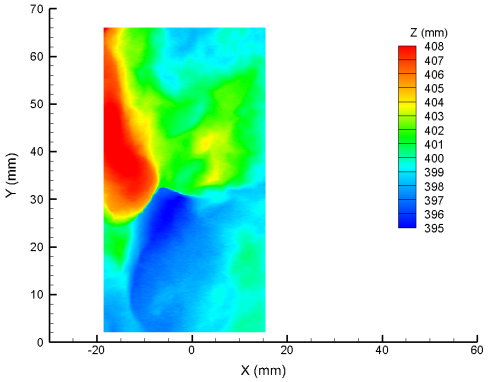

(A) Raw fracture surface data

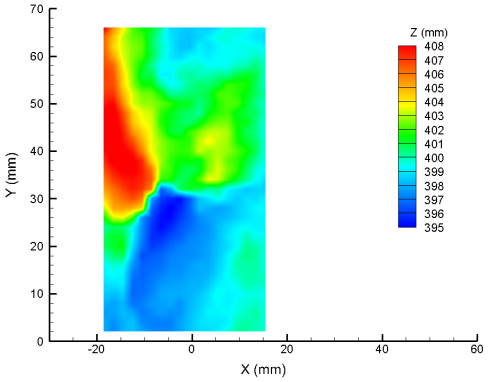

(B) Smoothed fracture surface data (2 mm interpolation)

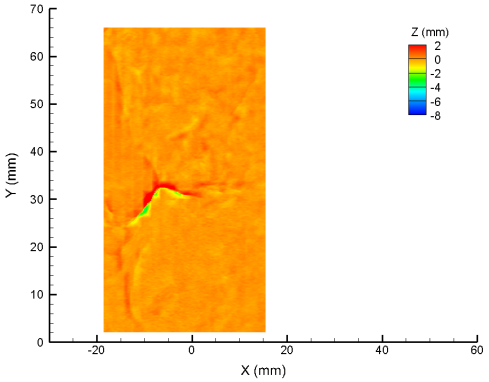

(C) Heletz H6A: Small scale roughness reference surface (raw-smooth)

FIGURE A.25: Heletz surface H6A (sample H6) - creation of a small scale roughness grid using a 2 mm smoothing technique

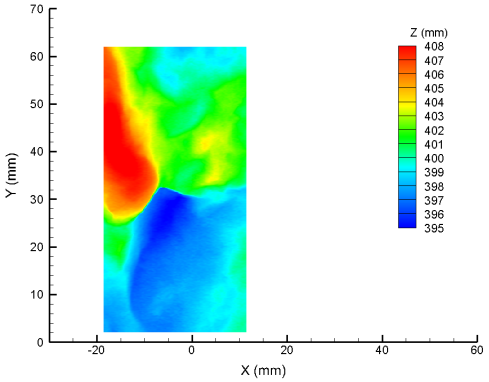

(A) Raw fracture surface data

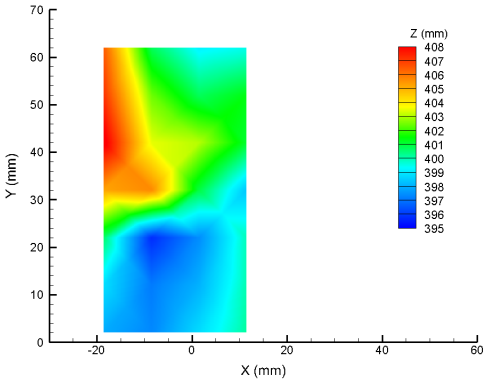

(B) Smoothed fracture surface data (10 mm interpolation)

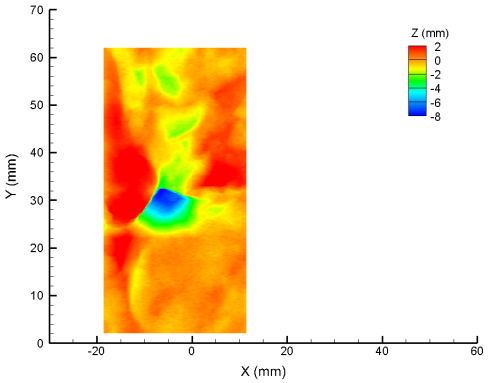

(C) Heletz H6A: Large scale roughness reference surface (raw-smooth)

FIGURE A.26: Heletz surface H6A (sample H6) - creation of a large scale roughness grid using a 10 mm smoothing technique

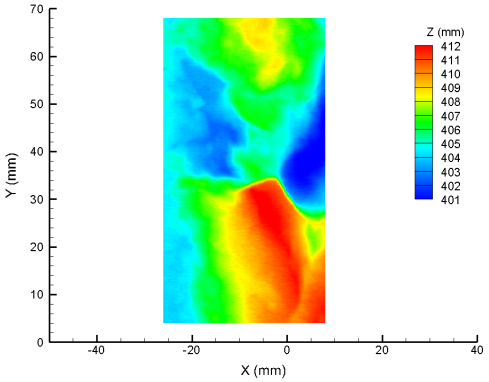

(A) Raw fracture surface data

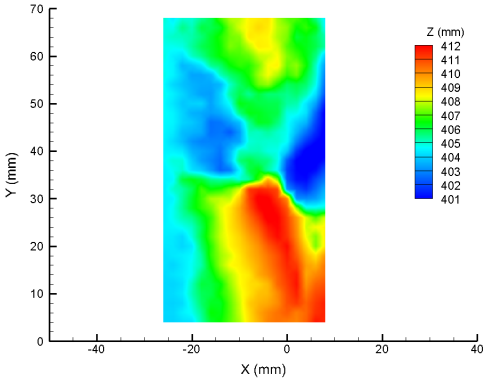

(B) Smoothed fracture surface data (2 mm interpolation)

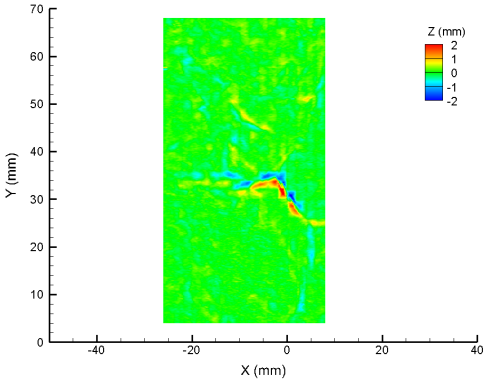

(C) Heletz D2B: Small scale roughness reference surface (raw-smooth)

FIGURE A.27: Heletz surface H6B (sample H6) - creation of a small scale roughness grid using a 2 mm smoothing technique

Appendix B

Calibration and testing of Validyne DP360 differential pressure transducer

B.1 Introduction

Calibration and testing of the Validyne DP360 differential pressure transducer was required prior to use of the instrument within the rig system during experiments. This appendix describes the methodology for undertaking the calibration, and associated testing. The accuracy of logged data measurements taken during the experiments is also reviewed and discussed.

Note that the diaphragm within the differential pressure transducer can be removed and replaced. This allows different pressure range diaphragms to be used within the same instrument. Following initial experimental studies, an 800 psi pressure range diaphragm was chosen for use during the main flow experiments, and this appendix describes the calibration procedure undertaken for this particular diaphragm. A full calibration is required whenever the diaphragm is exchanged.

The transducer is operated through a Validyne CP15 Sine Wave Carrier Demodulator which provides a DC output signal with a range of 0-10 V, which, once calibrated, provides a voltage of 0-10 V that is linearly correlated to differential pressures of 0-800

psi (or the range of the chosen diaphragm). The transducer is connected to the carrier demodulator using shielded cable.

The Validyne DP360 differential pressure transducer has a stated instrument accuracy of ± 0.5% FS (i.e. ± 0.5% of the full scale reading). Given the output voltage range of 0-10 V, this equates to an instrument error of ± 0.05 V, or ± 4 psi for the 800 psi diaphragm used during these experiments.

In order to allow continuous measurement of differential pressure during the experiments, the output signal from the differential pressure transducer is logged to a PC, via an Omega strain gauge meter, and an Omega data logger. The logging software allows a logging frequency to be selected - for the purposes of our experiments this data frequency is usually 5 seconds or 15 seconds. Transformation of the data signal occurs between the transducer and the PC (via the strain gauge), with an associated error. A review of the error associated with this is undertaken as part of the calibration process.

B.2 Calibration methodology

The methodology for setting up, calibrating and testing the differential pressure transducer prior to use has been split into two distinct sections:

B.2.1 Stage I: Calibration and line pressure testing

B.2.1.1 Calibration at zero line pressure

The calibration of the transducer was undertaken under zero line pressure (i.e. the downstream port of the transducer was open to atmosphere, 0 psig). Calibration involves adjustment of the carrier demodulator ZERO and SPAN controls to ensure that the output voltage range of 0-10 V corresponds to the full differential pressure range (in this case 0-800 psi). There should be a direct linear correlation between the voltage and the differential pressure ranges.

An experimental set-up was designed specifically for the calibration of the differential pressure transducer, this can be seen in Figure B.1. CO_2 was supplied to the upstream port of the transducer using an ISCO syringe pump. A valve was included to assist in

controlling the pressure (and to avoid pressure surges) within the connecting pipework. A very high accuracy digital pressure gauge[1] was connected directly upstream of the transducer - this provided the differential pressure measurement for calibration purposes as the downstream port of the transducer was open to atmosphere (0 psig).

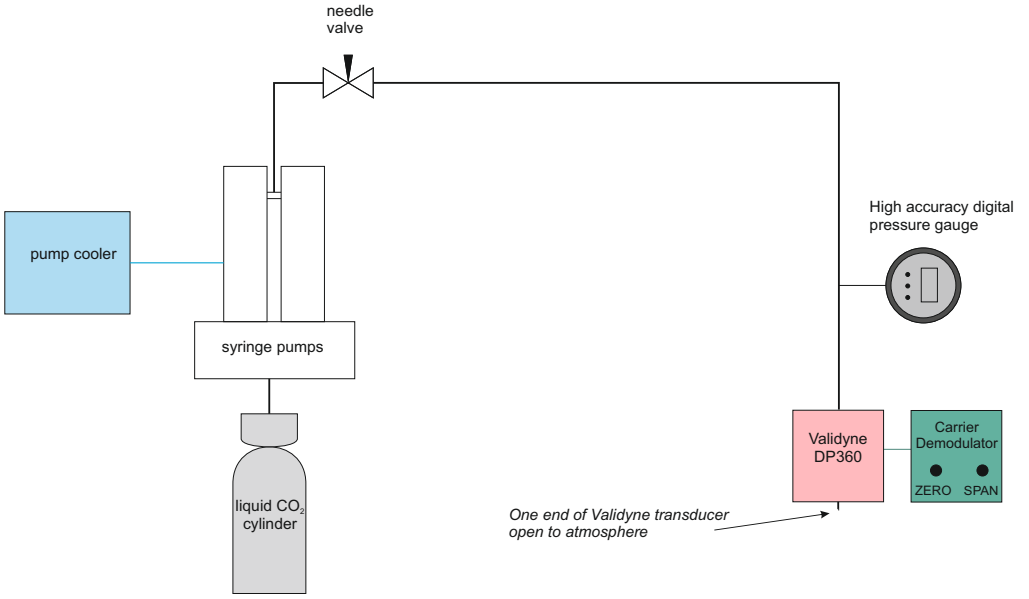

FIGURE B.1: Differential pressure calibration set-up

The steps involved in calibration are given below:

1. Prior to connecting the differential pressure transducer to the calibration rig (Figure B.1), a digital multimeter[2] was connected to the carrier demodulator to allow direct monitoring of the output voltage.

2. With both of the transducer ports open to atmosphere, thus ensuring a zero differential pressure, the carrier demodulator ZERO control was adjusted so that the output voltage was zero. Very minor fluctuations in the output voltage of ± 2.5 mV were observed on the multimeter at this stage - this is well within the error range of the differential pressure transducer (± 0.05 V) and therefore normal.

[1] Omega DPG4000, 0-1000 psig range, $\pm$ 0.05% FS
[2] digimess HM200

3. The transducer was subsequently connected to the calibration rig, and pressure was gradually applied to the upstream port of the pressure transducer, until the maximum differential pressure of 800 psi was achieved.

4. With the maximum differential pressure (800 psi) applied, the carrier demodulator SPAN control was adjusted to achieve an output voltage of 10 V.

5. A controlled leak off of upstream pressure was undertaken to return the differential pressure to 0 psi.

6. The output voltage was checked to ensure it was zero (or within the expected error range). On this occasion the voltage was 0.113 V - this is greater than the error range (±0.05 V), therefore the ZERO control was adjusted down. The reason for this was thought to be due to the bedding in of the new diaphragm. It may therefore be sensible to take the differential pressure up to full range and back to zero a couple of times prior to calibration when using a new diaphragm, to allow for bedding in.

7. Steps 3 and 5 (differential pressure increase and decrease) were repeated to allow for fine adjustment of the SPAN control following the small adjustment of the ZERO control undertaken in step 6. Following fine adjustment of the controls, the resulting control settings were established: ZERO = 6.183; SPAN = 5.067.

8. Steps 3 and 5 were repeated an additional two times to enable validation checks to be undertaken. In total 51 validation checks of the output voltage were undertaken, throughout the full differential pressure range. As an additional robustness check, the carrier demodulator power supply was switched off and on on one occasion during the validation checks to ensure that this action did not result in an output voltage shift.

All output voltages were accurate (within the error range of ±0.05 V), therefore the transducer was deemed to be accurately calibrated for the 800 psi diaphragm. Figure B.2 shows all the validation readings plotted against the calibration line. The maximum output voltage error magnitude from these validation data points was 0.03 V, and the mean error magnitude was 0.01 V. Therefore the validation checks were well within the stated instrument accuracy of ±0.05 V.

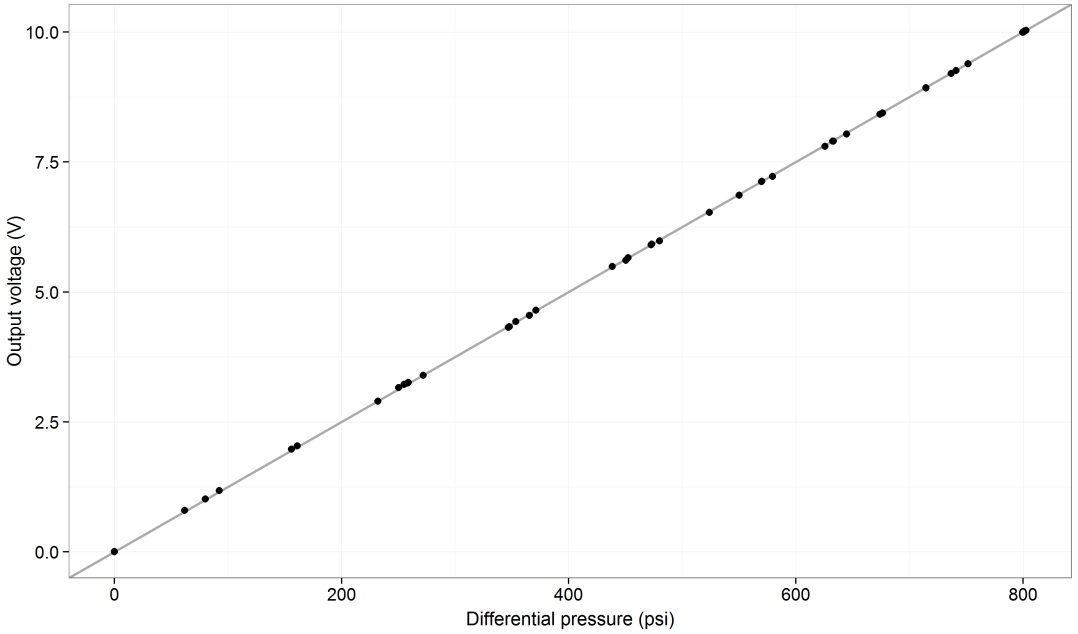

FIGURE B.2: Validation checks of output voltage following calibration

B.2.1.2 Line pressure testing

Following calibration, the instrument was connected to the experimental rig (Figure 5.2) and exposed to a range of line pressures while maintaining zero differential pressure (by keeping valves NV_F2, NV_F3 and NV_F4 open). This was carried out to ensure that the output signal was not unduly affected by changes in line pressure. The Validyne DP360 specifications state that the Line Pressure Error is 1% FS/1000 psi. As full scale output voltage is 10 V, the voltage shift due to a change in line pressure should therefore be within ±0.1 V per 1000 psi line pressure change.

The line pressure testing was considered particularly important for the transducer due to previous experience of voltage drift issues. The previous issues had been identified as being a result of transducer o-rings unsuitable for use with CO_2 (see section 5.4 for further details). Thus it was important to ensure that these issues were fully rectified.

Testing of the voltage drift was carried out on several occasions over four days, with a total of 44 readings recorded. Figure B.3 is a plot of all the readings, with a dashed line representing the maximum expected voltage drift (from the instrument technical specification data sheet). Table B.1 gives a brief description of pressure change direction for each category displayed in the Figure.

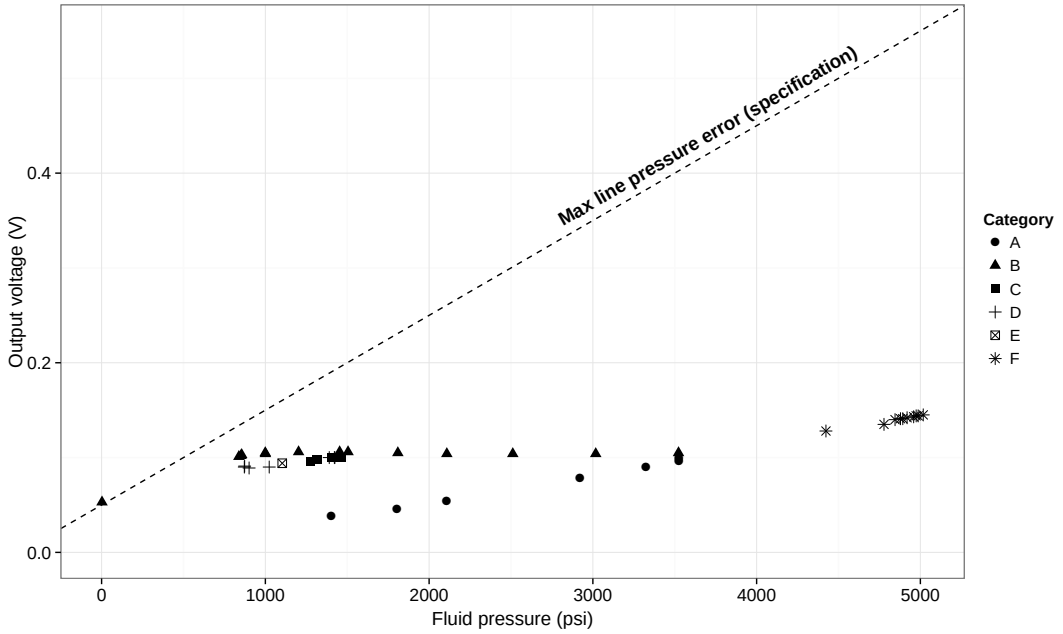

FIGURE B.3: Line pressure error review

TABLE B.1: Category descriptions

Category	Description
A	Pressure increase (1401-3526 psi)
B	Pressure decrease subsequent to A (3526-0 psi)
C	Small P increase then decrease, range 1275-1463 psi
D	Mainly P increase, range 869-1423 psi
E	Single reading, 1100 psi
F	High pressures, P increasing 4423-5016 psi

As can be seen from the graph, all but one of the readings are well below the maximum expected error line (taken from technical specifications). This indicates that there is not an issue with line pressure causing voltage drift. The one reading that is slightly above the line pressure error line was taken at almost zero fluid pressure, immediately after a large initial line pressure rise and fall cycle. Hysteresis is seen during this initial line pressure increase/decrease cycle: the voltage rise associated with the pressure rise is much greater than the subsequent voltage drop when fluid pressure is released. This hysteresis is the reason for the error in the low pressure voltage reading. Subsequent line pressure increase/decrease cycles did not result in the same degree of hysteresis, therefore this initial hysteresis could be associated with initial bedding in of the transducer diaphragm, and may be corrected by re-zeroing the transducer after initial testing.

During experiments, in order to remove the effect of voltage drift associated with line pressure change from experimental results, the differential pressure transducer is re-zeroed each time the fluid pressure is changed (ensuring there is zero differential pressure across the transducer when this is carried out). As the fluid pressure is changed at low frequencies (on average four times daily), this is felt to be a reasonable method to adopt.

Given the calibration equipment available, it was not possible to undertake full tests of the transducer calibration accuracy at high line pressures - only assessment of voltage drift. However, the coarser upstream and downstream pressure transducer data are used to sense-check the differential pressure data on a regular basis, and the instrument manufacturer does not suggest this is a requirement.

B.2.2 Stage II: Data logging operation and accuracy

Once full calibration and testing of the Validyne differential pressure transducer had been carried out (B.2.1), a review of the data logging was undertaken. It was observed that the logged data does not directly correspond to the transducer output voltage. The transformation of data required for the logger system to operate results in an associated systematic error. There may also be a component of electrical noise contributing to the error as a result of signal transfer. Therefore it was required to examine the relationship between the logged data and the calibrated transducer output voltage to fit a relationship that would allow logged data to be converted correctly to differential pressure. For this stage of the transducer set-up, we take the output voltages read directly from the calibrated transducer as the 'true' measurement of differential pressure, and use the relationship between these observations and the logged data values to define a simple model fit that will be used to convert the logging values to 'true' differential pressure readings.

In order to determine the relationship between the transducer output voltage and the logged data, the transducer output voltage was recorded periodically along with accurate time records (± 1 s). This was undertaken while the differential pressure was slowly increased from 0 to 800 psi to ensure data points across the full data range were considered. A total of 116 observations were recorded.

The 5 s frequency log data was subsequently combined with the 116 output voltage readings using linear interpolation between the 5 s frequency logged data points. For example, if a direct output voltage reading was manually recorded at 13:35:03, and the 5 s frequency logged data points occurred at 13:35:00 and 13:35:05, linear interpolation between the two logged data points at 13:35:00 and 13:35:05 would be carried out to provide an estimate for the logged data series at 13:35:03. This was felt to be valid as the differential pressure was steadily rising at a slow rate during the test periods. The first test period involved a differential pressure increase from 0 to 160 psi in 34 mins - an average rate of 4.7 psi per minute, or 0.4 psi per 5 s. The second test period involved a differential pressure increase from 0 to 800 psi in 2 hours 35 minutes - an average rate of 5.2 psi per minute, or 0.4 psi per 5 s. Thus, the error introduced as a result of interpolation is expected to be minimal relative to the instrument accuracy ($\pm$0.05 V or $\pm$4 psi).

For data analysis, we would like to transform the logged data values to differential pressure readings, in psi for ease (this can later be converted to Pa, if required). The manually recorded output voltages direct from the transducer (regarded to be the 'true' or accurate measurement of the differential pressure) were therefore converted to differential pressure values (psi) using a multiplication factor of 80, as the transducer is calibrated to output voltages of 0-10 V for the range 0-800 psi. The subsections below describe derivation of an appropriate model fit that describes the relationship between the logged data (V) and these 'true' differential pressure readings. As mentioned earlier, 116 observations were recorded, therefore 116 calibration points are available to determine the model fit.

B.2.2.1 Testing a linear model fit

A simple least squares linear regression model was initially used to fit a straight line to the data (using R software). From the figure (Figure B.4), it can be seen that there is a trend in the calibration data, such that there are negative residuals (calibration data is below the line) for both high and low values, with positive residuals (calibration data above the line) within the middle range. This can be seen more clearly in Figure B.5, which shows model fit analysis plots associated with the linear model.

The top left plot in Figure B.5 plots the residuals against the fitted values. The curved shape on this plot shows that there is not a constancy of variance within the data

range, and errors are not normally-distributed. This is further illustrated in the top right plot, which illustrates the calibration data against the theoretical normal distribution plot. The s-shaped curve shows departure from the normal probability plot (the dashed line) which suggests uniform error rather than normally-distributed error. This is not surprising given the error was expected to be a systematic error in data transfer/transformation. The bottom left plot is an alternative way of displaying the residuals: this shows that the residuals are smallest around 600 psi, but are higher for both low and high fitted values. The bottom right plot, standardized residuals against leverage, indicates that the data points associated with high differential pressures have the largest influence on parameter determination.

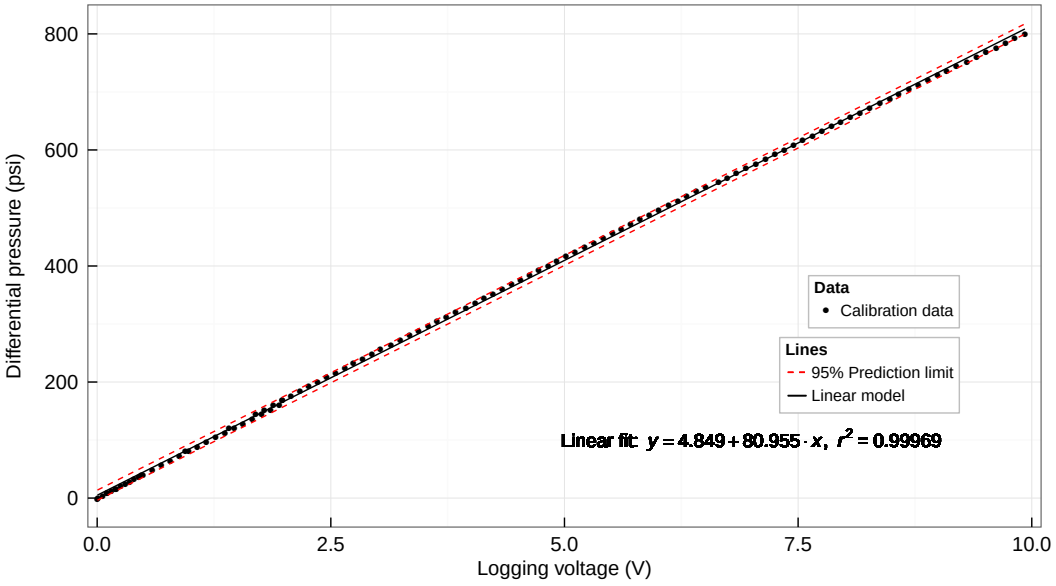

FIGURE B.4: Logged differential pressure data - linear model fit

Uncertainty limits for the linear model fit have been calculated from 95% prediction intervals [Crawley, 2012, Devore, 2011], which have been assumed to be valid despite the lack of normal error distribution. These uncertainty limits result in an uncertainty of ± 8.7 psi across the whole data range, and are included as red dashed lines in Figure B.4.

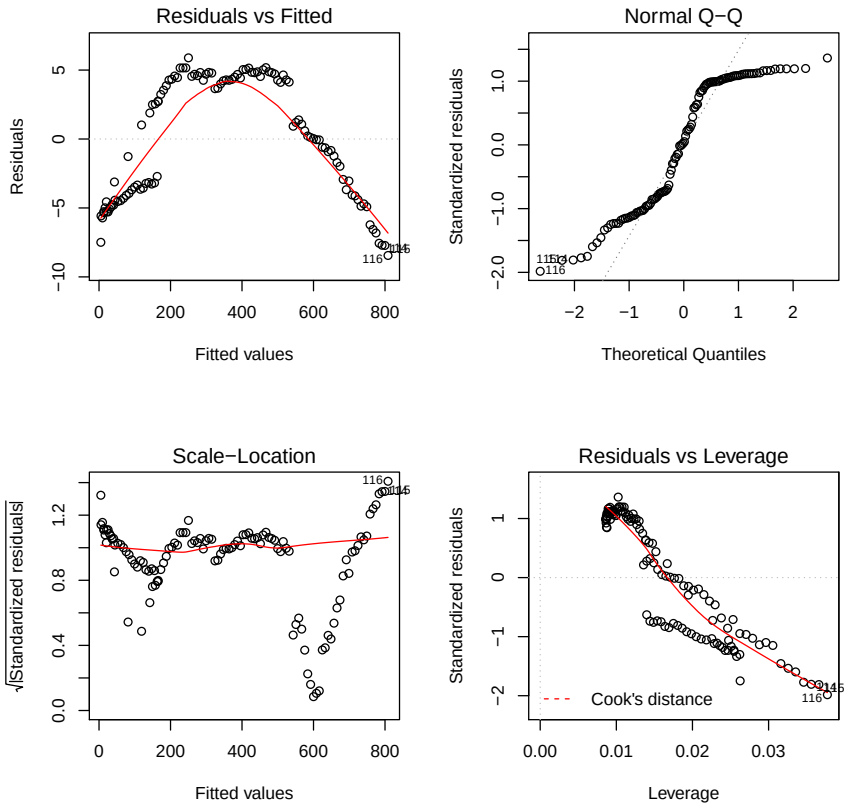

FIGURE B.5: Log data linear regression: model fitting plots

B.2.2.2 Testing a second order polynomial model fit

Due to the trend in the calibration data that suggests a linear model fit is not entirely appropriate, a second order polynomial model fit has also been tested. Figure B.6 plots the calibration data along with the second order polynomial fit and the 95% prediction limits associated with the model. Comparison of Figure B.6 with Figure B.4 indicates that the second order polynomial fit is an improvement to the linear model fit.

The model fit analysis plots associated with the second order polynomial model can be seen in Figure B.7. The top left plot (residuals against fitted values) shows a much more consistent variance across the data range than the linear fit, while the top right plot (calibration data against the theoretical normal distribution plot) shows a closer fit of residuals to the normal distribution than observed for the linear model.

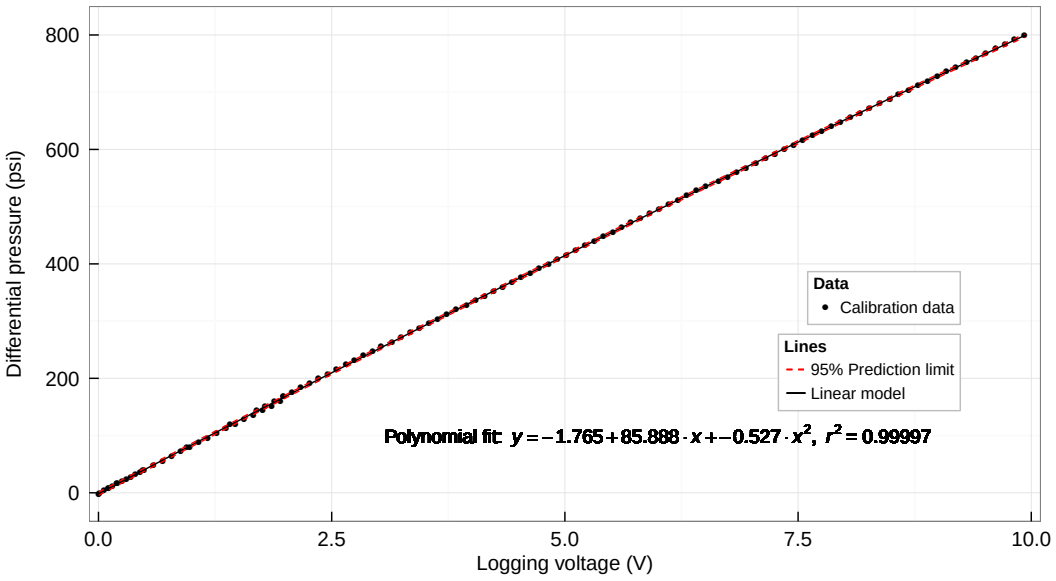

FIGURE B.6: Logged differential pressure data - second order polynomial fit

The uncertainty limits (shown in Figure B.6) for the second order polynomial model fit, calculated in the same manner as the linear model fit, are estimated to be ± 2.7 psi across the whole data range, notably lower than those estimated for the linear model fit. Due to the improved fit observed using a second order polynomial model over a linear model, the second order polynomial model has been adopted for conversion of logged differential pressure data for all flow experiments.

B.3 Discussion of measurement accuracy

As discussed in B.1, the differential pressure transducer instrument accuracy is stated to be ± 4 psi. The output voltages recorded during calibration of the instrument indicated that the observed error was well within this stated range, with a maximum error magnitude of ± 2.4 psi, and an average error magnitude of ± 0.8 psi observed (B.2.1).

However, in order to log the instrument output, the data is transferred and transformed via a strain gauge meter to a PC. An additional error is associated with this data recording process. Section B.2.2 describes how this data transformation is recorded

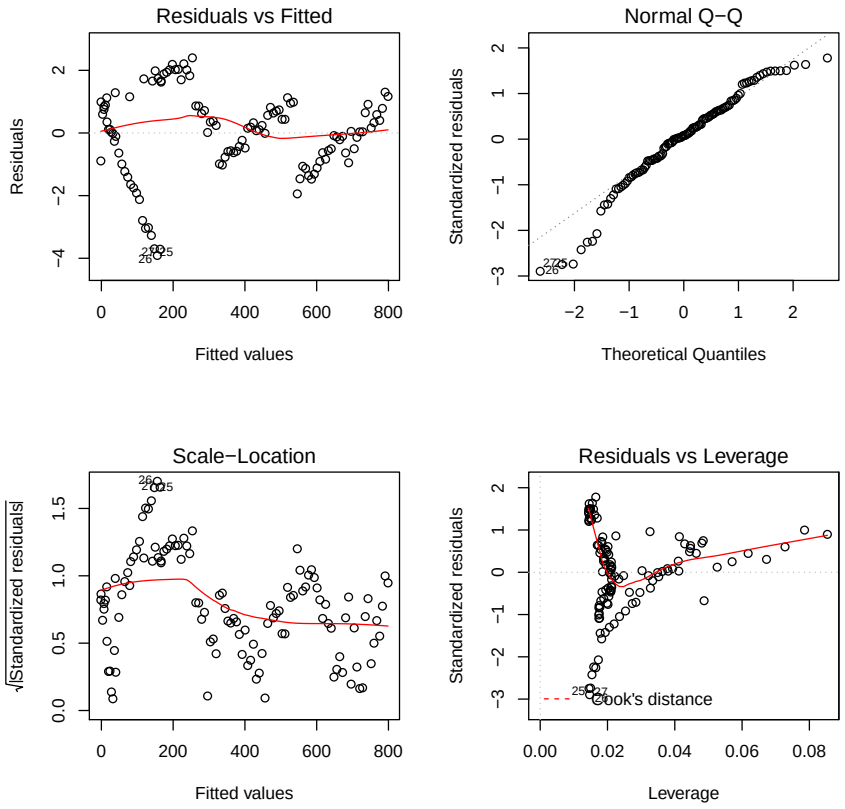

FIGURE B.7: Log data second order polynomial regression: model fitting plots

and analysed in an attempt to minimise uncertainty in the logged data. Section B.2.2 suggests that an error of ± 2.7 psi is associated with the process of real time logging of differential pressure transducer outputs to a PC, when utilising a second order polynomial model fit to calibrate the data transformation. This error, associated with the data logging process, is of slightly lower magnitude than the instrumental error.

The instrumental error ($e_i = \pm 4psi$) and the data logging error ($e_l = \pm 2.7psi$) can be combined using $e_t = \sqrt{e_i^2 + e_l^2}$ [Bevington and Robinson, 2003]. This gives a resultant error of ± 4.8 psi, which is slightly larger than instrumental error, as expected.

Appendix C

R data processing, analysis and presentation script files

This Appendix contains R script files representative of the data processing, analysis and presentation steps carried out for each sample experiment. The files included are listed below:

1. **omegacollate.R**: Collation and merging of all sample omega log files into a single dataset (East Brae B2b example file).
2. **omegaconvert.R**: Conversion of data within the omega log dataset from logged data values to meaningful data units, using calibration model data (East Brae B2b example file).
3. **iscoload.R**: Merging of files and conversion of data units within the isco pump log dataset using specified conversion factors (East Brae B2b example file).
4. **USBtempload.R**: Merging and quality checking of USB pump temperature log files (East Brae B2b example file).
5. **logmerge_eventextraction.R**: Merging of up to five separate log datasets (omega, pump and pump temperature), and an automated method for extracting representative event data for each of the logged parameters (East Brae B2b example file).

6. **logmerge_wisseyeventextraction.R**: Merging of up to five separate log datasets (omega, pump and pump temperature), and an automated method for extracting representative event data for each of the logged parameters, specifically written for the Wissey datasets, thus accounting for timing discrepancies observed between pump and omega log datasets.

7. **log_wissey_extract_Pc_events.R**: Automated event data extraction method adapted for constant fluid pressure and flow rate experiments where only confining pressure and temperature are changed (used for Wissey experiments C2, D and E).

File 1: omegacollate.R

```
## This file loads in all raw data from the omega logging software
## The data is saved in a single file in this folder

################### 1 - Load in and organise data from all omega csv files

#############################################################################################


# Set working directory
setwd("R:/EXPERIMENTAL DATA/LOGS/140618 EastBrae B2boffset/omega")

#First, remove all variables in R workspace to avoid clutter
rm(list=ls())

#Make empty data frame for combined dataset to be put in
omegadata<-data.frame()


#Import raw csv files from logging program into R - all files saved in the same
    folder.
#Headers are on row 7, so skip first 6 rows.
#Import all the data into R, extract the columns of interest, convert the
    datetime column
#to R datetime format, and create a data frame that contains all this
#data of interest.
temp = list.files(pattern="*.csv")
for(i in temp) {
  raw<-read.csv(file=i, skip=6)
  raw<-raw[,1:7]
  names(raw)<-c("Date","Time","P_conf","P_us","P_ds","P_diff","Templog")
  raw$DateTime<-paste(raw$Date,raw$Time)
  raw$Date<-NULL
  raw$Time<-NULL
  raw<-na.omit(raw)
  ds<-paste("data_",i, sep="")#this add "data_" to the name of file
  ds<-substr(ds, 1, nchar(ds)-4)#remove the last 4 char (.csv)
  rawsort<-data.frame(raw)
  omegadata<-rbind(omegadata,rawsort)
  assign(ds, rawsort)
}

#Tidy up the workspace once omegadata dataframe created
rm(list= ls()[!(ls() %in% c('omegadata'))])
str(omegadata)
#Make the date time information into POSIXct format
omegadata$Rdattim<-as.POSIXct(omegadata$DateTime, format="%d/%m/%Y %H:%M:%S")
omegadata<-omegadata[,c(7,1,2,3,4,5)] # This is to reorder the columns to put
    Rdattim at start (and get rid of DateTime)
```

```
## SORT DATA ##

sorted <- order(omegadata$Rdattim)
omegadata <-omegadata[sorted,]
str(omegadata)

#CHECK AND REMOVE DUPLICATES
test<-duplicated(omegadata)
duplicates<-omegadata[duplicated(omegadata),]
noduplicates<-unique(omegadata) #check these add up
#omegadata<-unique(omegadata) #update database to remove duplicates

### SAVING DATA
setwd("R:/EXPERIMENTAL DATA/LOGS/140618 EastBrae B2boffset")
write.csv(omegadata,file="omegadata_EBraeB2boffset_jun14.csv",row.names=FALSE)

# ### CHECK BY LOADING DATA BACK IN
# omegadatatest<-read.csv(file="omegadata_EBraeB2boffset_jun14.csv")
```

File 2: omegaconvert.R

```
## This file loads in the full omega log data series and applies calibration and
    unit conversions to the data as required

## Convert pressure log data to psi

#################### 1 - Load in omega data

rm(list=ls())
setwd("R:/EXPERIMENTAL DATA/LOGS/140618 EastBrae B2boffset")
omegadata <- read.csv("omegadata_EBraeB2boffset_jun14.csv") #Check folder for
    latest


#################### 2 - Load in calibration data

setwd("M:/Experimental/R/datafiles")
load ("lm_conf.Rdata") #CONFINING P calibration model
load ("lm_us.Rdata") #US P calibration model
load ("lm_ds.Rdata") #DS P calibration model
load ("poly2_diff.Rdata") #DIFF P calibration model
load ("lm_temp.Rdata") #TEMP calibration model

#################### 3 - Create new dataframe to work with

omegacal <- omegadata
# Need to set Rdattim class correctly otherwise searches and subsets won't work
    correctly
omegacal$Rdattim <- as.POSIXct(omegacal$Rdattim)

#################### 4 - Carry out calibration conversions (psi and C)
# uses calibration datafile/lm models

# Converted data as well as lower and upper 95% prediction intervals (according
    to model) are saved for each parameter

# Confining p (psi)
temp<-predict(lm_conf,list(Logging=omegacal$P_conf),interval='prediction')
omegacal$P_conf_psi <- temp[,1]
omegacal$Pc_lo <-temp[,2]
omegacal$Pc_hi <-temp[,3]

# US p (psi)
temp<-predict(lm_us,list(Logging=omegacal$P_us),interval='prediction')
omegacal$P_us_psi <- temp[,1]
omegacal$Pus_lo <-temp[,2]
omegacal$Pus_hi <-temp[,3]

# DS p (psi)
```

```
temp<-predict(lm_ds,list(Logging=omegacal$P_ds),interval='prediction')
omegacal$P_ds_psi <- temp[,1]
omegacal$Pds_lo <-temp[,2]
omegacal$Pds_hi <-temp[,3]

# Differential pressure (psi)
temp<-predict(poly2_diff,list(Logging=omegacal$P_diff),interval='prediction')
omegacal$P_diff_psi <- temp[,1]
omegacal$Pdiff_lo <-temp[,2]
omegacal$Pdiff_hi <-temp[,3]

# Temperature - converted to degrees celsius
temp<-predict(lm_temp,list(Logging=omegacal$Templog),interval='prediction')
omegacal$Templog_C <- temp[,1]
omegacal$Temp_lo <-temp[,2]
omegacal$Temp_hi <-temp[,3]

#Tidy up the workspace once calibrated dataframe created
rm(temp)

## Add, MPa columns to the calibrated file

omegacal$P_conf_MPa <- omegacal$P_conf_psi*0.00689475729
omegacal$P_us_MPa <- omegacal$P_us_psi*0.00689475729
omegacal$P_ds_MPa <- omegacal$P_ds_psi*0.00689475729
omegacal$P_diff_MPa <- omegacal$P_diff_psi*0.00689475729

### SAVING DATA TO RESEARCH DATASTORE

### !!!!!!!!!!!!!!!!!!!!!!!!!!!!!!!!!!!!!!!!!!!!!!!!!!!!!!!!
### !!!!!!!!!!! WARNING - THIS COULD TAKE A WHILE - CAREFUL NOT TO OVERWRITE BY
    ACCIDENT !!!!!!
### !!!!!!!!!!!!!!!!!!!!!!!!!!!!!!!!!!!!!!!!!!!!!!!!!!!!!!!!

setwd("R:/EXPERIMENTAL DATA/LOGS/140618 EastBrae B2boffset")
write.csv(omegacal,file="omegacal_POLY2M_EBraeB2boffset_jun14.csv",row.names=
    FALSE) # AMEND THE DATE IF UPDATING THE FILE


### LOADING DATA

# setwd("R:/EXPERIMENTAL DATA/CONVERTED")
# omegacal<-read.csv(file="omegacal_POLY2M_EBraeB2boffset_jun14.csv")

### WORKING WITH DATA

# TO WORK WITH A SUBSET TIME PERIOD OF THE DATA (USUALLY ADVISABLE DUE TO FILE
    SIZE)
# CREATE SUBSET DATASET
```

```
# sub_omegacal<-subset(omegacal,Rdattim>as.numeric(as.POSIXct("2014-02-01 00:00")
    )
#                   & Rdattim<as.numeric(as.POSIXct("2014-3-21 23:00")))
```

File 3: iscoload.R

```
## This file loads in all raw data from the ISCO logging software - first for
    Pump1 and then for Pump2
## The data is saved in a single file for each pump, in this folder

##### NOTE - THE TIME OF LOGGING NEEDS TO BE TIED IN WITH THE ISCO DATA OTHERWISE
     RESULTS ARE MEANINGLESS!!!! #####
#### THIS SCRIPT NEEDS TO REFER TO SPREADSHEET THAT CONTAINS THIS DATA AND THEN
    MUST CONVERT TIME TO A DATETIME FORMAT

################### 1 - Load in and organise data from all ISCO pump 1 csv files

#############################################################################################


###### LOAD IN ISCO LOG FILE ######

## FIRST PUMP 1 ##########################
########################################

#First, remove all variables in workspace to avoid clutter
rm(list=ls())

setwd("M:/Experimental/Logging/Pump/Pump1")
# Load in the Pump1 log starting datetime data (and check it's up to date)
pump1_datetime<-read.csv("pump1_datetime.csv") # This file can be updated outside
     of R - should be kept up to date
pump1_datetime$Rdattim <- as.POSIXct(pump1_datetime$Rdattim,format="%d/%m/%Y %H:%
    M:%S") #Makes sure DateTime are in correct format once loaded


#Try importing raw csv file output from logging program
# There are no headers in the raw output files
# These are added below, and unnecessary columns are removed

#Make empty data frame for combined dataset to be put in
iscodataP1<-data.frame()

#Now, import all UNLOADED data into R, extract the columns of interest, apply
    appropriate headers
#and create a data frame that contains all this data.
setwd("R:/EXPERIMENTAL DATA/LOGS/140618 EastBrae B2boffset/isco1")
temp = list.files(pattern="*.CSV")
for(i in temp) {
  #i="DATA_140610_P1.CSV"
  isco<-read.csv(file=i, header=FALSE)
  isco<-data.frame(isco)
  isco<-isco[,-c(4,5,6,7,8,9,10,21,22,23,24,25,29)]
```

```
  names(isco) <- c("Time","Pressure_A","Pressure_B","A_Flow","A_Vol","A_Status","
    A_Control","A_Problem","B_Flow","B_Vol","B_Status","B_Control","B_Problem","
    System_Flow","System_Pressure","System_Volume")
  isco<-na.omit(isco)
  isco$Pressure_A<-isco$Pressure_A/5 # Convert from psix5 to psi
  isco$Pressure_B<-isco$Pressure_B/5 # Convert from psix5 to psi
  isco$A_Flow<-isco$A_Flow/(1E7) #Convert from l/min*1E10 to ml/min N.B. mistype
    in ISCO technical bulletin
  isco$B_Flow<-isco$B_Flow/(1E7) #Convert from l/min*1E10 to ml/min
  isco$A_Vol<-isco$A_Vol/(1E6) #Convert from l*1E9 to ml
  isco$B_Vol<-isco$B_Vol/(1E6) #Convert from l*1E9 to ml
  isco$System_Flow<-isco$System_Flow/(1E7) #Convert from l/min*1E10 to ml/min
  isco$System_Pressure<-isco$System_Pressure/5 # Convert from psix5 to psi
  isco$System_Volume<-isco$System_Volume/(1E6) #Convert from l*1E9 to m3
  sel=which(pump1_datetime[,1]==i)
  isco$Rdattim= as.POSIXct(0.001*isco$Time,origin=pump1_datetime[sel,2])
  ds<-paste("data_",i, sep="")#this add "data_" to the name of file
  ds<-substr(ds, 1, nchar(ds)-4)#remove the last 4 char (.csv)
  iscodataP1<-rbind(iscodataP1,isco)
  assign(ds, isco)
}

#Tidy up the workspace once iscodataP1 dataframe created
rm(list= ls()[!(ls() %in% c('iscodataP1'))])


## SECONDLY PUMP 2 ##########################
##########################################

setwd("M:/Experimental/Logging/Pump/Pump2")

# Load in the Pump2 log starting datetime data (and check it's up to date)
#load("pump2_datetime.Rda")
pump2_datetime<-read.csv("pump2_datetime.csv") # This file can be updated outside
     of R - should be kept up to date
pump2_datetime$Rdattim <- as.POSIXct(pump2_datetime$Rdattim,format="%d/%m/%Y %H:%
    M:%S") #Makes sure DateTime are in correct format once loaded

#Try importing raw csv file output from logging program
# There are no headers in the raw output files
# These are added below, and unnecessary columns are removed

#Make empty data frame for combined dataset to be put in
iscodataP2<-data.frame()

#Now, import all the data into R, extract the columns of interest, apply
    appropriate headers
#and create a data frame that contains all this data.
setwd("R:/EXPERIMENTAL DATA/LOGS/140618 EastBrae B2boffset/isco2")
```

```
temp = list.files(pattern="*.CSV")
for(i in temp) {
  #i="DATA_140224_P2.CSV"
  isco<-read.csv(file=i, header=FALSE)
  isco<-data.frame(isco)
  isco<-isco[,-c(4,5,6,7,8,9,10,21,22,23,24,25,29)]
  names(isco) <- c("Time","Pressure_A","Pressure_B","A_Flow","A_Vol","A_Status","
    A_Control","A_Problem","B_Flow","B_Vol","B_Status","B_Control","B_Problem","
    System_Flow","System_Pressure","System_Volume")
  isco<-na.omit(isco)
  isco$Pressure_A<-isco$Pressure_A/5 # Convert from psix5 to psi
  isco$Pressure_B<-isco$Pressure_B/5 # Convert from psix5 to psi
  isco$A_Flow<-isco$A_Flow/(1E7) #Convert from l/min*1E10 to ml/min N.B. mistype
    in ISCO technical bulletin
  isco$B_Flow<-isco$B_Flow/(1E7) #Convert from l/min*1E10 to ml/min
  isco$A_Vol<-isco$A_Vol/(1E6) #Convert from l*1E9 to ml
  isco$B_Vol<-isco$B_Vol/(1E6) #Convert from l*1E9 to ml
  isco$System_Flow<-isco$System_Flow/(1E7) #Convert from l/min*1E10 to ml/min
  isco$System_Pressure<-isco$System_Pressure/5 # Convert from psix5 to psi
  isco$System_Volume<-isco$System_Volume/(1E6) #Convert from l*1E9 to m3
  sel=which(pump2_datetime[,1]==i)
  isco$Rdattim=as.POSIXct(0.001*isco$Time,origin=pump2_datetime[sel,2])
  ds<-paste("data_",i, sep="")#this add "data_" to the name of file
  ds<-substr(ds, 1, nchar(ds)-4)#remove the last 4 char (.csv)
  iscodataP2<-rbind(iscodataP2,isco)
  assign(ds, isco)
}

#Tidy up the workspace once iscodataP1 dataframe created
rm(list= ls()[!(ls() %in% c('iscodataP1','iscodataP2'))])

## SORT DATA ##

sorted <- order(iscodataP1$Rdattim)
iscodataP1 <-iscodataP1[sorted,]
str(iscodataP1)

sorted <- order(iscodataP2$Rdattim)
iscodataP2 <-iscodataP2[sorted,]
str(iscodataP2)

#CHECK AND REMOVE DUPLICATES
duplicates<-iscodataP1[duplicated(iscodataP1),]
noduplicates<-unique(iscodataP1) #check these add up
#iscoP1check<-unique(iscoP1check) #update database to remove duplicates

duplicates<-iscodataP2[duplicated(iscodataP2),]
noduplicates<-unique(iscodataP2) #check these add up
### SAVING DATA
```

```
setwd("R:/EXPERIMENTAL DATA/LOGS/140618 EastBrae B2boffset")
write.csv(iscodataP1,file="iscodataP1_EBraeB2boffset_jun14.csv",row.names=FALSE)
    # AMEND THE DATE WHEN UPDATING THE FILE
write.csv(iscodataP2,file="iscodataP2_EBraeB2boffset_jun14.csv",row.names=FALSE)
    # AMEND THE DATE WHEN UPDATING THE FILE
```

File 4: USBtemplload.R

```
# This file loads in all the USB temperature logger data and saves it in the
    correct
# data file, depending on what the data is from (i.e. Syringe Pump 1A, Syringe
    Pump 1B)

# Set folder to upload data from:

############################
# DO PUMP 1A FIRST##########
############################

setwd("R:/EXPERIMENTAL DATA/LOGS/140618 EastBrae B2boffset/temp1A")

#First, remove all variables in workspace to avoid clutter
rm(list=ls())

#Try importing raw csv file output from logging program

#Make empty data frame for combined dataset to be put in
tempdata_P1A<-data.frame()

#Now, import all the data into R from all files
#and create a data frame that contains all this data.
temp = list.files(pattern="*.txt")
for(i in temp) {
  tdata<-read.csv(file=i)
  tdata<-data.frame(tdata)
  tdata<-tdata[,c(2,3)]
  names(tdata)<-c("Rdattim","Temperature_C")
  tdata<-na.omit(tdata)
  tdata$Rdattim<-as.POSIXct(tdata$Rdattim, format="%d/%m/%Y %H:%M:%S")
  ds<-paste("data_",i, sep="")#this add "data_" to the name of file
  ds<-substr(ds, 1, nchar(ds)-4)#remove the last 4 char (.csv)
  tempdata_P1A<-rbind(tempdata_P1A,tdata)
  assign(ds, tdata)
}

#Tidy up the workspace once tempdata_P1A dataframe created
rm(list= ls()[!(ls() %in% c('tempdata_P1A'))])

############################
# DO PUMP 1B AS WELL #######
############################

setwd("R:/EXPERIMENTAL DATA/LOGS/140618 EastBrae B2boffset/temp1B")

#Try importing raw csv file output from logging program
```

```
#Make empty data frame for combined dataset to be put in
tempdata_P1B<-data.frame()

#Now, import all the data into R from all files
#and create a data frame that contains all this data.
temp = list.files(pattern="*.txt")
for(i in temp) {
  tdata<-read.csv(file=i)
  tdata<-data.frame(tdata)
  tdata<-tdata[,c(2,3)]
  names(tdata)<-c("Rdattim","Temperature_C")
  tdata<-na.omit(tdata)
  tdata$Rdattim<-as.POSIXct(tdata$Rdattim, format="%d/%m/%Y %H:%M:%S")
  ds<-paste("data_",i, sep="")#this add "data_" to the name of file
  ds<-substr(ds, 1, nchar(ds)-4)#remove the last 4 char (.csv)
  tempdata_P1B<-rbind(tempdata_P1B,tdata)
  assign(ds, tdata)
}

#Tidy up the workspace once tempdata_P1B dataframe created
rm(list= ls()[!(ls() %in% c('tempdata_P1A','tempdata_P1B'))])

## SORT DATA ##

sorted <- order(tempdata_P1A$Rdattim)
tempdata_P1A <-tempdata_P1A[sorted,]
str(tempdata_P1A)

sorted <- order(tempdata_P1B$Rdattim)
tempdata_P1B <-tempdata_P1B[sorted,]
str(tempdata_P1B)

#CHECK AND REMOVE DUPLICATES
duplicates<-tempdata_P1A[duplicated(tempdata_P1A),]
noduplicates<-unique(tempdata_P1A) #check these add up
#tempP1Acheck<-unique(tempP1Acheck) #update database to remove duplicates

duplicates<-tempdata_P1B[duplicated(tempdata_P1B),]
noduplicates<-unique(tempdata_P1B) #check these add up

### SAVING DATA

setwd("R:/EXPERIMENTAL DATA/LOGS/140618 EastBrae B2boffset")
write.csv(tempdata_P1A,file="tempdata_P1A_EBraeB2boffset_jun14.csv",row.names=
    FALSE) # AMEND THE DATE WHEN UPDATING THE FILE
write.csv(tempdata_P1B,file="tempdata_P1B_EBraeB2boffset_jun14.csv",row.names=
    FALSE) # AMEND THE DATE WHEN UPDATING THE FILE
```

File 5: logmerge_eventextraction.R

```
######################################################################
#
# 10 June 2014 East Brae B2b sample event extraction
#
######################################################################

############## FOR PLOTTING #################
library (ggplot2) # Needed for plotting
library (grid) # Needed for customising plot area
library (scales) # Needed for editing log tickmarks
theme_set(theme_bw())
############################################


###################################
#
# STEP 1 - LOADING DATA
#
###################################
rm(list=ls())
setwd("R:/EXPERIMENTAL DATA/LOGS/140618 EastBrae B2boffset")
omegacal<-read.csv(file="omegacal_POLY2M_EBraeB2boffset_jun14.csv")
iscodataP1<-read.csv(file="iscodataP1_EBraeB2boffset_jun14.csv")
iscodataP2<-read.csv(file="iscodataP2_EBraeB2boffset_jun14.csv")
tempdata_P1A<-read.csv(file="tempdata_P1A_EBraeB2boffset_jun14.csv")
tempdata_P1B<-read.csv(file="tempdata_P1B_EBraeB2boffset_jun14.csv")

# Need to set Rdattim class correctly otherwise searches and subsets won't work
    correctly
omegacal$Rdattim <- as.POSIXct(omegacal$Rdattim)
iscodataP1$Rdattim <- as.POSIXct(iscodataP1$Rdattim)
iscodataP2$Rdattim <- as.POSIXct(iscodataP2$Rdattim)
tempdata_P1A$Rdattim <- as.POSIXct(tempdata_P1A$Rdattim)
tempdata_P1B$Rdattim <- as.POSIXct(tempdata_P1B$Rdattim)

#####################################################################
# STEP 2 Create duplicate of omega data frame to manipulate
#####################################################################

loganalysis<-omegacal

#Tidy it up by removing unnecessary columns
loganalysis$P_conf<-NULL
loganalysis$P_us<-NULL
loganalysis$P_ds<-NULL
loganalysis$P_diff<-NULL
loganalysis$Templog<-NULL
```

```
#################################################################
#
#STEP 3 Create average fluid pressure for sample (average of us and ds)
#
#################################################################
loganalysis$P_fluid_avg_psi<-(loganalysis$P_us_psi+loganalysis$P_ds_psi)/2
loganalysis$P_fluid_avg_MPa<-(loganalysis$P_us_MPa+loganalysis$P_ds_MPa)/2

#####################
###
###   SAVING DATA
###
#####################

setwd("M:/Experimental/003 Experimental Results/140620 East Brae B2b offset
    experiment")
save(list=ls(), file="EBraeB2boffsetdata_poly2diff.Rdata")
rm(list=ls())
load("EBraeB2boffsetdata_poly2diff.Rdata")

#################################################
#
# STEP 4A Merge pump 1 data into log analysis file
#
#################################################

#Interim step (linear approximation, pull data out)
# This is the 'system flow', doesn't identify which pump is running (not
    necessary)
Pump1_flow<-data.frame(with(iscodataP1, approx(Rdattim, System_Flow, xout=
    loganalysis$Rdattim)))


########################################
#
#   STEP 4B PUMP P1 TEMP DATA
#
########################################

Pumptemp_1A<-data.frame(with(tempdata_P1A, approx(Rdattim, Temperature_C, xout=
    loganalysis$Rdattim)))
Pumptemp_1B<-data.frame(with(tempdata_P1B, approx(Rdattim, Temperature_C, xout=
    loganalysis$Rdattim)))
Pump_temp<-Pumptemp_1A
Pump_temp[,2]<-(Pumptemp_1A[,2]+Pumptemp_1B[,2])/2

# Check data - mostly Pump 1B temp is within 1C of Pump 1A temp, therefore mean
    used to represent the upstream pump temperature.
#
```

```
 c<-Pumptemp_1A-Pumptemp_1B
 c<-na.omit(c)
 max(c[,2])
 min(c[,2])
 mean(c[,2])
 qplot(seq_along(c$y),c$y)#+
   scale_y_continuous(limits=c(-3,2))

 ggplot()+
   geom_point(aes(x=Pumptemp_1A$x,y=Pumptemp_1A$y),col="blue")+
   geom_point(aes(x=Pumptemp_1B$x,y=Pumptemp_1B$y),col="red")#+
#   scale_y_continuous(limits=c(0,7))

#STEP 4C Pump B PRESSURE DATA
Pump2_pressure<-data.frame(with(iscodataP2, approx(Rdattim, System_Pressure, xout
    =loganalysis$Rdattim)))

################################################
# STEP 5 CREATING MERGED DATAFILE
################################################

# Incorporate interpolated data into loganalysis file.
loganalysis$Temp_pump_C<-Pump_temp[,2]
loganalysis$Flow_Pump1<-Pump1_flow[,2]
loganalysis$P_Pump2_psi<-Pump2_pressure[,2]

# Create and additional column to calculate differential pressure from the
# US and DS pressure (particualy for when DP too high for transducer to be used).
#loganalysis$P_diff2_calc_psi<-loganalysis$P_us_psi-loganalysis$P_ds_psi
loganalysis$P_diff2_calc_MPa<-loganalysis$P_us_MPa-loganalysis$P_ds_MPa

# Create moving average field (n=5) in loganalysis for Pdiff (smoothed series)
library("TTR")
loganalysis$P_diff_MPaSMA5<-SMA(loganalysis$P_diff_MPa,n=5)

#   CALCULATE EFFECTIVE STRESS
# In order to analyse mechanical effect on fracture aperture, calculate effective
     stress
# N.B. This is a simplified relationship (effective stress law, Terzaghi, 1936)
loganalysis$P_eff_MPa<-loganalysis$P_conf_MPa-loganalysis$P_fluid_avg_MPa
loganalysis$P_eff2_MPa<-loganalysis$P_conf_MPa-loganalysis$P_ds_MPa

#Calculate rate of change of Pdiff for each point in loganalysis (using moving
    average data)
str(loganalysis)
grad_Pdiff<-diff(loganalysis$P_diff_MPaSMA5,lag=2) # calculates x[3:n]-x[1:(n-3)]
#grad2_Pdiff<-diff(loganalysis$P_diff_psiSMA5,lag=2,differences=2) # 2nd order
grad_Pdiff<-c(NA,grad_Pdiff,NA)
#grad2_Pdiff<-c(NA,NA,grad2_Pdiff,NA,NA)
```

```
loganalysis$grad_Pdiff<-grad_Pdiff
max(grad_Pdiff,na.rm=TRUE)
min(grad_Pdiff,na.rm=TRUE)
summary(abs(grad_Pdiff))

# Check Pdiff comparisons
# uses P_diff_MPa (diff press transducer) for this sample
ggplot(data=loganalysis,aes(x=P_diff_MPa,y=value))+
  geom_point(aes(y=P_diff2_calc_MPa))+
  geom_abline(intercept=0,slope=1)#+
  #geom_point(aes(y=Pdiff_lo),col="red")+
  #geom_point(aes(y=Pdiff_hi),col="blue")#+
  #scale_y_continuous(limits=c(0,1000))

ggplot(data=loganalysis,aes(x=Rdattim,y=value))+
  geom_point(aes(y=(P_diff2_calc_MPa-P_diff_MPa)))#+
  #scale_y_continuous(limits=c(-25,25))

##################################################
#
# STEP 6
#
# CREATE SUMMARY TABLE OF 'EVENTS' WHERE EVENTS REPRESENT FLOW RATE SCENARIOS.
# i.e. new event commences when flow rate changes
#
##################################################

# Search for times when flow rate changes
temp<-diff(loganalysis$Flow_Pump1) #calculates difference between consecutive
    flow rates in time series
loganalysis$Flow_diff <- c(NA, temp) # add to log analysis file - need an NA at
    the start for the first row
# See plot p5
#abs(loganalysis$Flow_diff[45000:45050])

#This identifies which rows the flow rate changes at.
test<-which(abs(loganalysis$Flow_diff)>0.1)
# N.B. Assuming that the flow rate is reduced to <1ml/min in order
# to check DP ZERO value when fluid pressure changes occur, this should
# pick up all actual 'events'.
# However, remember that there will also be some 'non-events'.
#i.e. when fluid pressure is being changed and FR is 1 ml/min.

# Want to get rid of consecutive numbers in test vector
# This means when FR changes between timesteps (5s frequency),
# the latter times are excluded
# (it might take more than one timestep for the FR to fully change)
x<-diff(test)
```

```
x<-c(NA,x) # Add NA onto start of vector
y<-which(x==1)
test2<-test[-c(y)] #This is without the consecutive values
# i.e. only take first of consecutive values

#CREATE SUMMARY TABLE
# Contains only some of the fields from log analysis dataframe
str(loganalysis)
logsummary<-loganalysis[test2,c(1,14,17:30)]

# INCLUDE EVENT ID COLUMN
logsummary$id<-row.names(logsummary) #Create id for each 'event' for reference

# DEFINE EVENT PERIOD
logsummary$start<-logsummary$Rdattim # Create 'event' start time

# Identify end of 'event'
id_end<-c(logsummary$id[2:nrow(logsummary)],NA) #Set as start of following event
id_end<-as.numeric(id_end)-1 # Make sure events don't overlap - use timestep
    prior to FRstart for next event
logsummary$end<-loganalysis$Rdattim[id_end]
logsummary$id_end<-id_end

# N.B. LAST RECORD IN LOG SUMMARY DOESN'T HAVE END TIME
# THEREFORE REMOVE THIS RECORD
logsummary<-logsummary[-c(nrow(logsummary)),]

# Remove short events
temp<-which(logsummary$start+65>logsummary$end) #identify events that are less
    than 65s, and discard
logsummary[temp,] #check
logsummary<-logsummary[-c(temp),]#discard

# Remove events prior to experiment start date/time
temp<-which(logsummary$start<as.POSIXct("2014-06-20 10:38")) #identify events
    that are less than 480s, and discard
logsummary[temp,] #check
logsummary<-logsummary[-c(temp),]#discard

# ******************************************
# Shift event start time to the right until Pdiff gradient is less than set
    threshold

logsummary$start2<-logsummary$start #initial condition
str(logsummary)
t<-as.numeric(logsummary$id)+6 # Set initial start id to be id for 30s (x=6
    timesteps) later than start time
#N.B. Minimum event length previously was 65 seconds, therefore it's now 35 s
```

```
for (i in 1:nrow(logsummary))
{
  while ((abs(loganalysis$grad_Pdiff[t[i]])>0.01)|(mean(abs(
    loganalysis$grad_Pdiff[t[i]:logsummary$id_end[i]]))>0.005) & (t[i]<(
    logsummary$id_end[i]-12)))
      # while is a keyword
    # returns bool (true/false) value
    # C1 = 0.01/10=0.001 MPa/s as grad is difference between Pdiff across 2
    timesteps=10s
    # C2 = 0.005/10=0.0005 MPa/s as grad is difference between Pdiff across 2
    timesteps=10s
  { # opening curly brackets
    # Statements
    t[i]<-t[i]+1
  } # closing curly brackets
  logsummary$start2[i]<-loganalysis$Rdattim[t[i]]
}
logsummary$id_start2<-t


############################################################
#
#  STEP 7 - CALCULATING EVENT MEANS
#
############################################################

# ASSIGN INDICES TO LOGANALYSIS DATAFRAME RECORDS TO ASSIGN TO EVENTS (defined in
     logsummary)
# Line below creates list of what event each date falls into
event.indices = sapply(loganalysis$Rdattim, function(d) which(d>=
    logsummary$start2 & d<= logsummary$end))

# FOR LOGANALYSIS RECORDS NOT WITHIN EVENTS - set indices to NA
event.indices = sapply(event.indices, function(i) ifelse(is.null(i), NA, i)) #
    This applies NA if they don't fall into an event.
loganalysis$event<-event.indices
event_id<-as.integer((logsummary$id_start2+logsummary$id_end)/2)
str(logsummary)
logsummary$event_id<-event_id
logsummary$event<-loganalysis$event[event_id] #so you can see what event numbers
    the logsummary entries are (despite minor overlapping?)
logsummary$event

# Calculate average differential pressures for the revised 'events'
mean_Pdiff<-aggregate(loganalysis$P_diff_MPaSMA5,list(loganalysis$event),mean)
sd_Pdiff<-aggregate(loganalysis$P_diff_MPaSMA5,list(loganalysis$event),sd)
logsummary$mean_Pdiff<-c(mean_Pdiff[,2]) #add to log summary table
logsummary$sd_Pdiff<-c(sd_Pdiff[,2]) #add to log summary table
logsummary$eventtime<-loganalysis$Rdattim[logsummary$event_id]
```

```
# Now do for the whole of the log analysis file
logmeans<-aggregate(loganalysis,list(loganalysis$event),mean)
str(logmeans)
logmeans<-logmeans[,-c(32)] # Removes flow difference column as this is no longer
     relevant
str(loganalysis)

sd_Pdiff_logmeans<-aggregate(loganalysis$P_diff_MPa,list(loganalysis$event),sd)
logmeans$sd_Pdiff_calc<-sd_Pdiff_logmeans[,2]# N.B. This is sd of RAW Pdiff
    values

sd_Pf<-aggregate(loganalysis$P_ds_psi,list(loganalysis$event),sd)
sd_Pc<-aggregate(loganalysis$P_conf_psi,list(loganalysis$event),sd)
logmeans$sd_Pf<-c(sd_Pf[,2]) #add to log summary table
logmeans$sd_Pc<-c(sd_Pc[,2]) #add to log summary table

# Now logmeans is created, this supercedes logsummary, but may want to add
# START and END times to logmeans table
logmeans$start<-logsummary$start2
logmeans$end<-logsummary$end

# Remove events with pump flow <0.6 or >10.5ml/min
temp<-which(logmeans$Flow_Pump1<0.6|logmeans$Flow_Pump1>10.5)
# N.B. None >10.5
logmeans[temp,"Flow_Pump1"]
logmeans<-logmeans[-c(temp),]

sort(sd_Pf[,2])
sort(sd_Pc[,2])
plot(sd_Pc)

# Remove events with sd of Pf > 100 i.e. where Pf is being changed
temp<-which(logmeans$sd_Pf>100)
logmeans[temp,c("sd_Pf","start","end","Flow_Pump1","sd_Pf")]
logmeans<-logmeans[-c(temp),]

# Remove events with Pc changing
plot(logmeans$sd_Pc)
temp<-which(logmeans$sd_Pc>500) #NONE
logmeans<-logmeans[-c(temp),]

#Check event lengths (s)
eventlength<-logmeans$end-logmeans$start
eventlength<-as.numeric(eventlength)
summary(eventlength)

##############################################################################
```

```
#
# STEP 10 - Save the logmeans as a csv file for comparison with
# excel/manual averages
#
################################################################################

setwd("M:/Experimental/003 Experimental Results/140620 East Brae B2b offset
    experiment")
write.csv(logmeans,file="logmeans2_EBraeB2boffset_poly2_diff.csv",row.names=FALSE
    )

# Excel/manual averages have been manually added to the spreadsheet and saved as
    an xls.
# This can be used in the Validyne log calibration file as validation of the fit

################################################################################
#
# STEP 11 - SAVE DATAFILES NOW ANALYSIS COMPLETE
#
################################################################################

#First, remove variables/dataframes no longer required
rm(list= ls()[!(ls() %in% c('loganalysis','logmeans','logsummary'))])

setwd("R:/EXPERIMENTAL DATA/LOGS/140618 EastBrae B2boffset")
save(list=ls(), file="LD2_EBraeB2boffset_ALLDATA_POLY2Mdiff.Rdata")
rm(list=ls())
load("LD2_EBraeB2boffset_ALLDATA_POLY2Mdiff.Rdata")
```

File 6: logmerge_wisseyeventextraction.R

```
######################################################################
#
# 21 August 2014
# WISSEY DATA PROCESSING
# THIS INCORPORATES ADDITIONAL EVENT DURATION CORRECTIONS WITHIN SECOND
# PART TO ACCOUNT FOR PUMP LOG TIMING ERRORS AS WELL AS DIFFERENTIAL
# PRESSURE RESPONSE
#
######################################################################

############## FOR PLOTTING #################
library (ggplot2) # Needed for plotting
library (grid) # Needed for customising plot area
library (scales) # Needed for editing log tickmarks
theme_set(theme_bw())
#############################################

####################################
# LOADING DATA
####################################
rm(list=ls())
setwd("R:/EXPERIMENTAL DATA/LOGS/140702 Wiss3")
omegacal<-read.csv(file="omegacal_POLY2M_Wissey3_aug14.csv")
#omegacal<-read.csv(file="omegacal_LM_Wissey3_aug14.csv")
iscodataP1<-read.csv(file="iscodataP1_Wissey3_aug14.csv")
iscodataP2<-read.csv(file="iscodataP2_Wissey3_aug14.csv")
tempdata_P1A<-read.csv(file="tempdata_P1A_Wissey3_aug14.csv")
tempdata_P1B<-read.csv(file="tempdata_P1B_Wissey3_aug14.csv")

# Need to set Rdattim class correctly otherwise searches and subsets won't work
    correctly
omegacal$Rdattim <- as.POSIXct(omegacal$Rdattim)
iscodataP1$Rdattim <- as.POSIXct(iscodataP1$Rdattim)
iscodataP2$Rdattim <- as.POSIXct(iscodataP2$Rdattim)
tempdata_P1A$Rdattim <- as.POSIXct(tempdata_P1A$Rdattim)
tempdata_P1B$Rdattim <- as.POSIXct(tempdata_P1B$Rdattim)

#####################################################################
# Create duplicate of omega data frame to manipulate
#####################################################################

loganalysis<-omegacal

#Tidy it up by removing unnecessary columns
loganalysis$P_conf<-NULL
loganalysis$P_us<-NULL
loganalysis$P_ds<-NULL
loganalysis$P_diff<-NULL
```

```
loganalysis$Templog<-NULL

#####################################################################
# Create average fluid pressure for sample (average of us and ds)
#####################################################################
loganalysis$P_fluid_avg_psi<-(loganalysis$P_us_psi+loganalysis$P_ds_psi)/2
loganalysis$P_fluid_avg_MPa<-(loganalysis$P_us_MPa+loganalysis$P_ds_MPa)/2

#####################
#SAVE INTERIM DATA

setwd("R:/EXPERIMENTAL DATA/LOGS/140702 Wiss3")
#save(list=ls(), file="Wissey3data_poly2diff.Rdata")
rm(list=ls())
load("Wissey3data_poly2diff.Rdata")
# THE ABOVE FILE CONTAINS THE 5 LOG DATASETS (UNITS CONVERTED ALREADY)
# AND THE LOGANALYSIS STARTING FILE WHICH CONSISTS OF OMEGA LOG DATA ONLY
# STEPS 1 - 3 (COMPARING TO GENERAL LOGMERGE_EVENTEXTRACTION FILE ARE
# ALREADY COMPLETE)

#################################################
#
# Merge pump 1 data into log analysis file
#
#################################################

#Interim step (linear approximation, pull data out)
# This is the 'system flow', doesn't identify which pump is running (not
    necessary)
Pump1_flow<-data.frame(with(iscodataP1, approx(Rdattim, System_Flow, xout=
    loganalysis$Rdattim)))
Pump1_pressure<-data.frame(with(iscodataP1, approx(Rdattim, System_Pressure, xout
    =loganalysis$Rdattim)))

########################################
#
#   MERGE PUMP P1 TEMP DATA
#
########################################

# ************************************************************
# Note that the temp logging for 1A was faulty during 28-29 July
# The 1A and 1B temperatures are within 1C for the remainder of the period.
# The temperature for 1B is therefore used as a representative temperature
# for the whole of the experimental period (2 Jul - 5 Aug)
# ************************************************************

#Pump_temp<-data.frame(with(tempdata_P1B, approx(Rdattim, Temperature_C, xout=
    loganalysis$Rdattim)))
```

```
#If 1A wasn't faulty woudl calculate both,then average

Pumptemp_1A<-data.frame(with(tempdata_P1A, approx(Rdattim, Temperature_C, xout=
    loganalysis$Rdattim)))
Pumptemp_1B<-data.frame(with(tempdata_P1B, approx(Rdattim, Temperature_C, xout=
    loganalysis$Rdattim)))
Pump_temp<-Pumptemp_1B #1A drops out on one occasion (28 july) within the
    experiment, otherwise they're within 1C of each other
#Pump_temp[,2]<-(Pumptemp_1A[,2]+Pumptemp_1B[,2])/2 # Errors in 1A on 28-29 Jul

# Check data - mostly Pump 1B temp is within 1C of Pump 1A temp.
#
 c<-Pumptemp_1A-Pumptemp_1B
 c<-na.omit(c)
 max(c[,2])
 min(c[,2])
 mean(c[,2])
 qplot(seq_along(c$y),c$y)+
   scale_y_continuous(limits=c(-2,2))

 ggplot()+
   geom_point(aes(x=Pumptemp_1A$x,y=Pumptemp_1A$y),col="blue")+
   geom_point(aes(x=Pumptemp_1B$x,y=Pumptemp_1B$y),col="red")#+
#    scale_y_continuous(limits=c(0,7))

####################################################
#
# MERGE Pump B PRESSURE DATA
#
####################################################
Pump2_pressure<-data.frame(with(iscodataP2, approx(Rdattim, System_Pressure, xout
    =loganalysis$Rdattim)))


################################################
# CREATING MERGED DATAFILE
################################################

# Incorporate interpolated data into loganalysis file.
loganalysis$Temp_pump_C<-Pump_temp[,2]
loganalysis$Flow_Pump1<-Pump1_flow[,2]
loganalysis$P_Pump1_psi<-Pump1_pressure[,2]
loganalysis$P_Pump2_psi<-Pump2_pressure[,2]
#loganalysis$Pump2B_Problem<-Pump2B_problem[,2]

# Create and additional column to calculate differential pressure from the
# US and DS pressure (particualy for when DP too high for transducer to be used).
loganalysis$P_diff2_calc_psi<-loganalysis$P_us_psi-loganalysis$P_ds_psi
```

```
loganalysis$P_diff2_calc_MPa<-loganalysis$P_us_MPa-loganalysis$P_ds_MPa

ggplot(data=loganalysis,aes(x=P_diff_psi,y=value))+
  geom_point(aes(y=P_diff2_calc_psi))+
  geom_point(aes(y=Pdiff_lo),col="red")+
  geom_point(aes(y=Pdiff_hi),col="blue")+
  #scale_y_continuous(limits=c(600,800))
  scale_y_continuous(limits=c(0,1000))

ggplot(data=loganalysis,aes(x=Rdattim,y=value))+
  geom_point(aes(y=(P_diff2_calc_psi-P_diff_psi)))#+
  #scale_y_continuous(limits=c(-50,50))

ggplot(data=loganalysis,aes(x=Rdattim,y=P_us_psi))+
  geom_point()

#####################################################
# Create moving average field (n=5) in loganalysis for Pdiff
# (for use in automated event extraction procedure)
#####################################################

library("TTR")
loganalysis$P_diff_psiSMA5<-SMA(loganalysis$P_diff_psi,n=5)

#####################################################
#   CALCULATE EFFECTIVE STRESS
#####################################################

# In order to analyse mechanical effect on fracture aperture, calculate effective
     stress
# N.B. This is a simplified relationship (effective stress law, Terzaghi, 1936)

loganalysis$P_eff_psi<-loganalysis$P_conf_psi-loganalysis$P_fluid_avg_psi
loganalysis$P_eff2_psi<-loganalysis$P_conf_psi-loganalysis$P_ds_psi
loganalysis$P_eff_MPa <- loganalysis$P_eff_psi*0.00689475729
loganalysis$P_eff2_MPa <- loganalysis$P_eff2_psi*0.00689475729


# ggplot(data=loganalysis,aes(x=Rdattim,y=P_eff_psi))+
#   geom_point()


#####################################################
#
# PART 2: EVENT DATA EXTRACTION
#
#####################################################
#
# CREATE SUMMARY TABLE OF 'EVENTS' WHERE EVENTS REPRESENT FLOW RATE SCENARIOS.
```

```
# i.e. new event commences when flow rate changes
#
################################################
################################################
# STEP 1
# Search for times when flow rate changes
################################################

temp<-diff(loganalysis$Flow_Pump1) #calculates difference between consecutive
    flow rates in time series
loganalysis$Flow_diff <- c(NA, temp) # add to log analysis file - need an NA at
    the start for the first row
# See plot p5
#abs(loganalysis$Flow_diff[45000:45050])

#This identifies which rows the flow rate changes at.
test<-which(abs(loganalysis$Flow_diff)>0.1)
#test<-which(loganalysis$Flow_diff>0.1|loganalysis$Flow_diff<(-0.1))
# N.B. Assuming that the flow rate is reduced to <1ml/min in order
# to check DP ZERO value when fluid pressure changes occur, this should
# pick up all actual 'events'.
# However, remember that there will also be some 'non-events'.
#i.e. when fluid pressure is being changed and FR is 1 ml/min.

# Want to get rid of consecutive numbers in test vector
# This means when FR changes between timesteps (5s frequency),
# the latter times are excluded
# (it might take more than one timestep for the FR to fully change)
x<-diff(test)
x<-c(NA,x) # Add NA onto start of vector
y<-which(x==1)
test2<-test[-c(y)] #This is without the consecutive values
# i.e. only take first of consecutive values

#CREATE SUMMARY TABLE
str(loganalysis)
# Contains only some of the fields from log analysis dataframe
logsummary<-loganalysis[test2,c(1,2,5,8,11,14,21,23:26,34)] # N.B. This would
    miss the first FR row - not required
str(logsummary)

# INCLUDE EVENT ID COLUMN
logsummary$id<-test2 #Create id for each 'event' for reference - links to
    loganalysis file row number

# DEFINE EVENT PERIOD

# FR start time - Identify when log data suggests FR is changed
logsummary$FRstart<-logsummary$Rdattim
```

```
# Identify end of 'FR event' BEFORE ANY INTERMEDIATE EVENT REMOVAL
FRendrows<-c(logsummary$id[2:nrow(logsummary)],NA) #Set as start of following
    event
FRendrows<-FRendrows-1 # Make sure events don't overlap - use timestep prior to
    FRstart for next event
logsummary$FRend<-loganalysis$Rdattim[FRendrows]
logsummary$id_endFR<-FRendrows

# N.B. LAST RECORD IN LOG SUMMARY DOESN'T HAVE END TIME
# THEREFORE REMOVE THIS RECORD
logsummary<-logsummary[-c(nrow(logsummary)),]

#####################################################
# STEP 2
# REMOVE SHORT EVENTS (<60 s) #20 events
#####################################################

temp<-which((logsummary$FRstart+60)>logsummary$FRend) #identify
logsummary[temp,] #check
logsummary<-logsummary[-c(temp),] #discard

###########################################################
#
#  STEP 3 - CALCULATING INITIAL EVENT STATISTICS
#
###########################################################

# ASSIGN INDICES TO LOGANALYSIS DATAFRAME RECORDS TO ASSIGN TO EVENTS (defined in
     logsummary)
# Use FR event start and end dates for assigning events

# Line below creates list of what event each date falls into
event.indices = sapply(loganalysis$Rdattim, function(d) which(d>=
    logsummary$FRstart & d<= logsummary$FRend))

# FOR LOGANALYSIS RECORDS NOT WITHIN EVENTS - set indices to NA
event.indices = sapply(event.indices, function(i) ifelse(is.null(i), NA, i)) #
    This applies NA if they don't fall into an event.
loganalysis$event<-event.indices
#loganalysis[4200:4900,c("event","Rdattim","Flow_Pump1")]
logsummary$event<-loganalysis$event[c(logsummary$id)] #so you can see what event
    numbers the logsummary entries are
logsummary$event

# Calculate average flow rates for the 'events'
mean_FR<-aggregate(loganalysis$Flow_Pump1,list(loganalysis$event),mean)
sd_Pf<-aggregate(loganalysis$P_ds_psi,list(loganalysis$event),sd)
sd_Pc<-aggregate(loganalysis$P_conf_psi,list(loganalysis$event),sd)
```

```
logsummary$mean_FR<-c(mean_FR[,2]) #add to log summary table
logsummary$sd_Pf<-c(sd_Pf[,2]) #add to log summary table
logsummary$sd_Pc<-c(sd_Pc[,2]) #add to log summary table

# Calculate average Pdiff and sd_Pdiff for the 'events'
mean_Pdiff<-aggregate(loganalysis$P_diff_psiSMA5,list(loganalysis$event),mean)
sd_Pdiff<-aggregate(loganalysis$P_diff_psiSMA5,list(loganalysis$event),sd)
logsummary$mean_Pdiff<-c(mean_Pdiff[,2]) #add to log summary table
logsummary$sd_Pdiff<-c(sd_Pdiff[,2]) #add to log summary table


sort(sd_Pf[,2])
sort(sd_Pc[,2])
plot(sd_Pc)
plot(mean_FR)
sort(mean_FR[,2])

##################################################
# STEP 4 REMOVE NON-STATIONARY EVENTS
##################################################

# Remove events with us pump FR <0.5 or >10.5ml/min
temp<-which(logsummary$mean_FR<0.5|logsummary$mean_FR>10.5)
logsummary<-logsummary[-c(temp),]

# Remove events with sd of Pf > 100 i.e. where Pf is being changed
temp<-which(logsummary$sd_Pf>100)
logsummary[temp,c("sd_Pf","start")]
logsummary<-logsummary[-c(temp),]

# Remove events with Pc changing
plot(logsummary$sd_Pc)
temp<-which(logsummary$sd_Pc>500)
logsummary<-logsummary[-c(temp),]


#####################################################################
# SAVE DATA FOR RECOVERY LATER IF REQUIRED
#####################################################################

setwd("R:/EXPERIMENTAL DATA/LOGS/140702 Wiss3")
save(list=ls(), file="LD5midwork_Wissey3_POLY2Mdiff.Rdata")
rm(list=ls())
load("LD5midwork_Wissey3_POLY2Mdiff.Rdata")

str(loganalysis)

##################################################
# Calculate gradient for each point in loganalysis (could have been done earlier)
```

```
grad_Pdiff<-diff(loganalysis$P_diff_psiSMA5,lag=2) # calculates x[3:n]-x[1:(n-3)]
grad_Pdiff<-c(NA,grad_Pdiff,NA)

loganalysis$grad_Pdiff<-grad_Pdiff
max(grad_Pdiff,na.rm=TRUE)
min(grad_Pdiff,na.rm=TRUE)
summary(abs(grad_Pdiff))
plot(grad_Pdiff[1900:1930])

#####################################################
#
# STEP 5 DEFINE REVISED EVENT DURATIONS
#
#####################################################

#####################################################
# STEP 5A
#####################################################
# Set start time to be when Pdiff is within 1 sd of mean (using FR range)
str(logsummary)
logsummary$id_start<-logsummary$id # initial condition
logsummary$start<-logsummary$FRstart # initial condition
#logsummary$Pdiff_end<-loganalysis$P_diff_psi[logsummary$id_end] # initial
    condition
logsummary$id_end<-logsummary$id_endFR # initial condition
logsummary$end<-logsummary$FRend # initial condition
# logsummary$id_start<-as.integer(logsummary$id_start)
# logsummary$id_end<-as.integer(logsummary$id_end)
t<-logsummary$id_start
for (i in 1:nrow(logsummary))
{
  #i=67
  loganalysis$P_diff_psiSMA5[t[i]]
  #Statements to execute the loop sqr number of times
  while (abs(loganalysis$P_diff_psiSMA5[t[i]]-logsummary$mean_Pdiff[i])>
    logsummary$sd_Pdiff[i] & logsummary$id_start[i]<(logsummary$id_end[i]-6)) #
    while is a keyword
    # returns bool (true/false) value
  { # opening curly brackets
    # Statements
    logsummary$id_start[i]<-logsummary$id_start[i]+1 #Defines start as next
    timestep in loganalysis file
    logsummary$start[i]<-loganalysis$Rdattim[logsummary$id_start[i]]
    t[i]<-logsummary$id_start[i]
  } # closing curly brackets
}
logsummary$s_shift<-logsummary$id_start-logsummary$id
summary(logsummary$s_shift)
sort(logsummary$s_shift)
```

```
#####################################################
# STEP 5B
#####################################################
# Calculate 'new' event start time based on finding max gradient within
# +-50 sec from step 1 start time

logsummary$start2<-logsummary$start #initial condition
logsummary$id_start2<-logsummary$id_start # initial condition
for (i in 1:nrow(logsummary))
{
#i=78
a<-logsummary$id_start[i]-10 #N.B. Much better results using 10 than 6
b<-logsummary$id_start[i]+10
#abs(loganalysis$grad_Pdiff[a:b])
#plot(abs(loganalysis$grad_Pdiff[a:b]))
#
# logsummary$Rdattim[i]
# loganalysis$Rdattim[a]
# loganalysis$Rdattim[b]

#max(abs(loganalysis$grad_Pdiff[a:b]))
x<-which(abs(loganalysis$grad_Pdiff[a:b])==max(abs(loganalysis$grad_Pdiff[a:b]),
    na.rm=TRUE))
if (length(x)>1) {x<-x[length(x)]}
idstart<-logsummary$id_start[i]+x-11
if (idstart<(logsummary$id_end[i]-5))
{
logsummary[i,"id_start2"]<-idstart
logsummary[i,"start2"]<-loganalysis[idstart,"Rdattim"]
}
}

#logsummary[,c("id","id_start","id_start2","id_endFR","id_end")]
eventlength<-logsummary$id_endFR-logsummary$id_start2
summary(eventlength)
logsummary$s_shift<-logsummary$id_start2-logsummary$id

#####################################################
# STEP 5C
#####################################################

# Shift end as well (don't worry about conditions)
t<-logsummary$id_endFR+logsummary$s_shift
for (i in 1:nrow(logsummary)) #N.B. Can remove loop if no conditions -
    unnecessary
{
```

```
  #if (abs(loganalysis$P_diff_psiSMA5[t[i]]-logsummary$mean_Pdiff[i])<
    logsummary$sd_Pdiff[i])
  #{
    logsummary$id_end[i]<-t[i]
    logsummary$end[i]<-loganalysis$Rdattim[logsummary$id_end[i]]

  #}
}

#####################################################
# STEP 5D
#####################################################
# Shift start2 to the right until gradient is less than set threshold

# IDEA: Could consider adding condition that loganalysis$P_diff_psiSMA5[id_start3
    +idend/2]-mean<1.5*sd?

logsummary$start3<-logsummary$start2 #initial condition
logsummary$id_start3<-logsummary$id_start2 # initial condition
t<-logsummary$id_start3

#
t2<-logsummary$id_end
t3<-as.integer((t+t2)/2)
x1<-abs(loganalysis$P_diff_psiSMA5[t]-logsummary$mean_Pdiff)
x2<-abs(loganalysis$P_diff_psiSMA5[t2]-logsummary$mean_Pdiff)
x3<-abs(loganalysis$P_diff_psiSMA5[t3]-logsummary$mean_Pdiff)
sd<-logsummary$sd_Pdiff

summary(abs(x1)/sd)
summary(abs(x2)/sd)
summary(abs(x3)/sd)
test<-abs(x3)/sd
sort(test)
#& (abs(loganalysis$P_diff_psiSMA5[t3[i]]-logsummary$mean_Pdiff)<(2*
    logsummary$sd_Pdiff))

for (i in 1:nrow(logsummary))
{
  while ((abs(loganalysis$grad_Pdiff[t[i]])>3) & (logsummary$id_start3[i]<(
    logsummary$id_end[i]-5)) && (abs(loganalysis$P_diff_psiSMA5[t3[i]]-
    logsummary$mean_Pdiff[i])<(2*logsummary$sd_Pdiff[i])))
    # while is a keyword
    # returns bool (true/false) value
  { # opening curly brackets
    # Statements
    logsummary$id_start3[i]<-logsummary$id_start3[i]+1 #Defines start as next
    timestep in loganalysis file
    t[i]<-logsummary$id_start3[i]
```

```
    logsummary$start3[i]<-loganalysis$Rdattim[logsummary$id_start3[i]]
    t3[i]<-as.integer((t[i]+t2[i])/2)
  } # closing curly brackets
}

#Check for overlapping events
id_start2<-c(logsummary$id_start3[2:nrow(logsummary)],NA)
overlapcheck<-id_start2-logsummary$id_end
summary(overlapcheck)
test<-which(overlapcheck<0)
overlapcheck[test]

#Check event lengths
eventlength<-logsummary$end-logsummary$start3
eventlength<-as.numeric(eventlength)
summary(eventlength)

#####################################################
# STEP 5E
#####################################################

# Improve end time based on gradient and difference from mean
logsummary$end2<-logsummary$end #initial condition
logsummary$id_end2<-logsummary$id_end # initial condition
t<-logsummary$id_end2
for (i in 1:nrow(logsummary))
{
  while (((abs(loganalysis$grad_Pdiff[t[i]])>3)|(abs(loganalysis$P_diff_psiSMA5[t
    [i]]-logsummary$mean_Pdiff[i])>(2*logsummary$sd_Pdiff[i]))) & (
    logsummary$id_start3[i]<(logsummary$id_end2[i]-5)))  # while is a keyword
    # returns bool (true/false) value
  { # opening curly brackets
    # Statements
    logsummary$id_end2[i]<-logsummary$id_end2[i]-1 #Defines start as next
    timestep in loganalysis file
    t[i]<-logsummary$id_end2[i]
    logsummary$end2[i]<-loganalysis$Rdattim[logsummary$id_end2[i]]
  } # closing curly brackets
}



#####################################################
#
# STEP 6
#
#####################################################

# Review overlapping and negative length events and delete as appropriate
```

```
##################################################

# Event length and negative events
eventlength<-logsummary$end2-logsummary$start3
eventlength<-as.numeric(eventlength/60)
eventlength # event length in minutes
summary(eventlength)
logsummary$eventlength<-eventlength

test1<-which(eventlength<0) # NONE (28/08)
logsummary[test1,c("start3","end2","eventlength","event","FRstart","FRend")]

# Remove negative events
# *** IMPORTANT OTHERWISE RECALCULATION OF MEAN WON'T WORK
logsummary<-logsummary[-c(test1),]

#N.B. 2 events, 11/7 14:29 & 22/7 9:49 (for earlier versions, not this version)

#########################################################################

#Check for overlapping events
id_start2<-c(logsummary$id_start3[2:nrow(logsummary)],NA)
overlapcheck<-id_start2-logsummary$id_end2
summary(overlapcheck)
test2<-which(overlapcheck<(-3))
overlapcheck[test2]
logsummary[c(test2,(test2+1)),c("start3","event")]
logsummary[c(test2,(test2+1)),]

str(logsummary)
# Three with >15s overlap: event 173, 418 and 500:
# 4/7 12:22 (173) - requires manual shifting of end2 due to high sd value
# 11/7 10:10 (418) - due to accidental FR change mid-event - therefore 2 events
    overlap but same FR
# 11/7 14:23 (500) - Remove - the FR=5 event has been incorrectly shifted to the
    right to FR=10 event
# FR=5 event was too short.

# 11/7 14:23 event (500)
# Remove this event and the one it overlaps with (EDIT: 28 Aug REMOVED FOLLOWING
    EVENT TOO)
logsummary<-logsummary[-c(test2[3],(test2[3]+1)),]

# 4/7 12:22 event (173)
logsummary[test2[1],c("id_end2","end2")]
logsummary$id_end2[test2[1]]<-logsummary$id_end2[test2[1]]-15 # Manually shift
    first one
logsummary$end2[test2[1]]<-loganalysis$Rdattim[logsummary$id_end2[test2[1]]]
```

```
# All other overlapping events
id_start2<-c(logsummary$id_start3[2:nrow(logsummary)],NA)
overlapcheck<-id_start2-logsummary$id_end2

overlap<-which(overlapcheck<1)
overlapcheck[overlap]
logsummary$id_end2[overlap]
# Change start id and time to reflect how event.indices treats overlaps
x<-logsummary$id_start3[overlap+1]-(overlapcheck[overlap]-1)
logsummary$id_start3[overlap+1]
x
logsummary$id_start3[overlap+1]<-x
logsummary$start3[overlap+1]<-loganalysis$Rdattim[x]
logsummary$end2[overlap]
logsummary$start3[overlap+1]

#####################################################
# OTHER EVENTS - MANUAL REMOVAL
#
# Due to notes made in labbook and short event time,
# the Pds=10MPa results of 11/7 14:27 onwards have been removed:

logsummary[448:450,c("start3","mean_FR","mean_Pdiff","P_ds_psi")]
# Above should be 3 events as defined above
logsummary<-logsummary[-c(448:450),] #REMOVE

#####################################################
#
# STEP 7
#
#####################################################

# Recalculate mean and sd for Pdiff based on start3 and end2

# ASSIGN INDICES TO LOGANALYSIS DATAFRAME RECORDS TO ASSIGN TO EVENTS (defined in
     logsummary)
# Line below creates list of what event each date falls into
event.indices = sapply(loganalysis$Rdattim, function(d) which(d>=
    logsummary$start3 & d<= logsummary$end2))

# FOR LOGANALYSIS RECORDS NOT WITHIN EVENTS - set indices to NA
event.indices = sapply(event.indices, function(i) ifelse(is.null(i), NA, i)) #
    This applies NA if they don't fall into an event.
loganalysis$event2<-event.indices
#loganalysis[4200:4900,c("event","Rdattim","Flow_Pump1")]
event_id<-as.integer((logsummary$id_start3+logsummary$id_end2)/2)
str(logsummary)
logsummary$event2_id<-event_id
```

```
logsummary$event2<-loganalysis$event2[event_id] #so you can see what event
    numbers the logsummary entries are (despite minor overlapping?)
logsummary$event2

# Calculate average differential pressures for the revised 'events'
#mean_Pdiff2<-aggregate(loganalysis$P_diff_psiSMA5,list(loganalysis$event2),mean)
#sd_Pdiff2<-aggregate(loganalysis$P_diff_psiSMA5,list(loganalysis$event2),sd)
mean_Pdiff2<-aggregate(loganalysis$P_diff_MPa,list(loganalysis$event2),mean)
sd_Pdiff2<-aggregate(loganalysis$P_diff_MPa,list(loganalysis$event2),sd)
logsummary$mean_Pdiff2<-c(mean_Pdiff2[,2]) #add to log summary table
logsummary$sd_Pdiff2<-c(sd_Pdiff2[,2]) #add to log summary table
logsummary$eventtime<-loganalysis$Rdattim[logsummary$event2_id]

#########################################################
#
# Save DATA FOR PICKING UP LATER IF REQUIRED
setwd("R:/EXPERIMENTAL DATA/LOGS/140702 Wiss3")
save(list=ls(), file="LD5step7work3_Wissey3_POLY2Mdiff.Rdata") #28 Aug - edited
    work to work2
rm(list=ls())
load("LD5step7work3_Wissey3_POLY2Mdiff.Rdata")

# Now calculate means for the whole of the log analysis file
# THUS logmeans table contains means of all loganalysis fields for all events.
logmeans<-aggregate(loganalysis,list(loganalysis$event2),mean)
str(logmeans)
logmeans<-logmeans[,-c(35,36)] # Removes flow difference and first event column
    as these are no longer relevant
str(logmeans)
sd_Pdiff_logmeans<-aggregate(loganalysis$P_diff_psi,list(loganalysis$event2),sd)
logmeans$sd_Pdiff<-sd_Pdiff_logmeans[,2]# N.B. This is sd of RAW Pdiff values
# Now logmeans is created, this supercedes logsummary, but may want to add
# START and END times to logmeans table
logmeans$start<-logsummary$start3
logmeans$end<-logsummary$end2

logmeans$mean_FR_Pump1<-logsummary$mean_FR
str(logmeans)
#rm(logsummary)

#########################################################################
#
# SAVE DATAFILES NOW ANALYSIS COMPLETE
#
#########################################################################

#First, remove variables/dataframes no longer required
rm(list= ls()[!(ls() %in% c('loganalysis','logmeans','logsummary','omegacal','
    iscodataP1','iscodataP2','tempdata_P1A','tempdata_P1B'))])
```

```
setwd("R:/EXPERIMENTAL DATA/LOGS/140702 Wiss3")
save(list=ls(), file="LD5final3_25Apr_Wissey3_POLY2Mdiff.Rdata") #Edited final to
     final2 28 Aug
rm(list=ls())
load("LD5final3_25Apr_Wissey3_POLY2Mdiff.Rdata")
```

File 7: log_wissey_extract_Pc_events.R

```
#####################################################
# LOAD DATAFILES
#####################################################

setwd("R:/EXPERIMENTAL DATA/LOGS/140702 Wiss3")
rm(list=ls())
load("LD5final2_21Aug_Wissey3_POLY2Mdiff.Rdata")
load("logmeans_processed_140910.Rdata")
rm(iscodataP1,iscodataP2,logsummary,omegacal,tempdata_P1A,tempdata_P1B)

############## FOR PLOTTING #################
library (ggplot2) # Needed for plotting
library (grid) # Needed for customising plot area
library (scales) # Needed for editing log tickmarks
theme_set(theme_bw())
mytheme<-theme_bw()+
  theme (
    plot.title = element_text (vjust = 2, size = 20, face="italic"), # plot title
     attrib.
    plot.margin = unit (c(2, 2, 2, 2), "lines"), # plot margins
    legend.background = element_rect (colour="black",fill = "white"), #
    background colour
    legend.justification=c(0, 0), # lock point for legend
    legend.position="none",
    #legend.position = c(0.03, 0.6), # put the legend INSIDE the plot area
    legend.key = element_blank (), # switch off the rectangle around symbols in
    the legend
    legend.title = element_blank (), # switch off the legend title
    legend.text = element_text (size = 12), # sets the attributes of the legend
    text
    axis.title.x = element_text (vjust = 0, size = 15), # change the axis title
    axis.title.y = element_text (vjust = 0, angle = 90, size = 15), # change the
    axis title
    axis.text.x = element_text (size = 15, vjust = -0.25, colour = "black"),#
    change the axis label font attributes
    axis.text.y = element_text (size = 15, hjust = 1, colour = "black"), # change
     the axis label font attributes
    axis.ticks.length = unit(-0.25 , "cm"), # -ve length = inside ticks
    axis.ticks.margin = unit(0.5, "cm") # margin between the ticks and the text
  )

mytheme2<-theme_bw()+
  theme (
    plot.title = element_text (vjust = 2, size = 20, face="italic"), # plot title
     attrib.
    plot.margin = unit (c(2, 2, 2, 2), "lines"), # plot margins
    legend.background = element_rect (colour="black",fill = "white"), #
    background colour
```

```
    legend.justification=c(0, 0), # lock point for legend
    #legend.position="none",
    legend.position = c(0.05, 0.6), # put the legend INSIDE the plot area
    legend.key = element_blank (), # switch off the rectangle around symbols in
    the legend
    legend.title = element_blank (), # switch off the legend title
    legend.text = element_text (size = 12), # sets the attributes of the legend
    text
    axis.title.x = element_text (vjust = 0, size = 15), # change the axis title
    axis.title.y = element_text (vjust = 0, angle = 90, size = 15), # change the
    axis title
    axis.text.x = element_text (size = 15, vjust = -0.25, colour = "black"),#
    change the axis label font attributes
    axis.text.y = element_text (size = 15, hjust = 1, colour = "black"), # change
     the axis label font attributes
    axis.ticks.length = unit(-0.25 , "cm"), # -ve length = inside ticks
    axis.ticks.margin = unit(0.5, "cm"), # margin between the ticks and the text
    panel.border = element_rect (colour="black",fill = NA) # background colour
  )
theme_set(mytheme2)

###### DEFINE THE MULTIPLOT FUNCTION #############
# From http://www.cookbook-r.com/Graphs/Multiple_graphs_on_one_page_(ggplot2)/

setwd("M:/Experimental/R")
source("multiplot.R") #Providing you're in the right working directory, this will
     run the
# multiplot script file which contains the multiplot function only


#####################################################
#
# STEP 1 - Subset data from loganalysis file to review only C2, D and E time
    period.
#
#####################################################

loganalysis_sub<-subset(loganalysis,Rdattim>as.numeric(as.POSIXct("2014-08-02
    12:39")))

# C2
xlimC2<-as.POSIXct(c("2014-08-02 12:39", "2014-08-2 15:00"))
# D
xlimD<-as.POSIXct(c("2014-08-4 08:57", "2014-08-4 12:30"))
# E
xlimE<-as.POSIXct(c("2014-08-5 09:02", "2014-08-5 11:32"))

ggplot(data=loganalysis_sub,aes(x=Rdattim,y=value))+
  geom_point(aes(y=P_conf_MPa))+
```

```
  geom_point(aes(y=Flow_Pump1*5),color="blue")+
  geom_point(aes(y=Templog_C),color="red")+
  geom_point(aes(y=P_diff_psiSMA5*0.2),color="green")+
  geom_point(aes(y=P_diff_psi*0.2),color="dark green")+
  geom_point(aes(y=P_ds_MPa),color="orange")+
  geom_point(aes(y=P_us_MPa),color="pink")+
  #geom_point(aes(y=abs(grad_Pc)*3),color="purple")+
  scale_x_datetime(limits=xlimC2)

#####################################################
#
# STEP 2a - Remove times where FR is not 5ml/min (or thereabouts).
#
#####################################################

temp<-(which(loganalysis_sub$Flow_Pump1<4.7 | loganalysis_sub$Flow_Pump1>5.3))
loganalysis_sub<-loganalysis_sub[-c(temp),]

#is.na(loganalysis_sub$Flow_Pump1)
temp<-(which(is.na(loganalysis_sub$Flow_Pump1)==TRUE))
loganalysis_sub<-loganalysis_sub[-c(temp),]

max(loganalysis_sub$Flow_Pump1)
min(loganalysis_sub$Flow_Pump1)

#####################################################
#
# STEP 2b - Remove Pc data where gradient is > threshold
#
#####################################################

# Calculate confining pressure gradient
grad_Pc<-diff(loganalysis_sub$P_conf_MPa,lag=2) # calculates x[3:n]-x[1:(n-3)]
grad_Pc<-c(NA,grad_Pc,NA)
loganalysis_sub$grad_Pc<-grad_Pc

# ggplot(data=loganalysis_sub,aes(x=Rdattim,y=value))+
#  geom_point(aes(y=abs(grad_Pc)),color="purple")+
#   scale_x_datetime(limits=xlimE)+
#   scale_y_continuous(limits=c(0,0.5))

temp<-(which(abs(loganalysis_sub$grad_Pc)>0.1))
loganalysis_sub<-loganalysis_sub[-c(temp),]

#####################################################
#
# STEP 3 - DEFINE PC EVENTS WITHIN DATASET
#
#####################################################
```

```
# Search for times when confining pressure changes
temp<-diff(loganalysis_sub$P_conf_MPa) #calculates difference between consecutive
     Pc in time series
loganalysis_sub$Pc_diff <- c(NA, temp) # add to log analysis file - need an NA at
     the start for the first row

# Search for times where there is a large time gap i.e. overnight between
    experiments
temp<-diff(as.numeric(loganalysis_sub$Rdattim)) #calculates difference between
    consecutive Pc in time series
loganalysis_sub$t_diff <- c(NA, temp) # add to log analysis file - need an NA at
    the start for the first row

#This identifies which rows the Pc changes at and also overnight gaps.
test<-which(abs(loganalysis_sub$Pc_diff)>2 | loganalysis_sub$t_diff>100)

# Add first PC event - first row
test<-c(1,test)
# Check steps between events
x<-diff(test)
x<-c(NA,x) # Add NA onto start of vector
y<-which(x==1) #One entry (7)
#test2<-test[-c(y)] #This is without the consecutive values
# i.e. only take first of consecutive values

#FIND DATE_TIMES
str(loganalysis_sub)
check<-loganalysis_sub[test,c("Rdattim","P_conf_MPa","Pc_diff")]
check<-cbind(check,x)
check

####################################################
# CREATE PC SUMMARY TABLE WITH PC EVENT MEANS
####################################################

# Contains only some of the fields from log analysis dataframe
ExptCDEsummary<-loganalysis_sub[test,c("Rdattim","Templog_C","P_conf_MPa","
    P_diff_MPa")]
str(ExptCDEsummary)
ExptCDEsummary


# INCLUDE EVENT ID COLUMN
ExptCDEsummary$id<-test #Create id for each 'event' for reference - links to
    loganalysis file row number

####################################################
#
```

```
# STEP 5: DEFINE EVENT PERIOD (but done before STEP 4)
#
#####################################################

# Pc event start time - set as 60s after Pc change
ExptCDEsummary$start<-ExptCDEsummary$Rdattim+90

# Identify end of 'FR event' BEFORE ANY INTERMEDIATE EVENT REMOVAL
PCendrows<-c(ExptCDEsummary$id[2:nrow(ExptCDEsummary)],NA) #Set as start of
    following event
PCendrows<-PCendrows-6 # Make sure events don't overlap - use timestep prior to
    FRstart for next event
ExptCDEsummary$PCend<-loganalysis_sub$Rdattim[PCendrows]
ExptCDEsummary$id_endPC<-PCendrows

# N.B. LAST RECORD IN LOG SUMMARY DOESN'T HAVE END TIME
# THEREFORE ASSIGN AS LAST RECORD IN LOGANALYSIS_SUB
ExptCDEsummary
ExptCDEsummary$id_endPC[nrow(ExptCDEsummary)]<-nrow(loganalysis_sub)
ExptCDEsummary$PCend[nrow(ExptCDEsummary)]<-loganalysis_sub$Rdattim[
    ExptCDEsummary$id_endPC[nrow(ExptCDEsummary)]]
ExptCDEsummary[nrow(ExptCDEsummary),]

#####################################################
#
# STEP 4: REMOVE SHORT EVENTS (<60 s) #20 events
#
#####################################################

temp<-which((ExptCDEsummary$start)>(ExptCDEsummary$PCend)) #identify (already
    shifted start)
ExptCDEsummary[temp,] #check
ExptCDEsummary<-ExptCDEsummary[-c(temp),] #discard

# ASSIGN INDICES TO LOGANALYSIS_SUB DATAFRAME RECORDS TO ASSIGN TO PC EVENTS (
    defined in logsummary)
# Use FR event start and end dates for assigning events

# Line below creates list of what event each date falls into
event.indices = sapply(loganalysis_sub$Rdattim, function(d) which(d>=
    ExptCDEsummary$start & d<= ExptCDEsummary$PCend))

#####################################################
#
# STEP 6: CALCULATE EVENT MEANS
#
#####################################################

# FOR LOGANALYSIS RECORDS NOT WITHIN EVENTS - set indices to NA
```

```
event.indices = sapply(event.indices, function(i) ifelse(is.null(i), NA, i)) #
    This applies NA if they don't fall into an event.
loganalysis_sub$event3<-event.indices
#loganalysis_sub[c(4000:5601),c("event3","Rdattim")]
ExptCDEsummary$event3<-loganalysis_sub$event3[c(ExptCDEsummary$id+13)] #so you
    can see what event numbers the logsummary entries are
ExptCDEsummary$event3
event_id<-as.integer((ExptCDEsummary$id+12+ExptCDEsummary$id_endPC)/2)
ExptCDEsummary$eventtime<-loganalysis_sub$Rdattim[event_id]

# Calculate average parameters for the 'events'
ExptCDE_means<-aggregate(loganalysis_sub,list(loganalysis_sub$event3),mean)
sd_Pdiff<-aggregate(loganalysis_sub$P_diff_MPa,list(loganalysis_sub$event3),sd)
ExptCDE_means$sd_Pdiff<-sd_Pdiff[,2]
ExptCDE_means$start<-ExptCDEsummary$start
ExptCDE_means$end<-ExptCDEsummary$PCend
str(ExptCDE_means)
# N.B. There are some columns that are superfluous - these can be removed if
    desired
ExptCDE_means<-ExptCDE_means[,-c(34:41)]
str(ExptCDE_means)

#Check values
ggplot(data=loganalysis_sub,aes(x=Rdattim,y=value))+
  geom_point(aes(y=P_conf_MPa))+
  geom_point(aes(y=Flow_Pump1*5),color="blue")+
  geom_point(aes(y=Templog_C),color="red")+
  geom_point(aes(y=P_diff_psiSMA5*0.2),color="green")+
  geom_point(aes(y=P_diff_psi*0.2),color="dark green")+
  geom_point(aes(y=P_ds_MPa),color="orange")+
  geom_point(aes(y=P_us_MPa),color="pink")+
  geom_point(aes(y=abs(grad_Pc)*3),color="purple")+
  geom_point(data=ExptCDE_means,aes(x=start,y=P_diff_psi*0.2),color="red")+
  geom_point(data=ExptCDE_means,aes(x=end,y=P_diff_psi*0.2),col="red")+
  geom_point(data=ExptCDE_means,aes(x=Rdattim,y=P_diff_psi*0.2),col="red")+
  scale_x_datetime(limits=xlimC2)


#########################################################
# CREATE EXPT BOUNDARIES AND ASSIGN EXPT DATA
#########################################################

# Calculating Expt C2,D,E boundaries for ExptCDE_means table
Tdiff<-diff(ExptCDE_means$Templog_C) #calculates difference between consecutive
    Temp values in logmeans table
Tdiff<-c(NA,Tdiff)
expt_boundaries_CDE<-which(abs(Tdiff)>5)
```

```
ExptCDE_means$expt<-"X"
ExptCDE_means$expt[1:(expt_boundaries_CDE[1]-1)]<-"C2"
ExptCDE_means$expt[expt_boundaries_CDE[1]:(expt_boundaries_CDE[2]-1)]<-"D"
ExptCDE_means$expt[expt_boundaries_CDE[2]:nrow(ExptCDE_means)]<-"E"
ExptCDE_means$expt

#expt_boundaries_CDE<-expt_boundaries_CDE-0.5 # for figure lines

str(ExptCDE_means)

# %%%%%%%%%%%%%%%%%%%%%%%%%%%%%%%%%%%%%%%%%%%%%%%%%%%%%%%%%%%%%%%%%%%%%%%
# PLOT FIGURES FOR METHODS CHAPTER 4
# %%%%%%%%%%%%%%%%%%%%%%%%%%%%%%%%%%%%%%%%%%%%%%%%%%%%%%%%%%%%%%%%%%%%%%%
# C2
xlimC2<-as.POSIXct(c("2014-08-02 12:39", "2014-08-2 15:00"))
# D
xlimD<-as.POSIXct(c("2014-08-4 08:57", "2014-08-4 12:30"))
# E
xlimE<-as.POSIXct(c("2014-08-5 09:02", "2014-08-5 11:32"))

setwd("M:/Experimental/003 Experimental Results/140703 Wissey3 experiment/R
    figures/thesis")

str(logsummary)

plot_checkQ <- ggplot(data = loganalysis_sub, aes (x= Rdattim, y=P_conf_MPa))+
  geom_line(aes(col="US Pump flow rate"),size=0.8)+
  geom_vline(data=ExptCDEsummary,aes(xintercept=c(as.numeric(ExptCDEsummary$PCend
    )),col="Event end time"), linetype = "longdash")+
  geom_vline(data=ExptCDEsummary,aes(xintercept=c(as.numeric(ExptCDEsummary$start
    )),col="Event start time"), linetype = "longdash")+
  geom_vline(data=ExptCDEsummary,aes(xintercept=c(as.numeric(
    ExptCDEsummary$Rdattim)),col="US pump flow change time"), linetype = "solid")
    +
  scale_x_datetime(limits=xlimD)+
  scale_y_continuous(limits=c(30,60),expand=c(0,0))+
  #scale_y_continuous(limits=c(0,1000),expand=c(0,0))+
  scale_colour_manual(breaks=c("US Pump flow rate","Event start time","Event end
    time","US pump flow change time"),values=c("US Pump flow rate"="purple","
    Event start time"="dark green","Event end time"="dark red","US pump flow
    change time"="black"))+
  #scale_colour_manual(breaks=c("Differential pressure","Mean","Flow","Pfluid","
    Pconf","grad","logmean","Mean2","sd2"),values=c("Differential pressure"="dark
     red","Mean"="blue","Flow"="green","Pfluid"="purple","Pconf"="orange","grad
    "="brown","Mean2"="orange","sd2"="red"))+
  labs(x="Date time", y="Confining pressure (MPa)")+
  theme(legend.position = c(0.03, 0.80))
plot_checkQ
```

```
plot_checkPdiff <- ggplot(data = loganalysis_sub, aes (x= Rdattim, y=P_diff_MPa))
    +
  geom_line(aes(y=P_diff_MPa,col="Differential pressure"))+
  geom_line(aes(y=(P_diff_psiSMA5/145.037738),col="5 step Moving Average
    Differential pressure"))+
  scale_x_datetime(limits=xlimC2)+
  #scale_y_continuous(limits=c(-0.1,0.3),expand=c(0,0))+
  #scale_y_continuous(limits=c(0,1000),expand=c(0,0))+
  scale_colour_manual(breaks=c("Differential pressure","5 step Moving Average
    Differential pressure"),values=c("Differential pressure"="dark red","5 step
    Moving Average Differential pressure"="blue"))+
  labs(x="Date time", y="Differential Pressure (MPa)")+
  theme(legend.position = c(0.05, 0.85))
plot_checkPdiff


setwd("M:/Experimental/003 Experimental Results/140703 Wissey3 experiment/R
    figures/thesis")
pdf("ExptCDEmovingaverage_plot.pdf",width=11,height=8)
plot_checkPdiff
dev.off()

plot_checkPdiff2 <- ggplot()+
  geom_line(data = loganalysis_sub,aes(x= Rdattim,y=(P_diff_psiSMA5/145.037738),
    col="5 step Moving Average Differential pressure"))+
  geom_vline(data=ExptCDEsummary,aes(xintercept=c(as.numeric(ExptCDEsummary$PCend
    )),col="Event end time"), linetype = "longdash")+
  geom_vline(data=ExptCDEsummary,aes(xintercept=c(as.numeric(ExptCDEsummary$start
    )),col="Event start time"), linetype = "longdash")+
  geom_vline(data=ExptCDEsummary,aes(xintercept=c(as.numeric(
    ExptCDEsummary$Rdattim)),col="US pump flow change time"), linetype = "solid")
    +
  geom_errorbar(data=ExptCDE_means,aes(x=Rdattim,ymin=P_diff_MPa-sd_Pdiff,ymax=
    P_diff_MPa+sd_Pdiff),width=100,size=0.8)+
  geom_point(data=ExptCDE_means,aes(x=Rdattim,y=P_diff_MPa,col="Differential
    pressure - event mean"),size=2)+
  scale_x_datetime(limits=xlimD)+
  scale_y_continuous(limits=c(1,2.5),expand=c(0,0))+
  scale_colour_manual(breaks=c("5 step Moving Average Differential pressure","
    Differential pressure - event mean","Event start time","Event end time","US
    pump flow change time"),values=c("5 step Moving Average Differential pressure
    "="blue","Differential pressure - event mean"="red","Event start time"="dark
    green","Event end time"="dark red","US pump flow change time"="black"))+
  labs(x="Date time", y="Differential Pressure (MPa)")+
  theme(legend.position = c(0.03, 0.80))
plot_checkPdiff2

setwd("M:/Experimental/003 Experimental Results/140703 Wissey3 experiment/R
    figures/thesis")
```

```
pdf("ExptDeventwindow_plot2.pdf",width=11,height=10)
multiplot(plot_checkQ,plot_checkPdiff2)
dev.off()

multiplot(plot_checkQ,plot_checkPdiff2)

plot_steps_Pdiff_FRpump<-ggplot(data = ExptCDE_means, aes (x=P_conf_MPa, y=
    P_diff_MPa, colour=as.factor(expt)))+
  geom_errorbar(aes(x=P_conf_MPa,ymin=P_diff_MPa-sd_Pdiff,ymax=P_diff_MPa+
    sd_Pdiff),width=0.2,size=1)+
  geom_point(shape=24,size=3,fill="black")+
  #stat_smooth(se=TRUE,fullrange=TRUE)+
  stat_smooth(method = "lm", size = 1,se=FALSE)+
  #geom_vline(xintercept=c(expt_boundaries_step),colour="black", linetype = "
    longdash",size=2)+
  labs(x="Confining pressure (MPa)", y="Event differential pressure (MPa)")+
  #scale_x_continuous(limits=c(0,11),expand=c(0,0))+
  #scale_y_continuous(limits=c(0,2.5),expand=c(0,0))+
  #geom_text(aes(x = 25, y = 2.7, label = "Expt A"))+
  #geom_text(aes(x = 78, y = 2.7, label = "Expt B"))+
  #geom_text(aes(x = 112, y = 2.7, label = "Expt C1"))+
  scale_colour_manual(values=c("#0066CC","#00CC00","#e67600", "#B2DF8A", "#A6CEE3
    ","#1e601a",  "#ffa500", "#46f17d"),labels=c(expression(paste("Expt C2, ",
    theta," = 38",degree,"C")),expression(paste("Expt D, ",theta," = 58",degree,"
    C")),expression(paste("Expt E, ",theta," = 38",degree,"C")),"(iv) 20MPa", "(v
    ) 10MPa","(vi) 20MPa","(vii) 30MPa","(viii) 20MPa"))+
  #scale_colour_manual(values=c("#0066CC","#00CC00","#6600CC","#A6CEE3", "#B2DF8A
    ", "#33A02C", "#FB9A99", "#E31A1C", "#FDBF6F"))+
  mytheme2+
  theme(legend.position = c(0.03, 0.80))

plot_steps_Pdiff_FRpump

setwd("M:/Experimental/003 Experimental Results/140703 Wissey3 experiment/R
    figures/thesis")
pdf("CDE_eventdatacomparison_plot_PdiffPc_W3.pdf",width=11,height=10)
plot_steps_Pdiff_FRpump
dev.off()

#########################################################################

#####################################################################
# Calculate Q through SAMPLE
#####################################################################

#First, save subset file for use in RKWARD (NX CLIENT)
ExptCDE_means_Qcalc<-ExptCDE_means[,c("P_us_MPa","P_ds_MPa","P_fluid_avg_MPa","
    P_diff_MPa","Templog_C","Temp_pump_C","Flow_Pump1")]
```

```
setwd("M:/Experimental/003 Experimental Results/140703 Wissey3 experiment")
save(ExptCDE_means_Qcalc,file="ExptCDE_means_Qcalc1.Rdata")

#####################################################################
# GO TO NX CLIENT RKWARD TO RUN NEXT SECTION
#####################################################################
setwd("/home/s1164164/R/Naylor_scripts")
#setwd("M:/R/Naylor_scripts")

##install.packages("/home/s1164164/R/Naylor_scripts/CO2PhaseProperties.tar.gz",
    repos=NULL, type="source", dependencies=TRUE)
##install.packages("/home/s1164164/R/Naylor_scripts/H2OPhaseProperties.tar.gz",
    repos=NULL, type="source", dependencies=TRUE)
##install.packages("/home/s1164164/R/Naylor_scripts/GasPhaseProperties.tar.gz",
    repos=NULL, type="source", dependencies=TRUE)
##install.packages("/home/s1164164/R/Naylor_scripts/CO2Risk.tar.gz", repos=NULL,
    type="source", dependencies=TRUE)
##install.packages("/home/s1164164/R/Naylor_scripts/CO2GeoProperties.tar.gz",
    repos=NULL, type="source", dependencies=TRUE)

library(CO2GeoProperties)

## Import data from experiment on 130725
setwd("/home/s1164164/Experimental/003 Experimental Results/140703 Wissey3
    experiment")
load("ExptCDE_means_Qcalc1.Rdata")

# FIRST CALCULATE DENSITY AND VISCOSITY AT PUMP

## Sample inputs
names(ExptCDE_means_Qcalc)

# Pump parameters
temps_P1 = ExptCDE_means_Qcalc$Temp_pump_C
pressures_P1 = ExptCDE_means_Qcalc$P_us_MPa

# US sample
temps_S1 = ExptCDE_means_Qcalc$Templog_C
pressures_S1 = ExptCDE_means_Qcalc$P_us_MPa

# DS sample
temps_S2 = ExptCDE_means_Qcalc$Templog_C
pressures_S2 = ExptCDE_means_Qcalc$P_ds_MPa

# AVG sample
temps_Savg = ExptCDE_means_Qcalc$Templog_C
pressures_Savg = ExptCDE_means_Qcalc$P_fluid_avg_MPa

#temps = 60
```

```
#pressures = 45

sampleSize=length(temps_P1)

## Estimate densities (units: kg/m3)
density_P1 = CO2.getDensityFromPT(pressures_P1, temps_P1)
density_P1

density_S1 = CO2.getDensityFromPT(pressures_S1, temps_S1)
density_S2 = CO2.getDensityFromPT(pressures_S2, temps_S2)
density_Savg = CO2.getDensityFromPT(pressures_Savg, temps_Savg)

mean(density_P1)
length(density_P1)
mean(density_S1)
length(density_S1)
mean(density_S2)
length(density_S2)
mean(density_Savg)
length(density_Savg)

## Estimate viscosities (units: Centipoise)
viscosity_P1=density_P1  # initialise viscosities vector
if(length(density_P1)>0){
  for(l in 1:length(density_P1)){
    Rho = density_P1[l] ; T = temps_P1[l]
    viscosity_P1[l] = CO2.getViscosityFromDensity (Rho, T)
  }
}#viscosities = CO2.getViscosityFromDensity (densities[1], temps[1])

viscosity_S1=density_S1  # initialise viscosities vector
if(length(density_S1)>0){
  for(l in 1:length(density_S1)){
    Rho = density_S1[l] ; T = temps_S1[l]
    viscosity_S1[l] = CO2.getViscosityFromDensity (Rho, T)
  }
}#viscosities = CO2.getViscosityFromDensity (densities[1], temps[1])

viscosity_S2=density_S2  # initialise viscosities vector
if(length(density_S2)>0){
  for(l in 1:length(density_S2)){
    Rho = density_S2[l] ; T = temps_S2[l]
    viscosity_S2[l] = CO2.getViscosityFromDensity (Rho, T)
  }
}#viscosities = CO2.getViscosityFromDensity (densities[1], temps[1])

viscosity_Savg=density_Savg  # initialise viscosities vector
if(length(density_Savg)>0){
  for(l in 1:length(density_Savg)){
```

```
    Rho = density_Savg[l] ; T = temps_Savg[l]
    viscosity_Savg[l] = CO2.getViscosityFromDensity (Rho, T)
  }
}#viscosities = CO2.getViscosityFromDensity (densities[1], temps[1])

ExptCDE_means_Qcalc$density_P1<-density_P1
ExptCDE_means_Qcalc$viscosity_P1<-viscosity_P1

ExptCDE_means_Qcalc$density_S1<-density_S1
ExptCDE_means_Qcalc$viscosity_S1<-viscosity_S1

ExptCDE_means_Qcalc$density_S2<-density_S2
ExptCDE_means_Qcalc$viscosity_S2<-viscosity_S2

ExptCDE_means_Qcalc$density_Savg<-density_Savg
ExptCDE_means_Qcalc$viscosity_Savg<-viscosity_Savg

save(ExptCDE_means_Qcalc,file="ExptCDE_means_Qcalc2.Rdata")

############################################################
# RETURN TO RSTUDIO WINDOWS MACHINE
############################################################

setwd("M:/Experimental/003 Experimental Results/140703 Wissey3 experiment")
load("ExptCDE_means_Qcalc2.Rdata")

str(ExptCDE_means)
str(ExptCDE_means_Qcalc)
test<-cbind(ExptCDE_means,ExptCDE_means_Qcalc[,8:15])
str(test)
ExptCDE_means<-test # Update ExptCDE_means to include the density, viscosity
    values
# N.B. Flow_Pump1 can be used here instead of mean_FR_Pump1 as there are no flow
    changes therefore no discrepancies with timing
ExptCDE_means$Qsample_avg<-ExptCDE_means$Flow_Pump1*(ExptCDE_means$density_P1/
    ExptCDE_means$density_Savg)
ExptCDE_means$Qsample_1<-ExptCDE_means$Flow_Pump1*(ExptCDE_means$density_P1/
    ExptCDE_means$density_S1)
ExptCDE_means$Qsample_2<-ExptCDE_means$Flow_Pump1*(ExptCDE_means$density_P1/
    ExptCDE_means$density_S2)


# Create rounded FR values for ExptCDE_means file
# Round the mean FR values to integers to make processing easier
ExptCDE_FR<-round(ExptCDE_means$Flow_Pump1,digits=0)
# Add this column to the dataframe
ExptCDE_means$FR_pump1<-ExptCDE_FR
```

```
# Create step column in ExptCDE file - following on from Expt ABC1 steps
max(logmeans$step)
maxstep<-max(logmeans$step)
step<-c(1:nrow(ExptCDE_means))
step<-step+maxstep
ExptCDE_means$step<-step

# Create stage column (all 1) for ExptCDE
ExptCDE_means$stage<-1

# Create Pf_hyst column (all A) for ExptCDE
ExptCDE_means$Pf_hyst<-"A"

#########################################################################
# Calculate e (x 2 versions) to check magnitude for each solution
#########################################################################

# 1. Darcy's law

L=0.0276 # Length of sample (m)
D=0.0376 # Diameter of sample (m) (always width of fracture)
# N.B. Units need converting:
# Q:  ml/min to m3/s => x (1e-6/60)
# viscosity: Centipoise to Pa s => 1e-3
# P: MPa to Pa (1e6)

e_fracD<-(ExptCDE_means$Qsample_avg*(1e-6/60)*12*(ExptCDE_means$viscosity_Savg*1e
    -3)*L)/(ExptCDE_means$P_diff_MPa*1e6*D)
e_fracD<-e_fracD^(1/3)


# 2. Darcy's law compressible (Carman)

e_fracDc<-(ExptCDE_means$Qsample_avg*(1e-6/60)*12*(ExptCDE_means$viscosity_Savg*1
    e-3)*L*2*ExptCDE_means$P_ds_MPa*1e6)/((((ExptCDE_means$P_ds_MPa+
    ExptCDE_means$P_diff_MPa)*1e6)^2-(ExptCDE_means$P_ds_MPa*1e6)^2)*D)
e_fracDc<-e_fracDc^(1/3)

#####################################################################
# Add to logmeans table
ExptCDE_means$e_fracD<-e_fracD
ExptCDE_means$e_fracDc<-e_fracDc

################################################
#########################################################################

# Calculate k (m2) and K (m/s)
k<-(ExptCDE_means$e_fracD*ExptCDE_means$e_fracD)/12
ExptCDE_means$k<-k
```

```
k_comp<-(ExptCDE_means$e_fracDc*ExptCDE_means$e_fracDc)/12
ExptCDE_means$k_comp<-k_comp

K<-(ExptCDE_means$k*9.81*ExptCDE_means$density_Savg)/(
    ExptCDE_means$viscosity_Savg*1e-3)
ExptCDE_means$K<-K

K_comp<-(ExptCDE_means$k_comp*9.81*ExptCDE_means$density_Savg)/(
    ExptCDE_means$viscosity_Savg*1e-3)
ExptCDE_means$K_comp<-K_comp

##############################################################################

# Calculate Transmissivity (T)

T<-(ExptCDE_means$Qsample_avg*(1e-6/60)*ExptCDE_means$viscosity_Savg*1e-3*L)/(
    ExptCDE_means$P_diff_MPa*1e6)
ExptCDE_means$T<-T

T_comp<-(ExptCDE_means$Qsample_avg*(1e-6/60)*ExptCDE_means$viscosity_Savg*1e-3*L
    *2*ExptCDE_means$P_ds_MPa*1e6)/((((ExptCDE_means$P_ds_MPa+
    ExptCDE_means$P_diff_MPa)*1e6)^2-(ExptCDE_means$P_ds_MPa*1e6)^2))
ExptCDE_means$T_comp<-T_comp

##############################################################################
# Now, need to save the file and use the results to add data to plots
##############################################################################

str(ExptCDE_means)
setwd("R:/EXPERIMENTAL DATA/LOGS/140702 Wiss3")
save(ExptCDE_means, file="ExptC2DE_means_150428.Rdata")
rm(list=ls())
load("ExptC2DE_means_150428.Rdata")
```

Bibliography

Alexander, J. [1992], 'A discussion on the use of analogues for reservoir geology', *Geological Society, London, Special Publications* **69**(69), 175–194.

Alotaibi, F. M., Alkhaldi, M. H., Funk, Jim, J. and Shouwen, X. [2012], 'New Insights into Clay Swelling : Supercritical CO_2 Interaction with Montmorillonite', *Eighteenth SPE Improved Oil Recovery Symposium held in Tulsa* **cl**(Van 1977), 1–10.

Ameli, P., Elkhoury, J. E. and Detwiler, R. L. [2013], 'High-resolution fracture aperture mapping using optical profilometry', *Water Resources Research* **49**(10), 7126–7132.

Andreani, M., Gouze, P., Luquot, L. and Jouanna, P. [2008], 'Changes in seal capacity of fractured claystone caprocks induced by dissolved and gaseous CO_2 seepage', *Geophysical Research Letters* **35**(14), 1–6.

Angeli, M., Faleide, J. I. and Gabrielsen, R. H. [2013], 'Evaluating Seal Quality for Potential Storage Sites in the Norwegian North Sea', *Energy Procedia* **37**(0), 4853–4862.

Angeli, M., Soldal, M., Skurtveit, E. and Aker, E. [2009], 'Experimental percolation of supercritical CO_2 through a caprock', *Energy Procedia* **1**(1), 3351–3358.

Bachu, S. [2000], 'Sequestration of CO_2 in geological media: criteria and approach for site selection in response to climate change', *Energy Conversion and Management* **41**(9), 953–970.

Bachu, S. and Bennion, D. B. [2009], 'Experimental assessment of brine and/or CO_2 leakage through well cements at reservoir conditions', *International Journal of Greenhouse Gas Control* **3**(4), 494–501.

Bandis, S., Lumsden, A. and Barton, N. [1983], 'Fundamentals of rock joint deformation', *International Journal of Rock Mechanics and Mining Sciences & Geomechanics Abstracts* **20**(6), 249–268.

Barton, N., Bandis, S. and Bakhtar, K. [1985], 'Strength, deformation and conductivity coupling of rock joints', *International Journal of Rock Mechanics and Mining Sciences & Geomechanics Abstracts* **22**(3), 121–140.

Batenburg, D. V. and Milton-Taylor, D. [2005], 'Discussion of SPE 89325,'Beyond beta factors: a complete model for Darcy, Forchheimer, and Trans-Forchheimer flow in porous media'', *J. Pet. Tech* (August), 72–74.

Bear, J. [1972], *Dynamics of Fluids in Porous Media*, 1988 edn, Dover Publications, Inc.

Bensabat, J. [2013], Characterization and monitoring of an injection experiment at Heletz Israel, *in* 'Training Course on Geological Storage of CO_2, Göttingen, Germany, 9th-12th October', PANACEA.

Bevington, P. and Robinson, K. [2003], *Data reduction and error analysis for the physical sciences*, McGraw-Hill.

Biot, M. A. [1941], 'General Theory of Three-Dimensional Consolidation', *Journal of Applied Physics* **12**(2), 155.

Bjørlykke, K. [1993], 'Fluid flow in sedimentary basins', *Sedimentary Geology* **86**(1-2), 137–158.

Branter, S. R. F. [2003], 'The East Brae Field, Blocks 16/03a, 16/03b, UK North Sea', *Geological Society, London, Memoirs* **20**(1), 191–197.

Brenchley, P. J. and Rawson, P. F. [2006], *The Geology of England and Wales*, second edn, The Geological Society.

Broseta, D., Tonnet, N. and Shah, V. [2012], 'Are rocks still water-wet in the presence of dense CO_2 or H_2S?', *Geofluids* **12**(4), 280–294.

Brown, S. R. [1995], 'Simple mathematical model of a rough fracture', *Journal of Geophysical Research* **100**, 5941–5952.

Brown, S. R., Kranz, R. L. and Bonner, P. [1986], 'Correlation between the surfaces of natural rock joints', *Geophysical Research Letters* **13**(13), 1430–1433.

Brown, S. R. and Scholz, C. H. [1986], 'Closure of Rock Joints', *Journal of Geophysical Research* **91**(B5), 4939.

Busch, A., Alles, S., Gensterblum, Y., Prinz, D., Dewhurst, D., Raven, M., Stanjek, H. and Krooss, B. [2008], 'Carbon dioxide storage potential of shales', *International Journal of Greenhouse Gas Control* **2**(3), 297–308.

Busch, A., Amann, A., Bertier, P., Waschbusch, M. and Krooss, B. M. [2010], 'SPE 139588 The Significance of Caprock Sealing Integrity for CO_2 Storage', (November), 10–12.

Carman, P. [1956], *Flow of gases through porous media*, Butterworths Scientific Publications.

Cavanagh, A. J. and Haszeldine, R. S. [2014], 'The Sleipner storage site: Capillary flow modeling of a layered CO_2 plume requires fractured shale barriers within the Utsira Formation', *International Journal of Greenhouse Gas Control* **21**, 101–112.

Chadwick, A., Arts, R., Bernstone, C., May, F., Thibeau, S. and Zweigel, P. [2008], *Best Practice for the Storage of CO_2 in Saline Aquifers - Observations and Guidelines from the SACS and CO2STORE projects*, Vol. 14, British Geological Survey.

Chalbaud, C., Robin, M., Lombard, J., Martin, F., Egermann, P. and Bertin, H. [2009], 'Interfacial tension measurements and wettability evaluation for geological CO_2 storage', *Advances in Water Resources* **32**(1), 98–109.

Chiquet, P., Daridon, J.-L., Broseta, D. and Thibeau, S. [2007], 'CO_2/water interfacial tensions under pressure and temperature conditions of CO_2 geological storage', *Energy Conversion and Management* **48**(3), 736–744.

Cho, Y., Apaydin, O. G. and Resources, E. O. G. [2013], 'Pressure-Dependent Natural-Fracture Permeability in Shale and Its Effect on Shale-Gas Well Production', *SPE Reservoir Evaluation and Engineering* (May).

Crawley, M. J. [2012], *The R book*, John Wiley & Sons.

Credoz, A., Bildstein, O., Jullien, M., Raynal, J., Pétronin, J.-C., Lillo, M., Pozo, C. and Geniaut, G. [2009], 'Experimental and modeling study of geochemical reactivity

between clayey caprocks and CO_2 in geological storage conditions', *Energy Procedia* **1**(1), 3445–3452.

Cuss, R. J., Harrington, J. F., Noy, D. J., Sathar, S. and Norris, S. [2015], 'An experimental study of the flow of gas along synthetic faults of varying orientation to the stress field: Implications for performance assessment for radioactive waste disposal', *Journal of Geophysical Research : Solid Earth* pp. 1–14.

Cuss, R. J., Milodowski, A. and Harrington, J. F. [2011], 'Fracture transmissivity as a function of normal and shear stress: First results in Opalinus Clay', *Physics and Chemistry of the Earth, Parts A/B/C* **36**(17-18), 1960–1971.

Davies, O. M., Arnold, J. and Sulley, S. [1999], 'The mechanical properties of elastomers in high-pressure CO_2', *Journal of Materials* **4**, 417–422.

De Jong, S. M., Spiers, C. J. and Busch, A. [2014], 'Development of swelling strain in smectite clays through exposure to carbon dioxide', *International Journal of Greenhouse Gas Control* **24**, 149–161.

de Marsily, G. [1986], *Quantitative Hydrogeology*, Academic Press.

Deer, W. A., Howie, R. A. and Zussman, J. [1992], *An Introduction to the Rock-Forming Minerals*, second edition edn, Pearson Education Limited.

Deng, H., Fitts, J. P., Crandall, D., McIntyre, D. and Peters, C. A. [2015], 'Alterations of Fractures in Carbonate Rocks by CO_2-Acidified Brines', *Environmental Science and Technology* **49**(16), 10226–10234.

Devore, J. [2011], *Probability and Statistics for Engineering and the Sciences*, Cengage Learning.

Duan, Y., Jing, X., Meng, Y. and Luo, P. [2013], 'Closure Behaviour of Natural Rock Fractures', *SPE/AAPG Western Regional Meeting* .

Dupuit, J. [1863], *Etudes theoriques et pratiques sur le mouvement des eaux dans les canaux decouverts et a travers les terrains permeables avec des considerations relatives au regime des grandes eaux, au debouche a leur donner et a la marche des alluvions dans les rivieres a fond mobile*, Dunod.

Durham, B. [1997], 'Laboratory observations of the hydraulic behavior of a permeable fracture from 3800 m depth in the KTB pilot hole', **102**.

Durham, W. B., Bourcier, W. L. and Burton, E. a. [2001], 'Direct observation of reactive flow in a single fracture', *Water Resources Research* **37**(1), 1.

Edlmann, K., Haszeldine, S. and McDermott, C. I. [2013], 'Experimental investigation into the sealing capability of naturally fractured shale caprocks to supercritical carbon dioxide flow', *Environmental Earth Sciences* .

Forchheimer, P. [1901], 'Wasserbewegung durch boden', *Zeitsch-rift des Vereines Deutscher Ingenieure* **49**, 1736–1749.

Gaus, I., Audigane, P., André, L., Lions, J., Jacquemet, N., Durst, P., Czernichowski-Lauriol, I. and Azaroual, M. [2008], 'Geochemical and solute transport modelling for CO_2 storage, what to expect from it?', *International Journal of Greenhouse Gas Control* **2**(4), 605–625.

Gentier, S., Lamontagne, E., Archambault, G. and Riss, J. [1997], 'Anisotropy of flow in a fracture undergoing shear and its relationship to the direction of shearing and injection pressure', *International journal of rock mechanics and mining sciences & geomechanics abstracts* **34**(3-4), 412.

Giesting, P., Guggenheim, S., Koster van Groos, A. F. and Busch, A. [2012], 'Interaction of carbon dioxide with Na-exchanged montmorillonite at pressures to 640bars: Implications for CO_2 sequestration', *International Journal of Greenhouse Gas Control* **8**, 73–81.

Glennie, K. W. [1984], *Introduction to the petroleum geology of the North Sea*, Blackwell Scientific Publications, Palo Alto, CA.

Glover, P. and Hayasbi, K. [1997], 'Modelling Fluid Flow in Rough Fractures: Application to the Hachimantai Geothermal HDR Test Site', **22**(1), 5–11.

Glover, P. W. J., Matsuki, K., Hikima, R. and Hayashi, K. [1998], 'Synthetic rough fractures in rocks', *Journal of Geophysical Research* **103**, 9609.

Goodman, R. E. [1976], *Methods of geological engineering in discontinuous rocks.*

Greenwood, J. and Williamson, J. [1966], Contact of nominally flat surfaces, *in* 'Proceedings of the Royal Society of London A: Mathematical, Physical and Engineering Sciences', Vol. 295, The Royal Society, pp. 300–319.

Guglielmi, Y., Elsworth, D., Cappa, F., Henry, P., Gout, C., Dick, P. and Durand, J. [2015], 'In situ observations on the coupling between hydraulic diffusivity and displacements during fault reactivation in shales', *Journal of Geophysical Research : Solid Earth* **120**, 7729–7748.

Gunter, W. D., Bachu, S. and Benson, S. [2004], 'The role of hydrogeological and geochemical trapping in sedimentary basins for secure geological storage of carbon dioxide', *Geological Society, London, Special Publications* **233**(1), 129–145.

Gutierrez, M., Oino, L. and Nygård, R. [2000], 'Stress-dependent permeability of a de-mineralised fracture in shale', *Marine and Petroleum Geology* **17**, 895–907.

Hangx, S. J. T., Spiers, C. J. and Peach, C. J. [2010], 'Mechanical behavior of anhydrite caprock and implications for CO_2 sealing capacity', *Journal of Geophysical Research* **115**(B7), 1–22.

Hangx, S., van der Linden, A., Marcelis, F. and Bauer, A. [2013], 'The effect of CO_2 on the mechanical properties of the Captain Sandstone: Geological storage of CO_2 at the Goldeneye field (UK)', *International Journal of Greenhouse Gas Control* **19**, 609–619.

Harpalani, S. and Chen, G. [1997], 'Influence of gas production induced volumetric strain on permeability of coal', *Geotechnical and Geological Engineering* **15**(4), 303–325.

Harper, M. L. [1971], 'Approximate geothermal gradients in the North Sea basin', *Nature* .

Harrington, J. F. and Horseman, S. T. [1999], 'Gas transport properties of clays and mudrocks', *Geological Society, London, Special Publications* **158**(1), 107–124.

Haszeldine, R. S. [2006], 'Deep Geological CO_2 Storage: Principles Reviewed, and Prospecting for Bio-energy Disposal Sites', *Mitigation and Adaptation Strategies for Global Change* **11**(2), 369–393.

Haszeldine, S., Lu, J., Wilkinson, M. and Macleod, G. [2006], 'Long-timescale interaction of CO_2 storage with reservoir and seal : Miller and Brae natural analogue fields North Sea', *Greenhouse Gas Control Technology* **8**, 1–6.

Hebach, A., Oberhof, A., Dahmen, N., Ko, A. and Ederer, H. [2002], 'Interfacial Tension at Elevated PressuressMeasurements and Correlations in the Water + Carbon Dioxide System', *Engineering* (Figure 2), 1540–1546.

Hildenbrand, A., Schlomer, S., Krooss, B. and Littke, R. [2004], 'Gas breakthrough experiments on pelitic rocks : comparative study with N_2, CO_2 and CH_4', *Geofluids* **4**, 60–80.

Hinchcliffe, S. [2014], An investigation into multiphase flow behaviour during cyclic CO_2 injection and sequestration, BSc Environmental Geoscience dissertation, Technical report, University of Edinburgh.

Holloway, S. and Savage, D. [1993], 'The potential for aquifer disposal of carbon dioxide in the UK', *Energy Conversion and Management* **34**(9-11), 925–932.

Huang, F.-h., Li, M.-h., Lee, L. L., Starling, K. E. and Chung, F. T. H. [1984], 'An accurate equation of state for carbon dioxide', *Journal of Chemical Engineering of Japan* **18**(6), 490–496.

Huang, H. and Ayoub, J. [2006], 'Applicability of the Forchheimer Equation for Non-Darcy Flow in Porous Media', *SPE Annual Technical Conference and Exhibition* (March), 1–14.

Huerta, N. J., Hesse, M. A., Bryant, S. L., Strazisar, B. R. and Lopano, C. [2016], 'Reactive transport of CO_2-saturated water in a cement fracture: Application to wellbore leakage during geologic CO_2 storage', *International Journal of Greenhouse Gas Control* **44**, 276–289.

IEAGHG [2010], Corrosion and materials selection in CCS systems, Technical Report 2010/03, International Energy Agency.

Jaeger, J. C., Cook, N. G. and Zimmerman, R. [2009], *Fundamentals of rock mechanics*, John Wiley & Sons.

Jaeger, J. and Cook, N. [1979], *Fundamentals of Rock Mechanics*, third edn, Chapman ad Hall Ltd.

Jain, a. K. and Juanes, R. [2009], 'Preferential Mode of gas invasion in sediments: Grain-scale mechanistic model of coupled multiphase fluid flow and sediment mechanics', *Journal of Geophysical Research* **114**(B8), 1–19.

Javadi, M., Sharifzadeh, M., Shahriar, K. and Mitani, Y. [2014], 'Critical Reynolds number for nonlinear flow through rough-walled fractures: The role of shear processes', *Water Res* **50**, 1789–1804.

Jenkins, R. E. et al. [1960], Accuracy of porosity determinations, *in* 'SPWLA 1st Annual Logging Symposium', Society of Petrophysicists and Well-Log Analysts.

Ji, S. H., Lee, H. B., Yeo, I. W. and Lee, K. K. [2008], 'Effect of nonlinear flow on DNAPL migration in a rough-walled fracture', *Water Resources Research* **44**(11), 1–10.

Johnson, G., Mayer, B., Nightingale, M., Shevalier, M. and Hutcheon, I. [2011], 'Using oxygen isotope ratios to quantitatively assess trapping mechanisms during CO_2 injection into geological reservoirs: The Pembina case study', *Chemical Geology* **283**(3-4), 185–193.

Jossi, J. A., Stiel, L. and Thodos, G. [1944], 'The Viscosity of Pure Substances in the Dense Gaseous and Liquid Phases', *American Institute of Chemical Engineering* **8**(1), 59–63.

Klinkenberg, L. [1941], 'The permeability of porous media to liquids and gases'.

Kolditz, O. [2001], 'Non-linear flow in fractured rock', *International journal of numerical methods for heat & fluid flow* **11**(6), 547–575.

Kolditz, O., Bauer, S., Bilke, L., Böttcher, N., Delfs, J. O., Fischer, T., Görke, U. J., Kalbacher, T., Kosakowski, G., McDermott, C. I., Park, C. H., Radu, F., Rink, K., Shao, H., Shao, H. B., Sun, F., Sun, Y. Y., Singh, a. K., Taron, J., Walther, M., Wang, W., Watanabe, N., Wu, Y., Xie, M., Xu, W. and Zehner, B. [2012], 'OpenGeoSys: an open-source initiative for numerical simulation of thermo-hydro-mechanical/chemical (THM/C) processes in porous media', *Environmental Earth Sciences* .

Kranz, R., Frankel, A., Engelder, T. and Scholz, C. [1979], 'Permeability of whole and jointed barre granite', *International Journal of Rock Mechanics and Mining Sciences* **16**(4), 225–234.

Lee, D. S., Herman, J. D., Elsworth, D., Kim, H. T. and Lee, H. S. [2011], 'A critical evaluation of unconventional gas recovery from the marcellus shale, northeastern United States', *KSCE Journal of Civil Engineering* **15**(4), 679–687.

Legler, B. and Schneider, J. W. [2008], 'Marine ingressions into the MiddleLate Permian saline lake of the Southern Permian Basin (Rotliegend, Northern Germany) possibly linked to sea-level highstands in the Arctic rift system', *Palaeogeography, Palaeoclimatology, Palaeoecology* **267**(1), 102–114.

Lemmon, E., McLinden, M. and Friend, D. [2011], Thermophysical Properties of Fluid Systems, *in* P. Linstrom and W. Mallard, eds, 'NIST Chemistry WebBook, NIST Standard Reference Database Number 69', National Institute of Standards and Technology, Gaithersburg MD, 20899.

Li, S., Dong, M., Li, Z., Huang, S., Qing, H. and Nickel, E. [2005], 'Gas breakthrough pressure for hydrocarbon reservoir seal rocks: implications for the security of long-term CO_2 storage in the Weyburn field', *Geofluids* **5**(4), 326–334.

Liang, W., Yang, C., Zhao, Y., Dusseault, M. and Liu, J. [2007], 'Experimental investigation of mechanical properties of bedded salt rock', *International Journal of Rock Mechanics and Mining Sciences* **44**(3), 400–411.

Liteanu, E. and Spiers, C. [2011], 'Fracture healing and transport properties of wellbore cement in the presence of supercritical CO_2', *Chemical Geology* **281**(3-4), 195–210.

Liu, F., Lu, P., Griffith, C., Hedges, S. W., Soong, Y., Hellevang, H. and Zhu, C. [2012], 'CO_2–brine–caprock interaction: Reactivity experiments on Eau Claire shale and a review of relevant literature', *International Journal of Greenhouse Gas Control* **7**, 153–167.

Loring, J. S., Schaef, H. T., Turcu, R. V. F., Thompson, C. J., Miller, Q. R. S., Martin, P. F., Hu, J., Hoyt, D. W., Qafoku, O., Ilton, E. S., Felmy, A. R. and Rosso, K. M. [2012], 'In situ molecular spectroscopic evidence for CO_2 intercalation into montmorillonite in supercritical carbon dioxide.', *Langmuir : the ACS journal of surfaces and colloids* **28**, 7125–8.

Luquot, L., Abdoulghafour, H. and Gouze, P. [2013], 'Hydro-dynamically controlled alteration of fractured Portland cements flowed by CO_2-rich brine', *International Journal of Greenhouse Gas Control* **16**, 167–179.

Ma, H. and Ruth, D. W. [1993], 'The microscopic analysis of high forchheimer number flow in porous media', *Transport in Porous Media* **13**(2), 139–160.

McCraw, C., Edlmann, K., Miocic, J., Gilfillan, S., Haszeldine, R. S. and McDermott, C. I. [2016], 'Experimental investigation and hybrid numerical analytical hydraulic mechanical simulation of supercritical CO_2 flowing through a natural fracture in caprock', *International Journal of Greenhouse Gas Control* pp. 1–14.

McDermott, C., Haszeldine, R., Edlmann, K., Edwards, M., Robbins, B. and De la Rosa Illescas, A. [2012], *Report on the effect of Thermal, Hydraulic, Mechanical and Chemical coupled processes on caprock integrity from analogue analysis*, EU FP7 Project. The research leading to these results has received funding from the European Community's Seventh Framework Programme (FP7/20072013) under grant agreement no [227286].

McPhee, C. A. and Arthur, K. G. [1991], Klinkenberg Permeability Measurements: Problems and Practical Solutions, *in* P. F. Worthington and D. Longeron, eds, 'Advances in Core Evaluation II: Reservoir Appraisal', Gordon & Breach, 1991, pp. 371–391.

Metz, B., Davidson, O., de Coninck, H., Loos, M. and Meyer, L. [2005], IPCC Special Report on Carbon Dioxide Capture and Storage, Technical report, IPCC.

Michael, K., Golab, A., Shulakova, V., Ennis-King, J., Allinson, G., Sharma, S. and Aiken, T. [2010], 'Geological storage of CO_2 in saline aquifers-A review of the experience from existing storage operations', *International Journal of Greenhouse Gas Control* **4**(4), 659–667.

MicroEpsilon Messtechnik [n.d.], *Instruction Manual scanCONTROL 2700/2710*, MicroEpsilon Messtechnik.

Miocic, J. M., Johnson, G. and Gilfillan, S. M. V. [2014], 'Fault seal analysis of a natural CO_2 reservoir in the Southern North Sea', *Energy Procedia* **63**, 3364–3370.

Nasvi, M., Ranjith, P., Sanjayan, J. and Haque, a. [2013], 'Sub- and super-critical carbon dioxide permeability of wellbore materials under geological sequestration conditions: An experimental study', *Energy* **54**, 231–239.

Nelson, C. R., Evans, J. M., Sorenson, J. A., Steadman, E. N. and Harju, J. A. [2005], Factors affecting the potential for CO_2 leakage from geological sinks, Technical report, Plains CO_2 Reduction (PCOR) PArtnership.

Neuville, a., Toussaint, R. and Schmittbuhl, J. [2012], 'Fracture aperture reconstruction and determination of hydrological properties: A case study at Draix (French Alps)', *Hydrological Processes* **26**(14), 2095–2105.

Niemi, A., Bensabat, J., Shtivelman, V., Edlmann, K., Gouze, P., Luquot, L., Hingerl, F., Benson, S. M., Pezard, P. A., Rasmusson, K., Liang, T., Fagerlund, F., Gendler,

M., Goldberg, I., Tatomir, A., Lange, T., Sauter, M. and Freifeld, B. [2016], 'Heletz experimental site overview, characterization and data analysis for CO_2 injection and geological storage', *International Journal of Greenhouse Gas Control* .
URL: *http://linkinghub.elsevier.com/retrieve/pii/S1750583615301778*

Noy, D., Holloway, S., Chadwick, R., Williams, J., Hannis, S. and Lahann, R. [2012], 'Modelling large-scale carbon dioxide injection into the Bunter Sandstone in the UK Southern North Sea', *International Journal of Greenhouse Gas Control* **9**, 220–233.

Nur, A. and Byerlee, J. [1971], 'An exact effective stress law for elastic deformation of rock with fluids', *Journal of Geophysical Research* **76**(26), 6414–6419.

Nygård, R., Gutierrez, M., Bratli, R. and Høeg, K. [2006], 'Brittle–ductile transition, shear failure and leakage in shales and mudrocks', *Marine and Petroleum Geology* **23**(2), 201–212.

Ojala, I. O., Ngwenya, B. T., Main, I. G., Ojala, I. O., Ngwenya, B. T. and Main, I. G. [2004], 'Loading rate dependence of permeability evolution in porous aeolian sandstones', *Journal of Geophysical Research* **109**(B1), 1–14.

Olsson, R. and Barton, N. [2001], 'An improved model for hydromechanical coupling during shearing of rock joints', *International Journal of Rock Mechanics and Mining Sciences* **38**(3), 317–329.

Olsson, W. A. and Brown, S. R. [1993], 'Hydromechanical response of a fracture undergoing compression and shear', *International Journal of Rock Mechanics and Mining Sciences and* **30**(7), 845–851.

Parker, M. E., Meyer, J. P. and Meadows, S. R. [2009], 'Carbon Dioxide Enhanced Oil Recovery Injection Operations Technologies (Poster Presentation)', *Energy Procedia* **1**(1), 3141–3148.

Paul, S., Shepherd, R., Bahrami, A. and Woollin, P. [2010], Material selection for supercritical CO_2 transport, *in* 'The First International Forum on the Transport of CO_2 for Carbon Capture and Storage', Abington.

Peng, D.-Y. and Robinson, D. B. [1976], 'A New Two-Constant Equation of State', *Industrial & Engineering Chemistry Fundamentals* **15**(1), 59–64.

Perera, M., Ranjith, P., Airey, D. and Choi, S. [2011], 'Sub- and super-critical carbon dioxide flow behavior in naturally fractured black coal: An experimental study', *Fuel* **90**(11), 3390–3397.

Peters, C. A. [2001], Statistics for Analysis of Experimental Data, *in* S. Powers, J. Bisogni Jr, J. Burken and K. Pagilla, eds, 'AEESP Environmental Engineering Processes Laboratory Manual', Association of Environmental Engineering and Science Professors, Champaign, IL.

Pyrak-Nolte, L., Myer, L., Cook, N. G. and Witherspoon, P. [1987], 'Hydraulic And Mechanical Properties of Natural Fractures In Low Permeability Rock', *6th ISRM Congress, Montreal, Canada* .

Quinn, P. M., Cherry, J. a. and Parker, B. L. [2011], 'Quantification of non-Darcian flow observed during packer testing in fractured sedimentary rock', *Water Resources Research* **47**(9).

Ramajo, H., Jodar, J., Carerra, J. and Olivella, S. [2002], 'Conceptualization of gas tracer tests within a fracture', *Groundwater Quality* (275), 539–546.

Ranjith, P. G. and Darlington, W. [2007], 'Nonlinear single-phase flow in real rock joints', *Water Resources Research* **43**(9), 1–9.

Ranjith, P. G. and Viete, D. R. [2011], 'Applicability of the 'cubic law' for non-Darcian fracture flow', *Journal of Petroleum Science and Engineering* **78**(2), 321–327.

Ranjith, P. and Perera, M. [2011], 'A new triaxial apparatus to study the mechanical and fluid flow aspects of carbon dioxide sequestration in geological formations', *Fuel* **90**(8), 2751–2759.

Redlich, O. and Kwong, J. N. S. [1949], 'On the thermodynamics of solutions; an equation of state; fugacities of gaseous solutions.', *Chemical reviews* **44**(1), 233–244.

Renshaw, C. E. [1995], 'On the relationship between mechanical and hydraulic apertures in rough-walled fractures', *Journal of Geophysical Research* **100**, 629–636.

Russick, E. M., Poulter, G. a., Adkins, C. L. and Sorensen, N. [1996], 'Corrosive effects of supercritical carbon dioxide and cosolvents on metals', *The Journal of Supercritical Fluids* **9**(1), 43–50.

Ruth, D. and Ma, H. [1992], 'On the derivation of the Forchheimer equation by means of the averaging theorem', *Transport in Porous Media* **7**(3), 255–264.

Sathar, S., Reeves, H. J., Cuss, R. J. and Harrington, J. F. [2012], 'The role of stress history on the flow of fluids through fractures', *Mineralogical Magazine* **76**(8), 3165–3177.

Schaef, H. T., Ilton, E. S., Qafoku, O., Martin, P. F., Felmy, A. R. and Rosso, K. M. [2012], 'In situ XRD study of Ca2+ saturated montmorillonite (STX-1) exposed to anhydrous and wet supercritical carbon dioxide', *International Journal of Greenhouse Gas Control* **6**, 220–229.

Shi, J.-Q., Sinayuc, C., Durucan, S. and Korre, A. [2012], 'Assessment of carbon dioxide plume behaviour within the storage reservoir and the lower caprock around the KB-502 injection well at In Salah', *International Journal of Greenhouse Gas Control* **7**, 115–126.

Skurtveit, E., Aker, E., Soldal, M., Angeli, M. and Wang, Z. [2012], 'Experimental investigation of CO_2 breakthrough and flow mechanisms in shale', *Petroleum Geoscience* **18**(1), 3–15.

Smith, M. M., Walsh, S. D. C. and Mcnab, W. W. [2013], 'Experimental investigation of brine-CO_2 flow through a natural fracture : permeability increases with concurrent dissolution / reprecipitation reactions', *Thirty-Eighth Workshop on Geothermal Reservoir Engineering* .

Song, J. and Zhang, D. [2013], 'Comprehensive review of caprock-sealing mechanisms for geologic carbon sequestration.', *Environmental science & technology* **47**(1), 9–22.

Span, R. and Wagner, W. [1996], 'A New Equation of State for Carbon Dioxide Covering the FLuid Region from the Triple-Point Temperature to 1100K at Pressures up to 800MPa', *Journal of Physical Chemistry Reference Data* **25**(6).

Steinberg, J., Gvirtzman, Z., Gvirtzman, H. and Ben-Gai, Y. [2008], 'Late Tertiary faulting along the coastal plain of Israel', *Tectonics* **27**(December 2007), 1–22.

Tabor, D. [2002], 'Mohs's Hardness Scale - A Physical Interpretation', *Proceedings of the Physical Society. Section B* **67**(3), 249–257.

Teledyne Isco [2012*a*], 'Basic Operation of LabView Toolkit'. Syringe Pump Technical Bulletin TB06.

Teledyne Isco [2012*b*], 'CO_2 Applications and Technical Notes'. Syringe Pump Technical Bulletin TB08.

Teledyne Isco [2012*c*], 'D-Series Pumps - Installation and Operation Guide'.

Terzaghi, K. v. [1923], 'Die berechnung der durchlassigkeitsziffer des tones aus dem verlauf der hydrodynamischen spannungserscheinungen', *Sitzungsberichte der Akademie der Wissenschaften in Wien, Mathematisch-Naturwissenschaftliche Klasse, Abteilung IIa* **132**, 125–138.

Tonnet, N., Broseta, D. and Mouronval, G. [2010], 'Evaluation of the Petrophysical Properties of a Carbonate-rich Caprock for CO_2 Geological Storage Purposes', *Proceedings of SPE EUROPEC/EAGE Annual Conference and Exhibition* .

Tsang, C. F., Bernier, F. and Davies, C. [2005], 'Geohydromechanical processes in the Excavation Damaged Zone in crystalline rock, rock salt, and indurated and plastic clays - In the context of radioactive waste disposal', *International Journal of Rock Mechanics and Mining Sciences* **42**(1), 109–125.

Tsang, C.-F., Stephansson, O., Kautsky, F. and Jing, L. [2004], Coupled THM processes in geological systems and the DECOVALEX project, *in* O. Stephansson, J. A. Hudson and L. Jing, eds, 'Coupled Thermo-Hydro-Mechanical-Chemical Processes in Geosystems - Fundamentals, Modelling, Experiments and Applications', Elsevier, pp. 3–16.

Tsang, Y. W. [1984], 'The Effect of Tortuosity on Fluid Flow Through a Single Fracture', *Water Resources Research* **20**(9), 1209.

Tsang, Y. W. and Witherspoon, P. [1981], 'Hydromechanical behavior of a deformable rock fracture subject to normal stress', *Journal of Geophysical Research: Solid Earth* **86**(B10), 9287–9298.

Walsh, J. [1981], 'Effect of pore pressure and confining pressure on fracture permeability', *International Journal of Rock Mechanics Mining Sciences and Geomechanics Abstracts* **18**, 429–435.

Walsh, R., McDermott, C. and Kolditz, O. [2008], 'Numerical modeling of stress-permeability coupling in rough fractures', *Hydrogeology Journal* **16**, 613–627.

Wang, X., Alvarado, V., Swoboda-Colberg, N. and Kaszuba, J. P. [2013], 'Reactivity of dolomite in water-saturated supercritical carbon dioxide: Significance for carbon capture and storage and for enhanced oil and gas recovery', *Energy Conversion and Management* **65**, 564–573.

Washburn, E. [1921], Note on a method of determining the distribution of pore sizes in a porous material., *in* 'Proceedings of the National Academy of Science', pp. 115–116.

White, J. a., Chiaramonte, L., Ezzedine, S., Foxall, W., Hao, Y., Ramirez, A. and McNab, W. [2014], 'Geomechanical behavior of the reservoir and caprock system at the In Salah CO_2 storage project.', *Proceedings of the National Academy of Sciences of the United States of America* **111**(24), 8747–52.

Wilkinson, M., Haszeldine, R. S., Fallick, a. E., Odling, N., Stoker, S. J. and Gatliff, R. W. [2009], 'CO_2-Mineral Reaction in a Natural Analogue for CO_2 Storage–Implications for Modeling', *Journal of Sedimentary Research* **79**(7), 486–494.

Witherspoon, P. P., Wang, J., Iwai, K. and Gale, J. [1979], 'Validity of cubic law for fluid flow in a deformable rock fracture', *Water Resources Research* .

Wollenweber, J., Alles, S., Busch, a., Krooss, B., Stanjek, H. and Littke, R. [2010], 'Experimental investigation of the CO_2 sealing efficiency of caprocks', *International Journal of Greenhouse Gas Control* **4**(2), 231–241.

Xiao, W., Xia, C., Wei, W. and Bian, Y. [2013], 'Combined effect of tortuosity and surface roughness on estimation of flow rate through a single rough joint', *Journal of Geophysics and Engineering* **10**(4), 045015.

Yasuhara, H., Kinoshita, N., Ohfuji, H., Lee, D. S., Nakashima, S. and Kishida, K. [2011], 'Temporal alteration of fracture permeability in granite under hydrothermal conditions and its interpretation by coupled chemo-mechanical model', *Applied Geochemistry* **26**(12), 2074–2088.

Yasuhara, H., Polak, a., Mitani, Y., Grader, a., Halleck, P. and Elsworth, D. [2006], 'Evolution of fracture permeability through fluid–rock reaction under hydrothermal conditions', *Earth and Planetary Science Letters* **244**(1-2), 186–200.

Yeo, I., de Freitas, M. and Zimmerman, R. [1998], 'Effect of shear displacement on the aperture and permeability of a rock fracture', *International Journal of Rock Mechanics and Mining Sciences* **35**(8), 1051–1070.

Yielding, G., Lykakis, N. and Underhill, J. R. [2011], 'The role of stratigraphic juxtaposition for seal integrity in proven CO_2 fault-bound traps of the Southern North Sea', *Petroleum Geoscience* **17**(2), 193–203.

Zhang, Y., Gao, K. and Schmitt, G. [2011], 'Water Effect on Steel Under Supercritical CO_2 Condition', *Corrosion 2011, NACE International* (11378), 1–15.

Zhang, Z. and Nemcik, J. [2013], 'Fluid flow regimes and nonlinear flow characteristics in deformable rock fractures', *Journal of Hydrology* **477**, 139–151.

Zhang, Z., Nemcik, J. and Ma, S. [2013], 'Micro- and macro-behaviour of fluid flow through rock fractures: an experimental study', *Hydrogeology Journal* **21**(8), 1717–1729.

Ziegler, P. A. [1990], 'Geological Atlas of Western and Central Europe, Shell Internationale Petroleum Maatschappij BV/Geological Society of London'.

Zimmerman, R., Al-Yaarubi, A., Pain, C. and Grattoni, C. [2004], 'Non-linear regimes of fluid flow in rock fractures', *International Journal of Rock Mechanics and Mining Sciences* **41**(3), 384.

Zimmerman, R. W. and Bodvarsson, G. [1996], 'Hydraulic Conductivity of Rock Fractures', *Transport in Porous Media* **23**, 1–30.

Zoback, M. D. and Byerlee, J. [1975], 'Permeability and Effective Stress', *AAPG Bulletin* **59**(1), 154–158.